CONF-870961--Vol.2

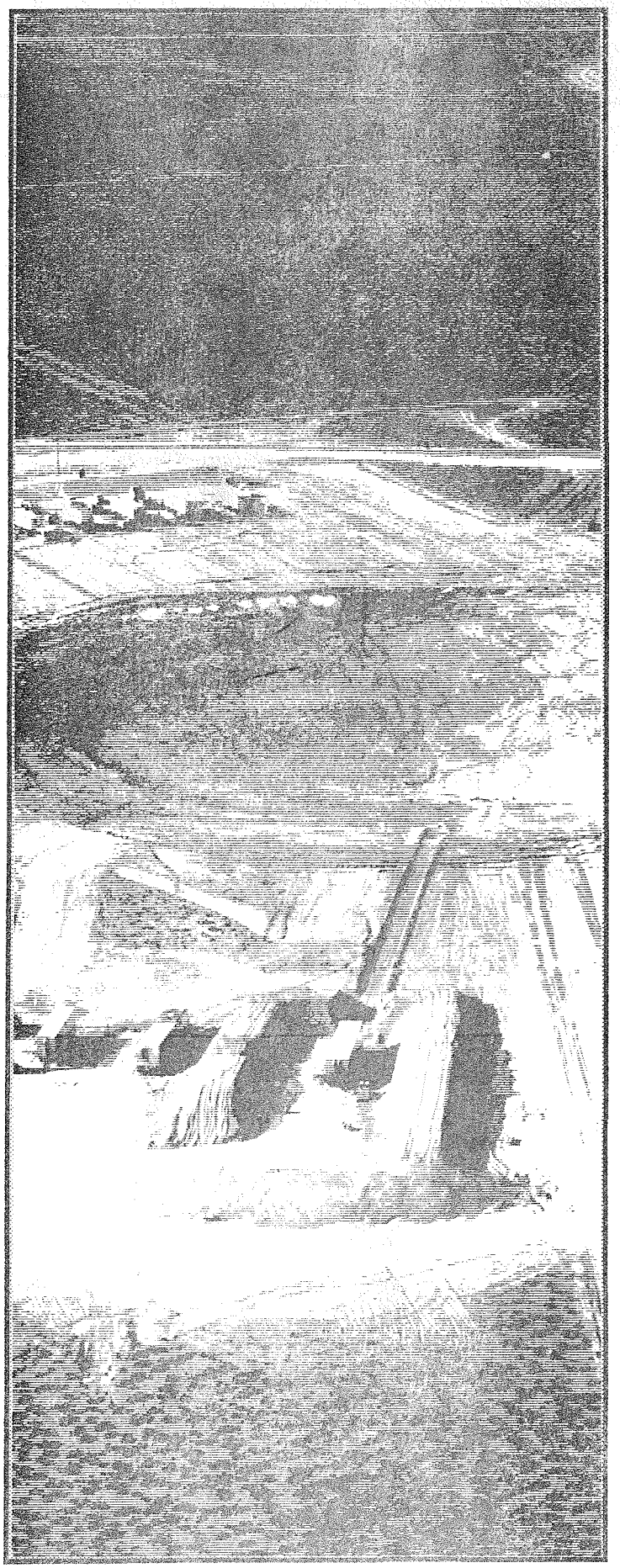

Fourth Symposium on Containment of Underground Nuclear Explosions

United States Air Force Academy, Colorado Springs, Colorado Sept. 21-24, 1987

Volume 2
PROCEEDINGS

CONF-870961

MASTER

DISTRIBUTION OF THIS DOCUMENT IS UNLIMITED

DISCLAIMER

This report was prepared as an account of work sponsored by an agency of the United States Government. Neither the United States Government nor any agency thereof, nor any of their employees, makes any warranty, express or implied, or assumes any legal liability or responsibility for the accuracy, completeness, or usefulness of any information, apparatus, product, or process disclosed, or represents that its use would not infringe privately owned rights. Reference herein to any specific commercial product, process, or service by trade name, trademark, manufacturer, or otherwise does not necessarily constitute or imply its endorsement, recommendation, or favoring by the United States Government or any agency thereof. The views and opinions of authors expressed herein do not necessarily state or reflect those of the United States Government or any agency thereof.

DISCLAIMER

Portions of this document may be illegible in electronic image products. Images are produced from the best available original document.

CONF-870961--Vol.2

DE89 009077

Proceedings of the Fourth Symposium on Containment of Underground Nuclear Explosions— **Volume 2**

United States Air Force Academy, Colorado Springs, Colorado

Sept. 21-24, 1987

Clifford W. Olsen, Scientific Editor
Maureen L. Donohue, Publication Editor
Sandra Wander, Editor

MASTER

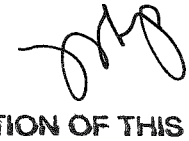

DISTRIBUTION OF THIS DOCUMENT IS UNLIMITED

Preface and Acknowledgments

This is Volume 2 of two unclassified volumes of the Proceedings of the Fourth Symposium on Containment of Underground Nuclear Explosions. The symposium was a meeting of workers at all levels in the containment community. Papers on containment and related geological, geophysical, engineering, chemical, and computational topics are included.

We would like to express our sincere thanks to the United States Air Force Academy for hosting the Symposium, and particularly to Janet Shea and Nancy Gass for their hospitality and excellent arrangements. We thank Col. Cary Fisher, Chairman of the Department of Engineering Mechanics, USAFA, and James Magruder, Assistant Manager for Operations and Engineering at the Nevada Operations Office of the USDOE, for their welcoming remarks. We thank Loraine Marshbank, Marie Kaye, Rochelle Hostetter, and Kim Dea for their invaluable support during the meeting. Special thanks are extended to Peter Zavattaro of E.G.&G. and to Augie Gurrola of Holmes and Narver for underwriting the Monday evening social.

Finally, the Program Committee wishes to thank all authors and attendees for their support, with a special thanks to the session chairpersons: Diana Hollis, James Plimpton, Edward Peterson, Wendee Brunish, Roger Thompson, Sidney Green, Robin Newmark, Donathon Krier, Gary Higgins, Stew Griffiths, Paul Orkild, and Lewis Thigpen.

The Program Committee

Bob Deupree, Los Alamos
Les Hill, SNLA
Cliff Olsen, LLNL
Roger Thompson, DNA
Paul Orkild, USGS

Organizers

Cliff Olsen, LLNL
Jack House, Los Alamos

Keynote Address

The opening address was presented by Irv Williams, Chief of the Weapons Research, Development, and Testing Branch at DOE Headquarters in Germantown, MD. Irv spoke on "Testing -- a Washington Perspective." He discussed the numerous branches of government that are vitally interested in nuclear testing and how highly visible testing is in Washington, both with the Administration and with Congress. He discussed the many steps required to obtain Programmatic and Detonation Authorities and the importance of the CEP and the containment community. He also discussed Arms Control activities. His final major area of discussion focussed on proposed Congressional actions related to testing limitations and treaty verification.

We thank Irv for his most interesting address.

Contents

Volume 2

Geology, Logging, and Databases

G-1 **Idealized Proximity Response of the DBS**
R. A. Fenster 3

G-2 **Borehole Inspection System for Large Diameter Holes**
W. L. Hawkins, R. D. Oliver, M. J. Lavelle 18

G-3 **Definition of Stratigraphic Units Between the Grouse Canyon and Rainier Mesa Tuffs in Los Alamos-Use Areas of Yucca Flat, Nevada Test Site**
S. L. Drellack, Jr., R. G. Warren, W. T. Hughes 27

G-5 **Pre- and Post-Event Elevation and Horizontal Surveys Across the Yucca and Topgallant Faults, Nevada Test Site**
D. Krier, F. N. App, L. Medina 56

Geophysics and Medium Properties

H-1 **Applications of Vertical Seismic Profiling at NTS**
N. R. Burkhard 77

H-2 **Shear Wave Velocities from Sonic Logs in Emplacement Holes**
R. L. Newmark 89

H-3 **A Possible Relation Between Sonic Velocity Measured at the Edge of a Large Borehole and Shear Failure**
J. T. Rambo and R. P. Swift 135

H-4 **Relationship Between Large-Hole Drilling Rates and Compressive Strength of NTS Rock Types**
G. D. Anderson, J. T. Rambo, A. S. Kusubov, H. A. Dockery, W. B. McKinnis 155

H-5 **Measurement of *In Situ* Strength Using Projectile Penetration: Tests of a New Launching System**
J. R Hearst, R. L. Newmark, J. A. Charest, C. S. Lynch 164

H-6 **Spectral Reflectance Characteristics of Clay-Bearing Soils: Applications to Downhole Environments**
J. C. Gradie, T. L. Roush 201

Cavity Pressure and Chemistry

I-3 **Fluid Dynamics of a Pressure Measuring System for Underground Explosive Tests**
R. C. Dykhuizen, C. W. Smith 229

I-4 **CORNUCOPIA Cavity Pressure Measurement**
B. Hudson, C. Cordill, L. Starrh, J. Kalinowski, T. Stubbs, C. Keller, E. Peterson, R. Nilson 237

I-5 **Chemical Considerations and Containment**
R. E. Duff 266

I-6 **Reaction Kinetics and Hydrogen Generation**
E. S. Gaffney 276

Late-Time Gas Flow

J-1 **Breathing on the Mesa**
E. C. Woodward, Jr. 285

J-2 **Estimation of the Bulk Diffusivity of Chimneys Using Post-Shot Holes**
N. R. Burkhard, J. R Hearst, J. M. Hanson 288

J-3 **Fickian Filtering of Cavity Gases Rising Through a Fractured Permeable Overburden**
R. H. Nilson, K. H. Lie, E. W. Peterson 316

J-4 **Dispersion of Contaminant During Oscillatory Gas-Motions Driven by Atmospheric Pressure Variations**
E. W. Peterson, K. Lie, R. H. Nilson 340

Hydrology and Radionuclide Migration

K-1 **High Fluid Levels in Drill Holes, Yucca Flat, Nevada Test Site**
D. L. Hoover, D. A. Trudeau 363

K-2 **Temperature Logging as an Aid to Understanding Groundwater Flow in NTS Boreholes**
J. Conaway 373

K-3 **Geologic and Hydrologic Investigations at the Aleman (U3KZ) Site and Other Sites in Yucca Flat, the Nevada Test Site**
W. L. Hawkins, A. P. Cavazos, P. H. Thompson 387

Collapse Phenomena

L-1 **Development for Centrifuge Modeling of Buried Explosions**
J. A. Brown, J. W. House, K. H. Wohletz, E. S. Gaffney 401

L-2 **Development of Centrifuge Modeling for Evaluating the Mechanisms of Collapse of Underground Openings**
B. C. Davis, B. L. Kutter, J. D. L. Chang 414

L-3 **Trends in Cavity Collapse Data**
R. G. Deupree, S. D. Noel, C. A. Watson 430

L-4 **Photogrammetric Method for Determining Sink Volumes at the Nevada Test Site**
M. N. Garcia 446

Geology, Logging, and Databases

DO NOT MICROFILM
THIS PAGE

IDEALIZED PROXIMITY RESPONSE OF THE DBS

Richard A Fenster
Los Alamos National Laboratory

ABSTRACT

The gamma-gamma density tool (DBS) used in containment borehole logging at the Nevada Test Site has two proximity indicators, devices intended to measure the gap between the density pad and borehole wall. These proximity indicators are located at each end of the density pad. The response of the proximity indicators is presently used to determine a correction factor for the basic (raw) density data . Proper interpretation of proximity log data is essential if valid corrections are to be made. The use of idealized response curves has long been a key to the interpretation of logging instruments and this technique will be used here to show the relationship of proximity data to density data. Proximity data, as presented on the density log, should not be used directly to correct the basic density values. An alternate density correction technique is presented. The response of a single proximity indicator, similar to that used in the single detector gamma-gamma density tool but centered between the source and detector, is also examined.

I. INTRODUCTION

The large-hole dual-spaced density sonde (DBS) is primarily a large carrier intended to hold a density measurement pad against an emplacement hole wall while logging upward. How well the pad conforms to the borehole wall is monitored by proximity indicators mounted at the top and bottom of the pad. Each indicator consists of two inch diameter wheel connected by a mechanical arm to a potentiometer which measures the movement of the wheel relative to the pad. The wheel stays in contact with the borehole wall as the pad moves away. The density pad contains two gamma detectors and a source of gamma radiation. The pad articulates about a vertical axis and a horizontal axis parallel to an emplacement hole wall, allowing the pad limited ability to follow borehole rugosity. The recorded proximities are calibrated for a scale of zero to one inch, with zero indicating that the pad face is flush with the emplacement hole wall. The density curves are calibrated using three large blocks of known election density values. The measuring points of the various detectors and sensors are spaced along the length of the sonde, so depth corrections are required during recording in order to align the various measuring points to a common depth.

II. PRESENT METHOD FOR DENSITY CORRECTIONS

The algorithm presently used to correct raw DBS long-spaced density incorporates proximity measurement as a term in the equation. An "effective prox" term is derived from the expression [(.336 x upper prox) + (.664 x lower prox)]. These weighting factors were determined empirically when other methods failed to yield satisfactory results. The assumption here is that a weighted average of the two proximity measurements will approximate the gap near the detector. It will be shown here that this may be a false assumption. The large-hole density, single detector density sonde (FDS) also uses proximity measurement directly to calculate corrected density. This device has a single proximity wheel located between the detector and source. It will be shown that this placement of the indicator provides a better approximation of gap, however, the lack of a second density detector severely limits the usefulness of the FDS instrument.

Recent changes in recording techniques will also affect the results of the present correction algorithm. Prior to the introduction of the Western Atlas International (present logging contractor at the NTS) CLS recording system, the logs were recorded on the Birdwell (previous logging contractor at the NTS) recorder at 20 samples per foot. During this period of time, the data was first reduced to 2 samples per foot after which the correction to density was applied. The CLS system logs are now

recorded and stored at 16 samples per foot and corrections are applied at the same data rate. Another point of interest is the fact that Birdwell density logs were filtered by the ratemeter panel prior to recording, and the CLS system imposes considerably less filtering of the density data. The higher data rate presently used (and less filtering) tends to make this discussion more pertinent. The ramifications of the switch to the Western Atlas CLS recorder are still not completely determined.

III. GENERATING THE IDEALIZED RESPONSE

Figure 1 shows the model of the DBS pad used in the these studies and was developed from Birdwell drawings. Since these drawings were produced, there has been a minor modification of the pad which changed the proximity spacing from 45 to 48 inches. While this modification affects actual tool response, it does not negate the analysis which follows.

The modeled proximity curves (Figures 2 through 5) were generated by moving a scale model of the pad along a simulated borehole situation and measuring the position of each proximity wheel. The curves are depth corrected to the zero point of the DBS which is the lower proximity measure point.

The modeled density response was based on tilt and standoff data taken in June, 1983. The conditions chosen for the model were:

1. A uniform formation density of 1.74
2. Water filled hole
3. A borehole anomaly of .5 inch (dashed line of proximity response)

The density response is depicted by a solid line for the long-spaced density and a dot/dashed line for the short-spaced density. The density curves were created by positioning the pad model along the simulated borehole and finding all places where abrupt changes in the pad tilt occurred or where gap changed suddenly. These pad positions generally coincided with those represented by standoff and tilt data. In this manner, fairly accurate apparent density values could be assigned to the short- and long-spaced density response curves. The points plotted by this technique were then connected by straight lines. The actual response between points is non-linear and beyond the scope of this work. Also, the plotted points represent steady-state response which is a good approximation for slow logging speeds only. Although specific conditions were assigned to model the density response, the purpose was solely to indicate density response with respect to proximity response and depth. Note also that borehole anomalies often occur at bed boundaries, and actual log response would reflect any density contrast.

IV. ANALYSIS

A. Upper and Lower Proximity Response

Figures 2 through 5 depict the response curves of the density and proximity logs to idealized borehole situations or anomalies. All curves are shown on depth. The proximity measure points are projected from the center of the wheels. The measure points for the long-spaced and short-spaced detectors are located midway between the gamma-gamma source and the center of the detector in each case. The idealized proximity curves show a dashed line for response corresponding to a .5 inch change in borehole radius and a solid line depicts the response if the change in radius were 2 inches on the caliper scale. The proximity wheels have a 1.0 inch deflection for full scale. In each case, the curves show pad response as the pad moves from the bottom of the figure towards the top.

The caliper log shows a differential trace based on bit-size (BS). The unlabeled mark on the scale indicates .5 inch deflection for the dashed proximity curves and density response, and 2 inches for the solid proximity curves.

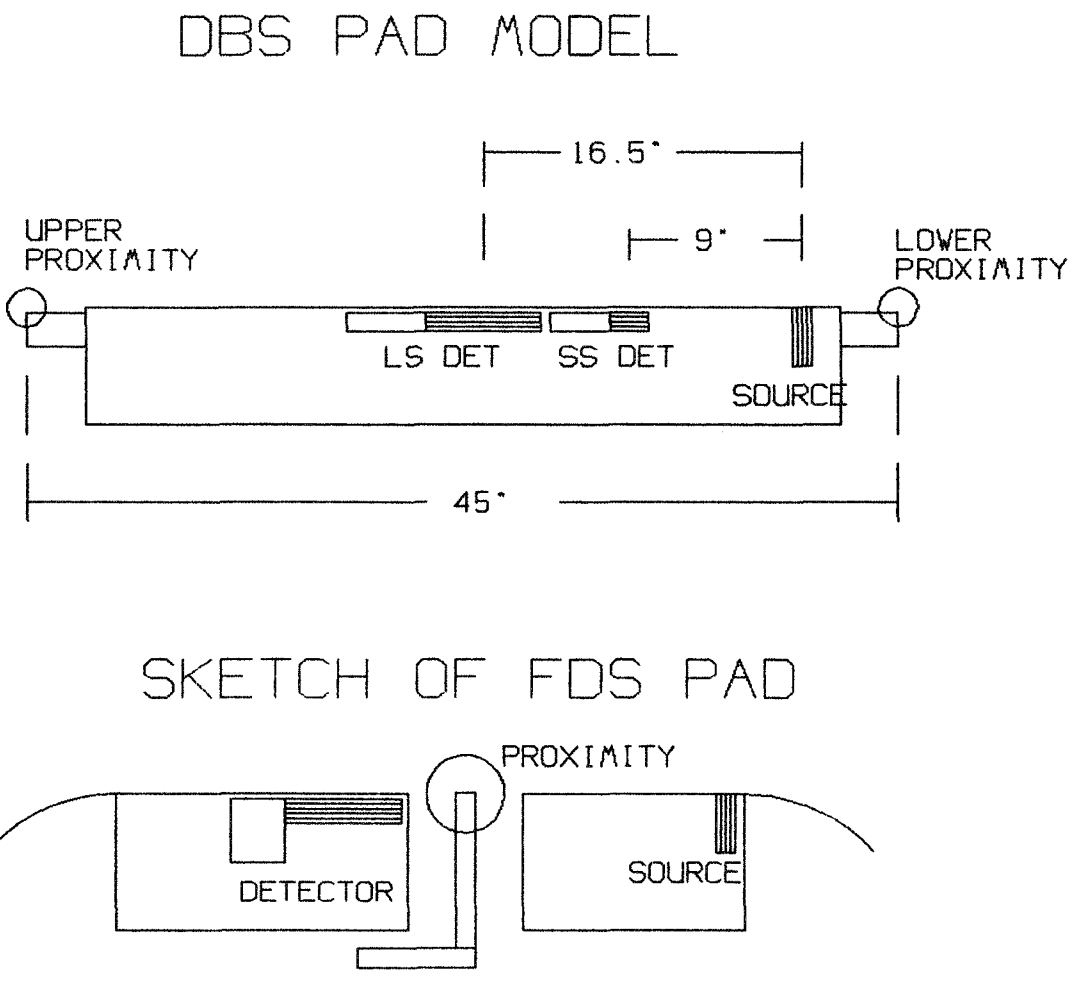

FIGURE 1 - DRAWING OF THE DBS PAD MODEL USED TO DEVELOPE RESPONSE CURVES. THE LOWER PORTION OF THE FIGURE CONTAINS AN UNSCALED SKETCH OF THE FDS PAD. NOTE THAT THE FDS PROXIMITY IS NOT CENTERED AT THE MEASURE POINT OF THE DENSITY LOG AND WHEEL IS LARGER DIAMETER.

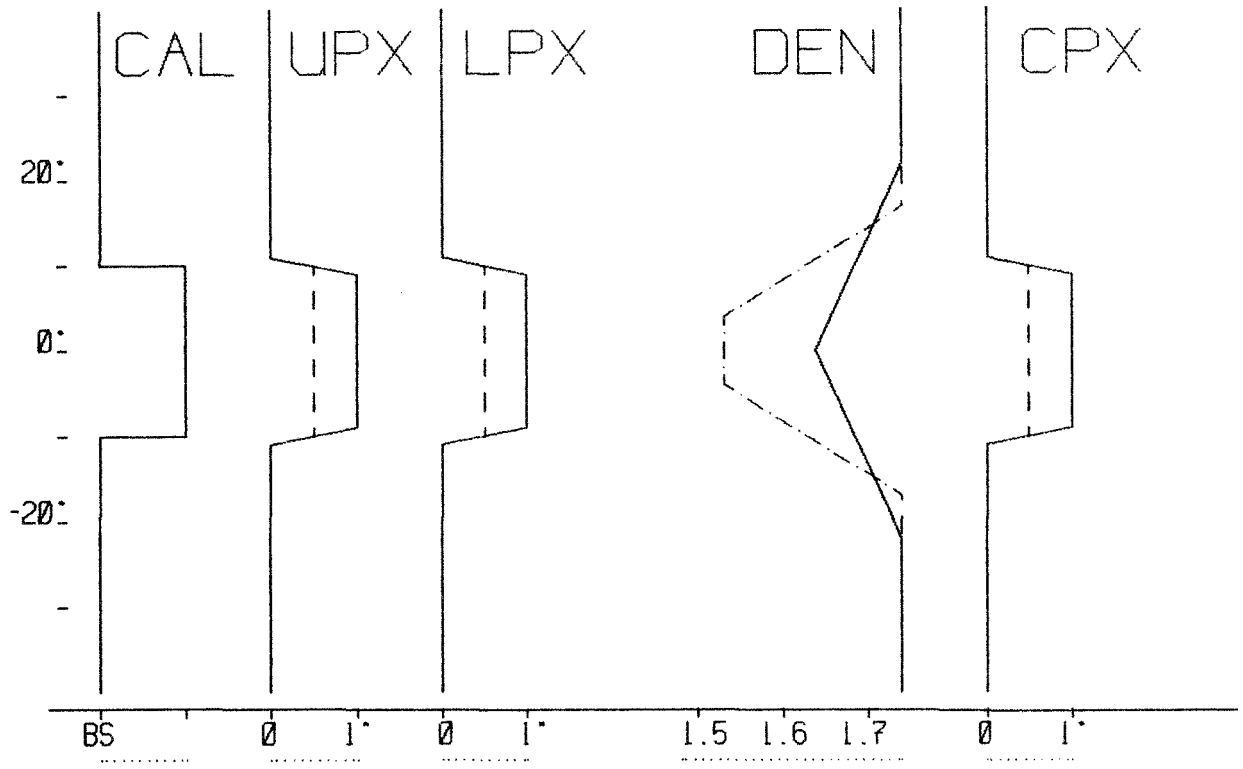

FIG. 2 - IDEALIZED DBS RESPONSE TO A WASHOUT (2' LONG. FROM LEFT TO RIGHT: CALIPER. UPPER PROX. LOWER PROX. DENSITY AND THEORETICAL CENTERED PROX.

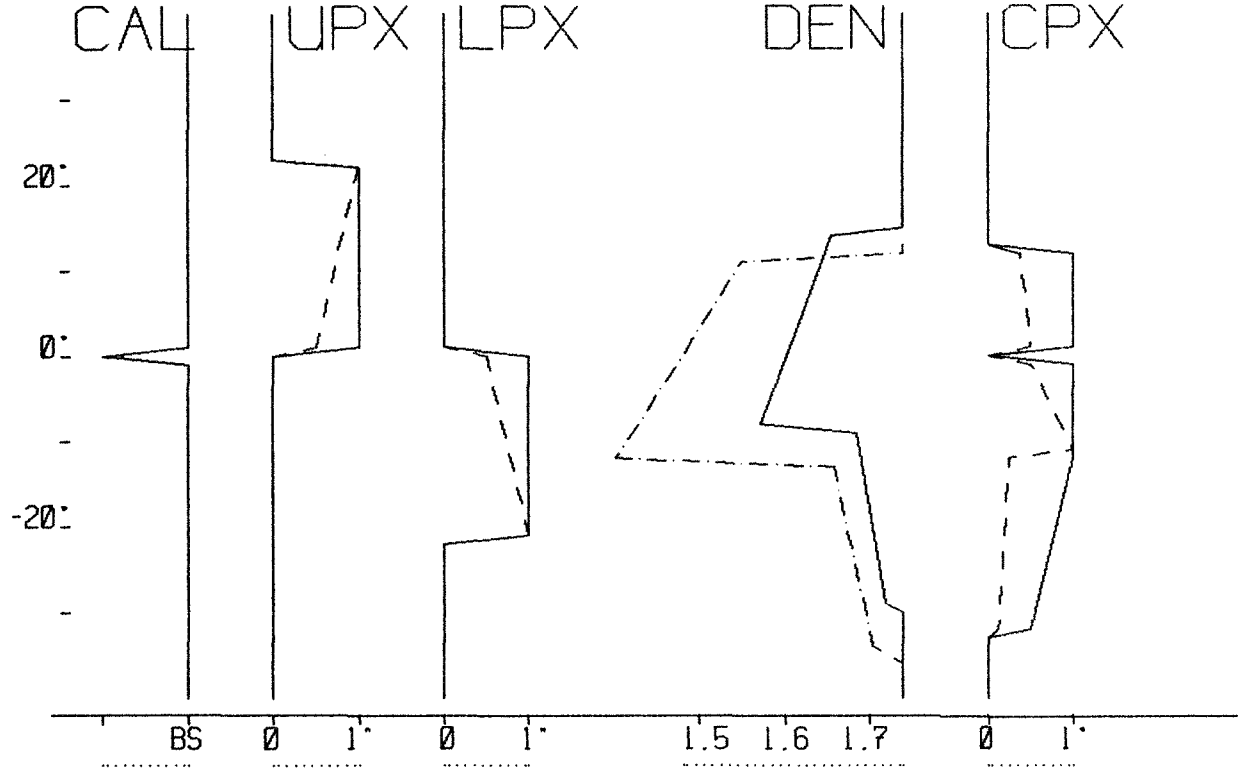

FIG. 3 - DBS RESPONSE FROM SMALL PROTUBERANCE ON BOREHOLE WALL.

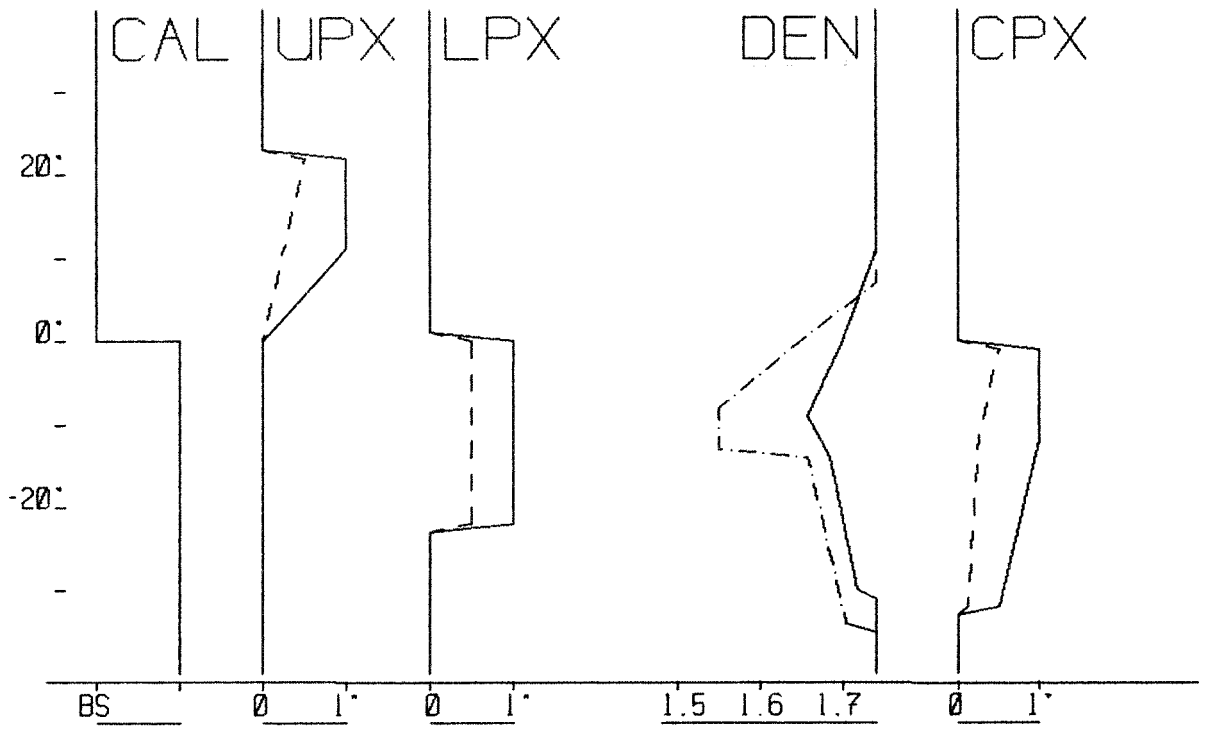

FIG. 4 - IDEALIZED RESPONSE OF DBS PAD EXITING A WASHOUT > 4' LONG.

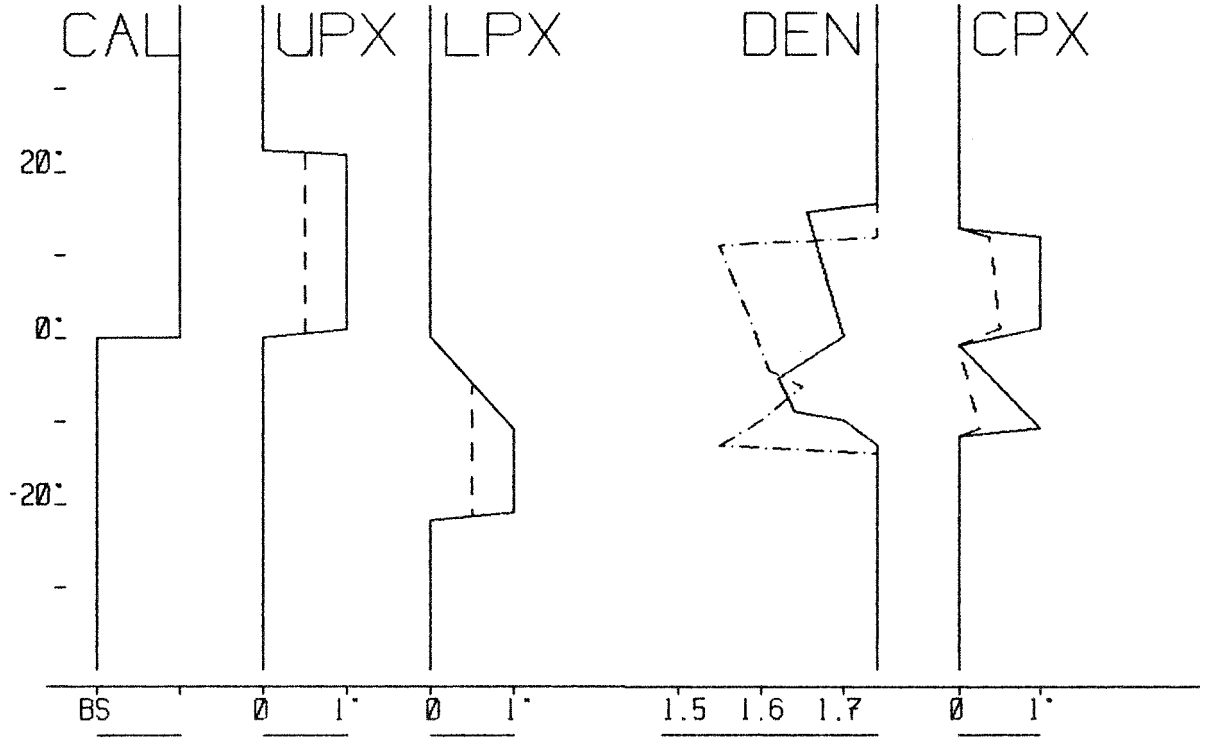

FIG. 5 - IDEALIZED RESPONSE OF DBS PAD ENTERING A WASHOUT > 4' LONG.

Figure 2 shows response of the DBS to an ideal washout with a width less than one half the pad length. The response of both proximity devices overlay and correlate well with the density curve. However, the proximity devices have a higher vertical resolution than the density curves because the effective length of the density sensor is the source to detector spacing (16.5 inches for the long-space and 9 inches for the short-space curves), as opposed to a 2 inch diameter proximity wheel. In the situation depicted, the length of the washout is 20 inches, the proximity devices response covers 20 inches (approx.), but the long-space density is affected over a 44 inch distance while the short-space density is affected over a 34 inch distance. It is also evident that proximity response is virtually constant over the anomaly while density compensation must vary over the distance of the anomaly to be accurate. Density corrections based on proximity, in this case, will over- and under-correct to some extent, but could yield improve density data.

Figure 3 shows the situation where the pad runs past a narrow protuberance which causes a pad tilt in both directions. A characteristic two foot offset is noticeable. The case is of particular interest because of the very poor correlation between the proximities, the accentuated errors caused by this anomaly, and the relatively frequent occurrence in NTS boreholes.

Figure 4 shows the DBS pad logging out of a wide washout. In this case the lower proximity correlates fairly well with the anomaly while the upper proximity is misaligned with most of the density response. Again, there is the same two feet of depth offset seen in the previous graph. Neither proximity can be used in applying corrections. Any sort of averaging technique would result primarily in over- or under-compensation.

Figure 5 shows the DBS response as the pad slides from a smooth borehole into a washout with a width longer than the pad.

The only situation where the proximity response is in reasonable alignment with density response occurs in a narrow washout. Even in this case, the proximity is fairly uniform in displacement whereas the density response varies and covers more depth. In all other situations where tilt occurs, the two proximity responses are not adjacent on the depth scale. They are shifted approximately two feet and the upper proximity is always higher than the lower proximity. This is a characteristic response useful in determing that a tilt condition exists. Neither the upper nor lower proximity correlates well to the density anomaly in a point-to-point comparison. An average of the proximities is also not useful in determining an effective gap figure. There are areas where maximum proximity deflection corresponds to unaffected density readings, and there are places where increasing density errors correlate to decreasing proximity indication. However, another useful observation besides tilt identification can be made. Wherever density effects are seen, proximity effects are present. The reverse is not true. This means that when separation between the short-spaced and long-spaced density is present, proximity information can be checked to determine if gap is present or not. If not, the separation may, for instance, be due to mud cake.

Proximity response will generally show what type of tilt situation the pad is experiencing. An examination of the curves in Figures 3, 4, and 5 shows that the slope of the two proximity curves from the midpoint position is also characteristic for each of the individual cases.

B. Centered Proximity

The idealized response of a hypothetical proximity wheel located at the measure point of the long-spaced density might be of interest, since a similar method is used in the FDS. The ideal response of a centered proximity is shown at the right side of Figures 2 through 5. It is obvious that the proximity response tracks the density better than either the upper or lower proximity of the DBS.

C. Scatter Plots

The data for the scatter plots was generated from Figures 2 through 5 by sampling data at four inch intervals along the y-axis of each chart. The resulting data is, of course, idealized and does not

truly represent real data. The object of the exercise is to demonstrate more clearly how little relationship exists between the present proximity information and ideal density on a point-by-point basis, and to show alternative relationships which might yield better algorithms.

The scatter plot (Figure 6) of long-spaced density vs. lower proximity indicates little potential for the development of a correction algorithm. The solid line represents measured density vs. gap as taken from testing, and shows poor agreement to the scattered lower proximity response.

In spite of the pessimistic appearance of the scatter plot (Figure 7) of the centered proximity response, there is little doubt that this would be an improved method of GAP measurement when compared to the present DBS method and might help explain why proximity corrections on the FDS are less troublesome than on the DBS.

The scatter plot (Figure 8) for the long-spaced density vs. short-spaced density is more promising, and shows improved agreement to the measured data represented by the solid line. The scatter plot of long-spaced vs. short-spaced density was drawn with the short-spaced curve shifted 4 inches to better overlay the long-spaced curve. This shift was made because an examination of the graphs indicated that, for all tilt conditions (the majority of proximity deflection) a four inch depth shift would improve the alignment. The relatively good match of the scattered points to the solid line representing measured response seems to encourage an attempt to correct long-spaced density with short-spaced density information rather than proximity information. The solid line in Figure 8 is the rib for the magnesium block density for the water filled hole, and represents a non-tilted pad configuration. The points lying near the solid curve are accurately corrected. Those points above the solid line will be under-corrected, and those below will be over-corrected. Those points which seem to lie near the spine do so by coincidence only and represent data affected by tilt of the upper end of the pad. That data which is affected by tilt of the source end of the pad will generally lie below the solid line. Those data points which miss the solid line may still be corrected within tolerance (if proximity is <.5 inches).

The relationship of long-spaced and short-spaced density is affected, as we have seen, by gap, but is also affected by hole conditions such as invasion, mud cake, crushed rock, etc. While this certainly complicates interpretation, utilizing all information available will allow a meaningful correction to be made.

V. ACTUAL DENSITY LOGS

In the real world of density logging, factors such as filtering, incorrect depth offsets, statistical errors, difficult borehole conditions and instrument problems tend to overshadow idealized modeling. Filtering particularly hinders a point-to-point correction algorithm. New recording techniques and procedures recently begun at the NTS will help minimize errors due to excessively filtered logging data and erroneous depth offsets. As recently as July, 1987, depth offset errors and/or excessive filtering prohibited accurate point-by-point correction of DBS logs.

An examination of an expanded depth scale of a DBS log reveals that a tilted pad condition is by far the most common cause of proximity deflection. Ther are very few examples of alignment of the lower- and upper-proximities. Much of the idealized response can be seen in actual logs. However, many of the situations seen in the proximity response are obviously combinations of the basic anomalies.

VI. PROPOSED DBS DENSITY CORRECTION ALGORITHM

A. Introduction

A spine and rib chart is used to depict the response of a dual detector density tool for a given mud cake density. The "spine" is merely a straight line of slope = 1 on a plot of short-spaced density

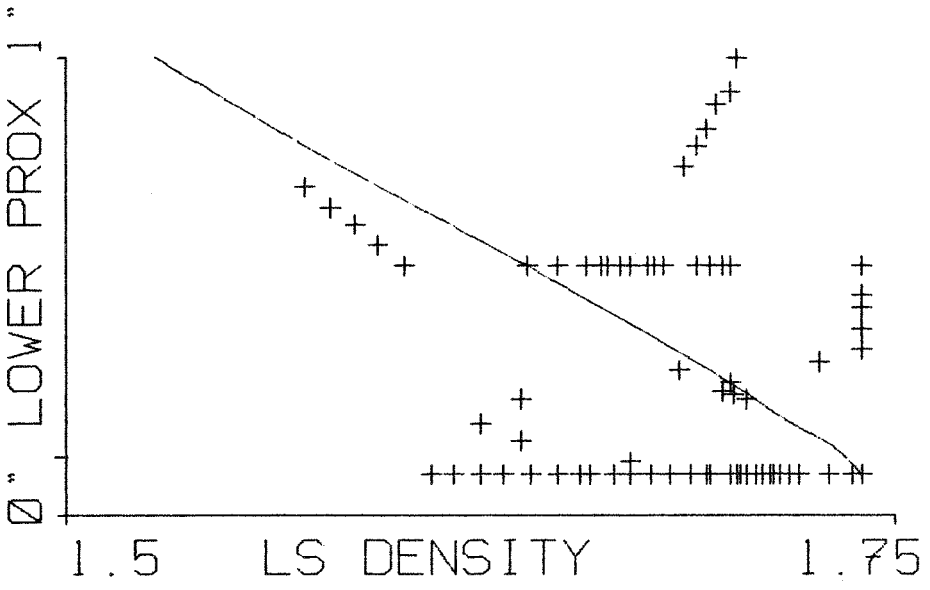

FIG. 6 - SCATTER PLOT OF LONG-SPACED DENSITY VS LOWER PROX.
SOLID LINE IS STANDOFF DATA FOR MAGNESIUM BLOCK. IN FLUID.

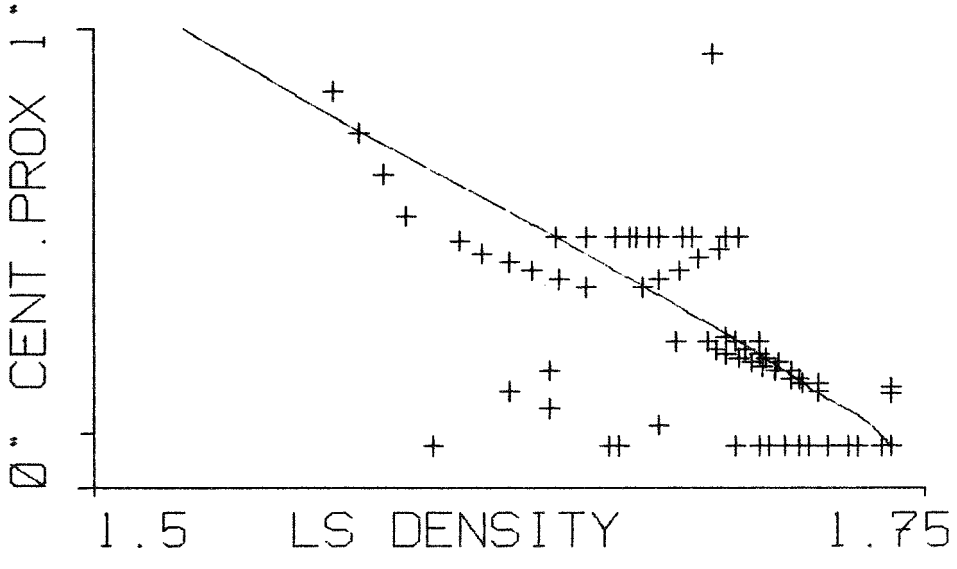

FIG. 7 - SCATTER PLOT OF CENTERED PROX VS. LONG-SPACED
DENSITY. SOLID LINE IS STANDOFF DATA FOR MAG. BLOCK.

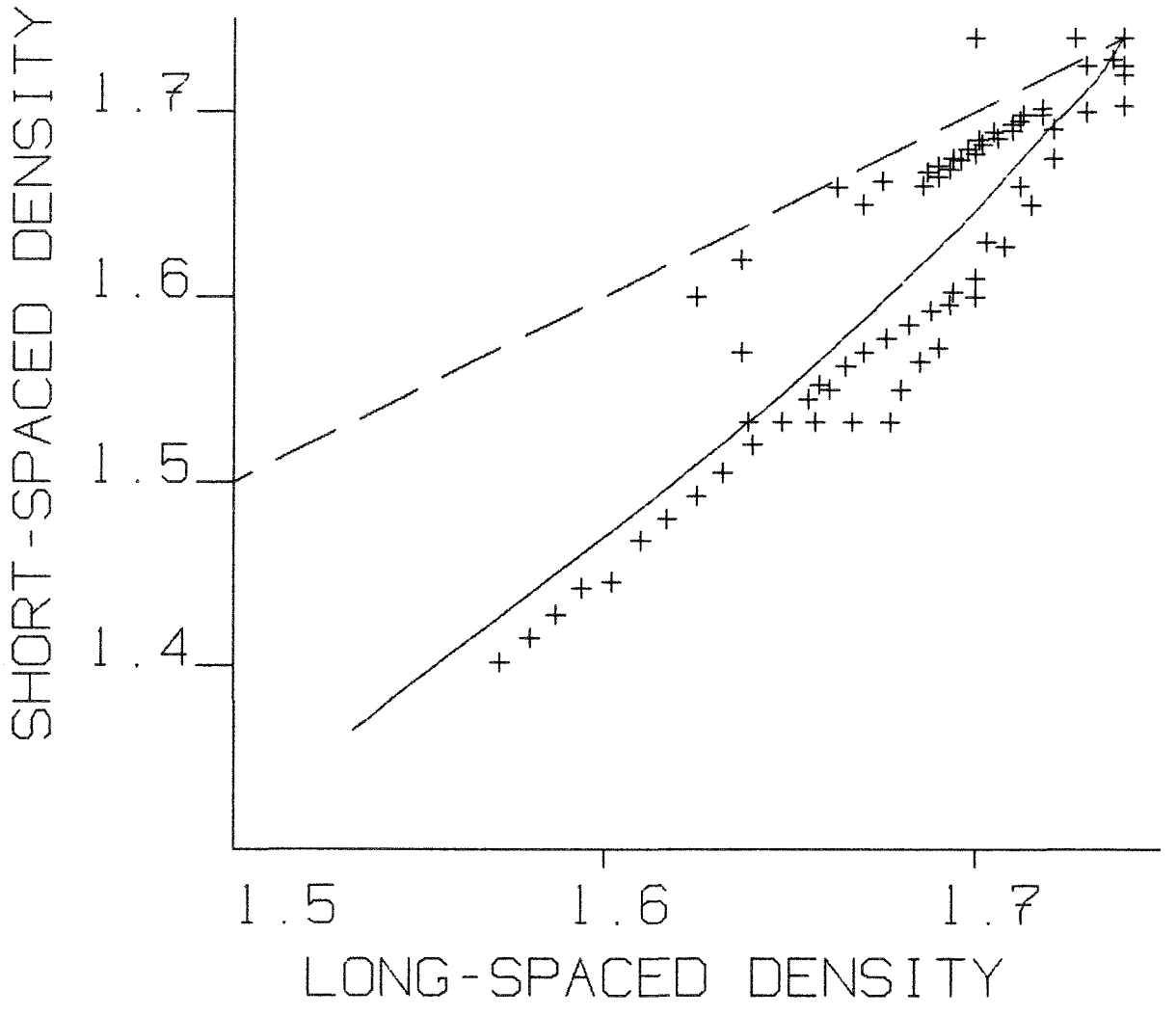

FIG. 8 - SCATTER PLOT OF SS VS. LS DENSITY. DASHED LINE IS SPINE. SOLID LINE IS RIB FOR MAGNESIUM BLOCK. FLUID FILLED HOLE.

(SSD) vs. long-spaced density (LSD). This is the response of both detectors when there is perfect coupling between the pad and the formation. The ribs are also plots of LSD vs. SSD, but are valid for situations when a constant gap (of variable thickness) exists between the pad and formation, with the gap filled with a constant density material. Conventionally, the slopes of the ribs are assumed to be constant over a range of formation densities but, in fact, the slopes of the ribs vary. The slope of the rib will also vary with mud cake density. The relationship of SSD to LSD gets quite complicated when test site logging parameters are considered. The following discussion is the author's attempt to explain and simplify the spine and rib chart components, the purpose being to develop a useful correction algorithm for density compensation. The material presented here was based on standoff and tilt tests performed at the Birdwell shop in June of 1983.

Certain operator inputs are required to process the density data. These are:

1. Choose air- or fluid-filled borehole parameters.
2. The density of the fluid.
3. The density of the mud cake, if present.

The proposed algorithm contains three sections for the three basic situations of air-filled hole, fluid-filled hole, and the presence of mud cake.

B. Density Compensation

Space limitations prevent a complete discussion of the algorithm in this paper so only the basic idea is presented here. When data from standoff tests are plotted on a spine and rib chart, it is immediately apparent that the slopes of the ribs vary with the density of the formation and the density of the material within the gap between the pad and the formation. Reference to the slope of a straight line is used because, in the range of interest, the rib plot is essentially straight, a fact used by other logging companies. To illustrate this point, data taken from the spine and rib plot are presented on graphs of density vs. gap (see Figures 9 and 10). By separating the LS and SS data and plotting on expanded scales, the obscure relationship of the ribs becomes more evident and approachable mathematically. The three solid curves in each graph represent standoff test data taken on the aluminum, magnesium, and plastic calibration blocks. It is apparent from the graphs that the slopes of the curves are not equal, which means that rib plots made from this data cannot have equal slopes. It is almost as apparent that there must be a relationship to describe mathematically a family of curves which could simulate a rib for various formation density and gap density. [Gap density is used here as a generic term to refer to material other than natural formation which fills the gap between the pad and the formation (which could be water, air, mud, mud cake, crushed rock, or shallow invasions)]. Using the available information, the author has proposed the straight line "family of curves" shown in Figure 9 as a solution for gap less than .5 inch. This will be refined after the next series of DBS standoff tests (which will include extensive standoff tests with simulated mud cake of various densities).

C. The Correction Algorithm

The development of the algorithm involves the following steps:

1. Find a mathematical relationship between long-spaced density and gap. Do this for air- and water-filled boreholes.

2. Find a mathematical relationship between short-spaced density and gap; also for air- and water-filled holes.

3. Find the same relationships for mud cake situations.

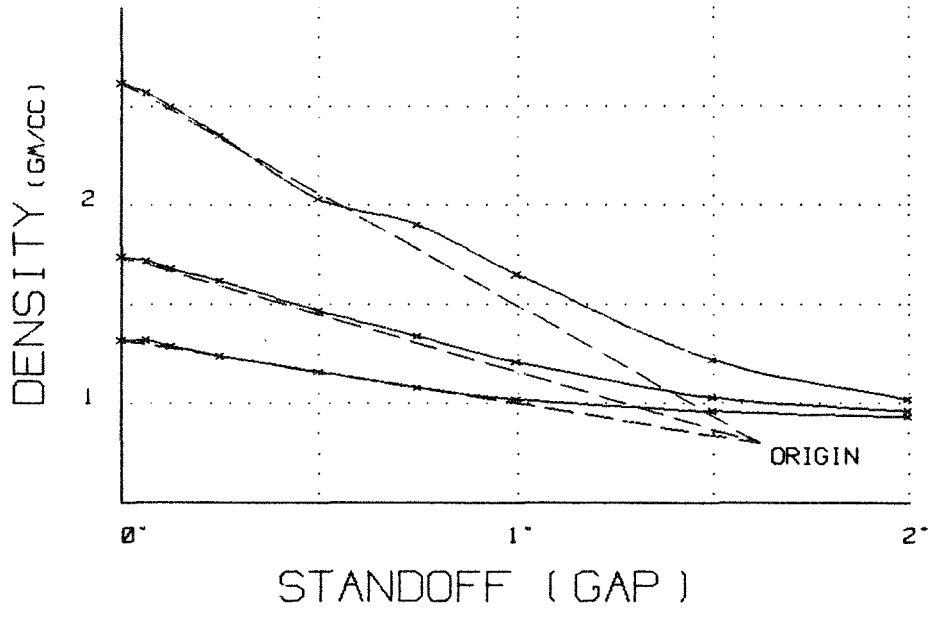

FIG. 9 - LONG-SPACED DENSITY VS. GAP, AIR FILLED BOREHOLE. SOLID LINES REPRESENT STANDOFF TEST DATA. DASHED LINES INDICATE THEORETICAL FAMILY OF CURVES.

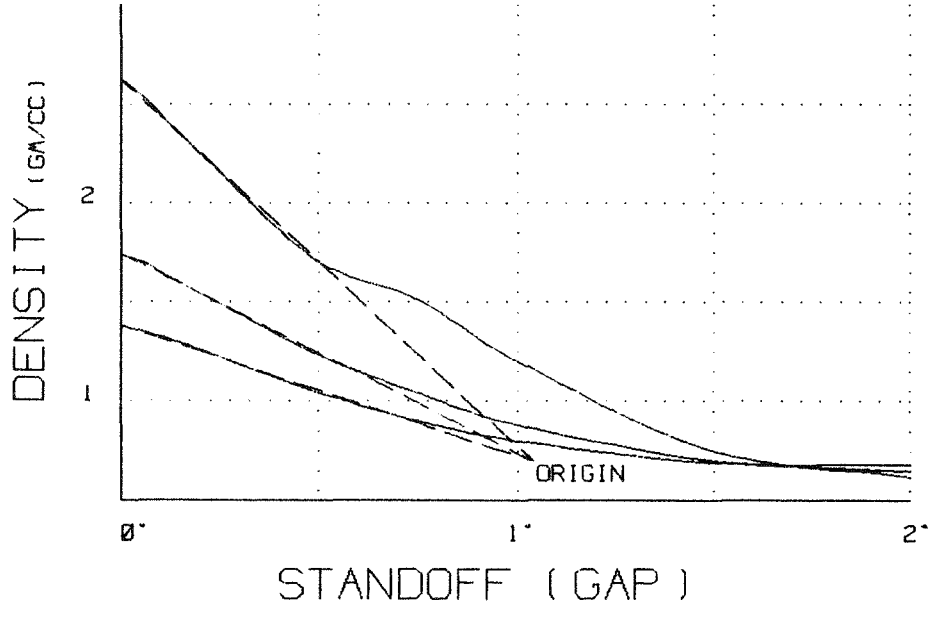

FIG. 10 - SHORT-SPACED DENSITY VS. STANDOFF, AIR FILLED BOREHOLE.

Data to develop the relationships for these first three steps are generated by extensive standoff testing of the DBS pad.

4. Determine which situation (air, water, mud) applies to the present data. This step is based on logical relationships between long- and short-spaced density and uses proximity data and initial operator inputs to help categorize the situation.

5. Assume that true density (unknown) and pad standoff is the same for the short- and long-spaced density and solve simultaneous equations. This step is equivalent to creating a "custom" spine and rib chart.

6. A level of confidence may be assigned if all data points are processed by this method. If a set tolerance is determined, such as ±.1 gm/cc, then only that data which meets this will be presented.

7. The presence of tilt can be detected by an algorithm which searches for the characteristic response which corresponds to tilt (see above text). Tilt may also be handled by simply disregarding data if proximity is greater than .5 inch. Within this range, stand-off data will yield results within tolerance.

D. The Math Solution

This discussion refers to Figures 9, 10 and 11. The mathematical relationship illustrated here is only for the air case. The fluid case is developed similarly and it is the author's contention that, when mud cake standoff data is available, the mud cake situation will also be modeled by the same expression. Although the equations are the same for all three situations, the origin points will be individually chosen from plotted standoff data; and only the constants of the origin points need be changed during a computer run to process the various situations.

List of Constants:

GOL - Gap Origin for LS (Long-Spaced Density)
GOS - Gap Origin for SS (Short-spaced Density)
PLO - Density Origin for LS
PSO - Density Origin for SS

List of Variables:

PLA - Density, LS, Apparent (Raw LS Density Data)
PSA - Density, SS, Apparent (Raw SS Density Data)
PLC - Density, LS, Corrected, Calculated
PSC - Density, SS, Corrected, Calculated
GX - Gap, Calculated

The constants are determined from standoff data, as illustrated in Figure 9 and 10. The point (GOL, PLO) defines the LS origin and (GOS, PSO) the SS origin.

Refer to Figure 11; this chart shows the LS and SS family of curves for the air-filled borehole. The solid lines represent a specific solution to a known PLA and PSA.

$$\frac{PLA - PLO}{GX - GOL} = SLOPE = \frac{PLC - PLO}{0 - GOL}$$

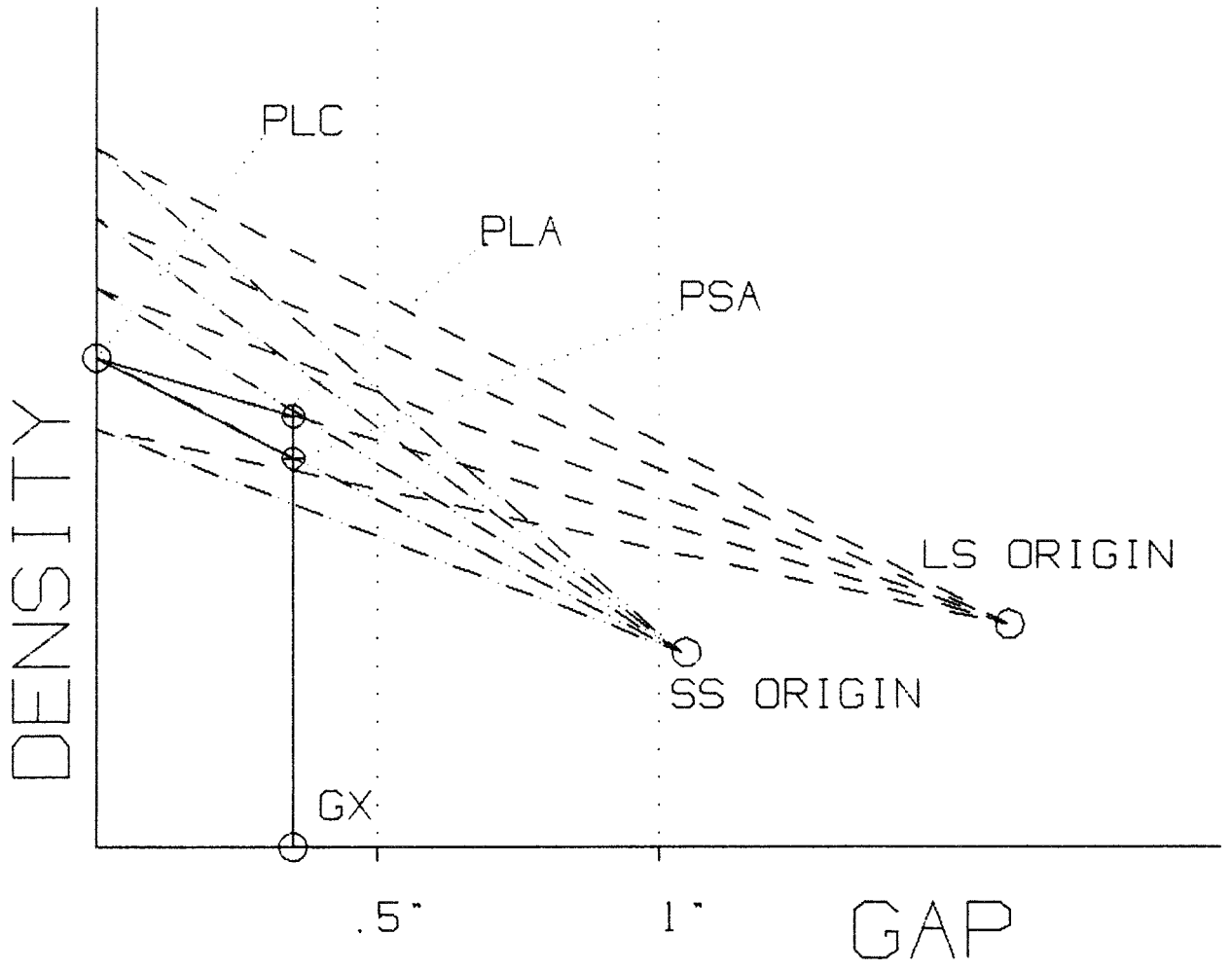

FIG. 11 - GRAPHICAL SOLUTION FOR AIR-FILLED HOLE. DASHED LINES SHOW SS AND LS FAMILY OF CURVES. PLA AND PSA ARE KNOWN. GX AND PLC ARE TWO UNKNOWNS FOUND BY SOLVING TWO SIMULTANEOUS EQUATIONS. SEE TEXT FOR EXPLANATION.

Solve for PLC:

$$PLC = \frac{(PLA - PLO)\ (-GOL)}{(GX - GOL)} + PLO$$

Similarly:

$$PSC = \frac{(PSA - PSO)\ (-GOS)}{(GX - GOS)} + PSO$$

Logically PSC = PLC and GX is the same for both equations, since the DBS pad is assumed to be in a constant density zone and standoff is the same for the LS and SS densities. Therefore, we have two equations and two unknowns (PLC and GX). The solution yields a preliminary corrected density and a calculated gap figure. The algorithm now will check other conditions to determine if this is the final processing. For example, does the calculated gap match the measured average proximity? Is GX > .5 inch? Is PLC - PLA within tolerance? Was PLA > PSA?

E. Categorizing the Data

The question of which set of origin points to use will be decided by the following criteria.

Situation 1: No correction applied

PLA - PSA = 0 (± Tolerance)
Average Prox = 0 (± Tolerance)

Situation 2: Air correction applied

Air-filled hole PLA > PSA
Average Prox > 0

Situation 3: Water correction applied

Water-filled hole PLA > PSA
Average Prox > 0

Situation 4: Mud cake correction applied

PSA > PLA
Average Prox = 0
Note: If mud cake density is unknown, then it may be calculated based on certain criteria.

Situation 5: Data flagged or sent to further processing.

GX > .5 inch and tilt situation exists

VII. SUMMARY

The dual proximity curves of the DBS log are useful for indicating the presence of pad standoff and identifing a tilted pad situation; however, the derivation of useful quantitative data from proximity response is not likely with present processing techniques.

If a proximity indicator were installed near the measure point of the long-spaced density, this centered proximity response would be more closely aligned with density response than the present dual proximities. The centered proximity could not reliably be used to indicate a tilted pad situation.

The modeled density response suggests that the short-spaced density curve should be shifted four inches to be more aligned with the long-space density curve. This shift occurs due to pad tilt, the most common pad situation found in boreholes. The short-spaced density curve relates more closely to long-spaced density deviations due to gap than to the proximities, and shows more promise as a means to determine corrected density.

ACKNOWLEDGEMENTS

This work has been supported by the United States Department of Energy and the Containment Program Office. I wish to thank Jack W. House, Containment Program Leader, for his support. I also wish to thank Mark Mathews and John Conaway for their significant help in editing this document.

REFERENCES

Wahl, J. S., Tittman, J., Johnson, C. W., and Alger, R. P., 1946, "The Dual Spacing Formation Density Log", Journal of Petroleum Technology, 16, 1511-1416.

Birdwell Wireline Services, Engineering Drawings No. LAHJ-8231, Sheet 219 - ASSEMBLY UNIVERSAL FRAME AND SUPPORT and LAHJ-8280, Sheet 271 -SOURCE/DETECTOR PAD ASSEMBLY.

BOREHOLE INSPECTION SYSTEM FOR LARGE DIAMETER HOLES

Ward L. Hawkins
Ronald D. Oliver
Los Alamos National Laboratory

Morgan J. Lavelle, EG&G

ABSTRACT

A color camera developed for underwater applications has been adapted for use as a large diameter Borehole Inspection System (BIS). This video/photographic system has pan and tilt capabilities and remotely interchangeable lenses. A compass provides an azimuth for orientation. It is designed to operate in boreholes ranging in diameter from 1.2 m to 3.0 m. The system has a 180 degree "fisheye" lens and an inspection lens with zoom. 35 mm photographs can be taken of the same view as the video for precise location. Video tape and 35 mm film is annotated.

The primary function of the BIS is geologic investigation. Various characteristics of the geologic medium can be viewed. Lithologic types and textures can be determined. Structural features such as faults, fractures, and bedding can be scrutinized. Detail descriptions of stratigraphic sequences and contacts are possible. In combination with other borehole data and sample information, many questions about hole conditions and the geologic medium can be resolved. Field operations often demand immediate resolution of borehole problems. This system offers on-the-spot visual inspection of the drill hole and associated hardware. Large eroded zones can be evaluated and casings and liners can be inspected. Other applications such as the location and configuration of hardware left in the hole and fluid entry points are possible.

I. INTRODUCTION

The Borehole Inspection System was developed to examine large diameter drill holes at the Nevada Test Site (NTS). The goal was to get immediate information from the video and obtain 35 mm color slides for later, more detailed analysis. A "fisheye" lens was chosen to provide a complete view of the hole when directed downward. An inspection lens with zoom would be used for close up work. The lenses had to be remotely interchangeable to allow a complete inspection with one downhole run. Slide photography would be taken through the same lens as the video for precise location. Compass orientation had to be provided. Versatile annotation on both video tape and slides for on-the-picture data was a requirement to facilitate later viewing. Continuous recording of narration had to be possible on the video tape.

II. CAMERA SYSTEM

An "off the shelf" underwater camera with lens switching capability was adapted for borehole use (Fig. 1). A full 360 degree view of the borehole is achieved with the "fisheye" lens (when oriented downward) to obtain a visual record of the entire hole. The 35 to 70 mm zoom lens provides undistorted detailed views. Pan and tilt adjustments allow complete flexibility in camera orientation. Over 200 slides can be taken during a logging run. Each slide exposure requires approximately twenty seconds. A ruggedized compass gives the azimuth. Lens selection, zoom adjustment, pan

and tilt, and focus and f-stop settings are all controlled from the surface. In the inspection lens mode the zoom can be adjusted. Information can be inserted on the video tape with a keyboard. A clear plastic shield protects the face of the camera.

III. LIGHTING

Lighting for the video is provided by eight evenly spaced, 250 watt tungsten halogen lamps, mounted above the camera beneath a stainless steel reflector (Fig. 1). A protective shield is mounted above the reflector. Lamp intensities can be controlled from the surface either individually or as a unit to obtain various light/shade conditions. Considerable effort was expended in the development of the lighting system to avoid hot spots and shadows. Twin strobe flash units with interchangeable heads; and, flash quenchers for proper film exposure are mounted on either side of the camera. A spotlight pointer immediately above the camera provides additional illumination for greatly enlarged portions of a hole where the other lighting may not reach.

IV. BOREHOLE VEHICLE

The overall length of the subsurface vehicle is approximately 4 m. There are two sets of four individually adjustable legs to centralize the system in the hole. The legs are off center so each 0.25 m diameter wheel is tracking its own path on the borehole wall. Washouts and undergauge sections are traversed smoothly and concentrically. The system is currently set up to run in holes with diameters from 1.2 m to 3.7 m. The pan and tilt unit has a tilt range from -90 degrees (vertically down) to + 60 degrees and a full 360 degree pan. Downhole mechanical response to surface commands is smooth and precise. Mounted just above the camera is a lens defogger (heater fan). This allows defogging of the protective lens cover during the logging run, thus eliminating the need to pull the entire tool out of the hole to clear the view. The electronics is housed in the central tube of the vehicle where there is adequate room for future modifications. The tool is deployed on a special sixteen conductor wireline with a central 75 ohm coaxial cable, and a quick disconnect cablehead. Logging speed during a general survey is 12 m/min.

V. SURFACE SYSTEM

The wellhead system consists of the logging (winch) truck, a dual sheave crane assembly with load indicator and depth encoder, and the monitor/control van (Fig. 2). Power is provided by an on-site generator. The hydraulically controlled winch system contains over 1800 m of the custom designed logging cable. The winch operator's console is equipped with a video monitor to observe the same real-time image as the logging engineer who is directing the operation from the monitor/control van. Winchman and logging engineer are in constant radio communication. Transport and well site rig-up is facilitated through the use of a special transporter built specifically for the borehole vehicle. The camera is handled separately in a special container. Rig-up and quality assurance procedures require sixteen man hours.

The monitor/control van is equipped with three video monitors (Fig 3); a viewing monitor for the geologist, a data and control display monitor, and a preview/review monitor. The data and control information which can be displayed includes: lighting configuration, temperature in the electronics housing, telemetry status, compass heading, pan and tilt angles, and depth and load. Microprocessors and digital communication links are used for transmissions over the wireline. The preview/review monitor is connected to one of the two 3/4 inch U-matic audio-video cassette recorders (VCR) through an editor. Immediate playbacks; or, recordings of other nearby holes, can be viewed for comparison with the real-time video. The editor also provides the capability to record two tapes simultaneously, and allows on-site studio quality editing.

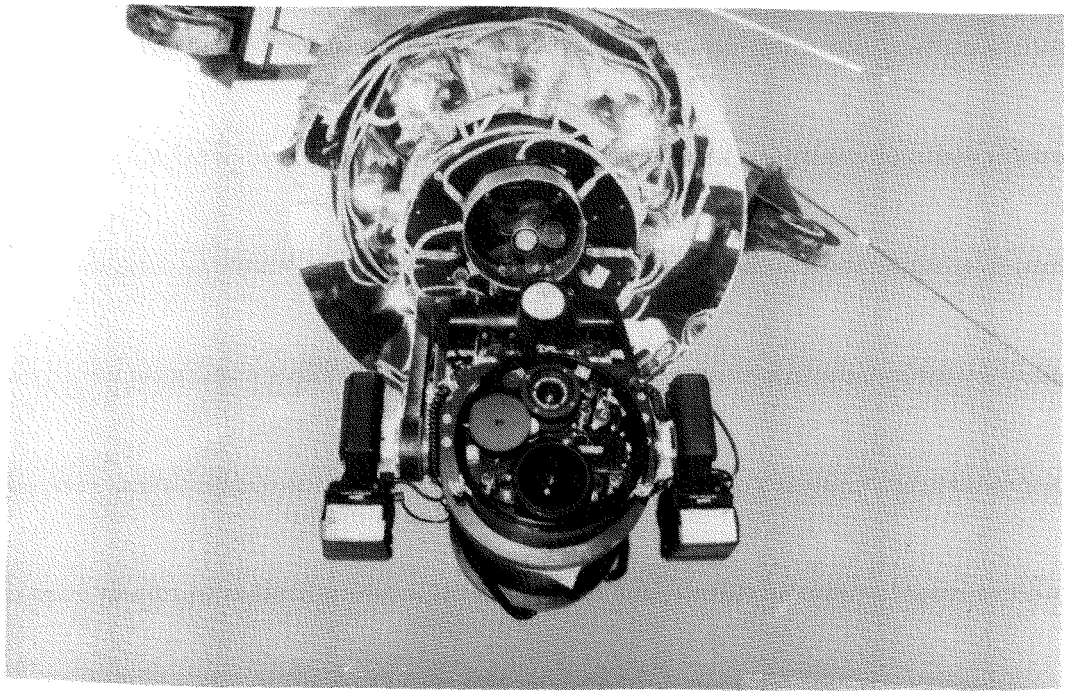

Fig. 1 Camera and lighting system.

Fig. 2 Wellhead system; winch truck, and control/monitor van.

The surface control system (Fig. 4) which manages the various camera functions includes the camera pan and tilt controller, the power distribution panel, and the data acquisition controller. A routing and patching system enables complete versatility in routing any video signal to any VCR or monitor. The video equalization panel compensates the loss imposed on the base band video when run over the long wireline. Video color calibrations, trouble shooting, and wireline compensation adjustments are accomplished with a waveform monitor and vector scope, multiburst generator, and color bar generator.

VI. GEOLOGIC CHARACTERIZATION

The primary reason for developing the BIS is geologic characterization. Figure 5 is a fisheye view of a fault in U7by. The annotation, from left to right, across the top of the photo is: frame number, lens (8 designates 180 degree fisheye lens), date, hole, depth (in feet), azimuth, tilt and pan angle (degrees from reference point on frame for lighting adjustments). In the photo the fault has a trend of approximately north 30 degrees west with an easterly dip. A closer view of the fault with the inspection lens zoomed to the maximum 70 mm reveals more detail (Fig. 6). Note the changes in the annotation along the top of the photo. The view is looking to the southeast at an angle of 16 degrees down from horizontal.

The feature shown in Fig. 7 would probably not have been detected with normal borehole sampling and logging procedures. In the center of the frame is a thin (~ 0.15 m), nearly horizontal air fall tuff unit interstratified with alluvium (Drellack, et al, 1986). Because of the ability of the BIS to identify it, this bed has become a very useful marker unit within the alluvium of southern Yucca Flat. Geophysical logging techniques do not have the resolution to detect such a thin feature. Cuttings samples taken during the drilling are a mixture of material from a 3 m interval making it extremely difficult to characterize a feature of this thickness. At times there have been sidewall samples taken in this bed; but, until its presence was verified through photography in several drill holes, meaningful characterizations and correlations could not be made.

In U6d the moderately to densely welded ash flow tuff of the Topopah Spring member of the Paintbrush tuff (Fig. 8) includes a 15 m thick lithophysal zone. The gamma-gamma density logging tool, which has to be in contact with the borehole wall to get reliable data, measured a 2.13 Mg/m^3 density for this zone (tool standoff eliminated 30% of the measurements). The gravimeter measured a formation density of 1.95 Mg/m^3 in the same interval. Although the difference is not great, an explanation based on the photography is obvious. The nature of lithologic zones such as a lithophysal layer which has large voids is important when considering the effects such a unit will have on phenomenology. Without the photography an accurate characterization of this zone would have been difficult.

Figures 9 and 10 are examples of operational concerns. A percussion gun sidewall sampling point is shown in Fig. 9. The sample cup which is explosively driven into the wall of the hole is approximately 0.03 m in diameter so the entire field of view for this photo, taken with the zoom inspection lens at 70 mm, is about 0.7 m across. The hole was drilled with a 2.44 m diameter bit. Roller stabilizers on the side of the bit made the diamond pattern in the mudcake left on the walls. Fig. 10 is the top of the liner at U4s. At times the nature of the liner cement job or fluid flowing over the top of the liner are of interest as are numerous other aspects of the transition from the open hole to the smaller diameter liner. Many questions about hole conditions can be easily answered with photography.

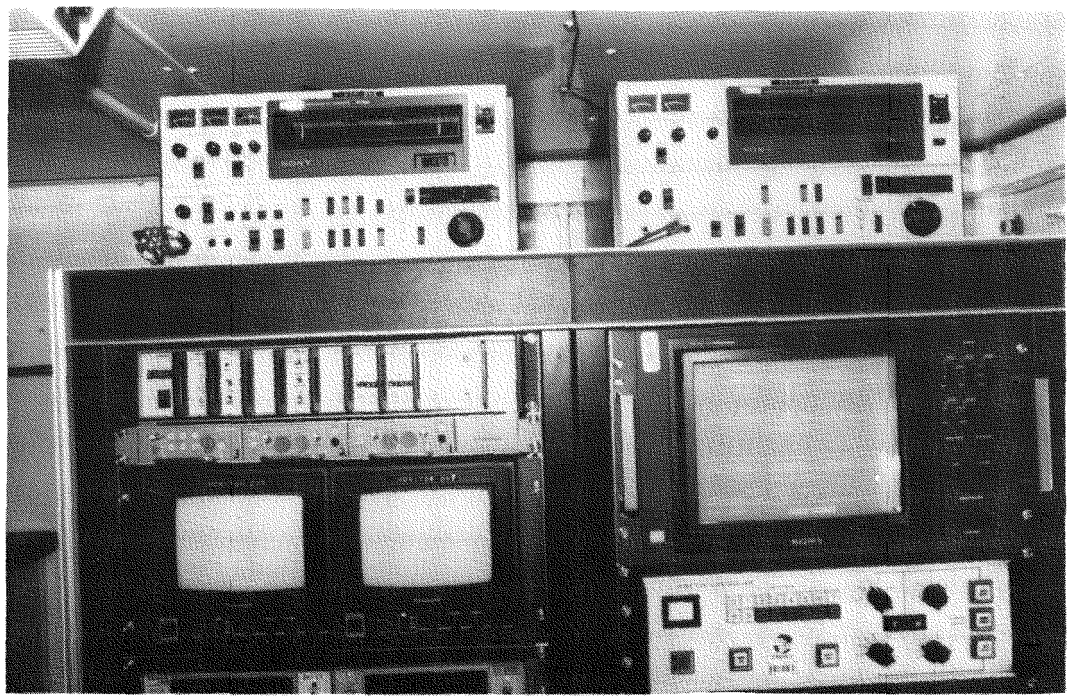

Fig. 3 VCRs and video monitors.

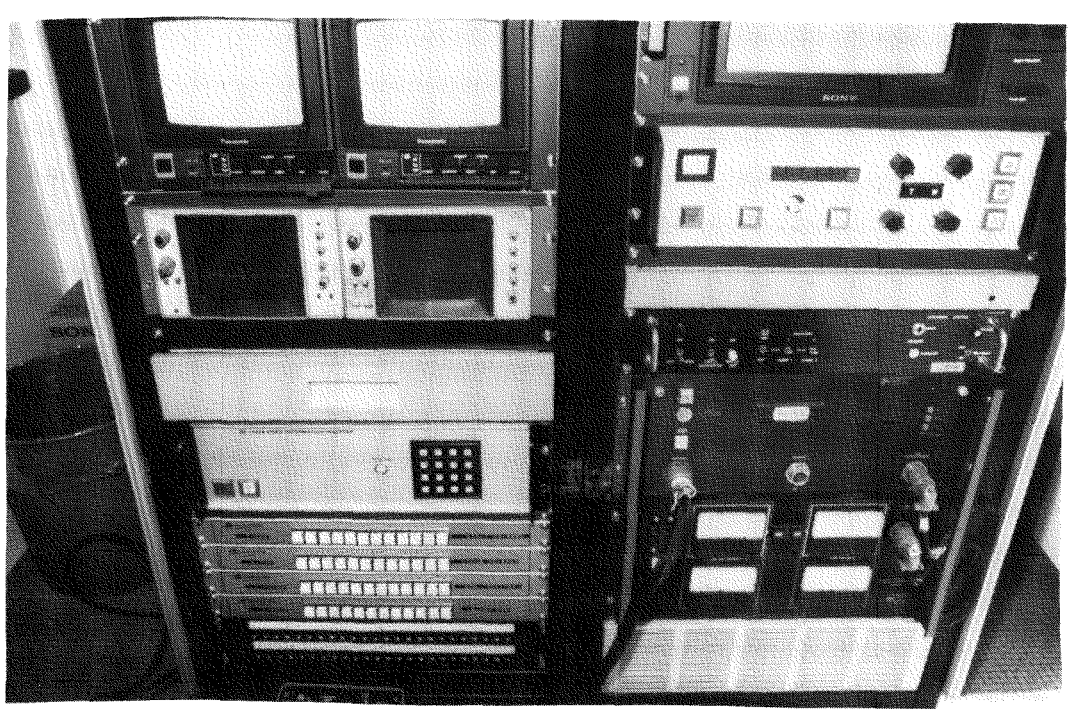

Fig. 4 Surface control system.

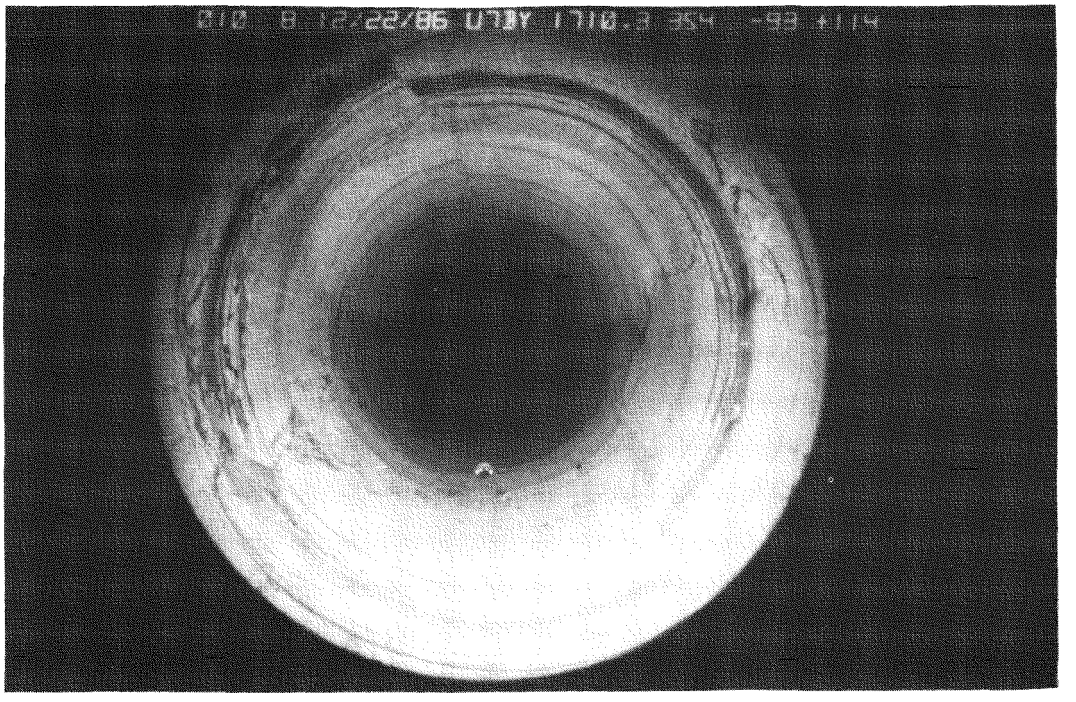

Fig. 5 Fisheye view of a small displacement fault.

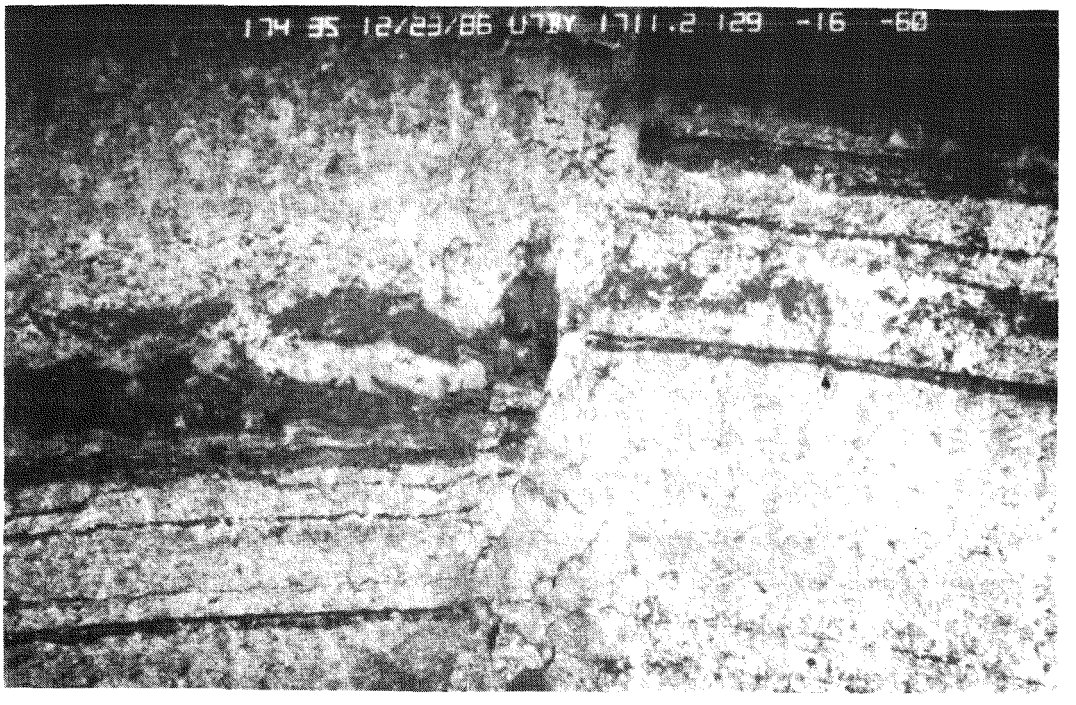

Fig. 6 Inspection lens view of the fault in Fig. 5.

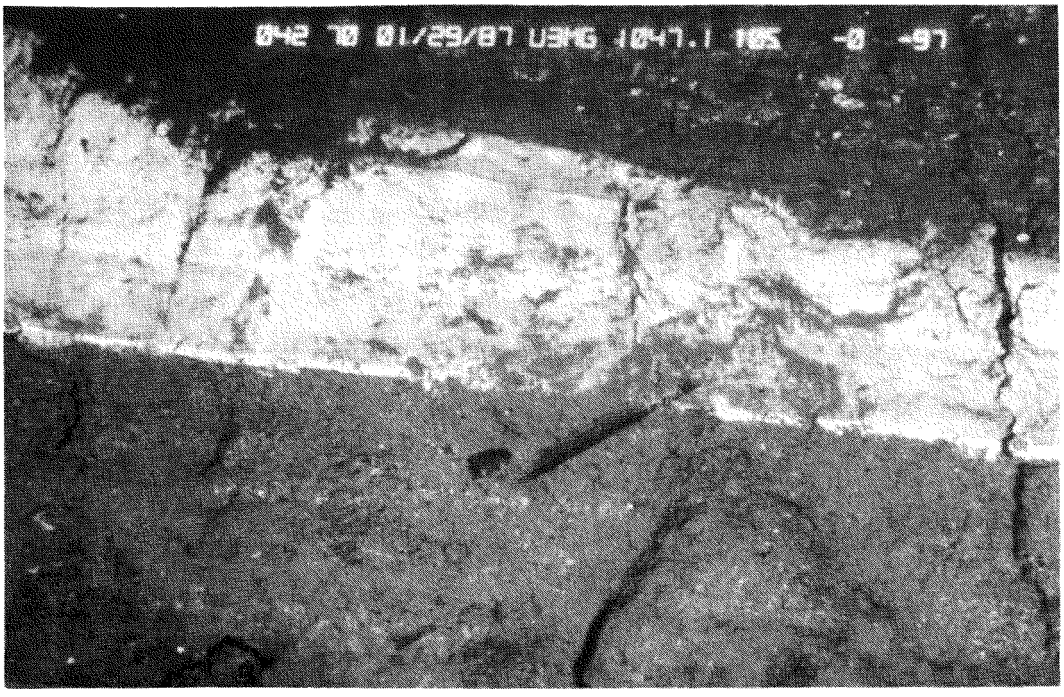

Fig. 7 Air fall tuff bed in alluvium.

Fig. 8 Lithophysal zone in a welded tuff.

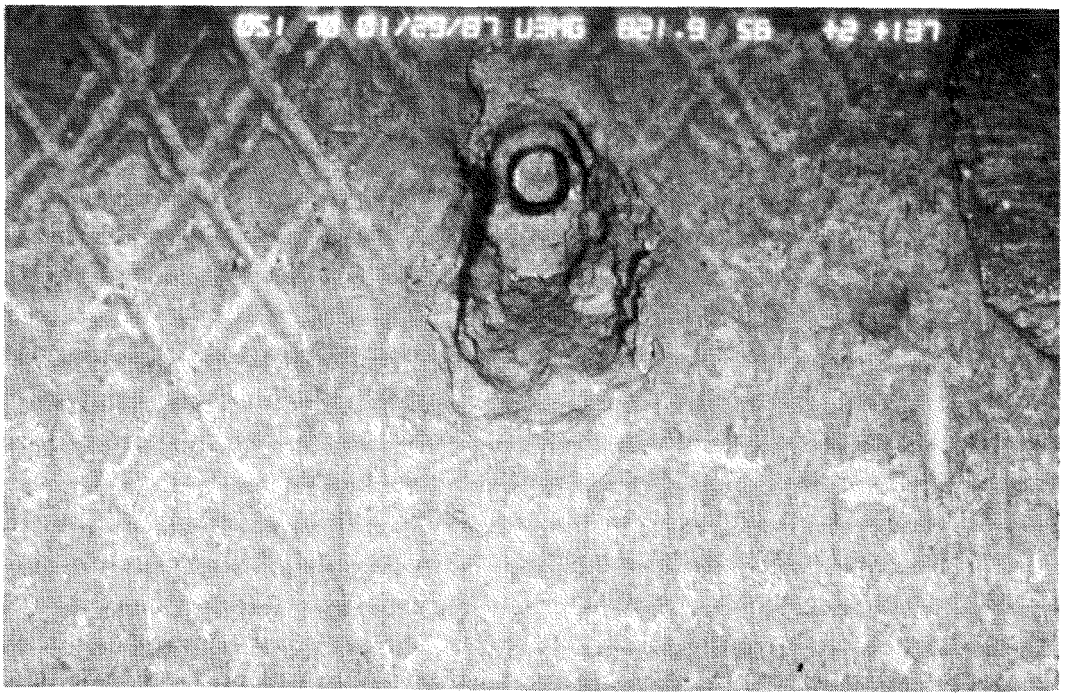

Fig. 9 Percussion gun sidewall sample location.

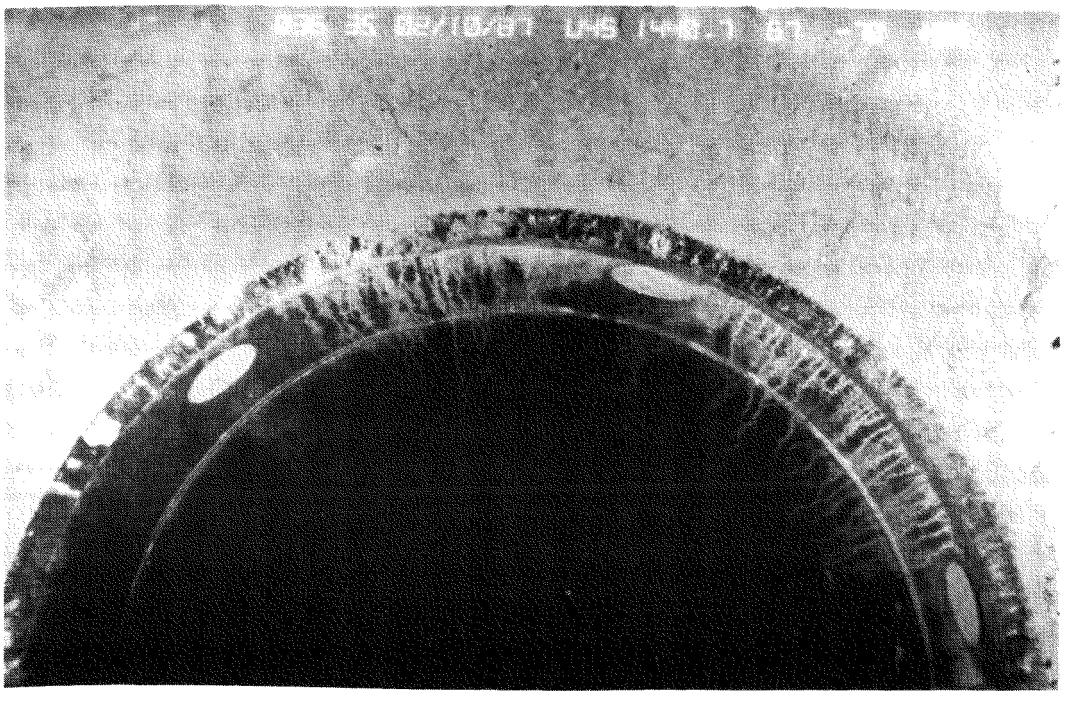

Fig. 10 Liner top.

VII. SUMMARY

The development of the BIS has been invaluable in the assessment of borehole conditions at the Nevada Test Site. Immediate observations are made from the video for time urgent investigations. With a single deployment a complete, permanent color video and still photo record of the hole is made. The interchangeable lens system provides a general borehole survey in the fisheye and close up photography with the zoom lens for later detailed analysis. Geologic and operational features which would be difficult to characterize by other means can now be quickly and accurately assessed.

VIII. ACKNOWLEDGMENTS

The authors are grateful to their colleagues (too numerous to name appropriately) for their comments and suggestions which were crucial to the successful development of this tool and its applications.

This work was supported by the United States Department of Energy.

REFERENCES

Drellack, S. L., Jr., Gonzales, J. L., and Cavazos, A. P., 1986, Lithology and stratigraphy of drill holes completed during 1985 in Los Alamos use areas of Yucca Flat, Nevada Test Site, Vol. VIII, Fenix and Scisson, Inc., Geologic Report, DOE/NV/10322-9, 76 p.

DEFINITION OF STRATIGRAPHIC UNITS BETWEEN THE GROUSE CANYON AND RAINIER MESA TUFFS IN LOS ALAMOS-USE AREAS OF YUCCA FLAT, NEVADA TEST SITE

DRELLACK, S. L., Jr., Fenix & Scisson, Inc., P. O. Box 498, Mercury, NV 89023;
WARREN, R. G., Los Alamos National Laboratory, Los Alamos, NM 87545;
[1]HUGHES, W. T., U. S. Department of Energy, P. O. Box 98518, Las Vegas, NV 89193

ABSTRACT

Our preliminary petrochemical work allows us to relate bedded tuffs between the 14.1-Ma Grouse Canyon (Tbg) and 11.6-Ma Rainier Mesa (Tmr) Tuffs in the subsurface of Yucca Flat to ash-flow tuffs and lavas that occur elsewhere within the region of the Nevada Test Site (NTS). Within this stratigraphic interval in Yucca Flat, presently assigned entirely to the Paintbrush Tuff, we find tuff from four formations defined within the region: the Crater Flat, Wahmonie, Area 20, and Paintbrush, in ascending order. We recognize an additional unit immediately beneath Tmr that correlates with the Transition tuff petrologic zone recently defined in subsurface of Pahute Mesa. Individual units within each formation of Yucca Flat (for example, the Bullfrog Member of the Crater Flat Tuff) are recognized by petrochemical and hand-sample characteristics that are nearly identical to those for the unit elsewhere within the NTS region.

We recommend routine subdivision of post-Tbg, pre-Tmr tuffs into individual units rather than assignment to the Paintbrush Tuff for several reasons. First, Paintbrush Tuffs are formally defined by a scarcity or absence of quartz phenocrysts, and the prominence of quartz phenocrysts within specific post-Tbg, pre-Tmr stratigraphic horizons is inconsistent with this definition. These quartz-bearing intervals are correlative with Area 20 and Crater Flat Tuffs. Second, the stratigraphic equivalence of the "mafic-rich zone of the Paintbrush" and the pre-Paintbrush age Wahmonie Formation has been firmly established by recent work. Third, the Tiva Canyon, Topopah Spring, and Stockade Wash ash flows are intercalated within the post-Tbg, pre-Tmr sequence of bedded tuffs in extreme southeastern Yucca Flat, complicating correlations within the present stratigraphic system. Finally, post-Tbg, pre-Tmr tuffs record more than half of the time interval for deposition of important volcanic units in Yucca Flat. Combined post-Tbg, pre-Tmr units tend to thin to the north and away from the central axis of Yucca Flat. Individual formations, however, display different thickness variations. Tuff of the Wahmonie Formation thickens towards the eastern edge of Yucca Flat, and the Paintbrush Tuff thins dramatically northward from 114m in UE-6d#2 to <15 m in UE-7ba. Thus, early structural development of Yucca Flat can be better understood if we utilize stratigraphic units within the post-Tbg, pre-Tmr sequence that represent well-defined, narrow time intervals.

I. INTRODUCTION

Continuous core from widely spaced exploratory holes UE-7f, UE-7ba, UE-7bc and UE6d#2, has provided a comprehensive set of samples representing tuffs postdating the Grouse Canyon Member of the Belted Range Tuff (Tbg), and predating the Rainier Mesa Member of the Timber Mountain Tuff (Tmr) in southern Yucca Flat, Nevada Test Site (NTS) (Figure 1). We have completed preliminary petrographic and geochemical studies on these samples and other samples from Yucca Flat for comparison with samples obtained from other regions of the NTS. By applying the

[1] formerly with Fenix & Scisson, Inc.

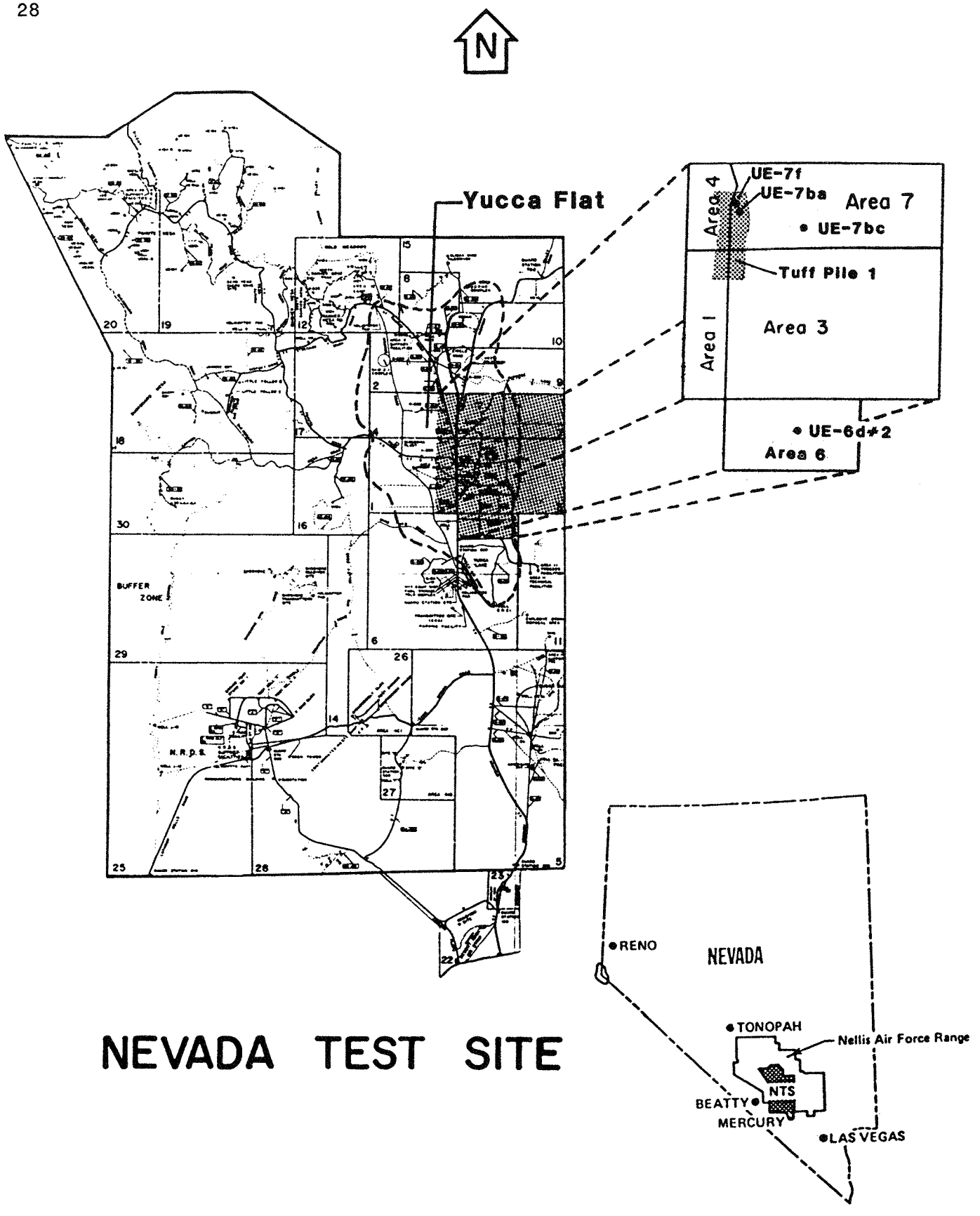

Figure 1. -- Map of Nevada Test Site showing areas covered in this report.

"petrologic zone" concept (Warren, 1983; Warren et al., 1985), our results establish an excellent petrographic and chemical, and therefore, stratigraphic correlation between bedded tuff units found in the subsurface of Yucca Flat and well-characterized ash-flow tuffs and lavas that occur elsewhere in the NTS region (Byers et al., 1976). These bedded tuffs can show considerable lithologic variability, which commonly is masked by strong zeolitization. Consequently, stratigraphic correlation is difficult if based solely on hand-sample lithologic characteristics. Practical criteria to precisely characterize these units have been inadequate. Consequentially, in the past these bedded tuffs were often grouped together and stratigraphically assigned to the "Paintbrush Tuff" ("Tp"). Our work defines a practical, preliminary stratigraphic framework for the pre-Tmr, post-Tbg sequence of volcanic units within Yucca Flat.

The Petrologic Zone

Petrographically and chemically distinctive stratigraphic units are termed "petrologic zones." Laterally, these petrologic zones may include several lithologies, analogous with facies changes in sedimentary rocks. For example, a single petrologic zone may consist of a prominent ash-flow tuff, distal and upper air-fall tuff, and a near-source lava flow (Figure 2). Several related petrologic zones may be grouped into a "petrologic assemblage". In Yucca Flat, where rhyolitic lavas are absent, we only need recognize the stratigraphic equivalence between petrochemically similar ash-flows and bedded tuffs.

II. Importance Of Subdividing These Units

Age dates for important tuff units of the NTS region are given in Figure 3. Most of the tuffs in Yucca Flat were deposited within a 3.6 million year interval between the 15.0 Ma Redrock Valley Tuff (Trv) and the 11.4 Ma Ammonia Tanks Member of the Timber Mountain Tuff (Tma). Post-Tbg, pre-Tmr tuffs span 2.5 m.y., or 69% of this depositional history (Figure 3). During this time span much structural activity occurred within the NTS region (Carr, 1984; Warren et al., 1985).

Drill hole data indicate that up to 798 m (2617′) of volcanic rocks were deposited in southern Yucca Flat. However, this thickness is extremely variable and can be as little as 305 m (1000′) in northcentral Area 7 where erosion, nondeposition, and structure are controlling factors. The post-Tbg, pre-Tmr section varies in thickness from 91.4 m (300′) in northcentral Area 7 to 295.7 m (970′) in UE-6e (Drellack et al., 1987). This sequence represents from less than 15% to approximately 40% of the total thickness of volcanic tuff in the subsurface of LANL-use areas of Yucca Flat. Stratigraphic logs from core holes studied in detail for this report are shown in Figure 4.

The pre-Tmr, post-Tbg stratigraphic interval includes common nonalluvium working point (WP) depths in the Tuff Pile 1, southern Area 7, northern Area 3, and southcentral Area 3 of the NTS (Figure 1). Ranges for typical WP depths near our example core holes are shown in Figure 4. This stratigraphic interval will continue to prove important for future tests as adjacent real estate is developed.

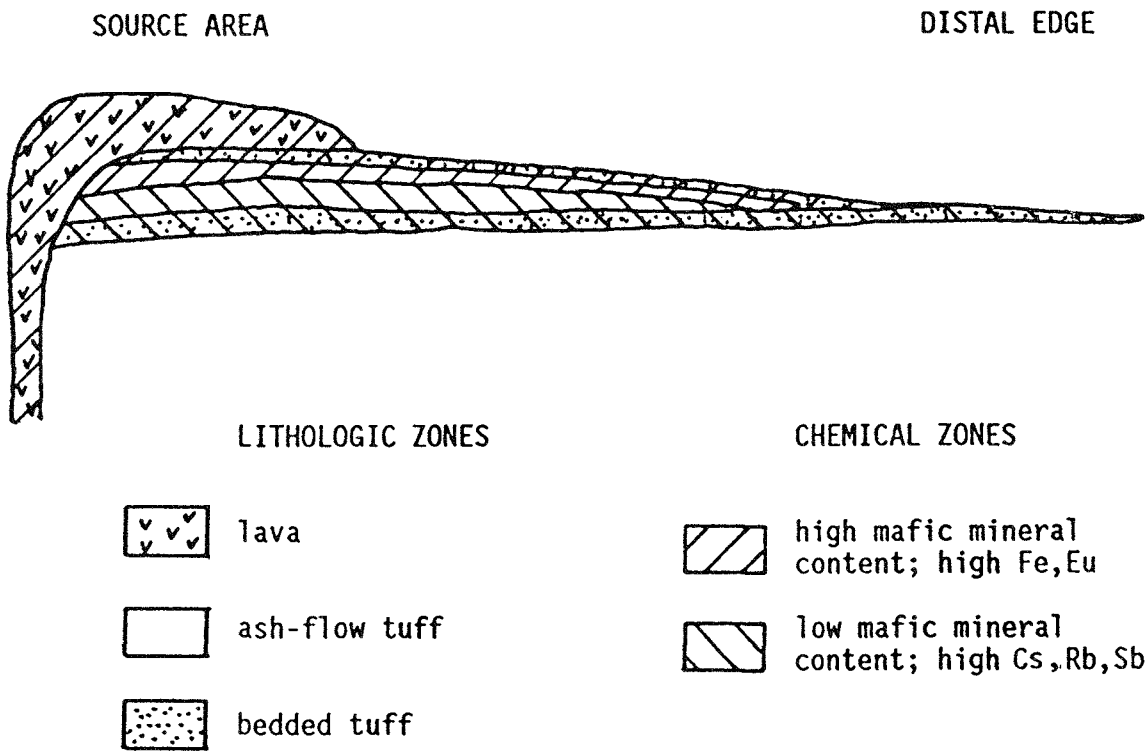

Figure 2.--Cross-section of an idealized petrologic zone. (from Warren et al., 1985)

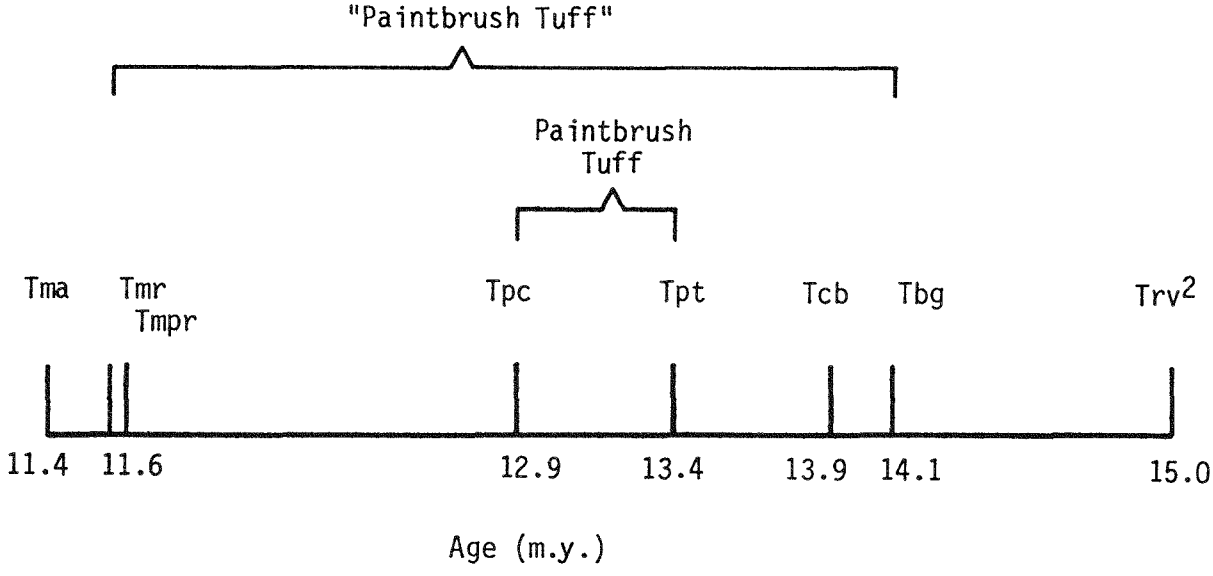

Figure 3.--Ages of important ash-flow tuffs in the NTS region and associated tectonic activity within the region.[1]

[1]Ages of units from Kistler (1968); Marvin et al. (1970); and Carr et al. (1986); ages corrected using new constants of Dalrymple (1979).

[2]Trv age was averaged from Kistler (1968) and Marvin et al. (1970); and corrected using new constants of Dalrymple (1979).

Figure 4.--Stratigraphic Logs For Continuously Cored Exploratory Holes Extensively Sampled For This Report.

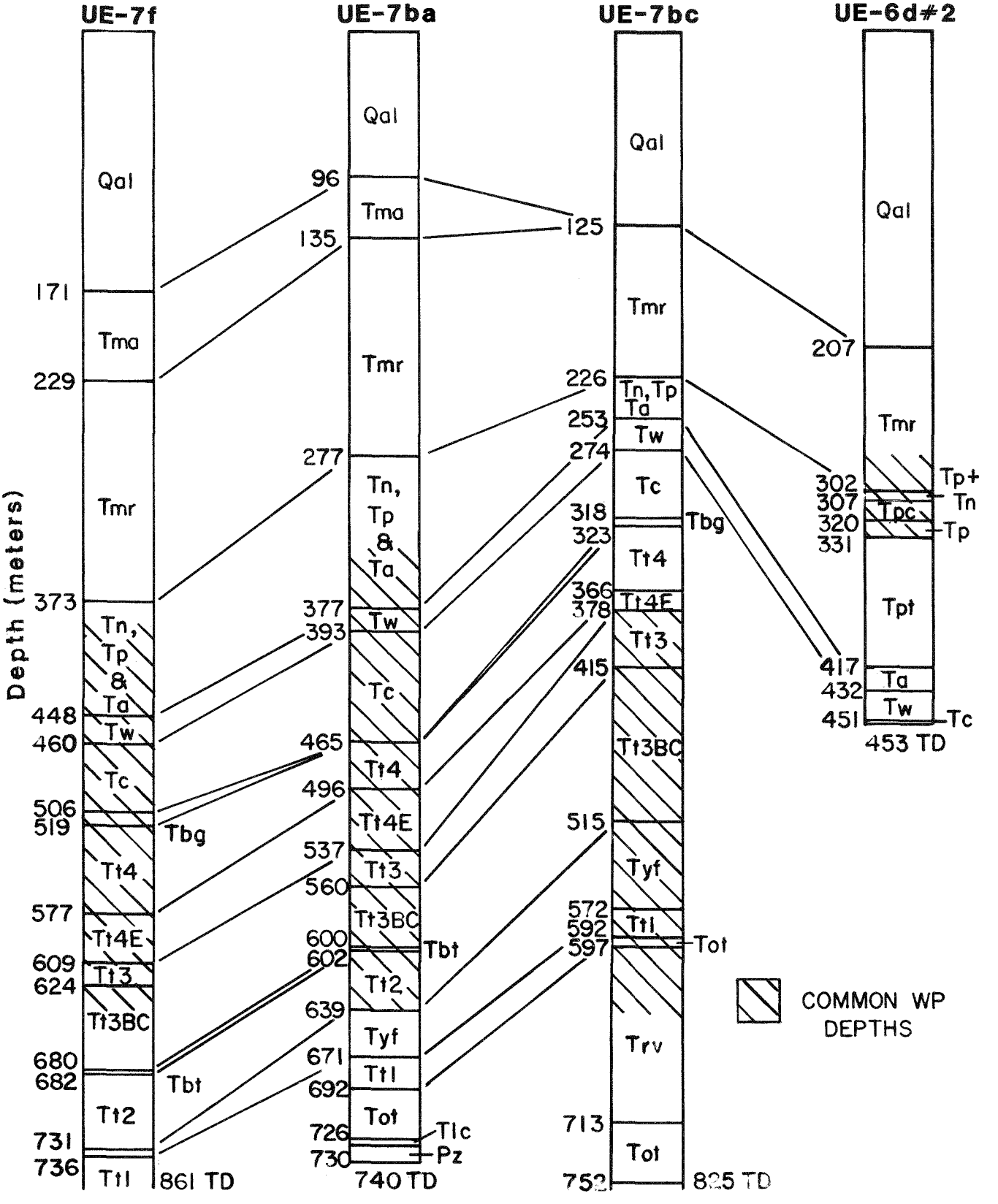

Table 1.--Stratigraphic Nomenclature Used in this Report

Qal	Alluvium
Tma	Ammonia Tanks Member of the Timber Mountain Tuff
Tmr	Rainier Mesa Member of the Timber Mountain Tuff
Tmpr	Pre-Rainier Mesa tuff of the Timber Mountain Tuff
Tnp	Pool tuff of the Transition tuff
Tnww	Windy Wash tuff of the Transition tuff
Tnqr	Quartz-Bearing tuff of the Transition tuff
Tx	*Pre-Rainier Mesa, post-Wahmonie bedded tuffs, undifferentiated
Tpc	Tiva Canyon Member of the Paintbrush Tuff
Tppr	Pyroxene-bearing rhyolite of the Paintbrush Tuff
Tpp	Pah Canyon Member of the Paintbrush Tuff
Tpr	Pre-Pah Canyon Member of the Paintbrush Tuff
Tpt	Topopah Spring Member of the Paintbrush Tuff
Ta	Area 20 tuff, undifferentiated
Tac	Calico Hills tuff of the Area 20 tuff
Tw	Wahmonie tuff, undifferentiated ("mafic-rich zone")
Tc	Crater Flat Tuff, undifferentiated
Tcp	Prow Pass Member of the Crater Flat Tuff
Tcs	Stockade Wash tuff of the Crater Flat Tuff
Tcb	Bullfrog Member of the Crater Flat Tuff
Tct	Tram Member of the Crater Flat Tuff
Tcl	Lower Crater Flat tuff of the Crater Flat Tuff
Tbg	Grouse Canyon Member of the Belted Range Tuff
Tt4	Tunnel beds, Unit 4
Tt4E	Tunnel beds, Subunit 4E Equivalent
Tt3	Tunnel beds, Unit 3
Tt3BC	Tunnel beds, Subunit 3BC Equivalent
Tbt	Tub Spring Member of the Belted Range Tuff
Tt2	Tunnel beds, Unit 2
Tyf	Yucca Flat Tuff
Tt1	Tunnel beds, Unit 1
Tot	Older Tuffs, undifferentiated
Trv	Redrock Valley Tuff
Tlc	Paleocolluvium
Pz	Paleozoic Rocks, undifferentiated

*Tx includes Tmpr, Tnp, Tnww, Tnqr, Tpc, Tppr, Tpt, Ta and Tac undifferentiated

III. Method To Establish Stratigraphy

Petrography, mineral chemistry and trace element analysis provide petrochemical data to define petrologic zones. These analyses are performed using the following established methods:

1. Petrographic microscope analysis of grain mounts and thin sections (for petrography)
2. Probe-section analysis of polished thin sections (for mineral chemistry)
3. Neutron Activation Analysis, or NAA (for trace-element chemistry)

We applied these techniques on samples of continuous core from widely spaced exploratory holes UE-7f, UE-7ba, UE-7bc and UE-6d#2 (Figure 1). The combination of excellent stratigraphic control and sample quality with high resolution petrochemistry enables the recognition of detailed characteristics. Published and unpublished data comprises a comprehensive geochemical data base for comparison. Our data base draws on petrochemical work for both the Weapons Program (primarily unpublished work of Warren), and the Waste Program (e.g. Broxton et al., 1986; Warren et al., 1983; Scott and Castellanos, 1984).

Petrography

Phenocryst contents for each of the volcanic samples are determined by petrographic microscope analyses of grain mounts and thin sections. Techniques for thin section analysis are described in Warren et al. (1984). Common minerals that can be accurately determined in thin section and used to define petrographic characteristics are felsic minerals and mafic minerals. Felsic minerals are quartz, sanidine, and plagioclase. Common mafic minerals are biotite, hornblende, and pyroxenes. The presence or absence of accessory minerals such as sphene are also important attributes that distinguish a particular stratigraphic unit.

Figure 5 shows quartz phenocryst content for a sequence of samples from the post-Tbg, pre-Tmr interval in two widely spaced core holes, UE-6d#2 and UE-7f. The Paintbrush Tuff (Tp) and Wahmonie Tuff (Tw) are characteristically quartz-poor to quartz-free, in contrast with adjacent formations, which have a considerably higher content of quartz phenocrysts. Phenocryst contents for one or more minerals may be very similar for several stratigraphically adjacent units. However, it is unlikely that such units will have similar phenocryst contents for all major minerals. In the above example, even though the Paintbrush Tuff and Wahmonie tuff exhibit very similar quartz phenocryst contents, they differ markedly in mafic mineral content and can readily be distinguished on this basis.

It is not uncommon for units (petrologic zones) to be compositionally zoned. The Rainier Mesa Member and the Topopah Spring Member of the Paintbrush Tuff (Tpt) are examples of compositionally zoned ash-flow tuffs which have a mafic-rich caprock. Far from the source large decreases in felsic phenocryst content commonly occur near the base of units normally considered to be unzoned. Thus problems often arise from sampling extreme tops and bottoms of units. An apparent atypical character may reflect extreme zonation or represent a "transitional unit".

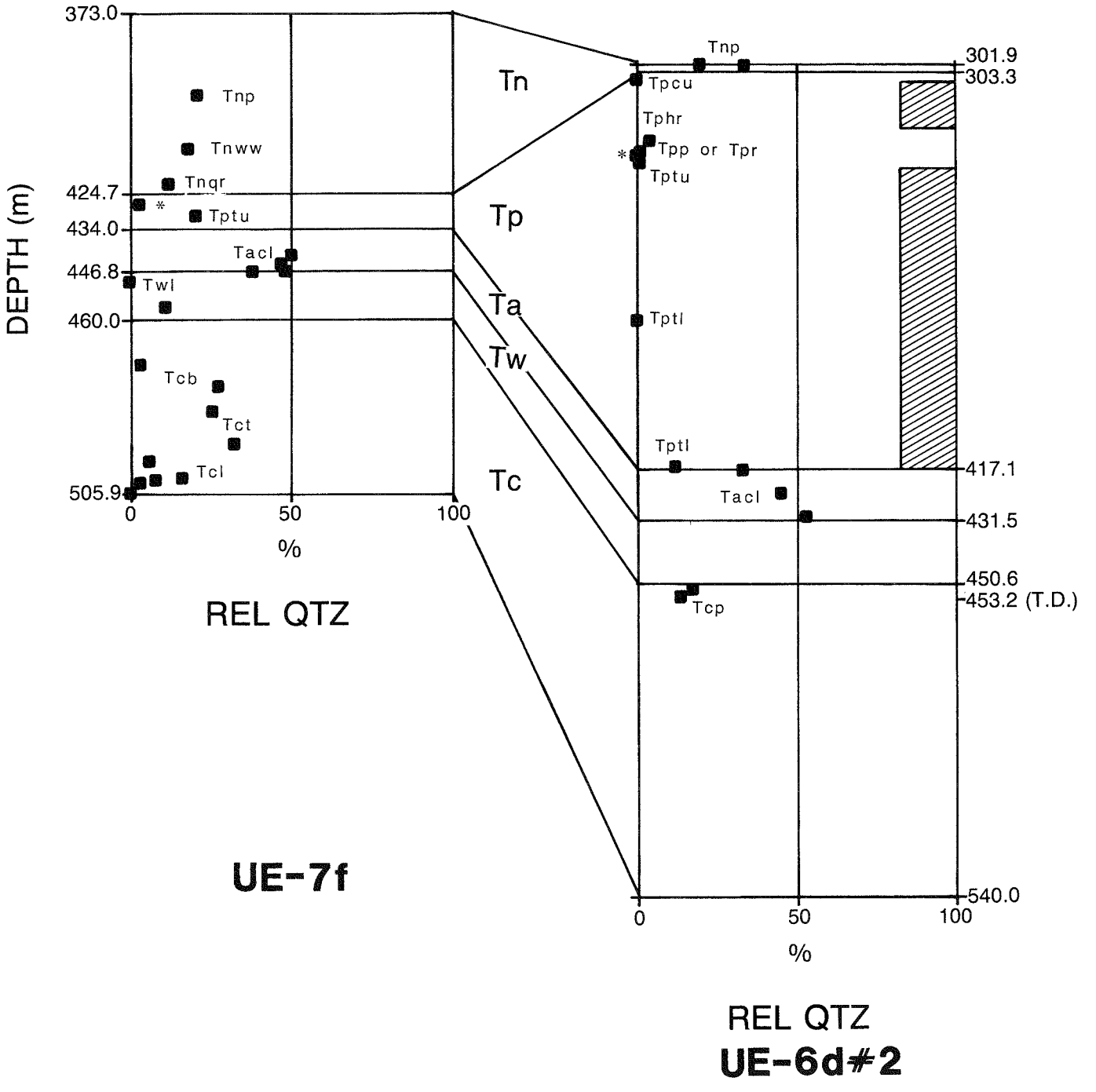

Figure 5.--Correlation of pre-Tmr, post-Tbg units in UE-7f and UE-6d#2, showing quartz as the percent of felsic phenocrysts (rel qtz). All data from petrologic analysis of grain mounts. Symbols for units are in Table 1; letters "u" and "l" in fourth position of symbol indicate "upper" and "lower" part of unit. Asterisk identifies plagioclase-rich tuff that correlates with pre-Tpr, post-Tpt "transitional" tuff of southwestern NTS. Ash flow cooling units shown with cross-hatched pattern.

Figure 6, which shows variations in plagioclase for units of the Paintbrush formation, illustrates typical petrographic variations within each petrographic group of units. Zoned units, such as the Topopah Spring and Tiva Canyon Members show extreme ranges in plagioclase content, and therefore the plagioclase content alone may not distinguish such units from stratigraphic neighbors. In general, statigraphic neighbors have overlapping ranges in plagioclase content and cannot be distinguished solely on this basis. However, much additional petrographic data are available for statigraphic identification, which usually allow unambiguous assignment. Some methods of representing these data are described below. When these additional data are considered, the petrographic ranges can be used to great advantage because this range is controlled largely by stratigraphic position within a zoned unit.

Ternary diagrams showing relative abundances of associated minerals are usually quite useful for illustrating petrographic characteristics. A petrographic comparison of the Wahmonie bedded tuff from the subsurface of Yucca Flat and the Wahmonie group of tuffs and Lavas near the Wahmonie-Salyer volcanic center, plotted on a quartz/K-spar/plagioclase ternary diagram is shown in Figure 7. Plagioclase constitutes roughly 95% of the felsic phenocrysts in both sets of samples, and represents a strong correlation.

The Tiva Canyon Member of the Paintbrush Tuff (Tpc) and Rainier Mesa tuff compositional fields are plotted for comparison (Figure 7) and demonstrate the distinctive petrographic character exhibited by some formations. Recognition of this petrographic character is enhanced when additional petrographic features are considered. For example, the hornblende/pyroxene/biotite ternary plot of the Wahmonie tuff and similar plagioclase-rich units is presented in Figure 8. There is an excellent match between the Wahmonie bedded tuff in Yucca Flat and the Lower Wahmonie at its source in the Wahmonie-Salyer Volcanic Center (Ekren and Sargent, 1965; Poole et al., 1965). The Upper and Middle Wahmonie is not presently recognized in Yucca Flat. The predominance of only the lower part of the Wahmonie formation in Yucca Flat follows a general observation that the lowest part of a cogenetic sequence becomes increasingly predominant with increasing distance from the source.

Mineral Chemistry

Mineral chemistry as determined by electron microprobe analyses of polished thin sections has proved to be the best method to define petrologic zones (Warren, 1983, Warren et al., 1985; Warren et al., 1984). Lithologic variations, petrographic zonation, and diagenetic alteration generally have little affect on primary mineral chemistry. Sanidine compositions for samples from a wide geographic area are extremely consistent. Other minerals, plagioclase and biotite for example, also exhibit a narrow range in chemistry or characteristic dominant composition for each particular unit. The histograms presented in Figure 9 compare plagioclase compositions for Wahmonie samples from Yucca Flat and the NTS region. These compositions are far more Ca-rich (An-rich) than most units of the NTS, but are more Ca-poor than those of other plagioclase-rich units of the region, such as the flow breccia of USW G-1 (Warren et al., 1983).

This distinctive chemical similarity within units is contrasted by dissimilarity between units. There is usually at least one primary mineral for which the composition differs significantly among units. This difference is usually substantially greater than the small analytical uncertainties allowing

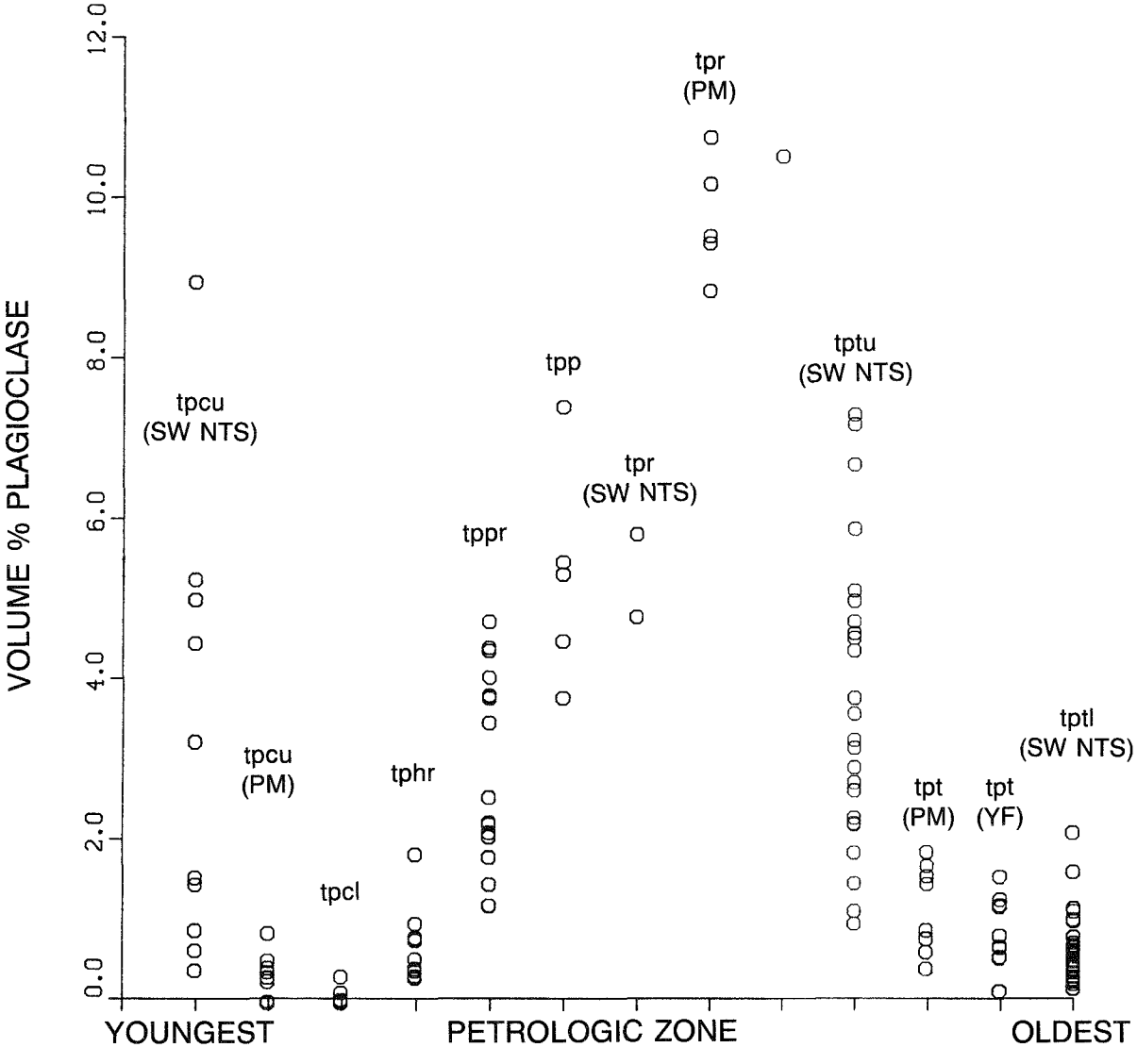

Figure 6.--Volume percent plagioclase in samples of the Paintbrush petrologic assemblage. Symbols for units are in Table 1; letters "u" and "l" in fourth position of symbol indicate "upper" and "lower" part of unit. Plagioclase content within many units differs strikingly among Pahute Mesa (PM), southwestern NTS (SW NTS), and Yucca Flat (YF) regions. Unlabelled point is "transitional" unit from southwestern NTS. Data from R. G. Warren (unpublished), F. M. Byers, Jr. (unpublished), Quinlivan and Byers (1977), and Scott and Castellanos (1984).

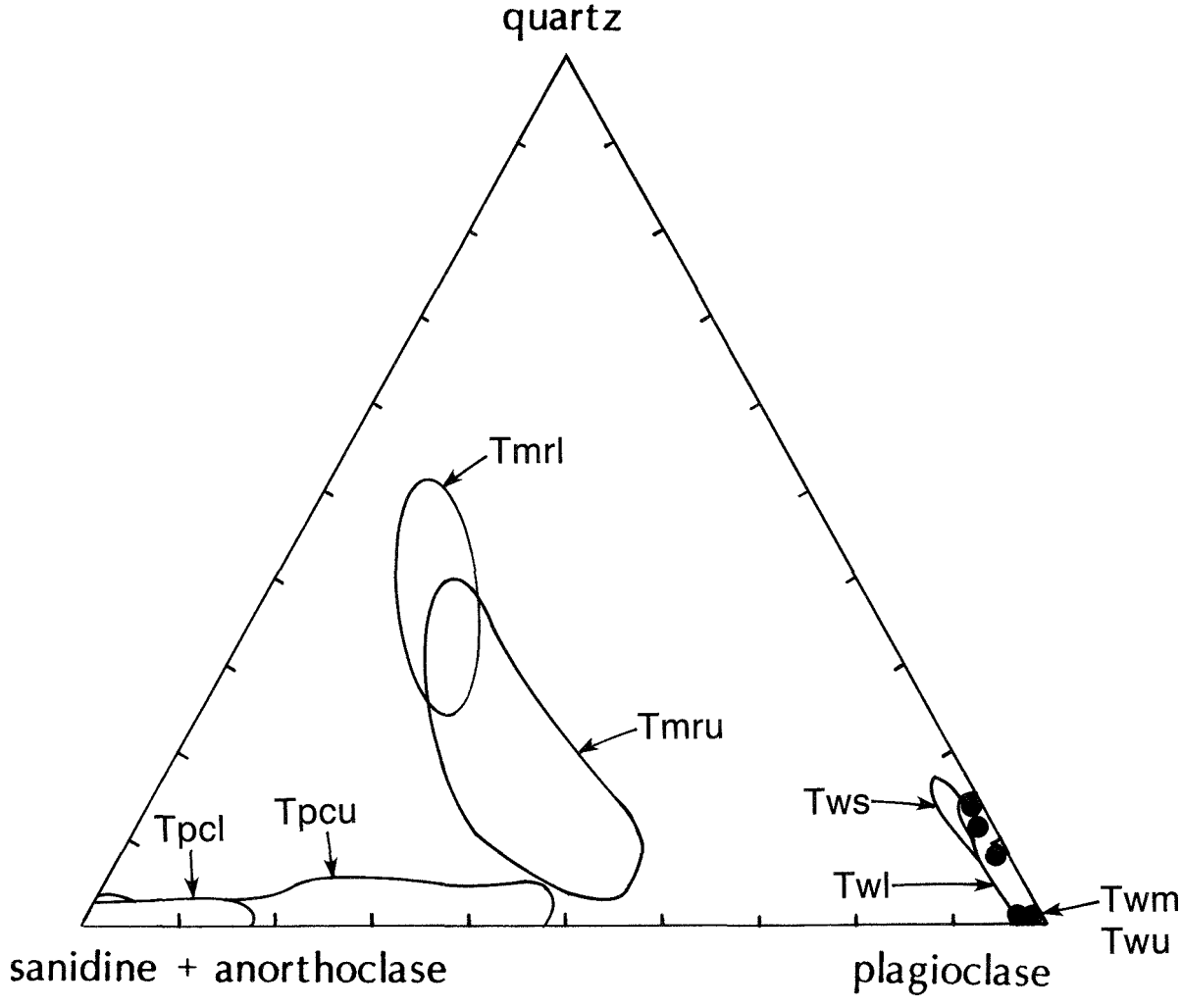

Figure 7.--Ternary diagram showing fields for relative felsic phenocryst contents of the Wahmonie (Tw), Tiva Canyon (Tpc), and Rainier Mesa (Tmr) tuffs. Units of the Wahmonie tuff are upper (Twu), middle (Twm), lower (Twl), and Salyer (Tws). Relative contents for seven samples of Wahmonie tuff from Yucca Flat are plotted individually; three points at plagioclase = 100% overprint. Data sources as in Figure 6.

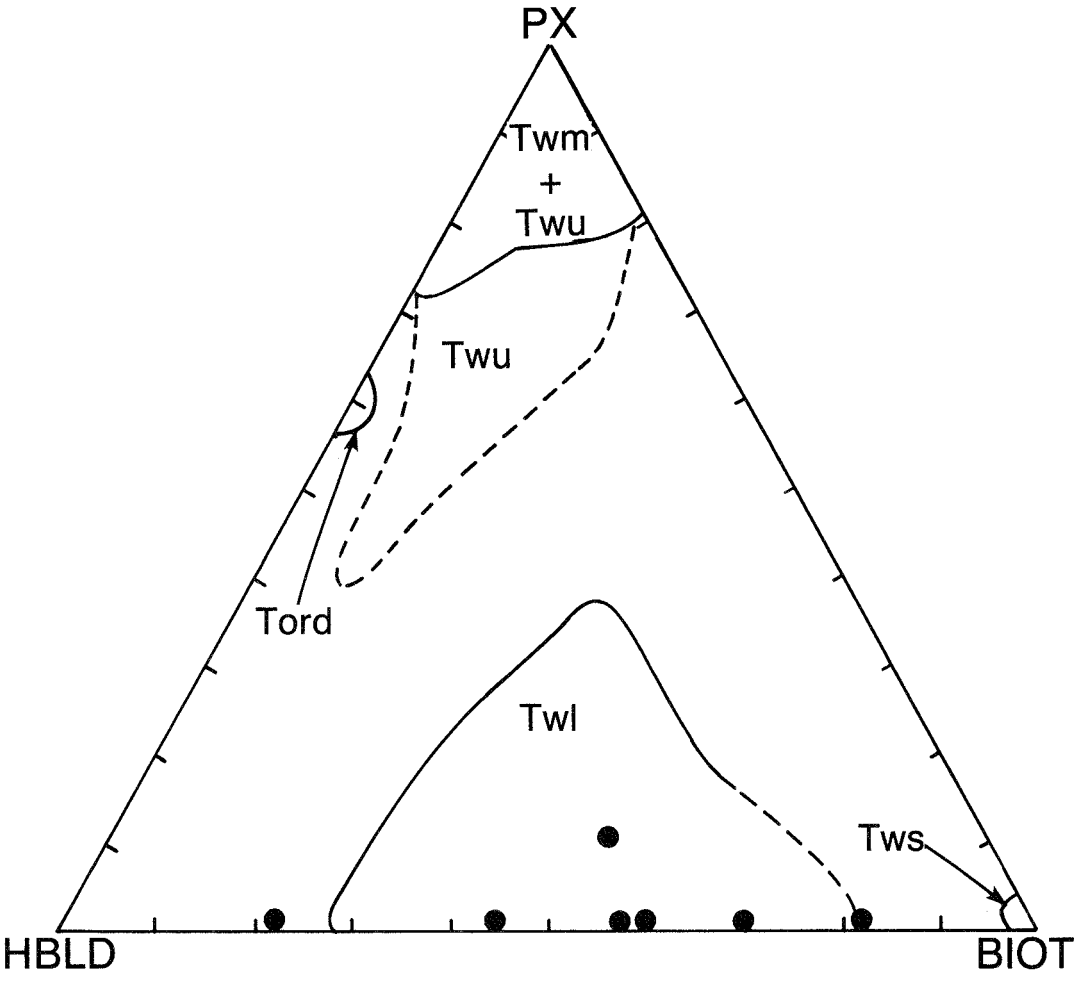

Figure 8.--Ternary diagram showing fields for relative mafic phenocryst contents of the Wahmonie tuff. Units of the Wahmonie tuff are upper (Twu), middle (Twm), lower (Twl), and Salyer (Tws). Relative contents for seven samples of Wahmonie tuff from Yucca Flat are plotted individually. For comparison, values from Warren et al. (1984) are also plotted for the plagioclase-rich flow breccia of USW G-1 (symbol Tord). Data for Wahmonie tuff and lava from R. G. Warren and D. E. Broxton (unpublished).

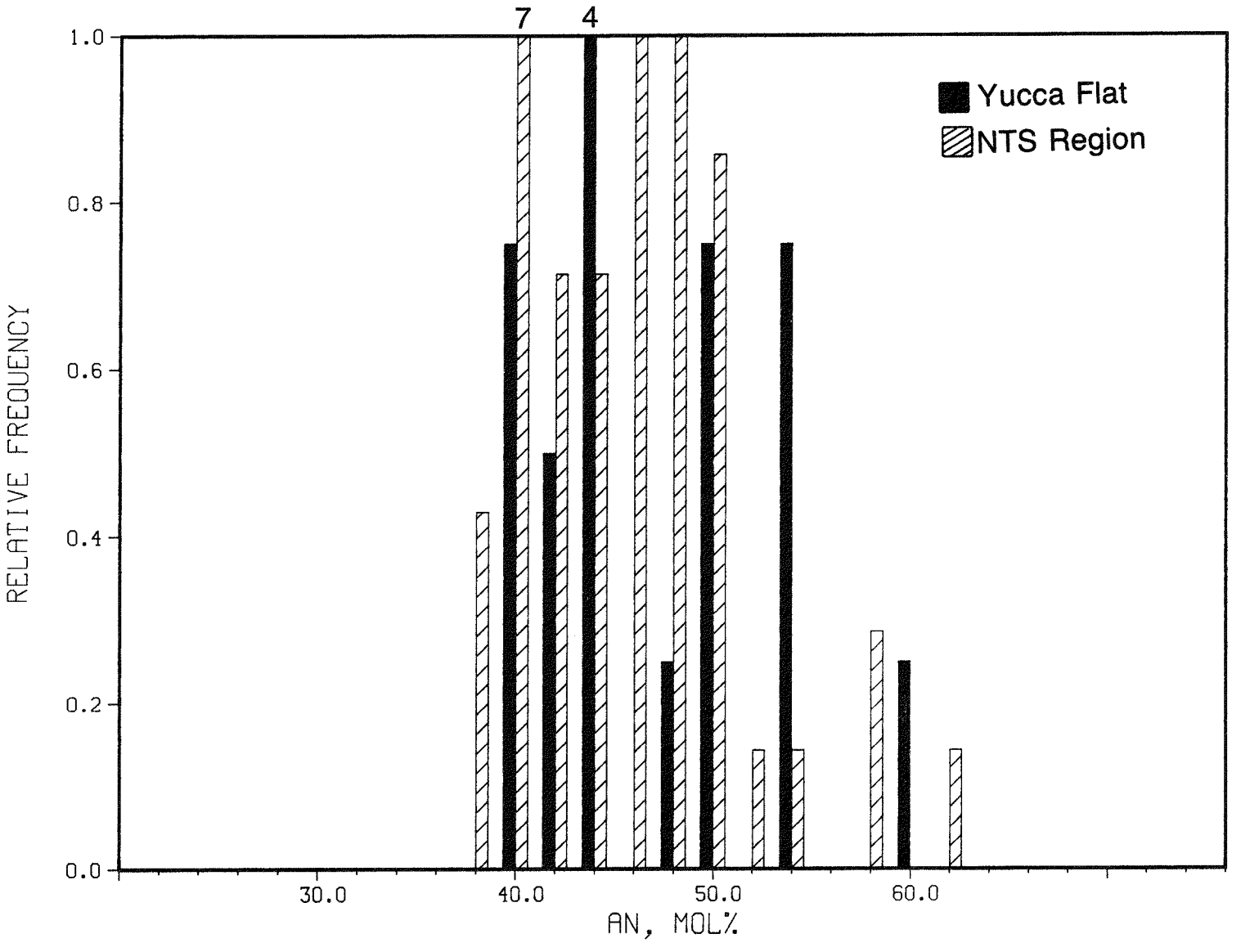

Figure 9.--Histogram comparing compositions of plagioclase in samples of Wahmonie tuff. Composition is for lower limit of bin; solid bars for Yucca Flat are left of this number, and cross-hatched bars for NTS region are right. Frequencies are scaled to maximum frequencies, shown at the top of the diagram. Data sources as in Figure 8.

correlations to be made with high confidence. Sanidine compositions for the Calico Hills tuff (Tac) and each member of the Crater Flat Tuff (Tc) for the NTS region are compared in Figure 10. Each unit has its own distinct sanidine composition. These histograms show excellent matches between samples of the Calico Hills tuff and Tram Member of the Crater Flat Tuff (Tct) from the subsurface of Yucca Flat and other samples from the NTS region.

Trace Elements

Whole-rock analyses for 45 elements by Automated Neutron Activation Analysis (ANAA) are routinely determined for NAA samples at LANL (Garcia et al., 1982). ANAA data for over 1000 samples from the NTS are available. Elements most valuable for stratigraphic assignments are Sc, Mn, Fe, Ba, La, Ce, Eu, Yb, Lu, Hf, and Th (Warren et al., 1985). The relative quantities of these elements are usually distinct enough to confidently assign a sample to a stratigraphic or petrologic zone. Depending upon variability factors of the particular element and geologic unit, one or more trace elements in agreement can produce significant confidence in a stratigraphic assignment. Sc values for samples from the Crater Flat formation and Calico Hills tuff are given in Figure 11. As with the sanidine chemistry, samples of Tram, Bullfrog and Calico Hills from the subsurface of Yucca Flat match quite well with Sc values for other samples of Tram, Bullfrog and Calico Hills in the NTS data base.

Trace element abundances in tuff are little affected by diagenetic alteration except for strontium, rubidium, and uranium (Broxton et al., 1986). Zeolitized rocks have extremely variable major-element chemistries. In these rocks there is significant mobilization and redistribution of Na, K, Ca, Mg, and Si during zeolitization. Thus, the trace element "fingerprint" may change little while the major element abundances undergo drastic changes.

IV. Results

A comprehensive set of samples from continuously cored exploratory holes in Yucca Flat representing bedded tuff units stratigraphically between the Grouse Canyon and the Rainier Mesa (Table 2) has been collected and analyzed. We have subdivided these tuffs, previously termed the "Paintbrush Tuff", into statigraphic units by applying the petrologic zone concept. By comparing our petrochemical data for Yucca Flat with regional data we recognize stratigraphic equivalence of Yucca Flat bedded tuff with formally recognized ash-flow tuffs and lava flows.

Within this stratigraphic interval, presently assigned entirely to the "Paintbrush Tuff", we find tuff from four well known formations defined within the region: the Crater Flat Tuff, Wahmonie tuff, Area 20 tuff, and the Paintbrush Tuff, in ascending order (Table 2). We also recognize an additional group of units immediately beneath the Rainier Mesa ash-flow tuff. These correlate with the Transition petrologic assemblage of Warren and Byers (manuscript in preparation), and we term them the Transition tuff. We also recognize individual units or members comprising each of these formations. Thus, a composite stratigraphic column is established (Table 2). With few exceptions, this column is identical to that established for Pahute Mesa (Table 3). With additional work, we expect that the correspondence in Table 3 will be exact.

Our preliminary stratigraphic column for pre-Tmr, post-Tbg units is based on the

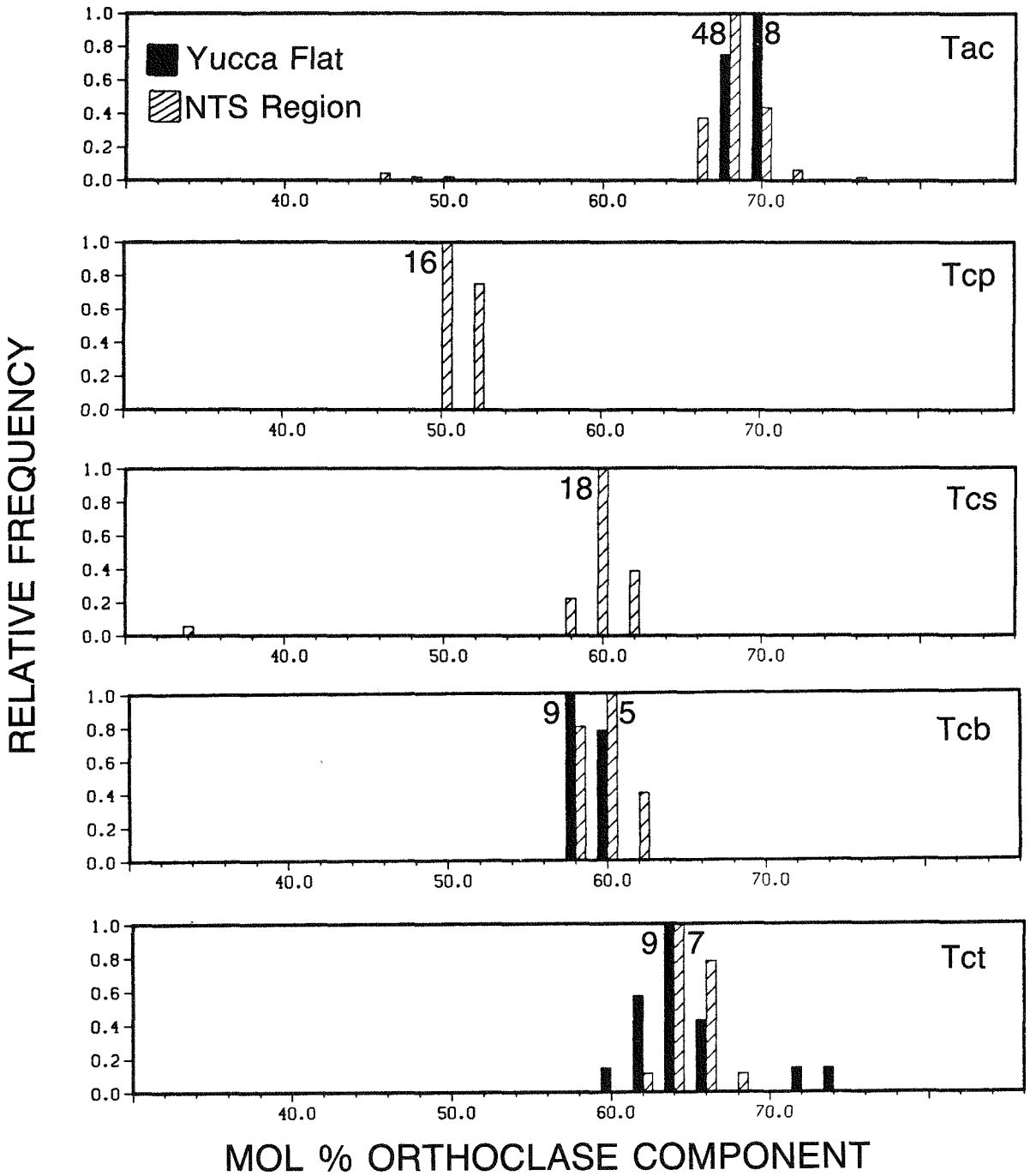

Figure 10.--Histograms comparing compositions of sanidine in samples of Area 20 (Ta) and Crater Flat (Tc) tuffs. Symbols for individual units are in Table 1. Histograms are constructed similar to Figure 9. Data from R. G. Warren (unpublished) for Yucca Flat, and from Broxton et at. (1982) for NTS region.

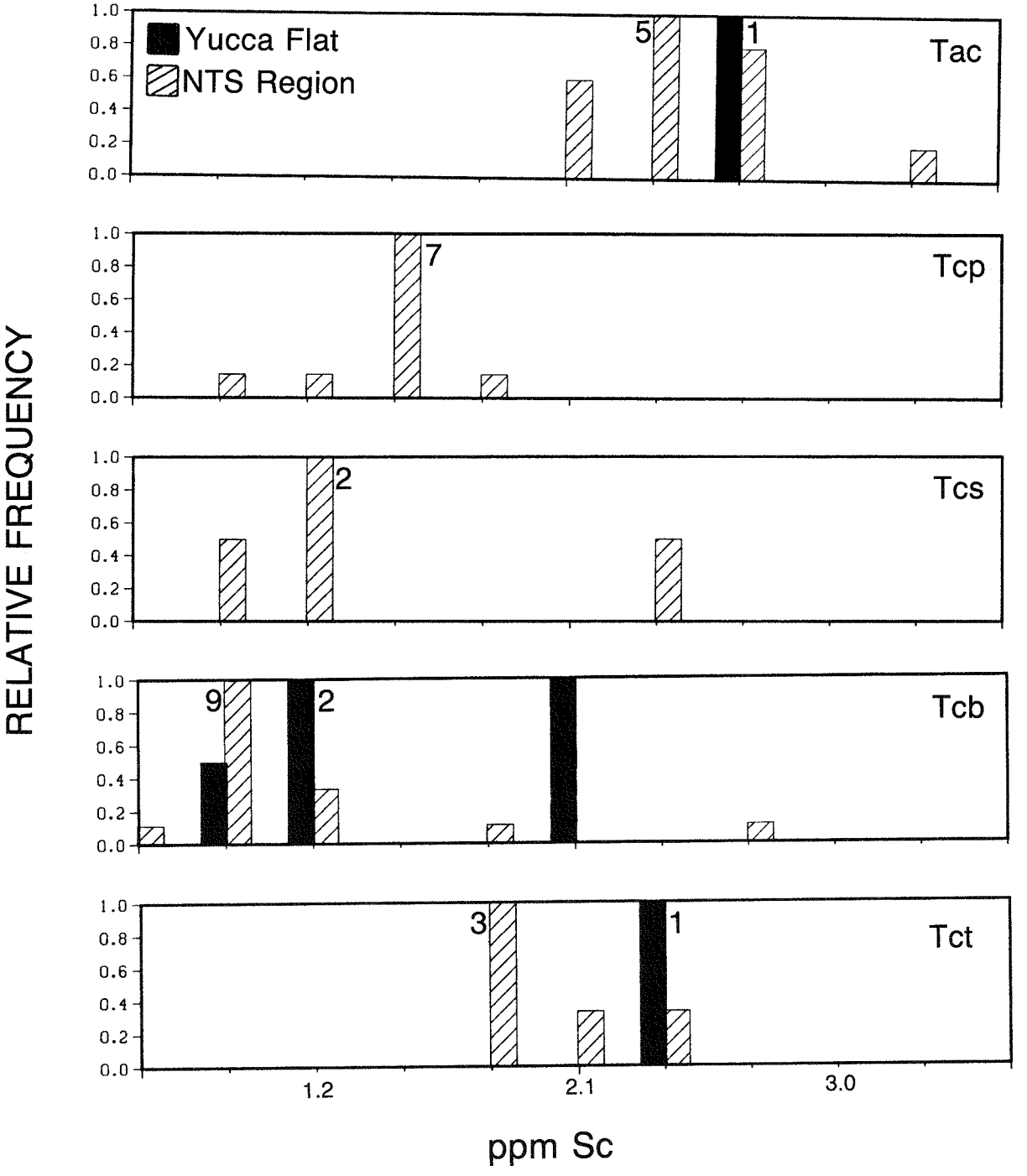

Figure 11.--Histograms comparing whole-rock scandium for samples of Area 20 (Ta) and Crater Flat (Tc) tuffs. Symbols for individual units are in Table 1. Histograms are constructed similar to Figure 9. Data from R. G. Warren (unpublished).

Table 2.--Pre-Rainier Mesa, Post-Grouse Canyon
Stratigraphic Column For Yucca Flat, NTS

Old System		New System	
Unit		Unit	Formation
Rainier Mesa Member		Rainier Mesa Member	Timber Mountain Tuff
Paintbrush Tuff		Pre-Rainier Mesa tuff	Transition tuff
		Quartz-Bearing tuff	
		Windy Wash tuff	
		Pool tuff	
		Tiva Canyon Member	Paintbrush Tuff
		Hornblende-Bearing tuff	
		Topopah Spring Member	
		Calico Hills tuff	Area 20 tuff
Paintbrush Tuff (mafic-rich zone)		Wahmonie tuff (Lower)	Wahmonie tuff
Paintbrush Tuff		Prow Pass Member	Crater Flat Tuff
		Bullfrog Member	
		Tram Member	
		Lower tuff	
Grouse Canyon Member		Grouse Canyon Member	Belted Range Tuff
Unit 4		Unit 4	Tunnel beds

Table 3.--Comparison of Stratigraphic Columns for Yucca Flat and Pahute Mesa

Yucca Flat			Pahute Mesa	
Lithology	Unit		Unit[a]	Lithology
Bedded	Pre-Rainier Mesa tuff		Pre-Rainier Mesa	Bedded
Bedded	Windy Wash tuff		Windy Wash	Lava
Bedded	Pool tuff		Pool tuff	Ash-flow/bedded
Bedded	Quartz-Bearing tuff		Quartz-Bearing Rhyolite	Lava/bedded
Bedded Ash-Flow	Tiva Canyon Member		Tiva Canyon	Ash-flow
Bedded	Hornblende-Bearing tuff		Hornblende-Bearing Rhyolite	Lava/bedded
			Pyroxene-Bearing Rhyolite	Lava/ash-flow
Bedded/ Ash-Flow	Topopah Spring Member		Topopah Spring	Ash-Flow
Bedded	Calico Hills tuff		Calico Hills	Lava/Bedded/ ash-flow
Bedded	Wahmonie tuff		Plagioclase-rich	Lava
Bedded	Prow Pass Member		Prow Pass (Upper & Lower)	Ash-Flow/ Lava/bedded
Bedded/ Ash-Flow	Bullfrog Member		Stockade Wash	Ash-Flow/bedded
Bedded	Tram Member		Tram	bedded
Bedded	Lower tuff			

[a]Petrologic zones of Warren et al. (1985).

same criteria used to define formal units of the region (Byers et al., 1976). Although we employ petrochemical methods to define each unit, such methods are far too time-consuming for practical routine application. However, just as formal units are defined by their petrochemical character, but recognized from their hand sample (field) characteristics, we define hand sample identification criteria (Table 4) for our informally defined pre-Tmr, post-Tbg statigraphic sequence (Table 5). We have found that hand sample methods alone generally suffice to distinguish units or formations within this stratigraphic interval. When assignments have been doubtful from hand sample inspection, simple grain-mount petrography has proven highly effective for certain stratigraphic assignments.

Although we employed the petrologic zone concept to establish the stratigraphic sequence, we define the pre-Tmr, post-Tbg statigraphic sequence as litho-stratigraphic units, like formal units of the region (Byers et al., 1976). Thus, our informal Tiva Canyon bedded tuff of the Paintbrush tuff is separate from the Tiva Canyon Member of the Paintbrush Tuff, although the unit nomenclature implies an obvious genetic relationship between the two. These two units are considered as different lithofacies of the same unit in the petrologic zone system. We prefer a lithostratigraphic stratigraphy within Yucca Flat because it is a familiar system, and because rhyolitic lavas do not occur within Yucca Flat. Rhyolitic lavas are associated with extreme facies changes, making the petrologic zone stratigraphic system far more useful at Pahute Mesa.

We identify several outstanding stratigraphic problems within the pre-Tmr, post-Tbg seqence for future resolution. The Transition tuff, a sequence of bedded tuff units between the Paintbrush Tuff and the Rainier Mesa ash-flow tuff has only recently been recognized and defined in Yucca Flat. Details of their chemical and petrographic characteristics as well as their overall distribution could be improved upon. Continued investigation of these units will contribute to a better understanding of the magma evolution and magma mixing exhibited in this sequence.

The exact relationship of the Bullfrog Member of the Crater Flat Tuff and the Stockade Wash tuff (Tcs) is unknown for Yucca Flat. In early work, the ash-flow tuff in Yucca Flat between the Wahmonie and the Grouse Canyon Tuffs was correlated with the Stockade Wash tuff of Byers et al. (1976). The Yucca Flat Tuff (Tyf) was erroneously correlated with the petrographically similar Bullfrog. However, the Yucca Flat Tuff is now recognized as being older and has been given a separate formational status. So, the question is now open, could the Stockade Wash Tuff in southern Yucca Flat be equivalent to the Bullfrog? They are very similar petrographically and extremely similar in age (Warren, 1983). Petrographically, the Stockade Wash ash-flow tuff from Area 6 falls between the Bullfrog and Stockade Wash (Figure 12). Mineral chemistry and some fieldwork will be necessary to resolve this question. For the present time, we assign the post-Tbg ash flow beneath the Wahmonie tuff to the Bullfrog.

We have recognized an additional complex bedded and ash-flow tuff unit beneath the Tram. We assign this new unit to the Crater Flat formation as the Lower tuff. The contact between the Lower tuff and the underlying Grouse Canyon Member is gradational. In UE-7f this contact lies within a welded zone. This indicates a strong magmatic relationship between the earliest Crater Flat (calc-alkaline) and latest Belted Range (peralkaline) magmas. This complex relationship may explain common difficulties defining the exact stratigraphic location for the top

Table 4.--Hand Sample Identification Criteria

Lithology
- Bedded Tuff
  - Air-Fall Tuff
  - Reworked Tuff
- Ash-Flow Tuff
  - Degree of welding
- Lava Flow

Phenocrysts Content
- Felsic Phenocrysts
  - Quartz
  - Sanidine
  - Plagioclase
- Mafic Minerals
  - Biotite
  - Hornblende
  - Pyroxene
  - Orthopyroxene
- Accessory Minerals
  - Sphene
  - Others
- Oxides
  - Magnetite

Stratigraphic Sequence

Color

Lithic Fragment Lithologies

Crystallinity
- Vitric
- Devitrified

Alteration
- Zeolitization
- Argillization
- Silicification

Table 5.--Unit Characteristics and Sample Identification Criteria for pre-Tmr, post-Tbg Units of Yucca Flat

Stratigraphic Unit			Lithology For Yucca Flat	Typical Felsic Phenocrysts as Percentage of Total Phenocrysts	
Formation	Member or Unit	Symbol		Quartz/K-Spar/Plagioclase	Mafic Minerals/Trace Elements
Timber Mountain Tuff	Pre-Rainier Mesa tuff	Tmpr	Bedded Tuff	40/25/35	rare biotite No sphene
Transition tuff	Pool tuff	Tnp	Bedded Tuff	20/35/45	Cpx, hbld, opx >> biotite; rare to common sphene; high Cr, Co (transition elements)
Transition tuff	Windy Wash tuff	Tnww	Bedded Tuff	20/60/20	biotite > hbld. common sphene
Paintbrush Tuff	Tiva Canyon tuff [Member]	Tpc	Bedded Tuff [ash-flow]	0/95/5 to 0/50/50 in mafic rich zone	Hbld Cpx, biotite in M.R. zone
Paintbrush Tuff	Hornblende-Bearing tuff	Tphr	Bedded Tuff	10/65/25	rare biotite plus hbld >> cpx; common sphene
Paintbrush Tuff	Clinopyroxene-Bearing tuff	Tppr[a]	Bedded Tuff	0/65/35	rare to common Biotite >> cpx; abundant sphene
Paintbrush Tuff	Pah Canyon tuff	Tpp[b]	Bedded Tuff	0/50/50	Common biotite, rare cpx and sphene
Paintbrush Tuff	Pre-Pah Canyon tuff	Tpr[b]	Bedded Tuff	0/40/60	Common to abundant biotite; No sphene
Paintbrush Tuff	Topopah Spring tuff [Member]	Tpt	Bedded [ash-flow]	0/70/30 (pheno. rich top) 10/30/60 (pheno. poor bottom)	Biotite > cpx > hbld; No sphene Lt. & Dk pumices
Area 20 tuff	Calico Hills tuff	Tac	Bedded Tuff	40/40/20	mafic-poor; reverse zoned (mafic-rich at base). Pumice & lithic-rich airfalls are common.
Wahmonie tuff	Wahmonie tuff	Tw	Bedded	5/0/95	mafic-rich bio, hbld>>opx, cpx

Table 5--Unit Characteristics and Sample Identification Criteria (cont.)

Stratigraphic Unit		Symbol	Lithology For Yucca Flat	Typical Felsic Phenocrysts as Percentage of Total Phenocrysts Quartz/K-Spar/Plagioclase	Mafic Minerals/Trace Elements
Formation	Member or Unit				
Crater Flat Tuff	Prow Pass tuff	Tcp	Bedded	15/40/45	rootbeer colored altered orthopyroxene; less biotite than Tcb.
Crater Flat Tuff	Stockade Wash tuff	Tcs[c]	Ash-Flow	20/60/20	rare to common biotite; rare hbld
Crater Flat Tuff	Bullfrog tuff [Member]	Tcb	Bedded Tuff [Ash-Flow]	20/40/40 0/50/50 at mafic-rich top	common biotite; conspicuous hornblende; biotite in pumice
Crater Flat Tuff	Tram tuff	Tct	Bedded Tuff	25/35/40 Feldspar are more Na-poor than Tcb	Common biotite; hornblende and cpx generally absent.
Crater Flat Tuff	Lower tuff	Tcl	Bedded Tuff	10/50/40 Low proportion of Qtz.	High mafic content; Hbld is conspicuous; clinopyroxene evident near top; cpx in pumice; reddish tunnel bed-like color. "Upper-buff"

[a]Not presently recognized in Yucca Flat.

[b]Sample UE-6d#2-327.0m is bedded tuff of Tpr (Chocolate Mountain type) or of Tpp. Also, samples in both UE-6d#2 and UE-7f correlate with transition unit between Tpr and Tpt units, described in Figure 6.

[c]We recognize Tcb in Yucca Flat, but the presence of Tcs has not been established. See discussion in text.

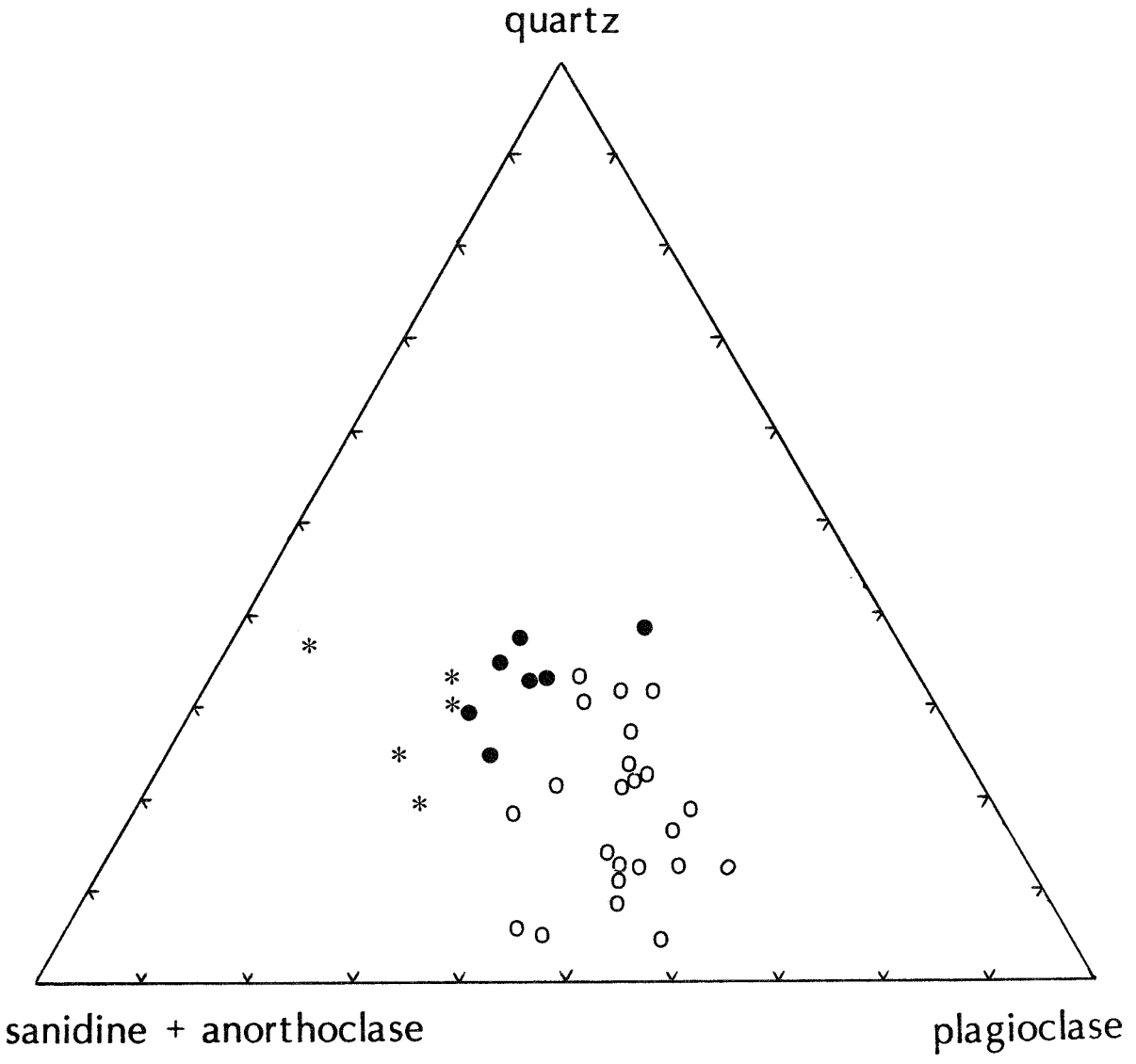

Figure 12.--Felsic phenocryst proportions for samples of Stockade Wash and Bullfrog petrologic zones. Data are from probe sections of Stockade Wash zone at or near Pahute Mesa (*), probe and glass-covered thin sections of Bullfrog zone from drill hole USW G-1 (o), and grain mounts of Bullfrog zone of Yucca Flat (●). Data for USW G-1 from Warren et al. (1984). All other data from R. G. Warren (unpublished).

of the Grouse Canyon member in many drill holes of Yucca Flat.

V. Application

The petrologic zone concept enables us to establish an unambiguous stratigraphic column of informal lithostratigraphic units for the pre-Tmr, post-Tbg interval in the subsurface of Yucca Flat. This sequence of mostly bedded tuffs is now known to have a simple and systematic stratigraphy similar to other areas within the NTS region. However, we recognize that routinely attempting to recognize every unit (i.e. Tnp, Tpc, Tphr, Tppr, etc) in Yucca Flat is well beyond our manpower resources. We suspect that these units are present at most locations in Yucca Flat as bedded tuffs, but some may be less than a meter thick. Often we could not account for every unit in our preliminary sampling. Subsequent and closer-spaced sampling programs revealed finer stratigraphic details; the units we found, or missed, were a function of our sampling programs. Recognition of such units in routine lithologic logging using cuttings and some sidewall samples would depend almost entirely on luck.

Due to these problems it is therefore more meaningful to correlate these units as groups (i.e. Tn, Tp, Ta, Tw and Tc). The ability to subdivide the post-Tbg, pre-Tmr tuffs into such groups for geologic site characterizations and general geologic problem solving should be more than satisfactory. In our routine work, where we are provided drill cuttings from 3 m (10′) intervals, our resolution is on the order of 3-6 m (10-20′). If necessary, individual units within each group can usually be identified in timely fashion by grain mount analysis (Figure 5). Thus, if greater stratigraphic detail is needed to better define a particular structural situation the methods and tools required are available and proven.

This stratigraphic system has made it possible to recognize additional "marker beds". Previously, the only consistently used marker bed within this interval was the "mafic-rich zone", which is the Wahmonie tuff of our stratigraphic column (Table 2). The stratigraphic location of quartz bearing units (Tn, Ta, Tc), previously a source of confusion, is now well understood. These units can now be recognized, distinguished from each other, and correlated.

From hand sample observation, we recognize normal zonation in the mafic mineral contents of each unit within the Crater Flat bedded tuffs immediately beneath the Wahmonie bedded tuff. On this basis, the Crater Flat formation can now be subdivided into several units, each with distinctive character. The Prow Pass tuff contains a low content of mafic minerals, and has highly distinctive rootbeer colored prismatic orthopyroxene, often in pseudomorphic form. The Bullfrog Member has common biotite and conspicuous hornblende. Biotite in the pumice, an obvious characteristic of the Bullfrog ash-flow, is also a characteristic of the Bullfrog bedded tuff lithology. The Lower Crater Flat (Tcl), an unrecognized unit until now is discernable by abundant mafic minerals, including both hornblende and pyroxene. These distinctive characteristics, and those for other pre-Tmr, post-Tbg units, are summarized in Table 5.

Many physical and mineralogical characteristics of these rocks manifest themselves as distinctive geophysical log responses. For example, a high mafic mineral content, particularly magnetite, produces a large response in the magnetic susceptibility log (Mathews et al., 1985). The total magnetic intensity log (or simply, the magnetometer log) will similarly reflect the mafic mineral content of bedded tuff formations via induced magnetism. These mafic-rich zones

also typically show a lower API reading on the natural gamma ray log. The mafic-rich Wahmonie tuff forms a familiar "W" signature on both the gamma ray and magnetometer logs and has long been used as a marker bed previously referred to as the "mafic-rich zone of the Paintbrush Tuff". Lithologic variations also affect resistivity and density logs which may be used in the future as our understanding of this sequence of tuffs grows. Responses in geophysical logs to mineralogical and lithological patterns in the Crater Flat Tuff are becoming discernable. A larger data base is necessary before we can confidently use these patterns as consistent correlative tools. However, we have gained valuable insight on how to use geophysical logs in conjunction with samples to help describe and correlate subsurface units.

The refined stratigraphic column will allow structure to be defined with greater confidence and precision as correlations between drill holes become easier and more accurate. Our detailed stratigraphic correlations have demonstrated substantial variations in thicknesses for individual units within the pre-Tmr, post-Tbg sequence of Yucca Flat. Figure 13, a schematic north-south cross-section along the eastern edge of Yucca Flat, shows how the presence of the Topopah Spring and Stockade Wash ash-flows greatly increases the composite thickness of the post-Tbg, pre-Tmr interval. The post-Wahmonie bedded tuffs thin considerably to the northeast. Widespread opal and calcite suggest this thinning in northeast Area 7 is due to erosion. Preliminary isopach maps of pre-Tmr, post-Tbg units not included here indicate that they will be useful in defining the early structural development of Yucca Flat.

VI. Summary and Conclusion

The post-Tbg, pre-Tmr tuffs represent a significant age span and thickness in the subsurface of Yucca Flat. This interval spans about 2.5 m.y., roughly between 14.1 Ma and 11.6 Ma., or 69% of major volcanic depositional history for Yucca Flat. With an aggregate thickness of 91.4 m (300′) to 295.7 m (970′), they can account for 15% to 40% of the total tuff sequence in the subsurface of Yucca Flat. This sequence of tuffs is important to containment because its position provides many of the nonalluvium WP depths in southern Yucca Flat.

The application of the petrologic zone concept enables us to confidently relate bedded tuffs in the Yucca Flat subsurface to formally recognized ash-flow tuffs and lavas found elsewhere in the NTS region. We have developed and demonstrated practical methods to identify and correlate units or groups of units. This detailed geochemical work has also contributed useful criteria for hand-sample analysis. The information developed in the course of this work enables the geologist to confidently make additional stratigraphic assignments without expensive and time-consuming analytical methods (i.e. microprobe, ANAA).

We have established a detailed stratigraphy for Yucca Flat similar to other regions at the NTS by petrochemical correlations. We have begun implementing this stratigraphic framework for LANL geologic work. It is, however, recognized that with continuing studies some details may be added or changed. We recommend routine subdivision, whenever possible, of post-Tbg, pre-Tmr tuffs in Yucca Flat, presently assigned entirely to the Paintbrush Tuff, into the lithostratigraphic units that we have defined.

Figure 13.--Schematic North-South Cross-Section Eastern Yucca Flat, NTS

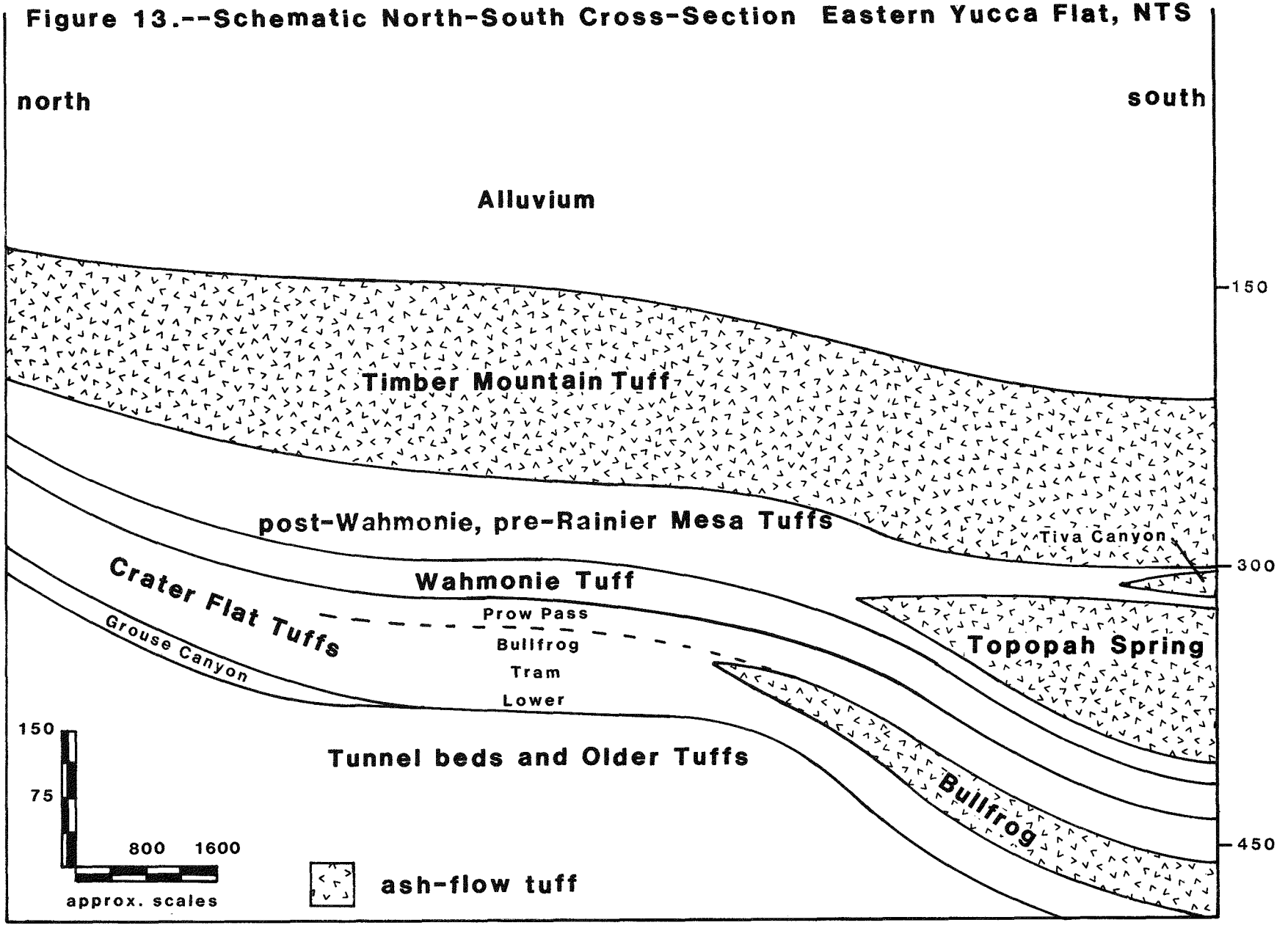

VII. Acknowledgements

This work is supported by the United States Department of Energy. The authors thank Anthony T. Garcia, Nancy L. Marusak and Susan H. Freeman for their assistance in preparing figures and tables, and Cindy Whittenburg for typing the manuscript.

REFERENCES

Broxton, D. E., Warren, R. G., Hagan, R. C., and Luedemann G., 1986, "Chemistry of Diagenetically Altered Tuffs at a Potential Nuclear Waste Repository, Yucca Mountain, Nye County, Nevada," Los Alamos National Laboratory report LA-10802-MS, 160 pp.

Broxton, D. E., Vaniman, D. T., Caporuscio, F. A., Arney, B. H., and Heiken, G. H., 1982, "Detailed Petrographic and Microprobe Data for Drill Holes USW G-2 and UE-25b-1H, Yucca Mountain, Nevada," Los Alamos National Laboratory report LA-9234-MS, 168 pp.

Byers, F. M., Jr., Carr, W. J., Orkild, P. P., Quinlivan, W. D., and Sargent, K. A., 1976, "Volcanic Suites and Related Cauldrons of Timber Mountain-Oasis Valley Caldera Complex, Southern Nevada," U. S. Geological Survey Professional Paper 919, 70 pp.

Carr, W. J., Byers, F. M., Jr., and Orkild, P. P., 1986, "Stratigraphic and Volcano-Tectonic Relations of Crater Flat Tuff and Some Older Volcanic Units, Nye County, Nevada," U. S. Geological Survey Professional Paper 1323, 42 pp.

Carr, W. J., 1984, "Regional Structural Setting of Yucca Mountain, Southwestern Nevada, and Late Cenozoic Rates of Tectoic Activity in Part of the Southwestern Great Basin, Nevada and California," U. S. Geol. Surv. Open-File Report 84-854, 109 pp.

Dalrymple, G. B., 1979, "Critical tables for conversion of K-Ar ages from old to new constants," Geology, Vol. 7, p.p. 558-560.

Drellack, S. L., Jr., and Cavazos, A. P., 1987, "Selected Stratigraphic Contacts for Drill Holes in LANL-Use Areas of Yucca Flat, NTS," Fenix & Scisson, Inc. report DOE/NV/10322-26, 44 pp.

Ekren, E. B., and Sargent, K. A., 1965, Geologic Map of the Skull Mountain Quadrangle, Nye County, Nevada," U. S. Geol. Survey Map GQ-387, Scale 1:24,000.

Garcia, S. R., Hensley, W. K., Minor, M. M., Denton, M. M., and Fuka, M. A., 1982 "An Automated Multidetector System for Instrumental Neutron Activation Analysis of Geological and Environmental Materials," Atomic and Nuclear Methods in Fossil Energy Research, R. H. Filby, B. S. Carpenter, and R. C. Ragaini, Eds., Plenum Press, New York, p.p. 133-140.

Kistler, R. W., 1968, "Potassium-argon ages of volcanic rocks in Nye and Esmeralda Counties, Nevada, in Nevada Test Site" Geol. Soc. America Mem. 110, p.p. 251-262.

Marvin, R. F., Byers, F. M., Jr., Mehnert, H. H., Orkild, P. P., and Stern, T. W., 1970, "Radiometric ages and stratigraphic sequence of volcanic and plutonic rocks, southern Nye and western Lincoln Counties, Nevada" Geol. Soc. America Bull., vol. 81, p.p. 2657-2676.

Mathews, M. A., Warren, R. G., and Taylor, K. A., 1985, "Investigation of Magnetic Susceptibility Logs Acquired in Satellite Holes in Areas 7 and 19," Proceedings, Third Symposium on Containment of Underground Nuclear Explosions, Idaho Operations Office of the DOE, Idaho Falls, Idaho September 9-13, Lawrence Livermore National Laboratory CONF-850953, Vol. 2, Clifford W. Olsen, Scientific Editor, p.p. 99-116.

Poole, F. G., Carr, W. J., and Elston, D. P., 1965, "Salyer-Wahmonie Formation of Southeast Nye County, Nevada," in Changes in Stratigraphic Nomenclature by the U. S. Geological Survey 1964, U. S. Geol. Survey Bull. 1224-A, G. V. Cohee and W. S. West, Editors, pp. A36-A44.

Quinivan, W. D., and Byers, F. M., 1977, "Chemical Data and Variation Diagrams of Igneous Rocks from the Timber Mountain-Oasis Valley Caldera Complex, Southern Nevada," US Geological Survey open-file report 77-724, 9 pp.

Scott, R., and Castellanos, M., 1984, "Preliminary Report on the Geologic Character of the Drill Hole USW GU-3 and USW G-3," U. S. Geological Survey Open-File report 84-491, 121 pp.

Warren, R. G., Byers, F. M., Jr., and Caporuscio, F. A., 1984, "Petrography and Mineral Chemistry of Units of the Topopah Spring, Calico Hills, and Crater Flat Tuffs, and Older Volcanic Units, with Emphasis on Samples from Drill Hole USW G-1, Yucca Mountain, Nevada Test Site," Los Alamos National Laboratory Report LA-10003-MS, 78 pp.

Warren, R. G., Byers, F. M., Jr., and Orkild, P. P., 1985, "Post-Silent Canyon Caldera Structural Setting for Pahute Mesa," Proceedings, Third Symposium on Containment of Underground Nuclear Explosions, Idaho Operations Office of the DOE, Idaho Falls, Idaho, September 9-13, Lawrence Livermore National Laboratory CONF-850953, Vol. 2, Clifford W. Olsen, Scientific Editor, p.p. 3-30.

Warren, R. G., 1983, "Geochemical Similarities between Volcanic Units at Yucca Mountain and Pahute Mesa: Evidence for a Common Magmatic Origin for Volcanic Sequences that Flank the Timber Mountain Caldera," Proceedings, Second Symposium on Containment of Underground Nuclear Explosions, Kirtland AFB, Albuquerque, NM, August 2-4, Lawrence Livermore National Laboratory CONF-830882, Vol. 1, Clifford W. Olsen, Compiler, p.p. 213-244.

PRE- AND POST-EVENT ELEVATION AND HORIZONTAL SURVEYS ACROSS THE YUCCA AND TOPGALLANT FAULTS, NEVADA TEST SITE

Don Krier
Frederick N. App
Lorraine Medina

Los Alamos National Laboratory

ABSTRACT

Three survey lines each were run across surface expressions of the Yucca and Topgallant faults in conjunction with the two nearby underground nuclear tests KINIBITO and GLENCOE. Survey data included both pre- and post-event elevations and horizontal displacements. Post-event, the faults are marked by an abrupt elevation loss of 24 to 48 cm superimposed on a background of general subsidence caused by spall compaction. The elevation loss recovers quickly to background spall compaction values over only short distances away from the surface trace. Both faults have slight elevation gains of their western (upthrown) block. Horizontal displacements were less indicative of fault movement, but the faults are marked by changes in azimuth of displacement. A net north to northeast movement of the survey area around KINIBITO and a net southward movement of the area around GLENCOE is recorded in the data. Several centimeters of right lateral motion may be indicated for the Topgallant fault; the Yucca fault data is more ambiguous. The elevation data show that relative block motion played only a minor role in the losses recorded across both faults. The similar magnitudes of elevation loss across the faults indicate that differential compaction of the thicker alluvial sections on the downthrown blocks was not a measureable result from either of these events. The rapid recovery of elevation to background values near the fault trace suggests that shock compaction is crushing the weaker alluvium adjacent to the tuff beds at depth where the units are juxtaposed by fault geometry. This decrease in pore space could result in the enhanced subsidence along the surface trace of the faults that is observed consistently in the surveys.

I. INTRODUCTION

In a continuing effort to study permanent ground displacement induced by underground nuclear testing at Yucca Flat, Nevada Test Site (NTS), Los Alamos National Laboratory sponsored pre- and post-event elevation and horizontal surveys in the vicinity of two intermediate yield tests: KINIBITO in drill hole U3me, and GLENCOE in U4i. These surveys were designed to describe the amount and geometry of motion across two major faults, the Yucca fault and the Topgallant fault, near the respective events and to provide evidence for general subsidence of the area outside the actual subsidence crater. Our concern with containment of underground tests lies (1) in the reduction of horizontal *in situ* stress, and its effect on a residual stress field surrounding an explosion cavity, which may result from differential compaction of geologic media by passage of a stress wave across a buried fault scarp and (2) in determining the amount, if any, of relative motion across a fault plane, produced by a nearby test, as manifested at the surface.

A study of the effects of differential compaction around the CARPETBAG event was performed by Rambo et al. (1983). In a study similar to the present one, App (1985) discussed pre- and post-event elevation differences across several buried faults in the eastern portion of Yucca Flat. He concluded that relative block motion, including rotation, could account for the observed surface displacements. Surface cracks produced by the events, which were field mapped immediately after execution, may or may not delineate zones of increased subsidence where accurate survey data may show dramatic elevation loss or, in some cases, gain. There was no unambiguous evidence for differential compaction across the faults in the study.

We hope this paper, which is descriptive in nature, adds constraints to computational approaches to the problems of subsidence near an underground test and to subsidence of Yucca Flat in general. The data from these surveys are available on paper or 3.5-inch floppy disk from the authors.

Techniques

Three survey lines were run at each of two event sites. The lines were oriented east-west and varied in length from 609.6m to 1218.6 m depending on their location relative to the expected surface collapse of the event in question. Small variations along the east-west trend were necessitated by a few cultural features, including a non- collapsed event site east of KINIBITO. Vertical and horizontal stations were established at 15.2 m intervals. The surveys were run by Holmes and Narver, Inc.

All of the surveys were second-order, requiring that a survey loop had to tie to a base station within 0.035 X (# miles traversed) ft. The base stations were located outside the expected spall radius of either event so that changes could be measured as accurately as possible. Vertical and horizontal angles were measured with a Hewlett-Packard 3820-A electronic surveying instrument, and elevations were read to the nearest 3 mm on a Wild NA-2 level. Field mapping of surface effects from the two events was done by the Los Alamos Geologic Support Group of Fenix and Scisson, Inc., Mercury, NV. Furthermore, each survey station was field checked after the surveys to determine any influence of roads, cableways, etc., on the data.

II. SURVEY RESULTS FROM THE YUCCA FAULT NEAR THE KINIBITO EVENT

General Statement

KINIBITO's relation to the survey lines and Yucca fault trace, and the geologic interpretation of the area, are shown in Figure 1. Three survey lines were run prior to and after the KINIBITO detonation. They run west to east along Nevada State Plane Coordinates N. 255,300 m, N. 255,718 m, and N. 255,941 m with only minor deviations as illustrated. Each survey line crosses the surface trace of the Yucca fault; closest approach from surface ground zero (SGZ) to the fault scarp is 274.3 m. Parts of each line were within the spall radius of events fired within the last seven years, except perhaps Line 1. This fact appears to have made no substantive difference to survey results. All of the survey lines were within the spall radius of KINIBITO. The KINIBITO device had a yield between 20 and 150 kt and was buried at 579 m depth. The working point medium was tuff beneath the water table on the west (upthrown) side of the fault. The stratigraphy overlying the working point includes 122 m of zeolitized bedded Paintbrush Tuff, 216 m of non- to densely welded Timber Mountain Tuff, and 241 m of tuffaceous alluvium.

The Yucca fault is an east-dipping, oblique-slip fault which extends nearly the length of Yucca Flat. Together with its presumed northern extension it can be traced 40 km (Barosh, 1968). It is the major structural feature observed at the surface in Yucca Flat and is a consideration when siting prospective underground tests. Near the survey lines at KINIBITO, the Yucca fault forms a weathered east-facing scarp with an elevation change of about 1.8-4.0 m down to the east over a 45 to 120 m distance. The grade is consistently 3-4%. At depth, the Yucca fault position is defined by drill hole data and surface gravity measurements which are used to estimate the thickness of the Cenozoic-age rocks above the Paleozoic carbonates and siltstones. The fault appears to dip eastward 75 degrees. The stratigraphic separation at the alluvium/tuff contact is about 285 to 375 m based on drill hole data and seismic interpretation. This results in an alluvium thickness of perhaps 200 m west of the fault and 500 m east of the fault at this locality. The width of the fault "zone" on Figure 1 is based on the combination of seismic evidence and the width of the zone of most intense surface fractures from underground tests. The KINIBITO working point was separated from the fault by approximately 420 m; distance from working point to surface scarp was about 650 m.

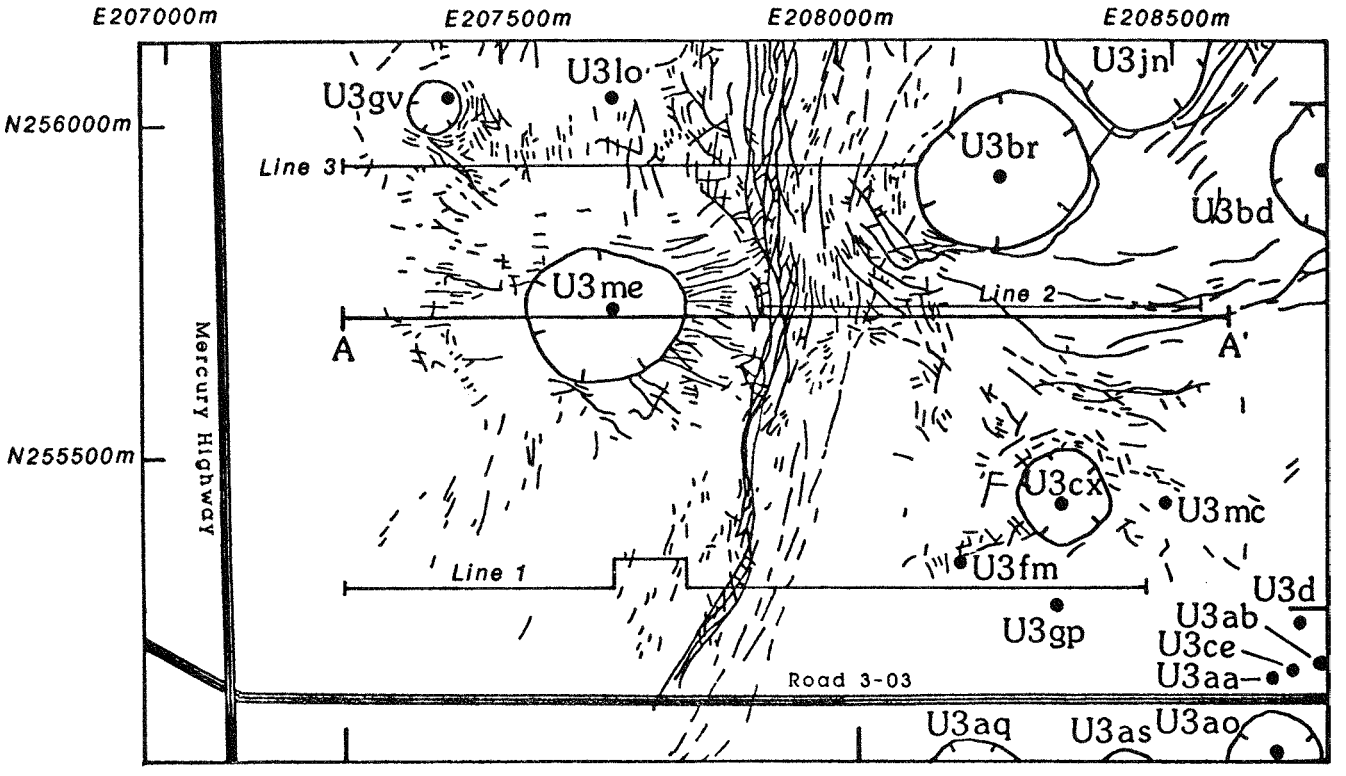

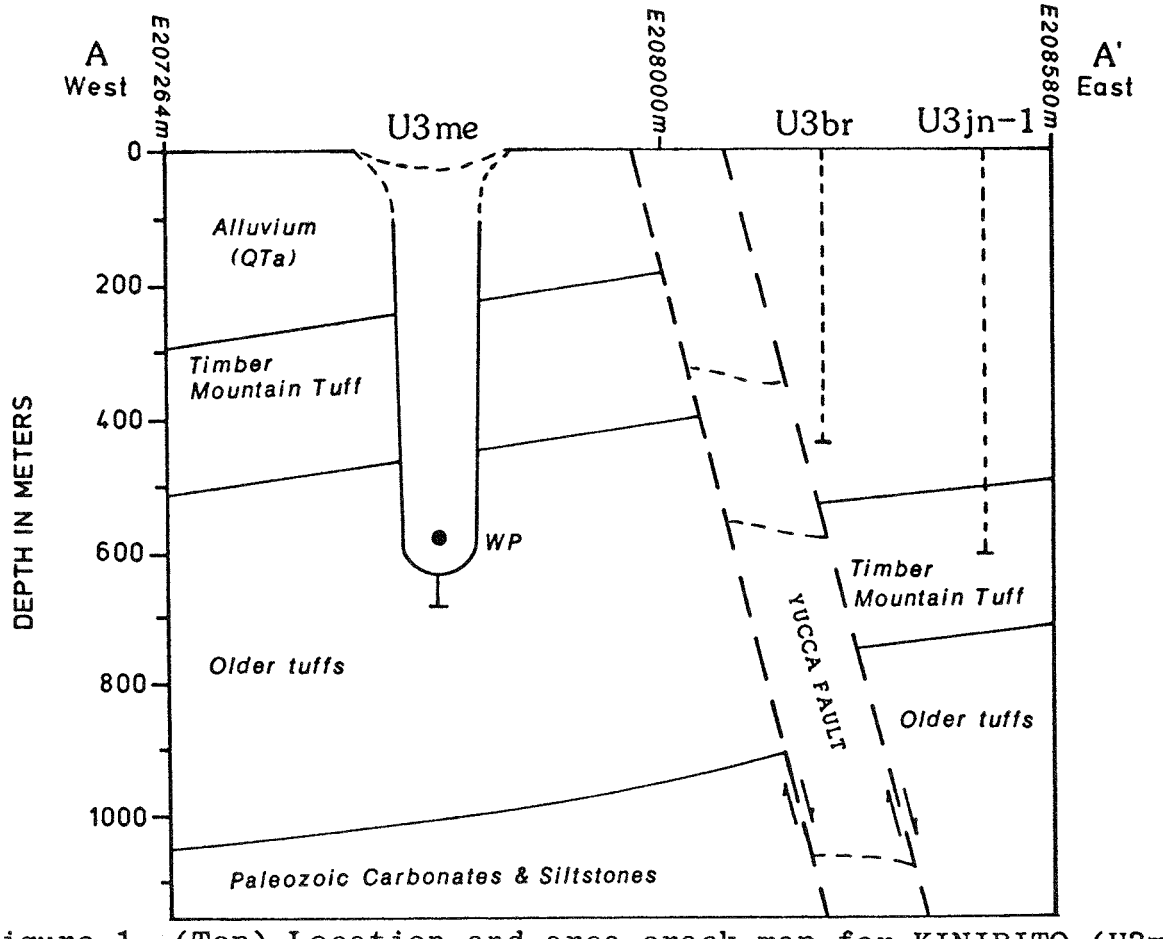

Figure 1. (Top) Location and area crack map for KINIBITO (U3me). Lines 1, 2, and 3 are survey lines. Line A-A' is cross-section line. (Bottom) Geologic cross section A-A'.

Results

Results of the surveys and the differences between pre- and post-event elevations are shown in Figures 2, 3, and 4. The top of each figure shows elevations along each line at a vertical exaggeration of 90:1. The bottom graphs the difference in elevation of each station after event execution. Line 1 (Fig. 2) shows a consistent elevation loss of 14 cm west of the fault. Elevation loss decreases to zero within 30 m of the surface scarp and an elevation gain of 7.6 cm marks the edge of the scarp. The fault trace is defined as the abrupt elevation loss of 22.5 cm. East of the fault, elevation loss quickly decreases, but is still 5.8 cm at the east end of Line 1, 792 m east of SGZ. A slight increase in elevation loss at E. 208,180 m may be recording a sagging of the surface around the uncollapsed event in hole U3fm.

Line 2 (Fig. 3) begins at the Yucca fault scarp. The survey records a 25 to 14 cm elevation change on the downthrown block. East of the scarp, an elevation loss of nearly 36 cm is recorded. Another loss of 30 cm appears at about E. 208,060 m, east of the fault trace, which coincides with the width of faulting shown in Figure 1. Elevation change decreases to 4.0 cm at E. 208,260 m, 598 m east of SGZ, but shows no sign of complete recovery in the spalled area covered by the survey.

Line 3 shows similar character to Line 1, with an elevation gain on the upthrown block and a loss of as much as 48 cm at the fault trace (Fig. 4). The increase in elevation loss to 52 cm near the west end of the line is due to the influence of a previously formed surface sink at hole U3gv (Fig. 1). Pre-shot survey data showed the presence of the sag outside the obvious sink; the KINIBITO explosion has accentuated this feature.

The horizontal surveys along the three lines near KINIBITO provide a type of data not obtained in the previous referenced studies. In Figure 5, direction and magnitude of each station is described by a vector, the magnitude being scaled up by a factor of 850 in order to plot visibly. Magnitude of horizontal displacement correlates somewhat with elevation change. As much as 58 cm of horizontal displacement is recorded along Line 1, and the greatest movement occurs on the west side of the fault (the same side as the event). Direction of movement is northeast (that is, toward SGZ) in the west third of Line 1, changing to southeast in the middle third, and again, to northeast on the eastern third of the line. There is a change in the data across the Yucca fault from a southeast direction of movement on the upthrown block to a northeast direction on the east side. The smooth transition to a southeast direction partly coincides with a nearby building where grading and packing of surface material for a foundation was done many years ago. Twelve stations along Line 1 were offset 45.7 m north between E. 207,660 m and E. 207,827 m to avoid the structure (Fig. 1; not shown on Fig. 5). The net southeast movement may be influenced by the building, but material on the scarp of the Yucca fault removed from the structure also moved southeast. As with most cultural features located along the survey lines, the width of the data anomaly far exceeds the dimension of the feature; hence the data appear to be recording a real effect. The dominant net movement of Line 1 is northeast on either side of the Yucca fault.

Horizontal survey results from Line 2 indicate a maximum of 87.2 cm of movement in an approximately N. 50 E. direction west of the fault, decreasing to 10 to 12 cm in a similar direction east of the fault. Note that this direction is not radial to SGZ, as might be expected. There is an abrupt change in direction and magnitude (and elevation) near E. 208,100 m, coinciding with the width of the fault zone shown in Figure 1.

Stations along Line 3 near KINIBITO record movement radially away from SGZ (Fig. 5). Maximum total horizontal displacement of 142 cm occurs between the easting of U3me and the Yucca fault trace. Direction of movement changes smoothly from northwest to northeast, with a subtle change of magnitude and direction across the Yucca fault.

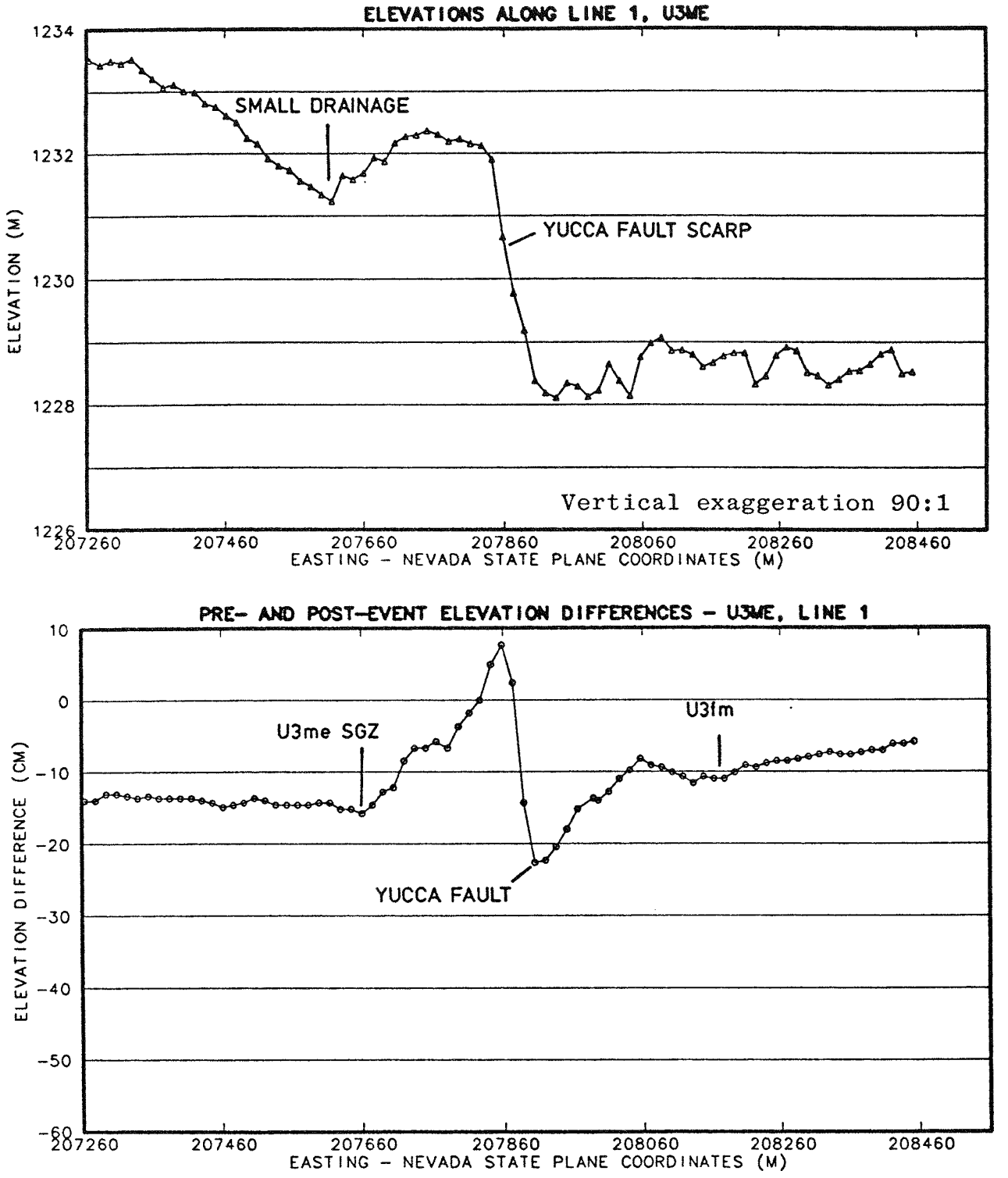

Figure 2. KINIBITO (U3me) survey elevations along Line 1. U3me SGZ projected 366 m south. U3fm projected 30 m south.

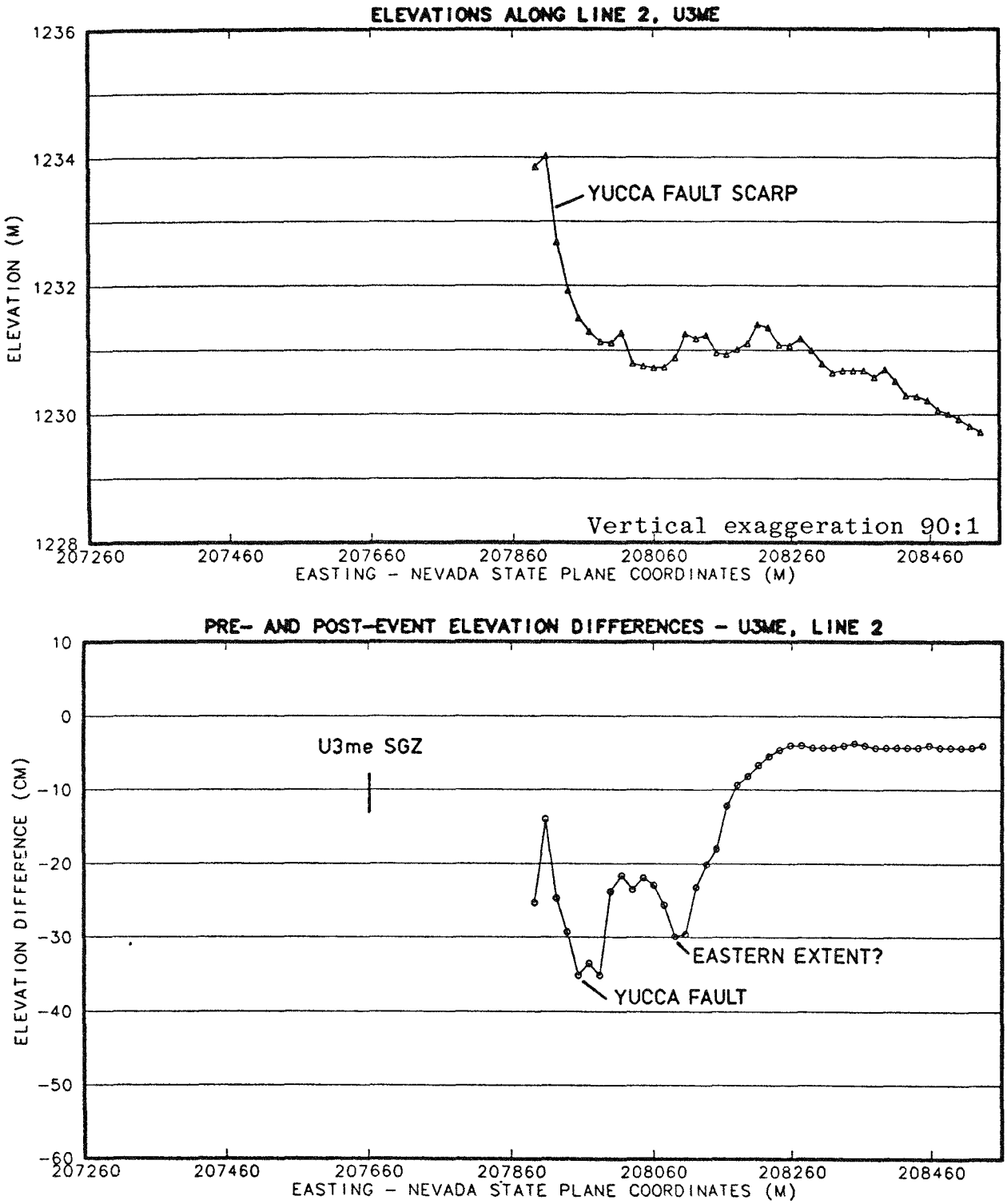

Figure 3. KINIBITO (U3me) survey elevations along Line 2.

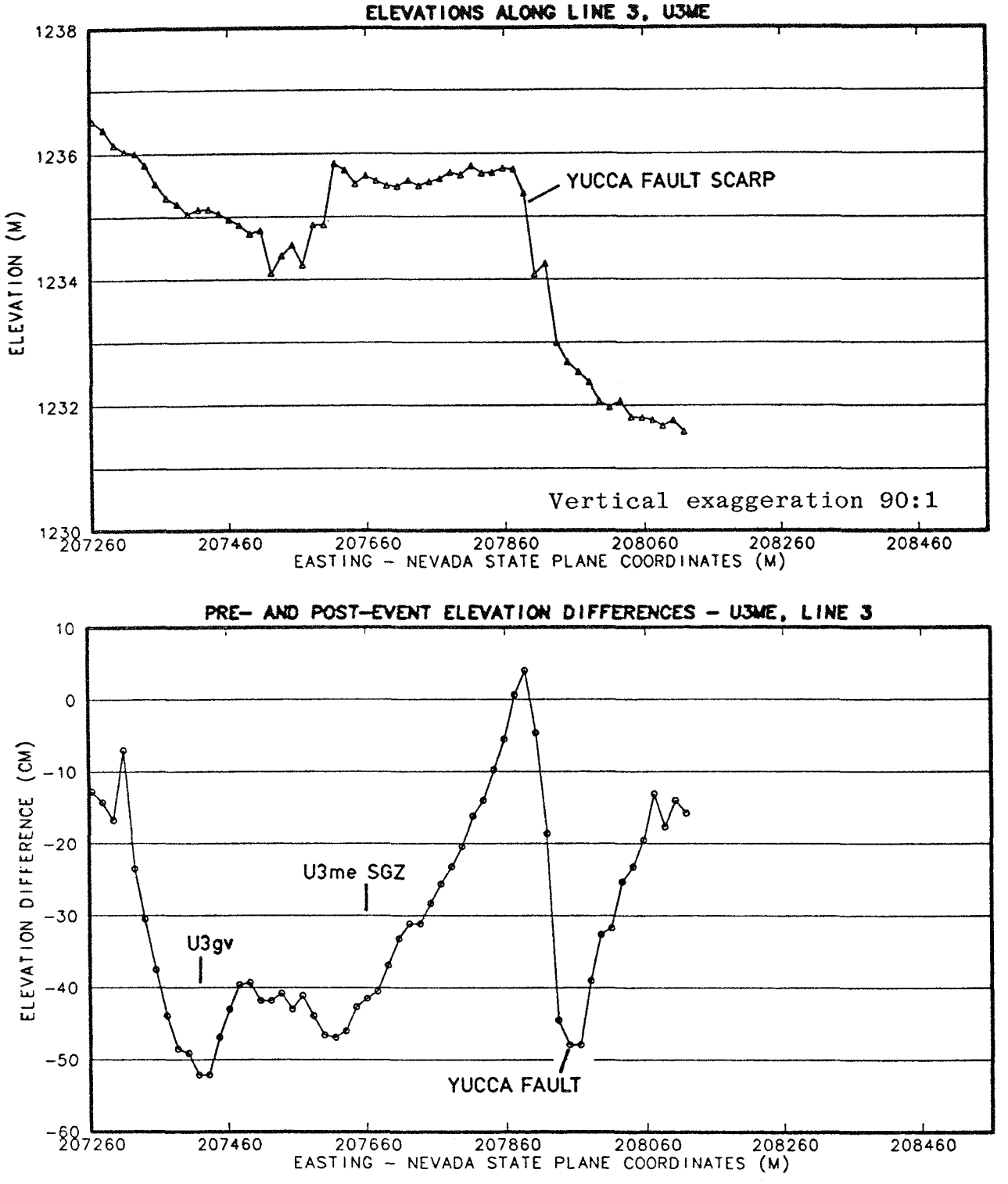

Figure 4. KINIBITO (U3me) survey elevations along Line 3. U3me SGZ projected 229 m north. U3gv projected 91 m south.

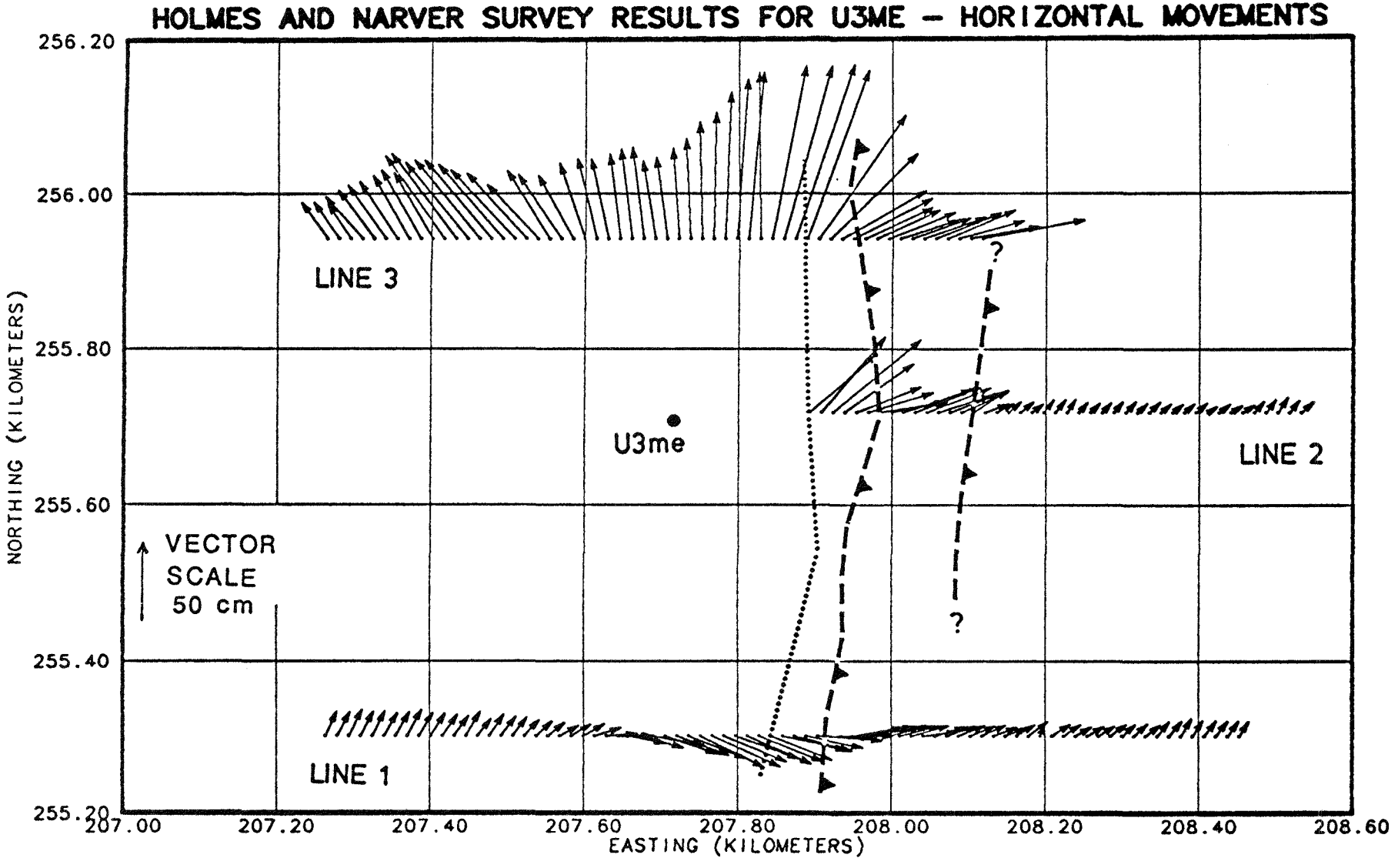

Figure 5. Direction and magnitude of horizontal movement of stations is described by vector. Magnitude scaled up by factor of 850. Dashed lines are Yucca fault traces, arrows on downthrown side. Dotted lines show topographic scarp.

Comparison of horizontal displacements with field mapped cracks is not very enlightening but comparison with elevation data reveals some effects. Along Line 1, the most surface cracking from KINIBITO is located east of the scarp, whereas the greatest change in elevation loss is at the foot of the scarp. Along Line 2, a mapped crack with about 20 cm of vertical offset has, according to the survey data, only a 6 cm elevation change recorded between encompassing stations. This indicates that rotation of small blocks (not easily observed in the field), is distorting some field data. Surface effects mapped near U3gv along Line 3 show the influence of previous collapse craters. Further collapse caused by KINIBITO around the U3gv sink is marked by concentric cracks. Uncollapsed U3fm also appears to have an elevation loss effect along Line 1, but this is not accompanied by any, even reactivated, cracking.

Topographic and horizontal data are important in interpreting the elevation changes. Topography shows a rise in elevation on the lip of the upthrown block of the Yucca fault. This is partly, but not entirely, due to the offset of survey Line 1 which climbs slightly upslope (see Fig. 1); Line 3 shows a similar elevated lip without the line offset, so the effect is real. The positive change-in-elevation on the lip shown by Lines 2 and 3 possibly is due to small-scale thrust faulting; the direction and magnitude of the horizontal survey results suggest this could render an elevation gain when, in fact, a loss may have occurred. However, the amount of horizontal movement of material does not seem large enough to account entirely for this result. Mapped surface cracks showed only dip-slip motion or were simply open, with no indication at the surface of thrust or reverse faulting. It appears that the elevation gain at the lip of the Yucca fault is real and possibly due to uplift of the block. Note that the collapse of the KINIBITO crater area west of E. 207,660 m (Fig. 2) has obscured the relation west of the fault. Similar elevation gains were recorded in surveys in eastern Yucca Flat where their geometry and consistency strongly suggested actual positive block motion along faults (App, 1985).

East of the fault, Line 1 shows results partially consistent with block rotation resulting in a west-sloping land surface. However, close in to the fault, a deeper subsidence has occurred. Such increased subsidence is also observed at Line 2. Line 3 also shows a similar subsidence but does not continue far enough east to characterize the motion.

To summarize, elevation and horizontal surveys near the KINIBITO event show dramatic elevation change from -4 to -52 cm. The Yucca fault shows a gain in elevation of from 5 to 8 cm at the edge of the upthrown block and a 23 to 48 cm loss on the downthrown block. Horizontal data show a net material flow northeast throughout the area with a small area of southeast flow south of SGZ. Field-mapped cracks are most frequent on the downthrown block of the Yucca fault, but not necessarily at the points of greatest elevation loss. In general, visible surface cracking is not found with high frequency where broad subsidence has taken place.

Little evidence is present for actual vertical block motion across the fault. The data suggest, however, that enhanced subsidence, or compaction, occurred at the base of the fault scarp. Aerial photography reveals small drainages trending along the base of the fault scarp so, while underground testing may be accentuating this trough effect, the feature is older than testing. Away from the fault trace, general subsidence occurred, the amount dependent on distance from the shot point. The lack of any difference in elevation loss across the Yucca fault, where the alluvial section thickens by as much as 300 m, strongly suggests that differential compaction is small enough an effect so as not to manifest at the land surface. A remaining puzzle from the survey data is the nearly "wholesale" northeast displacement of the area around KINIBITO.

III. SURVEY RESULTS FROM THE TOPGALLANT FAULT NEAR THE GLENCOE EVENT

General Statement

The GLENCOE event was an explosion with the equivalent yield of between 20 and 150 kt, buried in hole U4i at a depth of 610 m. The stratigraphy overlying the working point was 113 m of zeolitized bedded Paintbrush Tuff, 128 m of non- to densely-welded Rainier Mesa and Ammonia Tanks Members of the Timber Mountain Tuff, and 369 m of tuffaceous alluvium. The GLENCOE detonation did not result in a surface collapse, although a subsurface collapse was inferred from seismic activity within one hour after shot time. Three survey lines were run pre- and post-event (Fig. 6) and situated so as to span the surface projection of the seismically- and geologically-inferred Topgallant fault. The lines were numbered south to north and were located along Nevada State Plane Coordinates N. 258,684 m, N. 259,080 m, and N. 259,367 m. Their lengths were 1,219.2 m (Line 1), 609.6 m (Line 2), and 1,218.6 m (Line 3), and elevation and horizontal readings were recorded every 15.2 m.

The Topgallant fault in the area of U4i is less well-known than the Yucca fault previously described. It is inferred to cut rocks as young as Timber Mountain Tuff along two seismic lines located north and south of U4i. The seismic line evidence also suggests that the Topgallant fault strikes north-south in the vicinity of U4i. Together with data from drill hole Ue4b (Fig. 6), the information suggests that the fault dips about 72 degrees eastward, resulting in an abrupt thickening of about 100 m in the alluvial section within 370 m of the working point. The fault "zone" is depicted as two planes; this is based on reflection seismic profiles in which a hard-layer reflection is not observed within the "zone". The distance from the GLENCOE working point to the fault at depth is about 370 m; the distance to the surface projection is about 640 m. The tuff/alluvium interface in this area is about 370 m deep.

Prior to the GLENCOE event, there were no surface effects in the vicinity of U4i that would suggest the Topgallant fault extended through the alluvium. Figure 6 shows the sum of all mapped surface effects up to and including GLENCOE. The north-south trending cracks created by GLENCOE and located between U4i and Ue4b are surface manifestations of the Topgallant fault as interpreted from seismic lines in the area. These are associated with the western edge of the fault zone shown on Fig. 6 (top); cracks mapped around hole Ue4b which trend north may be related to the east edge of the zone. The northwest-trending cracks located north and southeast of U4i also created by GLENCOE appear to be a surface expression of a western branch of the Topgallant fault, as described below.

Results

Elevation change along Line 1 records a 16.8 cm loss at the west end of the line decreasing eastward toward the surface projection of the Topgallant fault (Fig. 7). The west end of the line is approximately 60 m from the U4al crater edge, indicating further subsidence of the U4al crater was caused by the GLENCOE detonation. The abrupt loss of 14.6 cm marks the fault trace at the ground surface. The loss quickly recovers to -2 cm east of this point and remains relatively constant. Beginning at about E. 206,288 m, three subtle step-like features are observed with decreasing elevation loss eastward.

Line 2 was positioned immediately east of the surface projection of the Topgallant fault (Fig. 8). It has a signature remarkably similar to the east half of Line 1, with a -11.9 cm change recorded at the edge of the downthrown block, recovering to approximately -3 cm change eastward. It also exhibits a rapid decrease in elevation loss close in to the surface projection. East of Ue4b (~E. 206,300 m, Fig. 8), a subtle increase in elevation loss over several stations may mark the trace of the main fault.

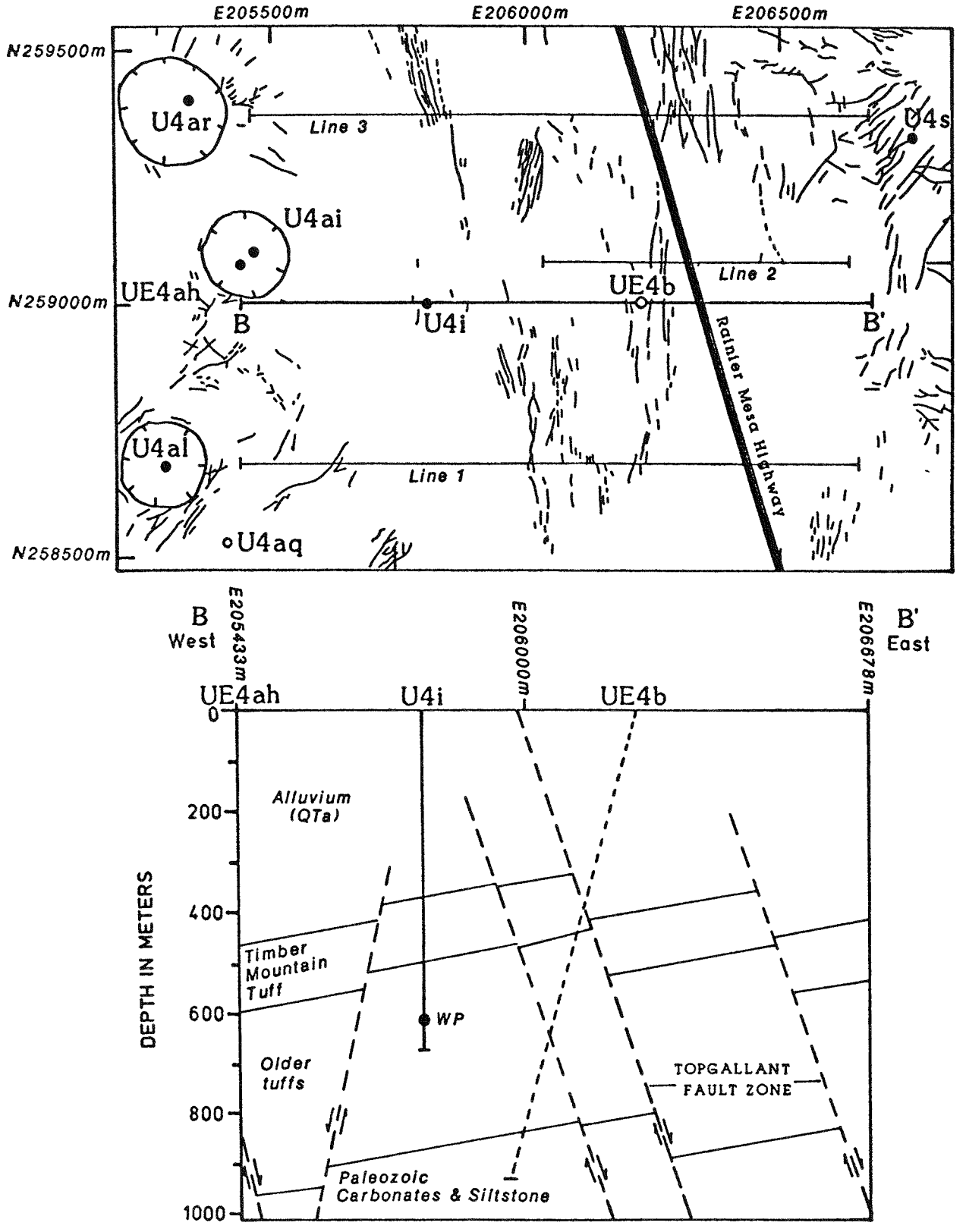

Figure 6. (Top) Location and area crack map for GLENCOE (U4i). Lines 1, 2, and 3 are survey lines. Line B-B' is cross-section line. (Bottom) Geologic cross section B-B'.

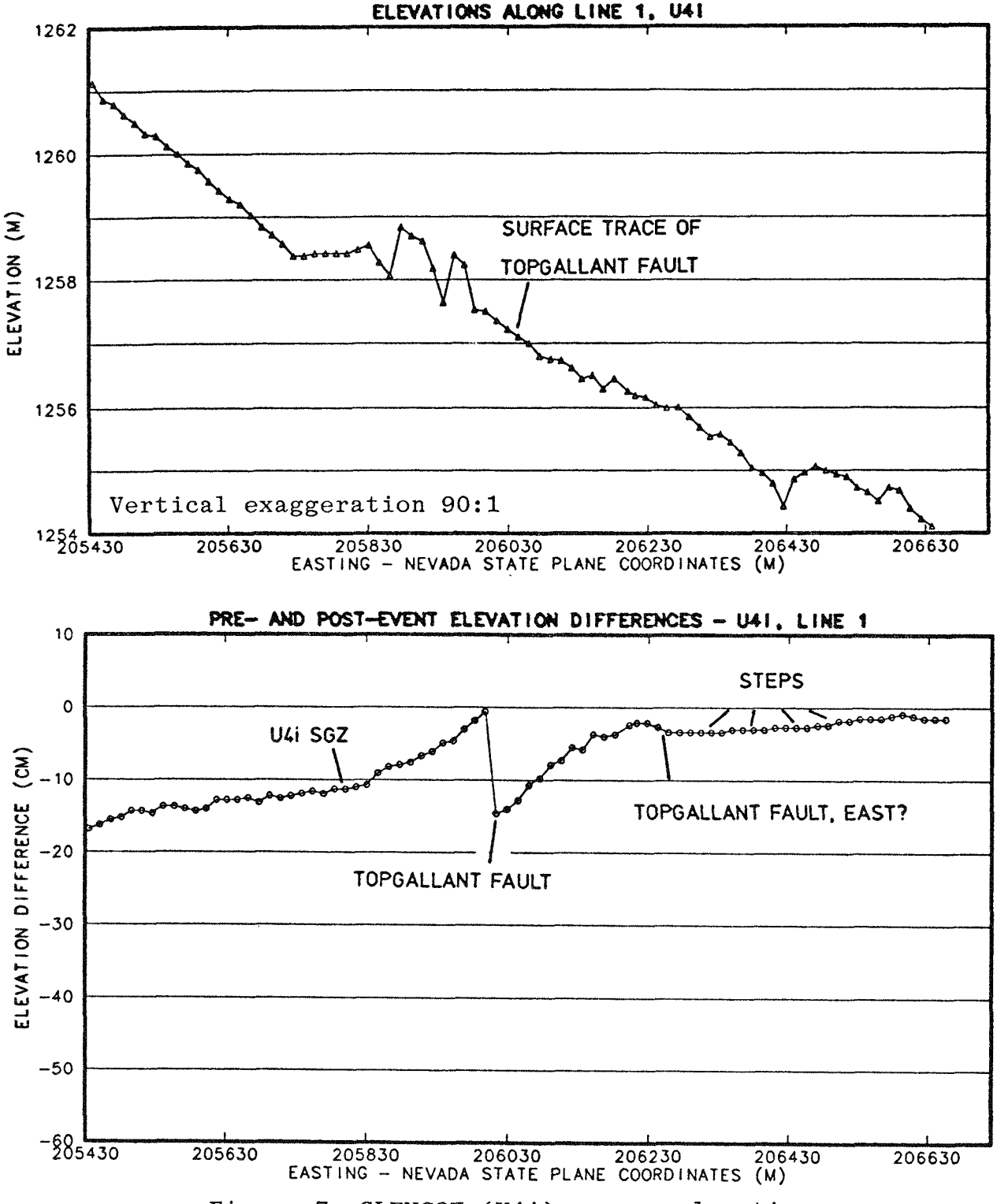

Figure 7. GLENCOE (U4i) survey elevations along Line 1. U4i SGZ projected 316 m south.

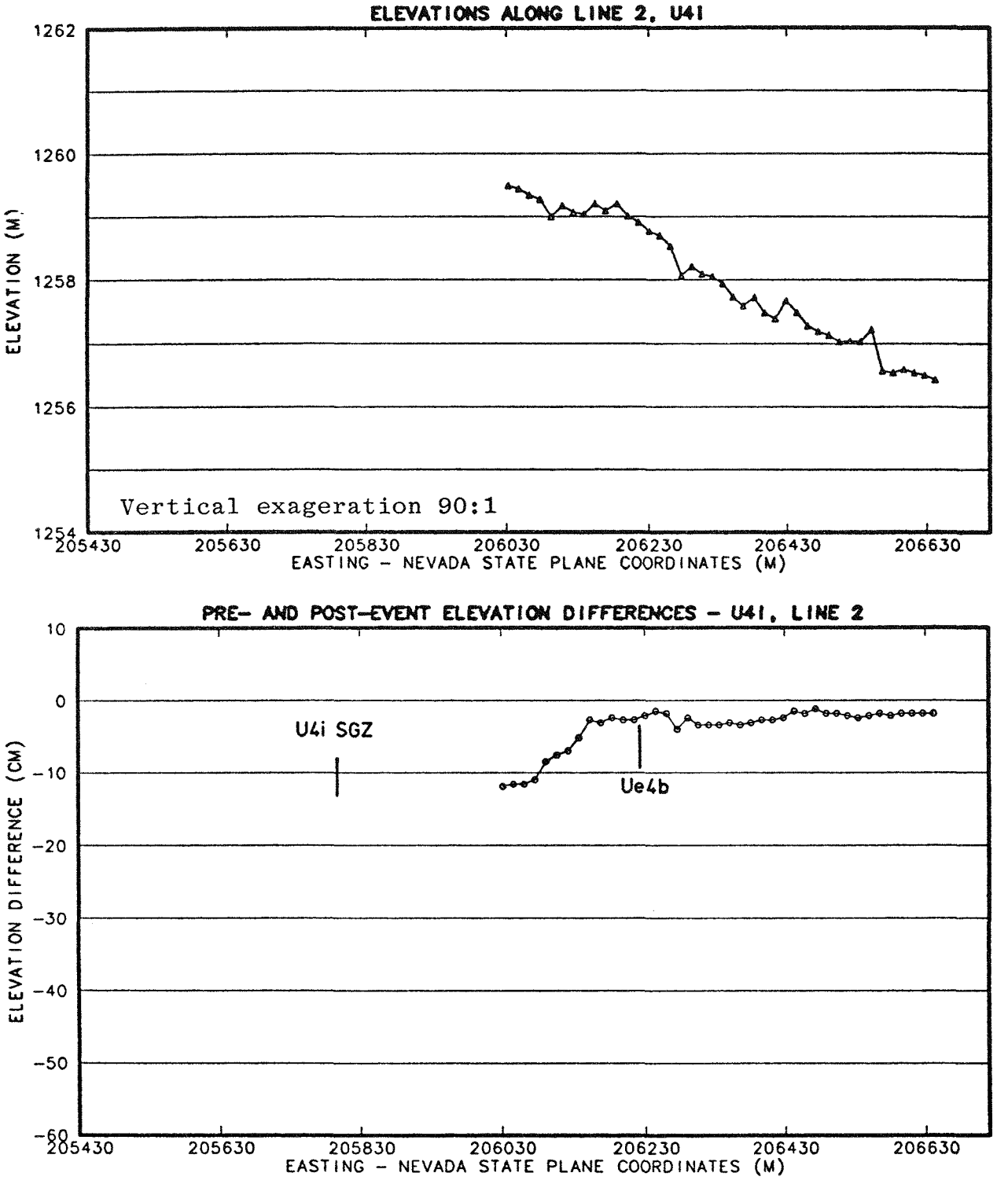

Figure 8. GLENCOE (U4i) survey elevations along Line 2. U4i SGZ projected 80 m north.

Line 3 (Fig. 9) shows an elevation gain of 2.5 cm at the upthrown lip of the block, with a 24.1 cm loss where the line crosses the fault. Again, rapid decrease in elevation loss occurs close to the surface trace. The fault in Line 3 is located west of where the main Topgallant fault is mapped from the seismic data. That data would place the surface trace of the Topgallant fault crossing Line 3 at ~E. 206,030 m. For now, we interpret the elevation surveys as picking up a western branch of the Topgallant fault. East of the fault, a -6 to -4 cm change characterizes the east half of the line, with subtle step-like features as was observed in Line 1.

Results from the horizontal data along Line 1 (Fig. 10) show a northeast to southeast movement on the west side of the fault and a southeast movement on the east side. The fault shows up well in this data set as the abrupt change from dominantly south to north component of azimuth. The maximum horizontal displacement along Line 1 is 21.0 cm. The zone of strong southeast movement on Line 1 between E. 205,680 m and the fault is about 275 m wide and is oriented approximately radial to SGZ. This may be "toss" of a surface layer from the spherical stress wave intersection with the ground surface. Together with data from Line 3, however, dilation of the surface around U4i SGZ is implied.

Line 2 shows a dominantly southeast component of movement becoming more easterly away from SGZ. Maximum displacement along Line 2 is 17.0 cm southeast.

The main trace of the Topgallant fault may be indicated on Line 3 (~E. 206,030 m) by the change in horizontal azimuth from southwest to southeast, although any elevation change is masked by the greater motion on the branch fault. The west branch of the Topgallant fault is marked by an abrupt change from southwest/northwest movement on the western block to south on the downthrown block (~E. 205,830 m). This change is coincident with the maximum elevation loss on Line 3. Maximum horizontal displacement is 25 cm in a southerly direction between the fault branches.

The data for all three lines shows a striking variability of direction of movement which appears to be more dependent on geologic structure than on the stations' position relative to SGZ. The horizontal surveys also show an overall net movement of the area toward the south to southeast.

The elevation changes along Lines 1 through 3 clearly depict movement associated with the fault known as the Topgallant in this part of Yucca Flat. As in the case of the Yucca fault survey, the elevation changes are most pronounced close in to the fault trace on the downthrown block; the recovery or decrease in elevation loss is rapid east of the fault trace and does not resemble simple dip-slip movement or block rotation across the fault. Some component of right lateral motion is supported by the horizontal survey data; an amount of movement on the order of 15 to 30 cm can be inferred from Lines 2 and 3.

In summary, major vertical change is restricted to the western side of the fault "zone" shown in Figure 6, that is, to the east-dipping fault identified in the Timber Mountain Tuff in drill hole Ue4b. The fault appears to branch northwestward where it crosses Line 3. Minor differential movement is possibly recorded along the eastern side of the "zone" along Lines 1 and 2. The horizontal data show dilation in the surface material of the block containing the event, and a net southward displacement of the survey area.

IV. DISCUSSION OF SURVEY RESULTS

The final displacements recorded by the surveys for both events are comprised of the effects from one or more processes including (1) general outward displacement from SGZ due to the spherically divergent ground shock interaction with the free surface, (2) near-surface spall compaction, (3) differential compaction of materials across material interfaces, (4)

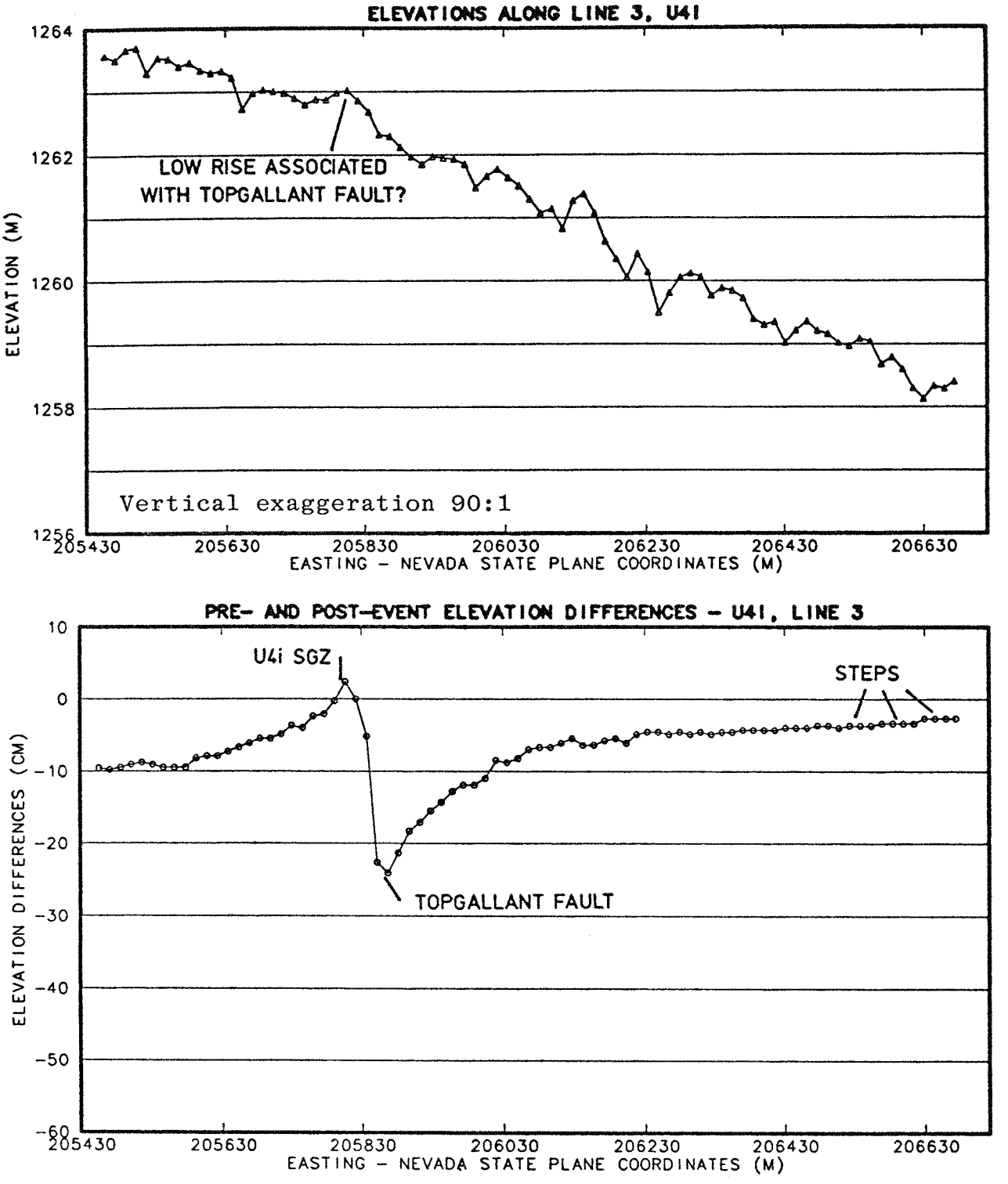

Figure 9. GLENCOE (U4i) survey elevations along Line 3. U4i SGZ projected 367 m north.

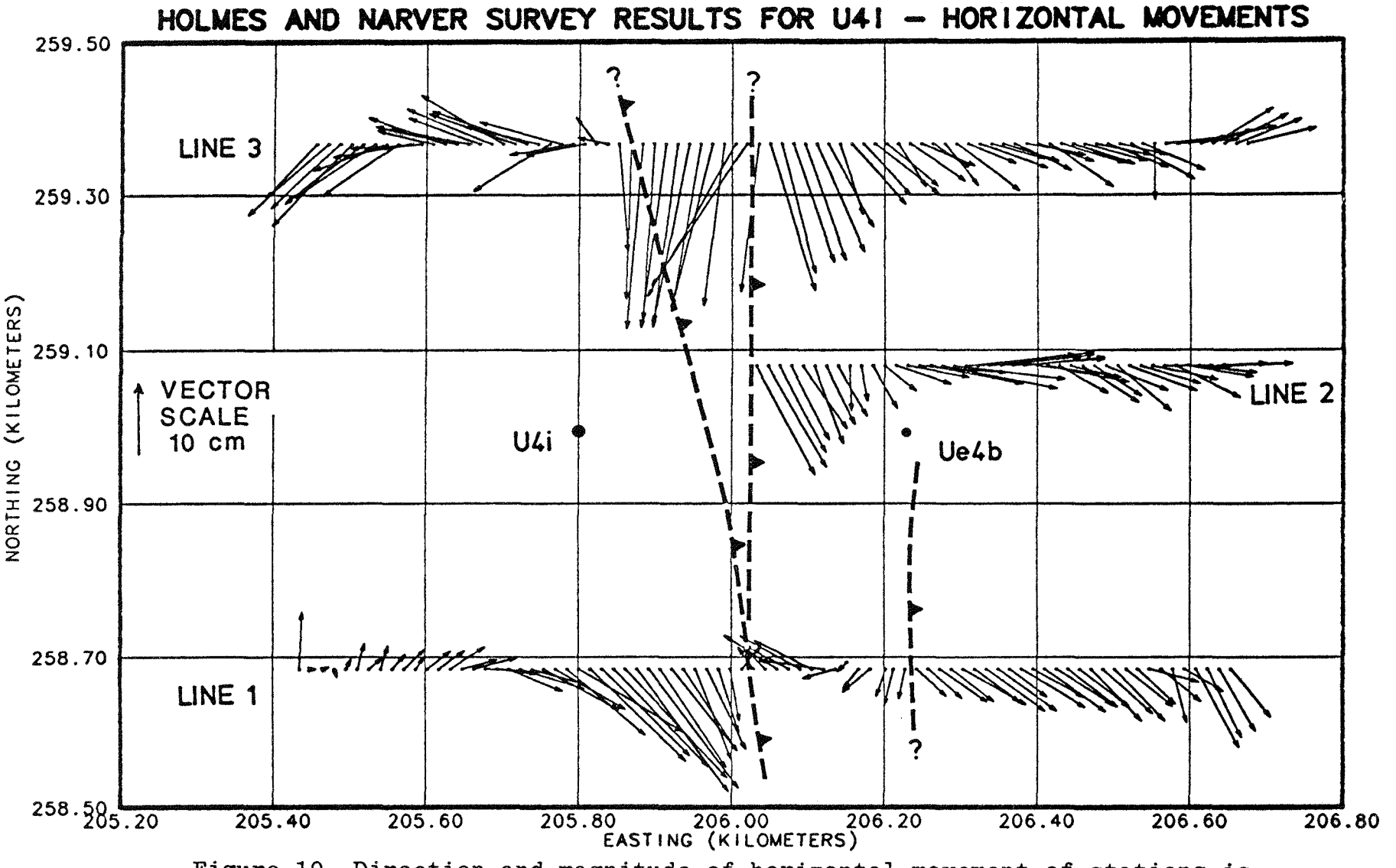

Figure 10. Direction and magnitude of horizontal movement of stations is described by vectors. Magnitude scaled up by 950. Dashed lines are traces of Topgallant fault with arrows on downthrown side. Little or no topographic scarp is observed in this area of Yucca Flat.

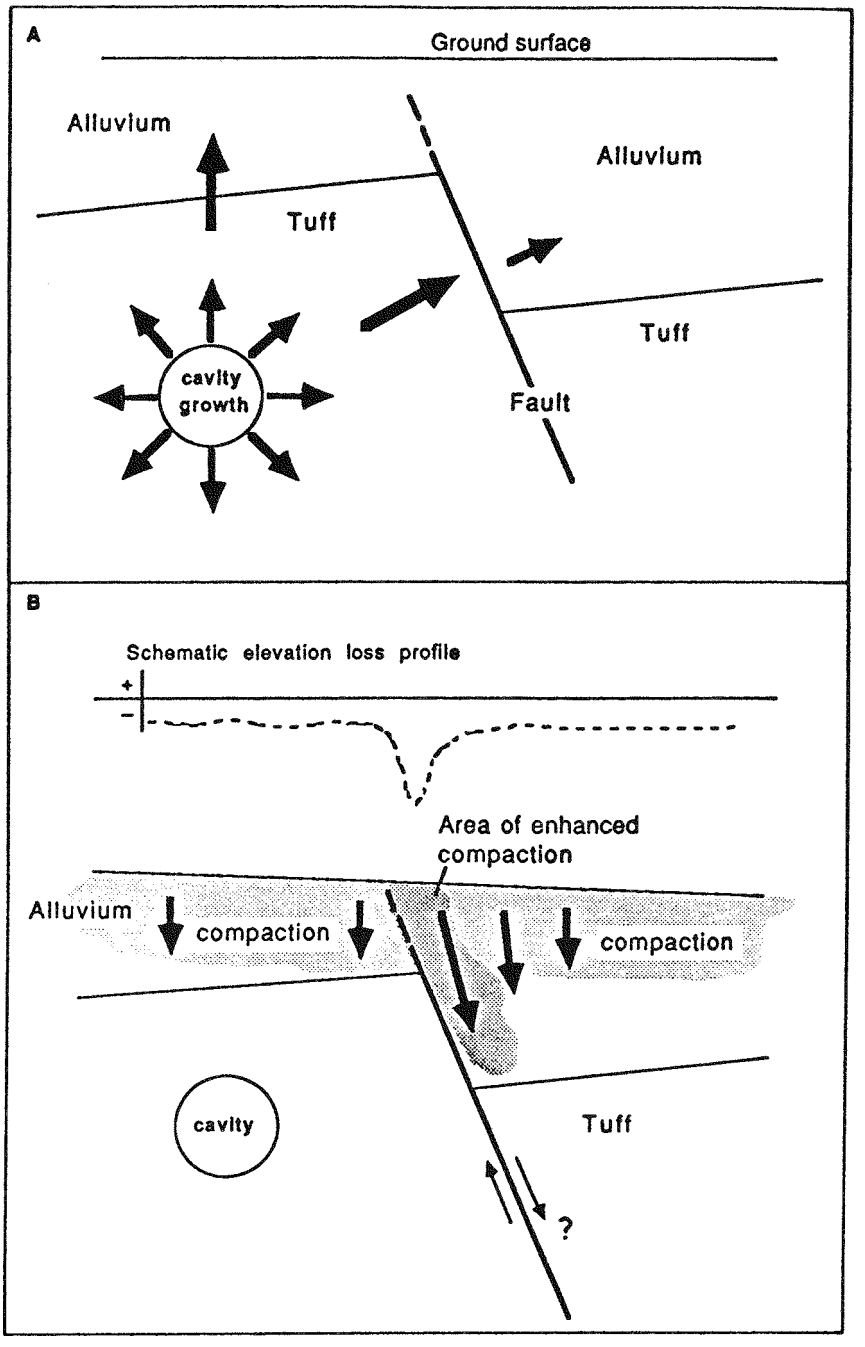

Figure 11. Model suggested to obtain elevation loss profile. (A) Outward motion of tuffs crushes pores in weaker alluvium along planar fault boundary. (B) Spall compaction combines with compaction at fault boundary to produce observed elevation loss profile.

chimney-associated subsidence, and (5) fault motion. It is beyond the scope of this preliminary treatment to account for all these processes; however, we advance some ideas on what, based on the more dominant and consistent observations, may be the more dominant mechanism.

Results from the surveys at KINIBITO and GLENCOE show that fault interaction with the surface alluvium can be verified with well-placed and careful surveys. Both the Yucca and Topgallant faults showed a significant elevation loss anomaly consistent with their known sense of displacement, but permanent (dip-slip) block motion was not confirmed by the elevation data. Spall compaction of alluvium appears to account for the general and somewhat uniform subsidence in the area around these underground blasts. Less straightforward are the horizontal motions which showed a net northeast movement of mass around KINIBITO, and a southerly movement around GLENCOE. Line 1 at KINIBITO showed some evidence for left-lateral motion across the fault (see Fig. 5) but this is not supported by data from the survey lines to the north. Data from the Topgallant fault may be interpreted as having a component of right-lateral displacement, but this is not conclusive due to the variable azimuths of station movement.

The common feature of the KINIBITO and GLENCOE events was the location of each working point west of a large displacement, east-dipping fault. If differential compaction of material across major faults is a real mechanism and is observable at the surface, then there should be some indication here. There is no broad effect. Once away from the immediate vicinity of the fault trace, subsidence appears to be similar on either side of the fault.

However, an "enhanced" elevation loss occurs close to the fault which is not addressable by any fault block motion we are familiar with. Differential compaction of the alluvium may play a role in explaining the unusual signature of elevation loss and rapid recovery observed close to the surface projection of the scarps. Increased elevation loss at the downthrown boundary might result from localized compaction along that inclined fault plane which separates materials of differing properties, as shown schematically in Figure 11. On both KINIBITO and GLENCOE, the ground shock peak stress probably was in the range 10 to 20 MPa at the tuff/alluvium interface where offset by faulting. Alluvium would readily crush at these stress levels, whereas tuff, particularly the moderately to densely welded unit of the Rainier Mesa Member present at both sites, should not crush. The effects of such compaction would be mitigated by the increasing range between survey station and explosion point, superimposing the effects of a diminishing radial stress wave on the elevation profile.

The impact of these data on containment of underground explosions clearly needs assessment by calculational models for which this study provides some constraints. Displacement of the free surface is very complex and not a simple function of scaled range from the working point. As the geologic structure increases in complexity, so does particle motion and final displacement. While some evidence in this study suggests that lateral movement of blocks did occur as a result of the explosions, we accept the conclusion as preliminary due to the lack of an unambiguous vertical component of block motion. The concept of differential compaction as applied to a broad region has no supporting evidence in these data, at least as measurable at the surface. However, localized differential compaction near the fault plane may, in part, explain the sudden downward displacement observed at the downthrown margin of the the Yucca and Topgallant faults.

V. ACKNOWLEDGEMENTS

The authors wish to thank Allen H. Cogbill for help in graphics display of the survey data. This work is supported by the United States Department of Energy.

VI. REFERENCES

App, Frederick N., 1985, Permanent displacement of the ground surface resulting from underground nuclear test induced ground shock, in Proceedings, Third Symposium on Containment of Underground Nuclear Explosions, September 9-13, 1985, Idaho Falls, ID, Vol. I, C. W. Olsen, editor, Lawrence Livermore National Laboratory CONF-850953.

Barosh, Patrick J., 1968, Relationships of explosion-produced fracture patterns to geologic structure in Yucca Flat, Nevada Test Site, Geol. Soc. America Mem. 110, p.199-217.

Rambo, J. T., D. E. Burton, F. A. Morrison, Jr., and R. W. Terhune, 1983, Calculation of early-time subsidence phenomena (A calculational study of the CARPETBAG event), in Proceedings, Second Symposium on Containment of Underground Nuclear Explosions, August 2-4, 1983, Albuquerque, NM, Vol., I, C. W. Olsen, editor, Lawrence Livermore National Laboratory CONF-830882.

Geophysics and Medium Properties

DO NOT MICROFILM
THIS PAGE

Applications of Vertical Seismic Profiling at NTS

Norman R. Burkhard
Lawrence Livermore National Laboratory
L-208, PO Box 808
Livermore, CA 94550

Abstract

Vertical Seismic Profiling (VSP) data can be used to refine the geologic interpretation of the structural setting around an emplacement hole at NTS. Recent upgrades to the seismic recording equipment routinely fielded by the NTS logging contractor permit VSP data to be obtained quickly as needed without external support. VSP data can be used in many different ways. Traditionally, VSP data have been used as a tool to assist in the interpretation of surface seismic Common Depth Point (CDP) reflection data. LLNL has been examining several direct applications to the geologic characterization of an emplacement site.

VSP data from a single surface seismic source location near an emplacement hole can be used to determine the depth and apparent dip of reflecting horizons below the bottom of the hole. With multiple surface seismic source locations, the true dip of a reflector can be determined. However, geologic interpretation is still required to properly identify the reflector. In some cases, the evidence of the presence or absence of the reflector is all that is required for containment evaluation. An example of this technique (along with its shortcomings) using data from hole, U20ar is presented.

Offset VSP data are obtained when the surface source is not near the well head. This technique uses the direct and reflected energy and differs from half-refraction techniques that utilize only the refracted head waves. A convenient method of imaging these data involves the transformation of these data from the traditional VSP domain to a CDP domain. In the CDP domain, the transformed VSP data resemble a CDP reflection section. Standard surface seismic reflection techniques can be utilized to determine the structure on a portion of the plane defined by the emplacement hole and the surface seismic source location. Data from experimental deployments of this technique at hole, U4ag are presented.

Introduction

A Vertical Seismic Profile (VSP) is a set of seismic data from a surface seismic source that is recorded on a borehole geophone at closely spaced depth intervals. VSP techniques have evolved from the technology of check-shot velocity surveys which are used to record direct arrivals of P wave energy. VSP techniques record data beyond the first arrival of the propagating pulse and record all subsequent arriving seismic waveforms. VSP data include the entire seismic signal from the surface seismic source and are analyzed to obtain the down-going and the up-going seismic wave fields at each geophone location. The up-going waves are reflected seismic energy. In order to be able to carry out this analysis, more geophone locations in the borehole are required than is typically used for a check-shot velocity survey and the data must also be recorded with full bit resolution. A typical VSP field data acquisition geometry is

displayed in Figure 1. In-field quality control for a VSP survey is much more important than it is for a check shot velocity survey; the quality of the entire seismic wavefield is important for VSP surveys.

At the Nevada Test Site (NTS), attempts have been made in the past to utilize VSP data for several applications. Lawrence Livermore National Laboratory (LLNL) has sponsored or conducted VSP experiments over the past ten years, typically, in an attempt to resolve structural setting issues around nuclear test emplacement holes. Experiments were conducted at hole U10bd [1] and at hole Ue8c [2]. In addition, old check-shot velocity data (hole Ue4ah for example) have been reanalyzed with VSP wavefield separation algorithms to determine whether reflections were present.

In all of these experiments, the VSP data gathered were either marginal to poor quality. At that time, VSP processing technology was not well developed. Neither the seismic industry nor LLNL really knew how to obtain useful structural information from the up-going wavefield. However, two things have happened in the last ten years.

First, the quality of the seismic equipment available at NTS for routine logging has been greatly improved. The locking borehole geophone has been improved so that the seismic data are no longer contaminated with tool resonances that would be excited by the first direct P arrival or by swinging of the logging cable. These tool resonances would obscure almost any reflected seismic wave that might be present. The seismic recorder in the field has been vastly upgraded. A modern digital recorder that is controlled by an in-the-field data quality control acquisition computer is now in routine use at NTS. A more powerful impulsive surface seismic source has been obtained. The entire seismic data acquisition system is now suitable for recording high quality VSP data. This capability is critical to the success of a VSP survey. Several authors discuss this topic at length [3,4].

Second, VSP data processing has matured;the method is no longer "experimental". Processing algorithms that will optimally carry out the critical wavefield separation and migrate the reflections to their true location have been developed. VSP data processing research is ongoing; however, enough has been done to make VSP data useable in real field situations.

In this paper, we concentrate on two specific applications of VSP data to help determine geologic structure and have direct application to the containment evaluation of a proposed nuclear test emplacement site.

Reflecting Horizon Below the Emplacement Hole

Calculations indicate that a reflecting surface near the working point for an underground nuclear test can reduce the strength of the residual stress field around the cavity. Strong material near the working point can confine the cavity and increase cavity pressure. An investigation for the presence or absence of such features is part of the containment evaluation of a proposed site.

VSP data can be used to "look" for reflecting horizons below the bottom of the emplacement hole. The up-going wavefield is used to determine whether reflectors are present. The depth and apparent dip of a reflector can be found from the arrival times of the direct wave and the identified reflected wave at a suite of geophone stations. The equation that relates the direct and reflected wave is:

$$T^2_R - T^2_D = (4/V^2)(z_p - z_r)(z_p \cos\varphi - x_s \sin\varphi) \cos\varphi \qquad (1)$$

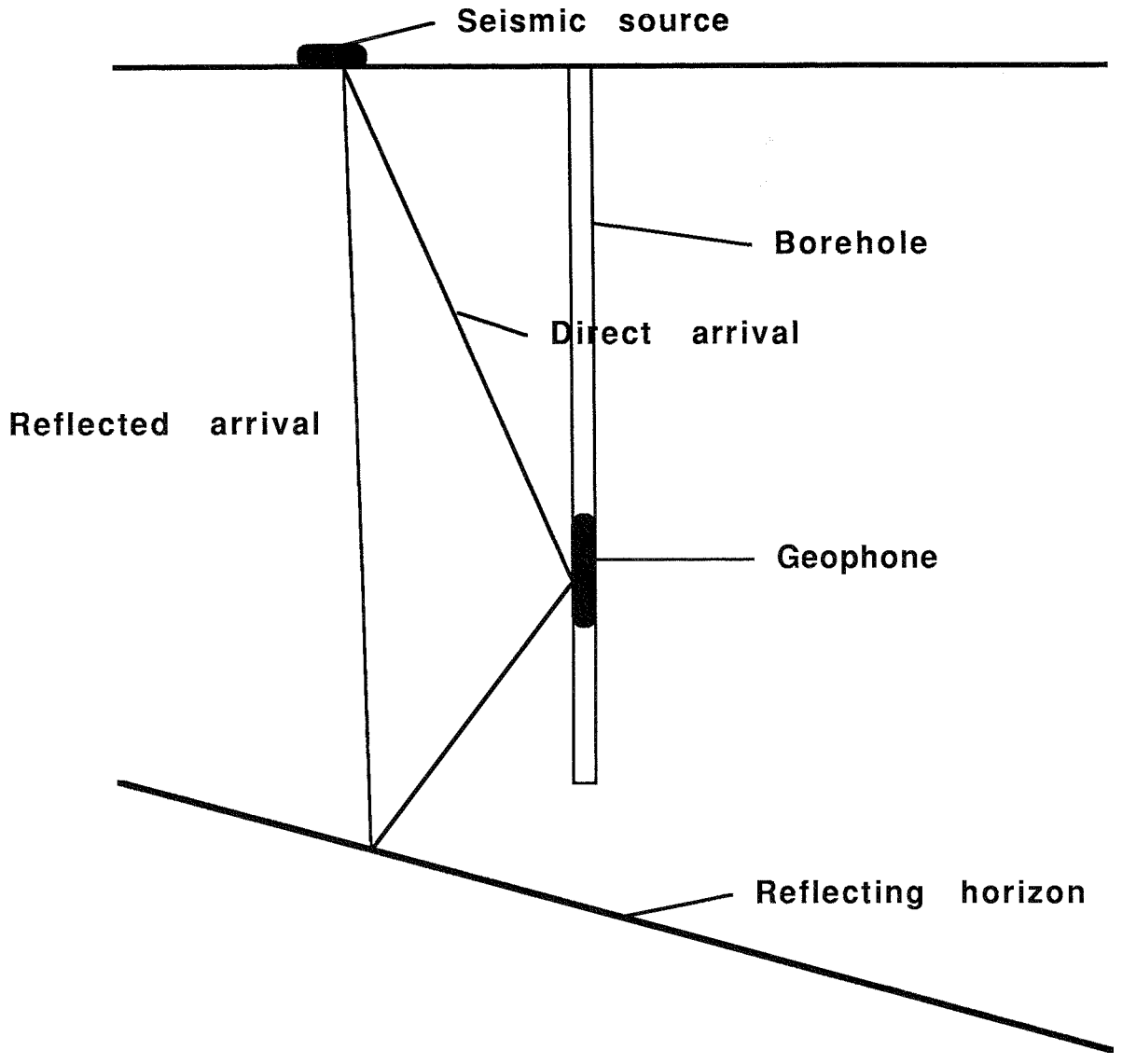

Geometry of a Typical Vertical Seismic Profiling Survey
Figure 1

where T_R = time of direct arrival at geophone at depth z_r
T_D = time of reflected arrival at geophone at depth z_r
V = seismic velocity of medium
z_p = depth of reflector at the hole
z_r = depth of geophone in the hole
x_s = offset of source from the hole
φ = apparent dip of reflector

This is a non-linear equation that can be solved numerically for φ and z_p. First, however, the VSP data from the hole must be separated into upgoing and downgoing wave fields. Second, the reflector of interest must be identified. Third, the arrival times for the direct and reflected waves must be picked. Then, from these travel times, a numerical solution to Equation 1 will give the apparent dip and depth of the reflector at the hole.

To illustrate the method I shall use data from U20ar. The U20ar velocity survey data were run through the standard VSP processing sequence available in the NTS field data acquisition computer to determine whether any reflectors might be below a proposed working point. Figure 2 is a corridor stack of the reflected energy from this survey. A corridor stack uses only the first part of the reflected traces at each depth and thus minimizes the existence of multiples in the stack. Note the broad reflector at 0.64 sec. (two-way time) from the surface. From the upgoing wave field (Figure 3), we obtained the reflected times. The reflected time of Figure 3 is in two-way time. Two-way time is the sum of the arrival time of the upgoing wave at the geophone and the time of arrival of the downgoing wave at the geophone. The depth of the reflector was calculated to be 573 ± 7 m; the apparent dip of the reflector was found to be 0 ± 9 degrees. The uncertainities were calculated from an assumption that the time pick accuracy was 3 ms.

This reflector was interpreted as a rhyolite lava that was seen at about that depth in hole U20a (located about 1 km east). After this interpretation, a hole, Ue20ar, was drilled to determine if a reflector that would be of concern for containment existed at this depth. The logging of the Ue20ar hole did not reveal a significant change in physical properties at this horizon. The initial interpretation of the reflector as rhyolite lava was based upon geologic correlation. The VSP data primarily tells us a depth; however, the frequency content of the signal can also be a diagnostic tool. The reflection is a broad pulse (≈37 msec long); this could mean that the reflection is coming from a gradational change. The standing water level in Ue20ar was measured at 563 m; it is likely that the broad reflection is the seismic response from the increased saturation and the water table. The original geologic interpretation of the VSP data appears to have been incorrect. The moral of the U20ar example is: Good geologic interpretation is still needed to properly use VSP data.

Offset VSP Data

An offset VSP survey is a VSP survey that has the seismic source located at some distance away from the wellhead. Offset VSP data can give structural information laterally away from the borehole. A potential application for offset VSP data in containment evaluation is to determine in detail the geologic structure away from the borehole. Geologic features such as

Figure 3. Upgoing wavefield from U20ar VSP survey.

Figure 2. Corridor stack of reflected energy from U20ar VSP survey. Arrow indicates the reflection from horizon below working point at U20ar.

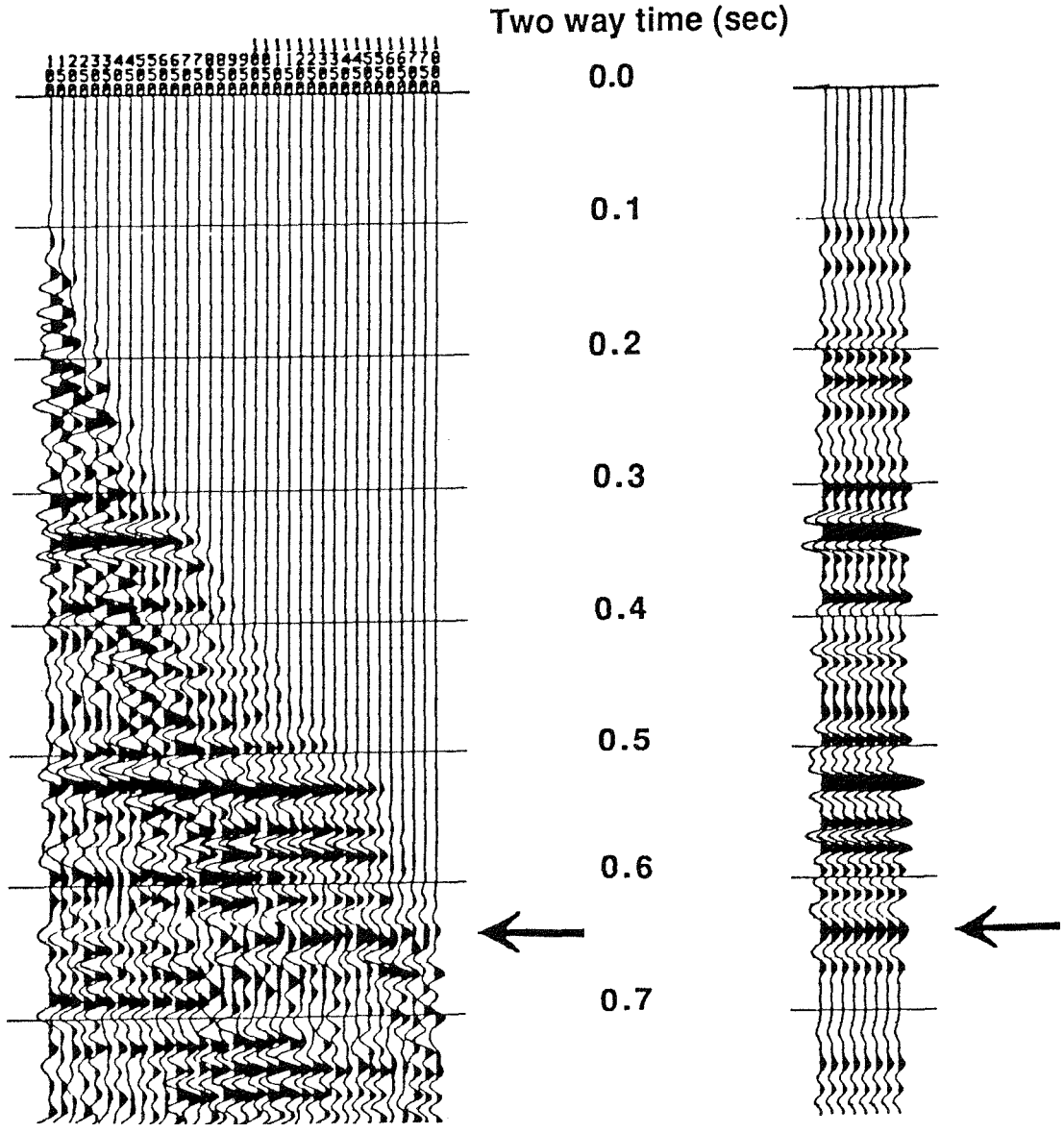

faults and scarps that are important in the containment evaluation of a site can be mapped in detail. To study the utility of the offset VSP technique, we designed a VSP experiment at U4ag. The structure around U4ag is complicated. Lithologic contacts in nearby holes, surface gravity, seismic reflection surveys, and surface magnetics were used to construct a preliminary Paleozoic isopach map and geologic cross section. The structural features that we wanted to examine are the locations of the two faults on either side of U4ag (Figure 4a).

To determine the optimum position for the offset source locations, we modeled the VSP ray paths for various offset source locations in the preliminary cross section to determine which offset position would give us the most information. Offset source locations at 304.8 m N 45^0 E and at 304.8 m S 45^0 W of U4ag were selected based upon the modelling results.

Offset VSP data from the two offset points and a normal vertically incident VSP were gathered over several days. Data were gathered on 20 ft. intervals with 8 good "pops" of the airgun at each level. The seismic signature of each pop was constantly monitored; bad pops were eliminated and additional pops taken until 8 good pops were obtained. The data were recorded in an unstacked format.

The data were processed by Western Atlas International Downhole Seismic Service. The processing steps were as follows: We processed the vertically incident VSP to obtain a velocity model for the area and to identify reflections. Next, the offset VSP data were separated into up-going and down-going wavefields. The preliminary cross section and the velocity model were used in an interactive computer modelling program to model a structure that would fit the travel times observed for the up-going reflections seen in the offset data sections. Then, based upon the models derived, the VSP data were transformed into a Common Depth Point (CDP) seismic section display. This process involves mapping the VSP data along the ray paths of the model. The data are summed within narrow offset ranges (binned) to produce a depth-migrated output section. Figures 4b -7 illustrate the steps.

From the CDP sections, we obtained more spatial resolution than is possible from the surface seismic reflection CDP data that was run in the area. The resolution is better for two reasons: The spatial coverage of CDP points is denser in the VSP data. The frequency content of the VSP data is higher than the surface CDP data because the seismic energy does not have to travel back through the high-attenuation zone in the near-surface alluvium. The final pseudo-CDP sections can now be interpreted using the standard seismic reflection interpretation tools. Although the two faults from the preliminary cross section do not appear in the models, the models do place some limits on the position of the faults. Basically, fault locations that would lie upon the mapped ray paths in the model are excluded. These locations for the faults are excluded because if the faults were located there, they would have either produced reflections that would have appeared in the offset VSP data or blocked the reflections that we do see that do not come from a faulted horizon in the model.

The VSP technique primarily obtains reflection data along a plane defined by the borehole and the seismic source. Therefore, the best images are obtained when the plane of the section is normal to the principal structure. When the structure is very complicated, a three-dimensional surface seismic reflection survey around the borehole might be a better method to define structure. Three-dimensional reflection data can be depth migrated (before stack) to place the reflections in their proper spatial location. Then images of the structure can be obtained at any azimuth from the hole or along any slice using three-dimensional reflection data. An accurate velocity model is required before the VSP data can be transformed into a CDP section. However, when the structure is very complicated, one needs to know what the general structure is like before processing to guide the development of the velocity model. This is not

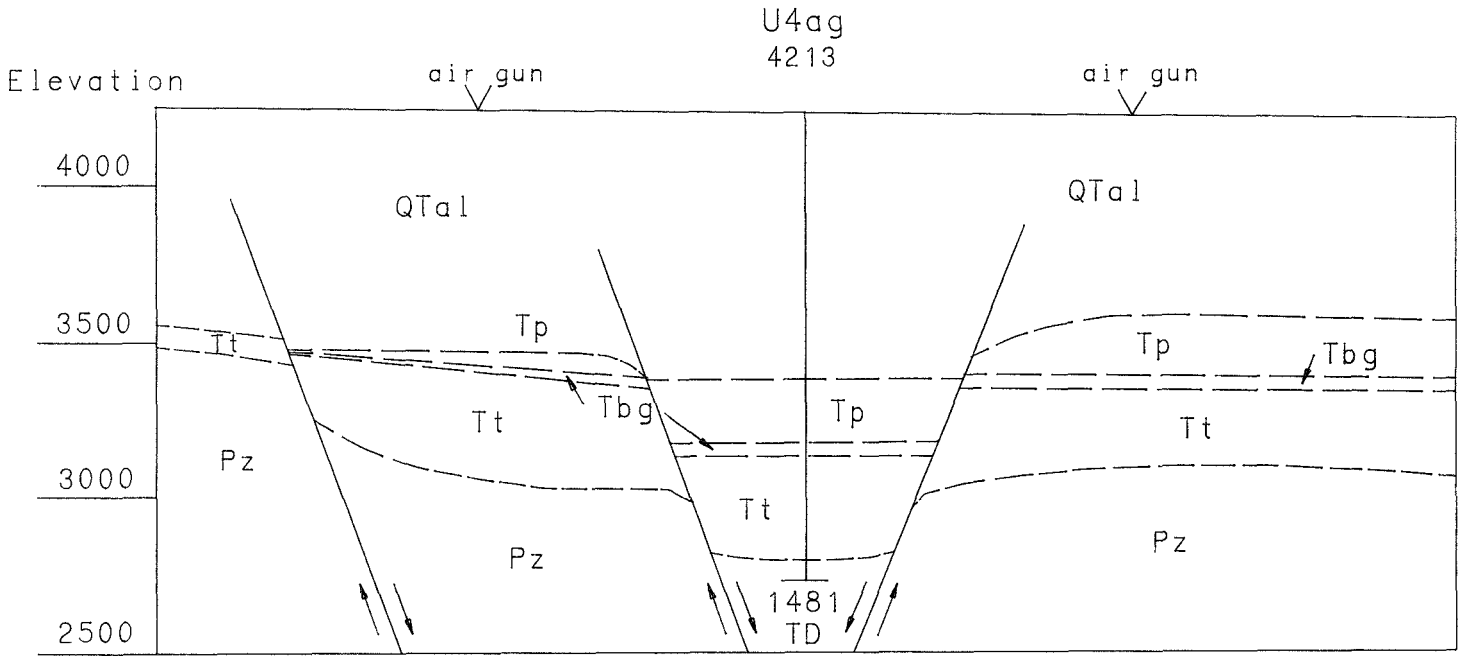

Legend

QTal	Alluvium
Tp	Paintbrush Tuff
Tbg	Grouse Canyon Member
Tt	Tunnel Beds and Older Tuffs
Pz	Paleozoic Rocks

GEOLOGIC CROSS SECTION A–A'
U4ag

Figure 4a

Figure 4b. "Raw" field data from U4ag 100 ft. offset VSP survey

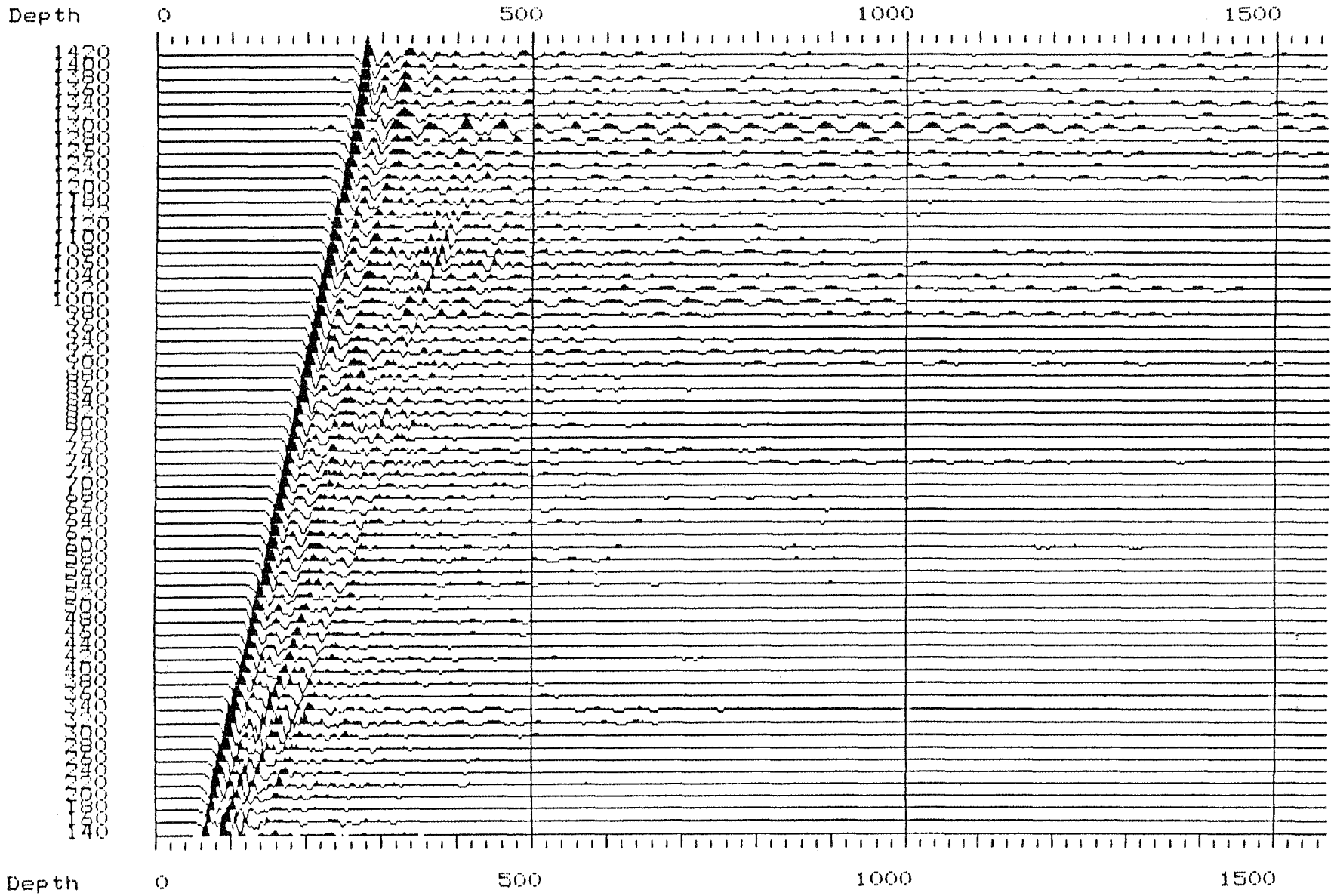

Figure 5a. U4ag 100 ft. offset downgoing wavefield

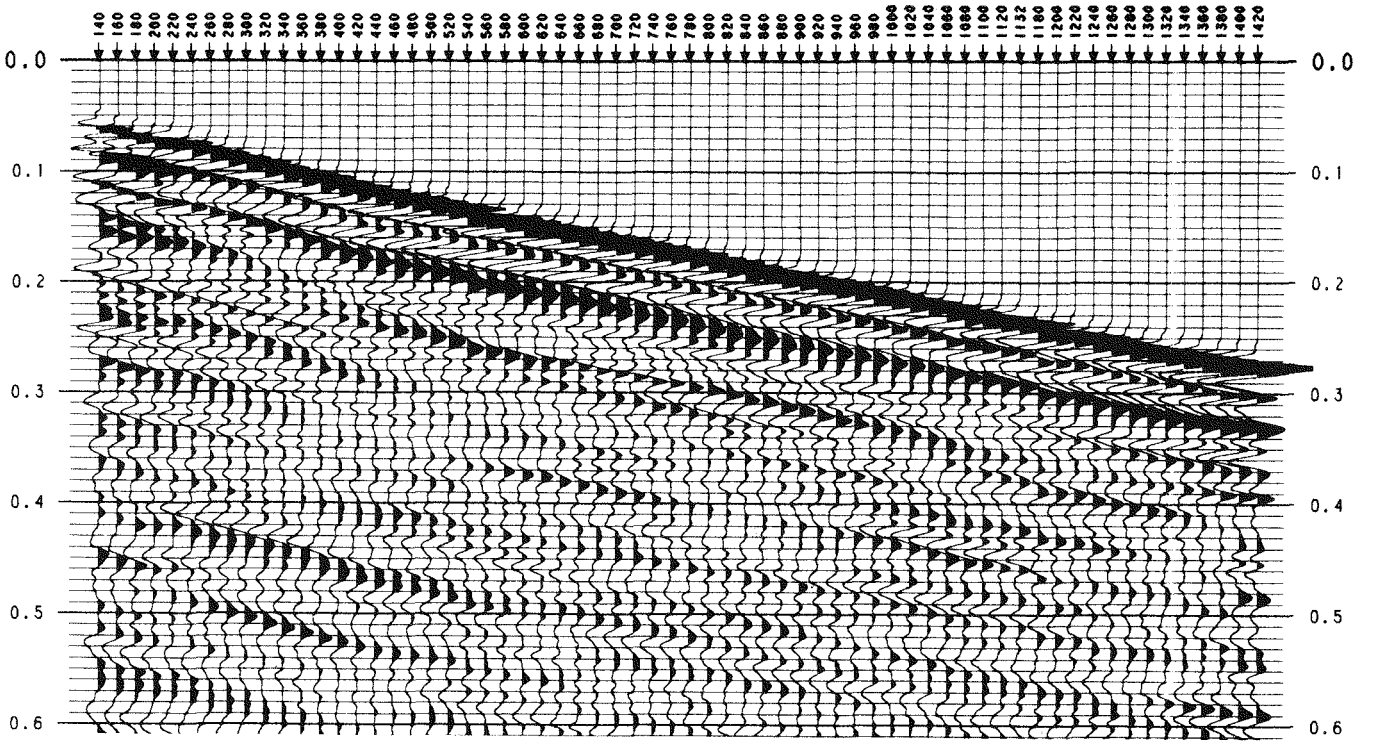

Figure 5b. U4ag 1000 ft. NE offset downgoing wavefield

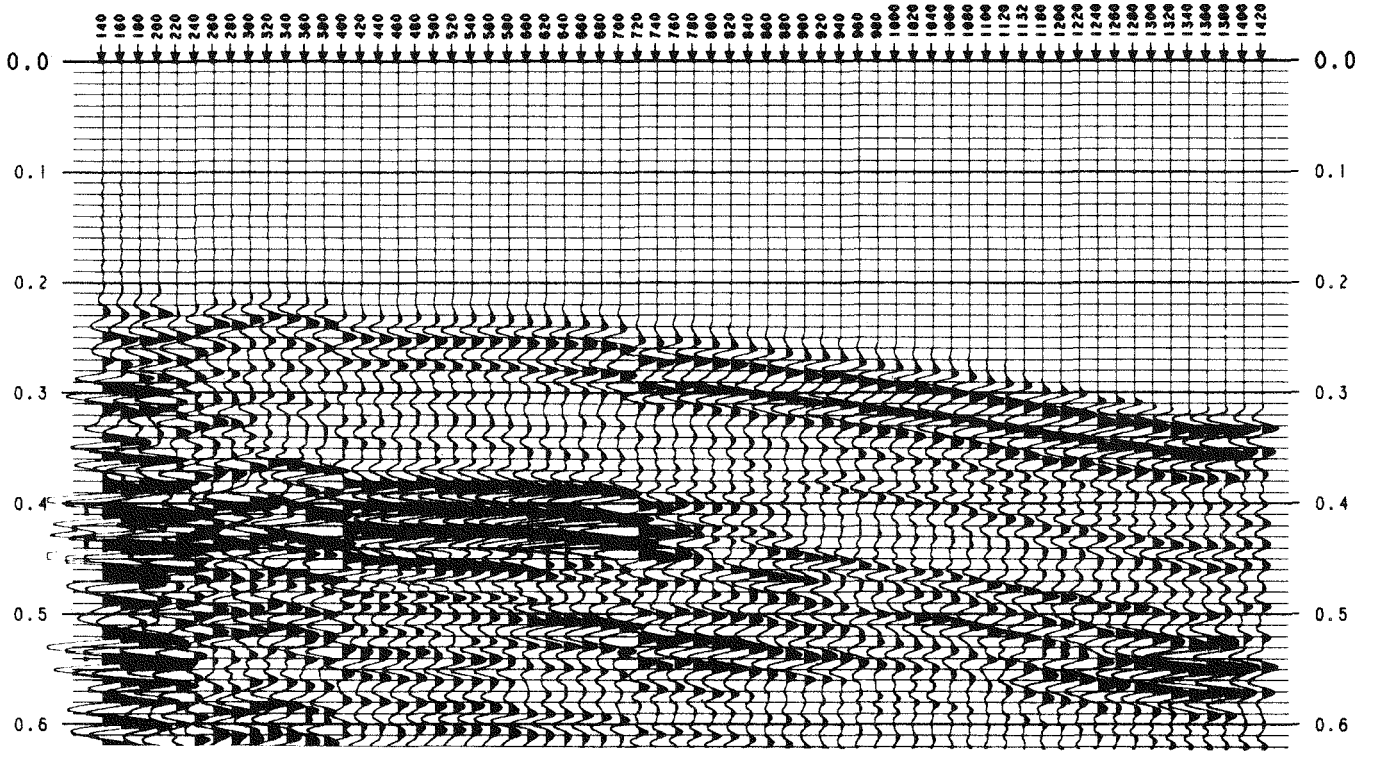

Figure 6a. U4ag 100 ft. offset upgoing wavefield

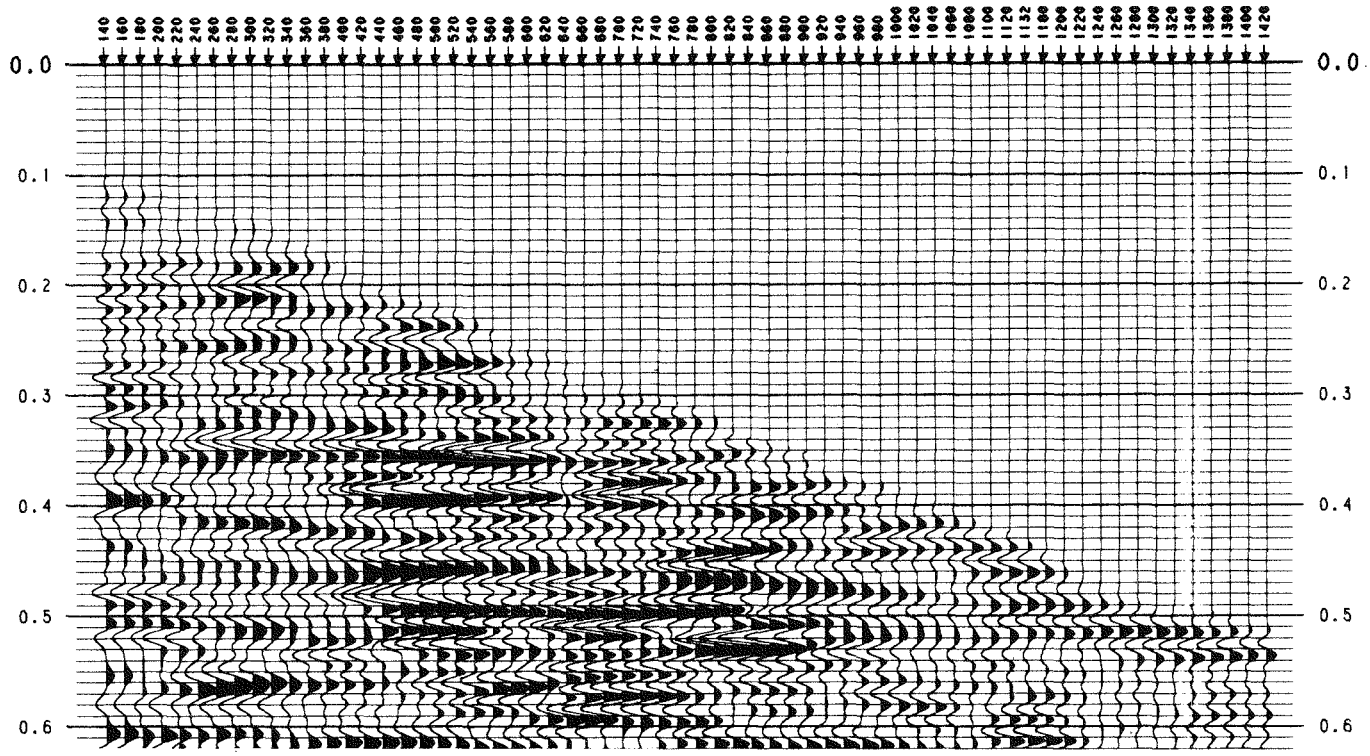

Figure 6b. U4ag 1000 ft. NE offset upgoing wavefield

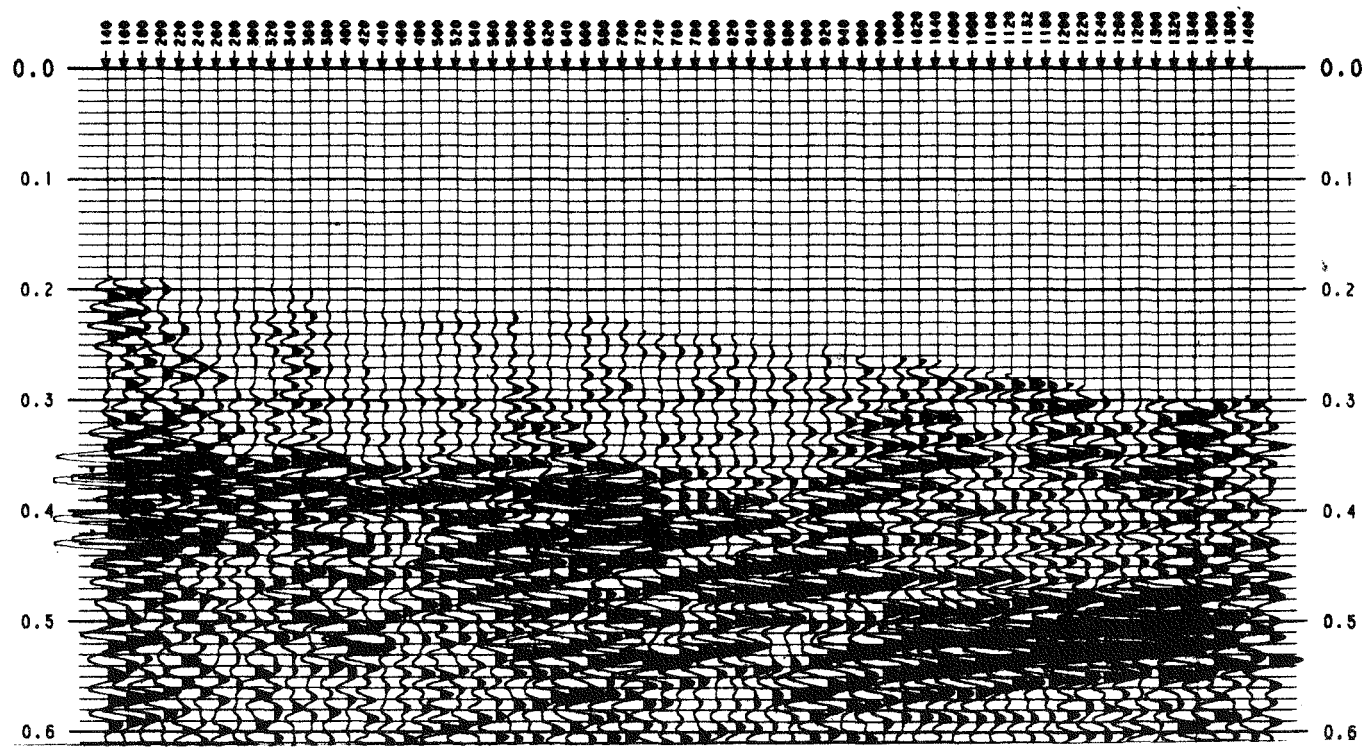

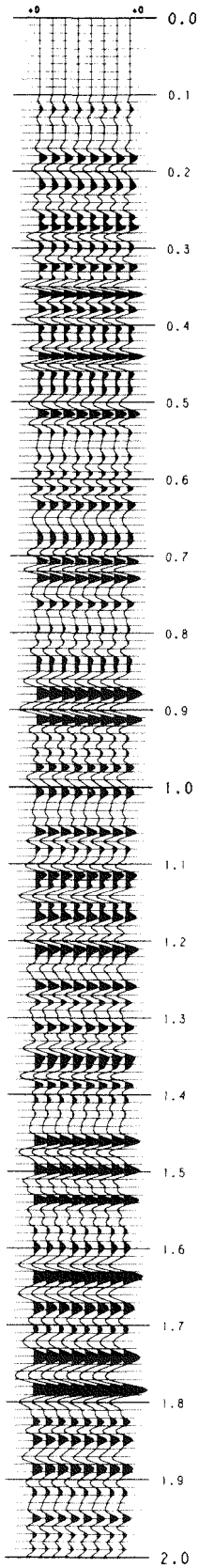

Figure 7a. U4ag 100 ft. offset corridor stack

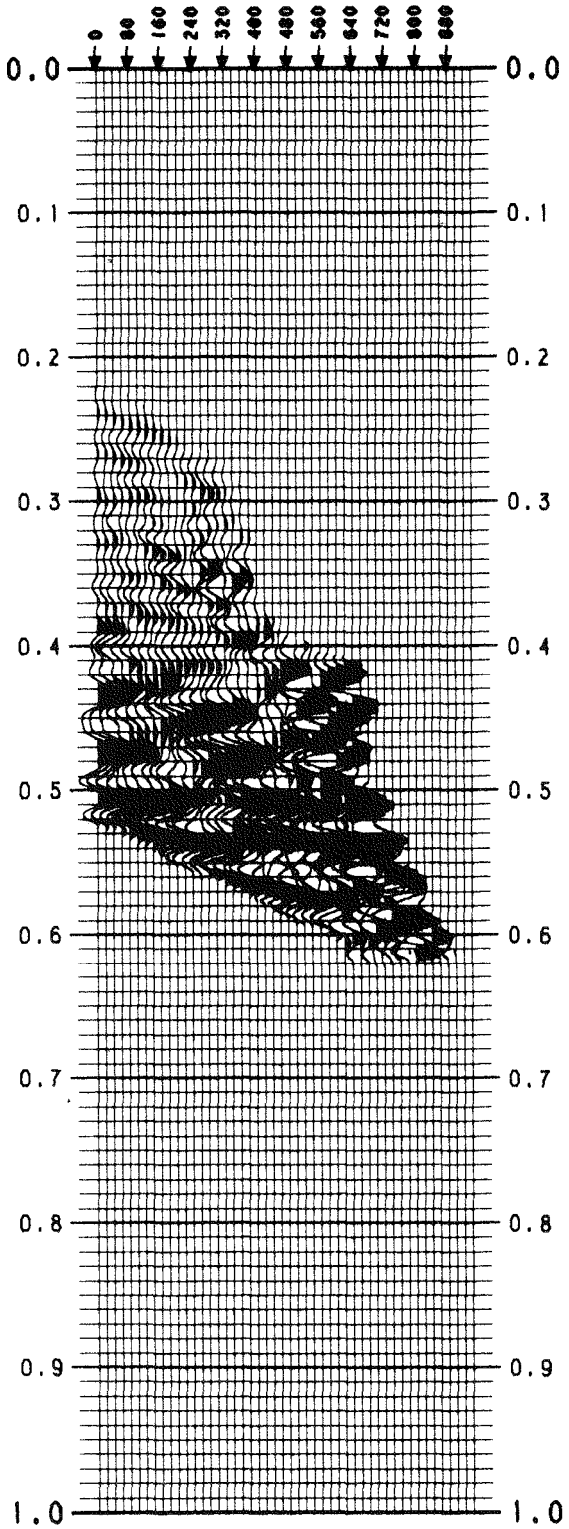

Figure 7b. U4ag 1000 ft. NE offset VSP-CDP section

always possible.

Conclusions

VSP surveys have the potential to help define the structure around a borehole. They give us another tool that can provide highly detailed information about the structure. The depth and apparent dip of a reflecting surface below the bottom of an emplacement hole can be determined with a vertically incident VSP. Offset VSP surveys can provide data about structures laterally away from the borehole. However, as with any seismic data, the quality of the final result still depends upon good geologic interpretation.

Acknowledgements

This work was supported by the Nuclear Test Containment Program at Lawrence Livermore National Laboratory. It was performed under the auspices of the U. S. Department of Energy under Contract Number W-7405-ENG-48. I would like to also acknowledge the support provided by Fenix & Scisson, Inc. in fielding the VSP experiments and the data processing conducted by Western Atlas International Downhole Seismic Services.

References

1. Balch, Alfred H., Lee, Myung W., and Muller, D. C., A vertical seismic profiling experiment to determine depth and dip of the Paleozoic surface at drill hole U10bd, Nevada Test Site, Nevada, USGS Open File Report, 1979.
2. GeoSurvey Report of Nevada Test Site Ue8c, Mercury, Nevada for Lawrence Livermore Labs, September, 1979.
3. Kiowski, John W., In-field quality control of VSP data, Oil & Gas Journal, Feb. 23, 1987, p.71-75.
4. Gal'perin, E. I., Vertical Seismic Profiling, Society of Exploration Geophysicists Special Publication No. 12, Tulsa, Oklahoma, 1971.

SHEAR WAVE VELOCITIES FROM SONIC LOGS IN EMPLACEMENT HOLES

Robin L. Newmark

Earth Sciences Department
Lawrence Livermore National Laboratory

ABSTRACT

The shear wave velocity (V_S) combined with the compressional wave velocity (V_P) yields a value of the dynamic Poisson's ratio. Poisson's ratio values are input to phenomenological calculations and are currently either derived from velocity measurements made on small core samples obtained in an emplacement hole or inferred from measurements made on samples obtained in nearby holes or similar materials. V_P is measured in emplacement holes by sonic logging (Dry Hole Acoustic Log–DHAL) and seismic methods. V_S is currently measured on selected core samples in the laboratory. **In situ** measurement of V_S would yield the variation of Poisson's ratio with depth.

Relative shear-wave velocities can be calculated from signals recorded by the two-receiver DHAL (DHAL MR). An energy packet within the DHAL signals has been identified as a pseudo-Rayleigh wave that travels along the wall of the empty borehole. Biot has shown that the velocity of the Rayleigh energy is related to the shear wave velocity. The signals from the two DHAL receivers are filtered, windowed and cross-correlated to obtain the best estimate of the time delay between the arrival of this Rayleigh energy at each of the receivers. From this time delay, the pseudo-Rayleigh wave velocity is calculated. Using Biot's relations and knowledge of the borehole diameter and signal wavelengths, Vs is calculated.

To check the accuracy of this correlation method, the same technique is applied to the compressional wave arrivals in the signal. V_P estimated using this correlation technique compares well with V_P obtained by picking first arrivals.

This technique is being applied to data obtained in holes drilled in a variety of materials at the Nevada Test Site (NTS). The signals arriving at the more distant receiver are often attenuated in lavas and in ash-flow tuffs, probably because of energy loss in units with more fractures or high gas-filled porosity. In the alluvium section of hole U2fh, V_P ranges from 1.0-4.0 km/s with a mean of 1.75 ± 0.50 km/s; V_S ranges from 0.53-1.6 km/s with a mean of 0.85 ± 0.22 km/s, and Poisson's ratio ranges from about 0.20 to over 0.40, with a mean of 0.33 ± 0.06. In the bedded tuffs of the lower portion of hole U20ai, V_P ranges from 1.10-2.65 km/s with a mean of 2.00 ± 0.35 km/s; V_S ranges from 0.56-1.29 km/s with a mean of 1.01 ± 0.16 km/s. Poisson's ratio varies between 0.23 and 0.43, with a mean of 0.33 ± 0.05. These values for V_P, V_S and Poisson's ratio are consistent with the range of values measured on similar materials in the laboratory or in the field.

INTRODUCTION

Computer calculations of the effects of underground nuclear explosions require fairly accurate knowledge of compressional (V_P) and shear (V_S) wave velocities. Combining V_P and V_S yields a value of the dynamic Poisson's ratio, a material parameter that can be used to characterize the elastic behavior of that material.

At present, V_P is measured in emplacement holes by sonic logging (Dry Hole Acoustic Log–DHAL) and seismic check shot methods. Occasionally, V_S is obtained from the seismic surveys. The seismic velocities are obtained over a long travel path (i.e., surface to hole bottom), and are not generally applicable to modelling of the elastic parameters of individual lithologic units. Due to their frequency ranges and areas of investigation, these **in situ** techniques provide acoustic information on a relatively large scale (tens of centimeters to hundreds of meters) and are affected by heterogeneities such as fractures, voids and material changes on a similar scale. These relatively large-scale features can strongly affect the manner of energy propagation, interaction, and resulting ground motion during and after an underground nuclear explosion. V_P determined from seismic methods is currently used as input for calculations.

Both V_P and V_S are also measured on relatively small core samples (centimeters to tens of centimeters long) in the laboratory. These measurements are made at high (ultrasonic) frequencies. The scale of heterogeneities sampled by these measurements is similarly much smaller and is not necessarily representative of the bulk formation properties, particularly those that determine how energy propagates and interacts during an underground nuclear explosion. These laboratory-measured V_S values are usually the only source of V_S data available from emplacement holes. Core samples are expensive and often difficult to obtain and measure. As a result, V_S values from samples obtained in nearby holes or in similar materials are used in the phenomenological calculations, which may not be representative of the emplacement hole formation properties.

Determination of V_S from downhole geophysical logs would prove a great improvement over the present procedure, providing a more representative measurement of V_S and some knowledge of how it varies with depth as well as an estimate of dynamic Poisson's ratio and how it varies with depth. This paper describes a technique whereby an estimate of V_S (and thus dynamic Poisson's ratio) can be made from the two-receiver DHAL (DHAL MR) data.

A relatively low-frequency energy packet is identified within the DHAL MR signals. Theoretical analyses show that (1) this energy results from surface, not shear wave propagation and (2) the surface wave can be described as a pseudo-Rayleigh wave that is nearly identical to a Rayleigh wave.

A combined filtering and cross-correlation analysis that extracts estimates of V_P and V_S from the DHAL MR records is described. Cross-correlation analyses are performed on DHAL MR logs from two holes drilled in different materials at NTS. Values of V_P, V_S,

and Poisson's ratio obtained from these analyses are compared with values obtained from (1) the same DHAL records by a different technique in the case of V_P and (2) laboratory and field experiments on similar materials for V_P, V_S, and Poisson's ratio to evaluate the accuracy of this technique. The cross-correlation technique provides values of V_P, V_S, and Poisson's ratio that compare favorably with existing data.

THE DATA

The first DHAL tool was designed to obtain velocity information, both compressional and transverse, in dry holes ranging in diameter from 1 to 4 m. The original tool, in use since 1966, consists of a single source and receiver, and is described by Hearst et al., (1970, 1973). The two-receiver DHAL (DHAL MR, in use since 1974) is very similar in design except that it has two receiver transducers (Fig. 1). The source and receiver transducers each consist of a stack of 20 piezoelectric transducers (PZT-4 ferroelectric disks, International Transducer Corporation model ITC-150A), a headmass, a tailmass, and a horn, each designed for 10 kHz. The transducers are 0.914 m (3 ft) apart in the original DHAL sonde and 1.0 m (3.28 ft) apart in the DHAL MR, with the two receivers mounted in a rigid section of the sonde, and the transmitter located in a hinged section, which provides for better coupling with the borehole wall. The full waveforms (about 8 ms long) are digitally recorded.

The region immediately surrounding a borehole is subject to invasion of the drilling fluid and subsequent flushing of formation fluids, and is often microfractured (e.g., Schlumberger, 1972, Zoback et al., 1983). The dry emplacement holes are thought to have a relatively deep zone of disturbance because of their large diameters. Thus, logging tools with relatively shallow depths of investigation might be expected to be strongly affected by the presence of the disturbed zone, and may not provide a very representative estimate of the formation properties. Velocities obtained using the DHAL logs were observed to be generally lower in large-diameter holes than in small-diameter ones (Howard, 1985). The DHAL MR was developed in the early 1970s using standard industry methods to investigate the depth of this disturbed zone in dry holes. The two source-receiver spacings each represent a different energy path, one of which has a longer residence time in the formation (Fig. 2). By differencing the travel times of the two receivers, it is possible to "cancel out" that part of the travel path common to both (i.e., the source-to-formation portion, part of the formation path, and the formation-to-receiver portion), leaving only that portion of the travel path actually travelling within the formation between the two receivers. The resulting travel time should be more representative of the actual formation travel time and less subject to near-borehole disturbances. The recording of waveforms at more than one receiver allows moveout calculations to be made for different energy packets (calculating the velocity from the difference in arrival time of an energy packet at different receivers).

At the Nevada Test Site, hole U2fh is a 2.44 m (8 ft) diameter emplacement hole that was drilled 390 m (1279 ft) into primarily dry Quaternary alluvium, and it bottoms in Paintbrush Tuff. Figure 3 shows the signals recorded by the near and far receivers at a DHAL location at a depth of 307.9 m. The signals show a strong resonance in the 5 to 11

kHz band, with a peak at about 8-9 kHz. This 8-9 kHz energy is dominant both in the raw recorded signals (Fig. 3) and in their Fourier spectra (Fig. 4). The first break of the compressional-wave arrival has been picked by hand; the standard processing procedure. The compressional-wave time picks are indicated by vertical lines, at 0.51 ms on the near-receiver signal, corresponding to a V_P of 1.96 km/s, and 0.85 ms on the far-receiver signal corresponding to a V_P of 2.35 km/s (Fig. 3). This yields a (far-near) time difference of 0.34 ms, corresponding to a V_P of 2.94 km/s. The remainder of the signal is dominated by the 8-9 kHz energy which is the resonant frequency of the source and receiver transducers. There appears to be a relatively low-frequency signal underlying this resonance from about 1.5 to 2.75 ms in the far-receiver signal. No corresponding low-frequency energy is evident in the near-receiver signal.

Removing the dominant resonant energy in the 6-10 kHz range by bandpass filtering reveals a different structure in the signal. Figure 5 shows the same signals with a notch filter from 6-10 kHz rejecting energy in that frequency band. The outgoing signal energy within the first 2 ms is more evident in the near-receiver signal, of nearly the same amplitude as the compressional arrival (at about 0.5 ms). The compressional wave arrivals are fairly low amplitude compared to the whole waveform, and are relatively easy to identify. The vertical lines indicating the first break of the compressional wave arrival no longer occur on the same part of the waveform as in the unfiltered signals. The bandpass filter is a two-pass process, and does not result in a phase shift of the signal. It is clear from this example that the time picks of the first arrival using the raw, unfiltered signal (Fig. 3) may be off by several tenths of milliseconds. The travel time to the center of the filtered near-receiver first signal peak is 0.48 ms (corresponding to a V_P of 2.05 km/s), and the center of the corresponding peak on the far-receiver signal is 0.90 ms (corresponding to a V_P of 2.22 km/s). This yields a (far-near) value of 0.42 ms, corresponding to a V_P of 2.38 km/sec. This is less than the V_P of 2.94 km/sec determined by differencing the first break travel times of the raw signals. However, it is higher than either $V_{P(near)}$ or $V_{P(far)}$, which is expected, as the differenced signal path traverses relatively undisturbed, and thus higher-velocity material.

When the signals are emergent, picking the exact center of a peak or the first break can be quite difficult. Cross-correlation techniques can provide a more accurate comparison of two signals, as they include more of the waveform. In cross-correlation, one signal is passed across another signal in time, and, at each time increment, the product of their amplitudes is computed. The maximum cross-correlation value occurs at the time delay required to shift one signal so that the product of the amplitudes is the greatest.

Cross-correlation techniques are applied to the U2fh DHAL MR data as follows. Windows are applied to the signal in order to isolate the first compressional wave energy (Fig. 6). These signals are filtered to remove the resonant 6-10 kHz energy (Fig. 7). The filtered signals are cross-correlated to determine the time delay between the arrival of the compressional energy at the near and far receivers (Fig. 8). For the example in Fig. 8, the peak value in the cross-correlation occurs at 0.43 ms. Because the two receivers are 1 m apart, this time delay corresponds to a velocity of 2.34 km/s, which compares favorably with the

velocities derived from the first arrivals in either of the raw signals. It is somewhat lower than $V_{P(far-near)}$.

A relatively high-amplitude, low-frequency energy packet appears in both the near- and far-receiver filtered signals, occurring between about 0.70 and 1.70 ms in the near-receiver signal and about 1.50 and 2.75 ms in the far (Fig. 5). Analysis of these signals determined that this energy dominates the 1-4 kHz band. Additional bandpass filtering to remove the high frequency components of these signals results in the waveforms shown in Fig. 9. The late-arriving, low-frequency energy is now very clear in the signals from both receivers. The waveforms appear nearly identical, with a small moveout, or difference in arrival time, at the two receivers. Cross-correlation of these filtered signals results in the curve plotted in Fig. 10, which identifies a peak time delay of 0.849 ms, corresponding to a velocity of 1.18 km/s. Energy of this frequency range occurs in nearly all the DHAL MR records from hole U2fh, with velocities ranging from about 0.58-1.4 km/s. The next sections will discuss theoretical analyses which show that (1) these arrivals result from surface, not shear wave propagation, and (2) the surface wave can be described as a pseudo-Rayleigh wave that is nearly identical to a Rayleigh wave.

LAMB'S PROBLEM

As the emplacement holes are generally dry and of large diameter (2-4 m), it is reasonable to model the DHAL MR source-receiver signals (for a first approximation) as an elastic disturbance propagating in a half space, which is referred to as Lamb's problem (Båth, 1968). In this idealized model, an impulse disturbance (point source) propagates in a half space, resulting in horizontal and vertical displacements such as those shown in Fig. 11 at some large distance from the source. Although the compressional and shear wave amplitudes fall off as $1/r^2$ (where r is distance from the source), the Rayleigh wave amplitude decreases as $1/r^{1/2}$. At sufficient distance, the large-amplitude Rayleigh wave amplitude dominates the signal; the shear wave arrival is a small bump just ahead of the Rayleigh wave. The theory defining Lamb's problem assumes a homogeneous elastic medium without layering and therefore with no dispersion. In a somewhat layered earth (a more realistic model for the DHAL configuration), dispersion might be expected. This idealized model supports the interpretation that the large-amplitude, relatively low-frequency arrival observed in the DHAL MR records is a Rayleigh or pseudo-Rayleigh wave, and not the shear wave.

WAVEFORMS IN A BOREHOLE

The propagation of elastic waves in a cylindrical borehole has been treated by Biot (1952). In addition to the compressional and shear waves that propagate as head waves along the borehole-formation interface, there are waves that propagate in other modes, including a dispersive surface wave analogous to a Rayleigh wave at the plane boundary of a semi-infinite solid. Considering an air-filled cylinder in an elastic solid of infinite extent, Biot derived expressions for the phase and group velocities of axial-symmetric surface waves along the bore. This mode differs from the classic Rayleigh wave in that the characteristic

velocity is a limited function of frequency, and the nature of the waves obtained along the bore is a function of the frequency of propagation, the diameter of the borehole, and the ratio of the compressional and shear velocities. Biot showed that a dispersive surface wave, called a pseudo-Rayleigh wave, may propagate along the borehole wall at a velocity between the Rayleigh-wave velocity at low wavelength/diameter ratios and the shear-wave velocity for high wavelength/diameter ratios.

At wavelengths above a cutoff wavelength, λ_c, the velocity of the surface waves becomes larger than the shear-wave velocity, and a disturbance propagating at the surface with such a velocity causes shear waves to be radiated, and the energy of the surface waves is dissipated. The ratio λ_c /D, where D= borehole diameter depends on the Poisson's ratio, is shown in Fig. 12, reproduced from Biot's paper. The range in Poisson's ratio for NTS tuff found in refraction surveys in tunnels at NTS (Carroll, 1986) and in laboratory measurements made on samples from boreholes (e.g., Constantino and Bonner, 1980) is from 0.20-0.40. Applying values appropriate to emplacement hole U2fh: diameter = 2.44 m, the V_S velocity range = 0.58-1.40 km/s, and the frequency range of 1-4 kHz, the ratio λ /D ranges from about 0.06 to about 0.57. This range falls substantially below the shear wave cutoff (λ_c /D) of about 1.5 for the observed Poisson's ratio range of 0.20-0.40, indicating that this energy observed in the U2fh example has the characteristics of an unattenuated dispersive surface wave.

When the characteristic wavelength of propagation becomes much smaller than the radius of curvature of the borehole (approximating a plane boundary), this mode becomes identical to the Rayleigh wave. Using the same values of borehole diameter, velocity range, and frequency for hole U2fh, we calculate a range of propagation wavelengths of about 0.15 to 1.4 m. Values in this range are near to if not less than the borehole radius of 1.22 m. Thus, this mode is found to be a pseudo-Rayleigh wave.

Biot derived the group-velocity curves for these surface waves; the value of V_R/V_S is plotted as a function of $\pi D/\lambda$ in Fig. 12, for various values of Poisson's ratio. For values of $\pi D/\lambda > 5$, these curves are relatively flat. Substituting appropriate D and λ values for NTS holes, for $\pi D/\lambda > 5$, the frequency must be $\geq$ 1 kHz. This condition is satisfied by the appropriate bandpass filtering, which for the pseudo-Rayleigh wave energy in the DHAL data is from 1 to 3 kHz. For a maximum range of Poisson's ratio from 0 to 0.5, V_R/V_S will range from 0.88 to 0.96. In this study, the shear wave velocity is calculated by dividing the pseudo-Rayleigh wave velocity by 0.92, which corresponds to a Poisson's ratio of 0.25, the value observed for many rocks (e.g., Aki and Richards, 1980). However, as discussed later in this paper, Poisson's ratio for many NTS materials generally ranges from 0.30-0.40. For the velocity range observed in this study, a range in Poisson's ratio of 0.0-0.50 results in a $\pm$4% variation in the resulting estimate of V_S. As Poisson's ratio almost certainly lies between 0.20 and 0.40, the uncertainty in the estimate of V_S due to the uncertainty in Poisson's ratio is $\pm$2%.

RESULTS

U2fh

Hole U2fh was drilled 427 m (1405 ft) into alluvium and tuff at the NTS. The lithology is described by Schmidt (1984). Cross-correlation analysis was performed on the DHAL MR log of hole U2fh. The compressional waveforms were windowed, filtered to remove the instrument resonance, and cross-correlated to determine V_P. The complete waveform was filtered to enhance the 1-3 kHz energy, and cross-correlated to determine V_R. V_S is calculated by dividing V_R by 0.92. The results are shown in Fig. 13A, along with the dynamic Poisson's ratio calculated from these velocities. Depths at which no data are available or no velocity determination has been made have zero values for velocity. In general, the velocities increase as a response to the increasing overburden. Besides this trend, however, there are depth intervals that display different characteristics such as greater or less variability, or changes in velocity gradient with depth. There is some agreement between the depth intervals that display similar velocity character and lithologic intervals as described by the preliminary lithologic log (Schmidt, 1984). Figure 13B displays the averaged velocity profiles along with the caliper log and the general lithology. The three curves indicate the range in estimate for V_S assuming a range in Poisson's ratio of 0.0-0.50. The range in uncertainty in V_S is less than its variability.

Both V_P and V_S decrease over the upper 90 m. From 90-164 m, V_P shows a gradual increase to about 1.65 km/s, while V_S remains nearly constant. The upper 159 m (Lithologic Unit 1) is described as mixed alluvium, 50-80% volcanic rock fragments and 20-50% Paleozoic rock fragments consisting dominantly of argillites and quartzites, with a lesser amount of dolomites and limestones. From 164-244 m, V_P remains relatively constant. Over this interval, V_S increases slightly from about 0.6 to 0.85 km/s at 164 m, remaining nearly constant about 0.8 km/s from 164-244 m.

Below 244 m, there is a distinct increase in both V_P and V_S, until about 267 m. From 267-335 m, both V_P and V_S are more variable than in the upper section of the hole. V_S remains nearly constant, about 1.1 km/s, while V_P varies about an average value of about 2.15 km/s. The lithology betwen 159 and 335 m (Lithologic Unit 2) is described as mixed alluvium, 75-80% Paleozoic rock fragments similar to those described above, with 25-20% volcanic tuff fragments. This material might be expected to have higher intrinsic velocities than the material overlying itbecause of the larger proportion of higher-velocity rock fragments (the tuff fragments generally have lower velocities because they often contain abundant gas-filled porosity, whereas most of the Paleozoic rock fragments do not). The variations in V_P and V_S over the lower part of this interval may reflect changes in the proportions of rock fragments with depth.

From 335-390 m, V_P increases to about 2.45 km/s while V_S doesn't appear to change. From 335-344 m (Lithologic Unit 3), the lithology is mixed alluvium, with 75-90% Paleozoic rock fragments, 10-25% volcanic tuff fragments. There is no strong velocity response to this change in the proportions of the dominant lithologic components, although both V_P

and V_S increase from 335-344 m. The tuff fragments increase at the bottom of the interval. From 344-390 m (Lithologic Unit 4), the lithology is described as tuffaceous alluvium, 90% volcanic tuff fragments and 10% Paleozoic fragments.

Below 390 m, the character of the recorded signals is quite different. Overall, V_P varies between about 1.8 and 3 km/s, and V_S between about 0.75 and 1.1 km/s. From 390 m to hole bottom (427 m), the hole penetrates Paintbrush Tuff (Lithologic Unit 5), described as glassy to massive. The DHAL MR records are of poor quality over this lower section of the hole. At several locations, only one receiver's signals are recorded. Attenuation is common on the signals recorded by the far receiver (see Fig. 15). This may be due to the structural heterogeneity of the formation (glass, cooling cracks, and massive units), reducing the energy of propagation, or hole enlargements affecting the quality of the tool's coupling with the borehole. Although the tool generally couples well to the borehole wall, hole enlargements may result in some reduction in coupling, which will also reduce the record quality. Only two locations provided good-quality records on both the near and far receivers.

Poisson's ratio is calculated from V_P and V_S, and is also shown in Fig. 13. There is considerable scatter in the individual values, which vary between about 0.21 and 0.44. However, some trends can be identified in the plot of the averaged values (Fig. 13B). From about 50-110 m, Poisson's ratio increases from about 0.25 to about 0.35. From 110-170 m, it decreases slightly. At about 183 m there is an abrupt increase in Poisson's ratio to about 0.35. Below 183 m Poisson's ratio varies a great deal about 0.32, and seems to decrease again to about 0.30.

U20ai

Cross-correlation analyses were performed on the DHAL MR records obtained in the lower 305 m of hole U20ai. This hole was drilled to a total depth of 656.5 m through a series of tuff and lava units characteristic of Pahute Mesa at the NTS. The results are shown in Fig. 14A, along with the Poisson's ratio calculated from these velocity values. Average velocities are displayed in Fig. 14B, including curves representing the range in V_S resulting from a range in Poisson's ratio of 0.0-0.50. Both the general lithology and the caliper log are also shown.

The DHAL MR records in the upper 96 m (from 305-400.5 m) are of poor quality. Many of the recorded signals are highly attenuated, and often signals from only one receiver were detectable (Fig. 15). V_P increases from about 1.75 km/s to about 2.75 km/s. V_S is about 1.0 km/s. This section of hole penetrates the lower portion of the Rainier Mesa Member of the Timber Mountain Tuff, which has moderate to minor cooling joints. It is described as a partially to moderately welded ash-flow. A short interval from about 369-378 m shows a constant high velocity of about 2.75 km/s. This interval coincides with the occurrence of a densely-welded vitrophyre (373-380 m).

At about 400.5 m, V_P drops abruptly to about 1.25 km/s. V_P decreases as well. From

400.5-457 m, V_P shows a gradual increase to about 2.25 km/s. Over this same interval, V_S increases from about 0.80 to 1.0 km/s. From about 450-470 m, the records decrease in quality, probably reflecting poor coupling in the large zone of hole enlargement. Both V_P and V_S drop over this interval. Extensive hole enlargement occurs over this depth interval. Excluding this disturbed zone, both V_P and V_S increase between about 400.5 and 548.6 m, V_P from about 1.25-2.25 km/s, V_S from about 0.75-1.15 km/s. This section of hole is described as bedded tuff, vitric to devitrified, partly zeolitized.

From 548.6-578.5 m, V_P is more variable and the average value decreases a bit, particularly at the bottom 6 m of the interval. V_S remains nearly constant. This section of the hole is described as zeolitized, bedded tuff, mostly reworked with abundant rhyolitic debris. The decrease in V_P at the bottom of this interval may be a response to larger scale heterogeneity at the bottom of this unit.

At 576.2 m, V_P drops from about 2.2 km/s to about 1.5 km/s. V_P increases steadily from 576.2-619 m to about 2.75 km/s. V_S varies about an average value of about 1.5 km/s to 591 m. Below this depth, it is not possible to extract V_S from the records. This lower section of the hole penetrates the upper part of a rhyolitic lava flow. The top 20 m (66 ft) are described as brecciated, frothy, devitrified to vitric, and partially zeolitized. From 591-610 m, the lava flow is vitric to partially devitrified and zeolitized. Signal strength is very high, and most of the records are clipped (Fig. 15), making cross-correlation analysis impossible. Changes in the current recording practice can correct this problem. V_P increases at the bottom of the section as the formation becomes more competent.

Poisson's ratio remains fairly constant at about 0.32 from 305-567 m (Fig. 14). It drops to below 0.20 at 567 m, then increases steadily to about 0.36 at 591 m, below which V_S is not available.

DISCUSSION

To evaluate the accuracy of the velocity determinations, comparisons can be made between the velocities obtained using different techniques. The common practice in processing the DHAL MR data is to first pick the travel time (Δt) of the first energy arrival (assumed to be the compressional wave) in both the near and far receiver records. If both the near and far receiver signals are of good quality, the Δt from the near-receiver signal is subtracted from the Δt from the far-receiver signal, and $V_{P(far-near)}$ is computed from the remainder Δt, dividing by the distance between the receivers (1 m). However, it is not always possible to use both the near and far receiver signals because of such factors as recording errors, noise and attenuation. In these cases, the V_P is obtained from either the near receiver ($V_{P(near)}$) or the far receiver ($V_{P(far)}$) alone. Since a significant portion of the travel paths for these signals traverses the disturbed zone along the borehole wall, these estimates of V_P are nearly always smaller than the estimates of V_P based on the differenced Δt. Signals reaching the near receiver have a larger proportion of their travel path in a more disturbed zone than those reaching the far receiver. V_P obtained from the near-receiver records might be expected to be lower than those obtained from

the far-receiver records. Figure 16 shows V_P determined from the near and far receiver signals alone ($V_{P(near-receiver)}$ and $V_{P(far-receiver)}$), the (far-near) travel time difference ($V_{P(far-near)}$), and the cross-correlation technique ($V_{P(cross-correlation)}$) for a 91 m (300 ft) section of hole U2fh. As expected, the $V_{P(near-receiver)}$ is generally the lowest estimate. Of all the travel paths, energy recorded at this receiver has spent the greatest proportion of its travel path in the more disturbed zone along the borehole wall. $V_{P(far-receiver)}$ is the next-highest estimate. $V_{P(far-near)}$ is generally the highest estimate. $V_{P(cross-correlation)}$ is higher than either of the single receiver estimates, yet it is commonly somewhat lower than $V_{P(far-near)}$. Comparison of these four estimates can provide some understanding of the reliability of the cross-correlation technique, at least compared to standard estimates.

The variation between two sets of velocity data are computed and plotted as percent difference in Figs. 17 and 18. For hole U2fh, 76% of the (nonzero) values of $V_{P(near)}$ and $V_{P(far)}$ lie within $\pm 20\%$ of each other (Fig. 17). The majority of the values of $V_{P(far)}$ are higher than $V_{P(near)}$. This means that if high-quality data were sparse, making it impossible to calculate $V_{P(far-near)}$ for much of the hole, the choice of $V_{P(near)}$ vs $V_{P(far)}$ could result in $\pm 20\%$ difference in 76% of the data, and a larger difference for the remaining 24%. By comparison, 84% of the (nonzero) values of $V_{P(cross-correlation)}$ and $V_{P(far-near)}$ lie within $\pm 20\%$ of each other (Fig. 18). Moreover, these results are generally less biased, with values distributed both above and below zero. The cross-correlation technique more closely approximates the preferred estimate of V_P than either $V_{P(near)}$ or $V_{P(far)}$. Also, since the cross-correlation technique utilizes a more accurate representation of the compressional waveform (the filtering removes the instrument resonance that dominates the raw signal), it is likely that it provides a more consistent estimate of V_P than that obtained by differencing the first arrival travel times picked using the raw signals.

Velocities measured on small samples in the laboratory are commonly higher than those measured in large-scale experiments **in situ** because they preferentially sample the more competent material and do not include large-scale heterogeneities such as large fractures that may be present in the formation. Moreover, they are rarely tested at conditions representative of their **in situ** environment (i.e., overburden pressure). In laboratory experiments, samples are often tested at inappropriately high pressures, which generally result in increased velocities. If tested at atmospheric conditions, the velocities would probably be slower.

The only laboratory measurements of ultrasonic velocities of NTS alluvium samples known to this author were made on cored and reconstituted material from hole Ue5n, area 5, Frenchman Flat, NTS by Constantino and Bonner (1980). These values are shown in Table I for comparison with the sonic results. The alluvium in this hole has been described as tuffaceous sediments (Ramspott and McArthur, 1977). For eight samples, mean values for all velocity/pressure runs were: $V_P = 2.15 \pm 0.25$ km/s, $V_S = 0.92 \pm 0.08$ km/s, and Poisson's ratio $= 0.38 \pm 0.04$. For hole U2fh, mean values are shown in Table II. Based on the lithologic descriptions, Lithologic Unit 4, (tuffaceous alluvium), is perhaps the unit most comparable to the material in Ue5n. Mean values of V_P, V_S, and Poisson's ratio for Lithologic Unit 4 compare well with the values obtained by Constantino and Bonner

(1980). **In situ** average velocities obtained from seismic surveys in Frenchman Flat and Yucca Flat alluvium are also shown in Table I. Velocities determined using cross-correlation analysis on the DHAL MR log of U2fh are generally higher than those obtained by seismic methods, yet lower than those measured on core samples in the laboratory. This is to be expected, because the scale of investigation of the DHAL MR is between that of seismic and laboratory experiments, and the sonic travel path probably traverses somewhat disturbed material.

In hole U20ai, only the original DHAL run (with a single receiver) was analyzed for V_P using first arrival travel time picks. Comparison between $V_{P(single-receiver)}$ and $V_{P(cross-correlation)}$ shows that, in areas of attenuation, scattering, or poor coupling due to hole enlargements or structural heterogeneities such as cooling joints, the cross-correlation technique gives less consistent results (Fig. 19). For example, in the upper 96 m of the analyzed section where cooling joints are common, only 33% of the (nonzero) $V_{P(single-receiver)}$ values are within ±20% of the $V_{P(cross-correlation)}$ values. However, below 400.6 m, 78% of the (nonzero) $V_{P(cross-correlation)}$ values are within ±20% of the (nonzero) $V_{P(single-receiver)}$ values. Between 450 and 470 m, major hole enlargements evident in the caliper log are responsible for poor signal quality, causing large data gaps. It would appear that, in sections of hole that are fairly competent (relatively few cooling joints, fractures, large-scale heterogeneities, hole enlargements, or low gas-filled porosity), the cross-correlation technique provides good estimates of V_P while also providing estimates of V_S and Poisson's ratio.

There are some problems with this technique. In zones of attenuation, scattering or poor coupling due to structural heterogeneities such as fractures, voids or hole enlargements, the cross-correlation technique gives less consistent results. Of course, the standard technique is less accurate in these circumstances as well. However, the standard technique requires good signal quality at at least one receiver, whereas the cross-correlation technique requires signals from both receivers. Similarly, in zones of high signal strength, where the recorded signals are clipped, this technique may fail. Changes in current data acquisition practices could improve the quality of the recorded signals and thus improve the analysis results.

Laboratory measurements of ultrasonic velocities were made on a sample of the Rainier Mesa member of the Timber Mountain Tuff (Schock et al., 1974), and on samples of Indian Trail Tuff from the Diamond Dust mine (Stephens et al., 1970) and the Diamond Mine site (Heard et al., 1971). Average **in situ** velocities of these tuffs were obtained from seismic surveys at two of these sites as well (Heard et al., 1971). These values are shown in Table III. Average values of V_P, V_S and Poisson's ratio for the lithologic units encountered in U20ai are given in Table IV.

The values of V_P, V_S, and Poisson's ratio obtained using the cross-correlation technique compare well with the range of values obtained in similar materials. The **in situ** confining pressure of the laboratory-measured sample of the Ranier Mesa Member of the Timber Mountain Tuff (Table III) is between 2 and 2.5 MPa, so the appropriate velocities

for comparison lie between those shown in Table III. As expected, the average velocities obtained by the DHAL are lower than those measured on samples in the laboratory. Values of Poisson's ratio are similar to the laboratory-derived values. The DHAL MR velocities are closer to those obtained using seismic methods than those obtained in the laboratory. This is to be expected, because the scale of investigation of the DHAL MR more closely approximates the scale of heterogeneities encountered by seismic methods.

In a porous material, the compressional sound speed, V_P, depends strongly on the number and "quality" of interparticle contacts. Increases in V_P of several hundred percent have been reported in unconsolidated materials (Bonner et al., 1972, Talwani et al., 1973) as application of hydrostatic stress to partially saturated samples increases both the number of contacts and their normal contact force (the "quality"). However, the shear-wave speed, V_S, should depend only on the effective stress. Constantino and Bonner (1980) documented the strong increase in V_P vs pressure (σ) until near-saturation is reached (Fig. 20). V_S increased weakly, and became constant at moderate σ. During hydrostatic loading, the V_P/V_S ratio increased smoothly, driven by the increase in V_P with respect to V_S. These results document the low sensitivity of V_S to changes in confining pressure at low to moderate pressures in unsaturated materials such as alluvium. This effect is quite relevant to the DHAL MR results. V_P obtained from the DHAL MR records may reflect changes due to increasing overburden with depth or local decreases because of microfracturing near the borehole resulting from stress relief or the formation of wellbore breadouts. However, the estimate of V_S from these records may be relatively insensitive for a wide range of low to moderate pressures (which includes the range expected near the borehole wall in emplacement holes), and thus may be a fairly reliable estimate of the intrinsic formation V_S.

SUMMARY AND CONCLUSIONS

A packet of relatively low-frequency energy within the DHAL MR records is identified. Theoretical analyses show that (1) this energy results from surface, not shear wave propagation, and (2) the surface wave can be described as a pseudo-Rayleigh wave that is nearly identical to a Rayleigh wave, and its velocity is directly related to the shear wave velocity.

A combined filtering and cross-correlation technique has been developed that provides an estimate of V_P, V_S, and thus dynamic Poisson's ratio from the DHAL MR records. Cross-correlation analyses have been performed on DHAL MR logs from two holes drilled at NTS that penetrate different materials, providing estimates of V_P, V_S, and Poisson's ratio. These values compare favorably with values obtained (1) from the DHAL using standard techniques and (2) in laboratory and field measurements in similar materials. Thus, this is the only technique currently available that provides an estimate of the shear wave velocity and its variations with depth in the dry emplacement boreholes.

It is not clear that the estimates of V_P determined using standard techniques are any more reliable than those obtained using the cross-correlation technique. In relatively

competent sections of hole, the cross-correlation technique yields compressional wave velocities, over 75% of which are within 20% of the velocities obtained by differencing the near and far receiver travel times (the preferred standard technique). Both techniques yield generally higher values than those obtained by picking the near or far receiver travel times alone. The advantage of this analysis is that it provides both an estimate of V_P and an estimate of V_S and thus dynamic Poisson's ratio as well.

REFERENCES

Aki, K., and P.G. Richards, 1980. *Quantitative Seismology, Volume I*, W.H. Freeman and Co., San Francisco.

Båth, M., 1968. *Mathematical Seismology*, Elsevier Publishing Co., New York.

Biot, M.A., 1952. Propagation of elastic waves in a cylindrical bore containing a fluid, *Journal Applied Physics, 23*, 997-1003.

Bonner, B.P., A.E. Abey, H.C. Heard, and R.N. Shock, 1972. High pressure mechanical properties of Merlin alluvium, *LLL Rept. UCRL-51252.*

Carroll, R.D., 1986. Shear-wave velocity measurements in volcanic tuff in Ranier Mesa tunnels, Nevada Test Site, Nevada, *USGS-474-321.*

Constantino, M.S., and B.P Bonner, 1980. Ultrasonic velocities and strength of Frenchman's Flat alluvium, *LLL Rept. UCID-18862.*

Heard, H.C., R.N. Shock, and D.R. Stephens, 1971. High-pressure mechanical properties of tuff from the Diamond Mine Site, *LLL Rept. UCRL-51099.*

Hearst, J.R., and R.C. Carlson, 1973. Working drawings of the LLL Dry Hole Acoustic Log, *Univ. of California SDK-732.*

Hearst, J.R., R.C. Carlson and J.T. Rambo, 1970. K-Division experimental work Part I: Geophysics research for underground explosion technology, *LLL Rept. UCRL-50855.*

Howard, N.W., 1985. Variation in properties of nuclear test areas and media at the Nevada Test Site, *LLL Rept. UCRL-53721.*

Ramspott, L.D., and R.D. McArthur, 1977. Results of the exploratory drill hole Ue5n, Frenchman Flat, Nevada Test Site, *LLL Rept. UCID-17392.*

Schmidt, C.S., 1984. Preliminary lithologic log for hole U2fh, *Memo of 28 August, 1984.*

Schlumberger, 1972. *Log Interpretation, Volume I - Principles*, Schlumberger Limited, New York.

Schock, R.N., B.P. Bonner, and H. Louis, 1974. Collection of ultrasonic velocity data as a function of pressure for polycrystalline solids, *LLL Rept. UCRL-51508.*

Stephens, D.R., H.C. Heard and R.N. Shock, 1970. High-pressure mechanical properties of tuff from the Diamond Dust Site, *LLL Rept. UCRL-50858.*

Talwani, P., A. Nur, and R.L. Kovack, 1973. Compressional and shear wave velocities in granular materials to 2.5 kilobars, *J. Geophys. Res., 78*, 6899.

Wagoner, J.L., 1985. Preliminary site characteristics summary, U20ai, *LLL Memo C-85-86.*

Zoback, M.D., D. Moos, L. Mastin, and R.N. Anderson, 1985. Well bore breakouts and in situ stress, *J. Geophys. Res., 90*, B7, 5523-5530.

ACKNOWLEDGMENTS

The content of this paper was greatly improved through discussions with Jose Rial, Steve Taylor, Howard Patton, and Norm Burkhard. In addition, Jose Rial provided guidance in my early attempts at Green's function modelling using his code. I would like to thank Norm Burkhard, John Rambo, Joe Hearst and Dick Carlson for reviewing the manuscript.

Work performed under the auspices of the U.S. Department of Energy by Lawrence Livermore National Laboratory under contract W-7406-Eng-48.

TABLE I
Velocities Obtained in Alluvium

Laboratory Measurements:

Sample #	Depth (m)	Overburden Pressure (bar)	Experimental Confining Pressure (bar)	V_p (km/s)	V_s (km/s)	Poisson's Ratio	Reference
Frenchman Flat Alluvium							
FF2-1	400	83.10	103.4	2.41	0.89	0.38	Constantino
FF2-2	400	83.10	103.4	2.48	1.02	0.40	
FF2-3	400	83.10	103.4	2.12	0.93	0.38	and
FF2-4	400	83.10	103.4	2.37	0.90	0.42	
FF3-1	400	83.10	103.4	1.97	0.74	0.42	Bonner (1980)
FF3-2	400	83.10	103.4	1.99	0.93	0.36	
FF4-1	400	76.05	103.4	1.77	0.97	0.28	
FF4-2	400	80.36	103.4	2.10	0.96	0.37	
				2.15 ± 0.25	0.92 ± 0.08	0.38 ± 0.04	
Seismic Velocity Surveys (in situ average):							
Frenchman Flat				1.63	0.89	0.20	Howard (1985)
Yucca Flat				1.67	1.01	0.21	Howard (1985)

6247J

TABLE II
U2fh
Mean Velocities

Lithologic Unit #	Depth (m)	Description	Vp (km/s)	Vs (km/s)	Poisson's Ratio
1	0-159	Mixed Alluvium	1.32±0.21 n=38	0.68±0.13 n=38	0.314±0.069 n=38
2	159-335	Mixed Alluvium	1.92±0.36 n=56	0.93±0.18 n=56	0.335±0.056 n=56
3	335-334	Mixed Alluvium	1.87±0.23 n=3	0.94±0.09 n=3	0.332±0.016 n=3
4	334-390	Tuffaceous Alluvium	2.31±0.89 n=13	1.12-0.29 n=12	0.346±0.082 n=12
5	390-427	Paintbrush Tuff	2.68±0.40 n=2	1.07±0.37 n=2	0.405±0.042 n=2
	Mean alluvium (units 1-4)		1.75±0.50	0.85±0.22	0.329±0.064

TABLE III
Velocities Obtained in Tuff

Laboratory Measurements

Sample #	Depth (m)		Experiemental Confining Pressure (bar)	V_p	V_s	Poisson's Ratio	Reference
Indian Trail Tuff: Diamond Dust Mine, Tunnel U16a05, Area 16:							
Unit 4a, i8	42.07		0	3.16	1.69	.300	
Unit 41, e1	109.15		0	2.61	1.51	.249	Stephens
Unit 41, e1	112.5		0	2.40	1.20	.334	et al (1970)
Unit 3, i6	13.72		0	2.87	1.39	.346	
mean				2.76±0.33	1.45±0.21	0.31±0.04	
Indian Trail Tuff: Diamond Mine, Tunnel U16a06, Area 16:							
4C (I) 71-1			0	3.17	1.72	0.294	
4C (II) 71-2	12.5	2.33	0	3.10	1.67	0.297	Heard et al.
4C (III) 71-3	12.5	2.33	0	3.21	1.62	0.328	(1971)
4C (IV) 71.4	12.5	2.36	0	3.14	1.60	0.324	
mean				3.16±0.05	1.65±0.05	0.31±0.02	

Seismic Velocity Surveys (in situ average)

Diamond Dust Mine	1.92	1.13	0.245	Stephens et al. (1971)
Diamond Mine	2.48	1.34	0.296	Heard et al. (1971)

TABLE IV
U20ai
Mean Velocities

Lithologic Unit #	Depth (m)	Description	V_p (km/s)	V_s (km/s)	Poisson's Ratio
6	149.7 - 400.5	Ranier Mesa Member Timber Mt. Tuff	2.108±0.437 n=18	1.017±0.211 n=14	0.304±0.095 n=12
7	400.5 - 548.6	Bedded tuff	1.895±0.529 n=37	1.001±0.172 n=37	0.334±0.046 n=37
8	548.6 - 578.5	Bedded tuff (zeolitized)	2.167±0.227 n=6	1.084±0.147 n=7	0.340±0.066 n=5
9	578 - 656.6	Rhyolite lava	2.259±0.334 n=3	1.076±0.308 n=3	0.321±0.044 n=3
Mean bedded tuff (units 7 and 8)			2.004±0.351 n=45	1.011±0.161 n=46	0.331±0.045 n=42

FIGURES

Figure 1. Multiple receiver Dry Hole Acoustic Log tool (DHAL MR). The lower transducer cone contains the source transducer stack, and the two upper cones contain the receiver transducer stacks. The clamping arm assures proper coupling with the borehole wall and is released for travel up the borehole.

Figure 2. Schematic travel paths for the DHAL MR. Abbreviations are: S = source, R_N = near receiver, and R_F = far receiver. Compressional and shear wave energy travels as head waves along the borehole wall at the formation velocity. Subtracting the travel time for the compressional wave arrival at the near receiver from that observed at the far receiver "cancels out" that part of the the travel path from the source into the formation, along the formation to near the near receiver, and back from the formation to the receiver, leaving only that part of the travel path within the formation between the two receivers.

Figure 3. DHAL MR signals from a depth of 307.9 m in hole U2fh. The upper signal is recorded at the near receiver, the lower one at the far receiver. The vertical line indicates the time at which the first (compressional wave) arrival has been picked. Amplitudes indicate relative gain. Energy within the first few milliseconds is part of the outgoing pulse.

Figure 4. Fourier spectrum of signals shown in Fig. 3. (A) Near receiver, (B) far receiver. Note the high-amplitude 5-11 kHz band.

Figure 5. Filtered signals. The signals shown in Figure 3 have been notch filtered, rejecting energy in the 6-10 kHz band. Note the emergence of energy of both high and low frequency.

Figure 6. Windowed compressional arrivals, raw signals.

Figure 7. Filtered, windowed signals. Note that the vertical lines indicating the travel time picks of the first (compressional wave) arrivals no longer occur at the beginning of the energy peak. The pick for the near receiver lies just past the peak of the first arrival, and the far receiver pick appears to be early. The arriving energy appears more emergent than on the raw records.

Figure 8. Cross-correlation of filtered, windowed signals. The high correlation near zero time delay is the correlation of the outgoing ringing pulse recorded by the tool. The peak time delay for the compressional arrival occurs at 0.427 ms.

Figure 9. Low-pass filtering of the entire waveforms. A low-pass filter has removed all energy above 4 kHz, revealing nearly identical energy packets occurring in both the near and far records, with a small moveout.

Figure 10. Cross-correlation of the filtered waveforms. The peak delay occurs at 0.849 ms.

Figure 11. Ground motion from a distant impulse (Lamb's problem). (A) initial pulse, (B) horizontal and vertical surface displacements (from Båth, 1968).

Figure 12. (A) Cutoff wavelength in an empty borehole. Above the cutoff wavelength, shear waves are propagated. For Rayleigh energy to propagate in materials with values of Poisson's ratio between 0.20 and 0.40, cutoff wavelength/borehole diameter must be $\leq$ about 1.55. (B) Group velocity/shear velocity in an empty borehole (from Biot, 1952). For $\pi D/\lambda > 5$, the curves for various values of Poisson's ratio are relatively flat.

Figure 13. Velocities determined using cross-correlation analysis on the DHAL MR log from hole U2fh. At depths where no data are available or no velocity determination could be made, the velocity is given as zero. (A) Individual values of V_P, V_S, and dynamic Poisson's ratio. (B) Average velocities, obtained using a 15 m moving window average, excluding any

zero values, along with lithology, Poisson's ratio, and caliper log for hole U2fh. The three curves for V_S are calculated using $V_R/V_S = 0.88$, 0.92, and 0.96, corresponding to Poisson's ratios of 0.0 (lower curve), 0.25 (middle curve), and 0.50 (upper curve), respectively.

Figure 14. Velocities determined using cross-correlation analysis on the DHAL MR log from hole U20ai. Zero values occur at depths where no data are available or no determination could be made. (A) Individual values of velocities and dynamic Poisson's ratio. (B) Velocities averaged with a 15 m moving window average, along with the lithology, caliper log, and dynamic Poisson's ratio. Curves are as for Fig. 13. In areas of hole enlargement (such as from about 450-475 m), poor signal quality often results in low estimates of V_p.

Figure 15. Examples of poor signal quality. (A) Near and far receiver signals from hole U20ai at a depth of 329.3 m. Although both signals are attenuated, the far signal is especially so, making correlation impossible. (B) Near and far receiver signals from hole U20ai at a depth of 603.7 m. Both signals are very strong, and have clipped. Proper amplitude ratios are not available, making cross-correlation impossible.

Figure 16. Different estimates of V_P. $V_{P(near-receiver)}$, $V_{P(far-receiver)}$, $V_{P(far-near)}$, and $V_{P(cross-correlation)}$ plotted over a 60 m section of hole U2fh. $V_{P(near-receiver)}$ is generally the lowest, $V_{P(far-receiver)}$ the next-lowest. Although $V_{P(far-near)}$ is generally the highest estimate, $V_{P(cross-correlation)}$ is very close to it, often exceeding it (e.g., 100-125 m). See text for discussion.

Figure 17. Comparison between $V_{P(near)}$ and $V_{P(far)}$ for hole U2fh. Percent difference between individual values of $V_{P(near)}$ and $V_{P(far)}$ for the DHAL MR log run in hole U2fh. Zero values in the original data sets plot off scale; 76% of the (nonzero) values lie within $\pm 20\%$ of each other. $V_{P(far)}$ is generally higher than $V_{P(near)}$.

Figure 18. Comparison between $V_{P(far-near)}$ and $V_{P(cross-correlation)}$ for hole U2fh.

Percent difference between individual values of $V_{P(far-near)}$ and $V_{P(cross-correlation)}$ for the DHAL MR log run in hole U2fh. Zero values in the original data sets plot off scale. 84% of the (nonzero) values lie within ±20% of each other. The difference between these values is less biased than in Figure 17.

Figure 19. Comparison between individual values of $_{P(far-near)}$ and $V_{P(cross-correlation)}$ for hole U20ai. Zero values in the original data sets plot off scale. Agreement in upper 96 m is not very good, with $V_{P(cross-correlation)}$ generally lower than $V_{P(far-near)}$. Agreement improves over the lower part of the hole. The bias in the distribution decreases over the lower part of the hole as well. See text for discussion.

Figure 20. Ultrasonic compressional and shear wave velocities of unsaturated Frenchman's Flat alluvium measured under undrained triaxial stress (from Constantino and Bonner, 1980).

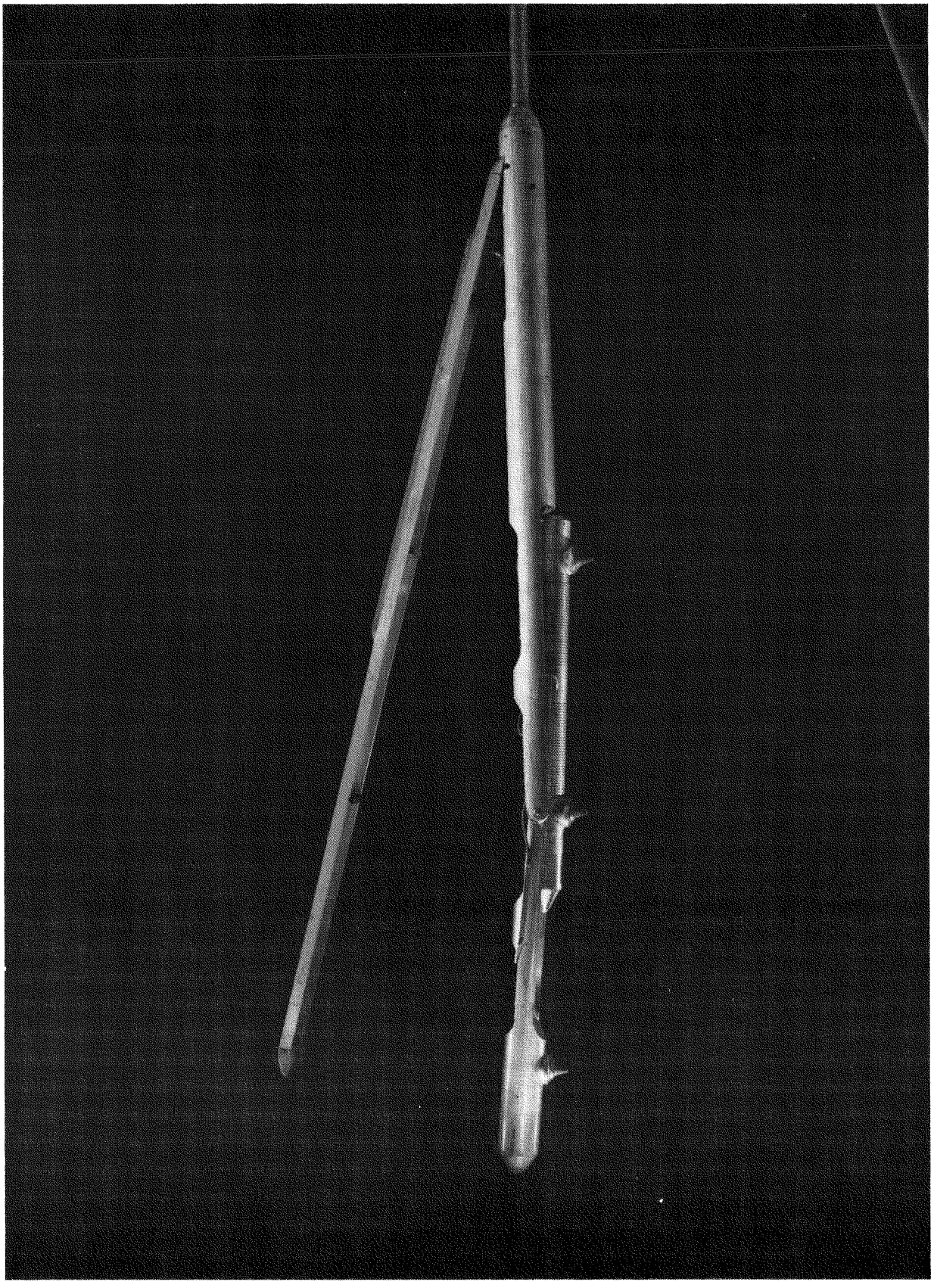

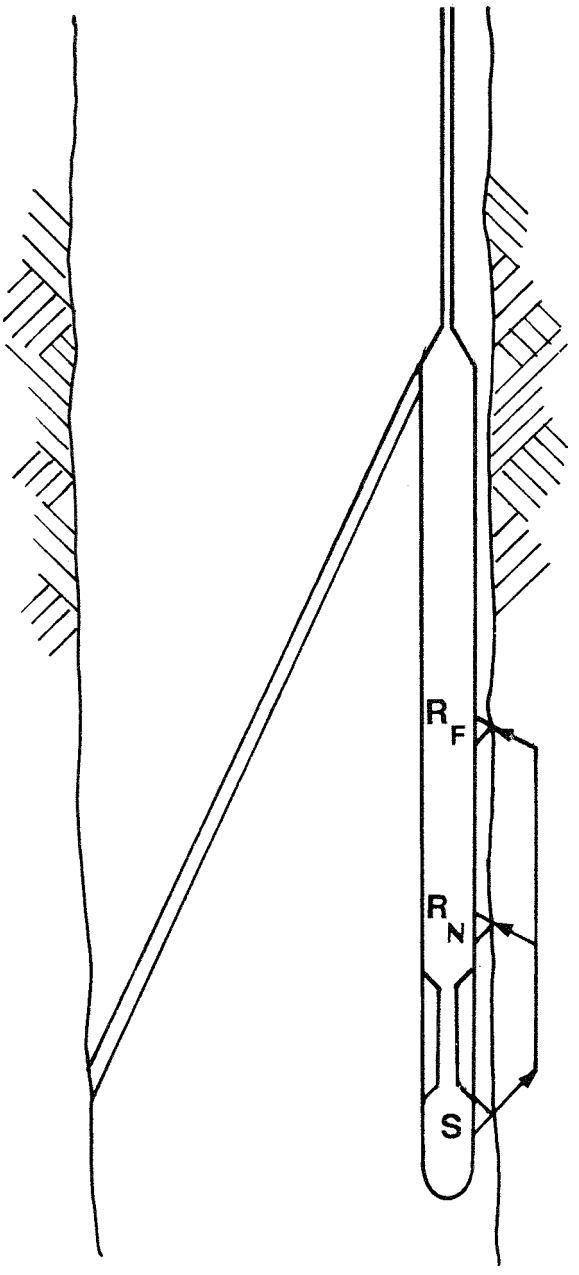

Figure 2

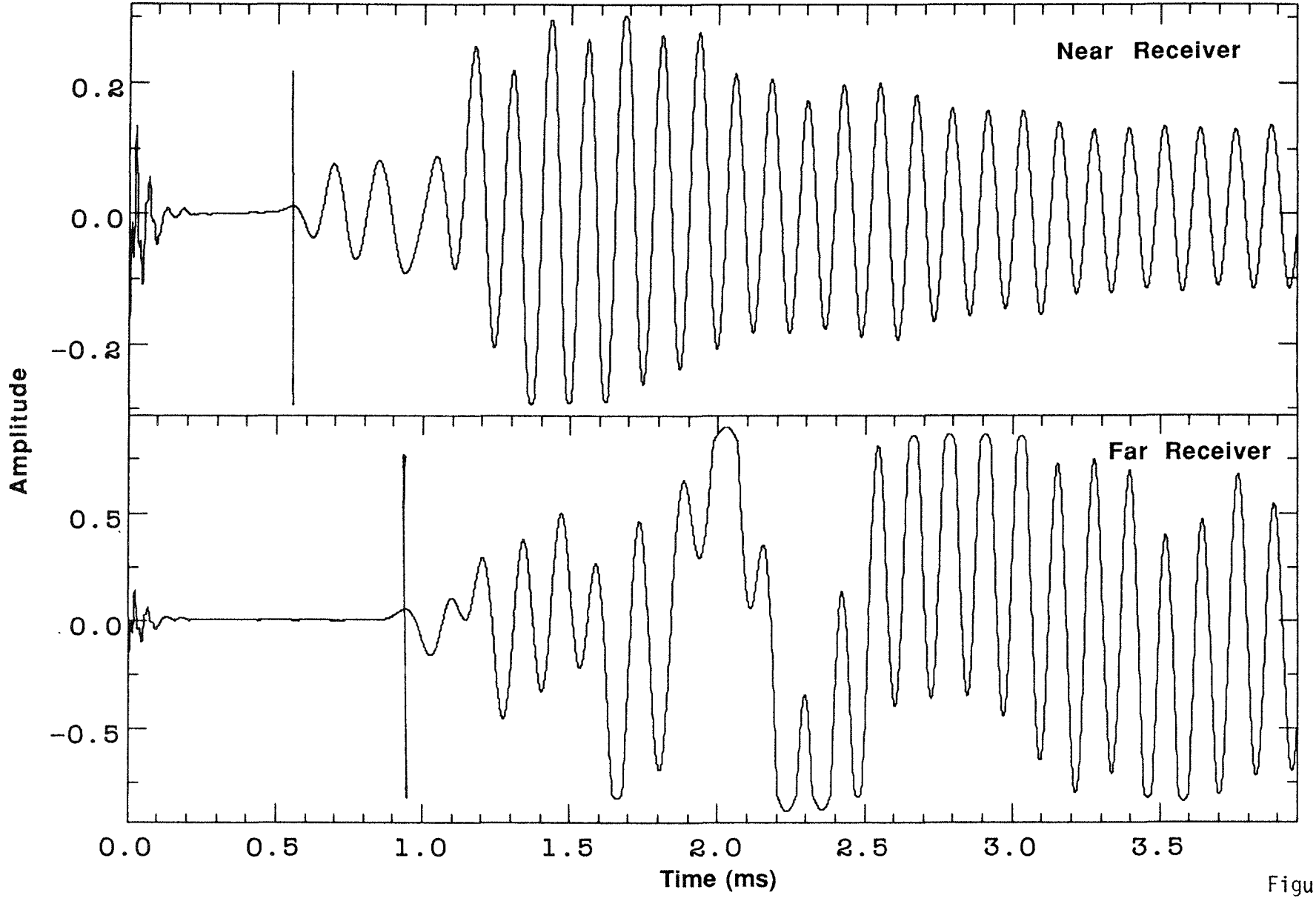
Near Receiver
Far Receiver
Amplitude
0.2
0.0
-0.2
0.5
0.0
-0.5
0.0
0.5
1.0
1.5
2.0
2.5
3.0
3.5
Time (ms)

Figure 3

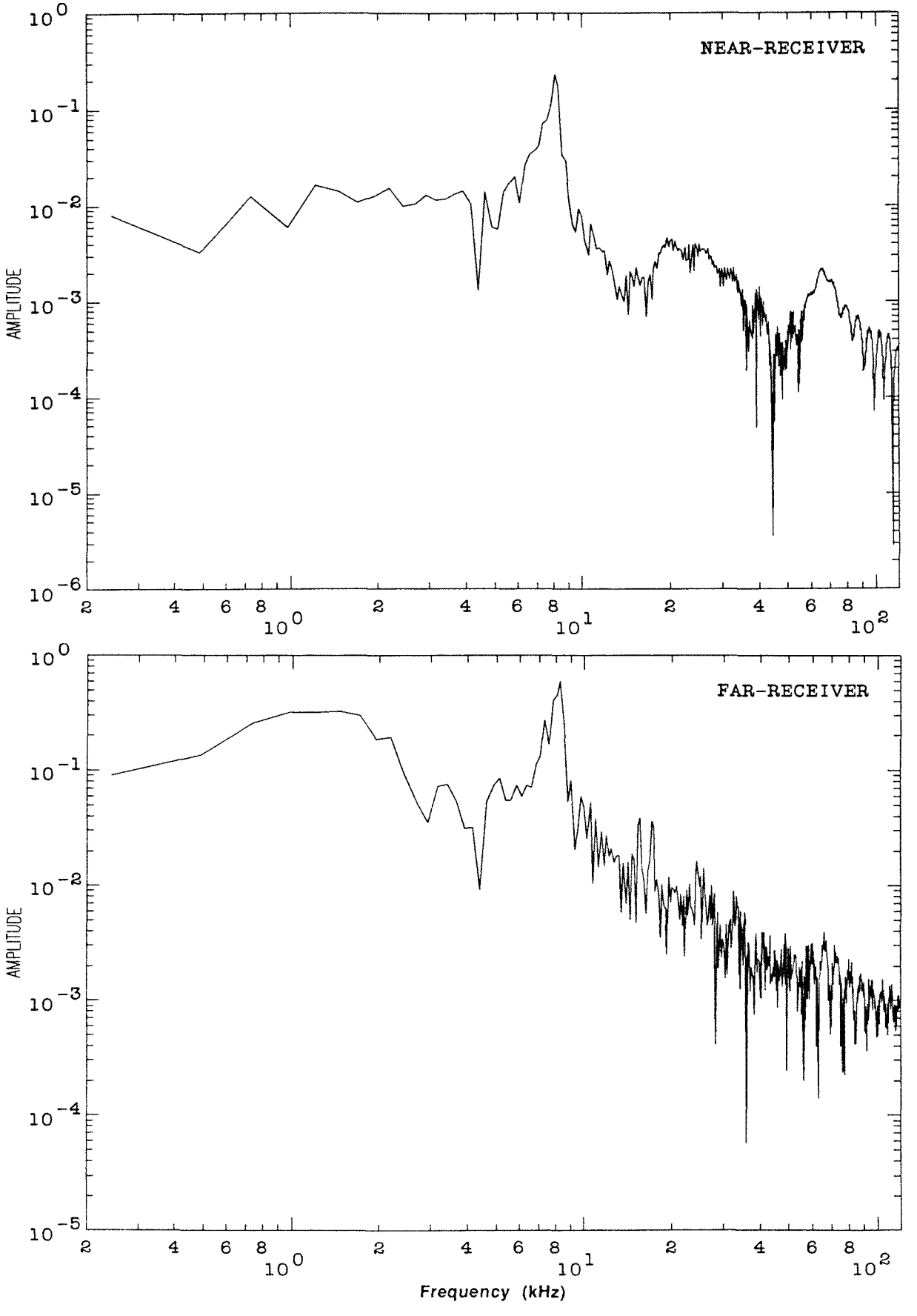
NEAR-RECEIVER
FAR-RECEIVER
AMPLITUDE
AMPLITUDE
Frequency (kHz)

Figure 4

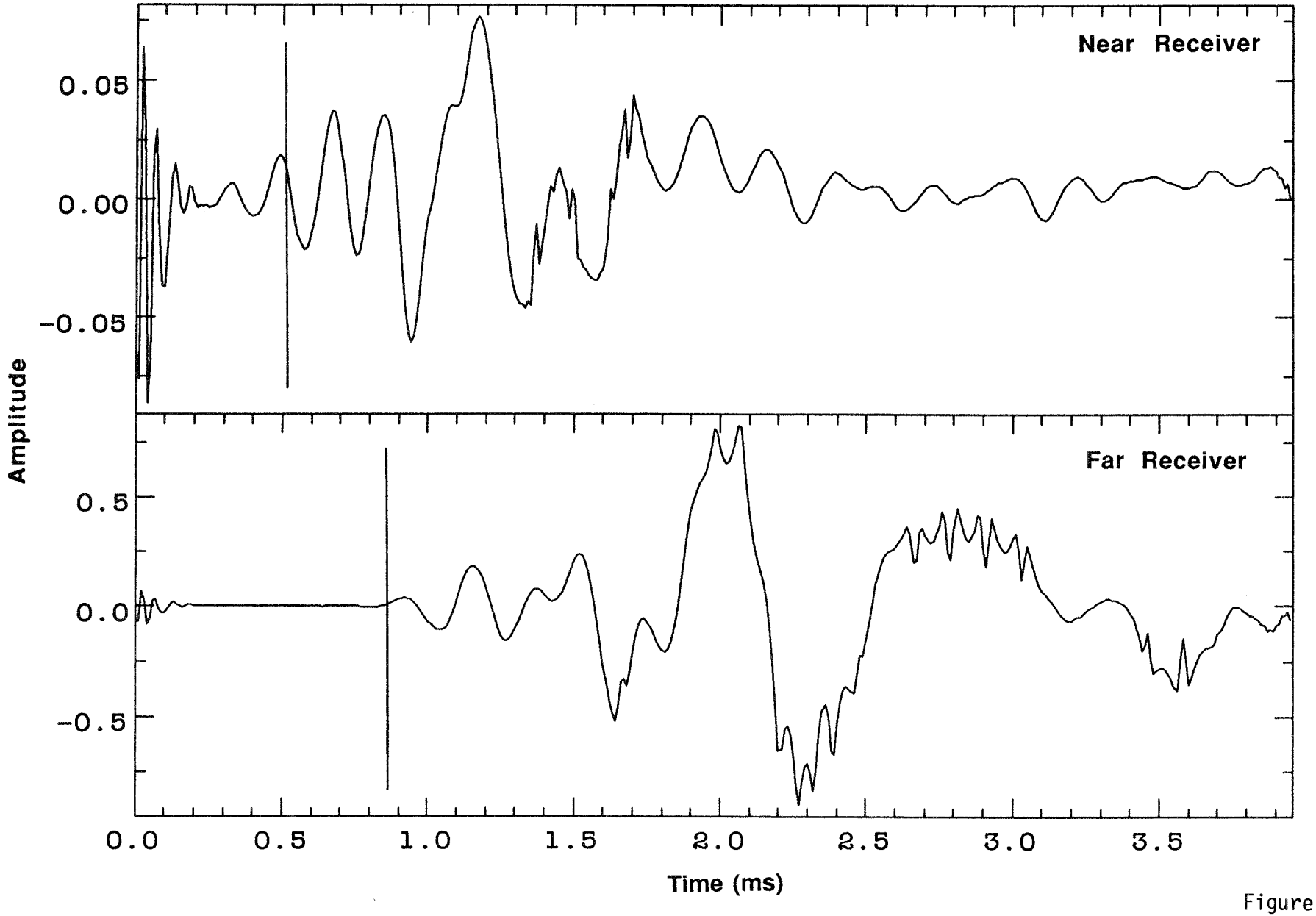
Near Receiver
Far Receiver
Amplitude
0.05
0.00
-0.05
0.5
0.0
-0.5
0.0
0.5
1.0
1.5
2.0
2.5
3.0
3.5
Time (ms)

Figure 5

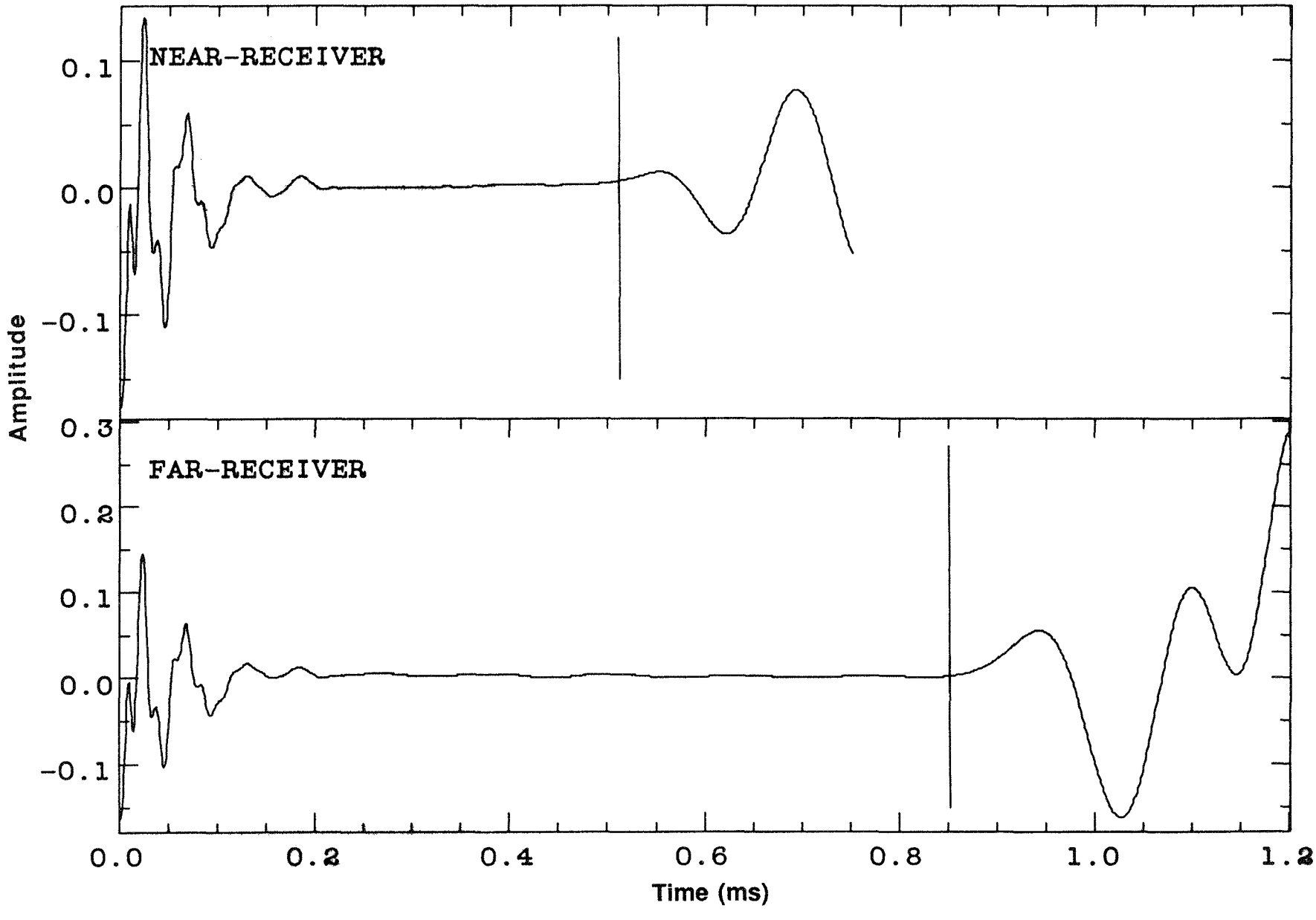
NEAR-RECEIVER
FAR-RECEIVER
Amplitude
0.1
0.0
-0.1
0.3
0.2
0.1
0.0
-0.1
0.0
0.2
0.4
0.6
0.8
1.0
1.2
Time (ms)

Figure 6

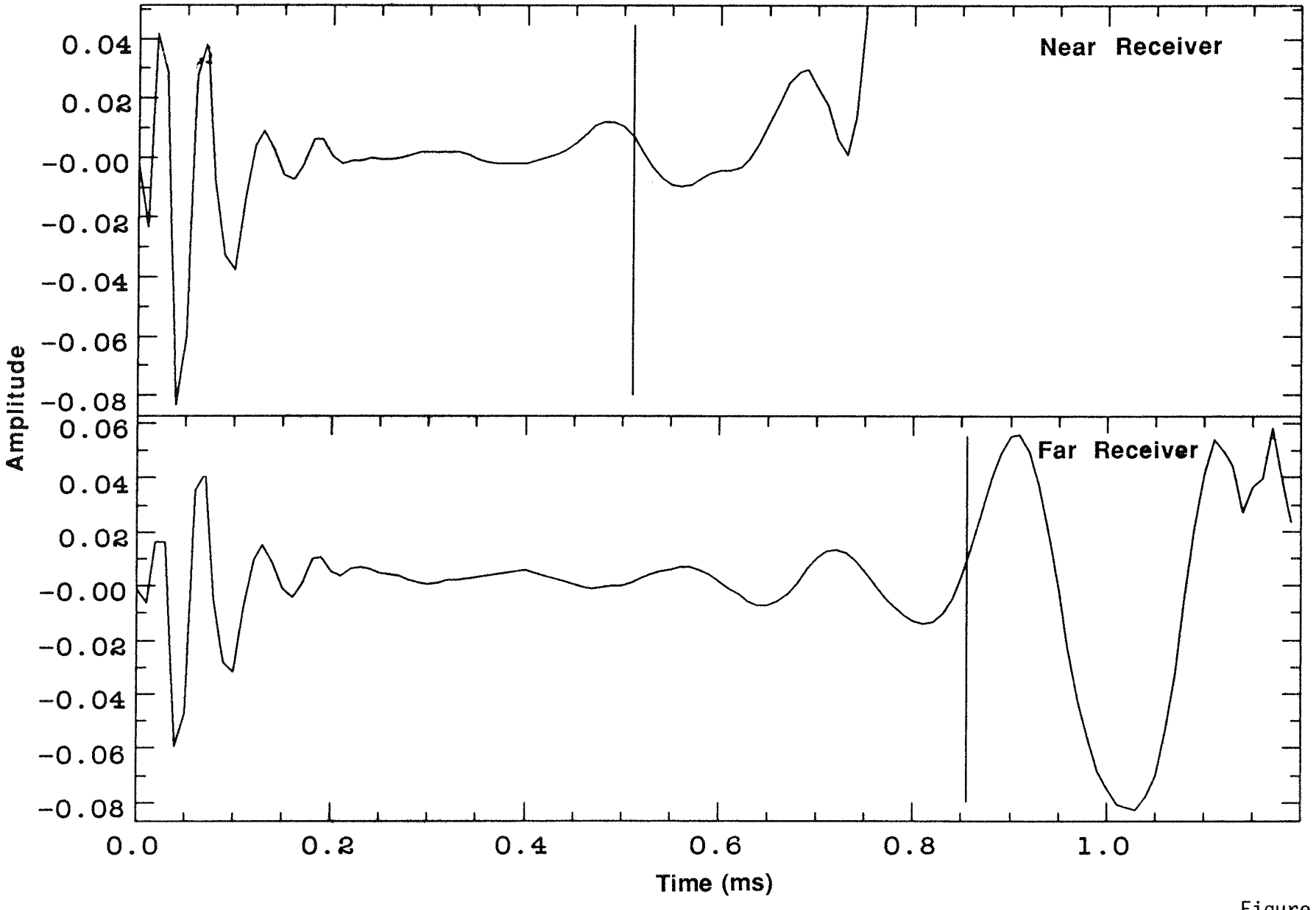
Near Receiver
Far Receiver
Amplitude
0.04
0.02
-0.00
-0.02
-0.04
-0.06
-0.08
0.06
0.04
0.02
-0.00
-0.02
-0.04
-0.06
-0.08
0.0
0.2
0.4
0.6
0.8
1.0
Time (ms)

Figure 7

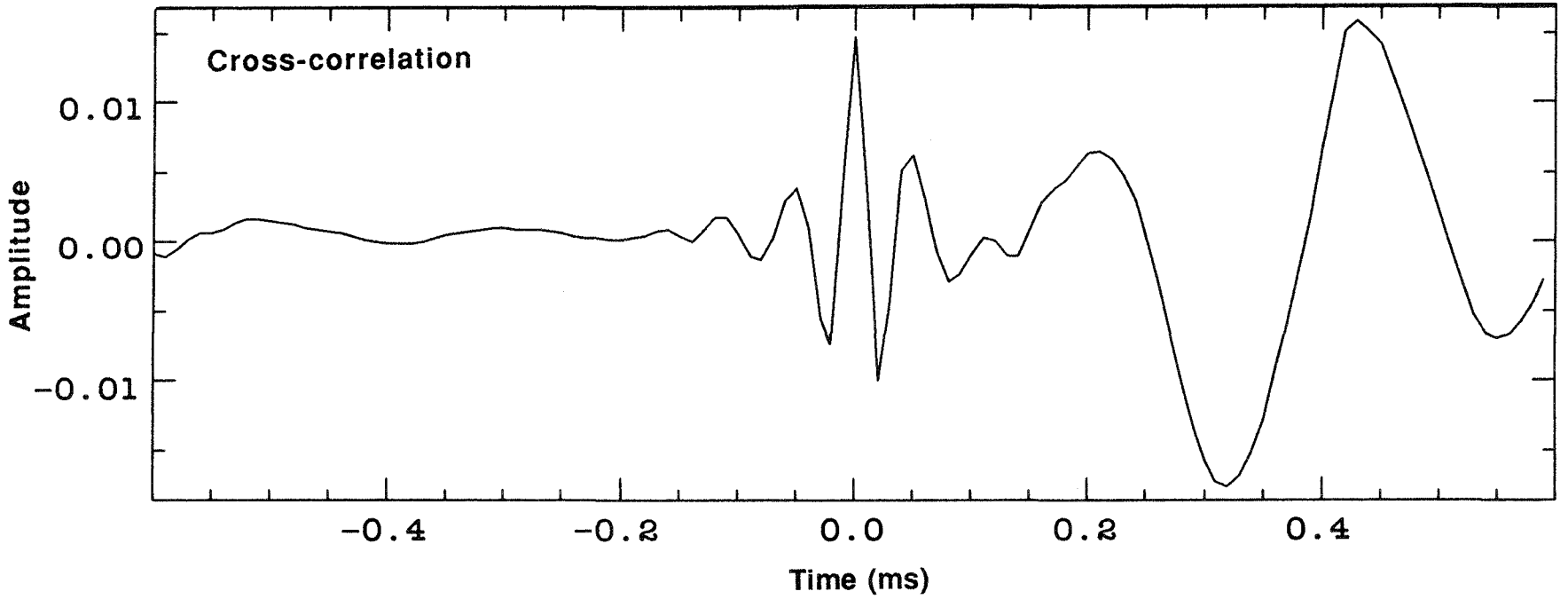
Cross-correlation
0.01
0.00
-0.01
Amplitude
-0.4
-0.2
0.0
0.2
0.4
Time (ms)

Figure 8

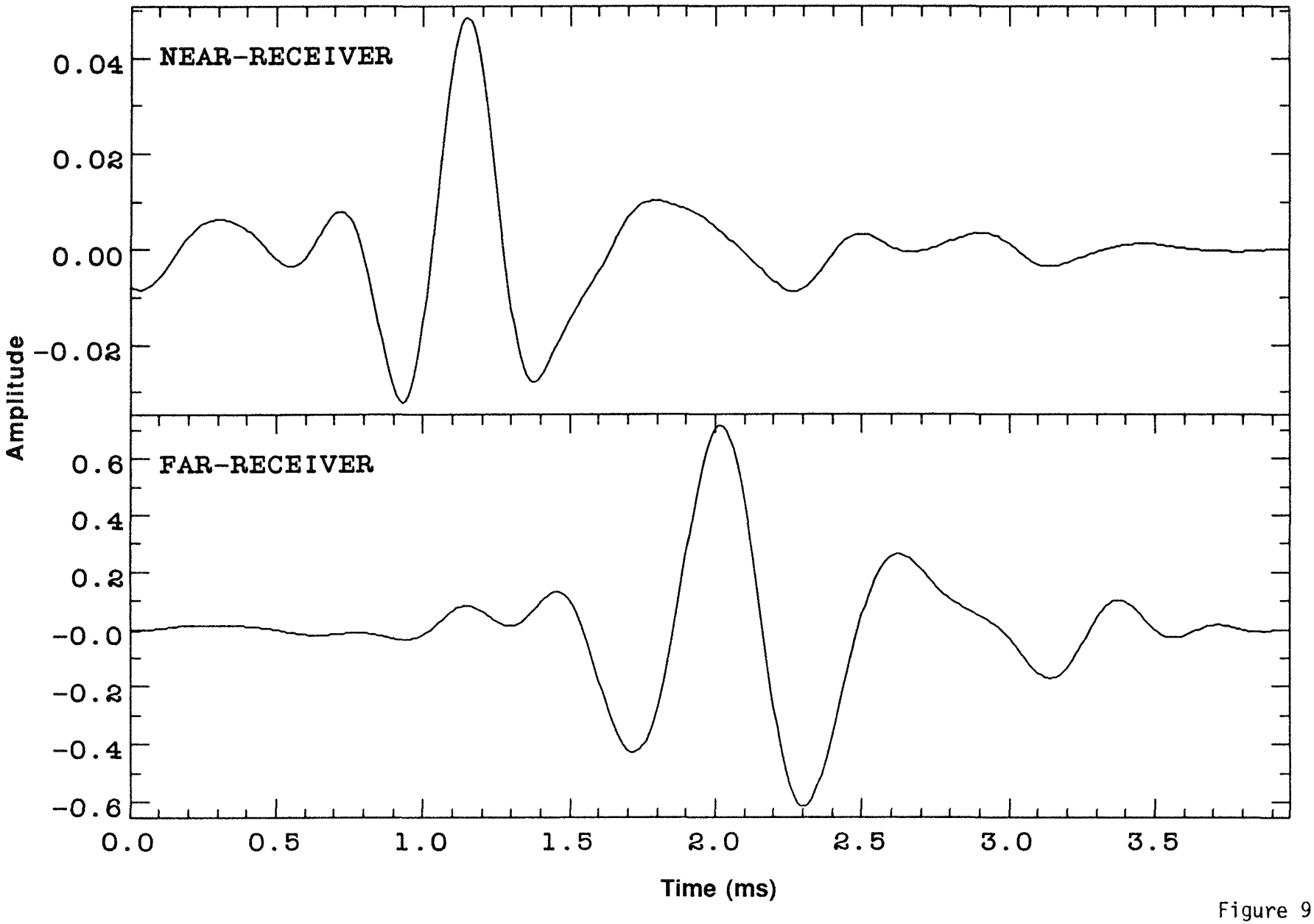
NEAR-RECEIVER
0.04
0.02
0.00
-0.02
FAR-RECEIVER
0.6
0.4
0.2
-0.0
-0.2
-0.4
-0.6
Amplitude
0.0
0.5
1.0
1.5
2.0
2.5
3.0
3.5
Time (ms)

Figure 9

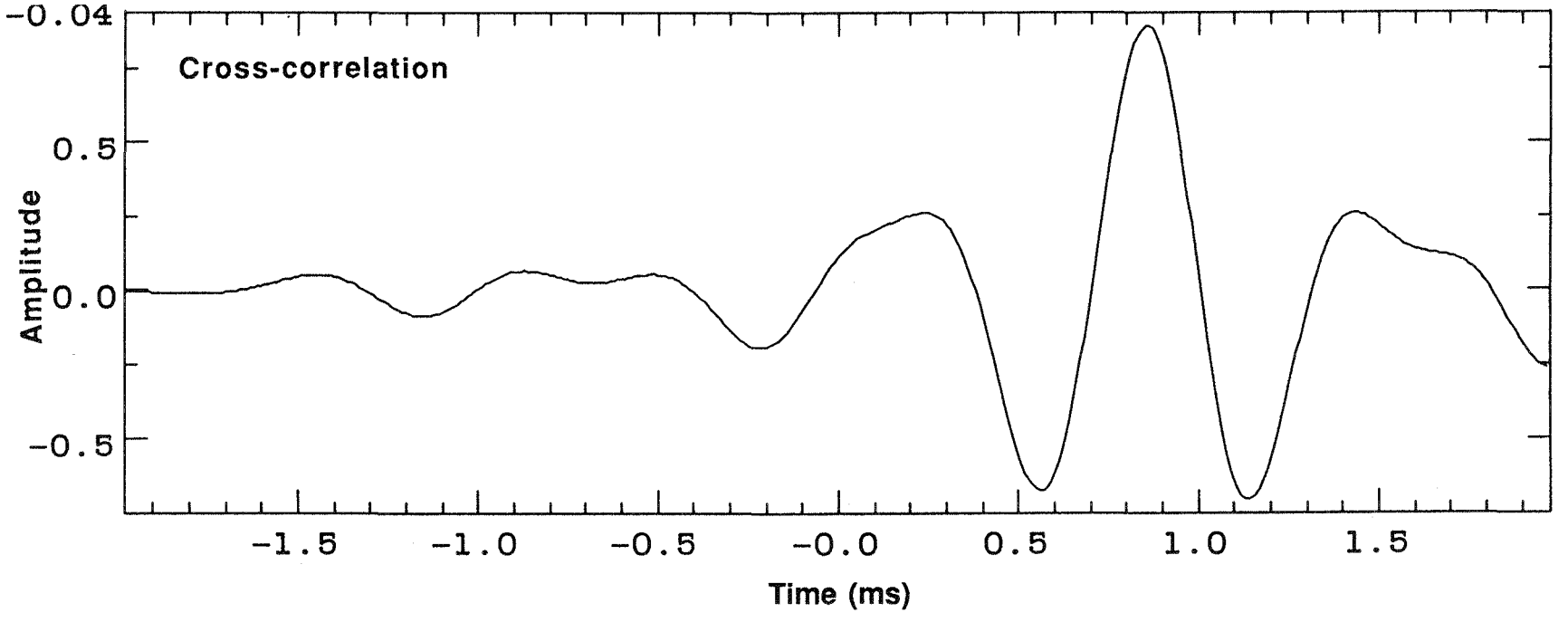
Cross-correlation
Amplitude
-0.04
0.5
0.0
-0.5
-1.5
-1.0
-0.5
-0.0
0.5
1.0
1.5
Time (ms)

Figure 10

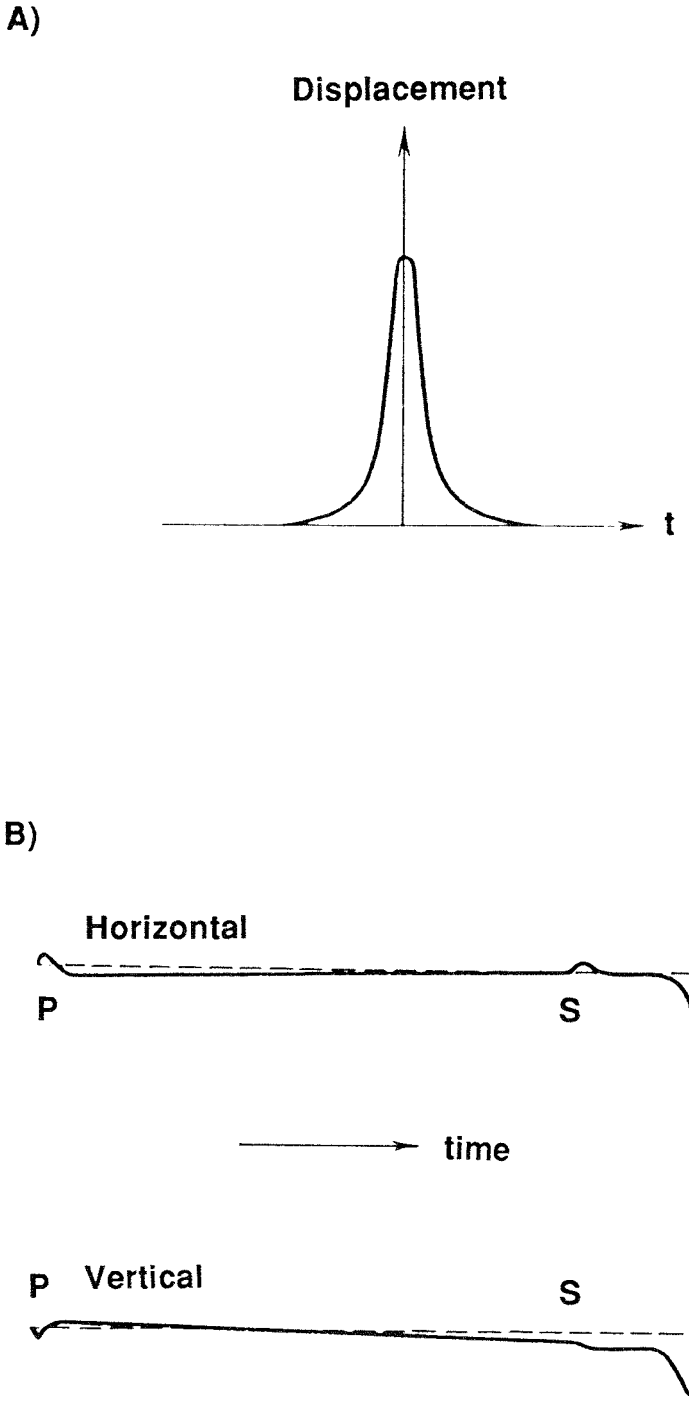

Figure 11

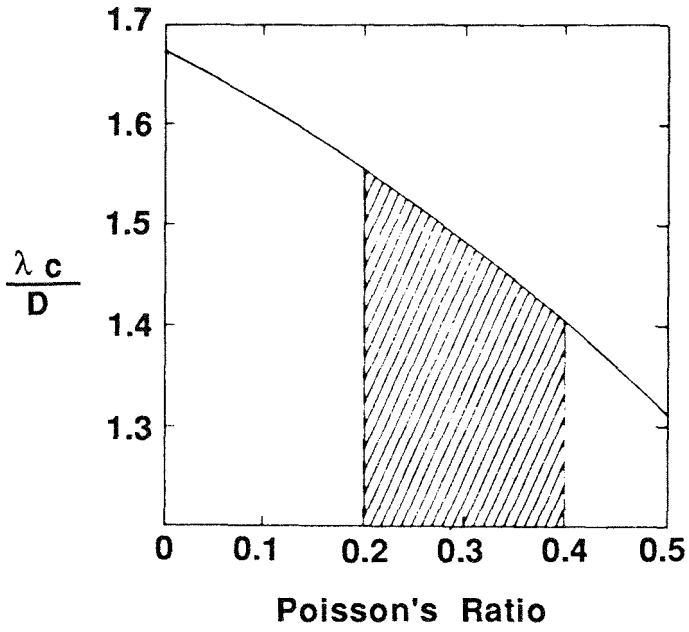
1.7
1.6
1.5
1.4
1.3
λ c / D
0
0.1
0.2
0.3
0.4
0.5
Poisson's Ratio

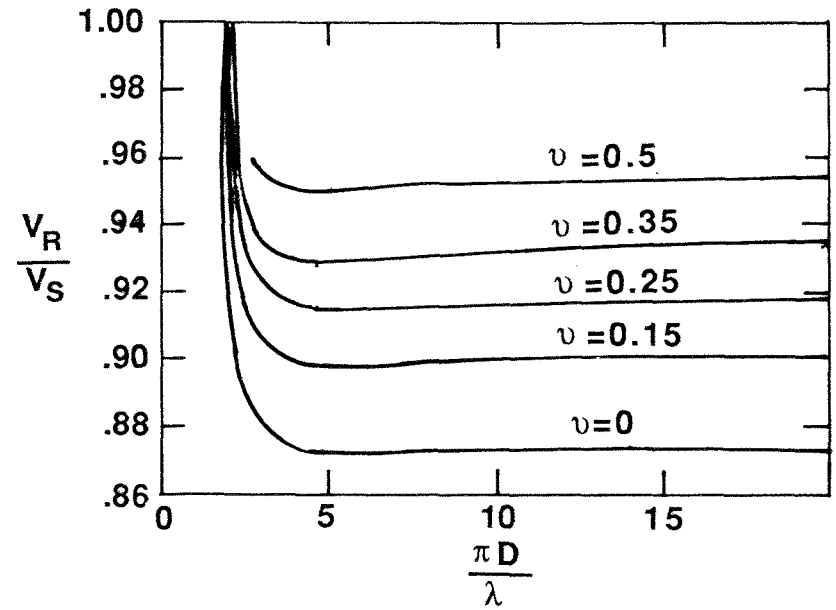
1.00
.98
.96
.94
.92
.90
.88
.86
V_R / V_S
υ =0.5
υ =0.35
υ =0.25
υ =0.15
υ=0
0
5
10
15
π D / λ

Figure 12

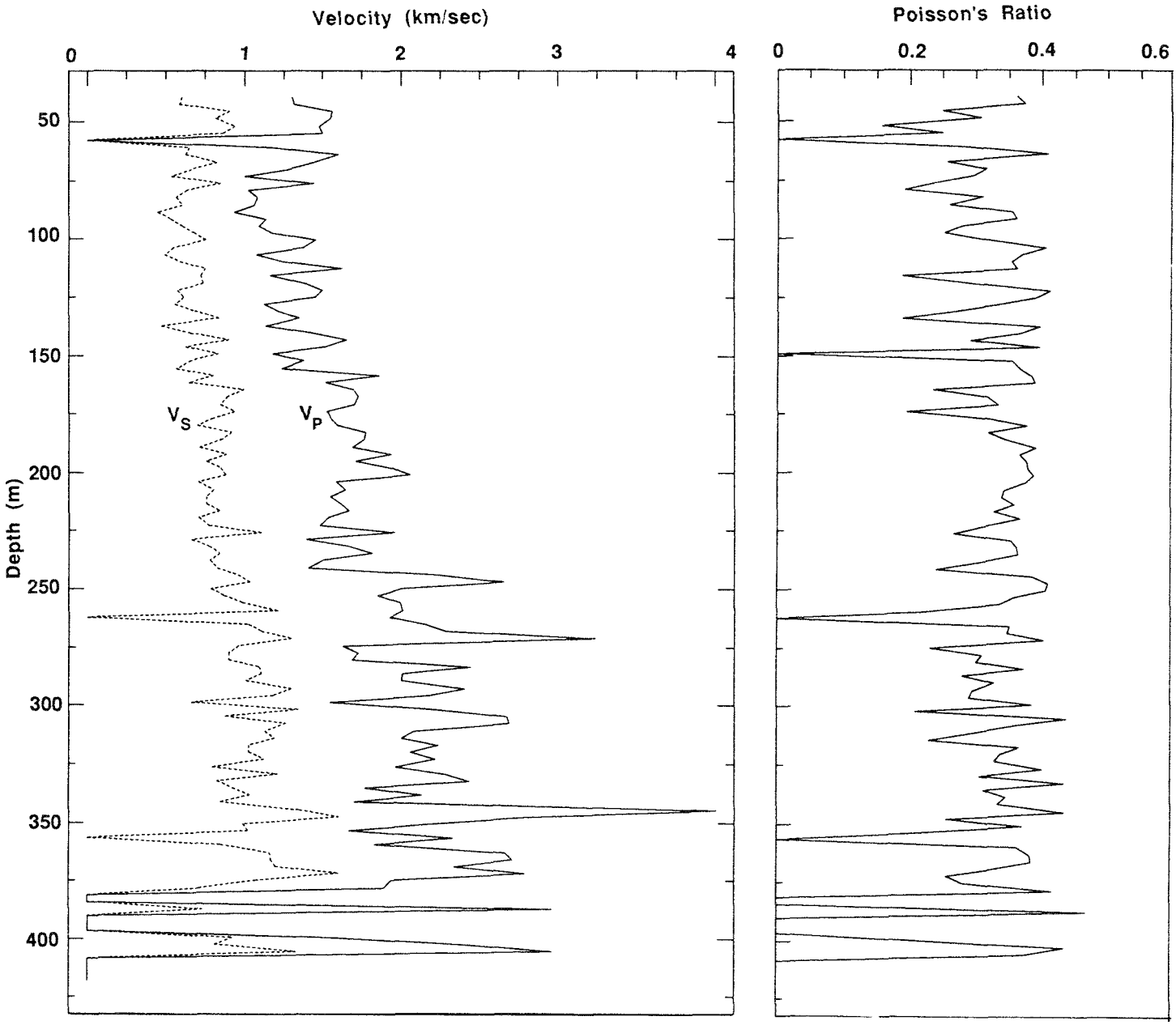
Velocity (km/sec)
0
1
2
3
4
Poisson's Ratio
0
0.2
0.4
0.6
Depth (m)
50
100
150
200
250
300
350
400
V_S
V_P

Figure 13A

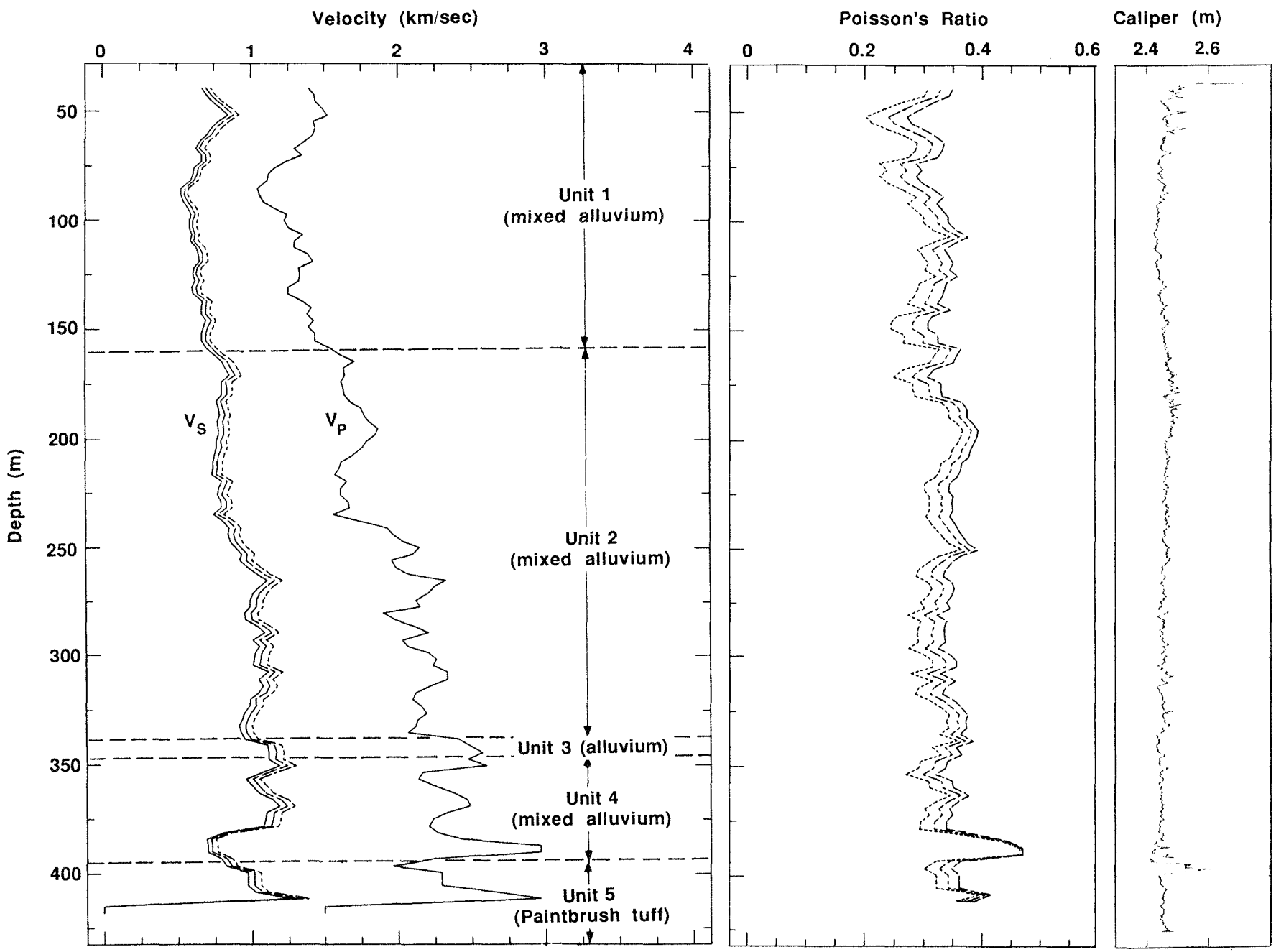
Velocity (km/sec)
0
1
2
3
4
Poisson's Ratio
0
0.2
0.4
0.6
Caliper (m)
2.4
2.6
Depth (m)
50
100
150
200
250
300
350
400
V_S
V_P
Unit 1
(mixed alluvium)
Unit 2
(mixed alluvium)
Unit 3 (alluvium)
Unit 4
(mixed alluvium)
Unit 5
(Paintbrush tuff)

Figure 13B

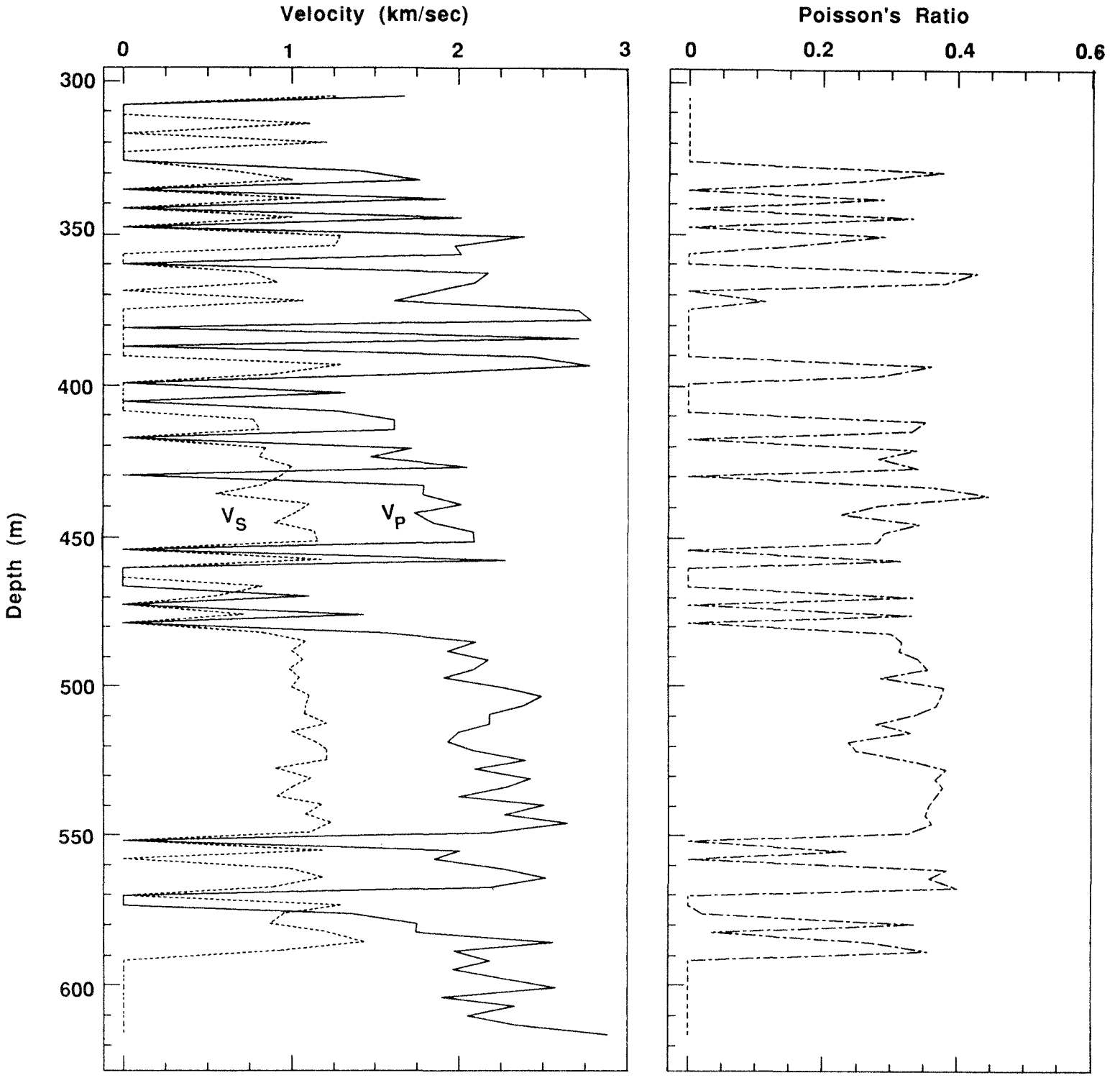
Velocity (km/sec)
0
1
2
3
Poisson's Ratio
0
0.2
0.4
0.6
Depth (m)
300
350
400
450
500
550
600
V_S
V_P

Figure 14A

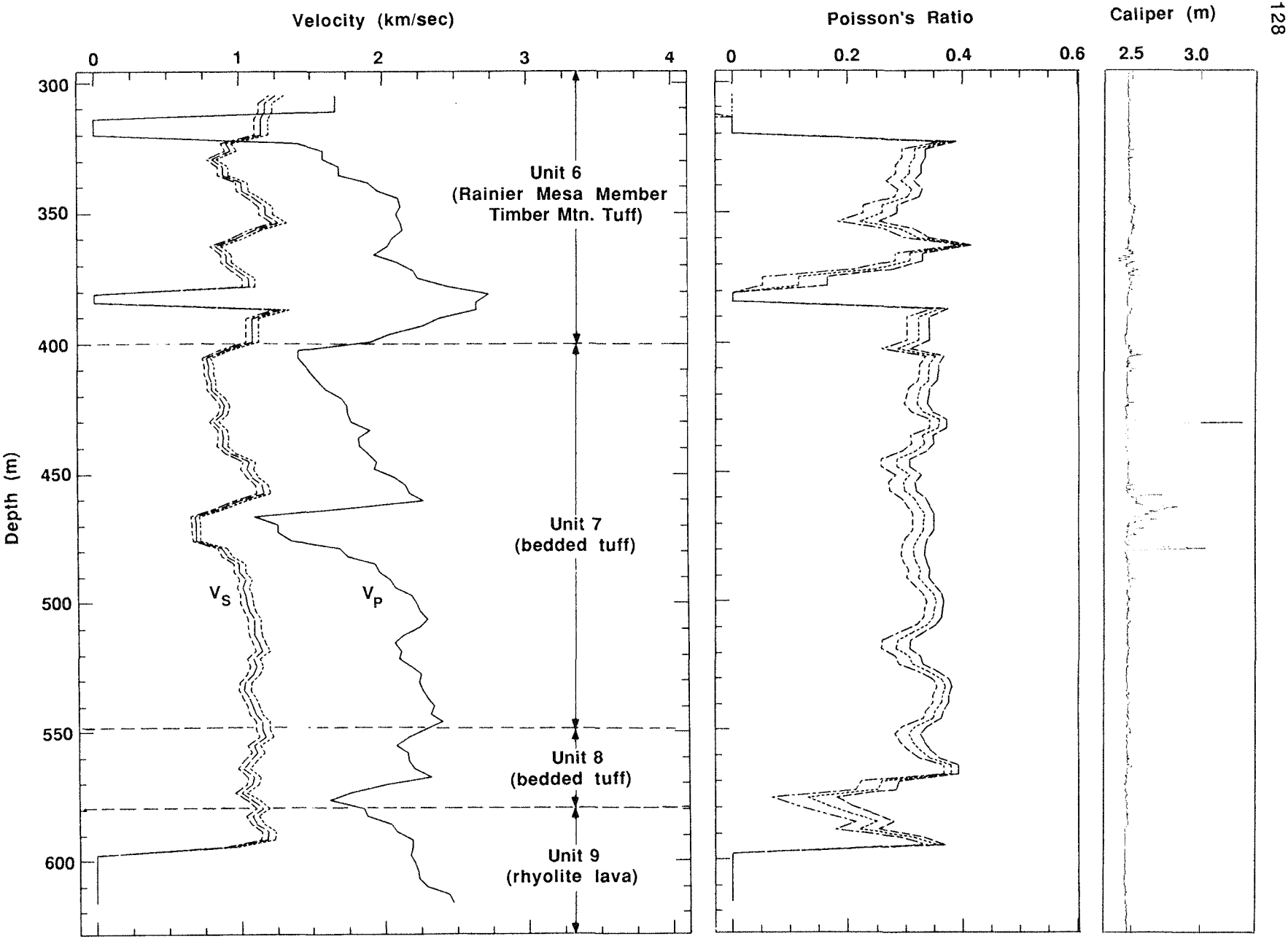
Velocity (km/sec)
0
1
2
3
4
Poisson's Ratio
0
0.2
0.4
0.6
Caliper (m)
2.5
3.0
Depth (m)
300
350
400
450
500
550
600
Unit 6
(Rainier Mesa Member
Timber Mtn. Tuff)
Unit 7
(bedded tuff)
Unit 8
(bedded tuff)
Unit 9
(rhyolite lava)
V_S
V_P

Figure 14B

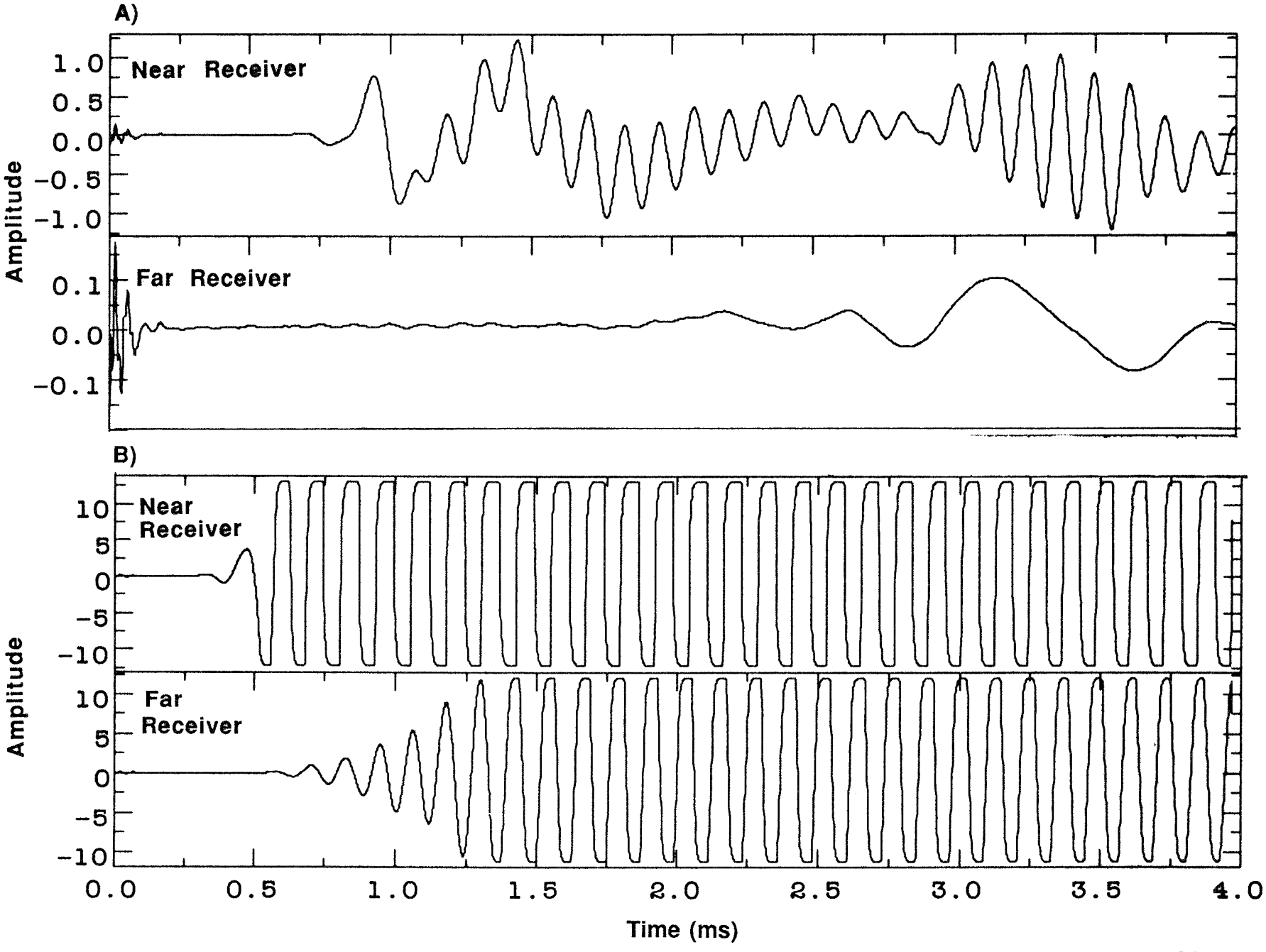
A)
Near Receiver
Far Receiver
Amplitude
1.0
0.5
0.0
-0.5
-1.0
0.1
0.0
-0.1
B)
Near Receiver
Far Receiver
Amplitude
10
5
0
-5
-10
0.0
0.5
1.0
1.5
2.0
2.5
3.0
3.5
4.0
Time (ms)

Figure 15

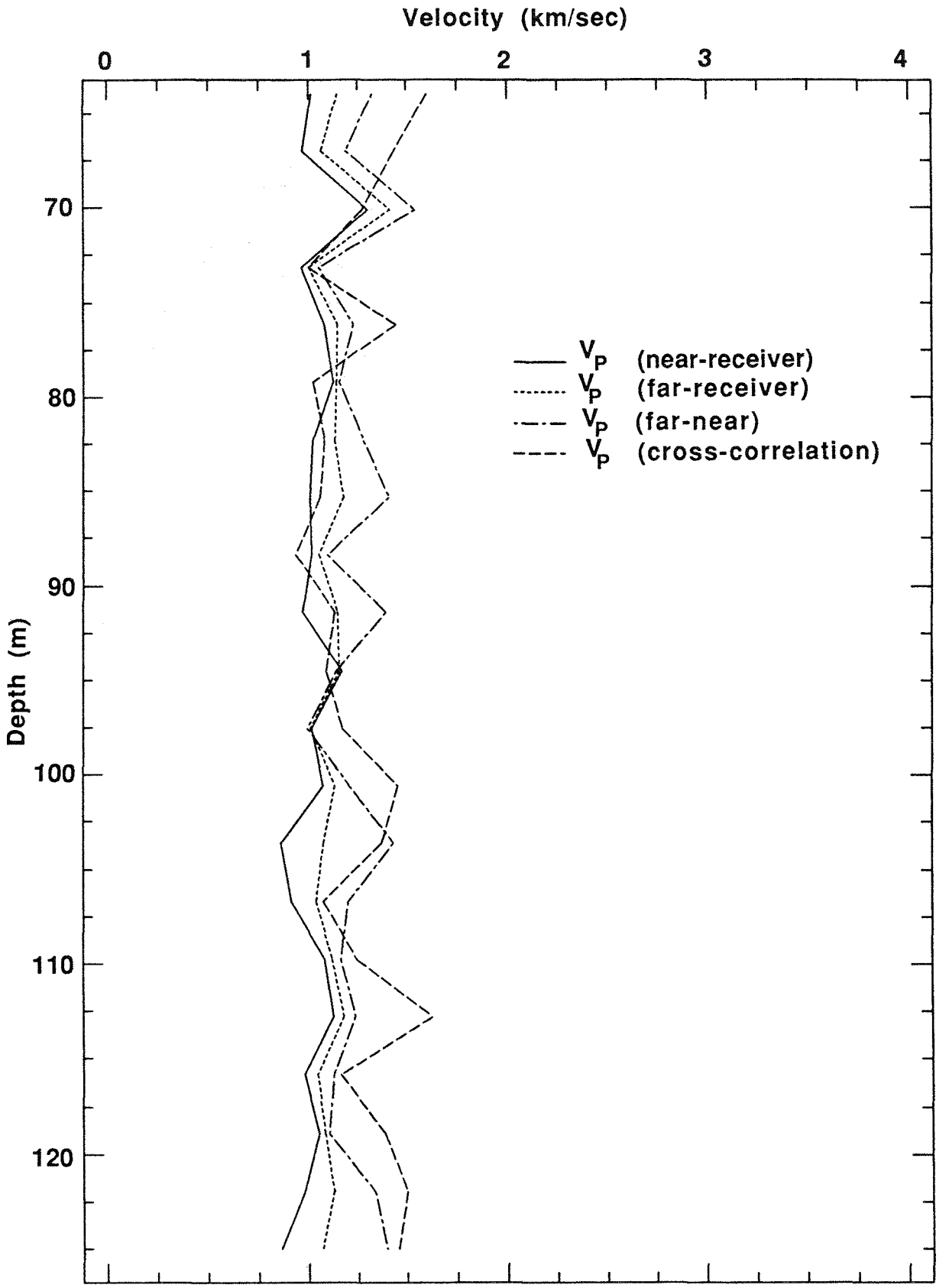
Velocity (km/sec)
0
1
2
3
4
Depth (m)
70
80
90
100
110
120
V_P (near-receiver)
V_P (far-receiver)
V_P (far-near)
V_P (cross-correlation)

Figure 16

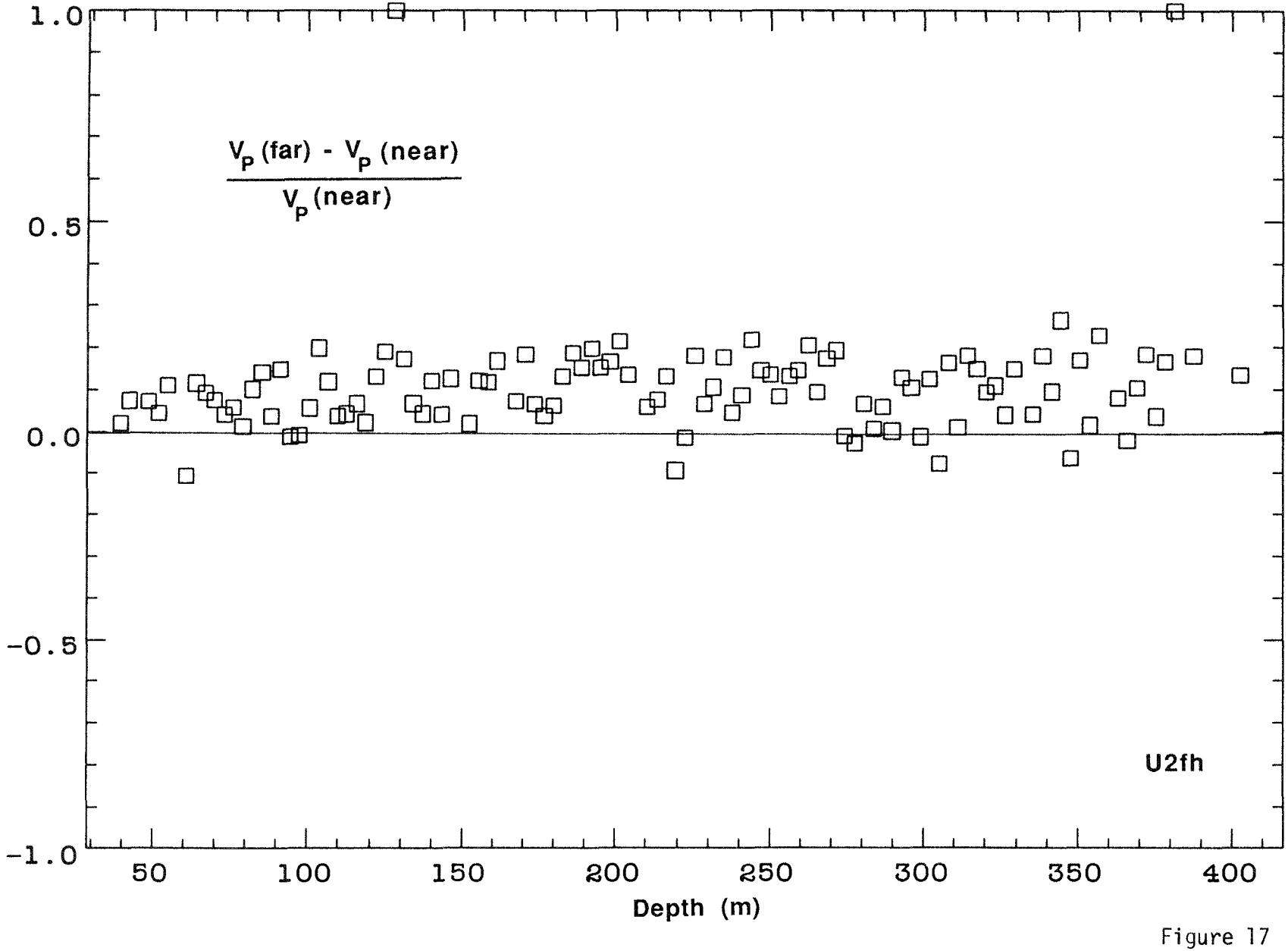
1.0
0.5
0.0
-0.5
-1.0
$\frac{V_P \text{ (far)} - V_P \text{ (near)}}{V_P \text{ (near)}}$
U2fh
50
100
150
200
250
300
350
400
Depth (m)

Figure 17

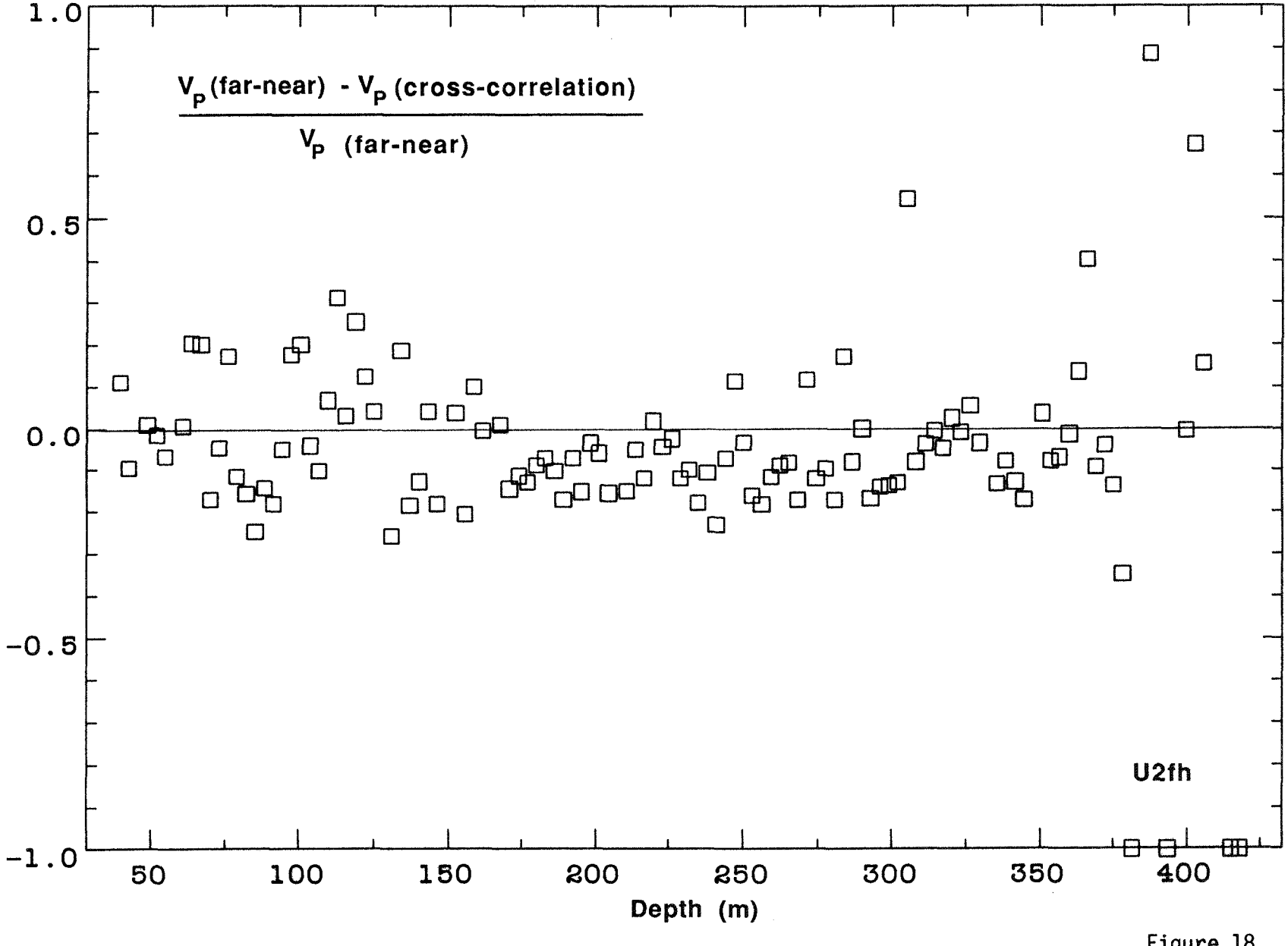
1.0
0.5
0.0
-0.5
-1.0
$\frac{V_P(\text{far-near}) - V_P(\text{cross-correlation})}{V_P(\text{far-near})}$
U2fh
50
100
150
200
250
300
350
400
Depth (m)

Figure 18

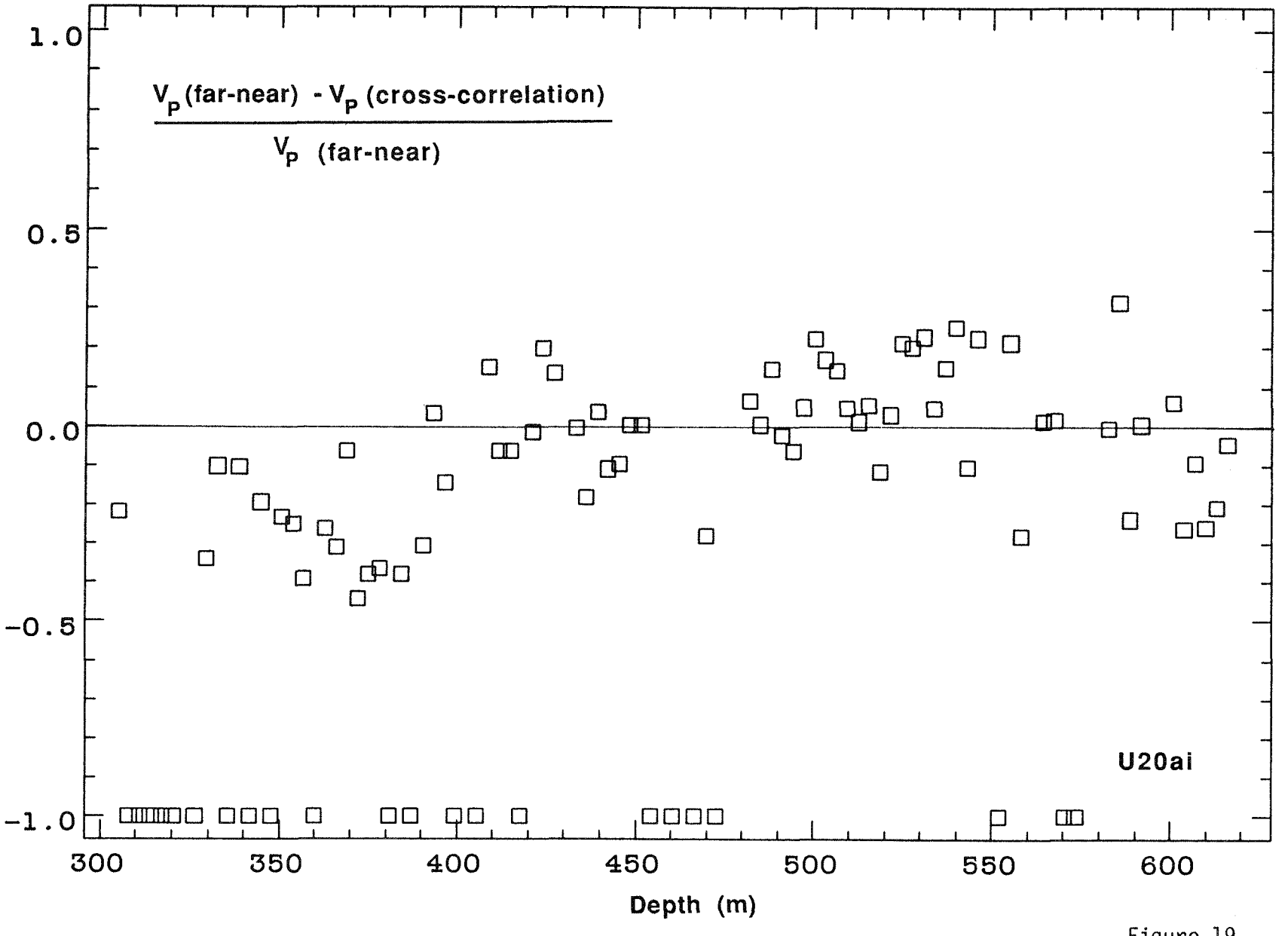
1.0
0.5
0.0
-0.5
-1.0
V_P(far-near) - V_P (cross-correlation)
V_P (far-near)
U20ai
300
350
400
450
500
550
600
Depth (m)

Figure 19

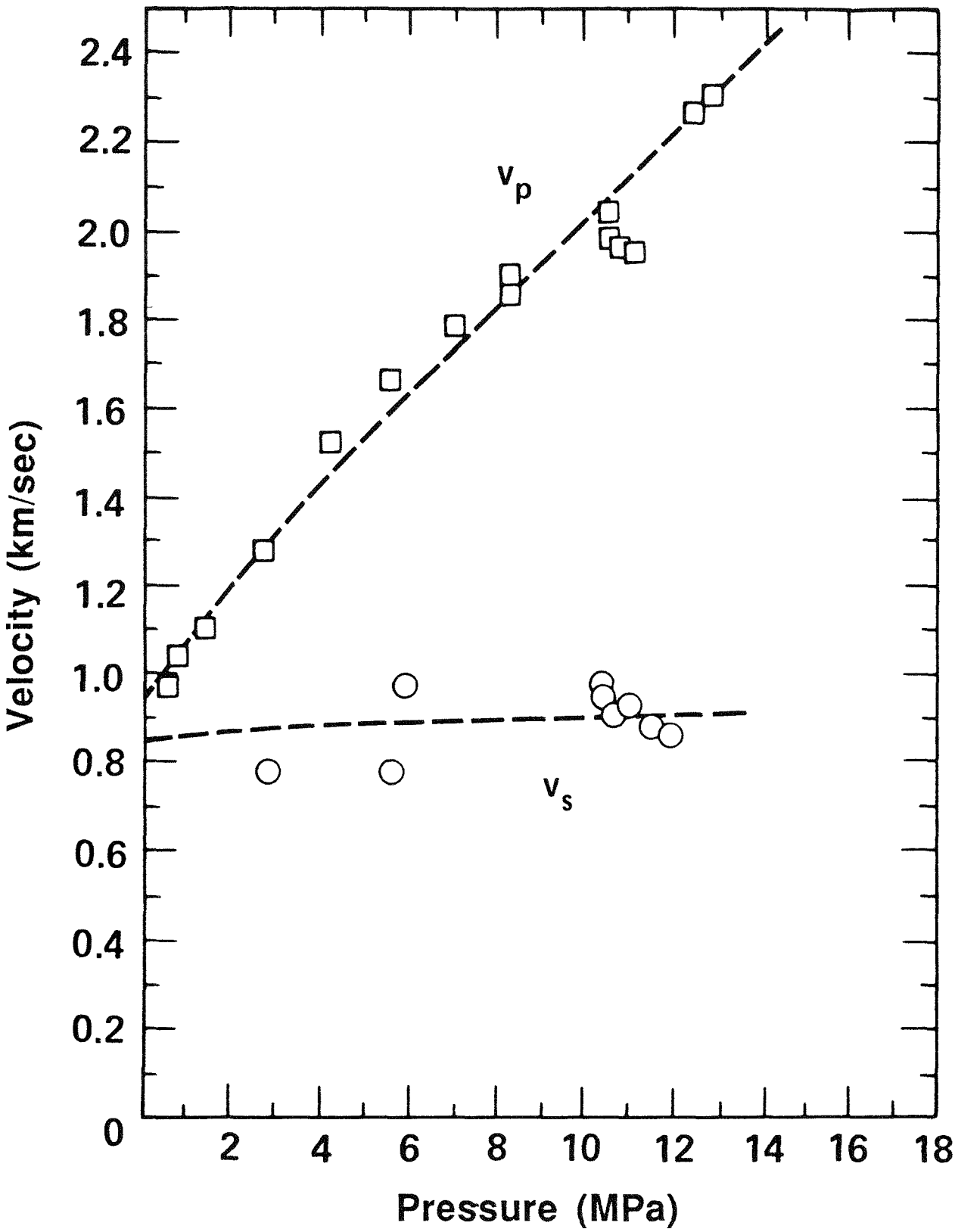
Velocity (km/sec)
2.4
2.2
2.0
1.8
1.6
1.4
1.2
1.0
0.8
0.6
0.4
0.2
0
v_p
v_s
2
4
6
8
10
12
14
16
18
Pressure (MPa)

Figure 20

A POSSIBLE RELATION BETWEEN SONIC VELOCITY MEASURED AT THE EDGE OF A LARGE BOREHOLE AND SHEAR FAILURE

John T. Rambo and Robert P. Swift
Lawrence Livermore National Laboratory

Abstract

Velocities of P-waves measured next to the walls of large-diameter boreholes with the dry-hole acoustic logger are typically lower than velocities across similar geologic media measured farther from the borehole wall using other techniques (Vibroseis). The difference in velocity is attributed to a weakened zone around the borehole wall, which in part may be due to disturbance from drilling and, in part, to the relief of overburden stresses in the vicinity of the borehole wall. P-wave velocity measurements in alluvium and tuffs show high sensitivities to confining pressures in the range of overburden stresses for many Nevada Test Site holes. When isotropic strength is assumed, elastic-plastic pressure-dependent strength models suggest that lower velocities should occur next to the borehole wall and that shear failure of the medium is necessary to reduce the mean stress and the P-wave velocity. The borehole walls of many holes appear to have failed sufficiently to relieve overburden stresses in major portions of large-diameter Nevada Test Site (NTS) holes. There are documented cases of radioactive gas proceeding past plug locations. On the basis of this analysis, it is prudent to consider the possibility that the damaged wall of the hole is a pathway. An analysis of the RIOLA and ROQUEFORT Events indicates that radioactivity could have bypassed the plug locations because of a weak annulus. We recommend that, where exact plug locations are not dominated by other factors, plugs be placed in regions where minimal annulus damage has occurred.

Introduction

The stress state around a circular opening was first formulated for the elastic case by G. Kirsch in 1889.[1] In addition to the elastic case, other situations occur in which shear stresses around the edge of a subsurface opening exceed the strength of the material (a plastic condition[2]) to some distance outward. In addition, SRI has studied overstressed conditions in the NTS tunnels.[3] There have been attempts to establish the outer boundary of overstressed material using velocity refraction surveys at the face of the tunnel wall.[4]

An application of a similar nature is suggested in this paper with velocity measurements in large Nevada Test Site (NTS) boreholes. We assert that the velocity logs can indicate a failed region of the borehole wall. Although weaknesses in some areas of the borehole wall are often revealed by surrounding erosion, borehole movie logs also indicate smooth or non-eroded areas of the hole. Velocity analysis of these areas suggests that many, including the usually smooth areas, have a weakened hole annulus. Because velocity measurements over short distances can have large error bars and because the stress-velocity relationship between all types of NTS soils and rock is not well characterized, we will make assumptions about the stress and velocity in order to assess damage in the hole annulus.

There is a large body of collected data consisting of local measurements taken against the edge of the borehole using the dry-hole acoustic logger (DHAL) and of seismic downhole velocity measurements with the Vibroseis technique[5] (Fig. 1). When travel times from both techniques are integrated over substantial distances, lower average velocities result from the DHAL technique. This may be attributed to a substantially large overstressed annulus around large boreholes. Disturbances caused by large-diameter drilling machinery (typically 2.44 m diam.) may also weaken the annulus. However, we believe that overstressed conditions in weak soil likely will affect a larger annulus zone than drilling alone would cause. The low DHAL velocities reported in LLNL geology reports of the NTS have no previous satisfactory explanation. We believe the lower velocities are caused by a lowered overburden stress condition at the edge of the large drill-hole walls.

Velocity Measurements in Nevada Test Site Holes

The DHAL is a single-station tool which consists of sending and receiving

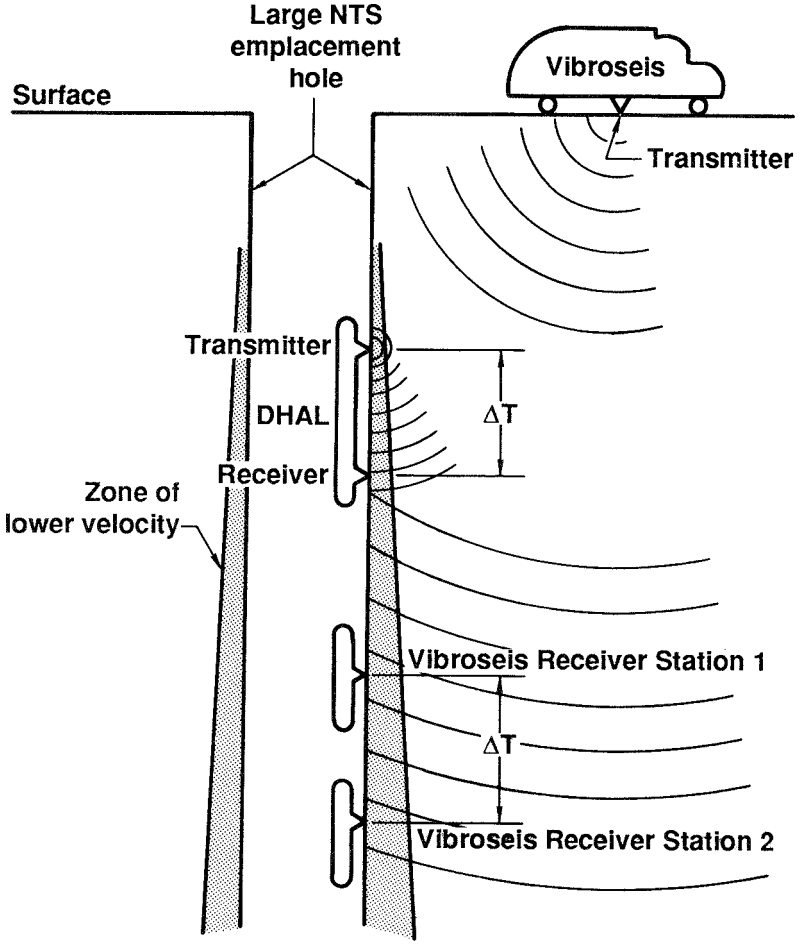

Fig. 1 Schematic of the DHAL and Vibroseis techniques.

units in contact with the borehole wall. The receiver transducer is located 0.914 m from the sending unit or at dual stations of 1.0 and 2.0 m in recent-model, multi-receiver units. The DHAL uses a 10-kHz design frequency. The Vibroseis technique uses a truck-mounted device, at the surface, which vibrates the ground in a linear sweep of 10 to 70 Hz, sending signals downward to receiving units in contact at the side of the hole. A cross-correlation data-processing technique establishes first arrival travel times to each receiving station.[6] The time difference between known locations establishes the velocity average of the interval. With this method, errors are large for small intervals because of errors in arrival-time determination. These errors are due to low frequency and to long, and likely different, travel paths to the receiving stations.[7] Fig. 1 shows a schematic of both techniques.

The schematic of the DHAL shows a low-velocity zone in the annulus. If the low-velocity region extends far enough into the annulus, the DHAL will measure only the low-velocity region. The Vibroseis signal travels down-hole, with first arrivals being representative of the fastest travel path. The first arrivals take the faster path outside of the low-velocity zone and refract across the low-velocity region to the receiver stations. The difference in arrival times between two stations cancels the times across the low-velocity annulus, thus giving a reasonable estimate of sonic velocity for the undisturbed material.

Travel times are reported for both techniques in most LLNL site characteristics reports. The travel path distances are from a planned working point location to the surface. Because the top of hole is cased for the first 30 m or so, the DHAL log is estimated over that region. An incomplete but random selection of these velocities is shown in Fig. 2.

In Fig. 2, the ratios of DHAL velocity to Vibroseis velocity are plotted for each site in a histogram. The populations are definitely biased to the left of the value of 1.0. In most cases, the average velocity of the DHAL is lower than that of the Vibroseis. Some NTS Areas show less of an average difference (19 and 20) than others (2,4,8,9, and 10). NTS Areas 19 and 20 generally are of stronger rock than are Areas 2, 4, 8, 9, and 10. The velocity in the annulus will be affected less in strong rock because less failure occurs in the annular region.

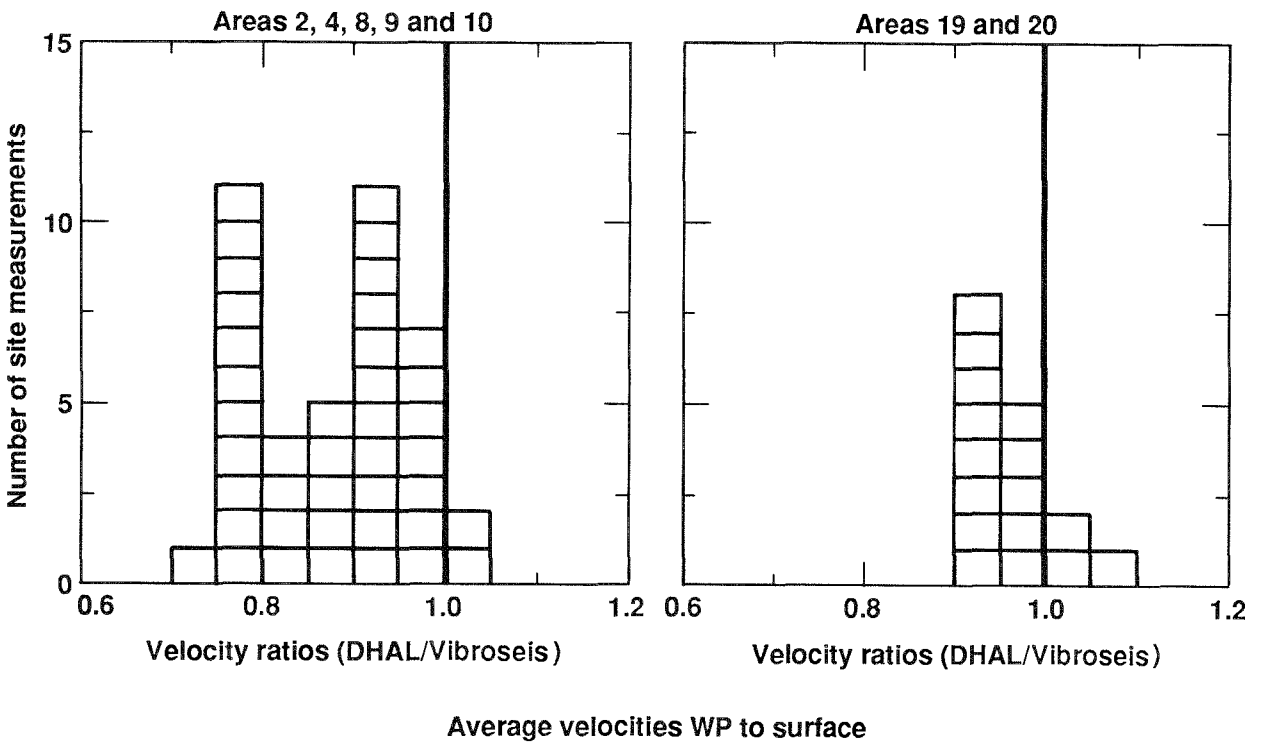

Fig. 2. Random selection of velocity ratios from several NTS Areas. Overburden DHAL velocities are usually lower than overburden Vibroseis velocities.

To observe the effect of hole diameter, we compare a large-diameter hole (2.44 m) and a smaller-diameter hole (0.311 m), separated by only 17 m at the surface. These holes are U2co and UE2co, respectively, and are relatively parallel. DHAL tools with the same spacing were run in both holes, with the result shown in Fig. 3. The large-hole DHAL velocity log is systematically lower than the small-hole DHAL.

A third observation determines which of the measurements gives the most correct arrival times. Comparison of pre-event velocity logging with arrival times from a nuclear event indicates that the Vibroseis compares quite favorably[7] (see Fig. 4). The nuclear case places a very large source at the bottom of the hole with detectors at the surface. With receivers away from the hole at the surface, the nuclear measurements likely represent good in-situ arrival times that are not affected by the hole annulus. By comparison, data from the Vibroseis, with its source away from the hole and the detectors in the hole, represent good in-situ measurements of comparable quality.

A corollary to the above is that the DHAL and the Vibroseis should agree in small-diameter holes in which the DHAL can penetrate past the low-velocity region. Figure 5, for hole UE2co with a 0.311-m-diam. hole, shows DHAL and Vibroseis velocities in fair agreement. The Vibroseis, which usually has a noisy interval velocity, still indicates some bias toward higher velocity. The overall average velocity of the Vibroseis of 1767 m/s is still high compared with the DHAL average velocity of 1569 m/s, to the maximum comparison depth of 472 m.

The four observations are consistent with the thesis that a low-velocity annulus exists around large holes. The DHAL tools with the current spacing, which may give reasonable velocities in small holes, usually do not adequately penetrate the thicker low-velocity annulus region of the larger holes. The two-receiver DHAL tool gives further verification. The receivers allow the travel path to be cancelled out across part of the disturbed zone. The resulting velocity is higher than what was obtained for the single receiver but not sufficient to reach the seismic velocity measurements.[8]

Velocity-vs-Pressure Measurements

There are only a few measurements relating P-wave velocity to mean stress (P_o) for NTS materials. Figure 6 shows velocity vs P_o for Timber Mountain tuff,[9] Merlin alluvium (U3ct),[10] and UE5n alluvium.[11]

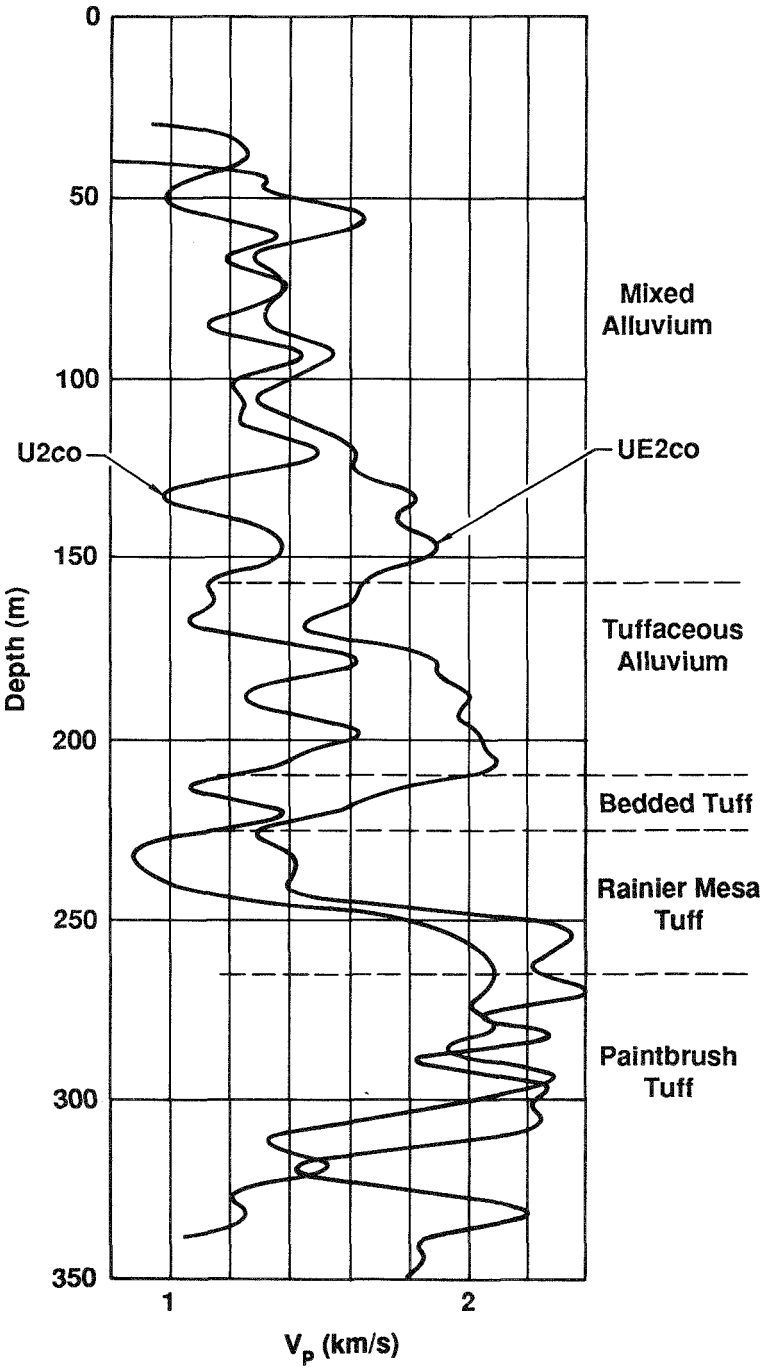

Fig. 3. Comparison of DHAL velocities in a large-diameter hole (U2co, 2.44 m) and a small-diameter hole (UE2co, 0.31 m).

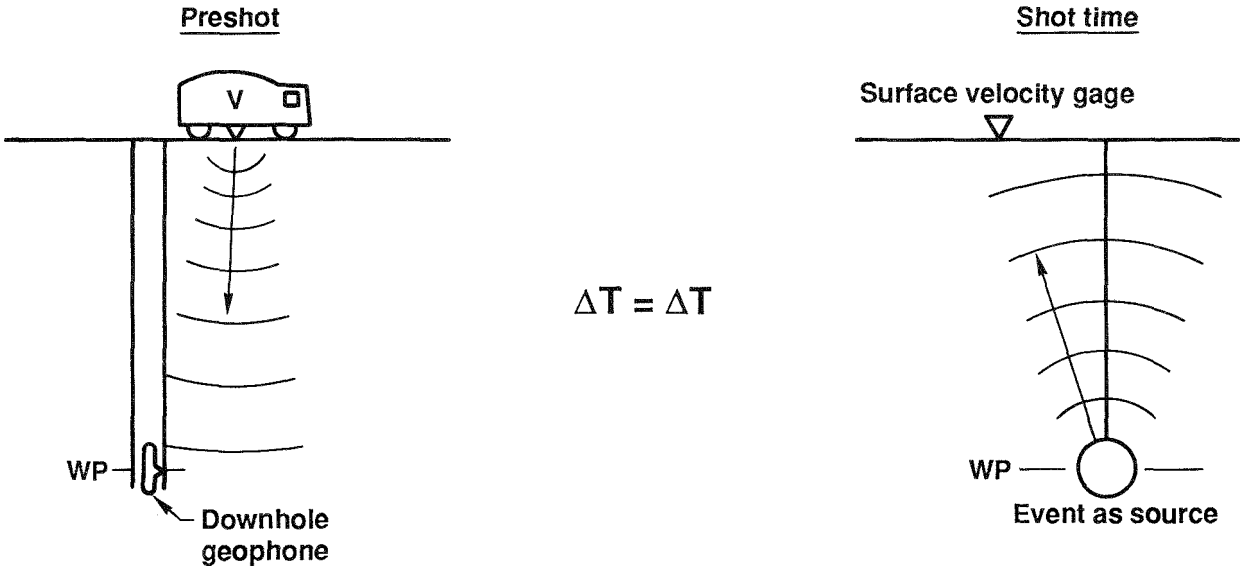

Fig. 4. Schematic of (1) pre-event Vibroseis velocity logging, and (2) arrival-time measurement from a nuclear event. The two compare favorably.

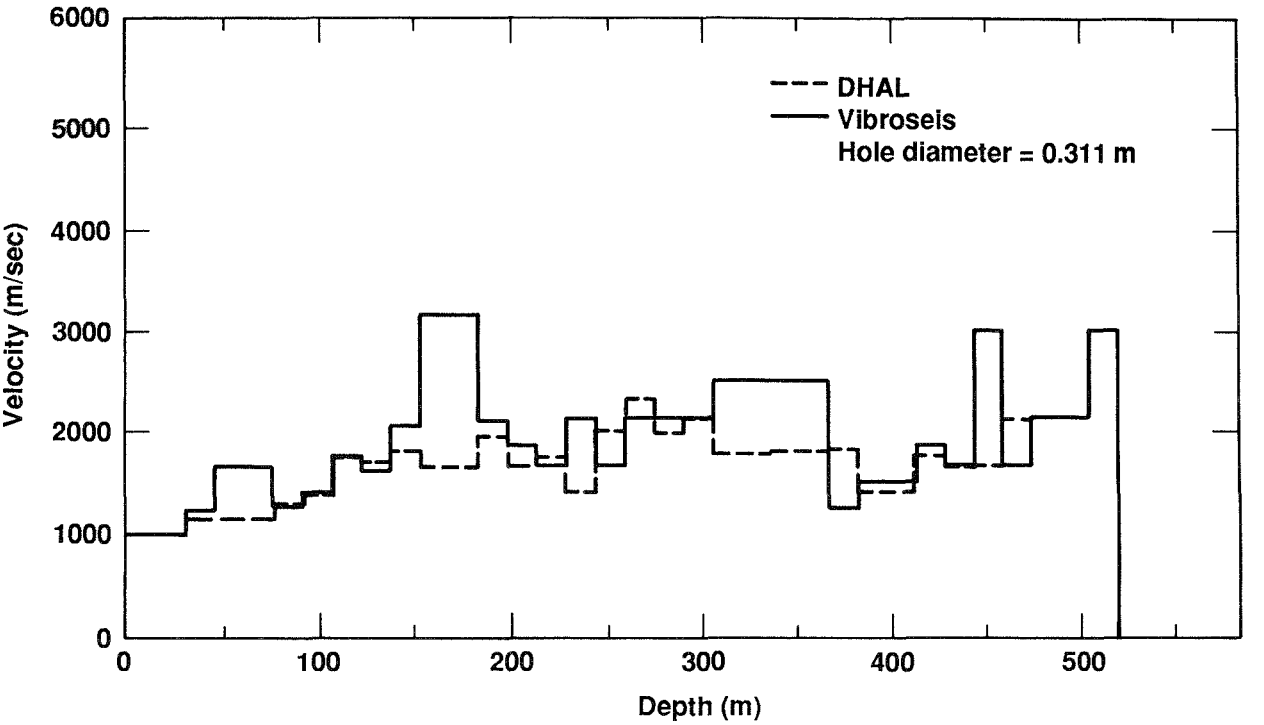

Fig. 5. Vibroseis velocity compared with DHAL velocity for a small-diameter hole (UE2co).

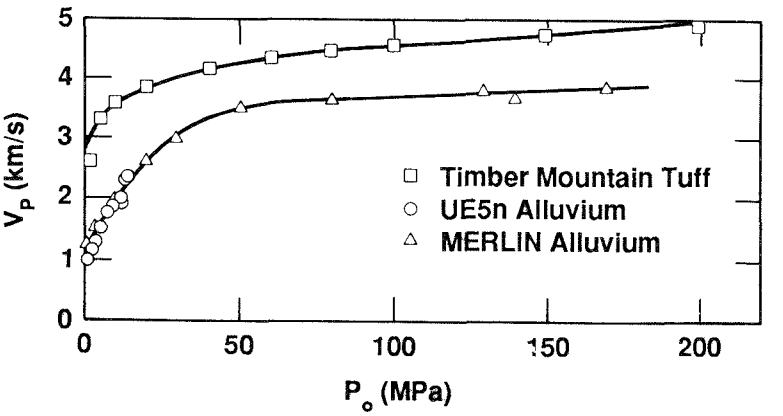

Fig. 6. P-wave velocity vs. mean stress, from laboratory measurements of three NTS materials.

In each case, the velocities increase with confining pressure. The soil-like alluvium material overplots reasonably well. The harder material of Timber Mountain tuff shows higher velocities separated by approximately a constant from the others. It is useful to assume for the later analysis that the slopes (first derivatives) for some NTS materials are similar.

It is generally accepted that Vibroseis velocities show sensitivity to the overburden pressure in the form of increased velocity with depth.[5,12] Figures 7a[13] and 7b[14] show such effects for two selected holes.

The laboratory data from UE3ct[10] were compared with those of the DHAL[15] and uphole surveys for that hole. Figure 8 shows reasonably good agreement, with some divergence at low confining stress. The laboratory data of UE5n[11] would give a better fit at low confining pressure.

Estimating the Pressure at the Hole's Edge

The method of estimating the stress state next to the edge of the hole may qualitatively indicate relative damage or weakness of the material along portions of the borehole wall. The method is considered qualitative because it uses differences in velocities between the DHAL and Vibroseis, which sometimes include large velocity errors over small intervals in the Vibroseis. If we assume that the overburden is isotropic and hydrostatic and that the first derivatives of the laboratory-measured velocities vs P_o are relatively similar for many NTS tuffs and alluviums, then a qualitative value of mean stress at the hole edge can be estimated.

The available data are the undisturbed velocity (Vibroseis), the velocity in the hole wall (DHAL), and the mean stress from overburden (calculated from the density log). In Fig. 9 the intersection of the mean stress at hydrostatic overburden is plotted at the observed Vibroseis velocity as a point representative of the undisturbed formation. The DHAL, which is usually lower, is plotted as a horizontal line. The slope of the displaced laboratory curve intersects the DHAL line from the Vibroseis point to give a mean stress value at the hole edge (P_{he}).

A Model of Reduced Stress at the Hole Wall

The elastic solution of stresses around a hole may be used if the material is sufficiently strong to withstand the applied stresses from overburden. The horizontal mean stress, P_o, which is related to the vertical overburden,

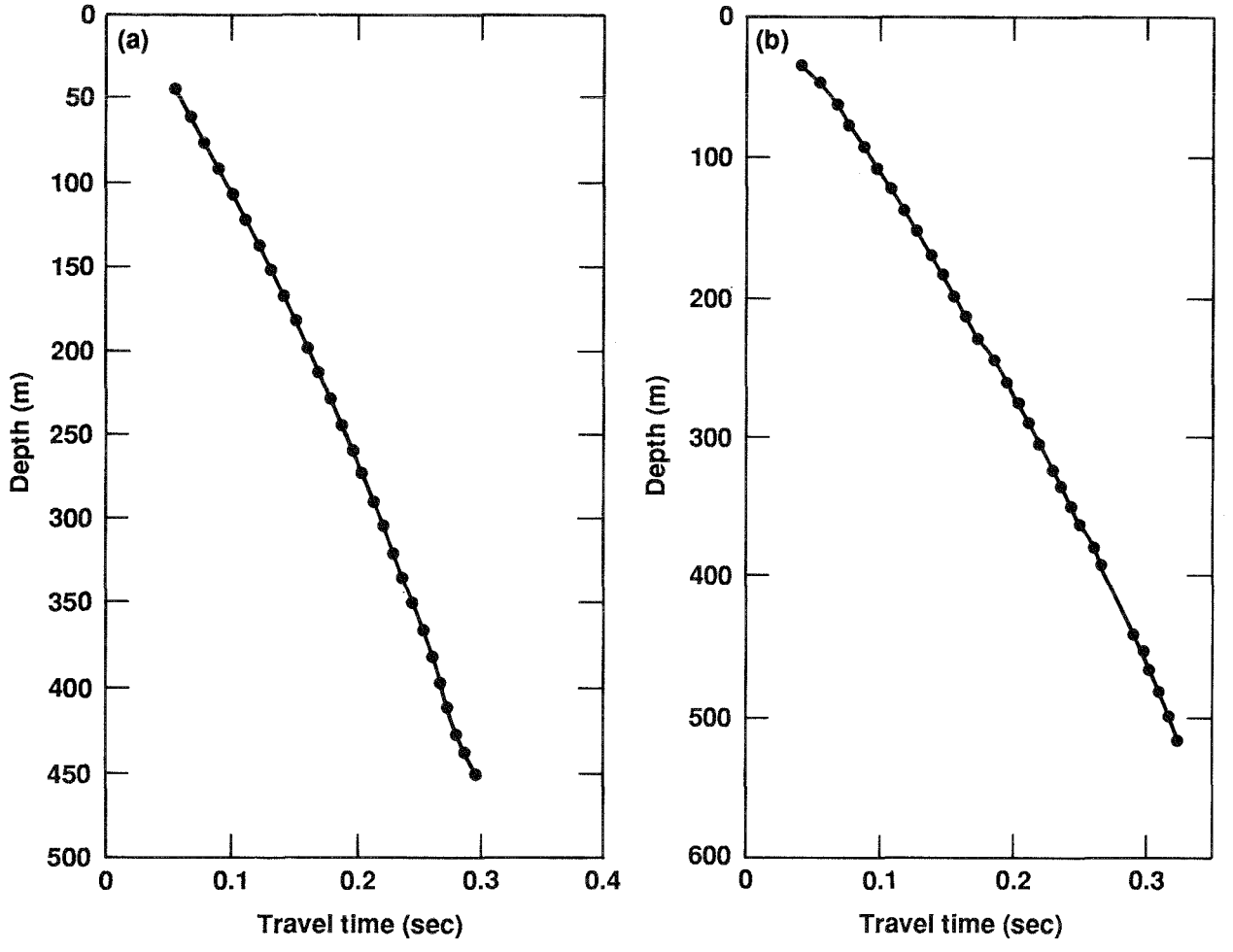

Fig. 7. Sensitivity of Vibroseis arrival times to depth. (a) U2ew Vibroseis Run 1, 8/31/82 (Ref. 13). (b) U2gb Vibroseis Run 1, 3/29/84 (Ref. 14).

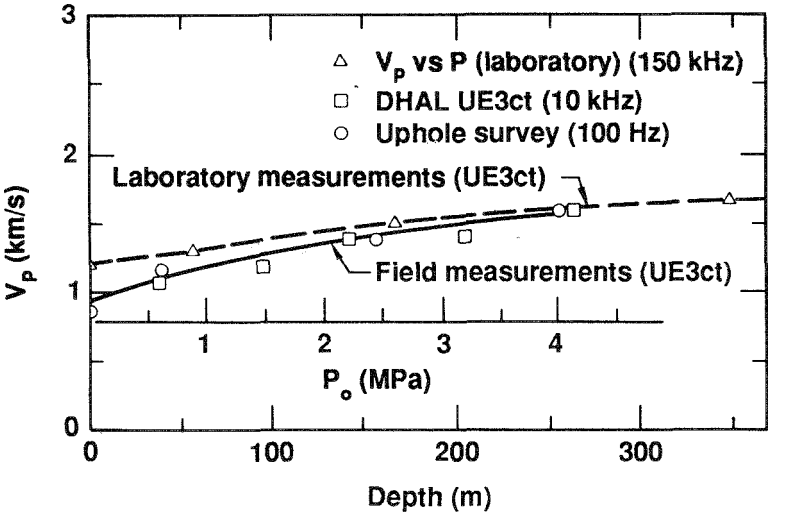

Fig. 8. Comparison between laboratory and field velocity measurements. The pressure scale is equivalent to the depth scale, assuming a constant average density for hole UE3ct.

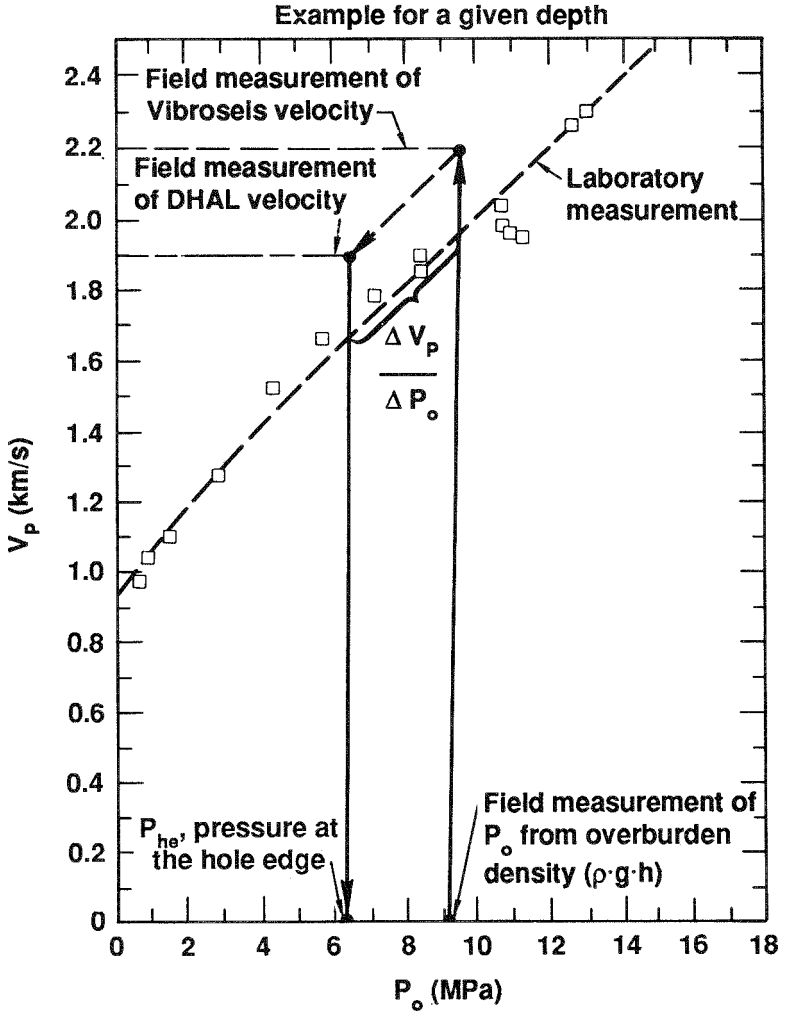

Fig. 9. Estimating the mean stress, P_{he}, at the hole edge. ρ is the average overburden density to a given depth, h, and g is the gravitational constant.

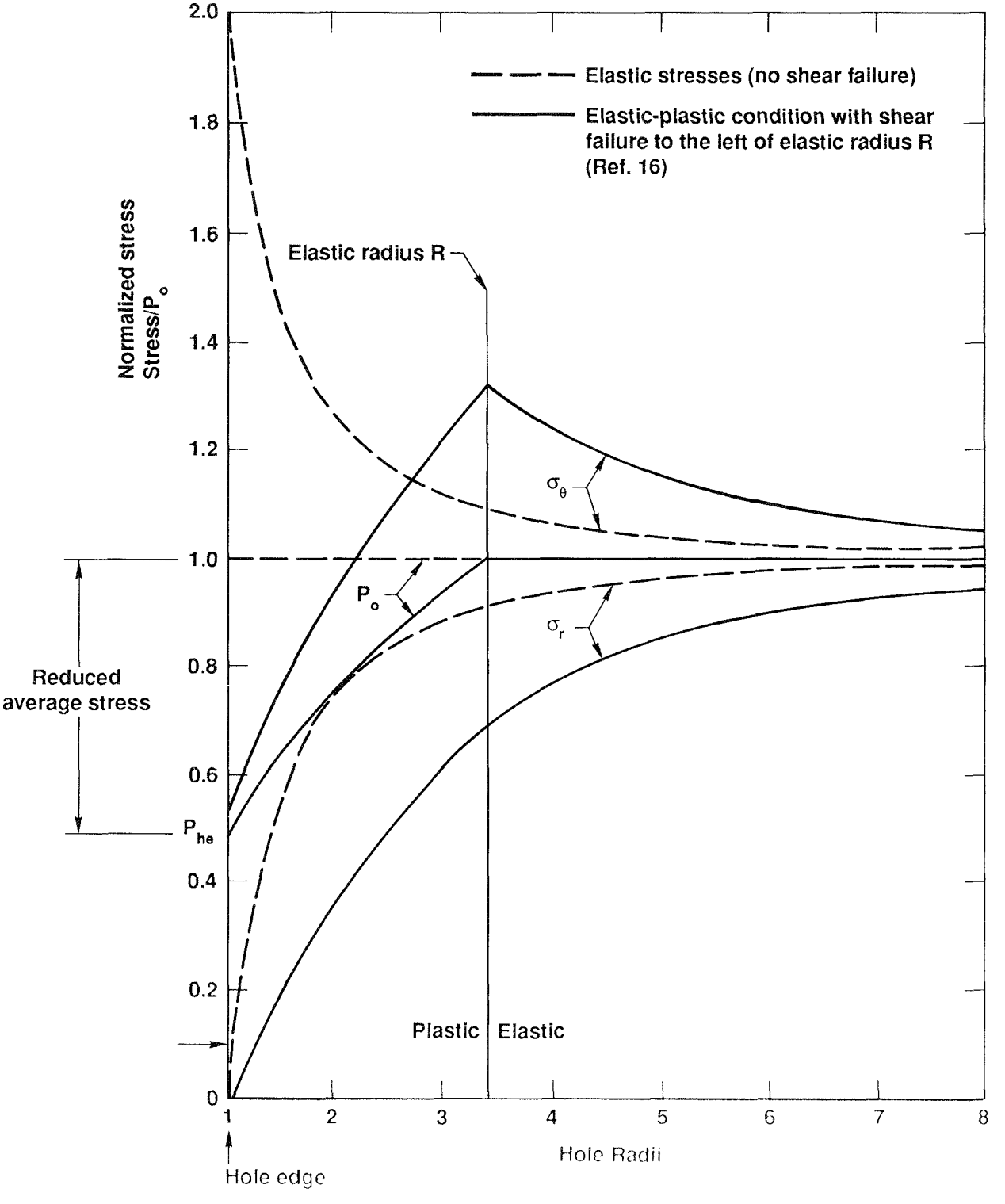

Fig. 10. Elastic model of stresses around a hole.

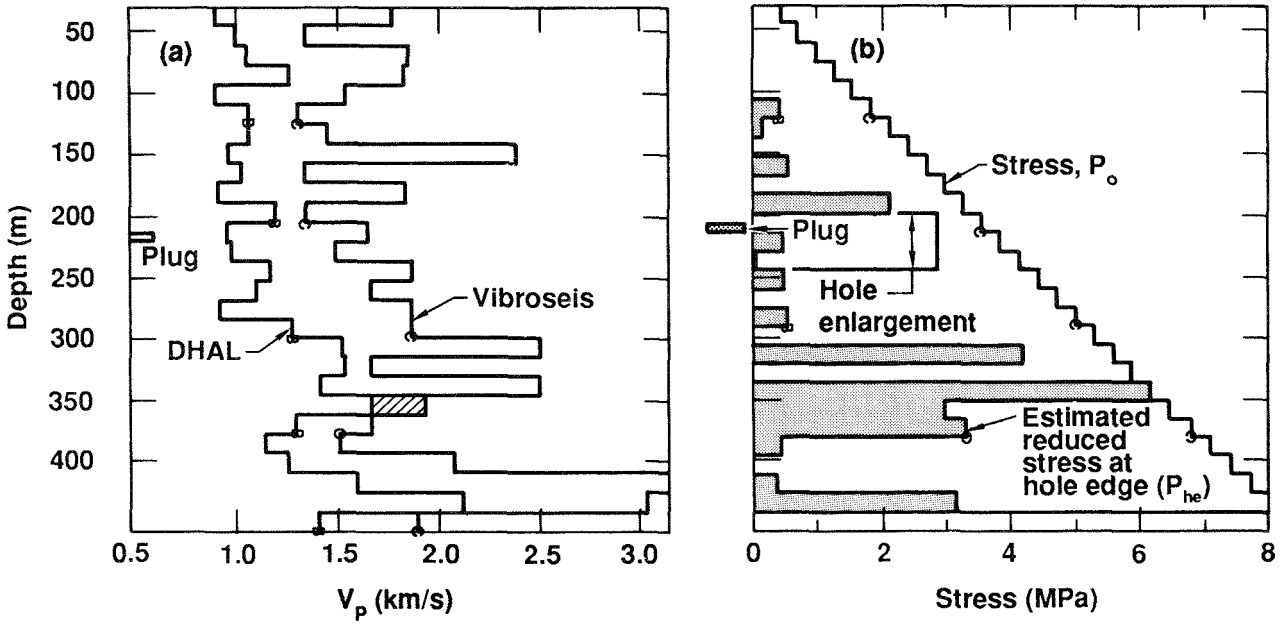

Fig. 11. RIOLA Event analysis (U2eq). (a) Downhole velocities. (b) Downhole stress. Cross-hatched regions in (a) are locations where the DHAL velocity exceeds the Vibroseis velocity.

σ_v, will remain constant, regardless of the distance to the hole edge. The elastic model is shown in Fig. 10 as dashed lines. As a boundary condition, the radial stress, σ_r (relative to the hole center), is zero at the hole edge. In a hydrostatic horizontal stress field, the hoop stress, σ_θ, increases to twice the applied horizontal stress. The shear that develops between the radial and the hoop stress may exceed the shear strength of the granular-like materials encountered at NTS.

It is likely that the applied overburden stress increases by 1.5-2.0 MPa per 100 m of depth. Unconfined strengths typically vary from 0 to 10 MPa, on the basis of recovered sidewall samples. The solid lines in Fig. 10 are an example of σ_r and σ_θ stress distribution in a Coulomb material under a failed condition.[16] As the hole edge is approached from a distance, the radial stress, σ_r, drops and the hoop stress, σ_θ, increases. The material is failed inside of a radius called the elastic radius. From this point to the hole edge, the radial stress continues to decrease to zero, and the hoop stress continues to decrease as well because the stress difference is limited by the strength of the material. The effect is that the mean horizontal stress will decrease to a lower value within the region where a shear failure occurs. The reduced average stress at the borehole wall shown in Fig. 10 includes the full vertical component σ_v (not shown), as well as σ_r and σ_θ. On the basis of the laboratory data in Fig. 9, the reduced stress would reduce the velocity at the hole edge as well.

The DHAL velocity data tends to support the stress model in that the observed velocities are almost always smaller than or equal to the Vibroseis data at the hole edge. In regions of the hole where the two velocity measurements tend to agree, we conclude that the hole annulus has not failed. DHAL velocities less than Vibroseis velocities indicate that failure has likely occurred in the hole annulus.

RIOLA Analysis

An example of the analysis outlined above is shown in Fig. 11 for the RIOLA Event. A comparison between the DHAL velocities and the Vibroseis velocities is shown in Fig. 11(a). The DHAL velocity is averaged over distance intervals equal to the Vibroseis velocity interval. The DHAL averages to a lower velocity everywhere except at a location near a depth of 350 m. Figure 11(b) shows the stress analysis from the data of Fig. 11(a). The staircase values of

stress are average values of mean stress based on the density log and with assumed hydrostatic overburden conditions. The laboratory data from Fig. 9 were used to estimate the reduced stress at the hole edge (P_{he}). The P_{he} estimates indicate complete unloading of the hole in many places.

This hole was picked to show how this analysis could be usefully applied. The RIOLA Release Report[17] gave information on the postshot radioactive seepage of the event as well as a seepage scenario. The plug and the material around the plug were both implicated in the resulting loss of stemming. The plug shown in Fig. 11 below a 200-m depth is in one of the extreme unloaded portions of the hole. A hole enlargement was also noted postshot over relatively unloaded portions of the hole between 200 and 245 m depth. The hole toward the surface above the 200-m depth did not appear to be eroded.

ROQUEFORT Analysis

Figure 12(b) shows the stress analysis and Fig. 12(a) the DHAL-Vibroseis comparisons for the ROQUEFORT Event. The DHAL in Fig. 12(a) is lower than the Vibroseis everywhere except at depths of 40, 190, 220, and 250 m. These values, however, are not greatly higher than the Vibroseis value.

Figure 12(b) shows plug locations along the depth axis of the stress plot. Postshot instrumentation indicated that radioactivity bypassed the two lower plugs and stopped below the plug located at about a 190-m depth.[18] There were known problems with the deeper two plugs.[19] The relatively low stress also shows the plugs to be located in regions where the annulus could have failed. The locations where the radioactivity stopped was below a plug in a region with a higher stress annulus.

In addition to analyzing ROQUEFORT and RIOLA, we placed the grout plug nearest the working point on the VILLE Event in a region of the hole shown to be a competent location by this analysis. Radiation did form below the plug but was not detected by radiation detectors just above the plug. These three examples do not provide conclusive evidence that the hole annulus is the problem, but they suggest that the annulus could have failed and that this type of analysis would be useful. Further investigative work into other event plug locations that have been challenged by radiation would be useful.

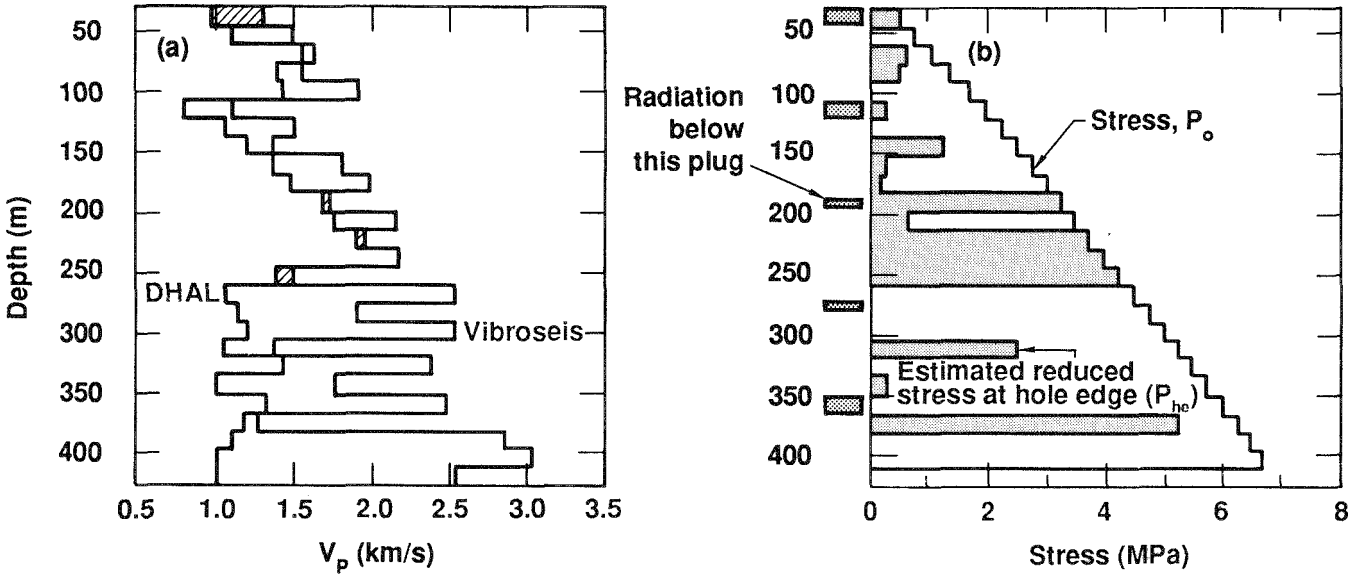

Fig. 12. ROQUEFORT Event analysis. (a) Downhole velocities. (b) Downhole stress. Cross-hatched regions in (a) are locations where the DHAL velocity exceeds the Vibroseis velocity.

Suggested Improvements

Better techniques are needed both to understand in-situ stresses and to reduce the noise in the velocity measurements. More laboratory measurements are needed on P-wave velocity vs mean stress of NTS tuffs and alluviums to add to the data base of NTS materials. Variations for the two materials presented are not well understood.

The laboratory measurements of velocity vs mean stress do not duplicate the stress conditions at the hole wall. We do not know how the DHAL P-wave velocities change in the presence of shear failed and shear cracked material. It may be that a more severe velocity decrease occurs, which might account for the lowest DHAL velocities appearing to be below those predicted by the laboratory curve. Velocity measurements across shear failed NTS material would be useful to better understand how the vertical stress differs from the horizontal stress.

Reducing noise in the Vibroseis analysis could be accomplished by taking larger distances for the velocity average. A seismic technique using an airgun source is now being employed to more accurately determine the P-wave arrival from the surface.

The current DHAL instruments do not penetrate very far into the annulus. The 0.91-m (3-ft) spacing would give a maximum of 0.10-m penetration, assuming a simple model of two concentric annuluses, that is, a low velocity surrounded by a 50% higher velocity. The two-receiver DHALs, with 2-m spacing, would give penetration to 0.2 m with similar assumptions. A wider spacing on the DHAL tool may allow greater penetration into the annulus, which would allow us to see past the disturbed zone in some instances.

Conclusions

We have established that the current DHAL tools measure a low annulus velocity in large holes. In NTS Frenchman Flat areas, we found that the shear strength is likely to be less than the shear stresses applied from overburden at the hole's edge. We have devised a method for indicating a qualitative picture of the hole damage based on the estimated mean stress at the hole wall. This method shows that cracks due to shear failure may occur in the annulus. These cracks can potentially align to produce a pathway around plug locations as derived from simple analyses of the RIOLA and ROQUEFORT failures.

We recommend that plugs be located in regions where less hole annulus damage is detected unless plug placement elsewhere is necessary for other containment considerations. To improve the quality of the measurements, we also recommend a longer-spacing DHAL and further study to better understand the process of reduction in stress at the hole wall, due to damage.

ACKNOWLEDGMENTS

We wish to acknowledge Francois Heuze for his guidance and useful suggestions, Cliff Olsen for his review of the paper, Jay C. Cherniak for his help in preparing the manuscript, Lydia Grabowski for her excellent typing, Miriam Lohmann for computer processing of the data for RIOLA and ROQUEFORT, and L. Lettis for writing the computer code (VEL17) to analyze the data. This work was performed under the auspices of the U.S. Department of Energy by Lawrence Livermore National Laboratory under contract No. W-7405-ENG-48.

REFERENCES

1. G. Kirsch, Verein Deutscher Ingenieure, Vol. 42, 1898.

2. K. J. Kim, D. D. Piepenburg, and D. Merkle, "Influence of the Intermediate Principal Stress on Rock Tunnel Behavior", DNA-TR-86-52, Applied Research Associates, Inc., Albuquerque, NM, January 20, 1986.

3. A. L. Florence and L. E. Scher, "Axial Symmetric Compression of a Mohr-Coulomb Medium Around a Circular Hole", International Journal for Numerical and Analytical Methods in Geomechanics, Vol. 2, pg. 367-379 (1978).

4. R. E. Goodman, Introduction to Rock Mechanics, John Wiley & Sons, New York, NY, pg. 235, 1980.

5. N. W. Howard, "Variation in Properties of Nuclear Test Areas and Media at the Nevada Test Site", Lawrence Livermore National Laboratory, Livermore, CA, UCRL-53721 (September 15, 1985).

6. J. M Crawford, W. E. N. Doty, and M. L. Lee, "Continuous Signal Seismogram", Geophysics, V. 25, pp 95-105 (1960).

7. J. M. Richter, EG&G, San Ramon, CA, May 1987, private communication.

8. R. C. Carlson, Lawrence Livermore National Laboratory, Livermore, CA, November 1987, private communication.

9. R. N. Schock, B. P. Bonner, and H. Louis, "Collection of Ultrasonic Velocity Data as a Function of Pressure for Polycrystalline Solids", Lawrence Livermore National Laboratory, Livermore, CA, UCRL-51508 (1974).

10. B. Bonner, A. Abey, H. Heard, and R. Schock, "High-Pressure Mechanical Properties of Merlin Alluvium," Lawrence Livermore National Laboratory, Livermore, CA, UCRL-51252, (July 7, 1972).

11. M. S. Constantino and B. P. Bonner, "Ultrasonic Velocities and Strength of Frenchman's Flat Alluvium," Lawrence Livermore National Laboratory, Livermore, CA, UCID-18862 (1980).

12. P. Fulan, "The Relation Between Dynamic Elastic Parameters and Depth of Soil", Soil Dynamics and Earthquake Engineering Conference, Southampton, U.K., pp 167-178 (July 13-15, 1982).

13. S. R. Clark and N. W. Howard, "U2ew Site Characteristics Report," Lawrence Livermore National Laboratory, Livermore, CA, Internal Report, CP-83-55, pg. 19 (1985).

14. G. Pawloski, "U2gb Site Characteristics Report," Lawrence Livermore National Laboratory, Livermore, CA, Internal Report, CP 85-83, pg. 19 (1985).

15. R. C. Carlson and J. R. Hearst "Physical Properties of (Mostly Northern) Yucca Flat Alluvium and Tuff," Lawrence Livermore National Laboratory, Livermore, CA, UCID-15848 (1971).

16. Jaeger and Cook, Fundamentals of Rock Mechanics, Third Edition, Chapman & Hall, Ltd., London, pg. 251 (1979).

17. E. C. Woodward, "RIOLA Release Report," Lawrence Livermore National Laboratory, Livermore, CA, UCRL-53437 (August 4, 1983).

18. B. C. Hudson, Lawrence Livermore National Laboratory, Livermore, CA, 1985, private communication.

19. V. E. Wheeler, "ROQUEFORT", Lawrence Livermore National Laboratory, Livermore, CA, Internal Memorandum UOPKL 85-38 (Oct. 14, 1985).

RELATIONSHIP BETWEEN LARGE-HOLE DRILLING RATES AND COMPRESSIVE STRENGTH OF NTS ROCK TYPES

G. D. Anderson, J. T. Rambo, A. S. Kusubov,
H. A. Dockery, and W. B. McKinnis

University of California
Lawrence Livermore National Laboratory

ABSTRACT

Calculations to simulate and evaluate nuclear test containment require data on the strength of the geologic media at the work point and in the surrounding region. Studies cited in the literature reveal correlations between mechanical properties of rocks and various drilling parameters of large horizontal boring machines that share similarities with drilling assemblies used at the Nevada Test Site (NTS). An extensive selection of downhole core samples spanning the strength range of NTS rocks has been collected, stratigraphically and petrologically identified, and tested for strength as a function of confining pressure. Detailed data on the drilling rates are available for similar geologic units identified in the compilation and also for the specific rocks from these vertical holes that were tested. These data are used to discuss a preliminary empirical correlation between reported laboratory-measured compressive strength and drilling rates for various NTS rock types.

INTRODUCTION

Computer calculations to simulate and evaluate nuclear test containment require data on the strength of the geologic media at the work point and surrounding media as a function of confining pressure. This information is usually obtained in the laboratory by testing core samples retrieved from drill holes. Over the past 20 years, many rock types from NTS have been tested in the rock mechanics laboratory at LLNL to provide material properties needed for containment calculations. The measurements include hydrostatic pressure-volume response, triaxial compressive strength as a function of confining pressure, and tensile strength. These data are available from the Lawrence Livermore National Laboratory's Library of Mechanical Properties of Geological and Related Materials.[1]

During the drilling of NTS boreholes, rate of drill-bit penetration as a function of depth is recorded routinely for each borehole and available from the NTS geolograph files.[2] Because both the strength data and the drilling rate data are available, a common question has been whether a correlation can be found between the compressive strength of the rock and the rate of drill bit penetration. Such a correlation would be useful for two reasons. First, it would enable us to estimate the compressive strength of individual rock sequences from the drilling rate as the hole is being drilled. If the strength of rock units could be estimated from the drilling rate, the data could be immediately incorporated into containment calculations. Thus, calculations could be completed in a more timely manner and problematical regions could be identified more quickly. Secondly, if we were drilling into a formation of known strength, this type of information would enable us to estimate the time required to drill to the bottom of that formation or particular rock type. Operations could make more accurate estimates of drilling time, thus scheduling equipment better.

A correlation between unconfined compressive strength and penetration rate was seen by Tarkoy[3] for large-scale horizontal tunnel boring machines (TBM) for a variety of rock types. However, Tarkoy points out that difficulty arises from indiscriminate attempts to use unconfined compressive strength for all rock types. Some samples contain a variety of flaws that have anomalous effects on the rock's mechanical behavior so they cannot be defined in terms of the unconfined compressive strength. A diagram from Tarkoy's work showing unconfined compressive strength vs penetration rate for a particular TBM is shown in Figure 1. Here the unconfined compressive strength of the rock varies from about 70 MPa to about 210 MPa.

For large vertical drill holes at NTS, we undertook a preliminary study to determine whether a correlation exists between penetration rate and compressive strength similar to Tarkoy's observations. The results of this preliminary study are presented in the following sections.

DRILLING RATE AND COMPRESSIVE STRENGTH OF NTS ROCKS

The drilling rate through a formation is dependent upon drilling parameters such as drill bit size and type, rotary speed of the drill bit, load on the drill bit, and type of drilling fluid or mud used, as well as

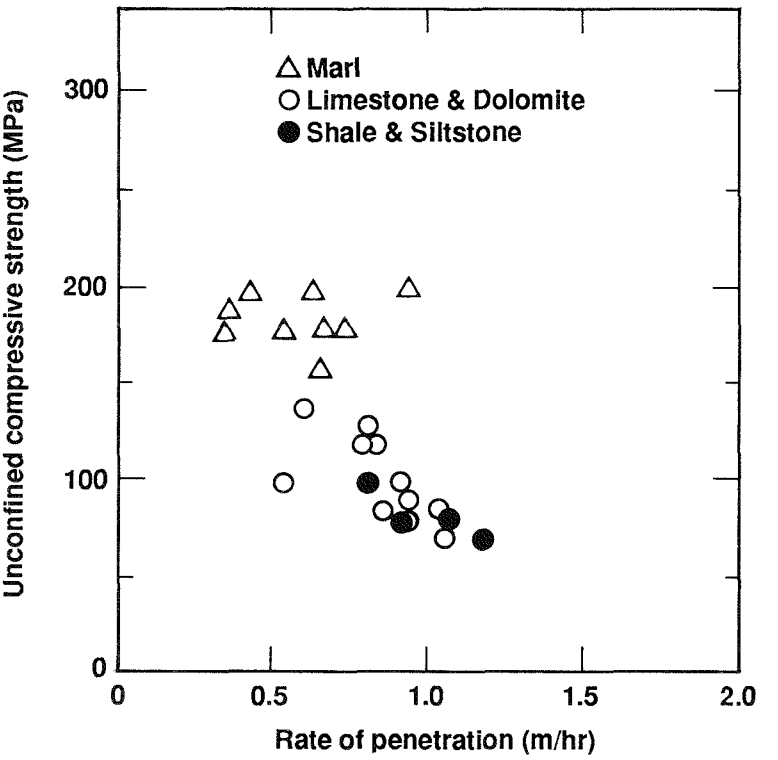

Figure 1. Rate of penetration of a horizontal tunnel boring machine vs unconfined compressive strength. From Tarkoy.[3]

mechanical properties of the rock. Under the constraints of this study, it was not possible to isolate and evaluate the effect of all these drilling parameters. Therefore, we selected holes of the same diameter, and we assumed that the holes were drilled with the same or a very similar type of drill to minimize the variation of drilling rate as a function of drilling parameters.

The restriction to use information from only one size of drill hole left us with a relatively small number of strength data points to correlate. In order to enlarge our data base of drilling rate data, we investigated nearby drill holes in the geologic formations from which strength data had been obtained. While a formation can change laterally in terms of welding, zeolitization, water content, and many other parameters, we believed that the properties of the same formation intersected in proximal drill holes would be similar. In order to identify these additional holes, we first geographically located each drill hole with strength information. Next, we centered each hole on a square 1500 m on a side. We identified all holes within each square that had a diameter of 2.44 m and that also penetrated to sufficient depth to intersect the formation(s) having strength data. After we had determined which holes belonged in the smaller set, we then looked at the stratigraphic and structural relationship each had with the central hole. Because we were dealing with thick-time stratigraphic formations exhibiting a wide range of physical properties and drilling rates, we next had to determine which portion of the formation in each hole was representative of the region that was measured for strength. A 5- to 10-m section of the formation, located at the appropriate stratigraphic level, was correlated according to the strength-tested sample according to the closest possible match in bulk density, grain density, porosity, and saturation. Drilling rates from these intervals were then obtained from the geolograph records.[2]

The holes and depths from which strength samples were taken are listed in Table 1, along with the corresponding drilling rates in m/hr. The third column lists the unconfined compressive strength of each material. In Figure 2, these data are plotted against the drilling penetration rate. The two points for rhyolitic lava appear to show a greater sensitivity in drilling rate vs compressive strength than do the weaker, nonwelded tuffs. The shaded areas are added to the figure to denote the regions in which more data, if available, would be expected to lie.

Table 1. Compressive strength and drilling rates for selected NTS rocks.

Drill hole sampled[a]	Depth (m)	Unconfined compressive strength (MPa)	Estimated strength at overburden confinement (MPa)	Rock type	Drilling rate (m/hr)
U8j[4]	427.	10.3	40.1	Ash flow tuff	1.3
U8j[4]	494.	12.3	34.6	Nonwelded tuff	1.1
U2cr[5]	250.	7.7	11.9	Nonwelded tuff	2.7
U2cr[5]	298.	4.6	17.2	Nonwelded tuff	2.3
U4as[6]	396.	0	4-6	Nonwelded tuff	2.9
U20av[7]	620.	11.1	21.	Nonwelded tuff	1.0
Ue2en[8]	685.	6.7	13.3	Nonwelded tuff	1.1
U19ac[9]	551.	49.	130.	Rhyolitic lava	0.5
U19yx[10]	506.	16.	26.	Rhyolitic lava	1.8

[a]Numbers refer to reference from which strength data was obtained.

When triaxial compressive strength tests are run on a material, a suite of tests is customarily run over a range of confining pressures varying between one atmosphere (unconfined) and several hundred MPa. Because this was done for the materials listed in Table 1, we could estimate the compressive strength of each of these materials at the confining pressure approximating the in situ overburden pressure. Under confining pressure, we assumed the compressive strength at failure equals the axial stress that the material can support minus the confining stress. The estimated compressive strength under appropriate confinement is listed in the fourth column of Table 1 and is plotted against drilling penetration rate in Figure 3. The effect is that the strength of all the materials is elevated because of increased confining pressure. Although the lower point for the rhyolitic lava now occurs nearer the points for the weak tuff, the rhyolitic lava still exhibits a greater sensitivity between strength and drilling rate than does the weak tuff.

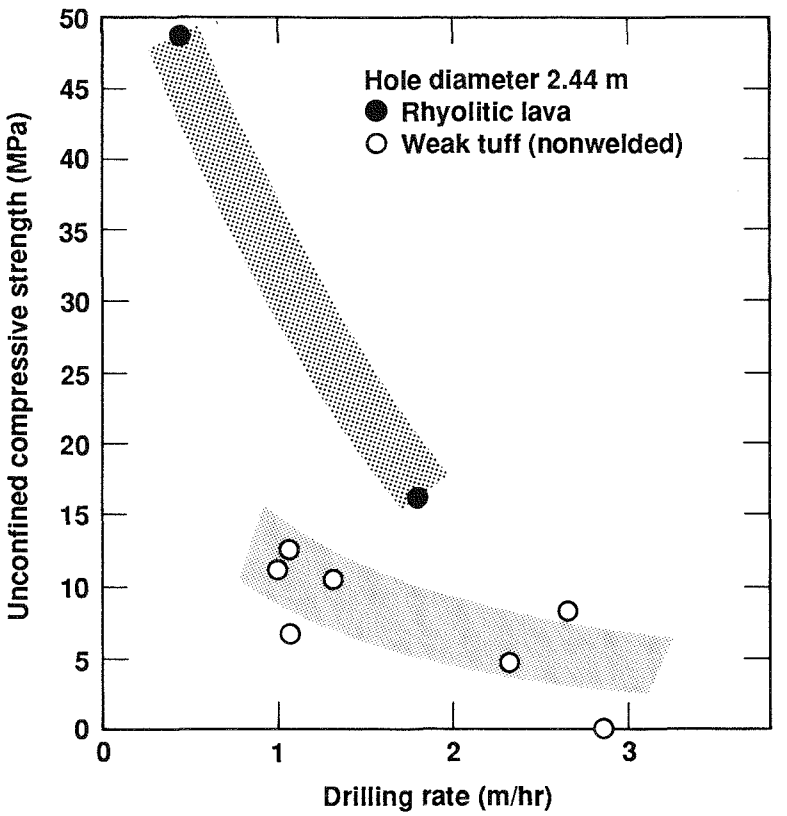

Figure 2. Unconfined compressive strength vs drilling rate for selected NTS rocks.

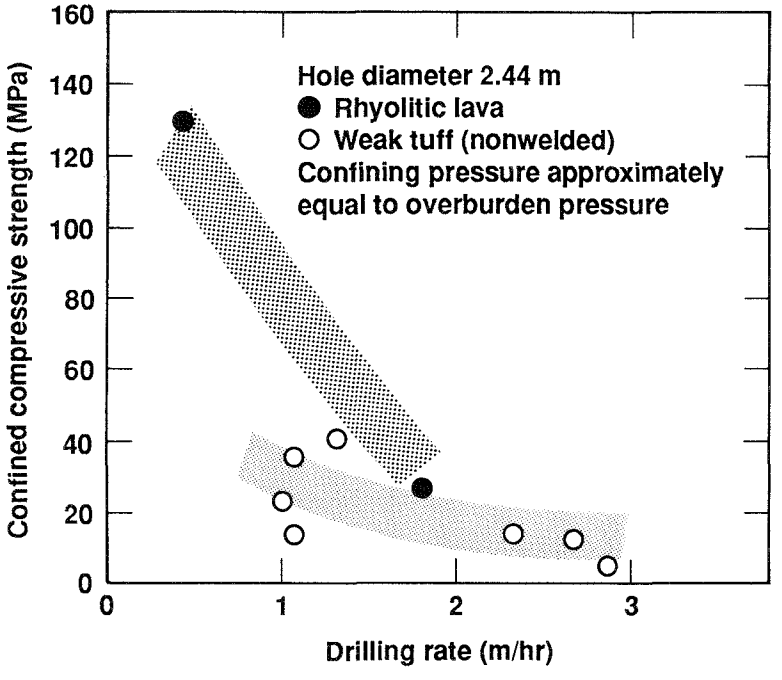

Figure 3. Confined compressive strength vs drilling rate for selected NTS rocks.

SUMMARY, CONCLUSIONS AND SUGGESTIONS FOR FUTURE WORK

From the limited data we studied, the stronger rock--rhyolitic lava--appears to exhibit a stronger correlation between drilling rate and unconfined compressive strength than does the weaker, nonwelded tuff. When drilling rate is plotted vs strength under confinement approximately equal to in-situ overburden, the scatter in the data is somewhat reduced. However, the strength of the stronger rhyolite is still more sensitive to drilling rate which we believe indicates that drilling rate in very weak rocks--such as the weak, nonwelded tuffs--is more sensitive to drilling parameters than to the compressive strength. Thus, a correlation may be useful only in the case of stronger, harder rocks.

A more thorough and complete study is suggested of the correlation between drilling rate and compressive strength. Specifically, more comparisons are needed for stronger, harder rock to assess the effects of drilling parameters such as drill bit size and type, load on the drilling assembly, and rotary speed of the drill. A procedure should be worked out to normalize the data with respect to the drilling parameters so that drilling data from all sizes of drill holes can be incorporated into the correlation. This process may require a more extensive understanding of the actual physics of the drilling process.

ACKNOWLEDGMENTS

We thank L. L. Schwartz and L. Thigpen for providing support for this study. A special thanks is due to S. P. Stull for editing this report and to T. A. Fletcher for typing the manuscript.

Appreciation is extended to Prof. H. F. Wang of University of Wisconsin, Madison, WI, for supporting this project.

REFERENCES

1. Kusubov, A. S., H. A. Dockery, and G. D. Anderson, Compilation of Mechanical Properties of Geological and Related Materials, Lawrence Livermore National Laboratory, Livermore, CA, UCID-20943, January 17, 1987.
2. Fenix and Scisson, Geolograph records, NTS Central Files, Mercury, Nevada.

3. Tarkoy, P. J., Rock Hardness Index Properties and Geotechnical Parameters for Predicting Tunnel Boring Machine Performance, Ph.D. Thesis in Civil Engineering, University of Illinois, Urbana-Champaign, IL, 327 pp., August 1975.
4. Anderson, G. D., and A. S. Kusubov, Static and Dynamic Mechanical Properties Tests of Core Material From Hole U8j at the Nevada Test Site, Lawrence Livermore National Laboratory, Livermore, CA, UCRL-92456, 16 pp., January 27, 1986.
5. Kusubov, A. S., and G. D. Anderson, Lawrence Livermore National Laboratory, Livermore, CA, Internal Memorandum to J. T. Rambo, 19 pp., May 29, 1984.
6. Anderson, G. D., and A. S. Kusubov, "Strength Tests on Material from Hole U4as," Lawrence Livermore National Laboratory, Livermore, CA, Internal Memorandum to J. T. Rambo, 4 pp., July 8, 1985.
7. Anderson, G. D., and A. S. Kusubov, "First Interim Report on Strength Data from Holes U20av and Ue20av," Lawrence Livermore National Laboratory, Livermore, CA, Internal Memorandum to J. T. Rambo, 10 pp., January 22, 1987.
8. Swift, R. P., "Compressive Strength Tests on Paintbrush Tuff from Ue2en," Lawrence Livermore National Laboratory, Livermore, CA, Internal Memorandum UCON 77-42, 6 pp., November 10, 1977.
9. Swift, R. P., and H. Washington, "Compressive Strength Tests on Pre-Pah Canyon Rhyolitic Lava from U19t and U319t," Lawrence Livermore National Laboratory, Livermore, CA, Internal Memorandum UCON 78-24, 6 pp., August 14, 1978.
10. Swift, R. P., "Compressive Strength Tests on Rhyolitic Lava from U19ys (PANIR)," Lawrence Livermore National Laboratory, Livermore, CA, Internal Memorandum UCON 78-14, 6 pp., April 27, 1978.

Work performed under the auspices of the U.S. Department of Energy by Lawrence Livermore National Laboratory under Contract W-7405-Eng-48.

Measurement of In situ Strength Using Projectile Penetration: Tests of a New Launching System

J. R Hearst and R. L. Newmark,
Lawrence Livermore National Laboratory

J. A. Charest and C. S. Lynch, Dynasen Inc.

ABSTRACT

The Lawrence Livermore National Laboratory has a continuing need to measure rock strength in situ, both for simple prediction of cavity size, and as input to computational models. In a previous report we compared two methods for measuring formation strength in situ: projectile penetration and a cone penetrometer. We determined that the projectile method was more promising for application to our large-diameter (2-4-m) hole environment. A major practical problem has been the development of a launcher and an apparatus for measuring depth of penetration that would be suitable for use in large-diameter holes. We are developing a gas-gun launcher system that will be capable of measuring both depth of penetration and deceleration of a reusable projectile. The current version of the launcher is trailer-mounted for testing at our Nevada Test Site (NTS) in tunnels and outcrops, but its design is such that it can be readily adapted for emplacement hole use.

We tested the current launcher on 60-cm cubes of gypsum cement, mixed to provide a range of densities (1.64 to 2.0 g/cc) and strengths (3 to 17 MPa). We compared depth of penetration of a 84-g projectile from a "Betsy" seismic gun--traveling on the order of 500 m/s--with the depth of penetration of a 13-kg projectile from the gas gun--traveling on the order of 30 m/s. For projectiles with the same nose size and shape, impacting targets of approximately constant strength, penetration depth was proportional to projectile kinetic energy. The ratio of kinetic energy to penetration depth was approximately proportional to target strength.

Tests in tuffs with a wide range of strengths at NTS gave a similar linear relationship between the ratio of kinetic energy to penetration and target strength, and also a linear relationship between deceleration and strength. It appears that penetration can indeed be used as a semiquantitative measure of strength.

INTRODUCTION

The Lawrence Livermore National Laboratory has a continuing need to measure the strength of tuff and desert alluvium, both for simple prediction of the size of cavities resulting from underground nuclear explosions (Terhune and Glenn, 1977), and as input to

computational models for calculating the effects of underground explosions. Measuring strength of core samples is not satisfactory, because the only possible method of obtaining core from the sites of interest is the use of a sidewall core machine in the wall of large-diameter (2-4-m) nuclear test emplacement holes. These cores are expensive, difficult (and sometimes impossible) to obtain, and not representative of the formation. There is, however, no currently accepted method for measuring in-situ strength with a borehole instrument.

Caudle et al. (1967) investigated the use of the penetration of projectiles to obtain soil strength. They observed qualitative correlation between projectile deceleration and soil strength. Rohani (1972) found that depth of penetration was inversely proportional to target strength. Butler (1975), in a series of calculations, determined that if projectile velocity and properties were held constant, the depth of penetration and deceleration depended strongly on unconfined compressional strength and the "locked" volume strain, but not on the initial target density. McNeill (1981) concluded, from experiments in soil, that projectile deceleration is directly proportional to strength.

One problem not treated by Caudle et al. (1967) or McNeill (1981) is the effect of initial projectile velocity. Although it would be possible to attempt strength measurements using constant projectile velocity, it is useful to vary the velocity to obtain greater flexibility in the measurements. Consequently it is important to understand the effects of initial velocity on penetration. Young (1969) listed several formulae relating depth of penetration, z, to initial velocity of a pointed projectile. He cited Robins (1742) and Euler (1745), both of whom assumed that resisting force was constant, and obtained

$$z = mV^2/2c, \qquad (1)$$

where m is the projectile mass and c is a constant. He also cited several authors: Poncelet (1829), Resal (1895), and Petry (1910), who assumed that force was a function of velocity and obtained results of the form

$$z = Km \ln(1 + cV^2), \qquad (2)$$

where K and c are constants. Young himself disagreed with all of these authors. He found that for velocities below 60 m/s,

$$z = CSN M^{1/2} \ln(1 + 2V^2 10^{-5}), \qquad (3)$$

and for velocities above 60 m/s

$$z = KSN M^{1/2} (V - 30), \qquad (4)$$

where C and K are constants, N depends on the projectile nose shape, S is a "soil constant," determined by fitting Eqs. (3) and (4) to the data, and M is the projectile mass per unit cross-sectional area.

In fact, his plots show approximate linear dependence of penetration on velocity at all velocities.

Bernard (1978) presented the following empirical formula, derived from dimensional analysis with a one-term model, relating penetration to both strength and projectile velocity:

$$z = KVm/A(\rho Y)^{1/2}, \qquad (5)$$

where ρ is the bulk density, Y is the strength, and K is a constant related to the "Rock Quality Designation," RQD.

Kumano and Goldsmith (1982), on the other hand, used spherical projectiles and found that z varied quadratically with kinetic energy.

In a previous report (Hearst and McKinnis, 1985) we compared two proposed methods for measuring formation strength in situ: projectile penetration and use of a cone penetrometer. We concluded that the projectile method was more promising for application to our large-diameter (2-4-m) hole environment. A major practical problem has been the development of a launcher and an apparatus for measuring projectile velocity, deceleration, and depth of penetration that would be suitable for use in large-diameter holes.

We have developed a prototype of such a launcher by modifying an existing 6.3-cm gas gun. The gun propels a heavy (about 13 kg) projectile to speeds on the order of 30 m/s. The modifications permitted us to make the required measurements. It appears that the basic mechanism can be adapted to the development of a remotely operated downhole apparatus.

This report describes the modified gun, and the tests made both in the laboratory and at the U. S. Department of Energy's Nevada Test Site (NTS) both on surface outcrops and in the walls of a mined tunnel.

APPARATUS

"Betsy" Seismic Gun

The Betsy, used in our previous work (Hearst and McKinnis, 1985), is an eight-gauge shotgun mounted on a wheeled platform (Fig. 1). Its normal charge is 6 g of gunpowder, and the projectile is an 84-g iron slug, 4 cm long, with a flat face 1.5 cm in diameter; 1.5 cm behind the face the diameter abruptly increases to 2 cm. The normal muzzle velocity is about 500 m/s.

For some experiments we reloaded the shotgun shells with a smaller powder charge to decrease the velocity. Two pick-up coils, through which the projectile passed enroute from the muzzle to the target, measured the projectile velocity. Consequently, we were able to both vary and determine the velocity at will.

Figure 1. Photograph of the "Betsy" seismic source.

The Gas Gun

The gas gun, designed originally for shock wave experiments, has a barrel 2 m long and 6.25 cm in diameter (Fig. 2). It has a compressed-gas chamber that can be operated up to about 12 MPa pressure. Projectile velocity is controlled by varying the pressure. The gun is fired by puncturing a stainless steel diaphragm with a solenoid-driven, pointed rod. For the laboratory experiments the gun was mounted vertically in a tower. For the fieldwork it was mounted on a trailer (Fig. 3), which provided a range of firing angles from horizontal to vertical.

The projectile, weighing 13.3 kg, is 1 m long (Fig. 4). The rear portion, the driver, is 50 cm long and 6.25 cm in diameter, and has Teflon bands for a tight fit in the barrel. The front portion, the penetrator, is 2 cm in diameter. It has a detachable nosepiece that is replaced for each experiment. For the laboratory experiments the nose was identical to the Betsy projectile. For the fieldwork the diameter of the rear portion of the nose was enlarged to 2.15 cm to reduce friction on the long penetrator.

For the laboratory work, we measured velocity either by using the coils described earlier, or by the projectile penetrating a pair of contact switches spaced a known distance apart. For the fieldwork we used a method developed by Charest et al. (1965). The operator wrapped a piece of paper with alternating white and black bands around the penetrator. A lamp focused on the penetrator served as a light source, and a photodetector monitored the reflected light (Fig. 5). The output of the photodetector was a sinusoidal signal, and the user obtained velocity as a function of time by determining the time between peaks in the signal. Thus both deceleration and penetration could be determined from the peaks.

A contact switch attached to the surface of the target provided a trigger signal on impact. We could therefore determine total penetration from the number of peaks recorded after impact. In practice we found that penetration determined in this manner was frequently as much as 1.5 cm greater than that measured directly. We do not understand the cause of this, although we suspect problems with early triggering of the contact switch and with surface spall; at present the method does not appear to be satisfactory for measuring depth.

LABORATORY-SCALE EXPERIMENTS

Gypsum Cement Targets

We performed the laboratory-scale experiments at the drop tower at Dynasen, Inc. The drop-tower target is a cavity 61 cm square and 46 cm deep, with sides made of 15-cm-thick steel plates. The target material was a mixture of gypsum cement and water with varying amounts of alluvium fines, expanded shale, or silica sand. We used materials with two bulk densities, 1.64 and 2.00 Mg/m^3. Changing the relative proportion of cement varied the strength from 2.5 to 17 MPa. Each target consisted of three side-by-side vertical batches with the same recipe, and we fired two or three shots into each

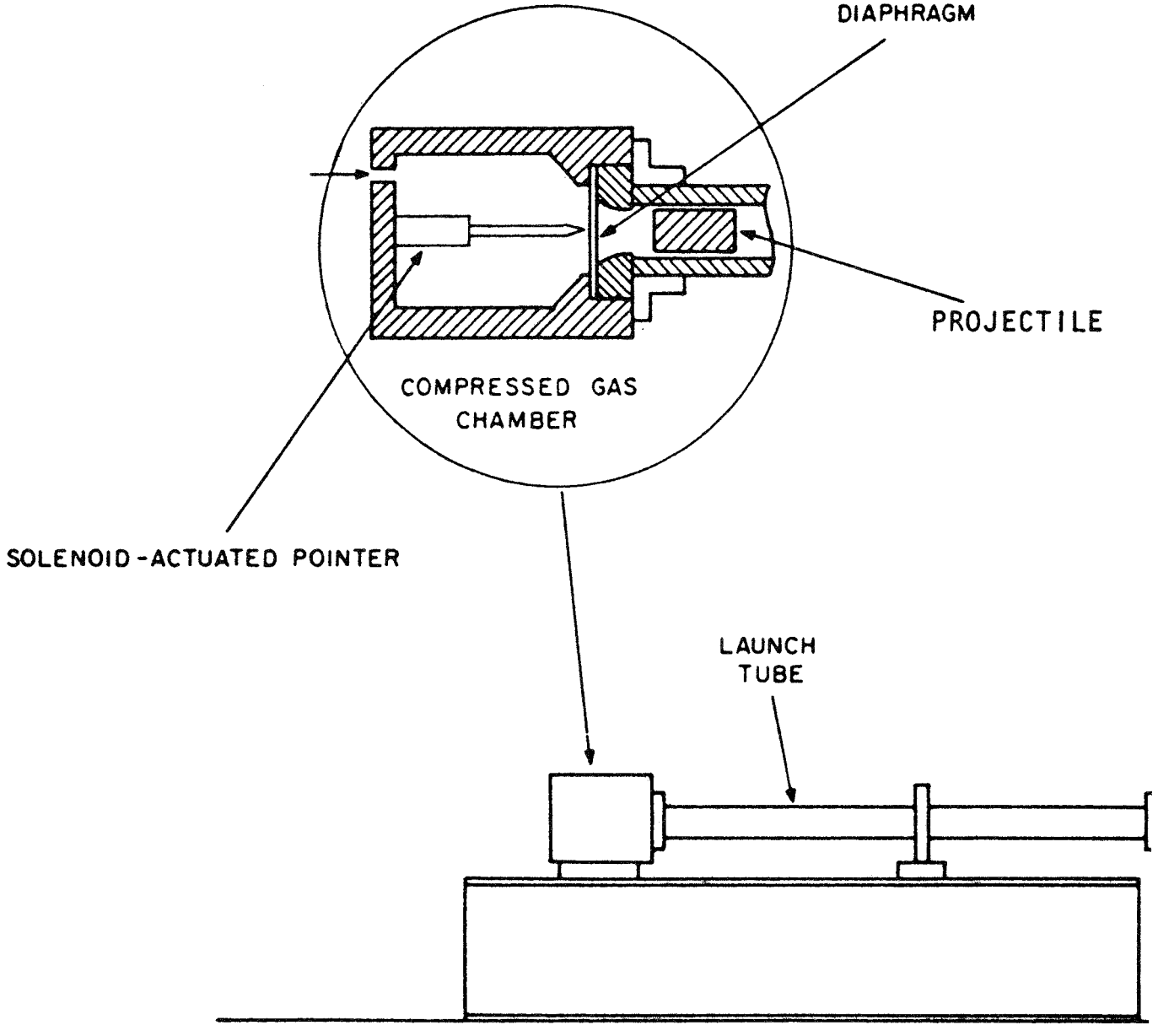

Figure 2. Design of the gas gun.

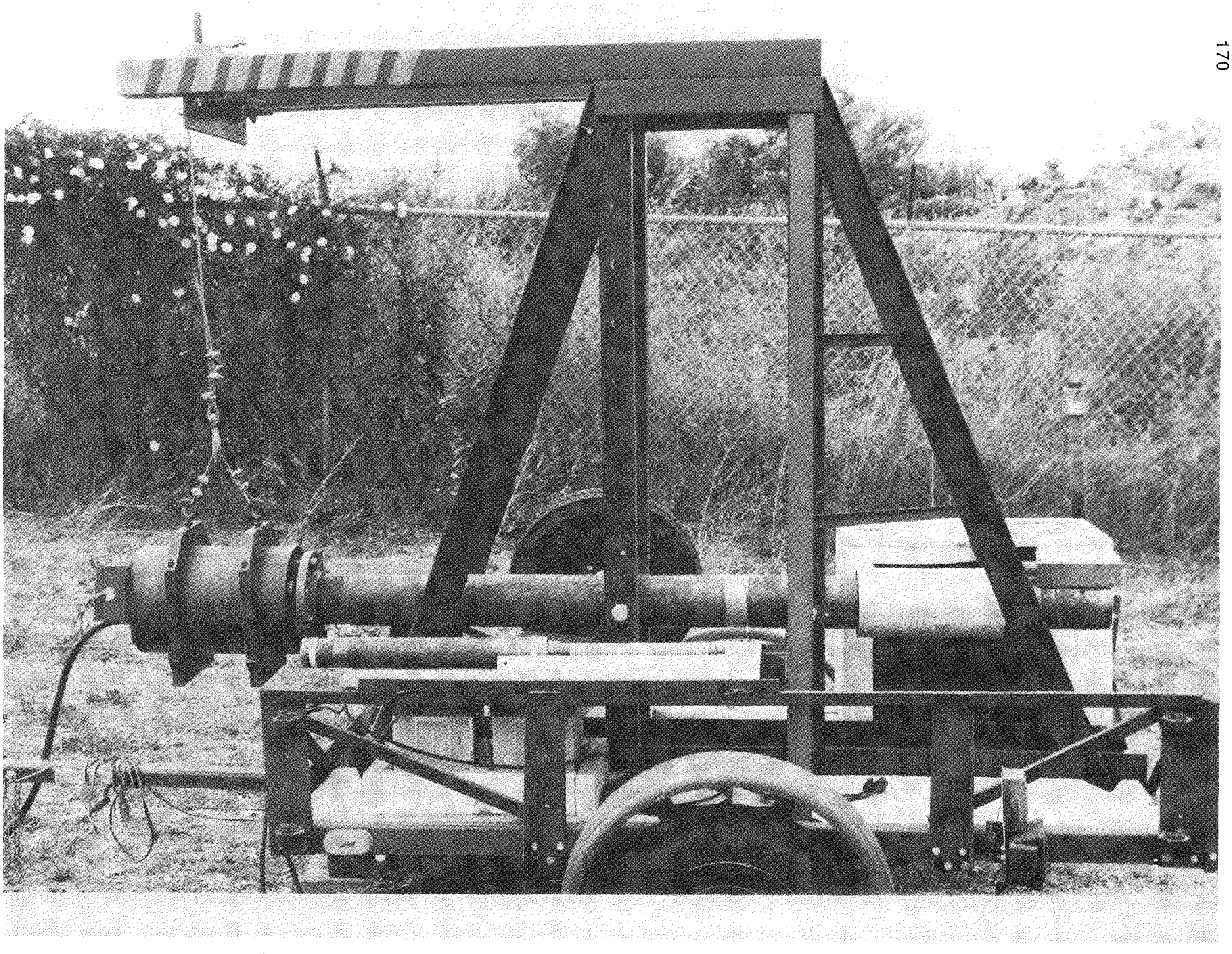

Figure 3. Photograph of the gas gun mounted on its trailer for field use.

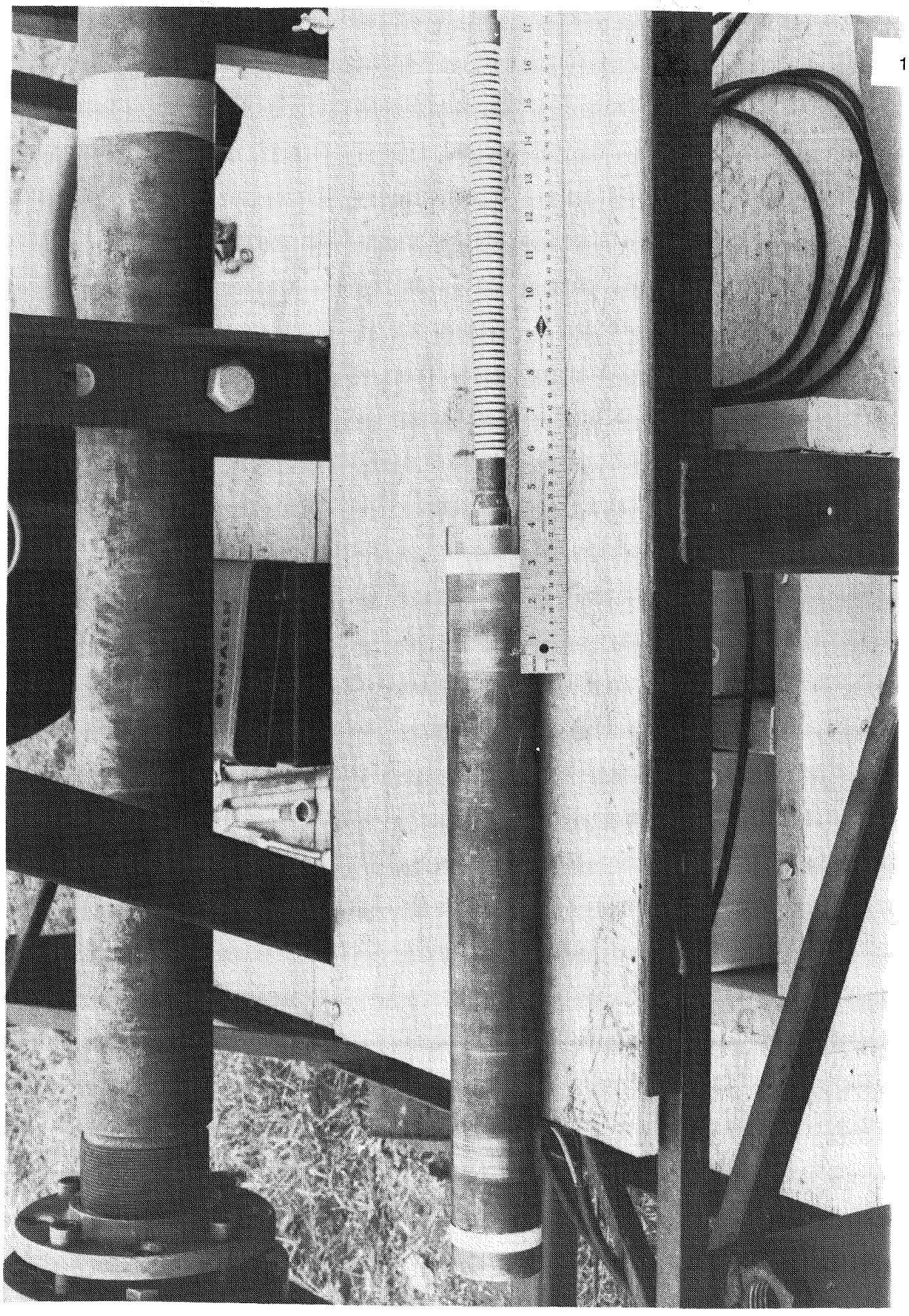

Figure 4. Photograph of the gas-gun projectile. Note the velocity-measurement stripes and the detachable nosepiece.

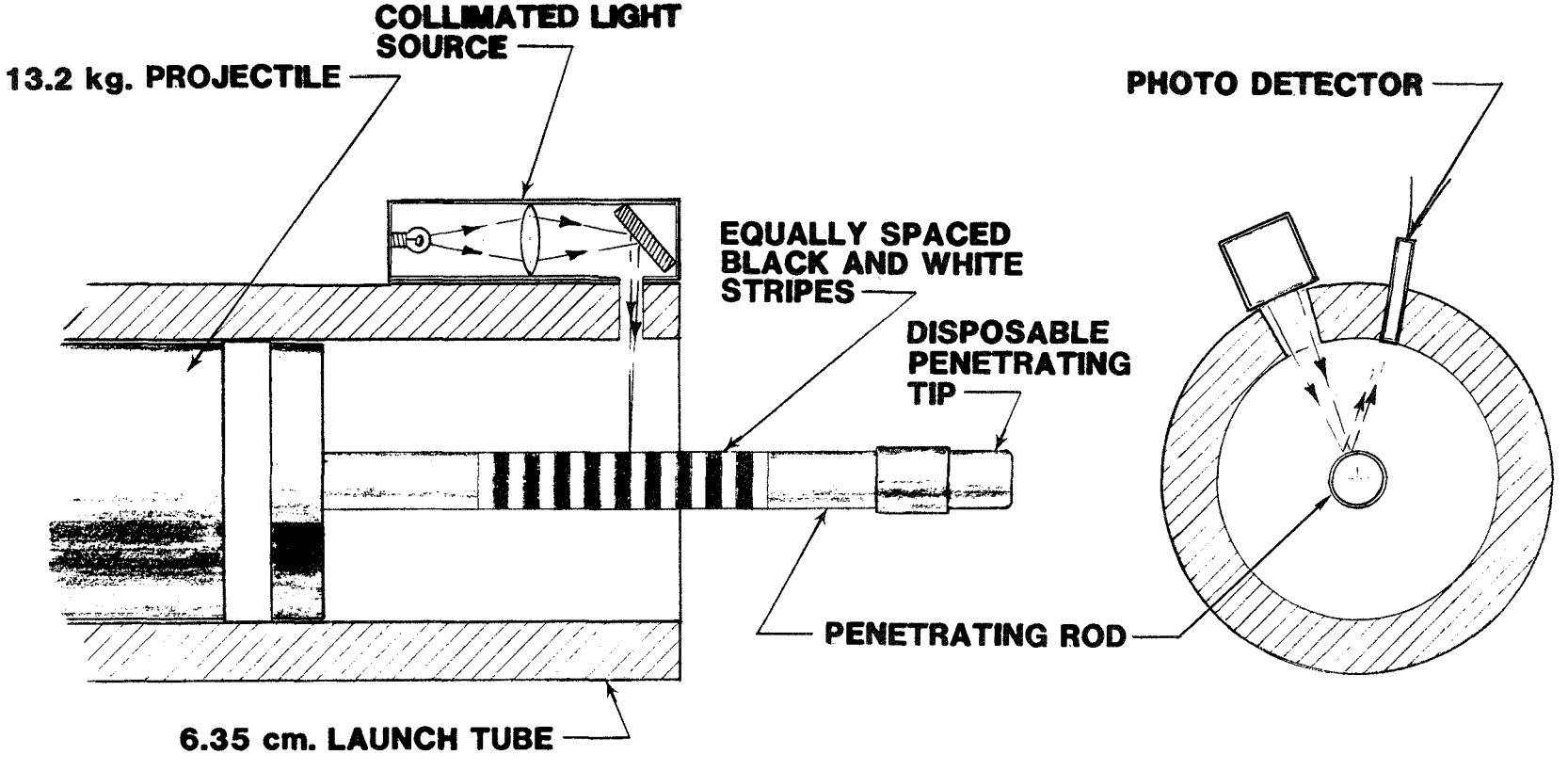

Figure 5. Drawing of the velocity-measuring apparatus.

batch. Standard unconfined compressional strength tests, performed on portions of each batch that had been poured into appropriately sized cylinders, gave values of material strength for each individual experiment.

Results

There were nine succesful sets of experiments with the Betsy, and four sets with the gas gun. In some of the Betsy experiments the projectile penetrated all the way through the target, and in others we changed the shape of the projectile to investigate possible improvements; those experiments are not discussed here. The results of the "normal" experiments are given in Tables I and II.

To obtain acceptable penetration depths (more than a few cm, and less than the depth of the target) using projectiles whose mass differed by more than two orders of magnitude, it was necessary to vary the projectile velocity. Betsy projectile velocities ranged from 250 to 500 m/s; gun projectile velocities ranged from 22 to 40 m/s. These experiments provided an excellent opportunity to investigate scaling of penetration with velocity.

Tests 6 and 7 with the Betsy and 12 and 13 with the gun had targets with approximately equal strengths. Figure 6 is an attempt to scale those results to Eq. (1). The fit is fair at best; the data from the Betsy and the gun appear to lie on different lines. If, however, we scale to $mV^{1.8}$ instead of mV^2 (Fig. 7), the fit is very good indeed. We shall discuss the implications of these fits later in this paper.

When we attempt to obtain a fit for strength, kinetic energy seems to be the most satisfactory parameter (Fig. 8). That is

$$z = KmV^2/Y, \qquad (6)$$

where K is a fitting constant and Y is strength. There is little segregation of the Betsy and gun data with this fit. The agreement between the two sets of data appears to be remarkably good, considering the great range of projectile mass and velocity.

FIELD EXPERIMENTS

Method

It was important to choose field sites with the widest possible range of strengths in natural, inhomogeneous materials present at NTS. We chose a total of 15 potential target sites, some in tuffs in G-Tunnel and some in tuff on the sides of road cuts and on horizontal surfaces at the top of Rainier Mesa. These materials ranged from poorly indurated bedded units, with abundant small pumice fragments and occasional organic matter (e.g., tree roots), which are soft enough to be etched with a fingernail (i.e., Sites 24 and 26), to massive ash-fall tuffs containing argillized pumice (individual pumice fragments range to about 1 cm), which would ring

Table I-A
Gypsum Data with Betsy;
Density 1.64 g/cc

Experiment	Strength (MPa)	Velocity (m/s)	Penetration (m)
2.1	17.55	509	0.165
2.2	17.55	516	0.178
2.4	17.55	516	0.203
2.5	17.55	332	0.067
2.6	17.55	493	0.200
2.7	17.55	504	0.200
2.9	17.55	497	0.187
3.1	11.04	503	0.269
3.2	11.04	508	0.269
3.3	11.26	511	0.269
3.4	11.26	505	0.276
3.5	11.70	510	0.276
3.6	11.70	507	0.263
3.7	11.70	324	0.130
3.8	11.26	325	0.130
3.9	11.04	317	0.121
4.4	5.72	333	0.186
4.5	5.86	342	0.219
4.6	5.79	344	0.196
5.4	2.92	332	0.295
5.5	2.93	337	0.381
5.6	3.31	328	0.357
5.7	3.05	254	0.176
5.8	2.93	245	0.140
5.9	3.31	251	0.173

Table I-B
Gypsum Data with Betsy;
Density 2.0 g/cc

Experiment	Strength (MPa)	Velocity (m/s)	Penetration (m)
6.2	16.24	503	0.136
6.5	16.24	325	0.073
6.6	13.89	323	0.070
6.8	16.24	489	0.139
6.9	13.89	493	0.149
7.1	15.73	498	0.142
7.2	15.36	500	0.155
7.3	14.70	494	0.146
7.4	14.70	339	0.076
7.5	15.36	333	0.076
7.6	15.73	330	0.066
7.7	15.73	499	0.146
7.8	15.73	499	0.142
7.9	15.36	494	0.135
8.2	10.90	500	0.199
8.4	6.73	338	0.176
8.5	10.90	339	0.119
8.6	6.58	325	0.155
8.7	6.58	496	0.358
8.8	10.90	494	0.204
8.9	6.73	501	0.352
9.4	3.25	363	0.329
9.5	2.59	342	0.445
9.6	3.83	343	0.207
9.7	3.83	268	0.143
9.8	2.59	269	0.229
9.9	3.25	266	0.165
10.1	14.63	507	0.136
10.2	14.79	502	0.150
10.3	13.97	502	0.160
11.3	16.82	502	0.209
11.4	16.82	508	0.196
11.6	16.82	501	0.211

Table II
Gypsum Data with Gun;
Density 2.0 g/cc

Experiment	Strength (MPa)	Velocity (m/s)	Penetration (m)
12.1	13.24	23	0.092
12.2	13.24	26	0.101
12.4	12.80	23	0.108
12.5	15.50	23	0.083
12.6	15.50	23	0.083
13.1	14.63	30	0.146
13.2	14.63	30	0.146
13.3	14.63	31	0.140
13.4	14.63	32	0.137
13.5	14.63	31	0.146
13.6	14.63	40	0.216
14.1	8.93	29	0.194
14.2	7.90	34	0.305
14.3	8.41	26	0.181
14.4	8.41	27	0.178
15.1	3.31	20	0.216
15.2	3.58	19	0.191
15.3	3.00	19	0.203

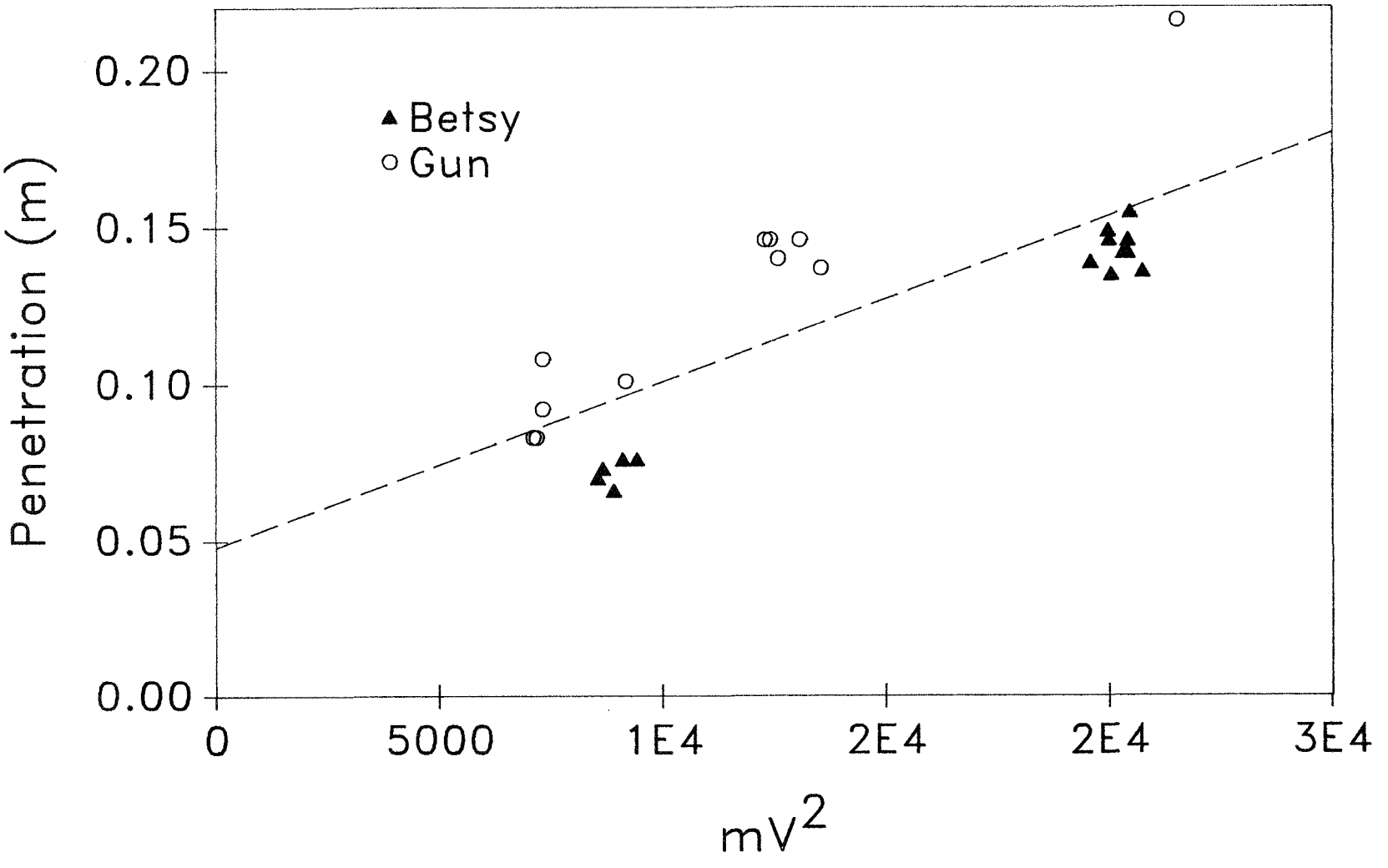

Figure 6. Projectile penetration vs mV^2 for four sets of data in targets with approximately equal strength. Note that the mass of the gun projectile was two orders of magnitude greater than that of the Betsy projectile.

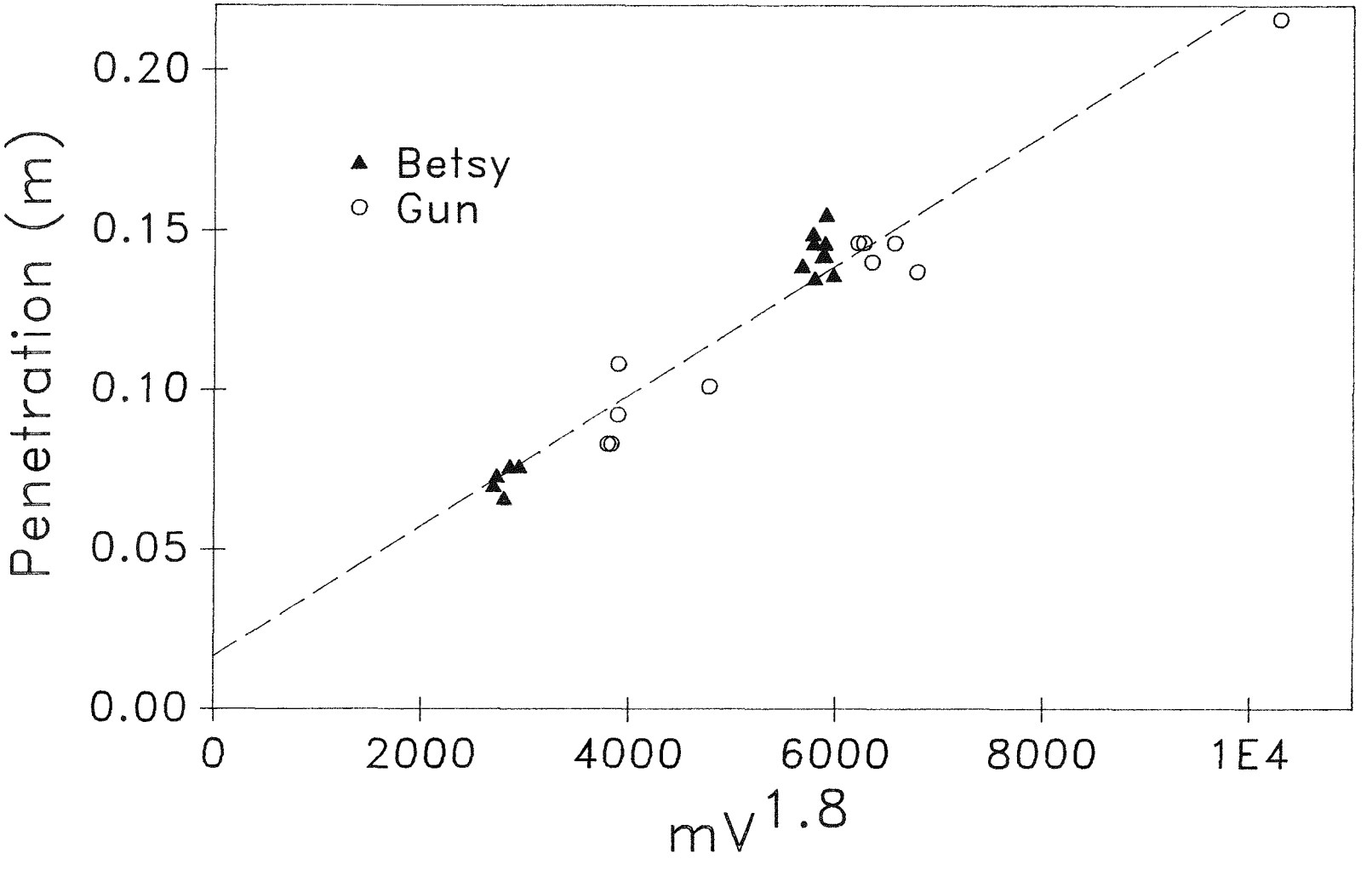

Figure 7. Projectile penetration vs $mV^{1.8}$ for four sets of data in targets with approximately equal strength.

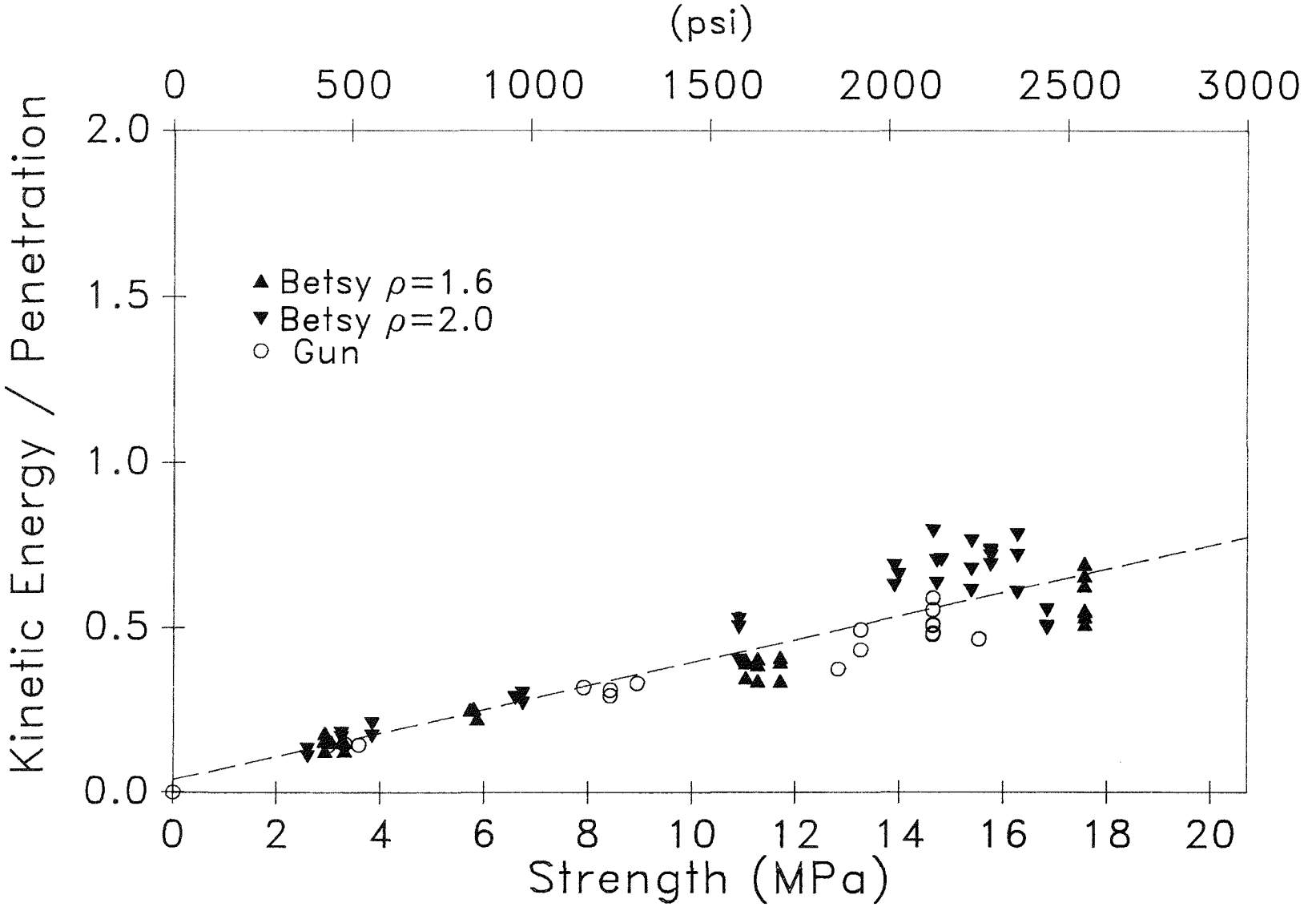

Figure 8. Strength vs mV^2/ penetration (newtons X 10^{-5}) for the laboratory experiments.

when struck with a hammer (i.e., Site 3). Table III gives geological descriptions of the ten sites we chose. Sites were given odd starting numbers in the tunnel and even starting numbers at the surface to designate pairs of consecutively numbered core holes.

Perhaps the most difficult part of the field experiments was obtaining core for strength measurements. At each site we planned to drill two 60-cm-deep core holes, from each of which we intended to obtain two 6.5-cm-dia, 13-cm-long cores. In practice, it was frequently very difficult to obtain cores with the appropriate length-to-diameter ratio, and it was necessary to drill several holes. It was unacceptable to drill deeper holes, as we needed near-surface samples representative of the material into which the projectile would penetrate. At many tunnel sites there was a "punky" spall zone several centimeters thick at the surface, presumably caused by stress relief after mining. When possible, miners removed this part of the rock before the experiment.

The drillers obtained at least four satisfactory cores from each site. A professional core-wrapper wrapped each core in aluminum foil and sealed it in beeswax within a short time after drilling. Two different laboratories, Holmes and Narver at NTS and Dynasen, each made standard unconfined compressional strength measurements on at least two cores. The range of strength for a given site was usually quite large. Knowing the strength and range of strength for each site, we chose shot sites to give both a wide range of strength from site to site, and the smallest possible variation of measured strength within a site. Table IV lists the strength data.

Figure 9 shows the gun rigged for an experiment at a tunnel site. The muzzle of the gun was set within a few centimeters of the surface of the target rock, and a trigger switch was taped to the target surface. For most shots, the gun was mounted either subvertically or subhorizontally. For some of the tests in the Paintbrush tuff, however (e.g., Shots 24-1 and 24-8), the gun was mounted at about 30^{o} from the horizontal so as to fire perpendicular to the surface. After the shot a crater could be seen on the rock surface, and a compacted zone surrounded the penetrator hole. A typical site with several craters is shown in Figure 10 and and a compacted zone is visible in Figure 11. During some of the tests performed on subvertical surfaces, particularly those in the relatively weak Paintbrush tuff (e. g., 24-3, 24-7, 24-8, 26-1), a large piece of the surface (up to about 30 cm in diameter and 8 cm deep) would flake off, leaving an augmented crater. This usually occured when the surface was not completely vertical. In those cases, the operator estimated the inital surface geometry, and measured the depth of penetration from the estimated surface. In some of these tests, a subvertical and/or subhorizontal crack would develop in the surface (parallel and perpendicular to the bedding in bedded units) reaching to about 20 cm from the penetrator. In those cases, we made successive tests at considerably larger distances along the surface from previous ones than at other sites.

Table III
Geological Descriptions of Sites

Site 1-2. A subunit of Tunnel Bed 4J, a massive red-brown ash-fall tuff containing abundent argillized pumice throughout. This specific site was located in a typical pumice "swarm" with occasional peralkaline lenses.

Site 3-4. A subunit of Tunnel Bed 4J, a medium- to coarse-grained ash-fall tuff. Specifically a silicified grey band 30 cm thick of medium-grained material, significantly harder than the surrounding tuff and located near the top of the 4J unit between the upper reworked subunit and the lower massive, red-brown ash-fall.

Site 9-10. Tunnel Bed 5, a massive peralkaline ash-fall tuff, yellowish-grey to dusky yellow, medium grained. Contains occasional small lithic fragments (0.5-1 mm).

Site 15-16. A subunit of Tunnel Bed 4K, a mottled red-grey ash-fall tuff, fine to medium grained. Contains occasional small lithic fragments (< 1mm).

Site 17-18. Tunnel Bed 4G, a massive, peralkaline, medium- to coarse- grained ash-fall tuff. Contains abundent lithic fragments from 1 mm to 1 cm and occasionaly 5-8 cm. Occasional thin silicified layering present.

Site 20-21. Upper Ammonia Tanks tuff. Pinkish-tan ash-flow, well indurated, slightly welded. Abundant quartz, sanadine and biotite phenocrysts, devitrified pumice fragments with vapor phase alteration from 2 to 50 mm, occasional small lithics.

Site 22-23. Top of Tiva Canyon tuff. Dark, brownish-grey ash-flow. Well indurated, partially welded, common fine-grained feldspar phenocrysts, brown pumice fragments 1-3 mm, occasional glass blebs and fine-grained lithics.

Sites 24-25; 26-27. Paintbrush tuff, bedded, light grey, poorly indurated. Small pumice fragments < 0.5 mm with occasional lithics and crystal fragments of the same grain size.

Site 30-31. Paintbrush tuff, air-fall, moderately well indurated, cream-colored, fine-grained glass shards with common lithics from 0.5-4 mm.

Table IV
Sample Densities and Strengths

Site	Density (g/cc)	Strength, H & N (MPa)	Strength, Dynasen (MPa)
1	1.92	15.6	
1	1.91	9.7	
1	1.92	14.0	
1			15.6
1			17.3
3	1.95	16.0	
3	2	19.3	
3	1.98	20.4	
3			13.1
3			28.9
9	1.65	8.8	
9	1.46	7.1	
9			9.3
9			9.5
15		10.5	
15	1.86	11.9	
15	1.89	9.7	
15	1.83	15.6	
15	1.9	9.3	
15		9.8	
15			15.4
15			20.2
17	1.78	8.1	
17	1.8	8.2	
17			8.2
17			11.4
20	1.76	6.2	
20	1.8	6.3	
20			4.7
20			5.9
20			6.4
20			7.0
22	1.31	6.8	
22	1.53	5.7	
22			4.3
22			7.0
22			7.3
24		0.2	
24		0.3	
26		0.9	
26		0.7	
26			1.4
26			1.7
30	1.73	2.1	
30	1.66	1.5	
30			2.7
30			2.9

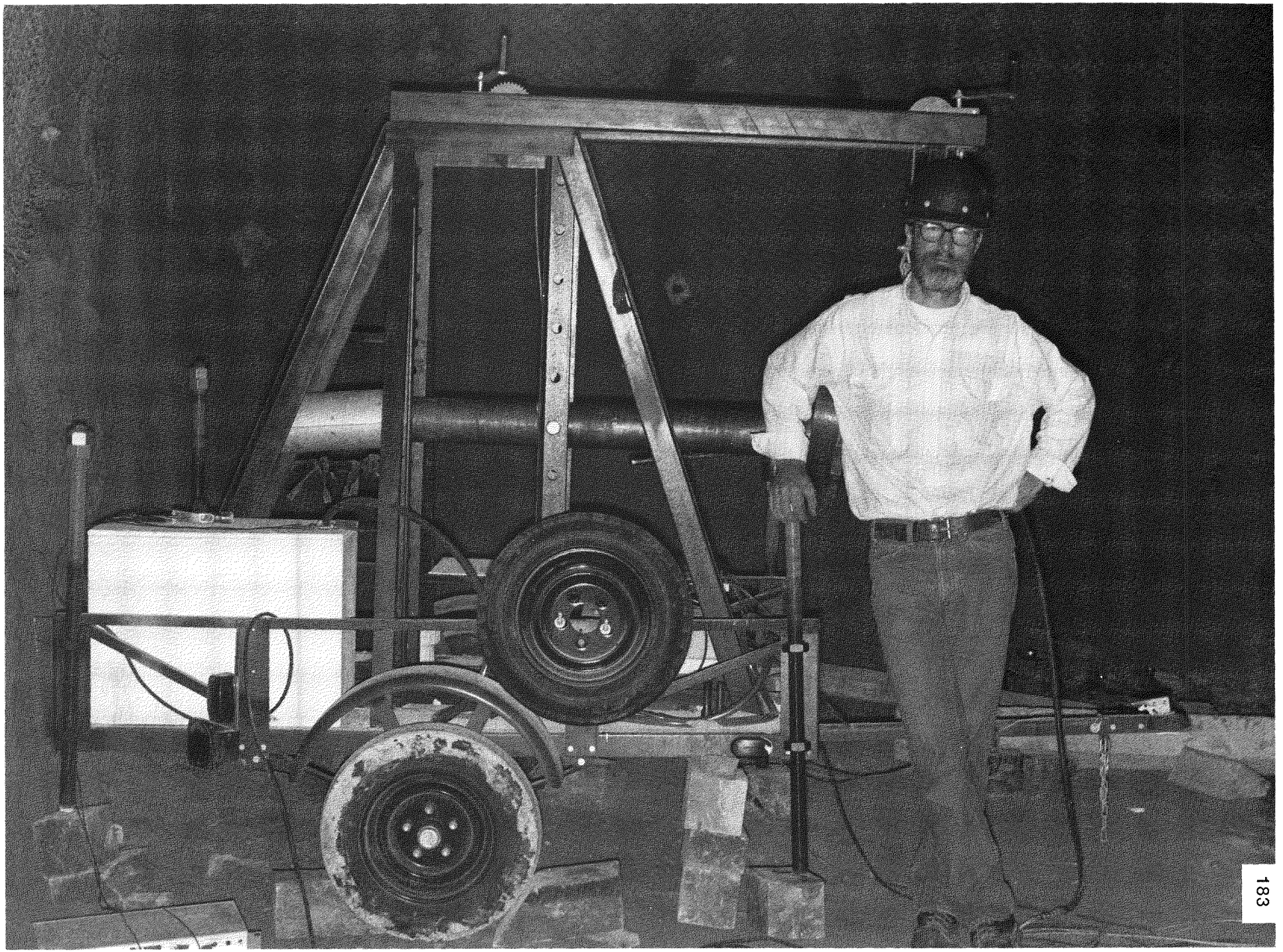

Figure 9. Photograph of the gun in place in G-Tunnel. (M. O'Brien)

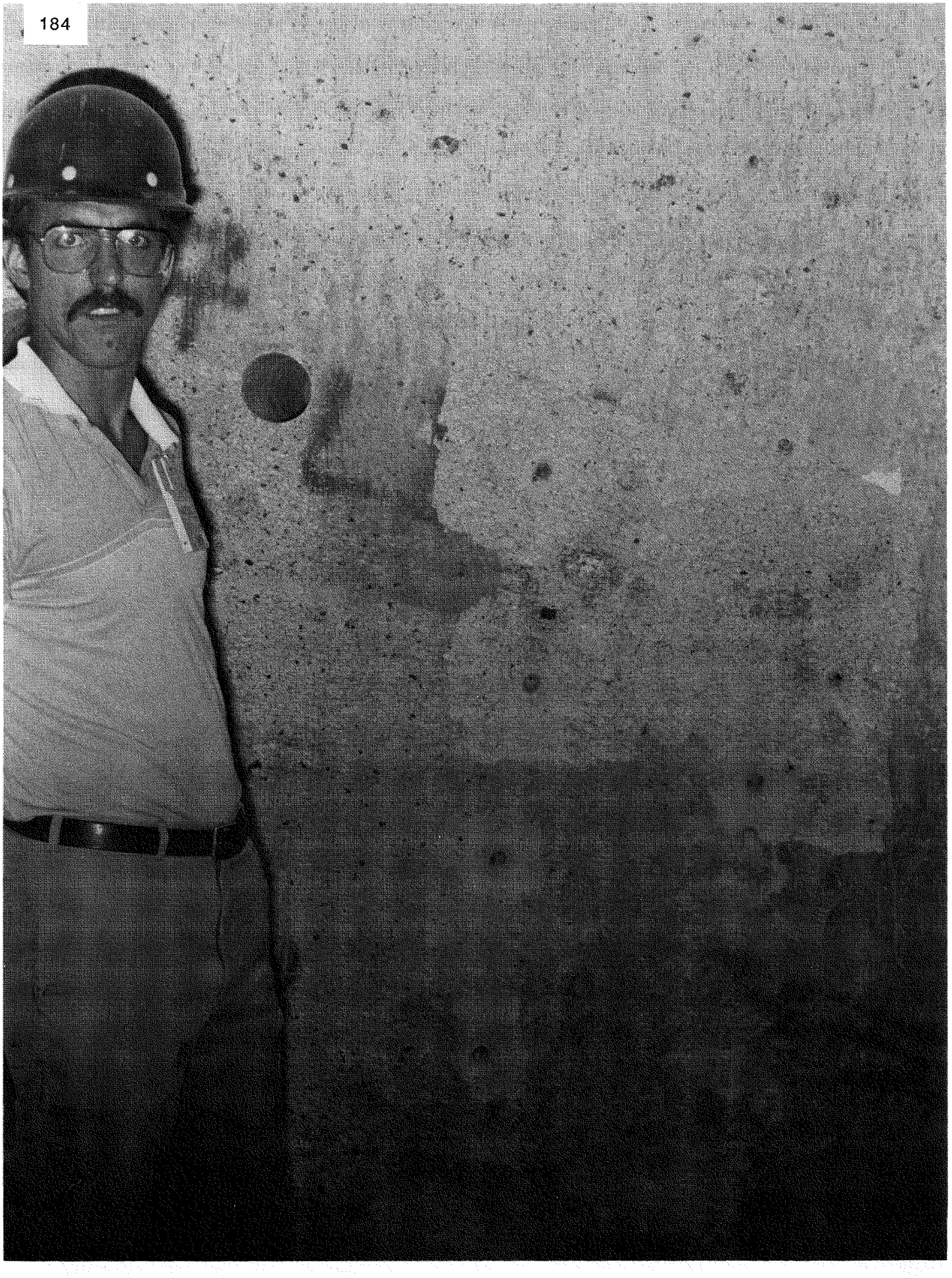

Figure 10. Typical craters at Site 17 (M. O'Brien).

Figure 11. Typical crater at Site 1 (M. O'Brien). Note the region of compaction surrounding the crater. The dark material is softer than that into which the projectile was fired.

Results:

Table V lists the results from all successful gun shots. Since velocity was constant for a given breech pressure, in the cases where velocity was not measured it was assumed to be the same as that for other experiments at the same pressure. The results are plotted in Figs. 12 and 13. In Fig. 13 the mean values of the gun data are fitted to Eq. (6). (It was not feasible to plot individual values, as in Fig. 8, because we could not match strength to penetration point-by-point.) On both figures the Betsy data from Hearst and McKinnis (1985) are included for comparison, but the line is fitted to the gun data only. Since most investigators have found that mass per unit area, rather than mass, is the important projectile parameter, the Betsy penetrations are divided by 1.2 to account for the difference in cross-sectional area of the projectiles. The error bars were derived from the sample standard deviations of strength and penetration.

Note that in general the higher-strength sites show a large variation in measured strength, but a small variation in penetration, whereas the lower-strength sites show a substantially larger variation in penetration. Two pairs of sites with approximately the same measured mean strength (Sites 20 and 22, and Sites 9 and 17) exhibit substantially different mean values of penetration; other sites with approximately the same penetration (e.g., Sites 15 and 17) have substantially different strengths. We discuss these anomalies in a later section.

Figure 14 is a typical plot of velocity vs time. The most interesting feature is the constant deceleration. Many investigators have used deceleration, rather than depth of penetration, as a measure of projectile performance. Consequently it is important to learn whether deceleration is an acceptable measure of strength. Moreover, decleration may be easier to measure in a downhole system. A plot of deceleration vs strength, shown in Fig. 15, is similar to Fig. 13. Since we were sometimes unable to obtain deceleration (because of trigger difficulties) we use penetration, which we measured directly, in the present work.

The miners described Sites 1 and 3 as particularly easy to mine, despite their high strengths. Shot No. 1 at Site 3 was fired into weak rock slightly below the bed in which the strength was measured and penetrated much deeper than the others. (It was in fact a bit tricky to choose the firing points at site 3, because of material variations.) At Site 17, Shot No. 6 was much shallower than the others; we learned that it was fired into a very hard bed that was hard to distinguish visually from the rest of the face. These two shots are left out of the plots. It should be noted that these two situations, in which anomalously weak and strong rock were found at a site of otherwise fairly constant strength, tend to confirm our ability to obtain strength from penetration.

It appears that Eq. (6) is a plausible fit to the data. We must now consider the implications of this result.

Table V-A
Tunnel shots

Site	Shot	Velocity (m/s)	Penetration (m)	Decleration (km/s^2)
1	1	32.9	0.16	4.4
	2	30.5	0.11	5.2
	3	30.5	0.12	
	4	30.5	0.11	
3	1	33.5	0.15	
	2	33.5	0.06	11.3
	3	37.2	0.07	
	4	33.5	0.06	10.1
	5	36.6	0.09	12.2
	6	36.6	0.06	
9	1	29.9	0.13	4.1
	2	29.9	0.14	4.2
	3	30.5	0.14	4.0
	4	30.8	0.14	3.6
	5	30.8	0.16	3.4
	6	29.9	0.14	
15	1	33.5	0.14	6.0
	2	32.6	0.12	4.6
	3	31.1	0.11	6.0
	4	32.6	0.12	5.6
17	1	30.5	0.10	6.1
	2	30.5	0.10	5.2
	3	30.5	0.16	
	4	30.5	0.11	
	5	30.5	0.10	
	6	35.1	0.08	10.1
	7	33.5	0.13	4.6

Table V-B
Surface Shots

Site	Shot	Velocity (m/s)	Penetration (m)	Decleration (km/s^2)
20	2	24.4	0.06	7.3
	3	29.9	0.12	3.3
	4	33.8	0.12	
	5	33.8	0.11	6.9
	6	35.1	0.15	5.9
	7	35.1	0.11	7.3
	8	35.1	0.11	6.6
	9	35.1	0.12	5.6
22	1	35.1	0.22	3.4
	2	33.8	0.21	3.1
	3	31.7	0.19	3.4
	4	31.7	0.25	2.5
	5	29.9	0.20	2.9
	6	29.9	0.21	
24	1	14.9	0.08	
	2	21.9	0.12	
	4	20.4	0.13	2.1
	5	22.9	0.16	1.8
	6	22.9	0.21	1.3
	7	20.4	0.17	1.2
	8	20.7	0.13	
26	1	26.8	0.19	2.9
	2	20.7	0.14	1.8
	3	21.0	0.11	2.4
30	1	25.3	0.16	2.6
	2	25.3	0.18	1.9
	3	25.3	0.12	3.4
	4	25.3	0.12	3.4
	5	25.3	0.11	3.7
	6	25.3	0.19	2.1

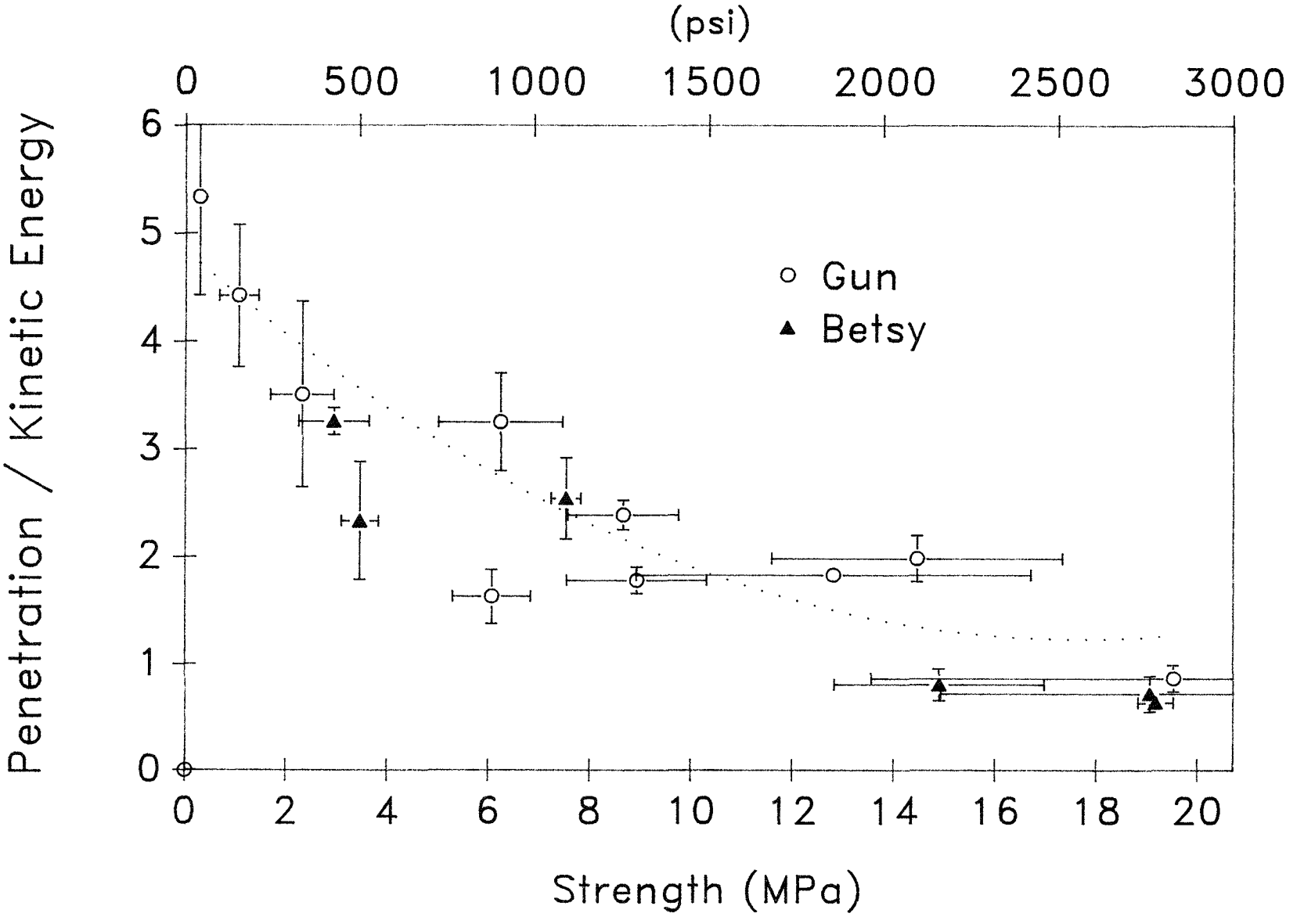

Figure 12. Strength vs penetration/mV^2 (units are 1/force, where force is in newtons X 10^{-5}) for the means of the field data.

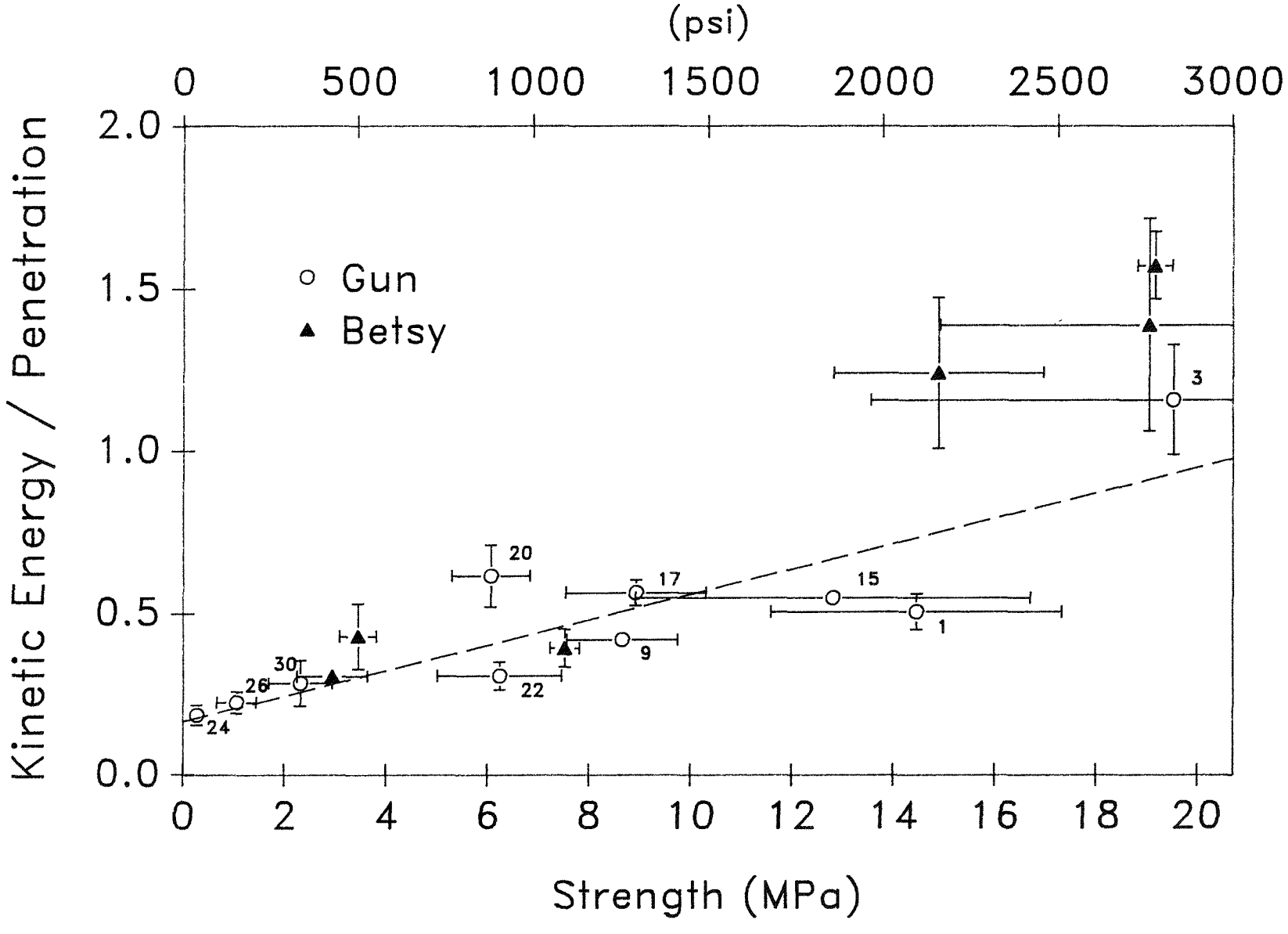

Figure 13. Strengths vs mV^2/ penetration (newtons X 10^{-5}) for the means of the field data. Numbers adjacent to the gun data points are site numbers.

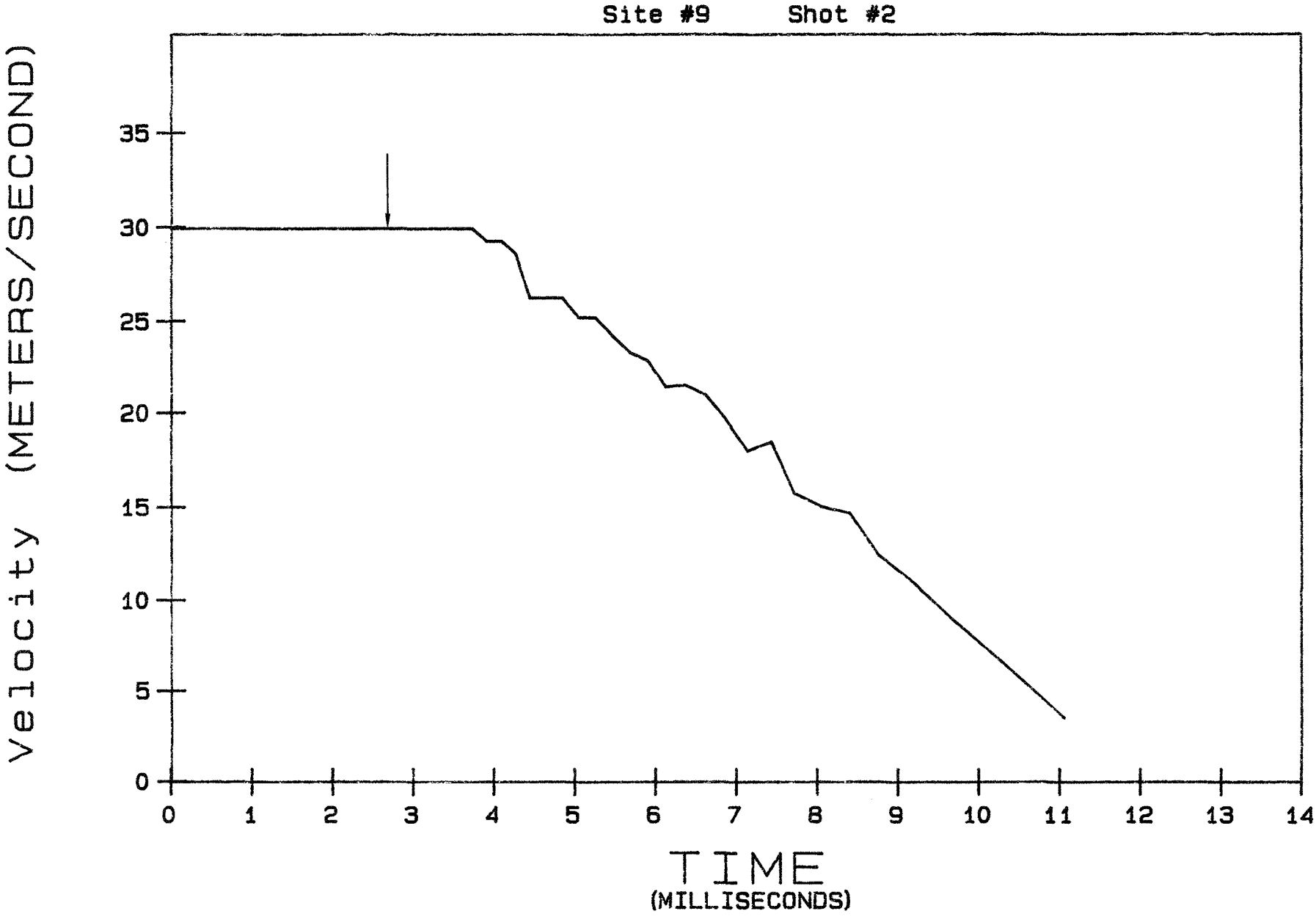

Figure 14. Typical plot of velocity vs time for a field experiment. The arrow is at the time of projectile impact.

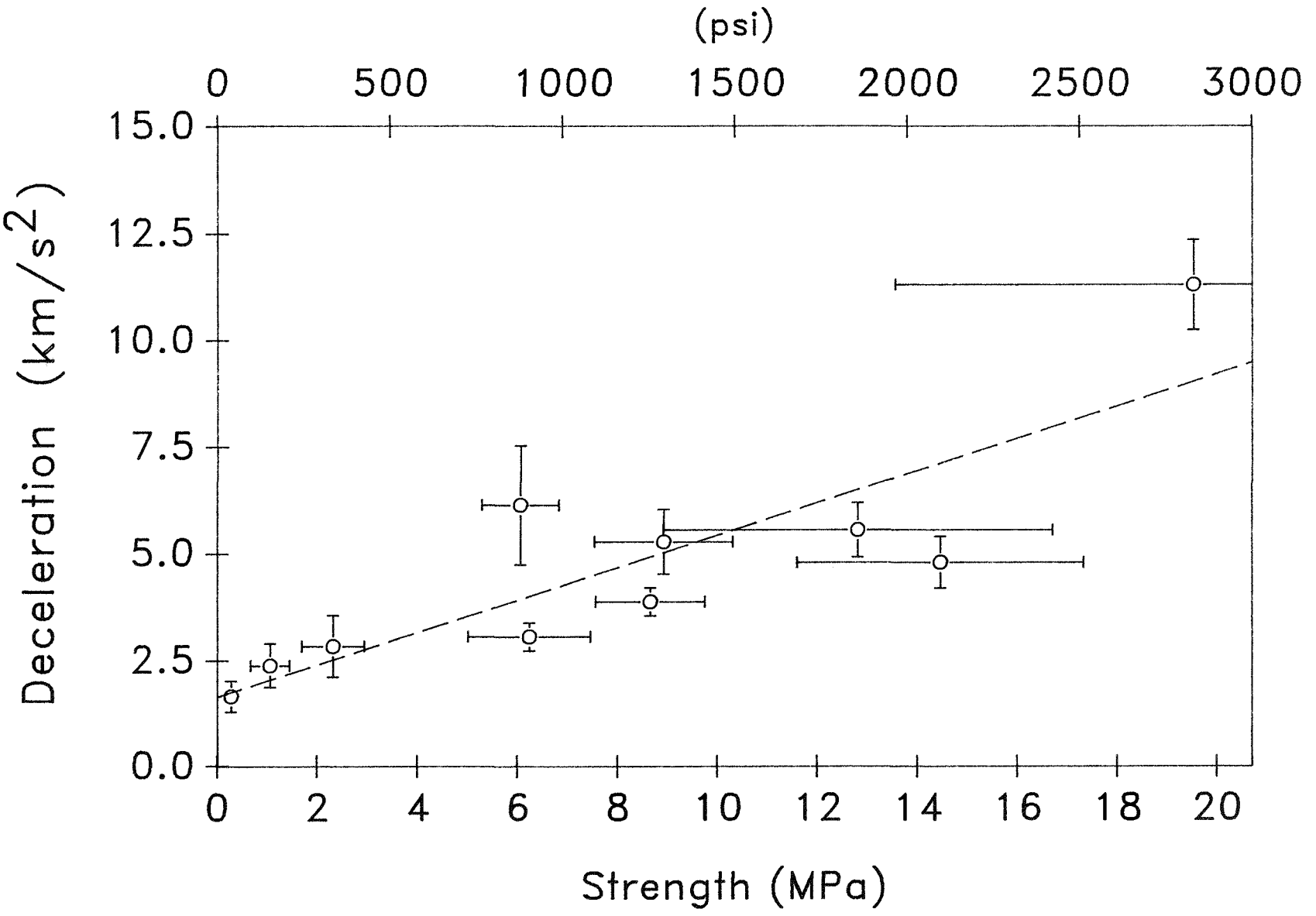

Figure 15. Deceleration vs strength for the means of the field data.

COMPARISON TO OTHER WORK

Velocity and Mass Scaling

Since the initial kinetic energy must be equal to the work done during penetration,

$$mV^2 = 2 \int_0^z F dx. \qquad (7)$$

If the force is constant, independent of velocity and depth, then

$$mV^2 = 2Fz.$$

We varied m over more than two orders of magnitude, and V by a factor of 25, holding strength approximately constant, and obtained the result described above: penetration is proportional to $mV^{1.8}$, but close to proportional to mV^2. If we accept the result that penetration is proportional to mV^2, then since $F = ma$, acceleration must be constant. In fact, as can be seen from Fig. 14, acceleration is essentially constant after an initial almost constant-velocity period.

The result that the depth of penetration, z, scales with $mV^{1.8}$ agrees with no other work. If, however, we assume that in fact the mV^2 scaling is correct, then these results agree with the oldest work, Eq. (1).

Thigpen (1974) used a large finite-difference code to predict penetration of an ogival projectile as a function of time and obtained the result shown in Fig. 16. Butler and Bernard (1975) used cavity expansion theory to obtain almost exact agreement with Thigpen. These results are remarkably similar to Fig. 14. Evidently, although our results appear to disagree with Eqs. (2-5), there is considerable reason to believe kinetic-energy scaling.

Strength Scaling

The most interesting result, from a practical point of view, is the fact that mV^2/z and deceleration are proportional to strength. Of the authors cited in the Introduction, all but Bernard (1978) either find inverse linear dependence of penetration on strength or linear dependence of deceleration on strength, or they do not give a specific form. Substituting the product of density and strength, or its square root, [based on Bernard's Eq. (5), derived from dimensonal analysis], for strength in Eq. (6) does not improve the fit. Since we have already seen that Bernard's velocity scaling does not fit the data, there is no reason to believe that Bernard's equation will fit these results better than Eq. (6).

Comparison of Field and Laboratory Data

The result that mV^2 is proportional to strength might lead one to expect that once the laboratory and field data have been scaled in that way, they would agree. A comparison of the fits in Figs. 8 and 13 shows that although the slopes of the fits are virtually identical, the intercepts are different. It is plausible to ascribe this difference to either a substantial difference in

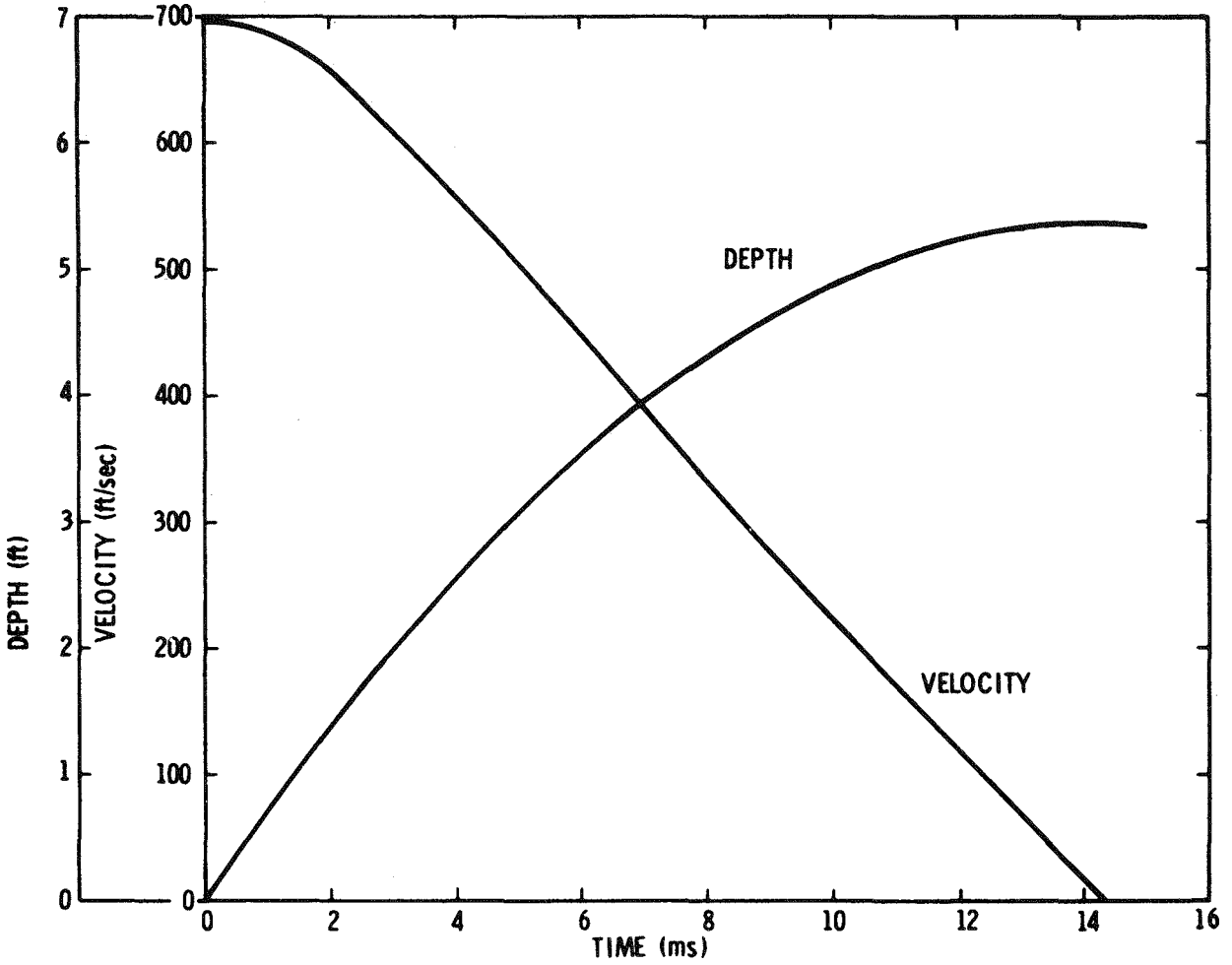

Figure 16. Velocity and penetration vs time from a finite-difference calculation for a projectile penetrating tuff (Thigpen, 1974).

material properties, particularly water content, of gypsum cement and tuff, or to edge effects resulting from the finite size of the gypsum experiments. High water content might increase penetration without decreasing strength. The finite size could make it possible for a rarefaction from the sidewalls of the container to fail the gypsum, or reduce its strength, while the projectile is penetrating the gypsum.

DISCUSSION

Quality of the Fit

Although the laboratory results in gypsum (Fig. 8) show a very good fit between mV^2/z and strength, the fit to field data is by no means as good. We have seen in Fig. 12 that at high strength there is a large variation in measured strength, but a small variation in penetration. Perhaps, in fact, z is a better descriptor of the *in situ* strength of the bulk medium than the measured unconfined compressional strength of core. There is a basic problem that two points with the same laboratory-measured strength have significantly different penetration (e. g., Sites 20 and 22), and two points with the same penetration have significantly different strength (e. g., Sites 15 and 17.)

If strength is indeed proportional to mV^2/z, then we must somehow explain those data points that lie far from the our best line fit. Tests in which penetration is less than predicted by the fit in Fig. 13 (points that lie to the left of the line) can be interpreted as a result of the targets being under confining stress. Microcracks in the rock, which could cause decreased strength in samples measured in the laboratory, can be closed by confining stress, and the strength can be thereby increased. If this were the case, than the strength would be greater than the measured value, and so the penetration would be less than expected. This is a plausible assumption for Site 3, near 20 MPa, as it is in the wall of G-Tunnel, 700 m or more below the surface of the ground, and the confining stress can be caused by overburden. The other such site, Site 20, at about 6 MPa, is on a horizontal free surface, so the confining stress must come from the stress field induced by the penetrator.

Tests exhibiting greater penetration than expected (points plotted to the right of the fit in Fig. 13) are more readily explained. It is reasonable to believe that intact core samples, drilled in the most homogeneous part of the surface, and representative of the intact formation, are probably stronger than the mass of the rock, which probably contains many micro- and even macro-cracks, voids, and other large-scale inhomogeneities. If this were not the case, it would have been easy to obtain intact cores. Furthermore, Price (1977) has shown, for tuffs considerably stronger than those we studied, that strength decreases with increasing sample diameter up to about 20 cm. His result, shown in Fig. 17, indicates that the strength for very large specimens is about 70% of that of specimens of the 6.67-cm diameter that we used. If the strengths of certain selected samples were reduced to 70% of the measured value, the fit in Fig. 13 would be very good indeed.

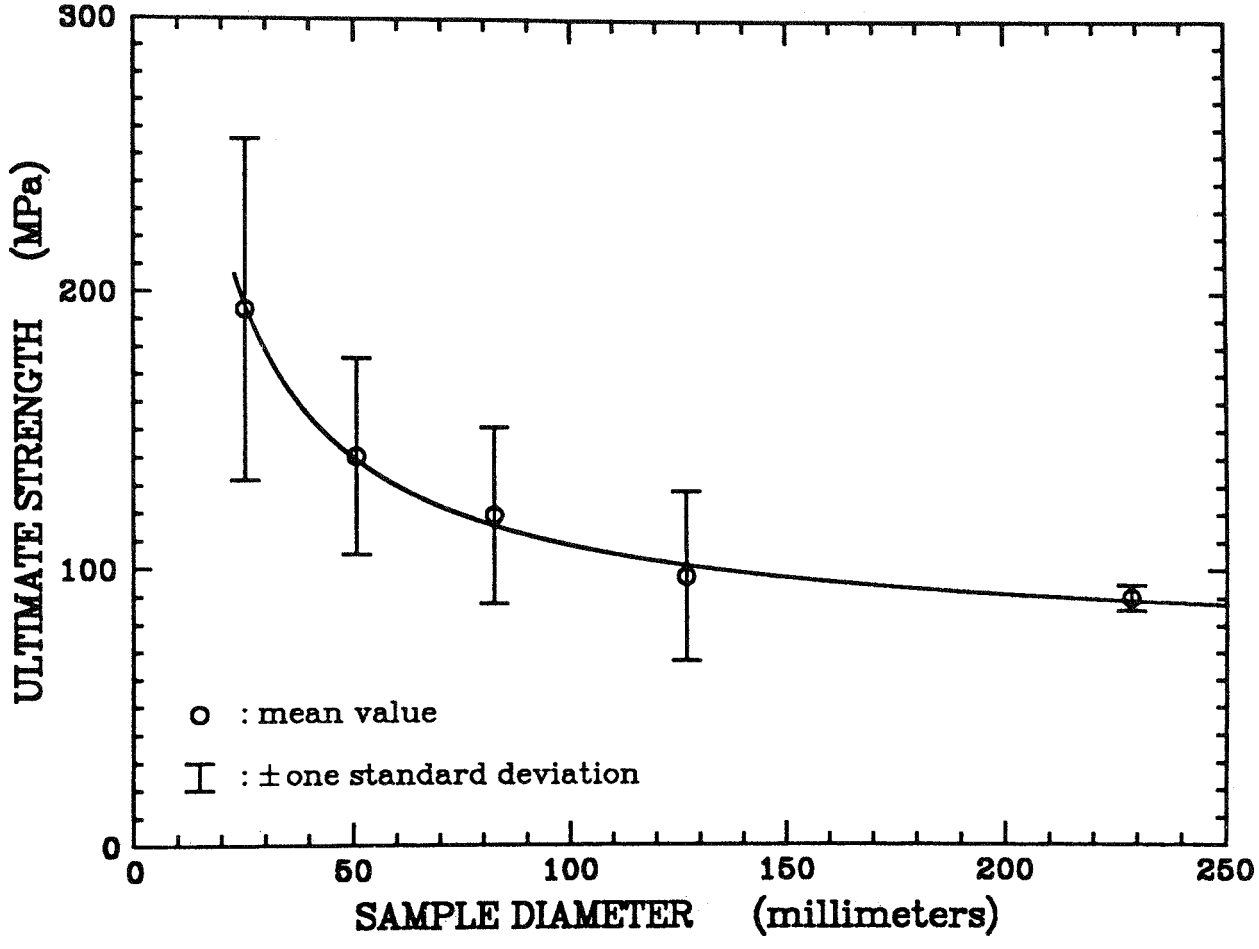

Figure 17. Measured unconfined compressional strength vs sample size for a strong Nevada tuff (Price, 1986).

The water content of the cores may not be representative of formation conditions. The cores were drilled with water, carefully preserved by sealing in wax, and then of necessity dried to some extent before testing. Consequently the water content at the time of testing may be greater or less than the bulk formation water content. Therefore, the measured strength may be either greater or less than the formation strength. Moreover, the laboratory measurement of strength is performed under quasi-static conditions. It is unlikely that values obtained in this manner are directly comparable to the strength obtained at high strain rate by a fast-moving projectile. This rate effect would imply that the measured strength is less than the strength seen by the penetrator.

By using these and other arguments, it is possible to explain almost any difference between the observations and the fit. Another plausible explanation is that the claim that mV^2/z is proportional to strength is in fact invalid. Therefore, we must consider what, in the absence of convincing reasons for the differences among the data, we should conclude about the feasiblity of using penetration as a measure of strength.

Feasibility of Strength Measurement by Penetration

If the fit in Fig. 13 is used to determine strength, there can be a difference of as much as 60% between the value determined from the fit and the end of the error bar closest to the line. This accuracy can be described as semiquantitative, but compared to currently available *in situ* methods, it is excellent.

It is unlikely that these results can be improved. We chose the best sites that could be found for the experiments and cored them as carefully as possible. It would be possible to make strength measurements at some confining pressure and see if those strengths would produce a better fit, but choosing an appropriate pressure would be difficult for the tunnel sites, and even more difficult for the sites on horizontal surfaces (which exhibit the worst disagreement). We can consider the effects of porosity (total or air-filled), density, and water content, all of which can be measured in boreholes and therefore used as corrections. But there is no obvious way to use these properties to improve the agreement among the data.

Although it may be possible to improve the fit by using some of these properties, the most important task is to decide whether the quality of the strength measurement made with this method is useful for predictions. There are two ways to approach this decision. The simplest and obvious approach is to make parameter studies using the various available predictive tools, to learn if strength measurements with the uncertainty that will be found using Fig. 13 will improve the predictive capability. If the improvement is significant, then it is desirable to develop a downhole instrument.

Meanwhile, theoretical work and perhaps some laboratory strength measurements under confining pressure will help us decide whether

the strength measured by the penetrator is more likely to be correct than the laboratory-measured unconfined compressional strength. If it is, then the parameter studies can be performed with a smaller range of strength.

CONCLUSIONS

For materials of constant strength with mass variations of more than two orders of magnitude and velocity variations of a factor of 25, penetration is proportional to $mV^{1.8}$, and approximately proportional to mV^2. To our knowledge there been no study of penetration in the past that used such a wide range of mass and velocity.

There appears to be a linear relationship between kinetic energy divided by penetration and target strength, and between deceleration and target strength. It appears that penetration can indeed be used as a rough measure of strength.

ACKNOWLEDGEMENTS

This work could not have been done without a great deal of help from others. Dan Sedgwick of Dynasen (shown in Fig. 9) was constantly involved in both the laboratory and field experiments. Mike O'Brien of Fenix and Scisson and Bill McKinnis of LLNL-Nevada found the sites for us and made sure we were on target. Dick Dye and John Talbutt of Sandia National Laboratories expedited both the administrative arrangements and the field operations. Without Lavelle Atkinson, Dale Pope, Aaron Jones, and the rest of the G-Tunnel crew our fieldwork would have been impossible. We also wish to thank Dave Kuhn and the REECo drill crew for obtaining the surface cores under difficult conditions. Work performed under the auspices of the U. S. Department of Energy by Lawrence Livermore National Laboratory under Contract Number W-7405-ENG-48

REFERENCES

R. S. Bernard, "Depth and Motion Prediction for Earth Penetrators", U. S. Army Engineer Waterways Experiment Station Technical Report S-78-4, 1978.

D. K. Butler, "An Analytical Study of Projectile Penetration in Rock", U. S. Army Engineer Waterways Experiment Station Technical Report S-75-7, 1975.

D. K. Butler and R. S. Bernard, "Projectile Penetration of Elastic-Plastic Earth Media", Jour. Geotechnical Engineering Division vol. 101, p71, 1975.

W. N. Caudle, A. Y. Pope, R. L. McNeill and B. E. Magason, "The Feasibility of Rapid Soil Investigations Using High-speed Earth-penetrating Projectiles", Int. Symp. on Wave Propagation and Dynamic Properties of Earth Materials, Albuquerque, August 1977.

J. A. Charest, P. Duler and J. S. Rinehart, " Mechanics of Penetration of Piles into Permafrost", U. S. Army Corps of Engineers Cold Regions Research Laboratory Report CRREL, TR, 122, 1965.

L. Euler, "Neue Grundsuatze der Artillerie", Berlin, 1745.

J. R Hearst and W. B. McKinnis, "A Comparison of Projectile Penetration and a Cone Penetrometer as Methods of Measuring Tuff Strngth", Proc. 3rd Symposium on Containment of Underground Nuclear Explosions, Idaho Falls, 1985.

A. Kumano and W. Goldsmith, "Projectile Impace on Soft, Porous Rock", Rock Mechanics, vol. 15 p. 113, 1982.

R. L. McNeill, "Approximate Method for Estimating the Strengths of Cohesive Materials from Penetrator Decelerations", Proc. Oceans 81, Boston, 1981.

L. Petry, "Monographies de Systems d'Artillerie", Brussels, 1910

J. V. Poncelet, "Cours de Mechanique Industrielle", 1829.

R. H. Price, "Effects of Sample Size on the Mechanical Behavior of Topopah Spring Tuff", Sandia National Laboratory Report SANDD85-0709, 1986

H. Resal, "Sur la Penetration d'un Projectile dans les Semifluides et les Solides", 1895.

B. Robins, "New Principals of Gunnery", London, 1742.

B. Rohani, "High Velocity Fragment Penetration of Soil Targets", Proc. Conf. on Rapid Penetration of Terrestrial Materials, Texas A&M University, 1972.

R. W. Terhune and H. D. Glenn, "Estimation of Earth Media Shear Strength at the Nevada Test Site", Lawrence Livermore National Laboratory Report UCRL 52358, 1977.

L. Thigpen, "Projectile Penetration of Elastic-Plastic Earth Media", Jour. Geotechnical Engineering Division vol. 100, p. 279, 1974.

C. W. Young, "Depth Prediction for Earth-penetrating Projectiles", J Jour. Soil Mechanics and Foundations Division vol. 95 p. 803, 1969.

SPECTRAL REFLECTANCE CHARACTERISTICS OF CLAY-BEARING SOILS: APPLICATIONS TO DOWNHOLE ENVIRONMENTS

JONATHAN C. GRADIE and TED L. ROUSH*

Planetary Geosciences Division
University of Hawaii

Visible and near-infrared spectral reflectance properties from 0.4 to 4.7 μm were used to characterize the mineralogy and chemistry of 23 soil samples from the Nevada Test Site. These samples represent primary materials, materials resulting from a range of primary and secondary alteration, alluvium, and tuff. The bi-directional reflectance spectra, measured with the Planetary Geosciences spectrogoniometer facility, show that the spectra of all altered materials exhibit absorptions. The presence of calcite can be identified in the spectra when it occurs in concentrations greater than 1 volume percent. In general, calcite absorption band depths correlate with the volume abundance of calcite present in a sample. Hydroxyl-bearing minerals are detected by absorption bands at 2.2-2.3 μm (Al cation) and 2.3-2.4 μm (Mg cation). The presence of zeolite in these samples appears to be correlated with the shape of the combination and/or overtone absorptions of water fundamentals at 1.4 μm, 1.9 μm and 3 μm. Spectra of all samples show a wide range of oxidation and, in addition, a range in the degree of crystallinity of the ferric-bearing materials. In conclusion, reflectance spectroscopy can provide a variety of information concerning the chemistry and mineralogy of these soil samples. However, before in situ *measurements are employed, the effects on the spectral reflectance of the hydration and dehydration of these samples must be characterized.*

I. INTRODUCTION

Visible and near-infrared spectral reflectance properties of soils and rock forming minerals have been used to characterize the mineralogy and chemistry of terrestrial and extra-terrestrial surfaces *(c.f.* Adams and Felice, 1967; Hunt, 1977; McCord, *et al.*, 1981). The spectral reflectance properties of rocks, minerals and soils (commonly called regoliths for extra-terrestrial surfaces) have broad applications in remote sensing. For example, spacecraft, aircraft, and even field spectrometers are used to investigate the mineralogy and chemistry of geologically interesting and important terrestrial scenes and planetary surfaces.

*Current address: NASA Ames Research Center, MS 245-3, Moffett Field, CA 94035.

Hunt (1977) discusses the variety of transitions which can result in absorptions of electromagnetic radiation in the visible and near-infrared (0.3-2.5 μm). Such transitions generally fall into two distinct categories, electronic and vibrational. Electronic transitions are mainly due to the presence of the petrologically significant Fe and Ti cations located in specific crystal sites. Vibrational transitions arise from the presence of a variety of molecular groups, of which the most prominent in the near- and mid-infrared (beyond 1 μm) are the water molecule, the hydroxyl ion, and several other anionic groups (e.g., carbonate, sulfate, etc.). Thus, use of reflectance spectra provides direct information concerning the chemistry and crystal structure of a surface, and hence its mineralogy.

Since reflectance spectra can be determined using remote sensing techniques, which require no sample preparation or destruction, remote sensing provides a unique means of characterizing surface mineralogical variation of the sample in question. If this mineralogical variation can be expressed on a spatial scale then remote sensing techniques can be directly applied to important geological problems such as: (1) mapping of structural formations, or alteration zones; (2) surveys of economically important materials; and (3) monitoring the containment of chemical or radioactive wastes.

Underground waste containment depends strongly upon the ability of the ground to hold or immobilize the waste product. The containment of the waste products resulting from underground nuclear explosions depends not only upon the ability of the rock strata to immobilize waste products but also upon the mechanical stability of the overlying rock strata. Since the mechanical stability of the ground can be affected by the presence of smectites (swelling clays), it is important to determine the composition of the strata through which the test hole is bored.

This study was directed at identifying those spectral features of water-bearing minerals that could help determine the presence (or absence) of a smectite component. Once identifying features are found, it is possible to develop techniques to determine, quantitatively, the amount and mineralogy (i.e., *which* clay, mineral, etc.) of the various rocks encountered (Clark and Roush, 1984).

II. SPECTRAL REFLECTANCE PROPERTIES OF WATER-BEARING MINERALS

The polar nature of the water molecule and its ubiquitous occurrence in the terrestrial environment cause it to be associated with minerals in a variety of ways. In our ensuing discussion concerning the specifics of water associated with clay minerals we rely heavily on the terminology and discussion originally presented by Bruckenthal (1987). *Physically adsorbed water* is found in pores, on surfaces, and around edges of clay particles. It consists of loosely bound water molecules held only by Van der Waals' forces. *Surface-bound water* consists of molecules which are electrostatically bound to the basal surfaces of the tetrahedral layers in the clay structure. At some distance from the basal structure, surface-bound water grades into physically adsorbed water. *Cation-bound water* consists of molecules which are electrostatically bound to the interlayer cations commonly present in smectite-like structures and, in general, these

molecules are more strongly bound than surface-bound water. Intrinsic water is similar to physically adsorbed water but is used here to include water molecules which are located in channels formed by some crystal structures (e.g., zeolites) and, additionally, those molecules which are trapped in micro-bubbles often referred to as fluid inclusions. The hydroxyl ion (OH^-), commonly referred to as constitutional or structural water, is a basic constituent of some crystal structures (e.g., phyllosilicates and clays), and in such structures it is coordinated with specific metal cations and located in specific crystal sites.

Important vibrational absorption bands from water, OH^-, and OH-cation bonds are shown in Table I, in which the wavelength (in microns), the mode (transition fundamental, overtones and combinations), and the molecule responsible for the band are shown. Note that the exact center of the band is dependent upon the exact structure encompassing the molecule. For example, the 2υ-OH^- band is only approximately centered at 1.4 μm. Similarly, the combination bands, 2υ-OH^-+ Al-OH and 2υ-OH^- + Mg-OH are approximately at 2.2 μm and 2.3 μm, respectively (Hunt, 1977).

TABLE I.

Some important H_2O and OH^- absorptions

λ (μm)	Mode	Molecule	
0.942	$3\upsilon_2 + 2\upsilon_3$	H_2O	
1.135	$2\upsilon_1 + 2\upsilon_2 + 2\upsilon_3$	H_2O	
0.379	$2\upsilon_1 + 2\upsilon_3$	H_2O	
~1.4	$2\upsilon_{OH^-}$	OH^-	
1.454	$2\upsilon_1 + 2\upsilon_2$	H_2O	
1.875	$2\upsilon_1 + \upsilon_2$	H_2O	
~2.2	$2\upsilon_{OH^-}$ + Al-OH	Al-OH	
2.3	$2\upsilon_{OH^-}$ + Al-OH	Al-OH	
~2.3	$2\,\upsilon_{OH^-}$ + Mg-OH	Mg-OH	
2.4	$2\,\upsilon_{OH^-}$ + Mg-OH	Mg-OH	
2.8	υ_{OH^-}	OH^-	Fundamental
2.903	υ_1	H_2O	Fundamental
3.04	$2\upsilon_2$	H_2O	
3.106	υ_3	H_2O	Fundamental
6	υ_2	H_2O	Fundamental

Although clay minerals represent an important class of water-bearing minerals, the abundance of other minerals whose reflectance spectra can exhibit strong water absorptions complicates the identification of smectites since the presence of water alone cannot be used as a unique test for the presence of smectites. For example, another important class of water-bearing minerals are the zeolites, which are abundant in the hydrothermally altered sediments of the western United States (Flanigen, 1977). The reflectance spectra of most water-bearing minerals have completely saturated 3 μm bands again complicating the unique identification of the various minerals. Presently, the most commonly used method of distinguishing between zeolites and smectites is X-ray diffraction which requires sample collection and subsequent preparation and analysis. The issue addressed here is whether zeolites can be distinguished from smectites by spectral reflectance techniques. If so, then remote sensing techniques can provide a rapid, in situ method of distinguishing a smectite-bearing layer from a zeolite-bearing layer.

III. SPECTRAL REFLECTANCE (0.7 - 2.5 μm) OF ZEOLITES

Zeolites are hydrated aluminosilicates of alkaline earths (Na, K, Ca, Ba) and are composed of a framework of $(Si,Al)O_4$ tetrahedra that are open and contain channels and cavities.

Zeolite minerals include phillipsite, chabazite, erionite, mordenite, and clinoptilolite. The spectral reflectance (0.7 to 2.5 μm) of these minerals is shown in Figure 1. The primary absorptions are due to water and are located at 1.45 μm and 1.9 μm. The short wavelength edge of the 3 μm water absorptions is seen as a dramatic decrease in reflectance beyond ~2.2 μm (Gaffney and Singer, 1985).

Also present, and indicative of zeolites, are the weaker absorptions that occur on the short wavelength side of the 1.4 μm and 1.9 μm water features. These features at 1.35 μm and 1.8 μm cause the bands to look somewhat asymmetric, which appears to be unique to the zeolites.

The depth of the 1.45 μm (and the 1.95 μm) absorption is well correlated with void space in the zeolite. Chabazite has the greatest void space (47%), whereas analcime has the least (18%). Values for the other zeolites in Figure 1 are: clinoptilolite (39%), erionite (35%) phillipsite (31%), and mordenite (28%). The correlation of void space with water absorption features is due to loosely bound water which fills the void spaces. The water, which ranges from 10-20% of the dehydrated phase, is given off continuously and reversibly on heating from room temperature to ~350 C. Because rehydration is an exothermic process, the water content at a given temperature is dependent upon the partial pressure of water in the atmosphere in contact with the zeolite.

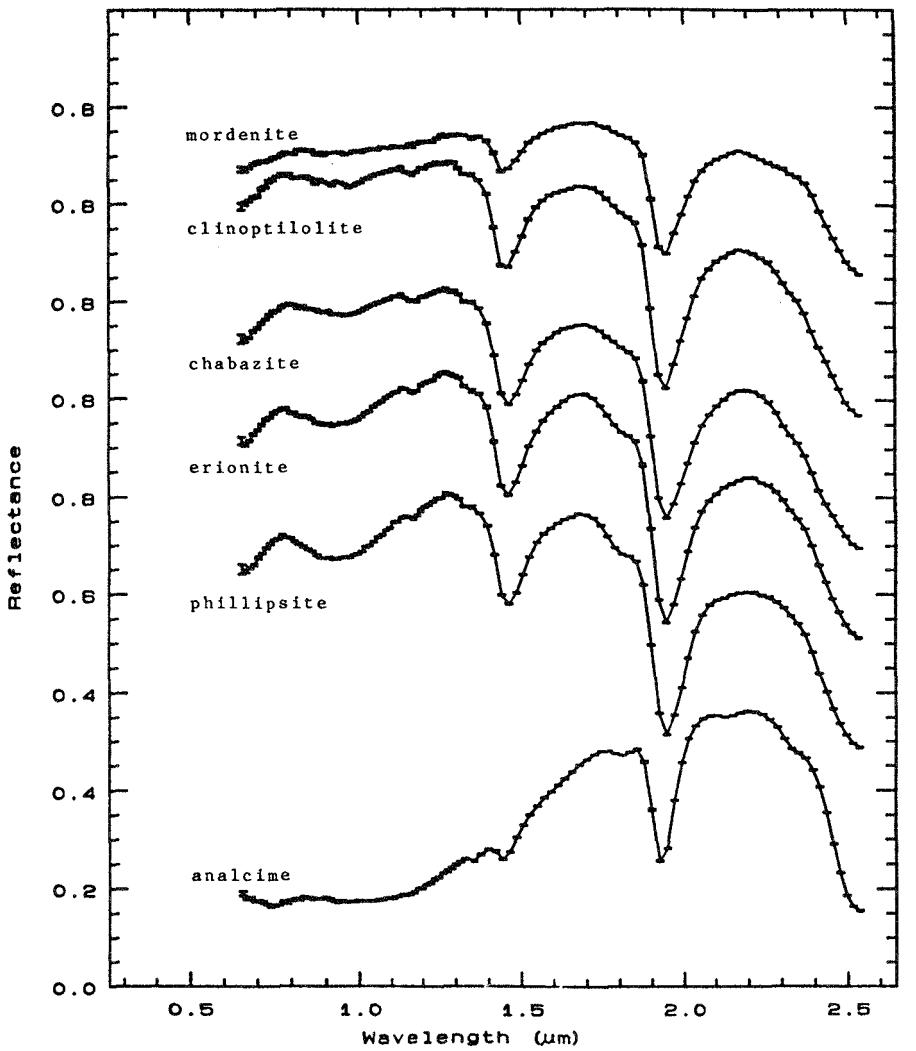

FIGURE 1. The spectral reflectance (λ = 0.7 to 2.5 μm) relative to halon of six zeolites (Singer, 1986).

IV. SPECTRAL REFLECTANCE (0.7 to 2.5 μm) OF Al-RICH SMECTITES

Smectites, or swelling clays, are phyllosilicates that form as alteration products of igneous rocks. Smectites, like zeolites, can lose or gain water reversibly as well as exchange constituent cations. However, unlike zeolites, the exchange of water causes major changes in the volume of the smectite. The exact chemistry of a smectite depends upon the chemistry of the source rock. Montmorillonite [$Al_2Si_4O_{10}$ (OH_{10},H_2O)] represents the di-octahedral Al-bearing species, whereas nontronite is produced if Fe replaces the Al in the octahedral layer. Saponite represents the tri-octahedral Mg-bearing species. The spectrum of nontronite generally exhibits strong Fe absorptions shortward of 1 μm (Adams and Filice, 1967). The spectra of saponite generally exhibit Mg-OH bands near 2.3 μm (Bruckenthal, 1987) while the spectra of montmorillonite usually exhibit Al-OH bands near 2.2 μm (Hunt, 1977).

Spectral reflectances (0.7-2.5 μm) of four samples containing Al-rich smectite clays are shown in Figure 2. Prominent are the water and hydroxyl bands at 1.4 μm and 1.9 μm. Also apparent, with varying strength is the Al-OH band at 2.25 μm. The variation in band depth is indicative of the amount of smectite present, in this case, probably montmorillonite. The absorption at 0.9 μm is related to ferric and ferrous iron in accessory minerals (probably geothite and hematite) in the sample (Gaffney and Singer, 1985). Absent in the spectra of the smectite clays is the short wavelength asymmetry in the 1.45 μm and 1.9 μm bands seen in the spectra of the zeolites. Also missing are the weak 1.35 μm, 1.80 μm absorptions and the strong short wavelength edge of the 3 μm water features found in the spectra of the zeolites.

Diagnostic differences between the clays and zeolites can be summarized as follows: spectra of zeolites show short wavelength asymmetry in the 1.4 and 1.9 μm bands whereas smectite clays do not; spectra of smectite clays show weak absorptions in the 2.2 to 2.4 μm region due to structural OH (Al-OH, Mg-OH) whereas zeolites do not, in general. Spectra of samples of unknown composition with both characteristics must be mixtures of smectite clays and zeolites.

V. EXPERIMENTAL PROCEDURE

To test the feasibility of distinguishing between zeolitic and smectite bearing rocks, twenty-three samples from eight different alteration types were obtained from the Nevada Test Site (Kunkle, 1985) and measured at the spectro-goniometric facility at the Planetary Geosciences Division at the University of Hawaii. Sample descriptions and assays provided by Los Alamos National Laboratory as well as the code number (1-23) used for our measurements are given in Tables II and III.

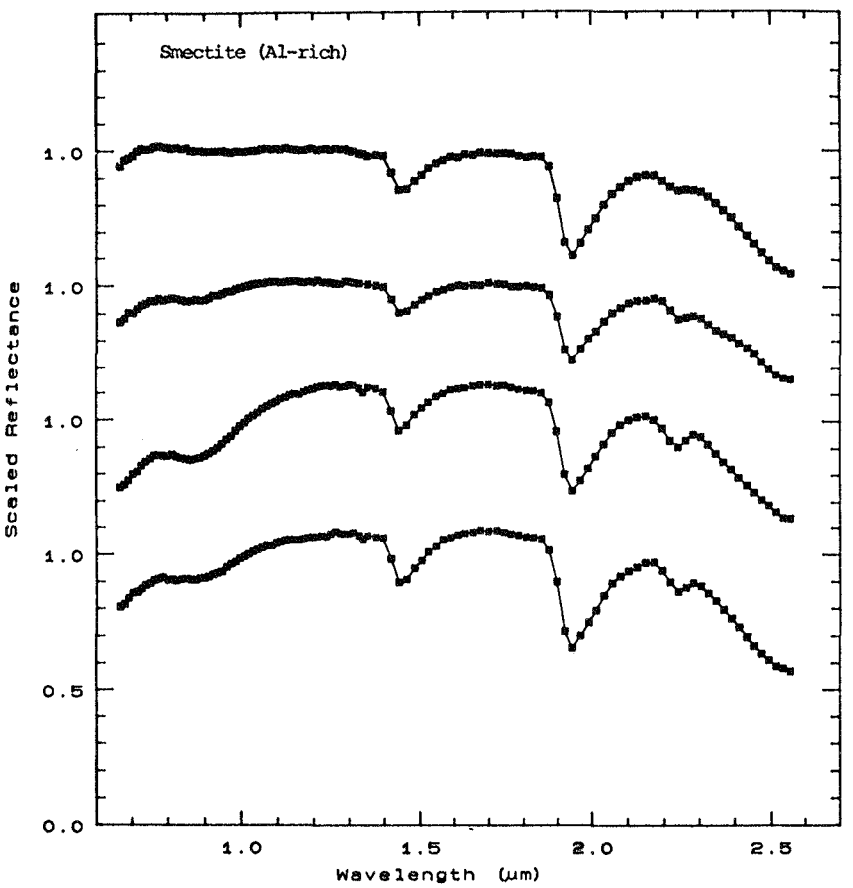

FIGURE 2. The spectral reflectance (λ = 0.7 to 2.5 μm) relative to halon of four clays of varying Al-OH content. The clay mineral in all the samples is primarily the smectite montmorillonite.

TABLE II.

Soil sample names

Number	Sample
1	U3Lz-550, QTa, S/W
2	U3Lw-300, QTa, S/W
3	U3Lc-500, QTa, S/W
4	U3Lf-1090-1100, QTa, cuttings
5	Ue7bc-2631, Paleocolluvium, S/W
6	Ue7bc-2687, Paleocolluvium, S/W
7	Ue7az-2289, Paleocolluvium, S/W
8	U19ak-445, tuff
9	U19ae-950, tuff
10	RW20a-13, Tpbr
11	RW29a-9
12	RW18a-4, Tpgl
13	RW18b-1, Tabw
14	Ue19fs-4662, Tram 2(b)
15	Ue19w-1-1859, Tbd
16	Ue20f-5799, Trap (b)
17	Ue19x-2301, Traul (b)
18	FB15d-4b, Siltstone lithics of Eleana
19	RW19f-13, Traul (b)
20	RW20a-4, Tphr(b)
21	DB28b-13, Tmrl
22	RWRYb-5, Tmrl
23	TB-2 GC, Tot2

Note: All samples were collected by D. Krier unless sample names begin with RW (R. Warren) or FB (F. Byers).

TABLE III.

Sample descriptions

These samples have been examined either by microprobe, x-ray fluorescence (XRF), x-ray diffraction, petrographic microscope, neutron activation, or some combination of these techniques.

Primary Materials (No alteration - vitric)

RW20a-13 (Tpbr): XRF analysis. Petrography incomplete.
RW29a-9 (Tptu): Vitrophyric with glass as analyzed by microprobe and XRF.

High-temperature primary devitrification

RW18a-4 (Tbgl): Minor secondary chalcedony and Ca-rich clinoptilolite as analyzed by microprobe.
RW18b-1 (Tabw): Vapor-phase alkalai feldspar and abundant vapor-phase silica (tridymite) as analyzed by microprobe.

High-temperature secondary alteration

Ue19fs-4662 [Tram2(b)]: kaolinite and chert.
Ue19w-1-1859 [Tbd(a)]: adularia and albite as analyzed by microprobe; drusy quartz and hematite after pyrite; extreme alteration, probably abundant clay.

Intermediate-temperature secondary alteration

Ue20f-5799 [Trap(b)]: analcime, adularia, and albite as analyzed by microprobe.

Low-temperature secondary alteration

Ue19x-2301 [Traul(b)]: alkalai-rich clinoptilolite as analyzed by microprobe; probably opaline.
FB15d-4b (Me): siltstone lithic in older volcanic assemblage (probably Torv unit). No data.
RW19f-13 [Traul(b)]: zeolitic with probably opaline; incomplete petrography.
RW20a-4 [Tphr(b)]: Ca-rich clinoptilolite and glass as analyzed by microprobe. Major-element analysis by XRF.
DB28b-13 (Tmrl): clay-rich(?); no glass; petrography incomplete.
RWRYb-5 (Tmrl): clay-rich(?); no glass.
TB-2 GC (Tot2): zeolitic with opal and psilomelane

TABLE III. cont'd.

Quaternary-Tertiary alluvium	
U13z-550:	quartz, calcite, minor feldspar, clinoptilolite, illite, kaolinite(?), and glass(?).
U31w-300:	quartz, feldspar, minor calcite, opal, clinoptilolite, illite, smectite, and glass.
U31c-500:	quartz, feldspar, glass, minor illite, smectite(?)
U31f-1090-1100:	quartz, feldspar, clinoptilolite, smectite, opal, calcite, illite.
Paleocolluvium	
Ue7bc-2631:	smectite, quartz, feldspar, and biotite.
Ue7bc-2687:	smectite, quartz, feldspar, and biotite.
Ue7az-2289:	smectite, calcite, quartz, feldspar, and illite.
Tuff	
Ue19ak-445:	smectite, feldspar, quartz, clinoptilolite, and illite.
Ue19ae-950:	smectite, quartz, feldspar, and cristobalite.

The samples were ground to particle sizes <150 μm diameter with a ceramic mortar and pestle. Some of the samples were already in a finely powdered form with the largest particle size much less than 150 μm; for that reason the particle size distribution among the samples is not uniform. This difference could, in principle, cause spectral reflectance effects dependent upon particle size (Adams and Filice, 1967). However, since small particles tend to cling to the larger particles, a size distribution of particles <150 μm will produce spectral reflectance properties that are closely mimicked by the smallest particles, which are always more abundant. The samples were placed into a sample cup (25 mm diameter, 5 mm deep) and leveled with a microscope slide. A dusting of the same size fraction was then sieved on top to produce a dusty, low density surface.

Each sample was measured at room temperature with the spectrogoniometer at the University of Hawaii Planetary Geosciences Division of the Hawaii Institute of Geophysics. Three different detectors were used for three parts of the spectrum. The spectral regions are divided into λ = 0.4 to 1.0 μm using two circular variable filters (CVF) and a silicon photo-diode detector, λ = 0.7 to 2.5 μm using two CVF's and a cooled (77K) InSb detector, and λ = 2.3 to 4.7 μm using two CVF's and another cooled (77K) InSb detector. Halon was used as a reflectance standard for $\lambda < 2.5$ μm. Sublimed sulfur was used as another reflectance standard for $\lambda > 2.5$ μm since halon

displays several prominent absorption bands at the longer wavelengths. Absolute reflectances were calculated using the absolute reflectance of halon (Weidner and Hsia, 1981) and the absolute reflectance of sulfur (Nash, 1986).

All samples were stored and measured at room temperature (295K) with a relative humidity of about 40%. Measurements of each sample were bracketed by measurements of the standard (either halon or sulfur) to identify any systematic effects due to variations in the light source, optical system or detectors. Systematic variations were less than 5% and were removed in the data processing stage. In general, up to 10 individual spectra of each sample were averaged together to obtain a signal-to-noise ratio (SNR) in excess of 100 for the darkest samples. Sometimes, as in the case of the 3 μm water band, the SNR was considerably less than the desired 100.

The reflectances used for the analysis are normalized at $\lambda = 1$ μm. The absolute reflectance of the samples at $\lambda = 1$ μm is given in Table IV. Digital data for all samples is available from the authors.

TABLE IV.

Absolute reflectances at $\lambda = 1$ μm

Sample	Reflectance
1	0.62
2	0.58
3	0.65
4	0.67
5	0.60
6	0.62
7	0.72
8	0.60
9	0.71
10	0.44
11	0.15
12	0.38
13	0.59
14	0.59
15	0.70
16	0.75
17	0.80
18	0.44
19	0.72
20	0.70
21	0.70
22	0.74
23	0.69

VI. RESULTS

The spectral reflectance for samples in each group is shown in Figures 3 through 11. An accompanying description of each group and sometimes of individual samples is provided and should be compared with the assays from other techniques given in Table III.

A. Primary materials (no alteration)

The normalized spectral reflectances of samples 10 and 11 are shown in Figure 3. A weak 1.9 μm band and a prominent 3 μm complex indicates the presence of water either adsorbed onto the surface or trapped as fluid inclusions. The lack of an OH^- feature at 1.45 μm, but the presence of one at 2.8 μm, indicates the amount of hydroxyl ion in the sample is small but still significant. The band at 2.25 μm indicates that the hydroxyl ion is probably in the form of Al-OH. The presence of the hydroxyl ion bands suggests that both of these samples have suffered some alteration. Based upon the relative strengths of the 2.25 μm Al-OH bands, it appears that sample 11 has been less altered than sample 10. A 4.25 μm feature in sample 10 indicates the presence of a small quantity of sulfate. The strong ultraviolet (UV) dropoff in sample 11 is indicative of a strong charge transfer centered further to the UV, due to metal-oxygen or metal-metal bonds.

The overall spectral reflectance properties cause us to question the statement that these samples are truly unaltered. A more accurate statement is that these samples are slightly altered or the least-altered in the set.

B. High-temperature primary devitrification

The minimal 1.9 μm and 3 μm bands in sample 13 (Figure 4) indicates that this sample has the least amount of water of all the samples measured. The broad nature of this band indicates the water is not site-specific, i.e., it is probably present as surface water or fluid inclusions. The lack of any OH^- features at 1.4 μm or in the 2.2 to 2.4 μm region indicates the absence of any clay component. The lack of other water bands indicates the absence of a zeolitic component.

The sharp 1.95 μm feature in sample 12 indicates the presence of site-specific water. The slightly asymmetric nature of this band suggests a weak 1.80 μm feature indicative of a zeolitic component, which is consistent with the strong 2.55 μm feature characteristic of zeolites. Clinoptilolite is assayed by microprobe analysis. A weak 1.45 μm feature is suggestive of an OH-bearing component. The 2.2-2.4 μm complex suggests a combination of Al-OH and Mg-OH bonds. However, since calcite is present at the 1% level, as indicated by the 4.0 μm band, the 2.2-2.4 μm feature is probably a barely resolved 2.35 μm calcite absorption. A strong UV absorption is probable due to Fe^{2+} and Fe^{3+} since the 0.7 μm feature is indicative of Fe^{3+} (probably hematite).

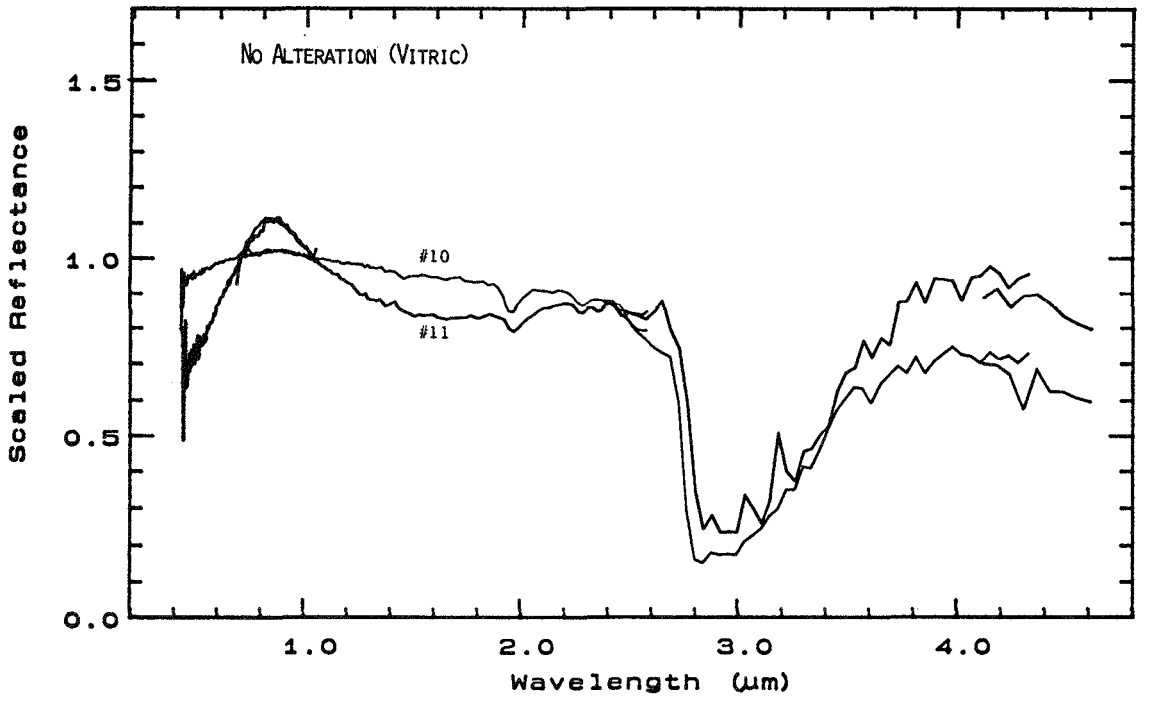

FIGURE 3. The normalized (at 1 μm) spectral reflectance (λ = 0.7 to 2.5 μm) of samples 10 and 11 (Table II) from the Nevada Test Site, which show evidence of no or little alteration.

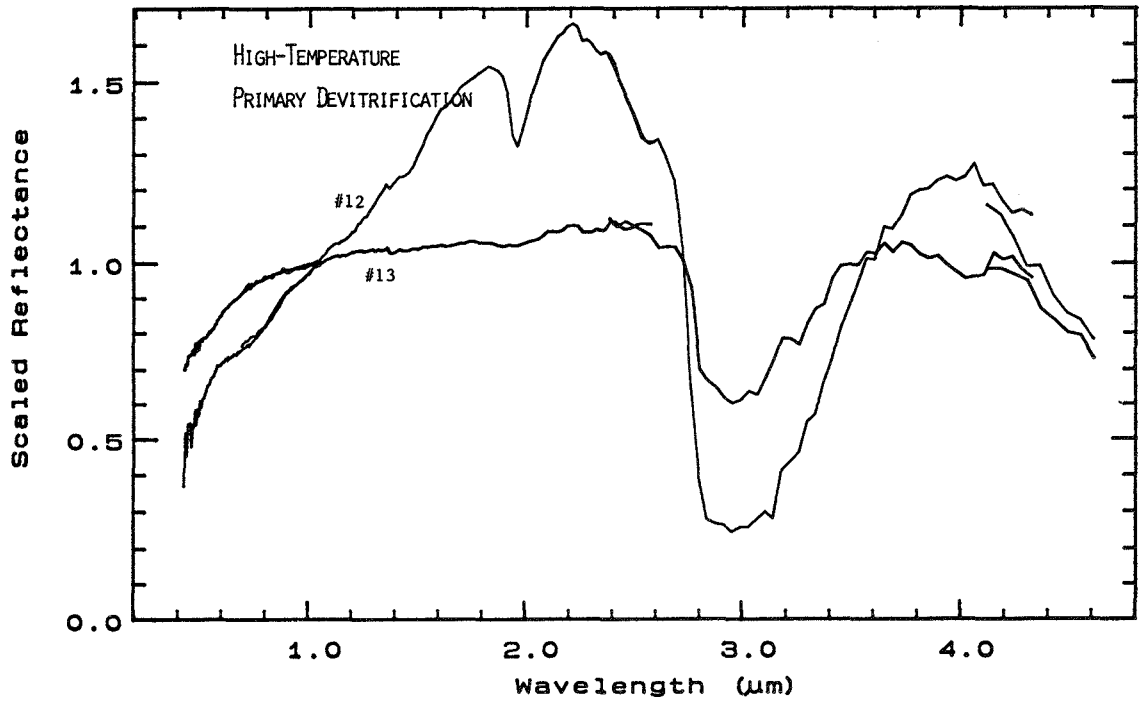

FIGURE 4. The normalized (at 1 μm) spectral reflectance (λ = 0.4 to 4.7 μm) of samples 12 and 13 (Table II) from the Nevada Test Site, which show evidence of high-temperature devitrification.

C. High-temperature secondary alteration

The band width of the 1.9 μm and 3 μm water bands (Figure 5) in both samples 14 and 15 suggest variations in the site of the bound water. The 1.45 μm band in combination with a 2.3 μm feature indicates an OH-bearing component which, based upon the 2.25 μm position of the Al-OH band, suggests a di-octahedral smectite (montmorillonite). The Al-OH absorption is comprised of a doublet at 2.2 μm (strongest) and 2.3 μm (weakest). The Mg-OH is comprised of a doublet at 2.3 μm (strongest) and 2.4 μm(weakest). Because our spectrometer cannot resolve these doublets we must rely on the general rule that we are seeing the strongest of the doublets, i.e. a band near 2.25 μm is indicative of Al-OH and a band near 2.35 μm is indicative of Mg-OH. The slight short wavelength asymmetries in the 1.45 μm and 1.95 μm bands are due to a zeolitic component, probably chert as mentioned in the assays. The 0.65 μm and 0.95 μm bands are indicative of Fe^{3+}, probably geothite or hematite, but could be due to nontronite, also.

D. Intermediate temperature secondary alteration

The sharp 1.9 μm and 3 μm features in sample 16 (Figure 6) are indicative of water coordinated to a narrow range of crystal sites. The 1.45 μm and 2.8 μm bands are indicative of an OH^- component which, from the presence of a 2.25 μm band, is probably Al-OH. A strong 2.55 μm band is suggestive of a zeolitic component but the lack of a 1.80 μm feature, that would cause the 1.95 μm water band to become asymmetric, is not apparent. Reference to Figure 1 shows that this is most likely due to the zeolite analcime which lacks a strong 1.80 μm band. The 0.65 μm band is due to oxidized iron (Fe^{3+}) in the form of hematite or geothite.

E. Low-temperature secondary alteration

All seven samples shown in Figures 7 and 8 show strong water bands at 1.45 μm, 1.9 μm and 3 μm. Samples 18 and 20 show slightly less of each component indicating a wide variation in the water content among these samples. The short wavelength asymmetries in the water and OH^- bands of samples 17, 19 and 20 indicate a significant zeolitic component; samples 18 and 21 show no significant zeolitic component.

The weak 2.25 μm band in all samples is indicative of Al-OH which must be in a clay component and not in a zeolite. The band position is suggestive of a di-octahedral component, i.e., montmorillonite. The broad 3 μm feature is the result of site disorder in the water-bearing component, another indicator of clay which from the presence of the Al-OH feature must be montmorillonite.

The 0.9 μm, 0.65 μm and UV drop off are indicative of Fe^{2+} and Fe^{3+} in either geothite or hematite. The variations in the strength of these features indicates a range of crystallinity in the iron oxides.

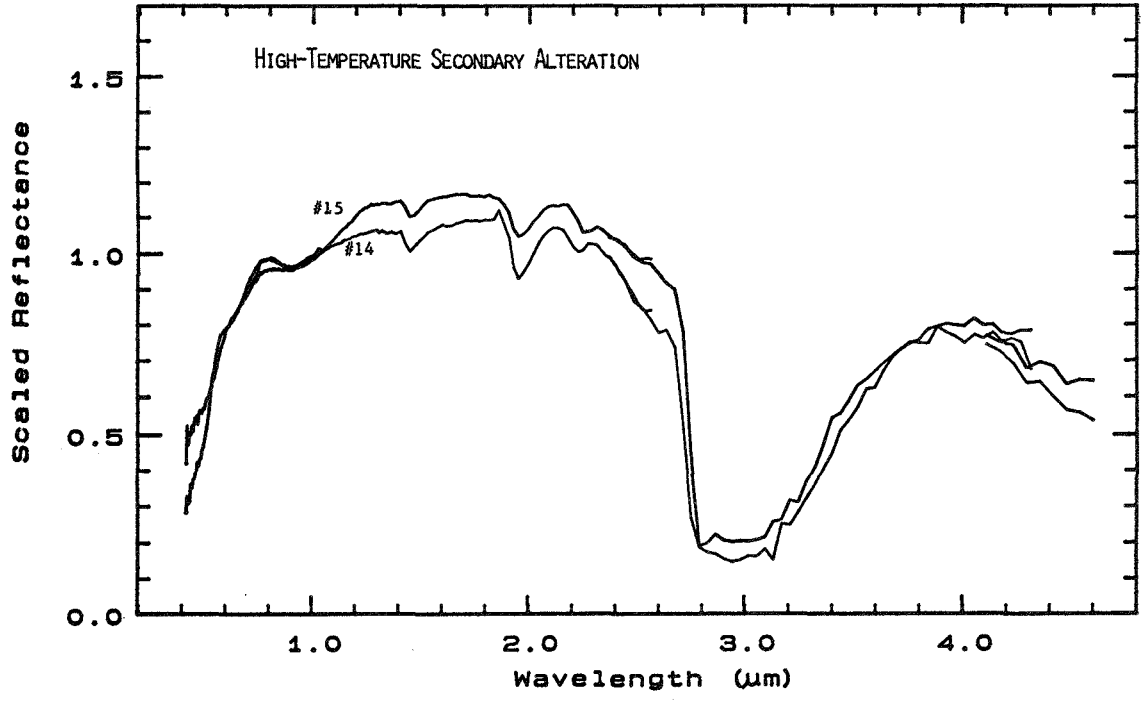

FIGURE 5. The normalized (at 1 μm) spectral reflectance (λ = 0.4 to 4.7 μm) of samples 14 and 15 (Table II) from the Nevada Test Site, which show evidence of high-temperature secondary alteration.

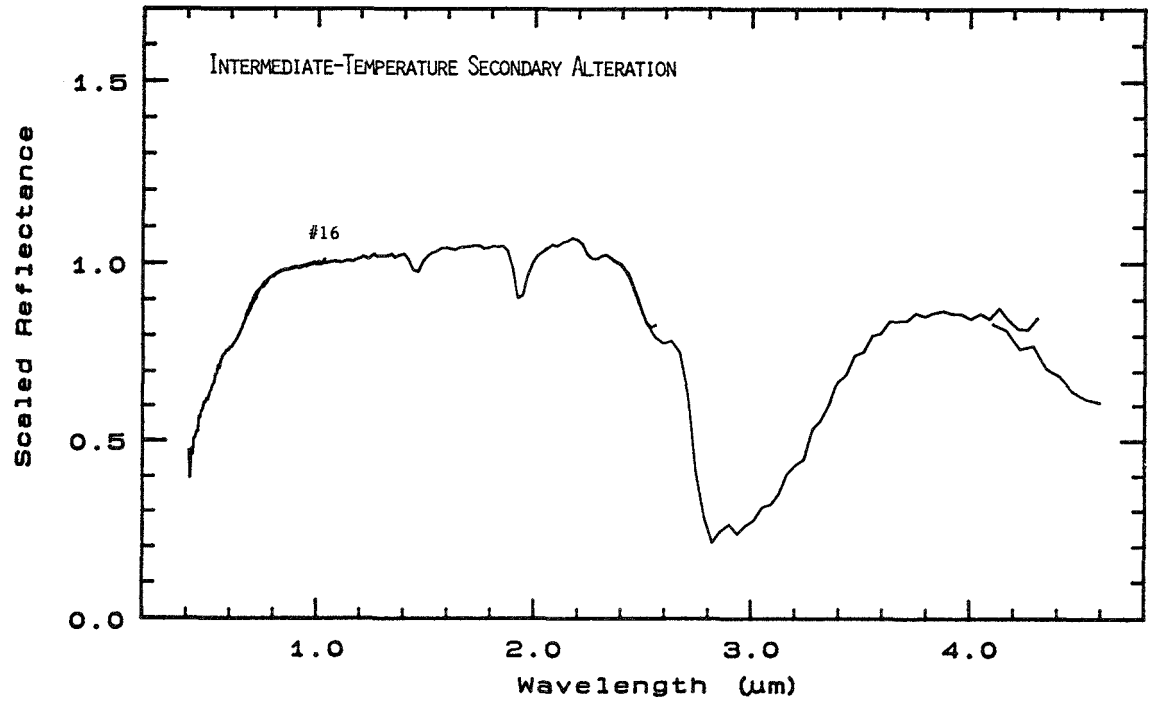

FIGURE 6. The normalized (at 1 μm) spectral reflectance (λ = 0.4 to 4.7 μm) of sample 16 (Table II) from the Nevada Test Site, which shows evidence of intermediate-temperature secondary alteration.

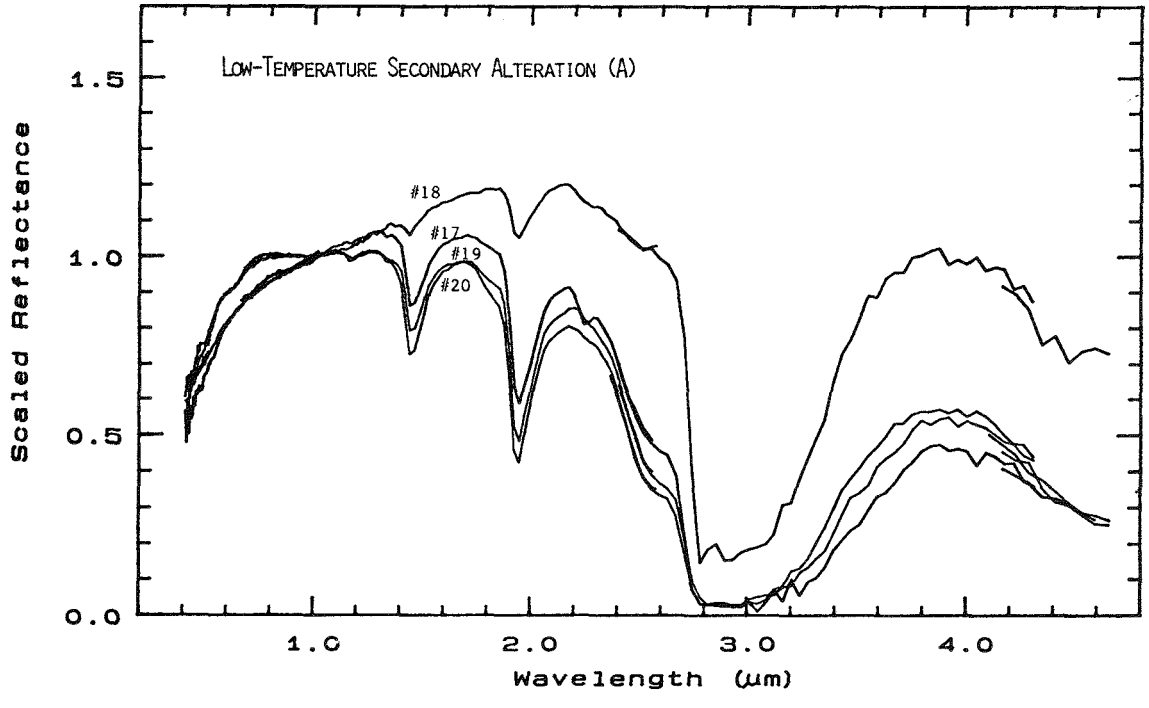

FIGURE 7. The normalized (at 1 μm) spectral reflectance (λ = 0.4 to 4.7 μm) of samples 17, 18, 19 and 20 (Table II) from the Nevada Test Site, which show evidence of low-temperature secondary alteration.

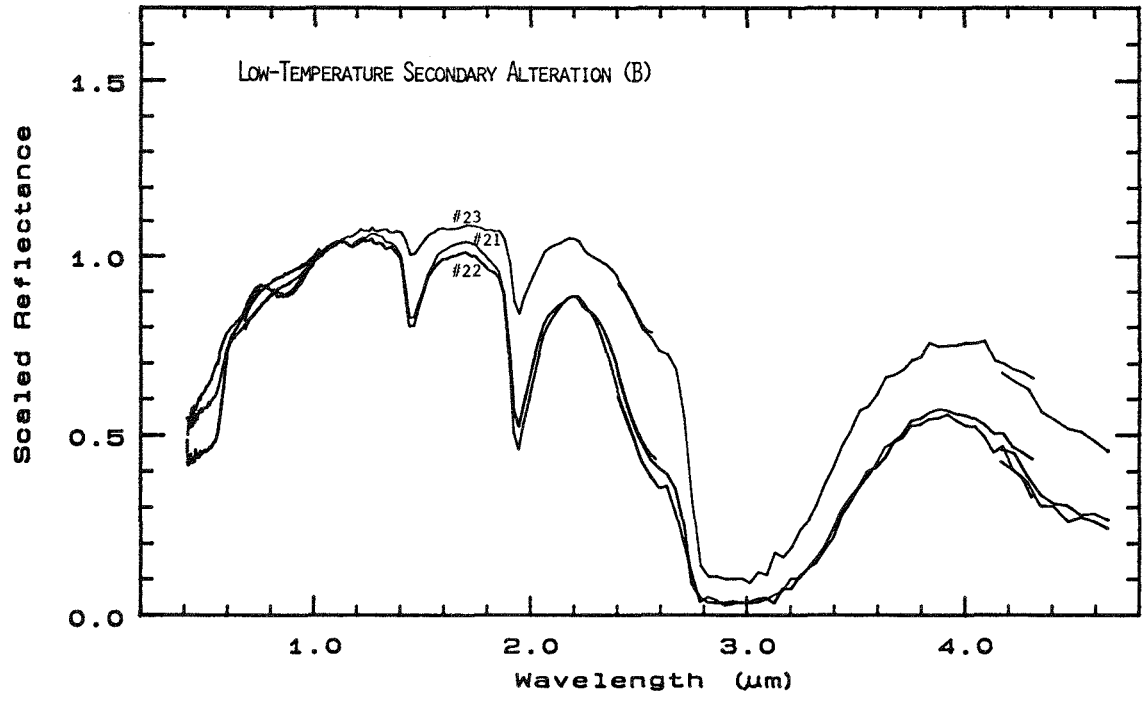

FIGURE 8. The normalized (at 1 μm) spectral reflectance (λ = 0.4 to 4.7 μm) of samples 21, 22, 23 (Table II) from the Nevada Test Site, which show evidence of low-temperature secondary alteration.

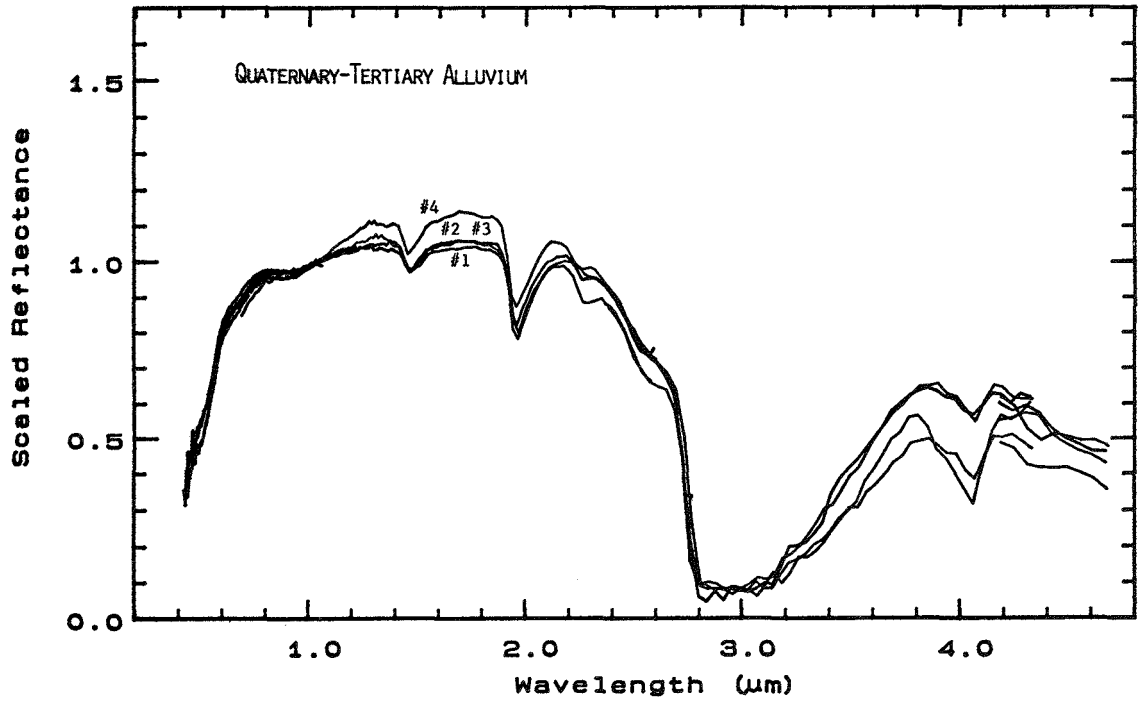

FIGURE 9. The normalized (at 1 μm) spectral reflectance (λ = 0.4 to 4.7 μm) of samples 1, 2, 3 and 4 (Table II) from the Nevada Test Site, which are Quaternary-Tertiary alluviums.

F. Quaternary-Tertiary alluvium

The broad 3 μm band and relatively broad 1.9 μm band suggest water with less site specificity for all four samples in Figure 9. The prominent 1.45 μm and 2.8 μm OH^- features combined with the broad water bands is indicative of a smectite. The Al-OH feature at 2.3 μm implies montmorillonite as the major smectite component. However, the presence of calcite (see below) which has bands at 2.35 μm and 2.55 μm makes the identification of a smectite component indeterminate.

The broad feature at 2.55 μm indicates a zeolitic component, although the lack of asymmetries in the 1.45 μm and 1.9 μm bands suggests this component is small and that most of the water is in the smectite component. The 4.0 μm calcite band correlates with the assayed abundance. The 0.9 μm band and the UV drop off are probably from Fe^{2+} and Fe^{3+}, which indicates a fair degree of crystallinity.

G. Paleocolluvium

As with the previous samples the broad 1.9 μm water band suggest site disorder in the water. The 1.45 μm and the 2.8 μm bands indicate OH which is in the form of Al-OH according to the position of the 2.25 μm band. The lack of asymmetries in the 1.45 μm and 1.9 μm bands suggest that any zeolitic component is minor. The major water-bearing mineral must be montmorillonite.

H. Tuff

The broad 1.9 μm water band indicates site-disordered water in both samples shown in Figure 11. The strong 1.45 μm and 1.9 μm OH bands indicate a major clay component, which according to the position of the 2.25 μm band must be the aluminous smectite montmorillonite. The water bands are so broad that smectite clays must be the major mineral component in these samples.

Sample 9 shows the asymmetries in the 1.45 μm and 1.9 μm bands that are indicative of a zeolitic component, whereas sample 8 can have only a minor component of zeolites. Sample 8 shows 0.65 μm and 0.9 μm bands indicative of Fe^{3+} which does not show in sample 9.

VII. SUMMARY

Visible and near-infrared spectral reflectance properties from $\lambda = 0.4$ to 4.7 μm were used to characterize the mineralogy and chemistry of 23 soil samples from the Nevada Test Site. These samples represent primary materials, materials resulting from a range of primary and secondary alteration, alluvium, and tuff. The bi-directional reflectance spectra, measured with the Planetary Geosciences spectro-goniometer facility, show that all altered materials exhibit absorptions due to the presence of water either intrinsic or adsorbed onto crystal surfaces. Calcite is easily identified from the spectra in amounts greater than 1 weight percent. In general, the

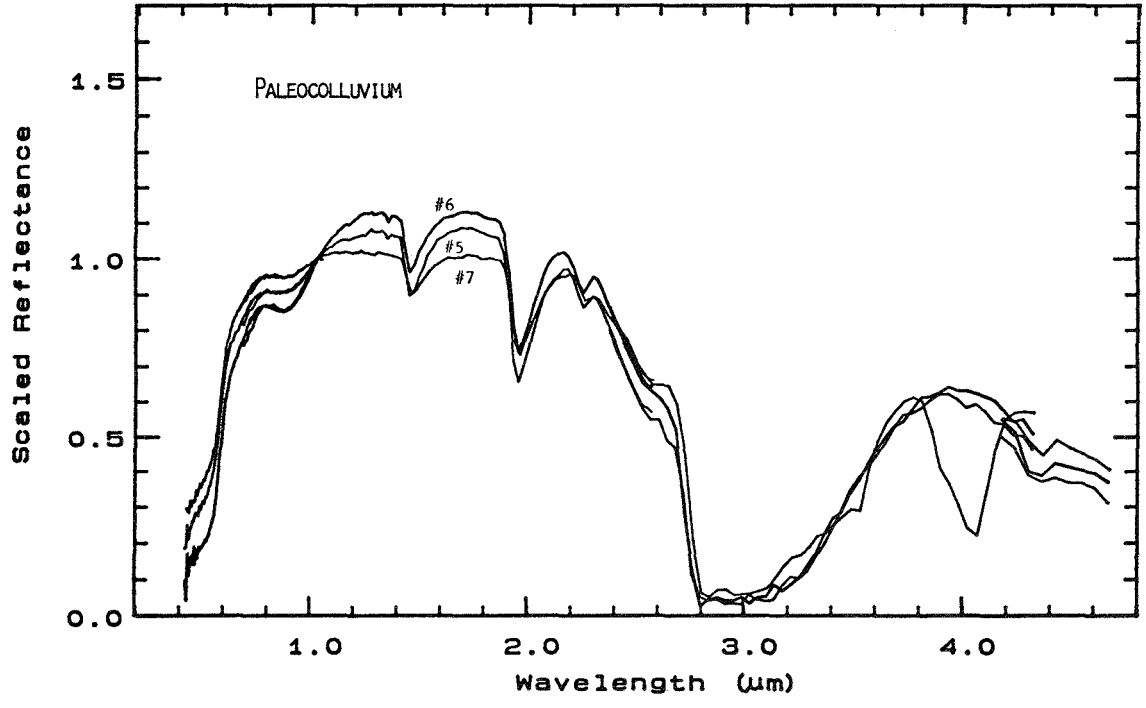

FIGURE 10. The normalized (at 1 μm) spectral reflectance (λ = 0.4 to 4.7 μm) of samples 5, 6, and 7 (Table II) from the Nevada Test Site, which are paleocolluvium.

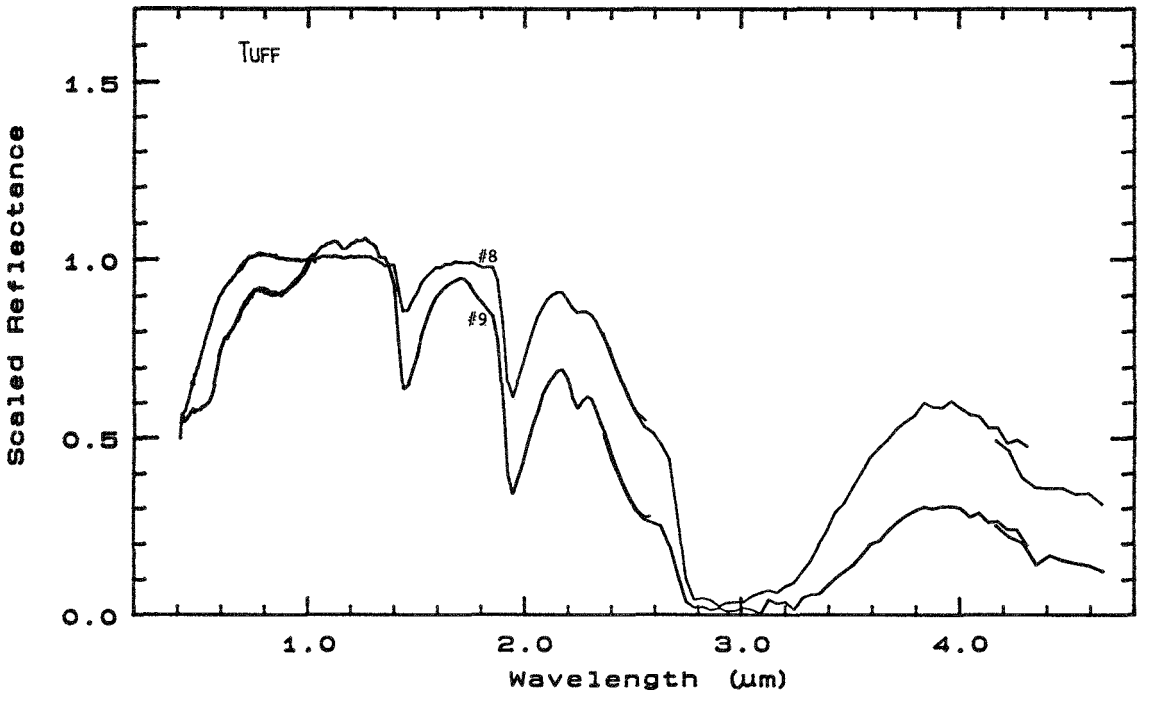

FIGURE 11. The normalized (at 1 μm) spectral reflectance (λ = 0.4 to 4.7 μm) of samples 8 and 9 (Table II) from the Nevada Test Site, which are tuff.

calcite absorption band depths and volume abundances correlate. Hydroxyl-bearing minerals are easily detected by absorption bands at 2.2-2.3 μm (Al cation) and 2.3-2.4 μm (Mg cation). The presence of zeolite in these samples appears to be correlated with the shape of the combination and/or overtone absorptions of water fundamentals at 1.4 μm, 1.9 μm and 3 μm. Spectra of all samples show a wide range of oxidation and, in addition, a range in the degree of crystallinity of the ferric-bearing materials. In conclusion, reflectance spectroscopy can provide a variety of information concerning the chemistry and mineralogy of these soil samples. However, before in situ measurements are employed, the effects on the spectral reflectance of the hydration and dehydration of these samples must be characterized.

ACKNOWLEDGMENTS

This work was performed under Contract No. 9-XDD-6114C-1 with the Los Alamos National Laboratories.

REFERENCES

Adams, J.B. (1975). Uniqueness of visible and near-infrared reflectance spectra of pyroxenes and other rock-forming minerals, in *Infrared and Raman Spectroscopy of Lunar and Terrestrial Minerals*, C. Karr, ed., pp. 91-116, Academic Press, Orlando, Florida.

Adams, J.B. and A.L. Filice (1967). Spectral reflectance 0.4 to 2.0 microns of silicate rock powders, *J. Geophys. Res.*, 72, 5705-5715.

Bruckenthal, E.A. (1987). The dehydration of phyllosilicates and palagonites: Reflectance spectroscopy and differential scanning calorimetry, Master of Science Thesis, Univ. Hawaii, 182pp.

Clark, R.N. and T.L. Roush. (1984). Reflectance spectroscopy: Quantitative analysis techniques for remote sensing applications. *J. Geophys. Res.*, 89, 6329-6340.

Farmer, V. C. (1974). The layer silicates.,in *The Infrared Spectra of Minerals* (V.C. Farmer, ed.). *Mineralogical Soc. Monograph 4, London,* 331-363.

Flanigen, E. M. (1977). Crystal structure and chemistry of natural zeolites, in *Mineralogy and Geology of Natural Zeolites*. (F. A. Mumpton, ed.) Mineralogical Soc. America, 19-52.

Gaffney, E.S. and R.B. Singer (1985). Zeolites on Mars: Prospects for remote sensing, *Bull. Amer. Astron. Soc., 16,* 710 (abstract).

Hunt, G.R. (1977). Spectral signatures of particulate minerals in the visible and near-infrared, *Geophysics*, 42, 501-513.

Kunkle, T. D. (1986). Personal communication (samples).

McCord, T.B., R.N. Clark, B.R. Hawke, L.A. McFadden, P.D. Owensby, C.M. Pieters, and J.B. Adams (1981). Moon: Near-infrared spectral reflectance, a first good look, *J. Geophys. Res.*, 86, 10883-10892.

Nash, D. B. (1986). Mid-infrared reflectance spectra (2.3-22 μm) of sulfur, gold, KBr, and halon, *Applied Optics, 25*, 2427-2433.

Singer, R. B. (1986). Personal communication (spectral reflectance measurements of zeolites).

Singer, R.B., T.B. McCord, R.N. Clark, J.B. Adams, and R.L. Huguenin (1979). Mars surface composition from reflectance spectroscopy: A summary, *J. Geophys. Res.*, 84, 8415-8426.

Weidner, V. R. and Hsia, J. J. (1981). Reflection properties of pressed polytetrafluoroethylene, *J. Opt. Soc. Am., 71*, 856-861.

DO NOT MICROFILM
THIS PAGE

Cavity Pressure and Chemistry

[illegible]

DO NOT MICROFILM
THIS PAGE

FLUID DYNAMICS OF A PRESSURE MEASURING SYSTEM FOR UNDERGROUND EXPLOSIVE TESTS

R. C. Dykhuizen
Fluid and Thermal Sciences Dept.

C. W. Smith
Field Sciences Dept.

Sandia National Laboratories
Albuquerque, New Mexico 87185

Abstract

Numerical and analytical models are used to optimize a pressure measuring system for underground nuclear tests. This system uses a long pipe filled with gas to communicate the pressure level to a transducer in a pressure chamber remote from the explosion cavity. The pressure chamber and pipe are pressurized above the final pressure expected from the explosion. During the explosion, the high pressure gas blows down, preventing debris from entering and clogging the system. The models were first checked against the Junior Jade test series, which used an underground non-nuclear explosion to simulate a nuclear test. It was found that the measured pressure oscillated for some time before settling down to a steady value. This is shown to be a result of an organ pipe oscillation that can develop in the short pipes used for this test series. The analytical model provided a simple means to optimize the system design parameters and showed that changing the working fluid from nitrogen to helium would improve the time response of the system significantly. The numerical model is then used to obtain more accurate predictions of the system response.

Introduction

It is desired to measure the pressure history in an underground cavity after a nuclear explosion. Due to the severe environment, the instrumentation system must be shielded from the test. In the current system, a sensor measures the pressure in a small reservoir which is connected to the explosion cavity through a long pipe. In order to minimize the chance of the pipe becoming clogged by the debris created by the explosion, the piping and reservoir are charged initially with high pressure gas. When this gas escapes, the pressure in the explosion cavity and the reservoir are equilibrated, and the sensor measures the cavity pressure level.

Figure 1 shows the geometry of the pressure measuring gas system. The pressure sensor is located in the reservoir, and the open end of the pipe is exposed to the explosion

This work was performed at Sandia National Laboratories, Albuquerque, New Mexico, supported by the U. S. Department of Energy under contract DE AC04-76DP00789.

cavity at some time after the nuclear event. This delay is accomplished by placing the pipe end in the host rock or grout. Then, as the explosion forces expand the cavity, it exposes the pipe end to the cavity gas. The pressurized gas in the piping system is then allowed to escape into the cavity. After equilibration of pressures, the pressure sensor measures the cavity pressure. However, subsequent cavity pressure changes with very short time constants cannot be resolved with this system due to its slow time response.

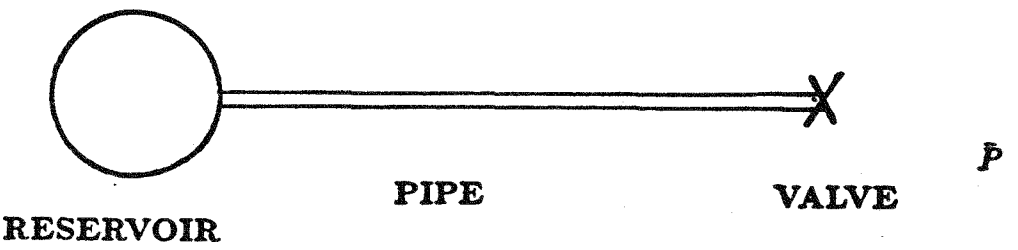

Figure 1: Flow Geometry.

Analytical and numerical models have been developed to optimize the design and predict the behavior of the system in a test environment. The models were used to predict the response of this pressure system which was used to measure the cavity pressure on the Junior Jade series of decoupled, high explosives underground tests.

Analytical and Numerical Models.

A simple analytical model was developed to gain insight on the response of the piping system. First, a mass balance equation is introduced for the reservoir:

$$\frac{dM}{dt} = -\rho v A \tag{1}$$

A momentum balance is introduced for the gas flow in the pipe:

$$\frac{d(\rho v)}{dt} = \frac{P - \bar{P}}{\ell} - f\rho v \mid v \mid \tag{2}$$

In the above equations, M represents the mass of gas stored in the reservoir; A represents the pipe cross-sectional area; v the pipe gas velocity; P and $\bar{P}$ the reservoir and explosion cavity pressures, respectively; f the friction coefficient; and ℓ the pipe length.

By limiting the model to two state equations, the analysis remains simple and tractable. Constitutive equations are then required to evaluate all variables in terms of two state variables. In this case, the reservoir pressure and the pipe gas velocity are chosen as the state variables. The reservoir mass is then determined by assuming a perfect gas. The temperatures are all assumed constant, and the pipe pressure is assumed to be the average of the reservoir pressure and the downstream cavity pressure. The pipe pressure level is used to calculate the density of the flowing gas. This yields the following two state equations (with V introduced to represent the reservoir volume):

$$\frac{V}{RT}\frac{dP}{dt} = -\frac{(P - \bar{P})}{2RT}vA \tag{3}$$

$$\frac{V}{2RT}\frac{dP}{dt} + \frac{(P + \bar{P})}{2RT}\frac{dv}{dt} = \frac{(P - \bar{P})}{\ell} - f\frac{(P - \bar{P})}{2RT}v|v| \tag{4}$$

If these equations are linearized about the equilibrium point (in this case, zero flow and equal pressures), the eigenvalues provides significant insight about the system response. Unfortunately, the friction term (being quadratic in the pipe velocity) disappears from the model when the linearization is performed. Without friction, the linear model displays two imaginary eigenvalues. This indicates a harmonic oscillator with no damping. The frequency of these oscillations is of interest since the pressure data from the Junior Jade test series exhibited an oscillation. The analytical frequency is given by:

$$\sqrt{\frac{ART}{V\ell}}/2\pi \tag{5}$$

A simple modification of the model is to assume that the gas in the reservoir behaves isentropically, instead of isothermally. The gas flow in the pipe is still assumed isothermal due to the good heat transfer with the massive pipe walls. Then, the following frequency is obtained:

$$\sqrt{\frac{kART}{V\ell}}/2\pi \tag{6}$$

In the above, the variable k represents the specific heat ratio of the flowing gas.

One might expect the actual oscillations to exhibit a frequency somewhere between the above estimates, since the reservoir will exhibit some heat transfer. This heat transfer will be insufficient to cause the reservoir to be isothermal, but too much to consider it isentropic.

The finite difference computer code, TOPAZ, [1] was also used to predict the pressure oscillations of this system. Use of this code removes some of the approximations that were made in the formulation of an earlier numerical model [2]. TOPAZ was developed to analyze gas piping networks. It assumes that the piping can be accurately represented using one-dimensional equations and a network of junctions connecting two or more pipe sections. The one-dimensional assumption limits the code to consideration of piping networks that have lengths much longer than their diameters. This condition is met with the pressure measuring system described here.

Use of this large code also eliminates many of the assumptions required for the analytical solution. The finite-difference equations in this code allow the velocity in the pipe length to vary both with time and location so the assumption of velocity variations only with time is avoided. The reservoir includes a heat transfer model so that neither the isentropic nor the isothermal assumption is required. Also, the equations are not linearized so the friction can be accurately represented.

Comparison to Junior Jade Test Results

Both the simple analytical model and the numerical code TOPAZ were used to predict the Junior Jade test series. The test results were not made available to the author until after the analytical and numerical results that are presented here were completed. Figure 2 shows the predicted response for the Junior Jade 5 test. This can be compared to Figure 3 where the test data is presented. In the numerical simulation, the downstream pressure is assumed to be constant. The experimental data displays a slight pressure decrease over time after equilibrium is established. This is due to cooling of the explosion gases after the explosion, which was not modeled. The fact that the undershoot was not predicted exactly was not a concern since any undershoot can easily be obtained from the analytic model by a slight change in the time delay between the valve opening and the explosion.

Table 1 compares predictions from the analytical and numerical models of the oscillation frequency to the experimental data of two tests; they agree fairly well. The disagreement between the analytically predicted frequencies for the Junior Jade 5 test and the other entries reflects the use of two different diameter pipe lengths connected in series. This was accounted for in the numerical model, but not in the analytical one.

Design Optimization

Numerical calculations of this system using the long pipes required for a nuclear explosion showed a discouragingly long time-constant for the pressure response. Figure 4, which shows the pressure in the reservoir and the pressure near the pipe end for a sample calculation, indicates that it requires approximately 1.25 sec before the sensor is

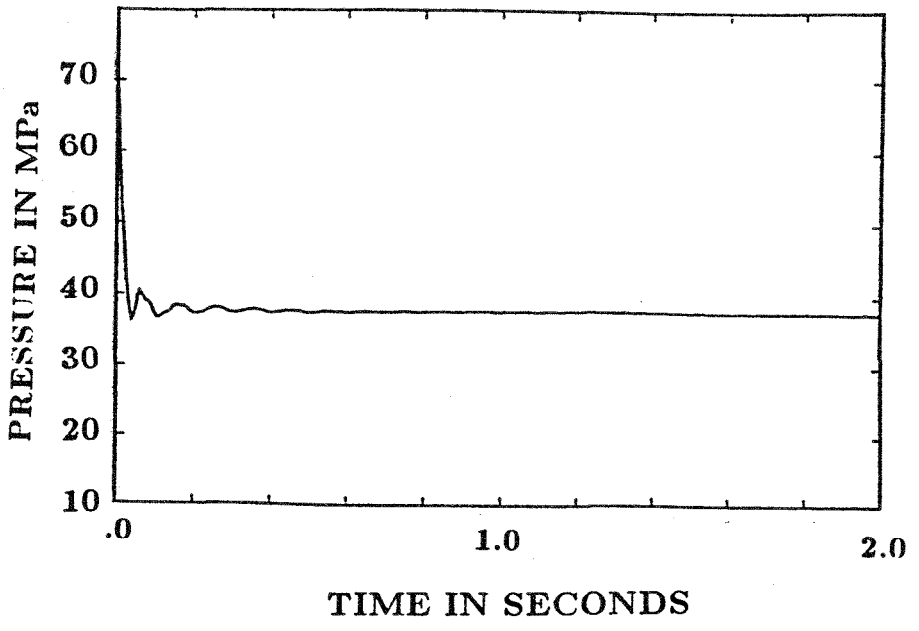

Figure 2: Predicted Reservoir Pressure Response for Jr. Jade 5 Test.

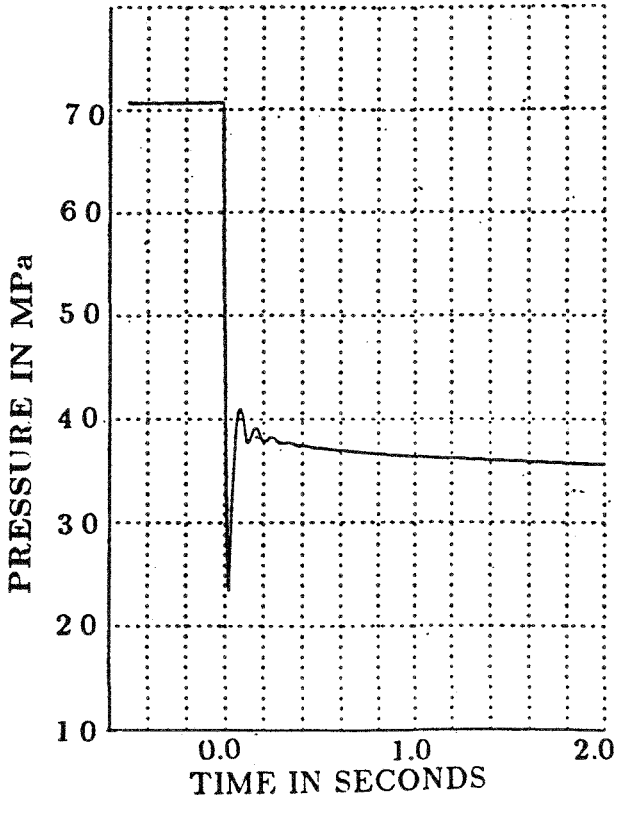

Figure 3: Measured Reservoir Pressure Trace for Jr. Jade 5 Test.

Table 1: Comparison of Oscillation Frequencies (cycles / second)

	Analytical Isothermal	Analytical Adiabatic	Numerical	Experimental
Jr. Jade 4	6	7	6.5	6.5
Jr. Jade 5	7.5	9	10.5	10.5

measuring the cavity pressure. Therefore, methods to improve the time response of the system were examined. The numerical results indicated that the pipe friction caused the pressure equilibrium between the explosion cavity and the reservoir to be delayed. Therefore, the analytical model presented above was modified since it did not include effects of the friction term after linearization. In an effort to keep the analysis simple, the acceleration term in Equation 2 is eliminated from the momentum equation. Then, this equation becomes algebraic and can be solved analytically for the flow velocity. When this is inserted into Equation 1, the following single-state equation results.

$$\frac{dP}{dt} = -\left(\frac{RT}{2f\ell}\right)^{\frac{1}{2}} \left(P^2 - \bar{P}^2\right)^{\frac{1}{2}} A/V \tag{7}$$

Assuming that the reservoir pressure is much larger than the downstream pressure, a single time constant is obtained.

$$\tau = (V/A)(2f\ell/RT)^{\frac{1}{2}} \tag{8}$$

This shows that to decrease the time constant, several choices are available. First, the friction coefficient can be decreased. This is mostly a function of the roughness ratio, so the roughness can be decreased or the pipe area increased. Increasing the pipe area initially looks like a promising method since it also appears in the denominator of the above time constant. Unfortunately, numerical simulations of the same case presented in Figure 4 with a larger area does not exhibit significant improvement in the time response of the system. This is because the pipe length is so long in this application that there is approximately 11 times the mass of gas stored in the pipe than stored in the reservoir. Therefore, any increase in the pipe area proportionally increases the total volume of high pressure gas that needs to be released. This counteracts any reduction in the friction and does little to improve the time response. This also limits the effect obtained by reducing the reservoir volume. Any reduction in the reservoir volume results in a negligible reduction in the effective volume of high pressure gas.

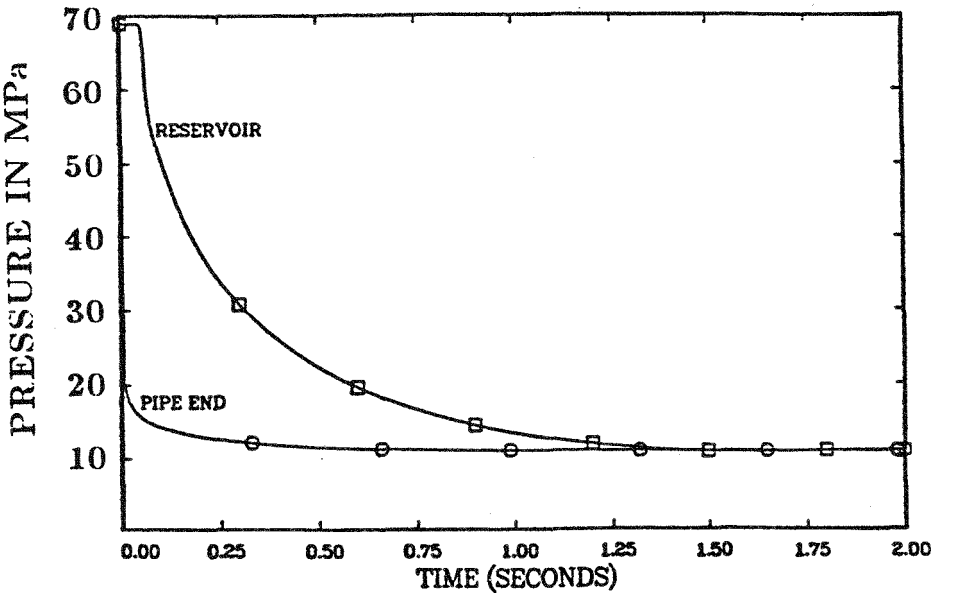

Figure 4: Pressure Response for Nitrogen System.

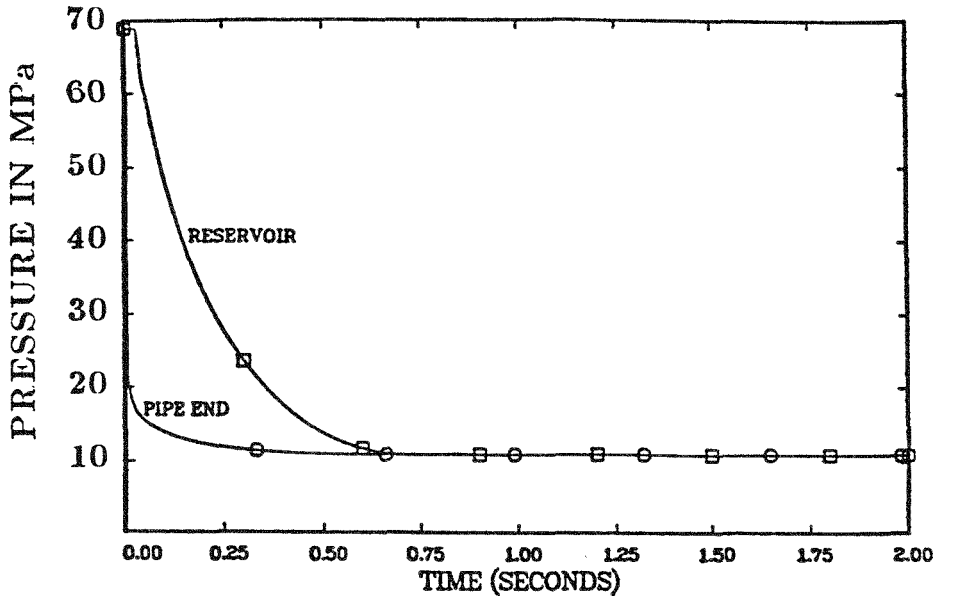

Figure 5: Pressure Response for Helium System.

Two other ways to reduce the time constant are to increase the temperature of the flowing gas or reduce the length of the pipe. Unfortunately, an increase in the gas temperature would make operations too complex, and the pipe length is fixed for other reasons. However, there still exists one way to reduce the time constant. That is to reduce the value of the specific gas constant, R. Previous designs used nitrogen as the working gas without consideration on how that choice might affect the performance of the system. A change to helium decreases the analytical time constant by a factor of approximately 2.5. Figure 5 shows the results of a numerical simulation of the same system shown earlier in Figure 4, with helium as the working fluid. The reservoir sensor reflects the pressure in the cavity after about 0.6 sec.

Conclusions

Analytical and numerical models aid in designing and optimizing a gas transfer system proposed for measurement of cavity pressures for an underground nuclear test. The predicted pressure levels and oscillations in pressure compare very well with measured values. The selection of the working fluid has a significant effect on the time response of the system and helium is shown to be a significant improvement over nitrogen.

References

1. W. S. Winters, "TOPAZ The Transient One Dimensional Pipe Flow Analyzer: Equations and Numerics," Sandia National Laboratories Report, SAND85-8248, December 1985.

2. S. N. Kempka and C. W. Smith, "Analysis of Cavity Gas Pressure Measurements in Underground Tests," Third Symposium on Containment of Underground Nuclear Explosions, Idaho Falls, ID, Sept. 9-13, 1985 Conf. 850953.

CORNUCOPIA Cavity Pressure Measurement

B. Hudson, C. Cordill, and L. Starrh
Lawrence Livermore National Laboratory, Livermore, California

J. Kalinowski and T. Stubbs
EG&G, Pleasanton, California

C. Keller
Science & Engineering Associates, Sante Fe, New Mexico

E. Peterson, and R. Nilson
S-CUBED, La Jolla, California

ABSTRACT

Many attempts have been made to measure cavity pressure over the past 25 years, but almost all have failed. A useful technique would give valid data from very soon after detonation until cavity collapse, and would be reliable enough to allow measurements on events with wide variations in geologic media, yield, and depth of burial. With these points in mind, a cavity-pressure measurement experiment was fielded on the CORNUCOPIA event. Electrical cables extended from a recording facility to an experiment package located deep in the emplacement hole, but not so deep as to be subjected to damaging stress levels from the outgoing shock wave. The experiment package contained high-pressure tanks, valves, and pressure transducers. A set of three stainless-steel tubes (approximately 0.25 in. O.D. x 0.15 in. I.D.) extended from the experimental package to the detonation elevation. These tubes were wound in the form of a helix with a pitch chosen such that as the cavity grew and the surrounding medium was displaced, axial compression and tension along the axis of each tube would balance. In addition, each tube was filled with water to prevent collapse from the high stresses (up to hundreds of kbars) in the ground shock wave. Within the experimental package each water-filled tube was connected to a high-pressure tank filled with dry nitrogen at about 12,000 psia. A few seconds before detonation, explosively driven valves were opened, pressurizing the water-filled tubes. Shortly after detonation, the strong shock wave vaporized and/or melted the end of each tube, allowing the pressurized water to be blown out.

The experiment performed very well, giving a complete pressure history for each of three independent sets of tube, transducer, and recording

channels, from a few seconds before detonation until cavity collapse, approximately nine hours later. Agreement between the three individual data channels was extremely good, showing a minus-time pressure from 10,700 to 11,400 psia, followed by a steep drop to a level of about 1500 psia at 10 s. After 1 min, the pressure underwent minor oscillations as it fell to about 160 psia at 2 1/2 h. From this time on, the pressure decreased monotomically, reaching about 100 psia approximately 35 min before collapse. The pressure then decreased at a much steeper rate until collapse, after which the record terminates as a result of electrical cable damage. After CORNUCOPIA, similar experiments were fielded on three other events, both to measure cavity pressure and as a means of obtaining a sample of gas from the cavity region. The technique performed well for cavity pressure on two events, and a gas sample was obtained on one event. Similar experiments are currently planned for two future events.

INTRODUCTION

An important constraint on our underground testing of nuclear devices is that no radioactive material should escape to the atmosphere. To accomplish this, we routinely bury the device in an emplacement hole hundreds of meters deep and then backfill the hole with sand, gravel, and concrete plugs. With this procedure, radioactive material not only fails to reach the surface through the emplacement hole but usually is contained near the explosion cavity itself.

We do not fully understand the details of cavity formation, although we believe a typical cavity contains radioactive gases under pressures of up to several megapascals (tens of atmospheres) for as long as several hours following the explosion, after which the cavity collapses and forms a rubble-filled chimney. The remaining cavity gas is displaced into the rubble and migrates some distance up the chimney.

From computer simulations of how nuclear explosions affect the surrounding rock, we are learning how cavities form and how geologic materials contain the explosion-generated pressures. These studies suggest that, immediately after the cavity forms, a compressive (hoop) stress develops in the region surrounding the cavity and that the resulting ground pressures are higher than the gas pressure in the cavity.

Consequently, an important criterion for containment of underground nuclear explosions has been that there be an adequate ratio of residual hoop stress to cavity pressure. During the past decade, no cavities have vented gases to the surface immediately following a nuclear test, lending credence to the concept that a residual hoop stress higher than cavity pressure is a good criterion for containment.

To test the concept's validity, we are examining the details of how the residual hoop stress and the cavity pressure vary with time, as well as the calculational tools to predict cavity pressure and ground stress histories. For such validation, we must develop a reliable means for measuring cavity pressure history so that we can model the potential long-term threat of leakage through the stemming column and permeable overburden media.

To be of greatest benefit, the data must be valid from shortly after detonation until the cavity collapses. Also, the technique must be reliable enough to allow measurements on events with wide variations in geologic media, yield, and depth of burial. Unfortunately, few attempts to measure cavity pressure history have succeeded over the past 25 years. Furthermore, the validity of the data from supposedly successful measurements has been difficult to establish.

With these thoughts in mind, we developed and fielded a cavity-pressure-measurement experiment on the CORNUCOPIA event.

EXPERIMENT DESCRIPTION

The downhole hardware is shown schematically in Fig. 1. Electrical cables extended from a recording facility to an instrument housing buried deep in the emplacement hole (Fig. 2), but far enough from the explosion to avoid being damaged by the shock wave. The housing contained high-pressure tanks, remotely operated valves, and pressure transducers.

A set of three stainless-steel tubes, wound in the form of a helix, extended from the housing to the detonation elevation (Fig. 3). We chose a pitch of the helix that would minimize axial compression and tension along the axis of the tubes as the cavity grew and displaced the surrounding rock. In addition, each tube was filled with water to prevent collapse from the high stresses in the ground shock wave.

Within the instrument package, each water-filled tube was connected to a high-pressure tank filled with dry nitrogen at about 12,000 psia. Each of the

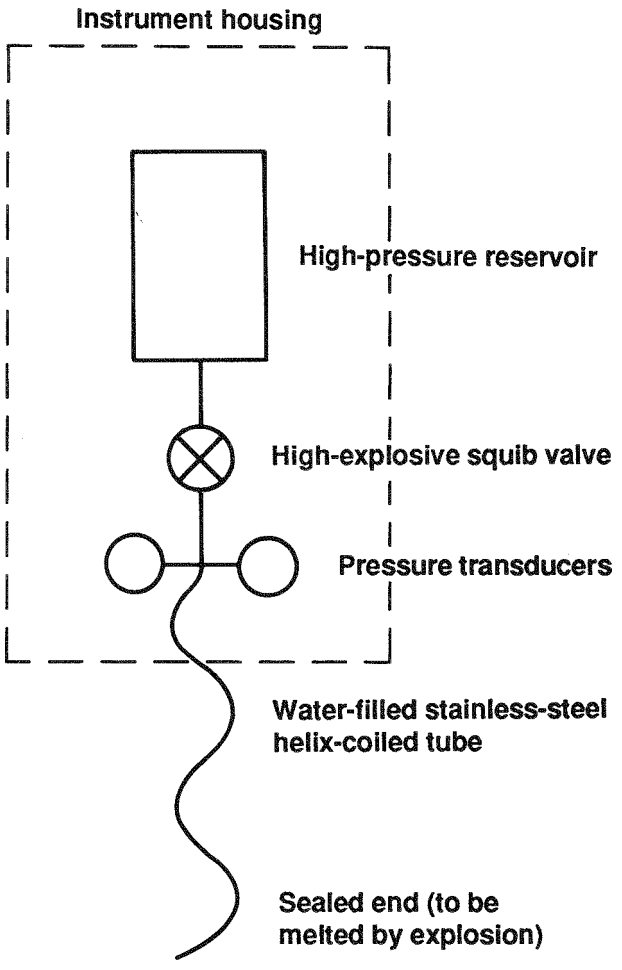

Figure 1. Schematic diagram of the apparatus (one of three) used for measuring cavity pressure.

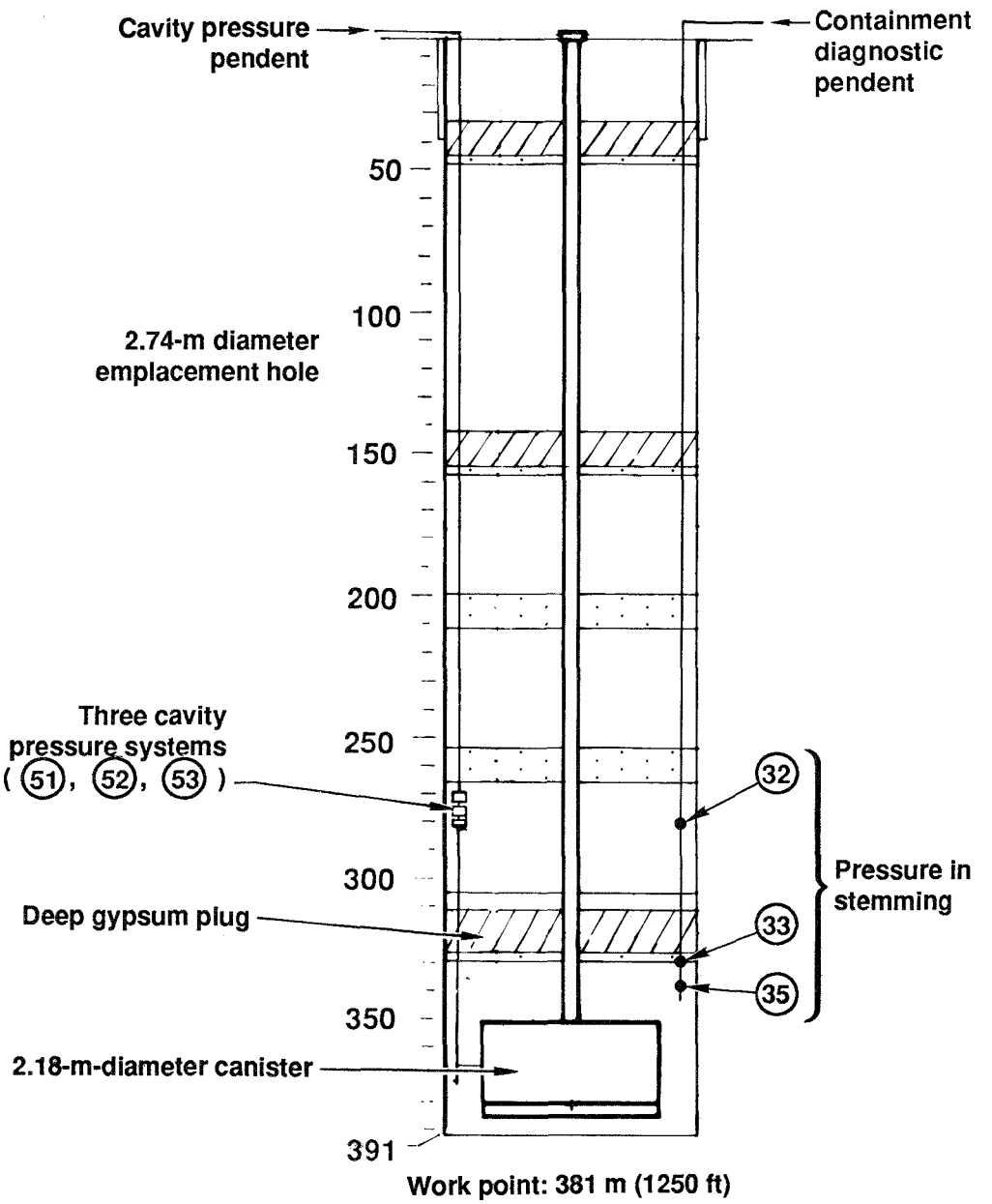

Figure 2. Stemming plan and major instrument locations for CORNUCOPIA.

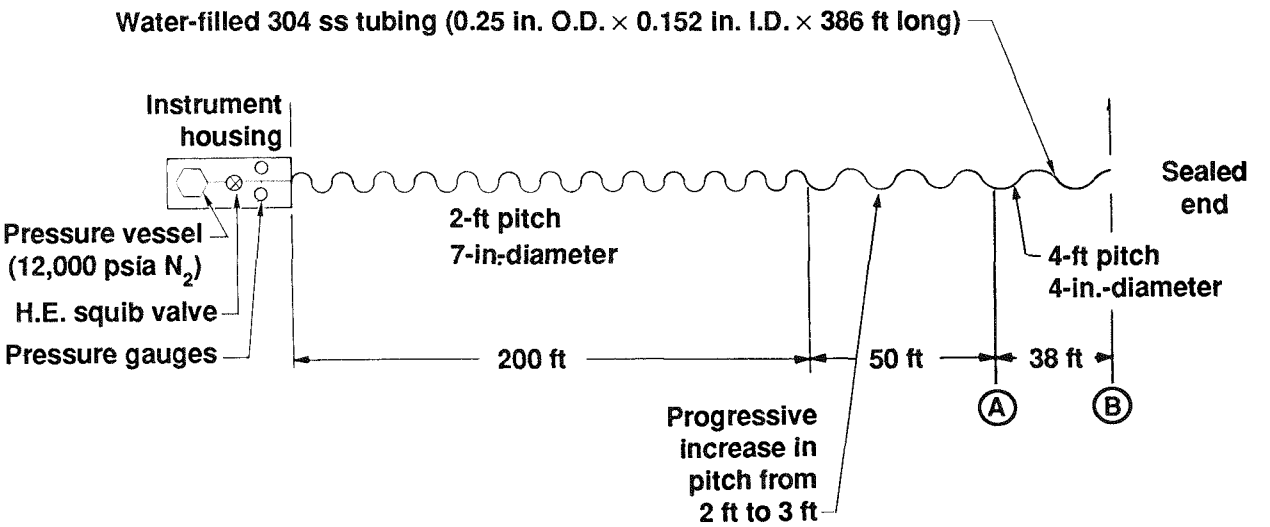

Figure 3. As-built cavity-pressure instrumentation geometry.

tube systems was fitted with two pressure gauges. A few seconds before the detonation, explosively driven valves opened to pressurize the water-filled tubes. Shortly after detonation, the strong shock wave vaporized or melted the end of each tube, letting the high-pressure nitrogen blow the water into the cavity and leaving the tube open to equilibrate with the pressure of the gases in the cavity.

RESULTS

Figure 4 shows the first 10 s of the measured pressure history from Validyne DP-360 gauges, which have a system range of 20,000 psia on each of the three systems. These data show that the squib valve opened at about -5 s, and system pressurization varied from 10,700 to 11,400 psia. All three gauges appear to have suffered a permanent offset in pressure at or shortly after zero time. Figure 5 shows the first minute of the pressure history as obtained from three Well Test 15k-006 gauges on each of the three systems, which can measure pressure up to 18,000 psia. These gauges converted a pressure value to a frequency output of around 40 kHz with a corresponding repeatability of 0.05% of full scale (~9 psia at 18,000 psia). Unfortunately, on CORNUCOPIA we were able to sample the pressure signal only about once every 3 s for each of the three data channels. Consequently, neither the time of valve opening nor the peak prezero pressure is accurately represented by these gauges.

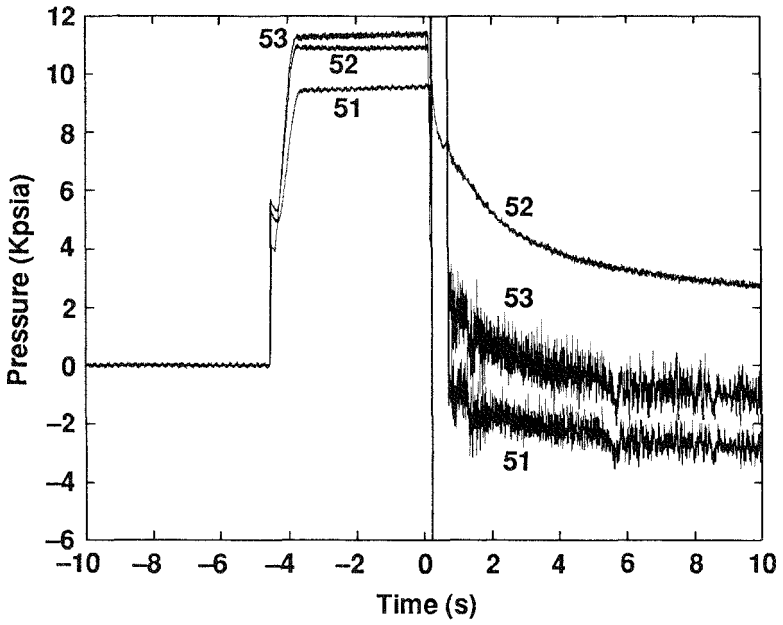

Figure 4. Early CORNUCOPIA pressure history taken from Validyne gauges.

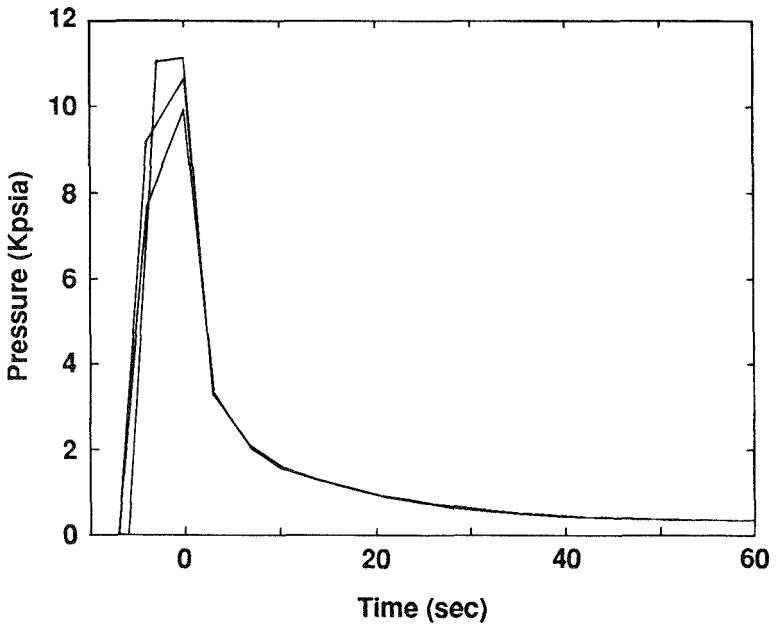

Figure 5. Early CORNUCOPIA pressure history taken from Well Test gauges.

Figure 6 shows the pressure data from the three Well Test gauges until collapse at about 9 h. Figure 7 shows the CORNUCOPIA cavity pressure data compared with other pressure measurements immediately above and below the deep gypsum plug (Fig. 2). These data show no significant pressure above the deep gypsum plug and indicate that the highest pressures are from deep in the emplacement hole, adding to our confidence that these data reflect the cavity pressure history.

At early times, the high-pressure nitrogen bottles are blowing down through the tubes that were originally filled with water, so the measured pressure is not identical to cavity pressure. To estimate the equilibration time of the pressure measurement system, a series of numerical calculations were executed at S-CUBED using the TOPAZ code.[1] This code simulates the process in which the high-pressure nitrogen flows from the reservoir through the valves and tubing, displacing the water that initially occupied the

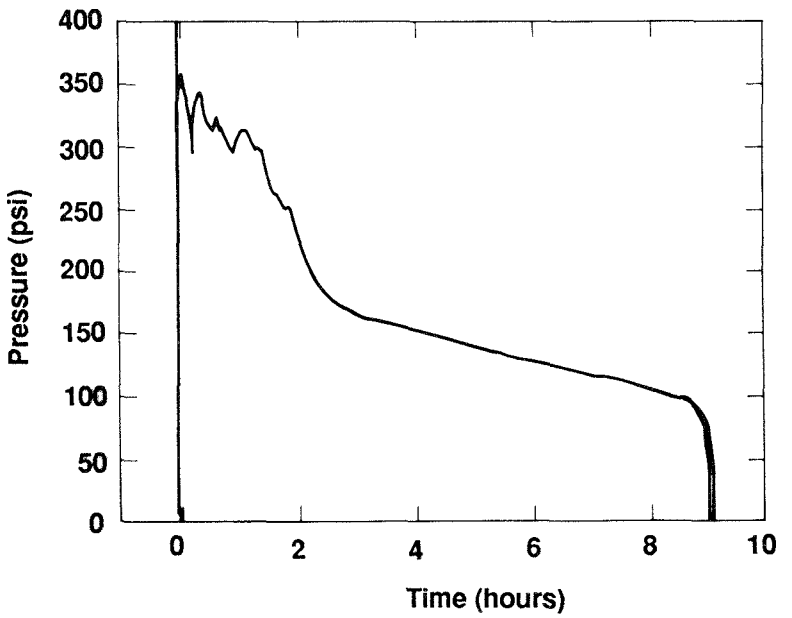

Figure 6. Complete pressure history of the CORNUCOPIA event cavity, from the explosion to cavity collapse about 9 h later. The increased rate of pressure drop in the minutes before collapse strongly suggests that reduced cavity pressure brought on, rather than resulted from, cavity collapse.

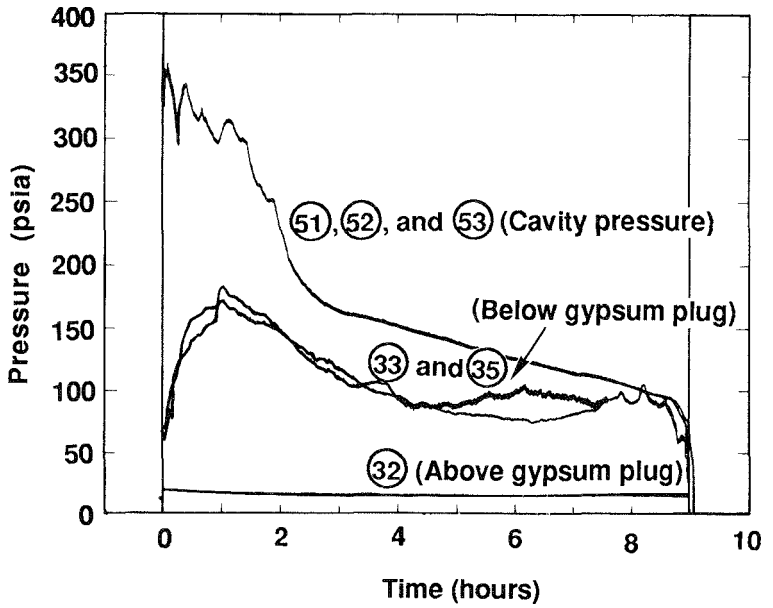

Figure 7. A comparison of pressure data from the steel capillary tubes with pressures measured higher in the stemming column.

lines. Figures 8 and 9 show TOPAZ predictions compared to CORNUCOPIA data. The results indicate that, for a constant cavity pressure of 25 bars, equilibrium would have occurred within 15-20 s. Similar calculations at SEA,[2] using the SEA code developed there, gave comparable results. Three different TOPAZ calculations corresponding to three different values of back pressure at the outlet of the tube (1450, 290, and 14.5 psi) are indicated by solid lines in Fig. 10. Superimposed on the calculational results are the three sets of experimental data that were observed on the MISSION GHOST, CORNUCOPIA, and HAZEBROOK events. All three sets of data appear to follow nearly the same curve to the pressure level at which they individually turn away onto a slower decay path, which is different for each event. Construction parameters of the measurement systems, initial reservoir pressures, and method of initiation differed for each event. Rather than emphasizing these differences, these plots suggest that all of the data sets are consistent with one another, with numerical models, and with an equilibration time of 10 s or more, depending on the pressure in the cavity. It seems likely that the CORNUCOPIA measurement system was in at least quasi-equilibrium at 20 s, with a cavity pressure equal to that of lithostatic overburden (70 bars). However, we cannot rule out the possibility of

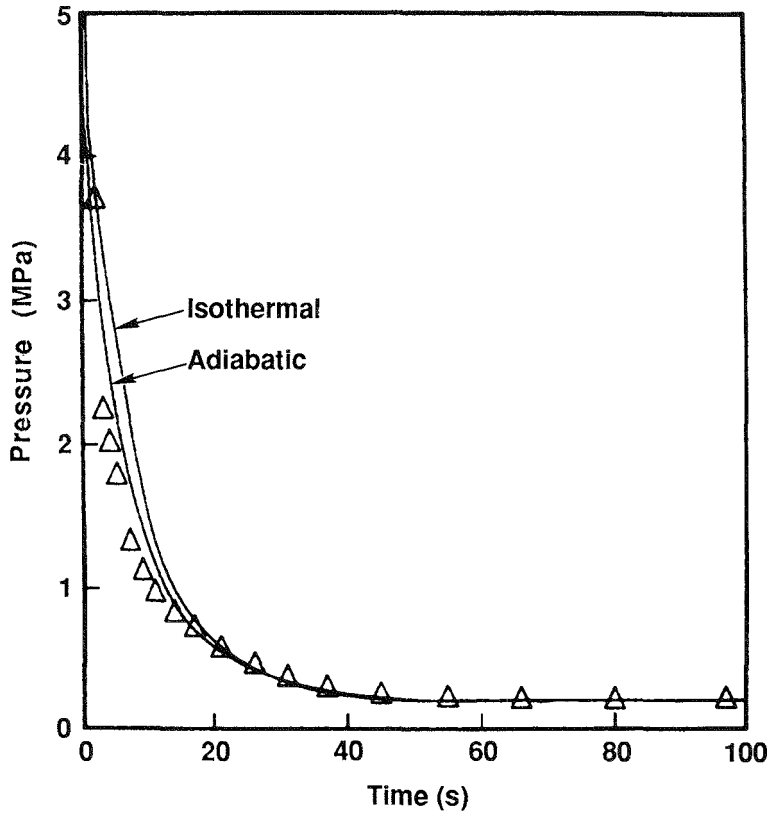

Figure 8. A comparison of blow-down pressure predicted by TOPAZ with data taken from CORNUCOPIA.

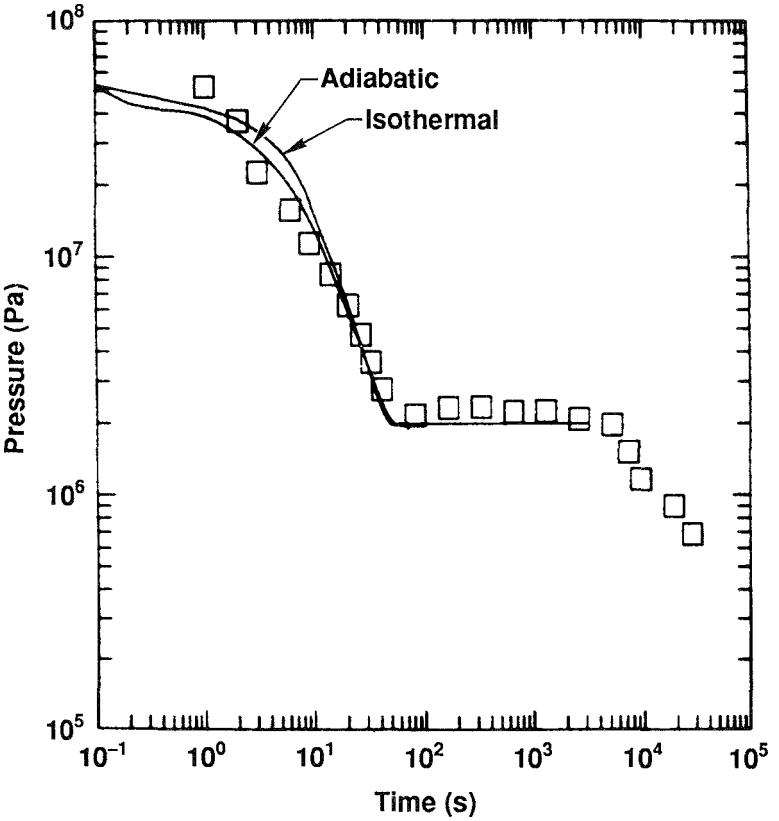

Figure 9. A comparison of blow-down pressure predicted by TOPAZ with data taken from CORNUCOPIA.

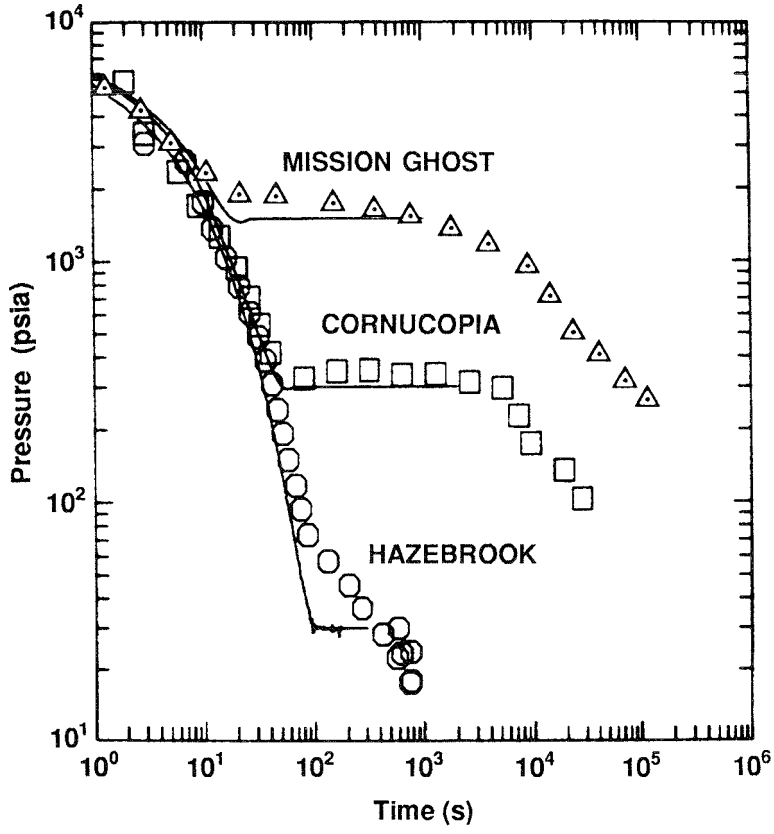

Figure 10. A comparison of three TOPAZ calculations, assuming different back pressures, with cavity pressure histories obtained from MISSION GHOST, CORNUCOPIA, and HAZEBROOK.

equilibrium being reached as late as 50 s, with a pressure (25 bars) that has been essentially constant since the end of cavity growth.

In addition, because we have no direct knowledge of how the tube pressures are coupled with the cavity pressure, we cannot rule out the possibility of the "true" cavity pressure being considerably higher than measured. However, if this were the case, we would expect greater similarity between the "cavity pressure" data and that observed somewhat higher in the stemming (Fig. 7).

DATA INTERPRETATION

A log-log plot of the CORNUCOPIA pressure data (Fig. 11) suggests three stages of pressure decay. The first stage, which extends to about 50 s, involves a rapid pressure decrease to a plateau value of less than half lithostatic overburden pressure. As discussed above, this stage involves the blowdown of the measurement system as well as the cavity pressure history.

The second stage includes the plateau with very little pressure change extending from about 50 s to 1 h. The third stage involves a monotonic pressure decrease extending from about 1 h until collapse at about 9 h.

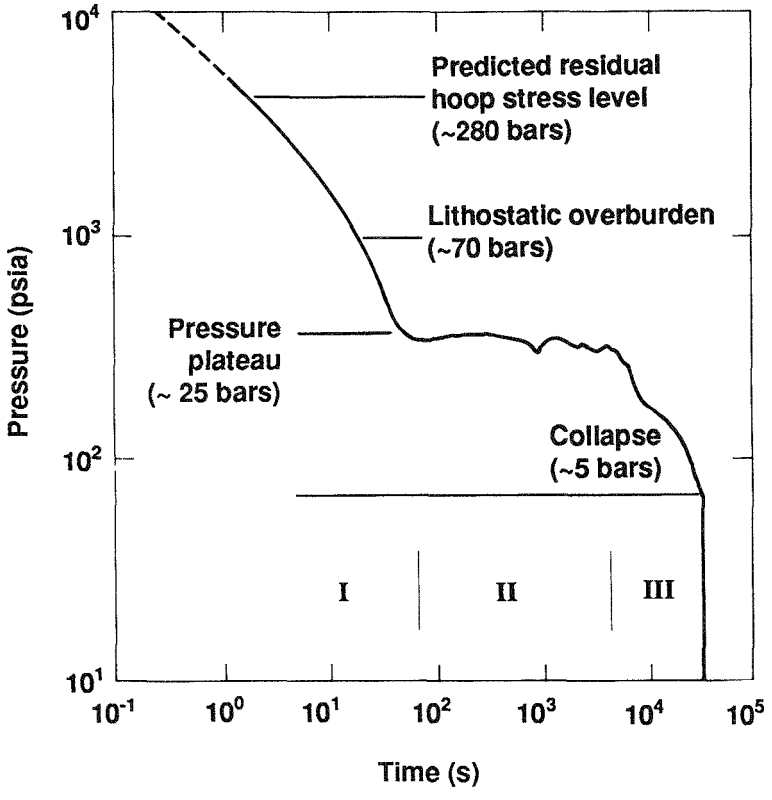

Figure 11. A log-log plot of the CORNUCOPIA cavity-pressure history, suggesting three stages of pressure decay. Stage I includes a pressure decay from above to well below overburden pressure. Stage II pressure is almost steady at about 20 bars. Stage III includes a monotonic pressure decay from the end of Stage II until collapse.

We believe that the observed pressure history is the collective result of these physical mechanisms:

1. Early-time cavity growth.
2. Mixing of wall material into the cavity.
3. Conductive heat transfer.
4. Darcian seepage.
5. Hydrofracture.

To understand the possible roles of these mechanisms, let us first examine each mechanism separately.

The effects of the various cavity cooling and leakage mechanisms can be understood in terms of:

$$P = (\gamma - 1) \frac{E}{V} \quad (1)$$

and

$$T = \frac{(\gamma - 1)}{R} \frac{E}{M} \quad . \quad (2)$$

Both are applicable to a so-called γ-law gas, where P = pressure, T = temperature, E = total energy in cavity, M = total mass, V = cavity volume, R = gas constant, and $\gamma = c_p/c_v$ is the ratio of specific heats at constant pressure and constant volume. Thus, pressure is basically a measure of energy per unit volume, and temperature is a measure of energy per unit mass. Although we do not use these equations directly in the upcoming analysis, they illustrate the way in which pressure and temperature can be altered by changes in the mass and energy contained within the cavity.

Early-Time Cavity Growth and Cavity Pressure

The early cavity growth and ground-motion phase of an event determines the initial conditions for the evolution of the cavity pressure. The volume of the cavity and the amount of energy remaining within the cavity depend on the yield of the device, burial depth, and properties of the surrounding geologic media. For a given class of media, calculations based on the results of previous measurements of cavity radius and ground motion suggest the approximate relationships:

$$R = 70\ W^{1/3}\ \rho H^{-1/4} \quad (3)$$

and

$$E = 0.33\ W \quad , \quad (4)$$

where R = cavity radius in meters, W = yield in kt, H = burial depth in meters, ρ = density, and E = energy remaining in the cavity after early cavity growth is completed.

Given these estimates of the cavity size and energy, and assuming that the amount of rock vaporized by the explosion is 70 tonnes/kt, the pressure in the newly formed CORNUCOPIA cavity would be about 108 bars (1620 psi). This value

is about 50% greater than the lithostatic overburden pressure (70 bars) and more than four times the measured plateau pressure.*

Mixing of Wall Material into the Cavity

The variation in temperature and pressure, as a function of mass addition (as predicted by the S-CUBED Cavity Cooling Code) is illustrated in Fig. 12. Given the cavity volume and energy predicted by Eqs. (3) and (4) and the composition of the rock, it is possible to calculate the pressure and temperature using the CHEST-24 equation of state of a rock/water mixture[4,5]. The results, which assume a water content of 17%, are shown in Fig. 12.

The process of adding mass always reduces the temperature, as shown by Eq. (2). However, what happens to the pressure is not as obvious. At very high temperatures, all of the energy is translational kinetic energy of the molecules, which results in a relatively large γ (approximately 5/3) and, hence, high pressures (Eq. 1). As the temperature falls, polyatomic molecules form, internal energy storage modes become available and the pressure decreases, even though the energy per unit volume remains nearly the same. However, for mass added over the first 70 tonnes/kt, very little pressure reduction occurs with added mass. In fact, the Cavity Cooling Code calculations suggest that the pressure will actually rise somewhat when the rock vapor is condensing and as energy is transferred from low-γ rock vapor to high-γ steam vapor.

Mass is assumed to be mixed into the cavity in two principal ways. First, the shock wave and the rock deformation cause sufficient energy deposition to induce vaporization, melting, and spalling ablation. Second, because the initial cavity gas temperature is well above the wall temperature, additional energy will be transferred to the wall, resulting in rock pore pressures

---

*In an independent calculation using the LLNL TENSOR code, John Rambo[3] predicted a cavity pressure of 70 bars. Rambo's calculation included an assumed "effective" shear strength of 119 bars. The 25-bar measured pressure would be consistent with an "effective" shear strength of about 20 bars, a value that would appear to be inconsistent with other physical properties at the CORNUCOPIA site.

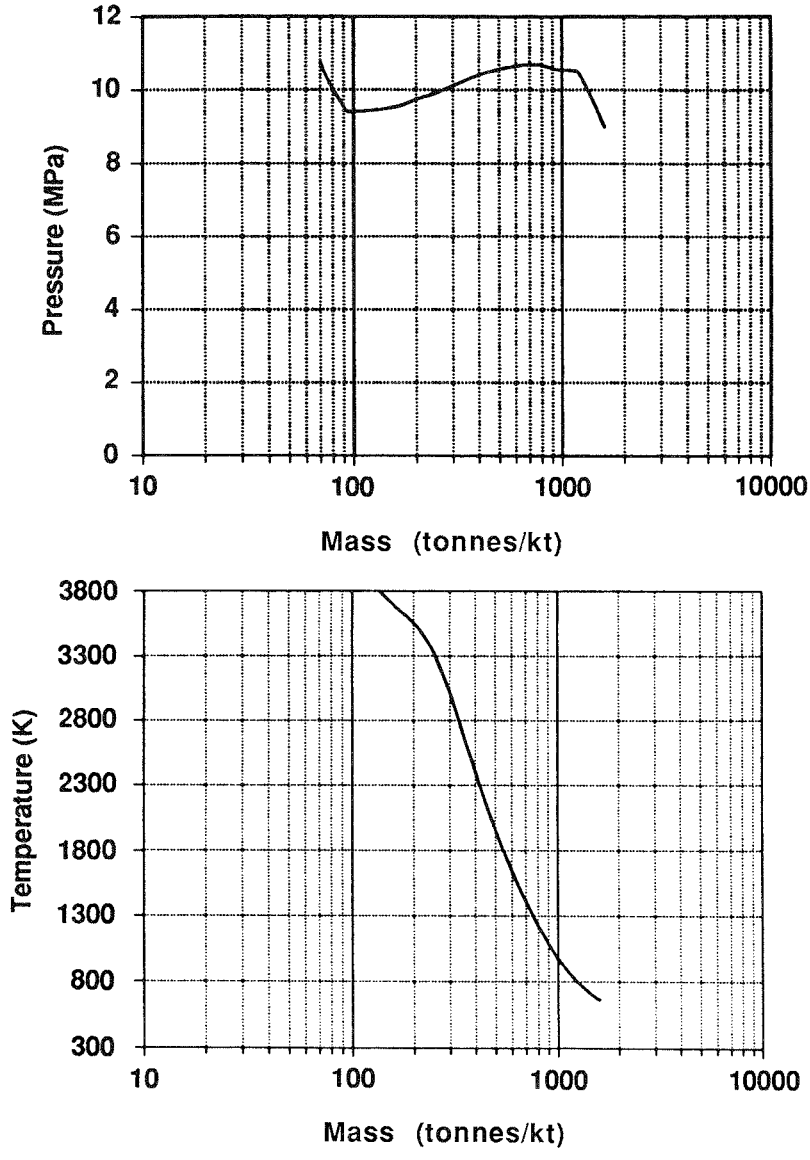

Figure 12. Pressure and temperature in a cavity as a function of the amount of wall material that has mixed into the cavity by vaporization and ablation.

higher than cavity pressure. Some milestones in this ablation and mixing sequence are:

- A mass of 70 tonnes/kt promptly vaporizes in the explosion.
- A mass of 140 tonnes/kt will lower the cavity temperature to the rock vaporization temperature (about 3800 K). The addition of more mass then causes rock vapor to condense within the cavity.
- A mass of 400–700 tonnes/kt includes all of the mass that has been shock-heated to an energy level high enough to cause the rock to melt. We expect this mass to be injected promptly into the cavity.
- A mass of about 1500 tonnes/kt includes all of the wall material that has been either melted or shock-heated to an energy level such that the pressure of the water vapor in the rock pores is greater than the cavity pressure. This much material can be "spalled" into the cavity by "popcorning" ablation, during the first few seconds after cavity formation.
- An additional mass of 1600 tonnes/kt could be "spalled" into the cavity by ablation as heat is transferred from the cavity gas to the walls.

We cannot state with certainty how much mass will be mixed into the cavity by these mechanisms, or how long the various processes will take. We believe the shock-related processes are essentially instantaneous, but the total heat transfer process could continue adding mass for hours.

The time scale of thermally induced mass addition depends on two considerations: the rate at which energy is transferred from the cavity gas to the wall and the amount of energy required to remove each increment of mass from the wall. Figure 13 shows the pressure and temperature vs time (instead of mass) for an ablative process that is limited by the rate of radiative and convective heat transfer. It is assumed that the energy absorbed by the wall is used to remove or ablate wall material. Depending upon the wall temperature, the removal energy is assumed to be the amount required to vaporize or melt the rock, or elevate the pore pressure of the rock above the cavity pressure. The calculation begins with only 70 tonnes/kt of vaporized rock within the cavity; the wall material remains in a cold state. The results suggest that, in the absence of shock-induced ablation, tens of seconds are required to drop the temperature below that required for vaporization (~3600 K), while hundreds of seconds are required to drop the temperature below that required for melting (~1400 K). Alternatively, the

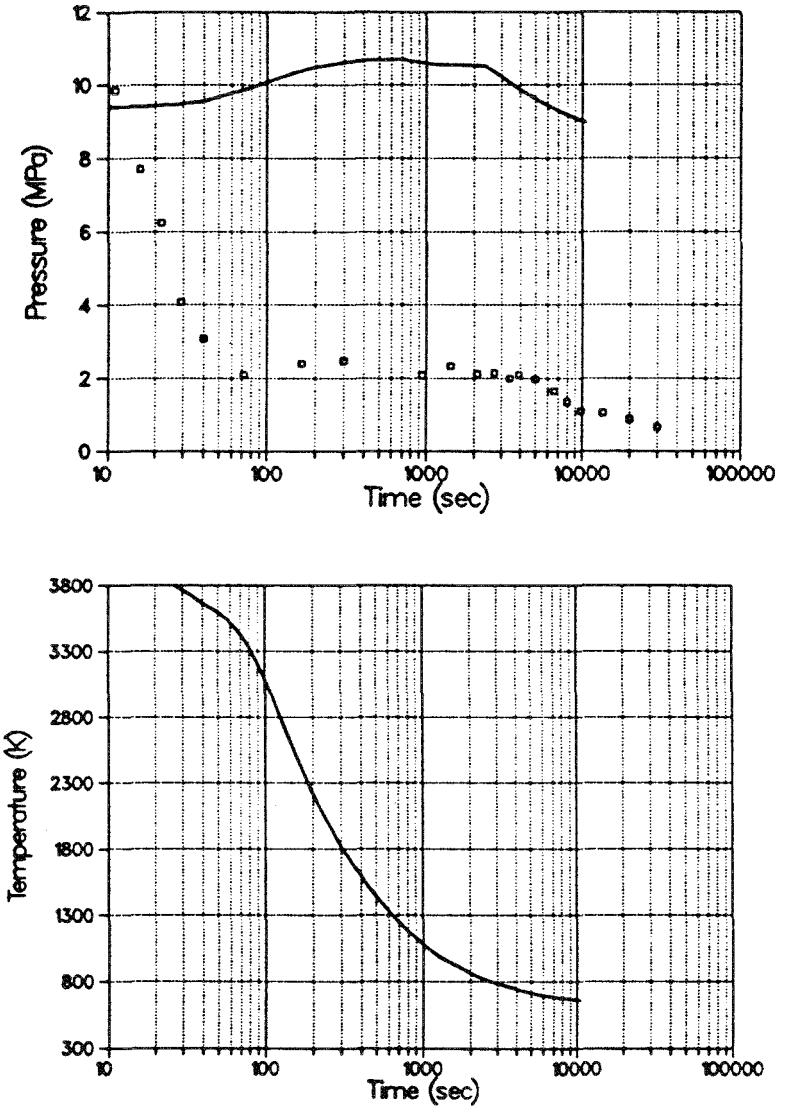

Figure 13. Pressure and temperature in the cavity during ablation and mixing compared with CORNUCOPIA pressure history.

injection of melted and shock-heated material may be instantaneous, as we will assume in subsequent discussion. However, this material may not be in immediate equilibrium with higher temperature material in the cavity.

Most importantly, these results (Figs. 12 and 13) show that very little pressure reduction is associated with mass additions ranging from 70 to 2000 tonnes/kt. Eventually, the process of mass addition lowers the temperature to a point at which the steam begins to condense and the pressure again begins to fall.

The buffered level, or plateau, of the cavity pressure, as determined by the mixing processes, is about 95 bars. This pressure is well above the

25-bar pressure plateau observed on CORNUCOPIA, suggesting that other physical processes must have been involved. The pressure levels associated with a mass addition process depend on the degree to which thermal equilibrium is maintained within the cavity; all of the calculations presented here assume that there is temperature equilibrium between the liquid and vapor phases in the cavity. Thus, cavity pressures would be higher if the gas were hotter than the liquid and vice versa. But the pressure differences predicted by reasonable models of this situation do not explain the discrepancy between that observed on CORNUCOPIA at 50 s and that predicted at the end of dynamic cavity growth.

Conduction Heat Transfer

Heat conduction into the surrounding wall rock reduces the energy within the cavity, which, in turn, reduces both the temperature and pressure in agreement with Eqs. (1) and (2). Figure 14 illustrates the calculated time-history of pressure decay that would occur by conduction alone. The starting point for this calculation is the melt temperature of the rock, 1400 K, which corresponds to a pressure of about 70 bars (lithostatic overburden) and a mass of about 700 tonnes/kt in the cavity. No additional mass was mixed into the cavity.

The time scale of the calculated pressure decay is roughly in agreement with CORNUCOPIA measurements, but the pressure level is clearly too high and the observed plateau is not indicated by the calculation.

Darcian Seepage

The energy and mass density within the cavity are probably reduced by Darcian seepage into the surrounding rock. The calculational results in Fig. 15 show both conduction heat transfer and Darcian seepage for a rock permeability of 1 mD. The pressure levels are reduced by the outflow of mass, which carries with it some of the cavity energy. But pressures are still too high at early and intermediate times, the plateau is absent, and the shape is wrong for Darcian seepage to entirely explain the pressure history. During Stage II, Darcian leakage may, in fact, be precluded by the rock pore pressure being higher than cavity pressure.

Different values of permeability are certainly plausible, that is, permeability could be smaller than 1 mD because of shock compression. Conversely, shock-induced fractures could substantially increase the

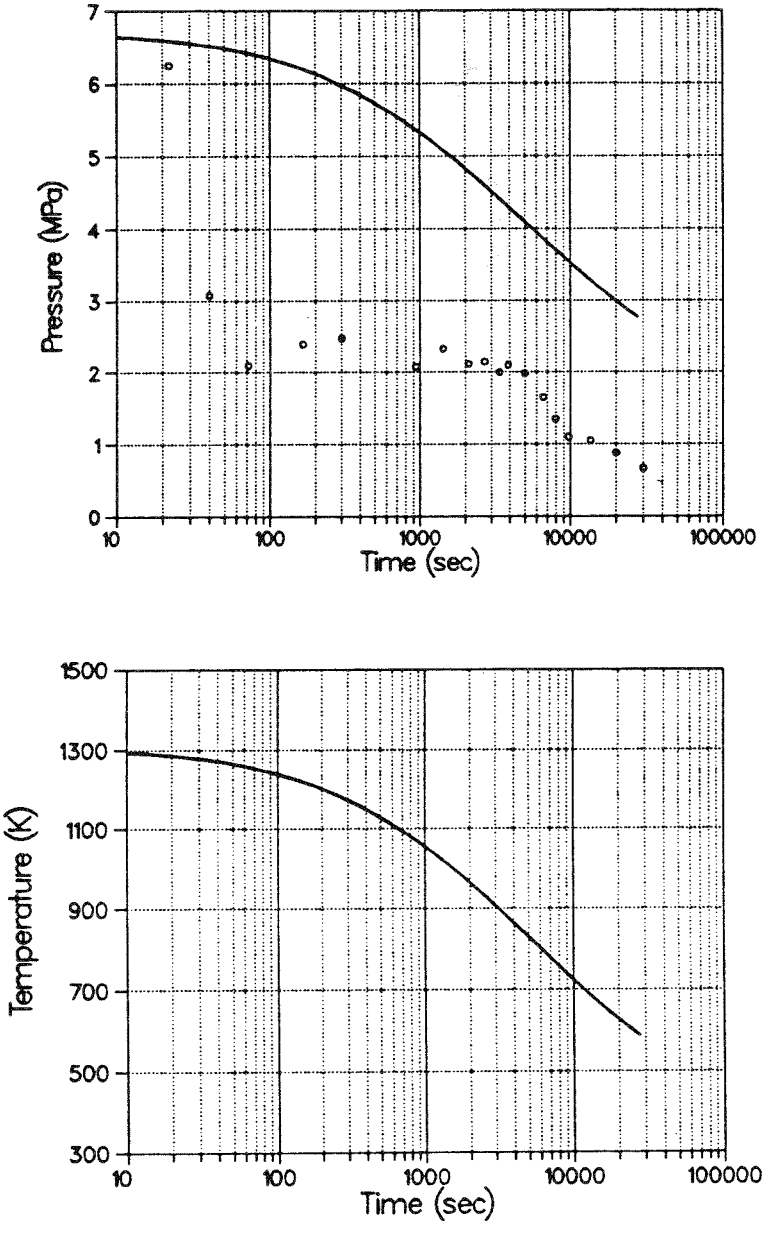

Figure 14. Pressure and temperature decay caused by conduction heat transfer into the surrounding rock, starting from the melt temperature with 700 tonnes/kt.

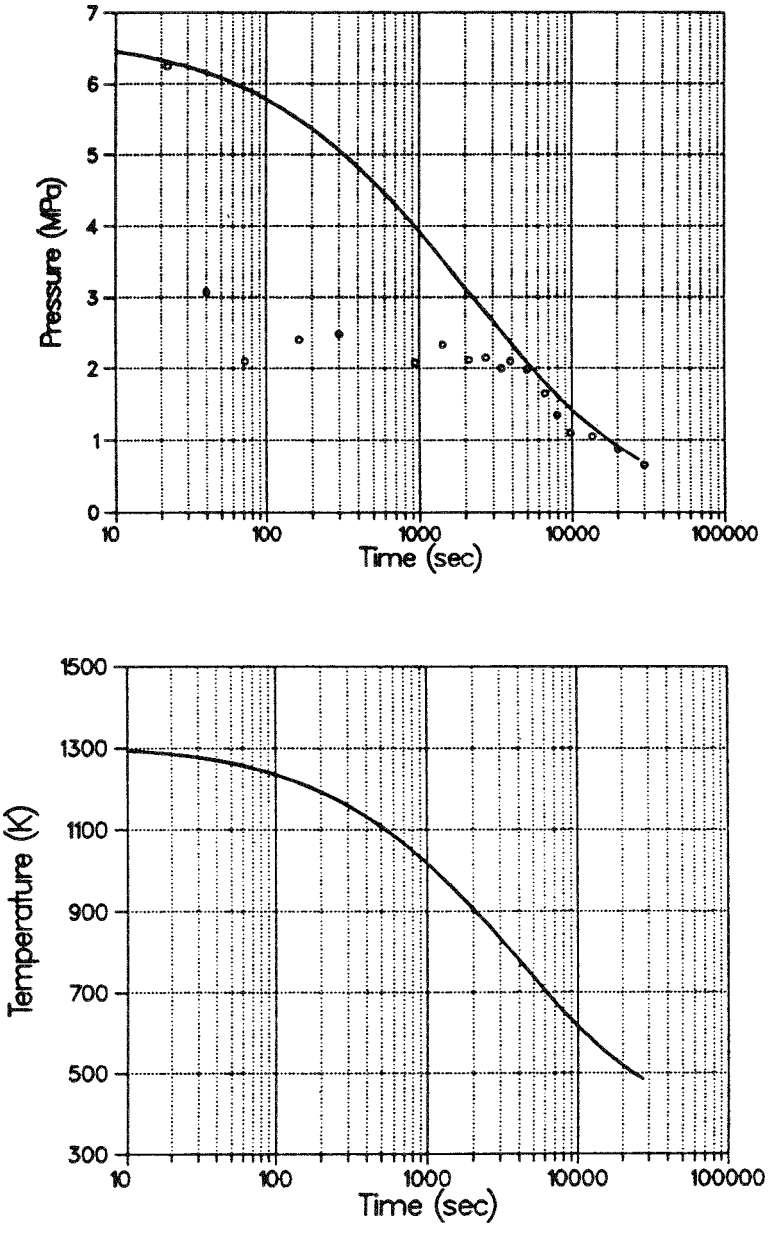

Figure 15. Pressure and temperature decay caused by heat conduction and Darcian seepage (k = 1 mD) starting with 700 tonnes/kt in the cavity.

permeability. But a change in the magnitude of permeability would alter only the time scale of the plot; it would not explain a sharp drop in pressure followed by a long plateau or the plateau by itself.

Fluid leaking out of the cavity could certainly reduce the cavity pressure to the level observed on CORNUCOPIA, but the leakage would have had to occur very rapidly at early times and then shut off very abruptly at the observed plateau.

Hydrofracture

The hypothesis that hydrofractures occur at relatively early times offers an explanation for the initial pressure observed on CORNUCOPIA. Based on an overburden pressure of 70 bars at the burial depth of CORNUCOPIA, the local minimum in situ stress acting in a horizontal direction is approximately 25 bars. If the peak residual hoop stress (140 bars) predicted by using the TENSOR code[3] was not achieved, or if it decayed rapidly, hydrofracture would be a viable mechanism for allowing the cavity pressure to drop to the observed plateau level.

The results presented in Fig. 16 indicate that the time scale for pressure decay from hydrofracture is on the order of seconds to tens of seconds,

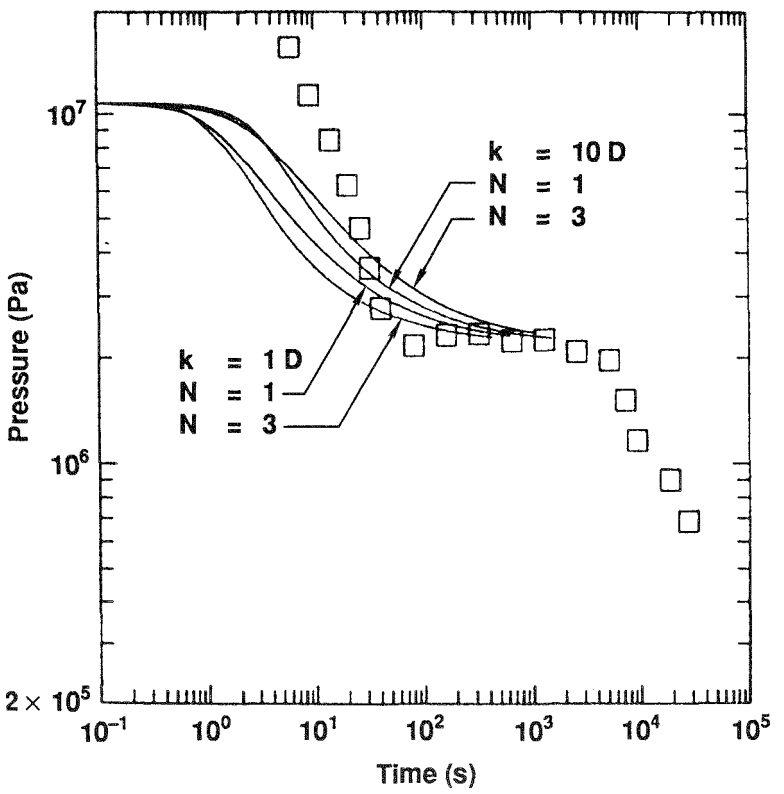

Figure 16. Pressure decay caused by hydrofactures beginning at zero time.

depending on the assumptions concerning numbers of fractures and permeability of the rock. Also, the corresponding fracture lengths in Fig. 17 appear to be within reasonable bounds. Figures 18 and 19 show comparable results assuming hydrofracture to begin at 10 s instead of zero time. These results were obtained using the FAST hydrofracture code[6,7] with the input data given in Table 1. Steam condensation was taken into account using the methodology described in Reference 4. Relatively high permeabilities are plausible in light of recent field data collected by LLNL on preexisting or shock-induced fractures.

The presence of hydrofractures might help explain the nearly cyclic pressure rises and falls that are superimposed on the base line of the plateau (Fig. 20). Mass additions (water) would drive the pressure up, while hydrofracture could act as a pressure-relief valve to prevent a rise substantially above the confining stress.

Composite Model

A review of the results from individual pressure-related mechanisms described above indicates that no single mechanism can explain the measured pressure history. Thus, we have developed a composite model, illustrated by Fig. 21, which includes the following sequence:

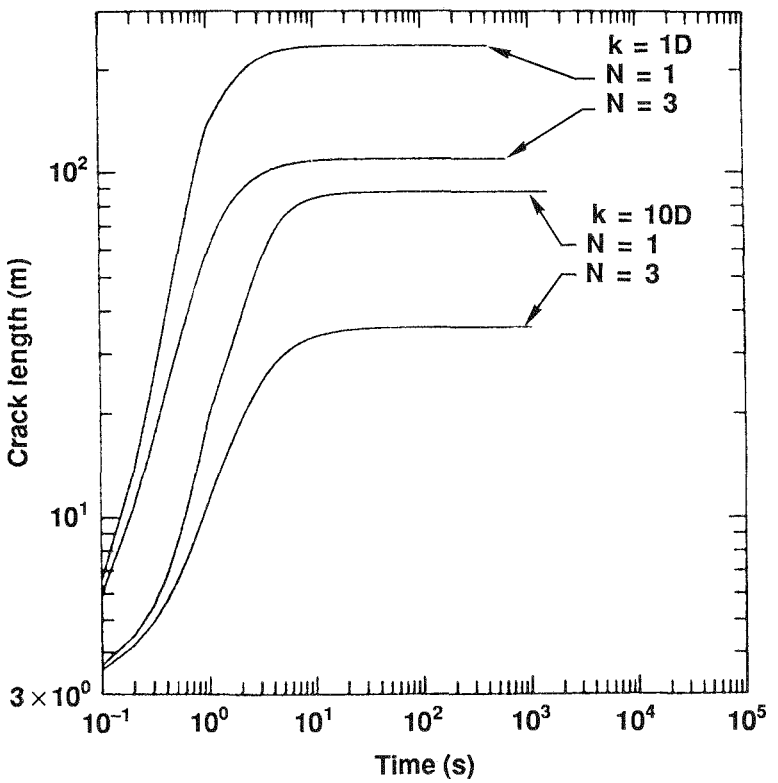

Figure 17. Fracture growth resulting from hydrofactures initiated at zero time. The number of fractures is indicated by N.

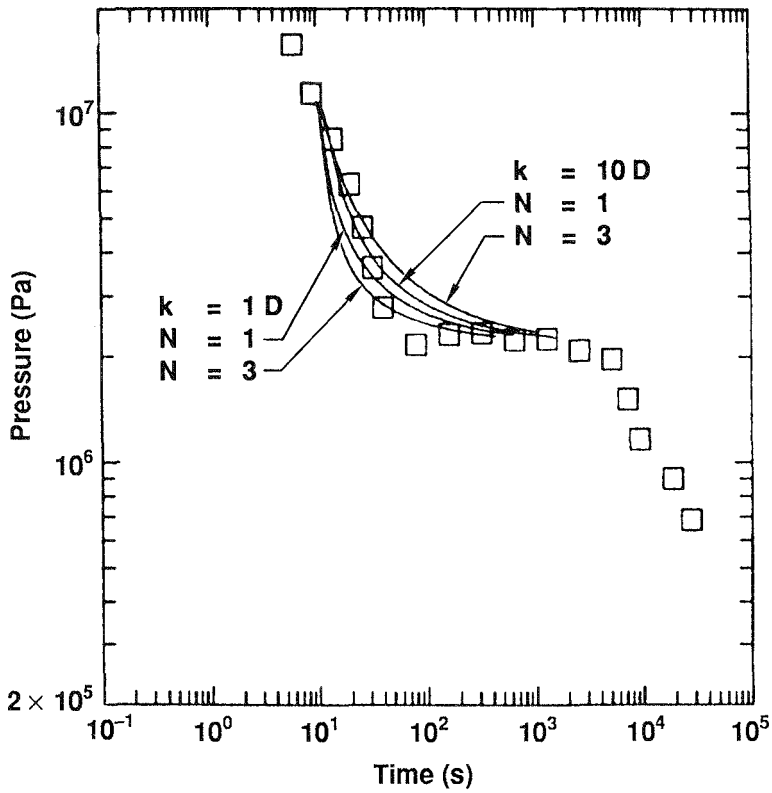

Figure 18. Pressure decay caused by hydrofractures initiated at 10 s.

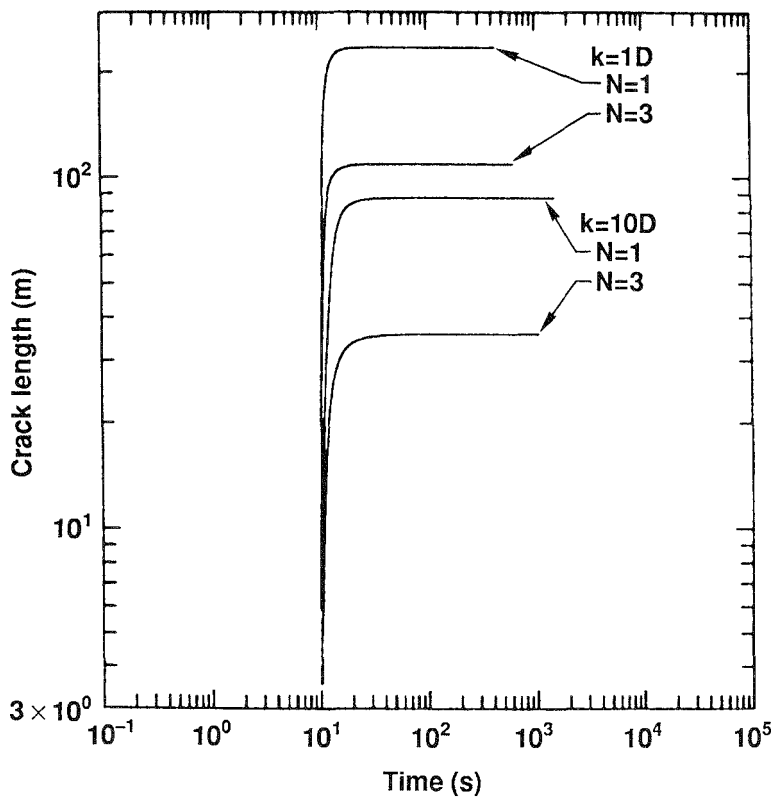

Figure 19. Fracture growth into surrounding rock resulting from hydrofracture initiated at 10 s.

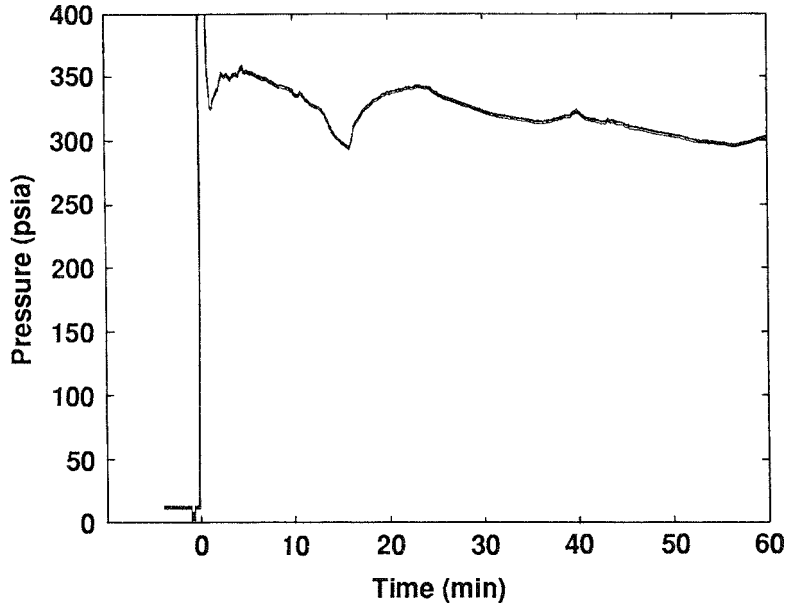

Figure 20. Cavity pressure variations during the first hour. Pressure rises are probably caused by water addition; falls are probably caused by heat conduction into the walls; and early upper limits may be controlled by hydrofracture.

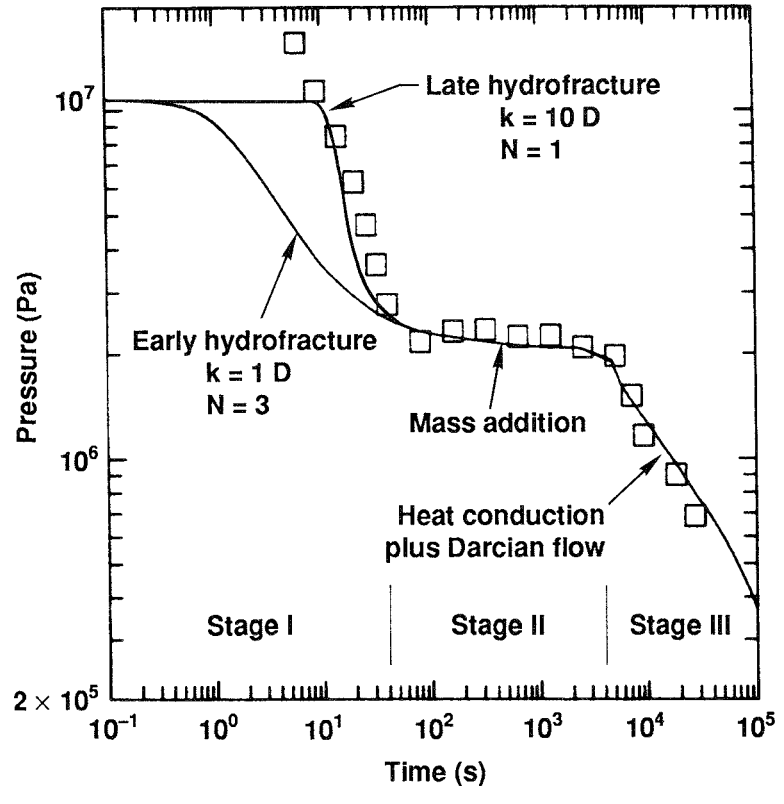

Figure 21. Composite model of CORNUCOPIA pressure decay includes hydrofracture, followed by ablative mixing and conduction cooling and Darcian flow.

- Rapid vaporization of 70 tonnes/kt and cavity growth could produce an initial pressure of over 100 bars at the temperature required to vaporize rock.
- Hydrofracture could allow the pressure to drop to about 25 bars within tens of seconds (Stage I). The temperature (i.e., energy per unit mass) would not be significantly affected by the outflow of gas.
- Mass addition from heat transfer and wall ablation could provide an additional 1600 tonnes/kt or more to be injected into the cavity material over a period of 1000's of seconds (Stage II), causing the temperature to drop to well below the melting point of rock (~1400 K) with little pressure change.
- Heat conduction could cool the steam vapor from 1400 K to 300 K with a commensurate fall in pressure while Darcian flow could reduce the pressure further (Stage III).

The first two steps in the sequence were calculated sequentially. The last two were calculated simultaneously, starting from the end-state of the hydrofracture, using a permeability of 1 mD for Darcian seepage.

The pressure plateau is the key feature that dictates the ingredients of the composite model. Other explanations are certainly possible, but a composite model is consistent with many qualitative and quantitative features of the data.

In summary, analysis of the CORNUCOPIA cavity pressure history leads us to suggest a three-stage model for pressure decay:

Table 1. Material property data.

Properties	Values	
Rock		
Shear modulus (GPa)	2.0	
Poisson's ratio	0.25	
Fracture toughness (MPa m)	1.0	
Porosity (%)	0.10	
Water saturation (%)	30	
Gas permeability (m^2)	1×10^{-12}	
Thermal conductivity (J/K-m-s)	2.0	
Thermal diffusivity (m^2/s)	5×10^{-6}	
Grain size (μm)	400	
Fluid properties	Steam	Air
Mass fraction	0.9	0.1
Molecular weight	18	28
Specific heat ratio	1.4	1.4
Latent heat (MJ/kg)	2.0	0.0
Viscosity (ns/m^2) (proportional to $T^{1/2}$)	2×10^{-5}	2×10^{-5}

Stage I--Initial pressure is either much lower than predicted, or hydrofracture allows the initial cavity pressure to drop to that controlled by non-event-related confining stresses within a very short time (about 50 s on CORNUCOPIA).

Stage II--Mass addition combined with additional hyrdrofractures maintains a nearly constant pressure for a relatively long period (about 1 h on CORNUCOP A) while the temperatures drop to near the melting point of rock (~1400 K).

Stage III--Heat conduction and Darcian flow out of the cavity cause a monotonic pressure decay until collapse.

Further Observations

Cavity pressure data obtained from MISSION GHOST and a comparison of MISSION GHOST and CORNUCOPIA pressure histories are presented in Figs. 22 and 23. The differences in pressure levels between the two events are probably due to differences in emplacement depth and media: CORNUCOPIA was detonated in unsaturated aluvium at 381 m depth, whereas MISSION GHOST was detonated in saturated tuff at 321 m. In addition, the CORNUCOPIA cavity had a volume much larger than that of MISSION GHOST. In spite of these differences, the measured pressure decay of both events appears to occur in three fairly distinct stages: the first dominated by the blowdown of the measurement system and perhaps hydrofracture, the second by mass addition, and the third by heat conduction and Darcian flow into the cavity wall.

As indicated in the introduction, an important reason for determining cavity pressure history is to the validate the residual stress-to-cavity pressure ratio as a viable criterion for containment. For CORNUCOPIA, we have concluded that either the initial cavity pressure was much lower than predicted, or hydrofracture allowed a significant flow of gas from the cavity within the first 50 s. A low initial pressure suggests a serious lack of understanding about the dynamics of cavity growth; an early pressure decay suggests that the predicted residual stress was not effective in controlling hydrofracture.

The MISSION GHOST data, on the other hand, suggest residual stress produced by the explosion on that event may have been effective for a significant period of time. The result was a much higher plateau pressure than observed on CORNUCOPIA and, consequently, a much greater challenge to the

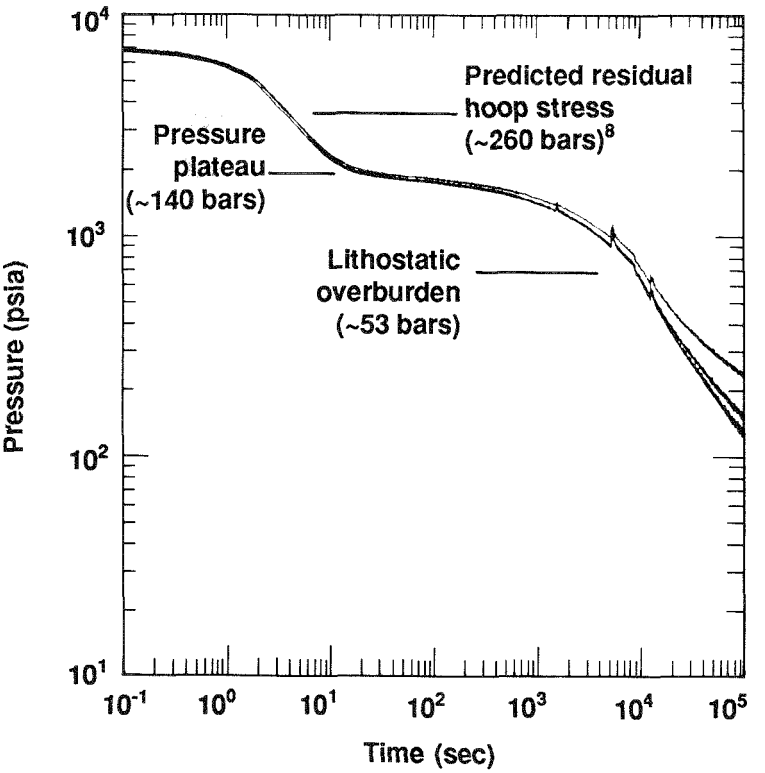

Figure 22. The cavity pressure history observed on MISSION GHOST. Pressure perturbations between 10^3 and 10^4 s are related to gas sampling operations.

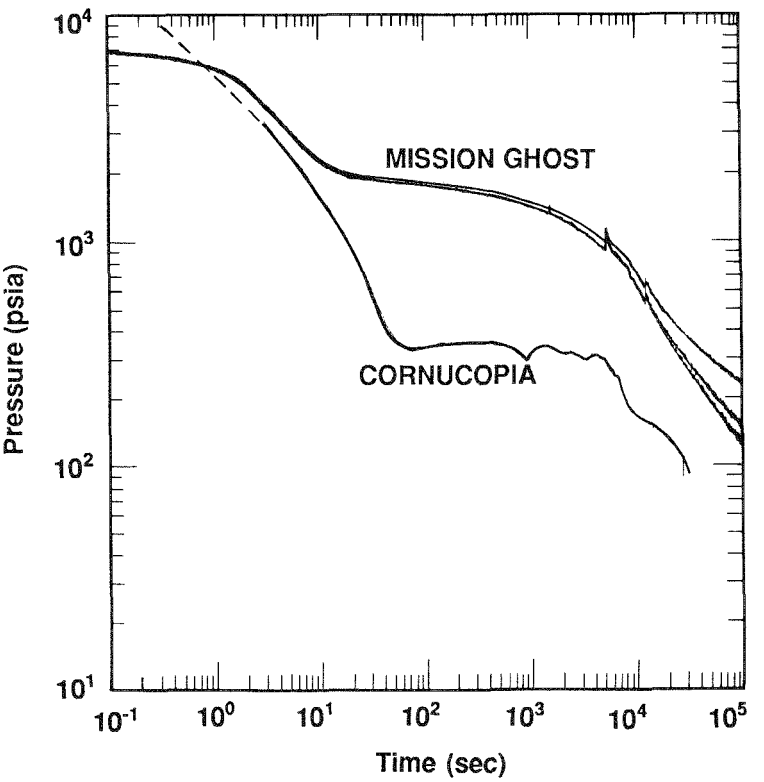

Figure 23. The MISSION GHOST cavity pressure appears to have three stages of decay, similar to that of CORNUCOPIA.

engineered features of the experiment, i.e., the tunnel stemming and pipe-closure hardware.

These points lead us to question whether a high residual stress to cavity pressure ratio is a necessary or sufficient condition for containment. Perhaps a containment criterion that includes the prediction of potential hydrofracture length and direction may be more valuable.

CONCLUSIONS

The pressure data obtained from CORNUCOPIA appear to give a valid representation of the cavity pressure history from 50 s, or earlier, until collapse at 9 h. Other measurements in the emplacement hole, the agreement among three independent pressure systems, and similarities to data obtained from MISSION GHOST support the validity of the pressure data.

Our proposed model explains how cavity pressure decay occurs in three fairly distinct stages: the first probably dominated by hydrofracture, the second by mass addition, and the third by conductive cooling and Darcian flow.

The decay of CORNUCOPIA cavity pressure to about one-fourth that of lithostatic overburden in less than 1 min suggests that the predicted residual stress was either not achieved or did not persist long enough to prevent hydrofracture.

Further measurements of cavity pressure are needed to better determine the pressure history before the plateau and the relation of plateau pressure to yield, depth of burial, and properties of the emplacement medium.

ACKNOWLEDGMENTS

We would like to thank the many people involved in fielding the CORNUCOPIA cavity-pressure-measurement experiment: Mel Hatch and the people in Department 1140 at EG&G, AVO; Del Wallace and the people in Department 1260 at EG&G, LVO; Denny Frischknecht and the others in the LLNL Nuclear Explosives Engineering Division's High Pressure System group at LLNL; and Tom Biesiada in the Nuclear Test Engineering Division's Containment Engineering group at LLNL. In addition to those above, we would like to thank Stu Griffith at Sandia, Livermore, and Gary Higgins from Fenix and Sisson for many helpful conversations; Kay Lie at S-CUBED, for carrying out many interpretive calculations; Sandra Dunn, Peter Smith, and Jim Cramer at SEA, Santa Fe, for

data interpretation and design-related calculations; and Larry Schwartz, Containment Program leader at LLNL, for programmatic support.

*This work was performed under the auspices of the U.S. Department of Energy by Lawrence Livermore National Laboratory under contract No. W-7405-Eng-48.

REFERENCES

1. W. S. Winters, TOPAZ--The Transient One-Dimensional Pipe Flow Analyzer: Users Manual, Sandia National Laboratories, Albuquerque, NM, SAND85-8215 (July 1985).

2. C. Keller, S. Dalvit-Dunn, Pl Smith, "Cavity Measurements Report," SEA, Santa Fe, NM (1987).

3. J. Rambo, Lawrence Livermore National Laboratory, Livermore, CA, private communication (1987).

4. E. W. Peterson and K. Lie, Evolution of the Post-Shot Cavity and Tunnel System Thermodynamic States, S-CUBED, La Jolla, CA, S-CUBED Technical Report, DNA-TR-86-134 (March 1984).

5. E. W. Peterson and K. Lie, Evolution of Late Time Cavity Pressure Decay, La Jolla, CA, S-CUBED Technical Report, SSS-R-80-4310 (January 1980).

6. R. H. Nilson, "An Integral Method for Predicting Hydraulic Fracture Propagation Driven by Gases or Liquids," Int. J. Numerical and Analytical Meth. in Geomechanics 10, 191-211 (1986).

7. R. H. Nilson, Effects of Condensation on Steam Flow and Hydraulic Fracture Propagation in Permeable Media, S-CUBED, La Jolla, CA, S-CUBED Technical Report, SSS-R-85-7145 (October 1985).

8. N. Rimer, E. Holda, K. Lie, and R. Nilson, Containment Review of the DNA MISSION GHOST Cavity Event, S-CUBED, La Jolla, CA, S-CUBED Technical Report SSS-R-88-8957 (1987).

CHEMICAL CONSIDERATIONS AND CONTAINMENT

Russell E. Duff
S-CUBED
A Division of Maxwell Laboratories, Inc.
P. O. Box 1620
La Jolla, CA 92038

ABSTRACT

Chemical reactions in a nuclear explosion cavity have long been recognized as a potential source of the noncondensible gases CO_2 and H_2 which might constitute a late-time threat to containment. The source of CO_2 is carbonate rock decomposition, and H_2 comes from oxidation-reduction reactions involving Fe or Al and water. Calculational results will be presented which show how equilibrium H_2 concentration changes with temperature under a variety of conditions. The potential advantage of oxidizing agents near the WP will be shown, but experimental results obtained when MnO_2 was used as a stemming material did not demonstrate improved containment. Another region where the oxidation-reduction reaction could be important is the stemming column of DNA HLOS experiments. The oxidation of LOS fragments by water in the grout may produce H_2 which generates late time pressure on the closures, sweeps radioactive gas into the tunnel complex, and provides the fuel for the fires and explosions seen recently. A laboratory experiment will be described which qualitatively demonstrated that this reaction proceeds rapidly at temperatures under 250°C, and it produces pressures greater than 1400 psi (9.7 MPa). This experiment also demonstrated that adding MnO_2 to the "stemming" suppressed the H_2 generation.

INTRODUCTION

All testing agencies recognize the potential threat to containment posed by noncondensible gases. Therefore, shot siting is done in such a way as to minimize the carbonate content of the formation in the vicinity of the working point. This follows because carbonates such as $CaCO_3$ decompose to produce $CaO + CO_2$ at high temperatures. The CO_2 may subsequently drive radioactive gases to the environment. In a similar way metals of construction such as iron or aluminum will react with water to produce hydrogen and metal oxides. The hydrogen may also react with water and CO_2 to make CO. Hydrogen is a noncondensible gas which would act as the CO_2 mentioned earlier to transport radioactive materials. Also, hydrogen and CO raise safety problems for reentry operations because of their flammable and toxic nature. These issues have been discussed by Dreiling and Hudson[1] and by Gaffney[2,3] among others.

There is ample precedent and evidence that chemical considerations may play an important role in understanding event related phenomena. S-CUBED has been consistent in its support for chemical studies for many years. We have argued that chemical measurements can give valuable insight into the conditions of pressure and temperature which may have existed in various places following an underground explosion. Such information may be difficult to obtain by other means.

The following sections will discuss investigations of cavity and stemming column chemical reactions and point out ways to moderate non-condensible gas generation and potential problems associated with it.

CAVITY CHEMISTRY

It has long been recognized that non-condensible gas generation in the cavity of a nuclear event represents a threat to containment which can be controlled by the choice of shot medium in the case of CO_2 and by minimizing iron in the case of hydrogen. The last significant problem the DNA test program had with carbonate was DIAGONAL LINE in 1971. In this case a relatively high carbonate content of 7.1 weight percent CO_2 is believed to have driven the late time seep of radioactive gases associated with that event.

More recently there has been increased concern about the seepage of radioactive materials from the vicinity of horizontal line of sight tests, and an investigation of ways this problem could be minimized was undertaken.

In the HLOS context, since emplacements are in tuff with a negligible CO_2 content, the only significant cavity non-condensible gas threat comes from hydrogen. This hydrogen can be generated from the oxidation-reduction reaction of metal with water to produce metallic oxides and hydrogen. Metal comes from Box A, the line of sight pipe and close-in instrumentation, as well as from rock bolts, wire mesh, and other materials of construction in the vicinity of the working point. Similar problems arise in DoE experiments, and the laboratories often add magnetite, Fe_3O_4, to the stemming for shielding and, to a lesser extent, chemical reasons. The argument is that at relatively high temperatures the preferred iron oxide is FeO. Therefore, the Fe_3O_4 provides some oxygen which can oxidize construction materials and reduce the hydrogen concentration.

The chemistry of this process was investigated in a series of simplified equilibrium calculations. The simplified calculations assumed that some of the device energy from a nominal 8 KT explosion remained in a fully formed nuclear cavity containing roughly 70 tonnes/kt of vaporized materials found in the vicinity of the working point. These materials included iron, aluminum, and plastic in representative

quantities. The cavity conditions were obviously dominated by an excess of vaporized tuff which was assumed to be 0.8 SiO_2 and 0.2 water. The chemical equilibrium was determined using the S-CUBED version of the TIGER code which is called ORAKL. The cavity was allowed to cool from a very high temperature at constant volume and mass, and the changing equilibrium was noted. At relatively high temperature, all of the iron which had been assumed to exist near the working point did indeed form FeO, and the hydrogen concentration was correspondingly high as shown in Figure 1. At lower temperatures, however, the equilibrium shifted as water was formed leading to a constant concentration below roughly 2300°K. Simultaneously at low temperature FeO and SiO_2 reacted to form Fe_2SiO_4, but this had no influence on the hydrogen concentration.

This generic nuclear explosion cavity model was used to investigate the efficacy of various stemming materials to control hydrogen generation. If magnetite is used as a stemming material as in DoE practice, the hydrogen concentration is suppressed as expected as the cavity temperature drops to about 2000 K. At still lower temperatures, the equilibrium shifts, magnetite reforms, and the hydrogen concentration returns to a value close to that found if no magnetite were used as a stemming material as also shown in Figure 1. One can, of course, question whether or not the equilibrium assumption which underlies this analysis is applicable at the relatively late time, relatively modest temperature conditions at which the magnetite reforms. We suspect that these reactions do occur, at least to some extent, perhaps locally in the puddle region. The water may come from material dissolved in the silicate melt, and the hydrogen release may help make the vesicles seen in the puddle glass.

It seemed appropriate to seek other materials which could be used as stemming which would not produce the reversible oxidation-reduction reaction shown by magnetite. Two potentially practical alternatives were identified. The first is CuO, the second MnO_2. Copper oxide could be obtained as a partially processed ore of copper, manganese dioxide, also known as the mineral pyrolusite, is an important item of commerce. It is used as the oxidizing agent in the production of dry cell chemical flashlight batteries. Large quantities of it are processed near the test site at Henderson, Nevada.

Figure 2 illustrates the potential influence of these and other possible stemming materials on hydrogen concentration as a function of assumed cavity temperature. CuO and MnO_2 both lead to irreversible reduction reactions whereby the available iron is oxidized, and the hydrogen concentration decreases to negligible amounts as expected. Hematite, Fe_2O_3, and MgO_2 also appear to be effective. Large quantities of the relatively expensive former are required, and the latter is prohibitively expensive.

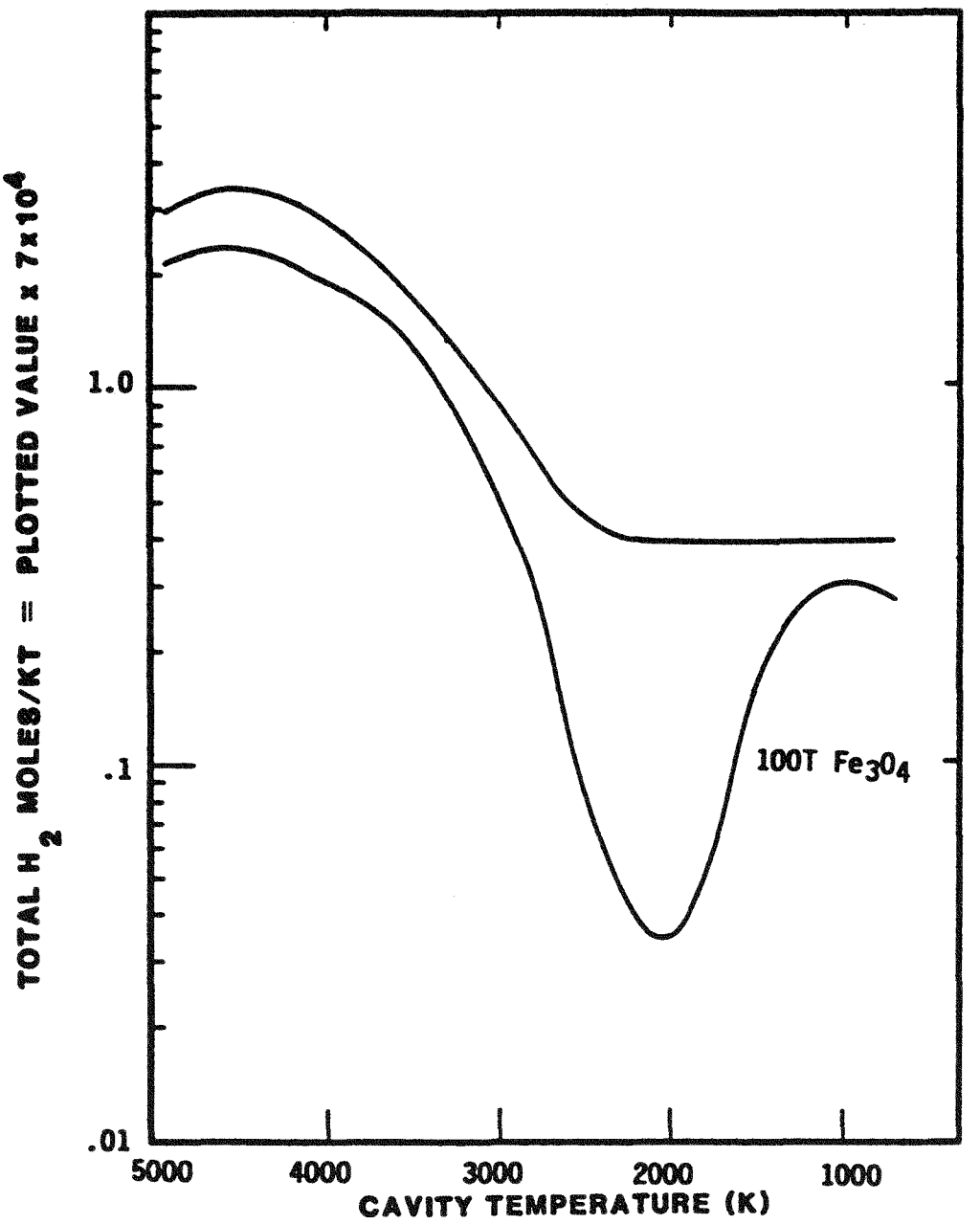

Figure 1. Calculated H_2 concentration in a 10 KT nuclear explosion cavity. The upper curve shows what to expect if no effort is made to influence the chemical state. The lower curve shows how the assumed equilibrium shifts if 100 tonnes of Fe_2O_3 is added to the cavity.

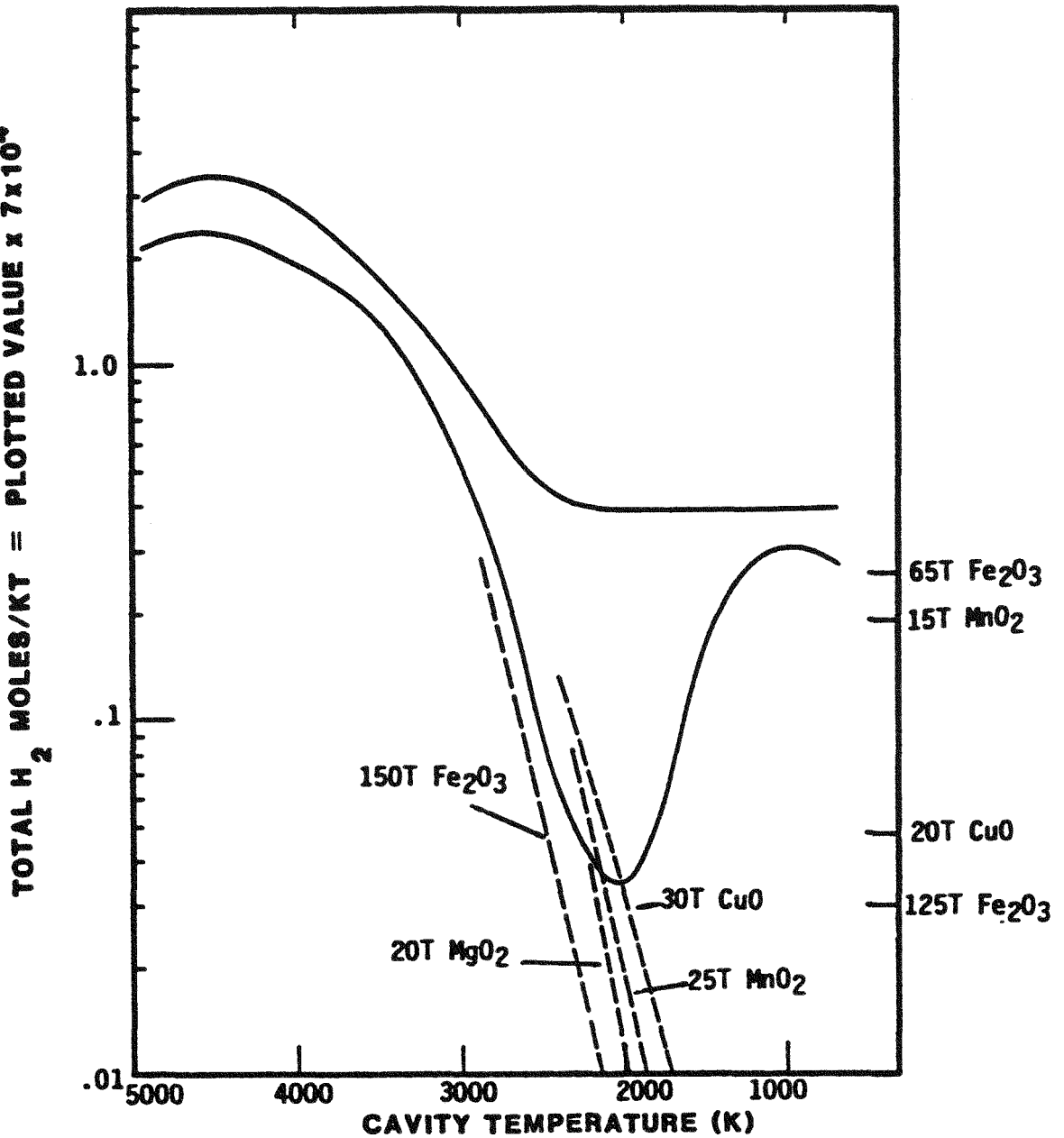

Figure 2. Calculated H_2 concentrations obtained when various materials are added to the explosion[2] cavity. The marks at the right margin of the graph show the low temperature equilibrium concentration when the indicated smaller quantities are used.

Since MnO_2 is readily available and much less expensive than CuO, recommendations were made that MnO_2 be used as a stemming material in the vicinity of the zero room of DNA HLOS events. Specifically, it could be used as the sandbag filling during buttonup around the zero room.

The force of this recommendation is moderated somewhat by the fact that MnO_2 had been used in the past to influence the chemistry of metal oxides and to improve the radiochemical yield determination process for the FADE event. Apparently its chemical influence was as expected. MnO_2 was also added to the stemming for CAMPHOR. In both cases, containment experience was less than desired. There is no evidence that the MnO_2 contributed to the problem, but it certainly did not assure containment. We hope future investigations will determine whether or not MnO_2 may contribute to reducing potential containment threats associated with non-condensible gas generation and whether or not it should become a feature of future DNA designs.

STEMMING CHEMISTRY

A feature of almost all DNA reentries into the vicinity of expended HLOS events has been the observation of flammable and toxic gases in the tunnel and LOS pipe. These gases are H_2 and CO. The results of measurements reported by Jim Metcalf of Sandia are shown in Table 1. On MISTY RAIN, DIAMOND BEECH and MIGHTY OAK, there is evidence that fires and/or explosions occurred in the tunnel complex at late time. In most cases the gases are not radioactive, but they are undesirable andpotentially dangerous from the health and safety point of view. We have speculated that these gases came from reactions of LOS metal and grout in the stemming column. The LOS provides the iron, the desert fines which was used in the preparation of superlean grout contains trace carbonate minerals which provide the carbonaceous material which is seen. This scenario is at least superficially consistent with the fact that very little of the LOS pipe is found on reentry. The problem has been to identify conditions under which the observed concentrations characterized by a predominance of hydrogen and much more CO than CO_2 can be produced.

Many calculations were undertaken in an effort to identify appropriate conditions. This effort was successful. The important reactions appear to be

$$2Fe + 2H_2O + SiO_2 \rightleftarrows Fe_2SiO_4 + 2H_2$$

$$CaCO_3 + SiO_2 \rightleftarrows CaSiO_3 + CO_2$$

$$CO_2 + H_2 \rightleftarrows CO + H_2O$$

Table 1.

Gas composition measured in the LOS pipe for several events. Cases where fires or explosions probably occurred are noted.

EVENT	H_2	CO	CH_4	O_2	N_2
DIAMOND SCULLS	> 60	0.65	-	-	-
HUSKY ACE	22	1.2	-	-	-
MING BLADE	25	1.0	1.0	-	-
DINING CAR	70	0.75	1.25	-	-
HUSKY PUP	84	0.4	0.5	-	-
MIGHTY EPIC*	9	1.2	1.5	16.7	70
DIABLO HAWK	65	1.0	1.0	< 5	25
MINERS IRON	2	0.15	-	20	78
HURON LANDING	60-65	~ 1	0.5	~ 8	~ 28
MISTY RAIN	Fire and Explosion				
MIGHTY OAK	Fire and Explosion				
DIAMOND BEECH**	Fire possible				
	2.5	1.6	-	16	79

* This data was taken from a gas sample obtained two days after pumping out an unknown depth of water behind the TAPS began. Contamination with air was inevitable.

** This measurement was made behind the Facility Drift Protection Plug.

These reactions are assumed to occur in the stemming column under conditions where both Fe and SiO_2 are in local excess. The Fe comes from fragments of the LOS pipe and, of course, SiO_2 is the major constituent of grout. An additional restriction is imposed, namely, that carbon will not precipitate as graphite during these reactions. This assumption seems reasonable since the reaction temperature is too low to produce significant C_2H_2, the usual precursor of graphite.

Equilibrium calculations show that the H_2/CO and CO/CO_2 ratios are essentially independent of reaction temperature over the interval between 500 and 1200°K as shown in Table 2. The H_2/CO ratio exceeds 100 and the CO/CO_2 is greater than 5 over this interval for a particular set of initial conditions. Careful study of the calculated output shows that the excess Fe and SiO_2 react to adjust the H_2O/H_2 ratio so as to keep CO/CO_2 essentially constant in spite of the fact that the equilibrium constant for the water-gas reaction (the third in the series above) changes quite dramatically over this temperature range.

The significance of this investigation is that apparently credible conditions have been identified under which warm LOS pipe fragments can react with their environment to produce non-condensible gases which can subsequently diffuse through the grout and leak past the closures into the LOS pipe and, perhaps, into the tunnel complex. In some cases there is evidence that a small amount of radioactive material has been mixed into the grout presumably by early time processes. The gaseous components of this radioactivity can then be swept from the grout into the LOS and tunnel complex by these non-condensible gases long after dynamic processes are over.

Several methods have been suggested which could reduce this mechanism for non-condensible gas generation. The easiest way to remove the CO would be to formulate superlean grout using clean quartz sand rather than desert fines. This would remove the only credible source of carbon species which has been identified.

The more important H_2 could be reduced by minimizing or eliminating iron from the stemming column. The MIDDLE NOTE LOS pipe was redesigned to make it thinner and somewhat smaller with this thought in mind. Also, the internal helix was redesigned to significantly reduce its mass. Perhaps these reductions in potentially reactive materials contributed to the success of the MIDDLE NOTE experiment. Alternatively one might make the LOS from Cu which does not react under these conditions.

A final possibility would be to add an oxidizing agent such as MnO_2 as a convenient and effective oxidizing agent. This material is used to prevent the development of hydrogen gas in dry cell batteries. Calculations have shown that it would effectively eliminate the hydrogen concentration and simultaneously oxidize CO to CO_2 in the stemming column. There may be toxicity problems associated with handling large amounts of MnO_2, however.

Table 2.

Calculated equilibrium concentrations following the reaction of excess iron in HSSL 50/50 grout at several temperatures. Eight other potential gaseous species were included in the calculational system. None of them appeared. The pressure was assumed to be 10.0 atm.

CONSTITUENT CONCENTRATIONS - MOLES PER KGM OF REACTANTS

	T =	1200	1100	1000	900	800	700	600	500°K
H_2	Gas	4.1967	4.4518	4.6822	4.8799	5.0590	5.1686	5.2320	5.2587
H_2O	Gas	1.0691	0.8140	0.5837	0.3860	0.2068	0.0974	0.0339	0.0072
CO	Gas	0.0317	0.0318	0.0319	0.0318	0.0320	0.0319	0.0318	0.0316
CO_2	Gas	0.0059	0.0058	0.0057	0.0058	0.0056	0.0057	0.0059	0.0060
SiO_2	Solid	2.3618	2.2341	2.1190	2.0202	1.9304	1.8758	1.8441	1.8308
Fe	Solid	7.0555	6.8003	6.5699	6.3723	6.1929	6.0835	6.0202	5.9937
FeO	Solid	0.0000	0.0000	0.0000	0.0000	0.0000	0.0000	0.0000	0.0000
Fe_3O_4	Solid	0.0000	0.0000	0.0000	0.0000	0.0000	0.0000	0.0000	0.0000
Fe_2SiO_4	Solid	2.1142	2.2418	2.3570	2.4558	2.5455	2.6002	2.6318	2.6451
$CaCO_3$	Solid	0.0000	0.0000	0.0000	0.0000	0.0000	0.0000	0.0000	0.0000
$CaSiO_3$	Solid	0.0376	0.0376	0.0376	0.0376	0.0376	0.0376	0.0376	0.0376
TOTAL	Gas	5.3034	5.3035	5.3035	5.3035	5.3035	5.3035	5.3035	5.3035

These calculations were qualitatively confirmed with a simple laboratory test wherein small sections of steel pipe were filled with a sand/cement/water and iron filings mixture with and without added MnO_2. The pipe sections were fitted with pressure gages and thermocouples and heated in an ordinary kitchen oven. As the temperature of the system reached 60°C, a small increase in pressure was observed. The pressure increase was very rapid when the temperature reached 130°C. The measured pressure exceeded transducer band edge of 1400 psi within a minute or two of the beginning of the fast reaction. The specimen containing MnO_2 showed a significantly later pressure rise than did the one without. The oven was then turned off, and the pipes gradually cooled. The MnO_2-containing specimen showed a pressure back on scale within 33 min. The rate of pressure decrease was rapid until the pressure fell to the value corresponding to the vapor pressure of water at the measured temperature. The specimen which did not contain MnO_2 showed pressures less than 1400 psi only after 2-1/2 hr, and we believe there was a small gas leak in this system.

This very simple experiment demonstrated three things: (1) the hydrogen-producing reaction between iron and grout occurs at modest temperatures, so chemical kinetics does not appear to be a serious limitation; (2) these reactions can generate high pressures comparable to those seen at the MINERS IRON MAC; (3) MnO_2 added to the grout significantly moderates the hydrogen generation.

We hope in the months and years ahead it becomes possible to confirm these experimental findings and to develop appropriate techniques which will eliminate or minimize the possibility of late-time, non-condensible gas generation in the stemming region of horizontal line of sight underground nuclear tests.

I gratefully acknowledge the assistance provided by Dr. Kay Lie. She performed the numerous chemical equilibrium calculations required for this investigation.

REFERENCES

1. L. A. Dreiling and B. C. Hudson, "Non-Condensible Gas Generation", Lawrence Livermore National Laboratory Report UOPLL-80-17 (1980) (CFRD).

2. E. S. Gaffney, "Hydrogen Gas Generation in Underground Nuclear Tests," Los Alamos National Laboratory Report ES/CPO-82-28 (1982) (CFRD)

3. E. S. Gaffney, "Thermodynamics of Hydrogen Generation," Second Symposium on Containment of Underground Nuclear Explosions, p. 306 (1983).

REACTION KINETICS AND HYDROGEN GENERATION

E.S. Gaffney, Ktech Corporation, Albuquerque, NM 87110

ABSTRACT

Kinetics of reactions between cavity gases and steel, iron oxides and iron silicates will limit the rate at which chemical equilibrium is approached in the production of noncondensible gas by underground nuclear tests. A preliminary estimate based on only a few published data for steel-steam reactions indicates that reaction rates will be very low at temperatures below about 1000 to 1200 K. The physical state of the metal, oxides and silicates, especially the specific surface, also has an important effect on the reaction rates.

I. INTRODUCTION

Production of non-condensible gases during an underground test (UGT) can be a threat to containment of the event because such gases maintain a high pressure in the explosive cavity even after temperatures drop to nearly ambient. Carbon dioxide produced by decomposition of carbonate minerals in the media surrounding the event presents a potential hazard which can be reduced to safe levels by selecting a site with only minor amounts of calcite or dolomite.

The importance of hydrogen as a non-condensible gas produced by UGTs was first documented in 1980 when it was noted that steel from the experiment rack could reduce water in the surrounding formations with iron oxide and hydrogen as products:

$$H_2O + Fe \rightarrow FeO + H_2 \qquad (1)$$

Since Fe is always present as steel in the rack and water is always present as a few percent or more of the surrounding formation, this reaction can always be expected to produce some hydrogen. The amount of hydrogen produced will always be controlled by the amount of Fe available because so much water is available in the rock. This gas must be contained in the explosive cavity so high pressures (which may threaten containment) can be expected when the cavity is small (low yield) and the rack is large.

At the Second Containment Symposium, Gaffney (1983) pointed out that reaction (1) was not the only reaction possible. In the simple oxide system the reaction:

$$3Fe + 4H_2O \rightarrow Fe_3O_4 + 4H_2 \qquad (2)$$

may occur, but so may:

$$Fe + Fe_3O_4 \rightarrow 4FeO \qquad (3)$$

which produces no hydrogen. In fact, at temperatures above about 1500 K, (3) is the preferred reaction. Only at lower temperatures does equilibrium favor reaction (1). Recently, Duff at S[3] has used a numerical equilibrium thermodynamics code to calculate hydrogen production histories involving these and many other reactions.

In the present paper I discuss the nature of some of the important reactions and how kinetic factors can affect the amount of hydrogen generated by a UGT. The next section presents a brief discussion of the nature of the "chemical system" of a typical UGT. In Section III, the reactions considered are described and some remarks are made about the processes which will affect the kinetics. Section IV presents a quantitative analysis of the kinetics of a single reaction as an example of how kinetics can affect the oxidation of steel by water vapor. The final section consists of discussion, conclusions and suggestions for further investigations.

II. THE UNDERGROUND TEST AS A "CHEMICAL SYSTEM"

Calculations of chemical equilibrium, and frequently of kinetics as well, are based on the notion of a chemical system. A chemical system is the aggregate of all of the mass which is accessible for chemical reaction. In the kitchen chemistry case of boiling an egg, the system consists of everything inside the eggshell. Upon heating, the protein molecules in the egg react with each other to yield a more solid product called boiled egg. No material from inside the shell gets out (if you do it right) and no material from outside gets in; the reactions are limited to those within the chemical system.

In a UGT we can also speak of a chemical system, although its exact bounds may be less clear than in the case just described. Certainly all of the rack, water and rock that is vaporized is available for reaction; gas phase reactions are usually quite fast, especially at high pressures. Given the violent displacement of material which accompanies cavity growth it seems likely that most of the material within the final cavity, including molten rock and steel, is part of the chemical system initially. There will also be some amount of exchange of fluids between the cavity and the shallower parts of the surface surrounding it; however, the extent of this interaction is unclear.

Just how much of the mass of the rack should be included is also unclear if part of it extends beyond the cavity. Conservative design calculations assume that all of the mass can react but that is surely an overestimate. More light might be shed on this issue by reentry observations (very unlikely in a VLOS test), complicated 2-D hydrodynamic calculations or scaled experiments. Until such time as investigations such as those just mentioned can be undertaken, one can only state the plausible limits. I suggest that a reasonable upper limit to the amount of steel to be included is all of the rack at a range closer than one free-field cavity

radius. The steel which is initially at that range will be moved outward with the ground shock and thus should actually be slightly outside the cavity after cavity growth. As a lower limit one might use the mass of steel within the melt radius radius (1350 Mg per kilotonne).

Having defined the extent of the UGT chemical system, the next step is to describe its contents. The vast majority of the material for reaction will be rock, except perhaps for the very low yield events. If we take the radius of a typical cavity to be 14 $m/kt^{1/3}$, that is equivalent to about 11,500 Mg/kt. But much of the volume of the cavity represents rock shoved aside. Perhaps about 5000 Mg/kt is a better estimate. If this rock contains only 4 percent water, we have enough water to oxidize 125 Mg/kt of Fe in the rack, certainly enough that water will be in excess on events of yield greater than about a kilotonne. However, for lower yield events in dry media, water may limit the amount of iron which can be oxidized.

III. OXIDATION-REDUCTION REACTIONS IN THE SYSTEM Fe-O-H(-SiO^2)

All of the above discussion has considered reactions of iron and water. But the majority of the material in the system is rock. This is typically about 70 percent SiO_2, 15 percent Al_2O_3 and 15 percent other oxides. Almost none of the rock consists of material which can be readily reduced or oxidized. But the SiO_2 can react with iron oxides producing minerals which are more stable than the simple oxides. In particular, the reaction:

$$2FeO + SiO_2 \rightarrow Fe_2SiO_4 \qquad (4)$$

produces fayalite. The Fe^{2+} in FeO is not very stable, indeed below about 875 K it is not stable at any value of oxygen pressure. But fayalite is very stable and can coexist with much higher oxygen pressures than FeO. Thus fayalite will tend to reduce the amount of H_2 produced by reducing water. In the absence of metallic iron, fayalite can be oxidized by water to produce H_2 by the following reaction:

$$3Fe_2SiO_4 + 2H_2O \rightarrow 2Fe_3O_4 + 3SiO_2 + 2H_2 \qquad (5)$$

This reaction is apparently important in Duff's (1985) finding of increasing H_2 pressure at low temperatures.

We have already listed four of the reactions which are involved in controlling hydrogen production in a UGT. One other reaction can either produce or consume hydrogen:

$$3FeO + H_2O \leftrightarrow Fe_3O_4 + H_2 \qquad (6)$$

High temperatures favor the left side of this relation; low temperatures, the right. For many events magnetite (Fe_3O_4) is included in the stemming.

This can be expected to suppress hydrogen and lead to formation of FeO at early times when temperatures are high (Gaffney, 1983). However, as the temperature drops, the FeO will react with water and lead to a late time build up of equilibrium levels of hydrogen as Duff (1985) has calculated. Whether this should happen in a system with excess SiO_2 may be debated.

If we consider the reactions (1), (2) and (6) [Note that (6) = (1) - 3x(2)], one can reconstruct the history of a small piece of steel in a UGT. Let us consider a steel piece that is close enough to the device to be vaporized. As temperatures drop it, and adjacent material, will condense. If we assume that Fe_3O_4 is absent in the initial medium (see Gaffney (1983) for a discussion of Fe^{3+} in the formation) this initial condensate will be some mixture of Fe, FeO, and Fe_3O_4 with H_2 present in accord with the amount of each of these materials. If the oxides are present there will be substantial pressures of H_2 in the cavity gas. If metal is present, the cavity gases will be relatively poor in H_2. In any event, the presence of substantial quantities of metal outside the vaporization region will dominate the later behavior.

Consider a piece of un-reacted steel exposed to this water-rich atmosphere. As the temperature drops, we can expect an oxide film to develop. At high temperatures, above the eutectic melting point of Fe and FeO at 1645 K, this will be a film of liquid FeO. Hydrogen gas will be produced with the FeO. Further reductions in temperature would move equilibrium to the right in reaction (6), causing oxidation of FeO to Fe_3O_4 with hydrogen production. This would produce a three layer structure with Fe_3O_4 over FeO over Fe.

IV. REACTION KINETICS

Kinetic studies of reactions between water and various steels and pure iron provide data to evaluate the situation just described. Hauffe and Pfeiffer (1953) studied the oxidation of iron at elevated temperatures and found that diffusion of 0 through FeO was so rapid that reaction rates were constant (reactions which are limited by diffusion of one of the reactants through one of the products, as might be the case for 0 diffusing from the vapor/FeO surface to the FeO/Fe surface, are characterized by a decreasing rate with time reflecting the progressive thickening of the layer of product). Bittel et al., (1969) find similar behavior for both mild steel and stainless steel in steam. Stainless steel differs from steel at temperatures above 1250 K only in its reaction to air; in steam they react similarly. Bittel et al. found linear behavior to last for several minutes, after which the decreasing ("parabolic") rate was observed. By comparing their linear and parabolic rates, we can see that the linear rate will dominate for the first 10 minutes at 1800 K, but for the first 30 minutes at 1000 K. At 1600 K, an oxide film 700 μ thick will form before diffusion begins to dominate. But at 1200 K only 10 μm of oxide is needed to have diffusion dominating. Microscopic observations show the oxide to be Fe_3O_4.

Thus we can see clearly that the details of the kinetics are intimately entwined with the temperature history. We also see that the typical thickness of the reacted region decreases very rapidly as the temperature decreases.

Lower temperature kinetic results for steam reacting with stainless steels are reported by Gaul and Pearl (1961) and by Wanklyn and Jones (1962). Figure 1 shows their data with that of Bittel et al. (1969) in a Ahrennius plot. It can be seen that all of the data for temperatures above about 850 K lie nearly on a straight line. Thus the reaction rate (r) can be expressed as a single function of temperature:

$$r = 0.18 \exp\left(\frac{-163780}{RT}\right) \qquad (7)$$

where r is the reaction rate in Mg $m^{-2}s^{-1}$, R is the gas constant (8.3Jmole^{-1}K^{-1}), and T is the absolute temperature. Bittel et al. reported $r=1.1 \exp\left(\frac{-185150}{RT}\right)$ for their data alone; the difference is probably not significant). But the rate at 550 K clearly is not on the trend. The lower temperature corrosion must be different either in the mechanism or the reaction.

We can apply this data to see how reaction kinetics can affect hydrogen generated by a UGT, especially at low temperatures. Consider a 0.1 kilotonne event producing a cavity of 6.5 m radius. Each mole of oxygen (0.032 kg) consumed produces two moles of hydrogen. So the hydrogen production rate can be obtained from equation (6) as:

$$r_{H_2} = 1.1 \times 10^4 \, e^{\left(-\frac{19730}{T}\right)} \text{ moles } H_2 \,/\, (m^2 \cdot s) \qquad (8)$$

The number of moles of H_2 can be expressed as pressure using an equation-of-state. An ideal gas equation-of-state (P = nRT/V) will give a lower limit:

$$r_p = 79 \, T \, e^{\left(-\frac{19730}{T}\right)} \text{ Pa}/(m^2 \cdot s) \qquad (9)$$

To proceed further we need an estimate of the specific surface of the rack materials after cavity expansion. Development of such an estimate is non-trivial[2,3]. For the present we will present results for specific surfaces of 10^2, 10^3, 10^4 m^2/Mg corresponding to uniform cubical grains of dimension 7.5 mm, 0.75 mm and 0.075 mm, respectively. Equation (8) then becomes:

$$r_p = (7.9 \text{ to } 790) T \, e^{\left(-\frac{19730}{T}\right)} \frac{\text{KPa}}{\text{Mg} \cdot \text{s}} \qquad (10)$$

Using this relation we can calculate that after exposure of a 100 Mg rack dispersed as cubes 75 μm on a side to cavity water vapor for 3000 seconds at a steady temperature of 1100 K, only 4 MPa of cavity pressure due to hydrogen can be expected (about equal to the overburden pressure at 200 m). For coarser particles these numbers are correspondingly less; 7 MPa after

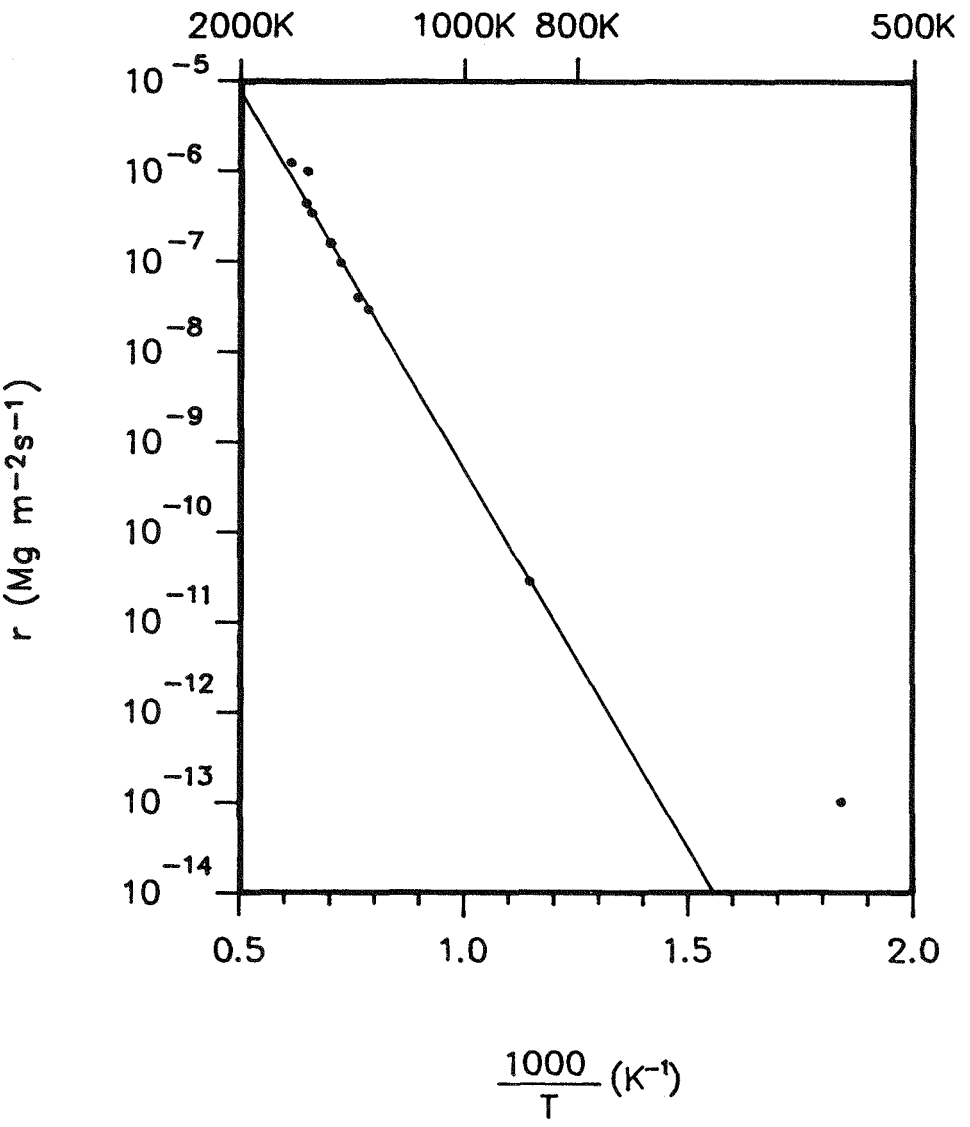

Figure 1. Ahrennius plot for steel-water reaction rate.

50 minutes at 1500 K for 7.5 mm steel cubes. So we can see that for temperatures in the range of 1100 to 1500 K reaction rates are likely to limit the amount of hydrogen produced at late times.

V. DISCUSSION

The reaction kinetics just described can provide no more than general guidance for understanding of hydrogen generation by a UGT because only one of several possible reactions has been addressed. Of particular interest, because of the large amount of SiO_2 available for reaction, is reaction (5). But we have argued that diffusion of water through the Fe_3O_4 products of reaction (2) controls the rate of that reaction for much of the time of interest. Fe_3O_4 is also a major product of reaction (5), along with quartz, so the diffusion may be similar. If so, we see that the amount of H_2 produced by reactions (2) or (5) at temperatures below about 1100 K to 1500 K will be limited by kinetics. However, this encouraging conclusion must remain tentative until tested by studies of kinetics in silica-bearing systems.

It is also clear that on assessment of the quantitative effects of chemical kinetics on containment requires a better knowledge of the physical state of the solid material in the cavity. This includes not only the mineralogical and metallurgical species, but also the size and shape of the grains.

REFERENCES

Bittel, J.T., L.H. Sjodahl and J.F. White, 1969, Oxidation of 304L stainless steel by steam and by air. Corrosion 25, 7-14.

Gaffney, E.S., 1983, Thermodynamics of hydrogen generation, Proc. 2nd Symp. Containment of Underground Nuclear Explosions, 305-322, CONF-830882.

Gaul, G.G. and W.L. Pearl, 1961, "Corrosion of Type 304 Stainless Steel in Simulated Superheat Reactor Environments", General Electric Co., GEAP-3779.

Hauffe, K. and H. Pfeiffer, 1953, Kinetics of Wustite Formation in Oxidation of Iron, Z. Metallk., 44, 27.

Wanklyn, J.N. and P.J. Jones, 1962, The aqueous corrosion of reactor materials. J. Nucl. Materials 6, 291-329.

ACKNOWLEDGEMENT

This work was conducted under Los Alamos National Laboratory Subcontract 9-XFE-1419G-1.

Late-Time Gas Flow

BREATHING ON THE MESA

WOODWARD, JR., E. C., Lawrence Livermore National Laboratory, P.O. Box 808, Livermore, CA 94550

Subsequent to the execution of several events on Pahute Mesa noble gas samplers have detected radioactive noble gas. This has been attributed to atmospheric pressure cycling ("breathing") assisting diffusion in enabling gaseous radioactive fission debris to reach the surface.

The geology of an event site, in particular the depth of the Rainier Mesa Member of the Timber Mountain Tuff, may well play a role in the amount and timing of this phenomenon.

Radioactive gases are produced by nuclear explosions. The gases of concern in this study are the long lived isotopes of Krypton and Xenon. These gases diffuse outward from the cavity region of an underground nuclear detonation. Their migration upward to the surface is assisted by atmospheric pressure cycling ("breathing").

Late in 1983 a sampling station for radioactive noble gases was located on Pahute Mesa at the Area 20 camp. Since that time radioactive noble gases have been detected subsequent to four nuclear events. After the second of the four I sought to determine whether there might be a feature of the event site which might explain the phenomenon and possibly predict its future occurrence.

Figure 1 shows the location of Pahute Mesa events since October 1983. Table 1 lists these events with their depths of burial and certain characteristics of the site geology. The figure shows that all four sites where radioactive gases were detected subsequent to the event were east of the West Greeley fault with Timber Mountain members at the surface. The table shows that in all four cases the top of the Rainier Mesa member was less than 100 metres distant from the surface.

Taken as a whole the figure and table indicate that, when the surface member is of the Timber Mountain group, there is about one chance in two that radioactive gas will be detected after the event. So far no event having a Thirsty Canyon member at the surface has had a postevent detection of radioactive gas.

The implication can be made that the Thirsty Canyon members act as "forgiving alluvium" for Pahute Mesa Events.

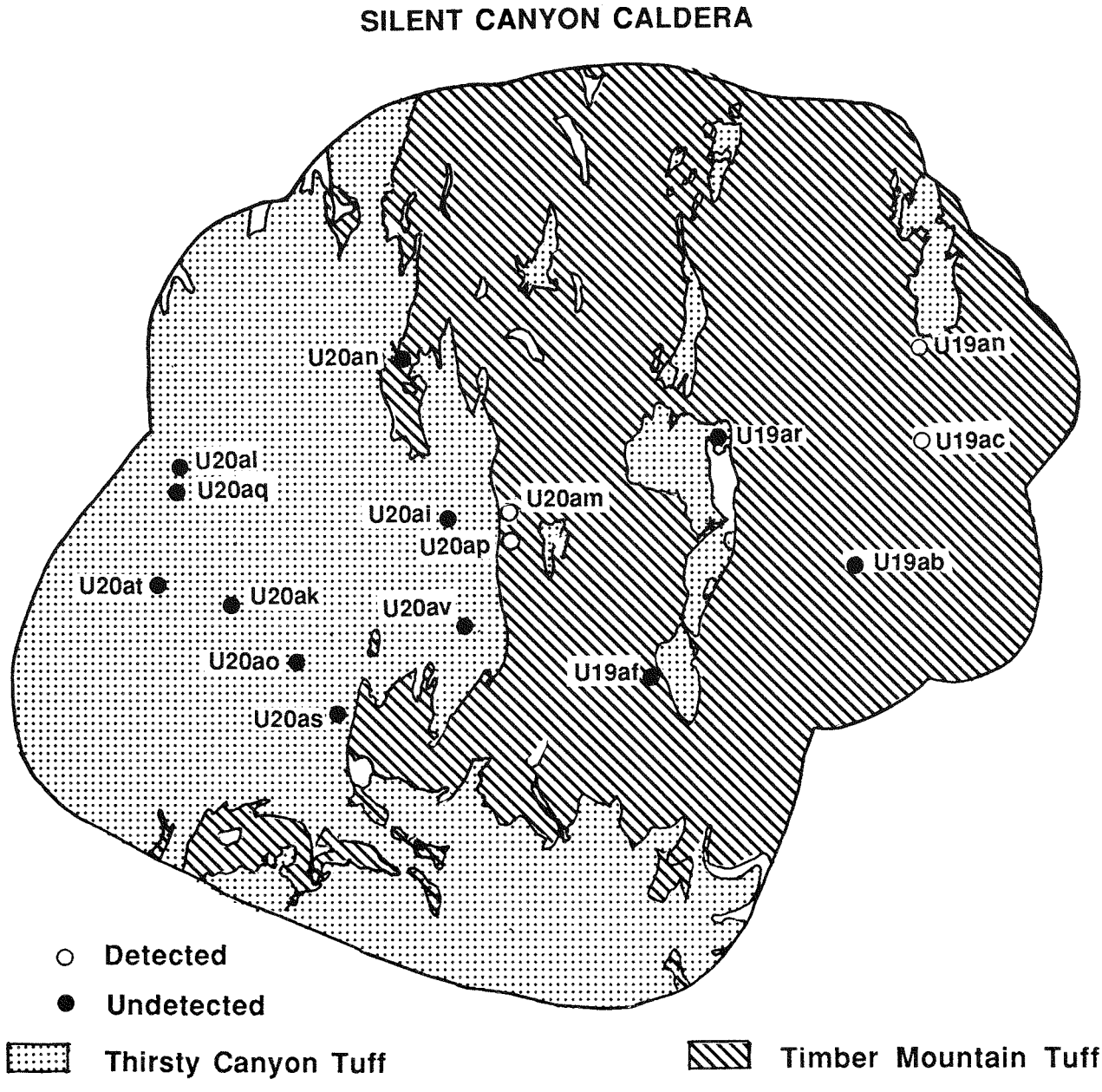

Adapted from

Geologic Map of Pahute Mesa, Nevada Test Site

by

Paul Orkild, K. A. Sargent, and R.P.Snyder

Figure I

TABLE I

PAHUTE MESA EVENTS 1984 - 1987 TO DATE

HOLE	EVENT	DOB (M)	SURFACE MEMBER	TOP OF RAINIER MESA (M)	BOTTOM OF RAINIER MESA (M)	DATE	RADIATION DETECTED
U20AM	KAPPELI	640	Tmr	0	168	7/25/84	YES
U20AL	EGMONT	546	Ttt	179	507	12/09/84	NO
U19AC	TIERRA	640	Tma	71	402	12/15/84	YES
U19AB	TOWANDA	665	Tma	15	358	5/02/85	NO
U20AK	SALUT	608	Ttt	168	640	6/12/85	NO
U20AN	SERENA	597	Tma	43	618	7/25/85	NO
U20AO	GOLDSTONE	549	Ttt	152	655	12/28/85	NO
U20AI	JEFFERSON	609	Ttt	150	654	4/22/86	NO
U20AQ	DARWIN	549	Ttt	584	584	6/25/86	NO
U19AR	CYBER	628	Ttt	165	493	7/17/86	NO
U19AF	GALVESTON	488	Tma	68	328	9/04/86	NO
U19AN	LABQUARK	616	Tma	73	370	9/30/86	YES
U20AS	BELMONT	605	Ttt	126	200	10/16/86	NO
U20AP	BODIE	635	Tmr	0	148	12/13/86	YES
U20AT	DELAMAR	544	Ttt	143	299	4/18/87	NO
U20AY	HARDIN	625	Ttt	169	359	4/30/87	NO

Tmr = Rainier Mesa member of Timber Mountain Tuff
Tma = Ammonia Tanks member of Timber Mountain Tuff
Ttt = Trail Ridge member of Thirsty Canyon Tuff

Estimation of the Bulk Diffusivity of Chimneys using Post-Shot Holes

Norman R. Burkhard and Joseph R Hearst
Lawrence Livermore National Laboratory
L-208, PO Box 808
Livermore, CA 94550

Jonathan M. Hanson
Hanson & Associates
PO Box 8047
Salt Lake City, UT 84108

Abstract

LLNL has been calculating the bulk diffusivity of chimney regions using measurements of atmospheric pressure variations. Fluctuations in atmospheric surface pressure and subsurface pressure (measured in a post-shot hole of opportunity) are compared to determine the diffusivity. The diffusivities calculated to date range from about 130 to 31000 m^2/hr. Time and frequency domain techniques have been utilized to determine this range of diffusivity Some limitations of this method of diffusivity determination have been discovered. Useful data have been obtained in the frequency band 0.002-0.03 cycles/hour. The effect of the water table upon our measurements has been determined. The theoretical impulse response functions for a typical geologic setting can be quite long (> 300 hours). Therefore, the surface pressure history for time spans greater than this or the entire initial pressure distribution (p(z,t=0)) in the geologic setting must be known before gas transport predictions from transport models can be reliably made, as the driving pressures for transport depend upon these initial conditions.

Introduction

The hydraulic diffusivity of the chimney and surrounding media can play an important role in the containment of radioactive gas generated during an underground nuclear explosion. Molecular diffusion of gas through the matrix or fractures, atmospheric pumping of gas to the surface, and steam-drive fracture extension depend upon the diffusivity and/or permeability. The stimulus for this work is a series of observations of late-time gas seepage from several sites on Pahute Mesa on the Nevada Test Site (NTS). We are now developing a data base of bulk diffusivity measurements in order to determine whether these sites are anomalous. Bulk diffusivity is our term for the diffusivity determined in a medium that contains both matrix and fractures. The importance of this parameter in the transport of radioactive gas to the surface is discussed by other investigators at this symposium [1,2]. In addition, we are attempting to determine whether it would be possible to predict the occurrence of late-time gas seepage from pre-shot measurements of diffusivity. The first step in our study is the determination of post-shot bulk diffusivity at many emplacement sites. This paper reports on this portion of the

study.

Lawrence Livermore National Laboratory (LLNL) has been making estimates pre-shot and post-shot of the diffusivity around emplacement holes. Estimates of the pre-shot diffusivity for alluvium and tuff sites were reported by Hanson and Hearst [3]. Since then, LLNL has developed a technique to estimate the diffusivity of the chimney and surrounding region using post-shot gas sampling holes. LLNL also did work on this problem in the early 1970's [4,5,6]. Interest in this work was rekindled by the observations of late-time seepage from several events.

The estimates of the diffusivity are obtained from atmospheric pressure measurements made simultaneously on the surface and downhole in the cavity region. Several time domain techniques and a frequency domain technique have been developed to obtain the estimates of diffusivity. As part of this process, analytical models for several simple cases have been derived. These models lead to a better understanding of the value and limitations of these measurements.

Theory

The hydraulic diffusivity of the medium combines the permeability and the porosity of the medium into one term in the diffusion equation:

$$\frac{\partial^2 p}{\partial z^2} = \frac{1}{C}\frac{\partial p}{\partial t} \qquad (1)$$

where $C = kp_0/\mu\varphi$ (2)

and where k = permeability
p_0 = static pressure
μ = viscosity of air
C = diffusivity
φ = porosity

and at normal atmospheric conditions, $C \approx 16\ k/\varphi$
with k in darcys,
and C in m^2/hr.

Solutions of this equation were formulated in the time domain using finite difference techniques. We have used the finite difference techniques to estimate the diffusivity of chimney regions at several different sites around NTS. In addition, we have obtained analytical solutions for the Green's function for this problem in the frequency domain for one dimensional horizontally homogeneous layered media as a tool in helping us understand the measurements and their possible limitations.

The Green's function is simply the impulse response of the system and is independent of either the surface or subsurface pressures. Examination of the characteristics of the Green's functions can help clarify fundamental properties of the diffusive system and reveal limitations that might occur in the interpretation of our pressure data sets to obtain diffusivity.

We have calculated the Green's function for the models illustrated in Figure 1. The

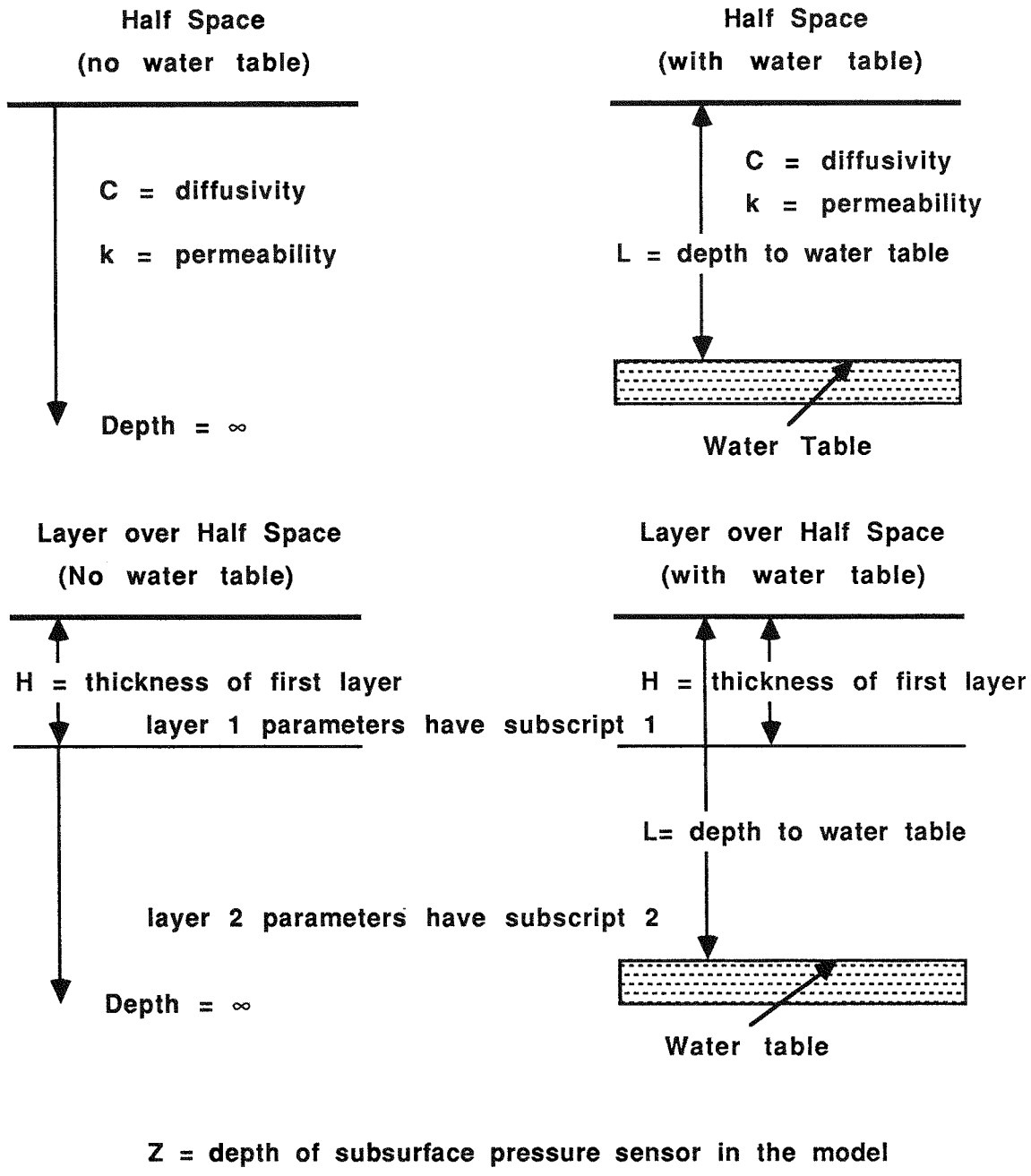

Figure 1. Models used in Green's function calculations

horizontally layered models use the appropriate combinations of the following boundary conditions for p(z,t) in their solution:

$$p(0,t) = \delta(t) \qquad \text{Surface condition for impulse response} \qquad (3)$$

$$\lim_{z \to \infty} p(z,t) = 0 \qquad \text{No pressure at infinity} \qquad (4)$$

$$\frac{\partial p(L,t)}{\partial z} = 0 \qquad \text{No flow at water table (z=L)} \qquad (5)$$

$$p_i(z=z_i,t) = p_{i+1}(z=z_i,t) \qquad \text{Continuity of pressure at layer boundary} \qquad (6)$$

$$k_i \frac{\partial p_i(z,t)}{\partial z} = k_{i+1} \frac{\partial p_{i+1}(z,t)}{\partial z} \qquad \text{No mass accumulation at layer boundary} \qquad (7)$$

The appropriate combinations of boundary conditions are used with Eq. 1 to obtain the Green's function for a homogeneous half space (with and without a water table) and a homogeneous layer over a half space (with and without a water table). These cases are illustrated in Figure 1. Assuming a time dependence of $\exp(-i\omega t)$, the solution to Eq. 1 for $p(z,\omega)$ in any layer can be represented as:

$$p_i(z,\omega) = A_i \exp(-\alpha_i z) + B_i \exp(\alpha_i z) \qquad (8)$$

$$\text{where } \alpha_i = \sqrt{-i\omega/C_i}$$

and where A_i and B_i depend on ω and are determined from the particular boundary conditions that apply to that problem and where C_i is the diffusivity.

The Green's function for a homogenous half space with no water table (solution to Equation 1 with boundary conditions 3 and 4) is:

$$G(z,\omega) = \exp(-\alpha z) \qquad (9)$$

The Green's function for a homogenous half space with a water table at z=L (solution to Equation 1 with boundary conditions 3 and 5) is:

$$G(z<L,\omega) = \frac{\cosh[\alpha(L-z)]}{\cosh(\alpha L)} \qquad (10)$$

The Greens' function solution for a homogeneous layer (thickness = H) over a homogeneous half space with no water table (solution to Equation 1 with boundary conditions 3, 4, 6, and 7) is:

$$G(z>H,\omega) = \frac{\exp(-\alpha_2 z)}{\exp(-\alpha_2 H)[\cosh(\alpha_1 H) + \kappa \sinh(\alpha_1 H)]} \qquad (11)$$

$$\text{where } \kappa = (k_2/k_1) \times \sqrt{C_1/C_2}$$

The analytical Green's function for a homogeneous layer (thickness = H) over a homogeneous half space with a water table at z = L (solution to Equation 1 with boundary conditions 3, 5, 6, and 7) is:

$$G(L>z>H,\omega) = \frac{\cosh[\alpha_2(L-z)]}{\cosh[\alpha_2(L-H)]\cosh(\alpha_1 H) + \kappa \sinh[\alpha_2(L-H)]\sinh(\alpha_1 H)} \qquad (12)$$

$$\text{where } \kappa = (k_2/k_1) \times \sqrt{C_1/C_2}$$

The Green's function can be used to determine the downhole pressure response of for any arbitrary surface pressure data set. In the frequency domain, this is simply a multiplication:

$$p_D(z,\omega) = G(z,\omega) \cdot p_S(0,\omega) \qquad (13)$$

In the time domain, this operation is represented by the convolution:

$$p_D(z,t) = \int_{-\infty}^{t} G(z,t-\tau)p_S(0,\tau)\partial\tau \qquad (14)$$

Note that in general, the subsurface pressure depends on the entire history of the surface pressure. For practical situations, we never have an infinitely long surface pressure record. It is sometimes assumed that the data lengths are long enough to approximate a stationary time series. In our interpretation technique, we also will assume that the data set is long enough to approximate a stationary time series.

Length of Impulse Response

The impulse response of the diffusive system can be very long. Figure 2 illustrates the impulse response for a homogeneous half space (k = 10 darcies, φ = 10%, C = $\approx$1600 m^2/hr) with a water table at 700 meters. Note that there is a significant contribution to the impulse response at depth out to times of about 300 hours (or 12 days). One of the effects of a long impulse response is that either the entire surface pressure history for time spans greater than this or the entire initial pressure distribution p(z,t=0) in the media must be known before gas transport predictions from transport models can be reliably made as the driving pressure for transport depends upon these initial pressure conditions. Figure 3 illustrates the decay of subsurface pressure with time for an initial subsurface pressure that is 0.1 psi greater than the surface pressure (surface pressure, p(0,t) = 0.0) in the homogeneous half space example of Figure 2.

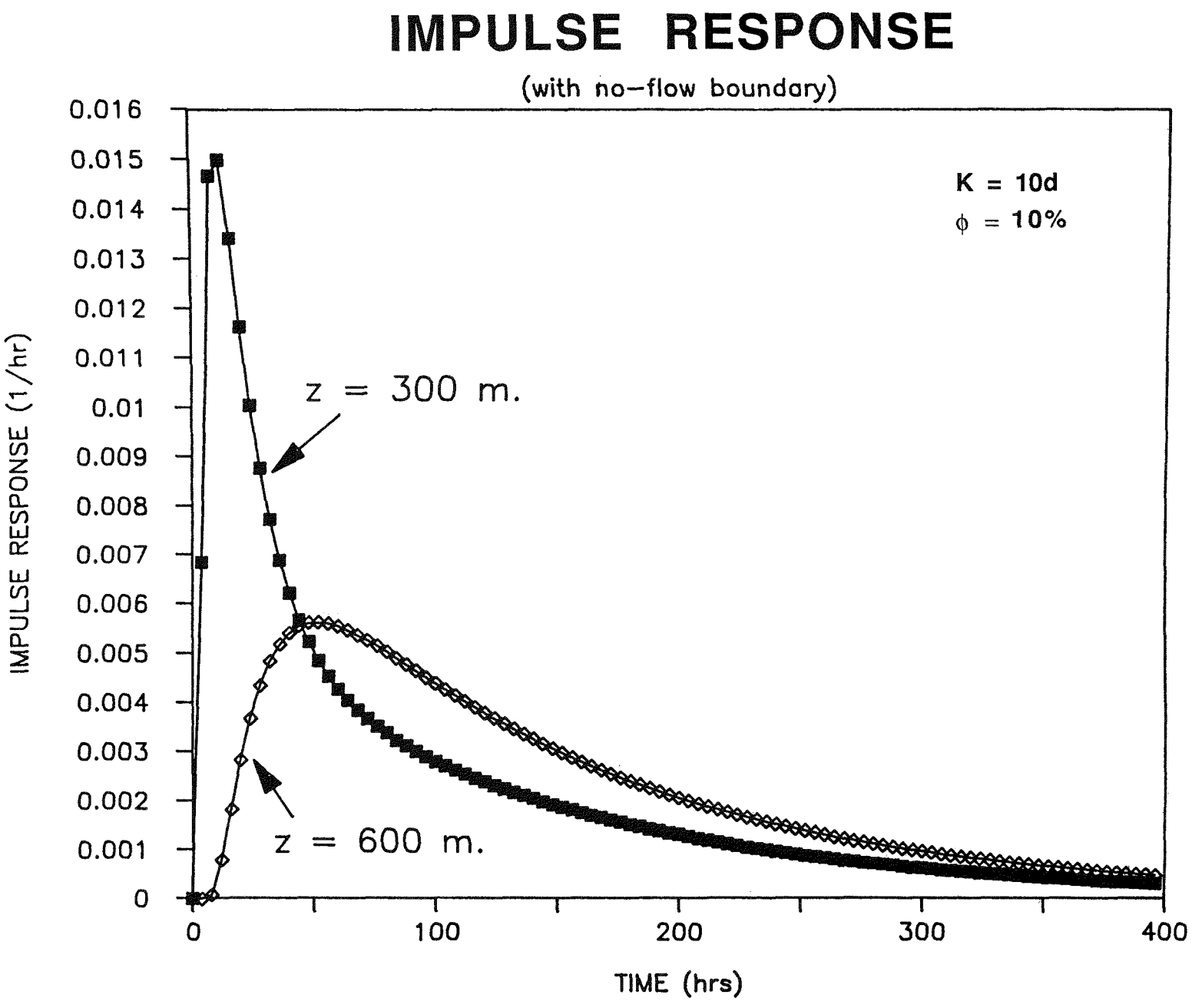

Figure 2. Impulse response (Green's function) of half space with a water table at 700 m. Subsurface sensors are located at 300 and 600 m.

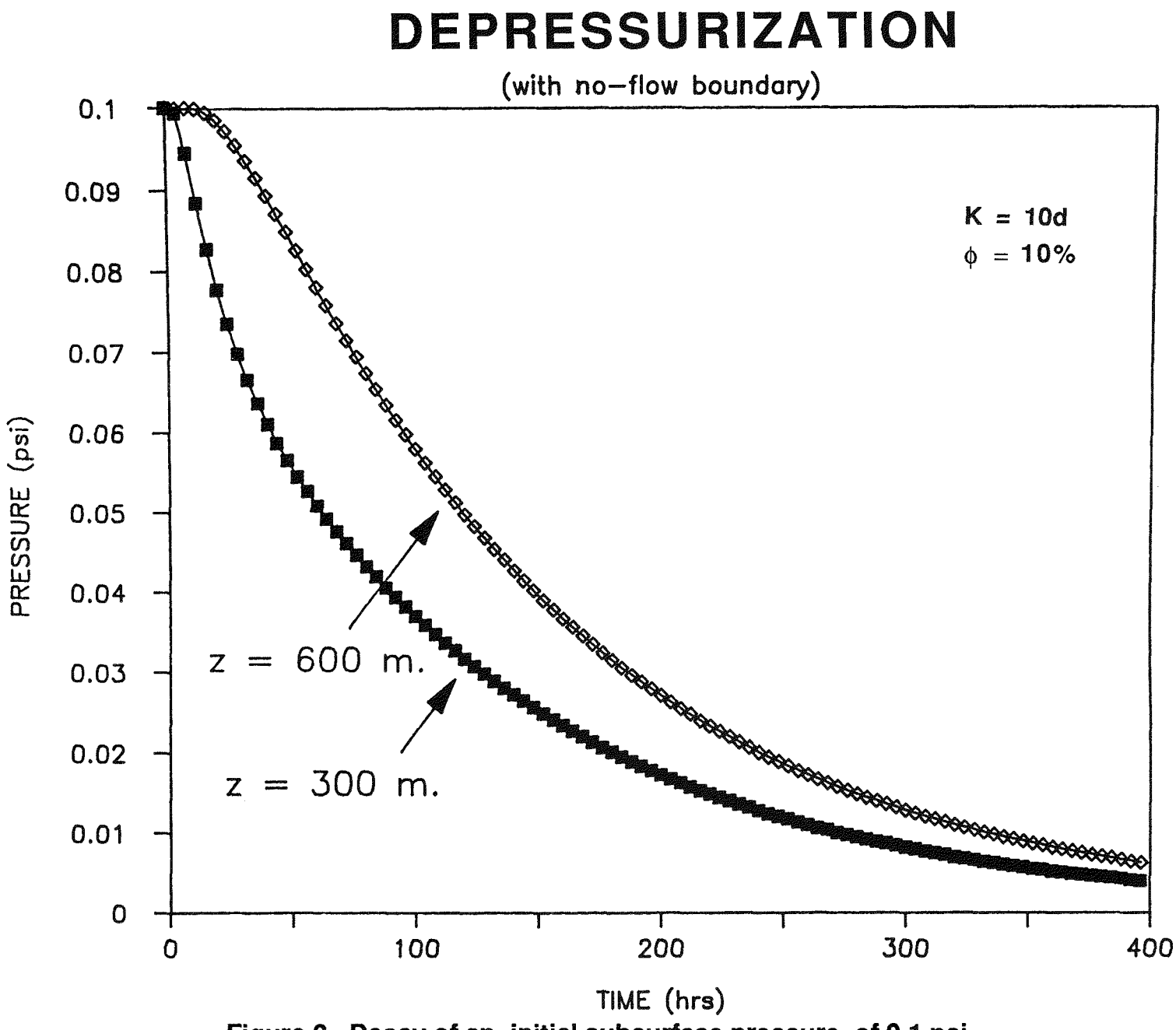

Figure 3. Decay of an initial subsurface pressure of 0.1 psi for a half space with a water table at 700 m with surface pressure held at 0.0 psi. Subsurface sensors are located at 300 and 600 m.

Data Acquisition

Surface and downhole atmospheric pressures have been recorded from post-shot holes that were completed for gas sampling. The typical configuration is illustrated in Figure 4. The holes have been cemented around the tubing for a significant fraction of the total hole depth. The holes penetrate the cavity region and/or chimney region. The instrumentation consists of two high precision quartz pressure gauges. Both gauges are buried several feet under ground on the surface in order to reduce thermal effects upon the gauges. The subsurface pressure sensor is connected by hose to the interior of the post-shot hole tubing. The surface pressure sensor is connected to the atmosphere with a hose. A digital recorder (a modified Commodore SX-64 computer) samples the pressures every 10 seconds. The digital data stream is then desampled (with digital anti-alias filtering if desired) to a sample time interval of 30 minutes (2 samples/hour) and recorded on a floppy disk. A typical data set length is about 300 to 500 hours of data (12-21 days). This length was chosen by balancing the desire to instrument several different sites in a finite time period and the natural occurence rate for pressure fronts at NTS. The maximum length for continuous recording at 2 samples/hour is about 40 days; the size of the floppy disc on the computer determines this length.

Data Interpretation (Time Domain)

Several finite difference codes have been written to solve the diffusion equation with the boundary conditions for the geometry appropriate to post-shot completion (length of cement and total depth of hole) [7]. These codes can take a large amount of CPU time for complicated geometries. Therefore, to rapidly get an estimate of the bulk diffusivity of the chimney region, we initially interpret the data assuming a homogeneous medium. An iterative forward modelling scheme in the time domain is used to match the subsurface data using the surface data as input. The iterative calculation is terminated when the value of chi-square for the fit between the measured subsurface data and the predicted subsurface data does not change significantly. The data gathered to date are in Table 1.

The surface (or elevation of the ground surface in the models) was assumed to be the elevation of the post-shot hole. However, this is not always a good assumption. A large surface crater that is 25 meters deep means that the subsurface pressure sensor is 25 meters closer to the boundary where the surface pressure is applied than we assumed in the interpretation. For the Agrini site with its bottle-shaped crater 68.6 meters deep, we also interpretated the data with the surface sensor being 68.6 meters closer to the subsurface sensor and obtained 1374 m^2/hr (a reduction of about 50%). Assuming a porosity of 10%, the range of diffusivities calculated (132-31000 m^2/hr) correspond to a permeability range of about 1-200 darcies. For volcanic rocks, laboratory measured matrix permeabilities are typically in the millidarcy range. The large values for the Pahute Mesa sites (U19ac, U20am, U20ap) would indicate that a combined fracture-matrix bulk diffusivity is being estimated and not just a matrix diffusivity. It should be noted that calculating the permeability from our estimates of diffusivity requires that the value of connected porosity be known. In general, the porosity is not known very well. Estimates range from less than 1% for volcanics to 30% for alluvium at NTS.

Figure 4. Schematic of gas sampling post shot hole used for atmospheric pressure measurements.

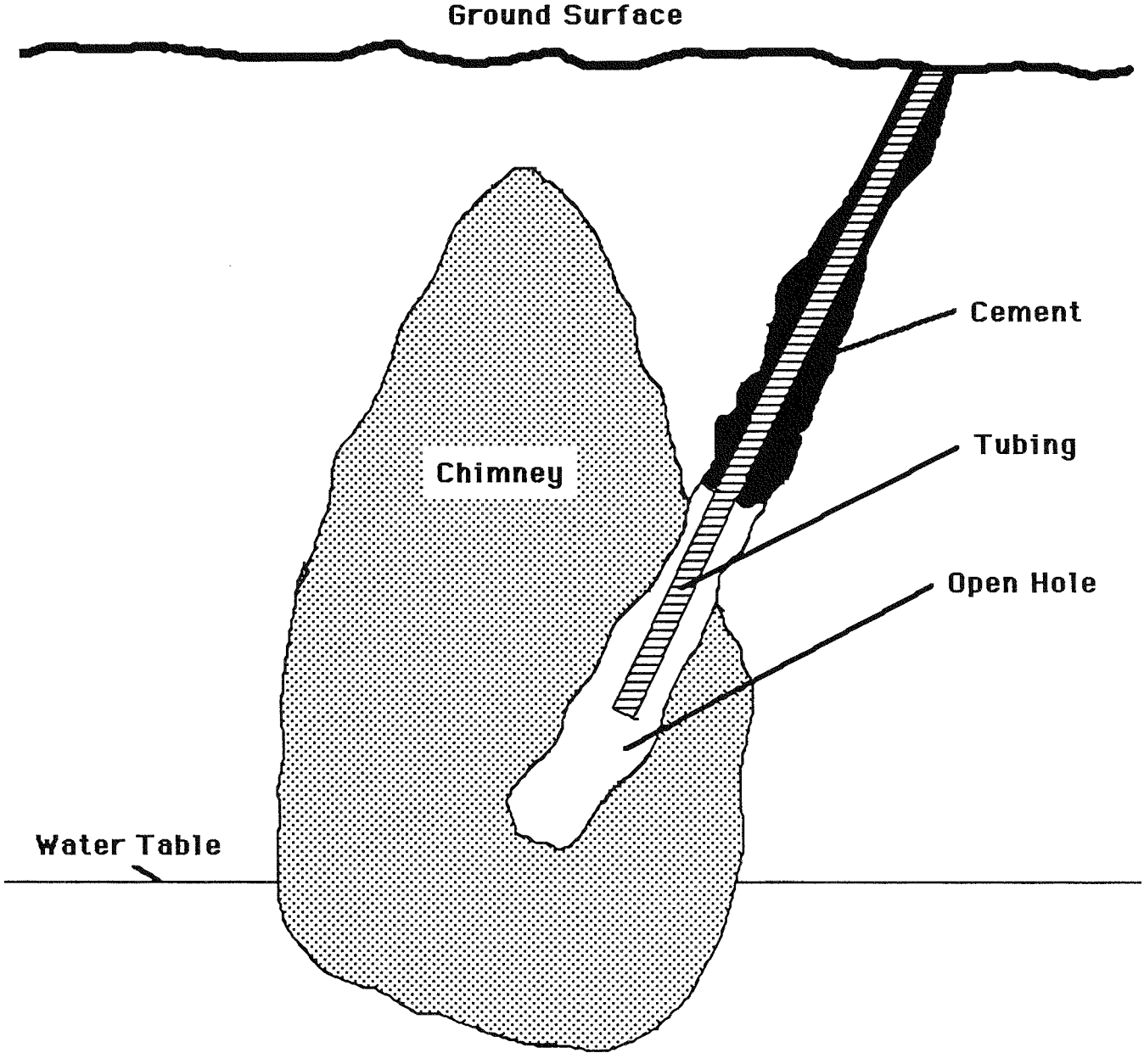

Table 1

Estimates of Chimney Diffusivity from Independent Pressure Data Sets

Hole	Event	Independent Diffusivity (m^2/hr) Estimates			Depth of Cement (m)
U2et	Cheedam	312			194.5
U2ev	Agrini	2790	2288	1374 **	117.3
U2##		414	398	384	214.0
U2fd	Tarko	1335			242.9
U2ff	Laban	182	188		200.6
U4ar	Breton	132			333.5
U8c	Norbo	400			217.6
U19ac	Tierra	3599			387.0
U20ac	Colwick	7412			557.0
U20am	Kappeli	30000	31000		495.0
U20ap	Bodie	551	415		202.1

** using crater depth of 68.6 meters as the elevation of the surface sensor.
U2## is an unannounced event in alluvium.

Data Interpretation (Frequency Domain)

We have also developed a method to rapidly estimate the diffusivity using a frequency domain representation of the data. The method assumes that the data sets are long enough to approximate a stationary time series. This method is quite simple. First, we calculate in the frequency domain the complex transfer function between the surface and subsurface pressure data (The complex transfer function is the impulse response of the system or the Green's function for a delta function pressure input.). Second, from the amplitude of the complex transfer function, we calculate an apparent diffusivity by using the following transformation:

$$C_{apparent} = \frac{\omega z^2}{2 (\ln |\text{transfer function}|)^2} \qquad (15)$$

where $|\ |$ is the modulus of the complex transfer function.

This transformation is based upon the modulus of the Green's function for a homogeneous half

space without a water table (Eq. 9). The $C_{apparent}$ transformation has several advantages over the transfer function as a means of representing the data. First, the units are the same as the desired physical property. Second, for a nearly homogeneous earth without a water table, the $C_{apparent}$ curves will be constant and have the value of the diffusivity of the earth. Third, the $C_{apparent}$ curves are in general simpler than the transfer function, and changes in their curvature define frequency ranges where different zones in the earth are influencing the data. A similar transformation is routinely used to simplify the interpretation of electrical resistivity data.

Theoretical master curves were calculated for a measurement at a depth z in a homogeneous half space of diffusivity, C, with a water table (Eq. 10). Figures 5 and 6 plot the apparent diffusivity, $C_{apparent}/C$, and the phase as a function of $\omega z^2/C$ for different ratios of the water table depth, L, to measurement depth, z. To determine the diffusivity from a real data set, we obtain the complex transfer function by dividing the complex Fourier transform of the subsurface pressure data by the complex Fourier transform of the the surface pressure data. We transform the transfer function according to Equation 15 and then determine which theoretical curve best fits our data. For the phase data, we simply plot our data and then determine which theoretical curve best fits our data.

Let us illustrate this process with an real example. Atmospheric pressure data from U2## ($\approx$360 hours long) are shown in Figure 7. The "glitches" in the data correspond to data drop outs in the raw data stream. We have not removed these "glitches" in our interpretation of these data. These data had the mean and a linear trend removed and have been Fourier transformed into amplitude and phase spectra. Figure 8 gives the amplitude spectrum of the surface and subsurface data along with an estimate of a transfer function calculated by dividing these two spectra. Note that the U2## data have power in a frequency band from about 0.004 to 0.025 cycles/hour. Data at lower frequencies give a physically unreasonable transfer function value that is greater than 1.0; data at higher frequencies do not appear to have much power (this is particularly true in the subsurface pressure sensor data). The amplitudes are partially transformed in Figure 9 and the phase differences are displayed in Figure 10.

In order to obtain diffusivity using Figure 5 as an interpretation tool, we need to know the depth of the downhole pressure sensor. Hanson [7] has shown that it is a good approximation to use the midpoint between the bottom of the cement and bottom of the post-shot hole as the depth of the subsurface pressure sensor. Figure 9 gives a value of about 0.0055 for $C_{apparent}/Z^2$. With Z=267.3 m, the flat portion of the curve in Figure 9 ($C_{apparent}/C$ = 1.0) yields a value of 393 $\pm$ $\approx$50 m^2/hr (error based upon scatter in plot) for a homogeneous half space model. The value of 393 m^2/hr compares favorably with the average value of 397 m^2/hr calculated with the time domain finite difference technique for the same data set. The phase difference plot for a homogeneous half space model also gives diffusivity values in this range.

Limitations of the Frequency Domain Diffusivity Estimation Technique

The pressure data have a limited spectrum; our data have a frequency range (0.002-0.03 cycles/hr) for useful information. Above 0.03 cycles/hour (or periods shorter than about 33 hours), there are significant sources of "noise" from solid earth tides which do not obey Eq. 1 and thermal effects on the sensors. At frequencies lower than 0.002 cycles/hour (or periods longer than 500 hours), the data sets that we typically obtain are just not long

Figure 5. Theoretical master curve for apparent diffusivity in a half space of diffusivity, C, for a measurement at depth, z, with a water table at depth, L.

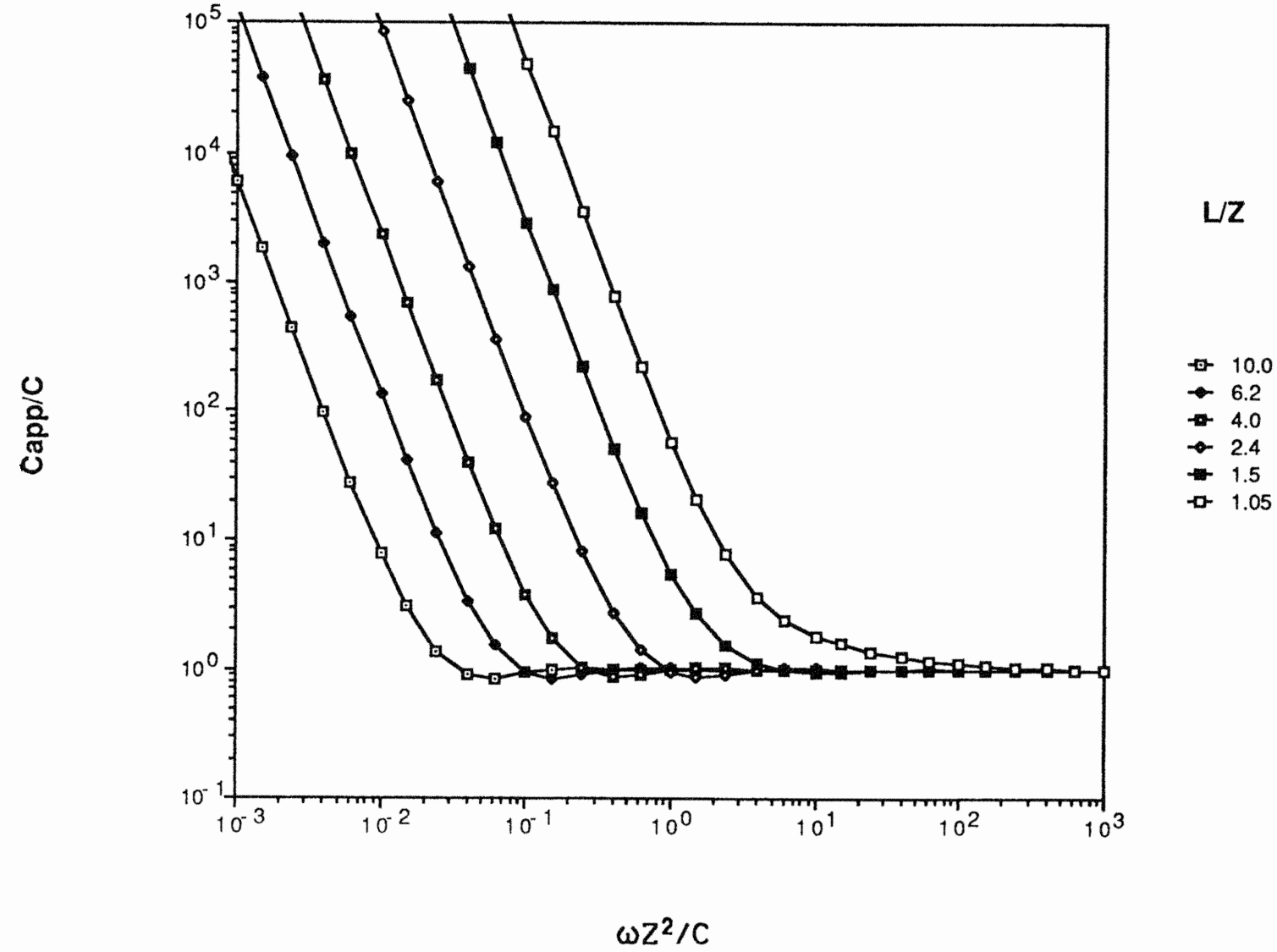

Figure 6. Theoretical master curve for the phase response in a half space of diffusivity, C, for a measurement at depth, z, with a water table at depth, L.

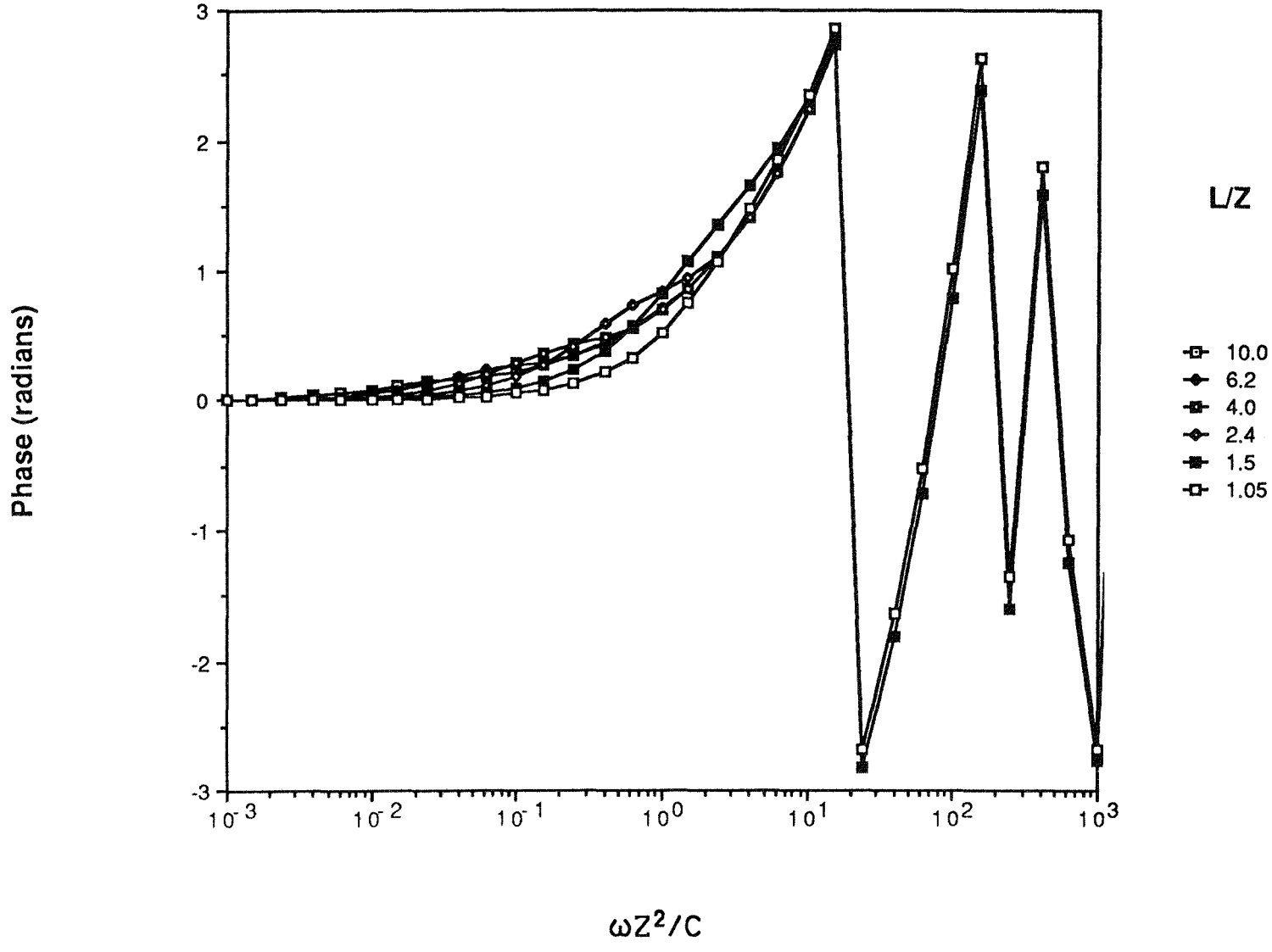

Figure 7. U2## atmospheric pressure variations

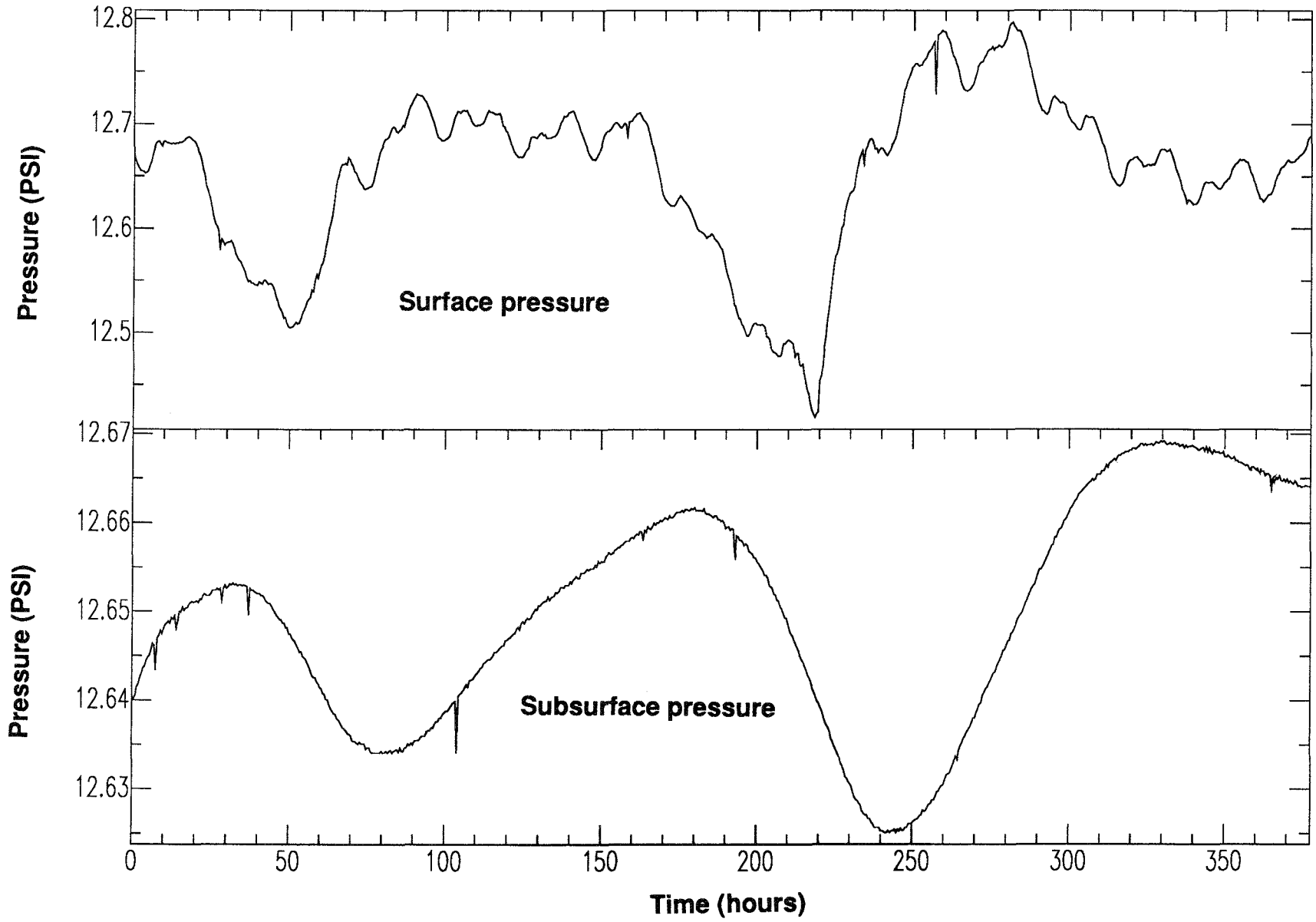

Figure 8. U2## transfer function and amplitude spectra

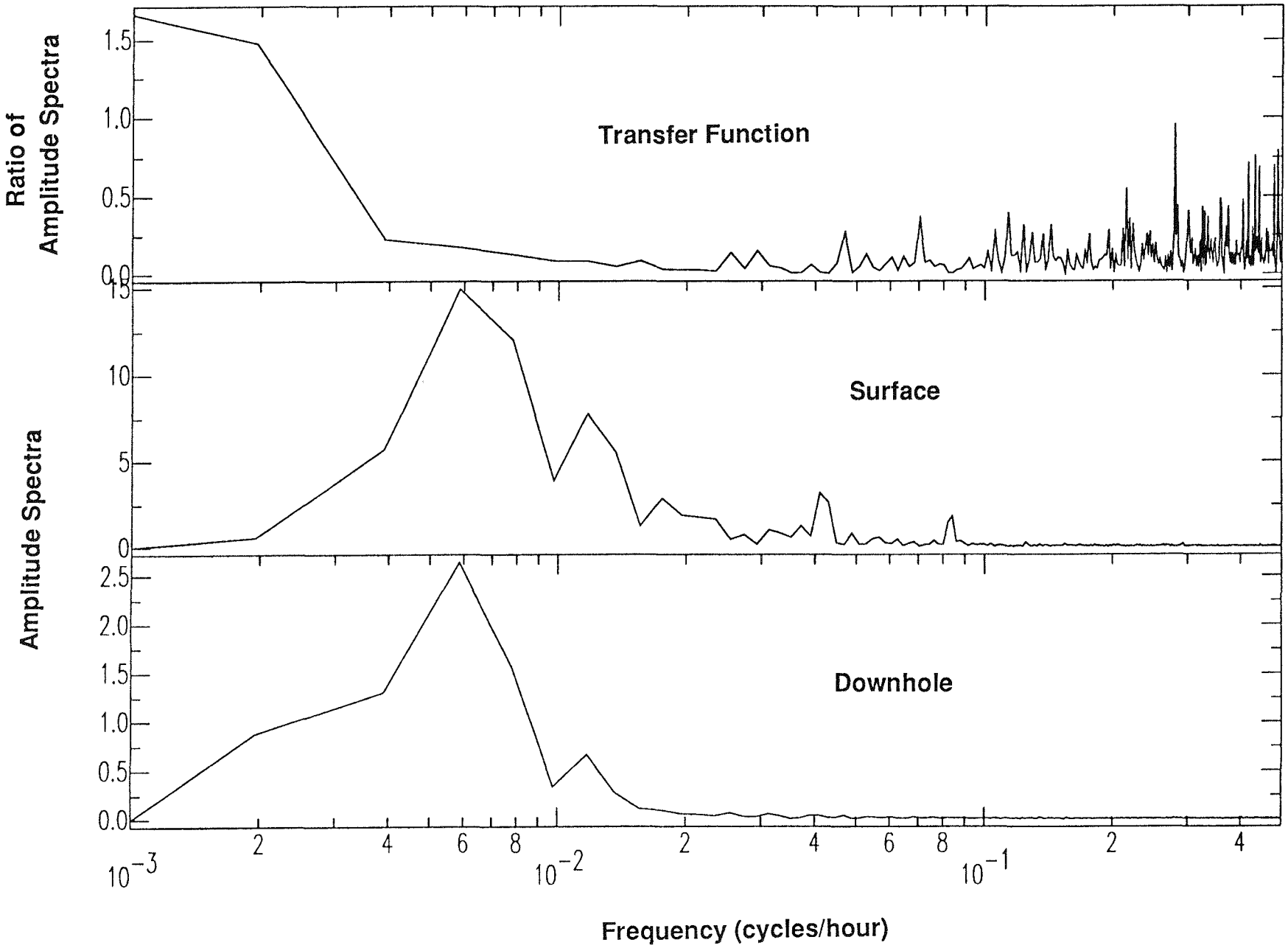

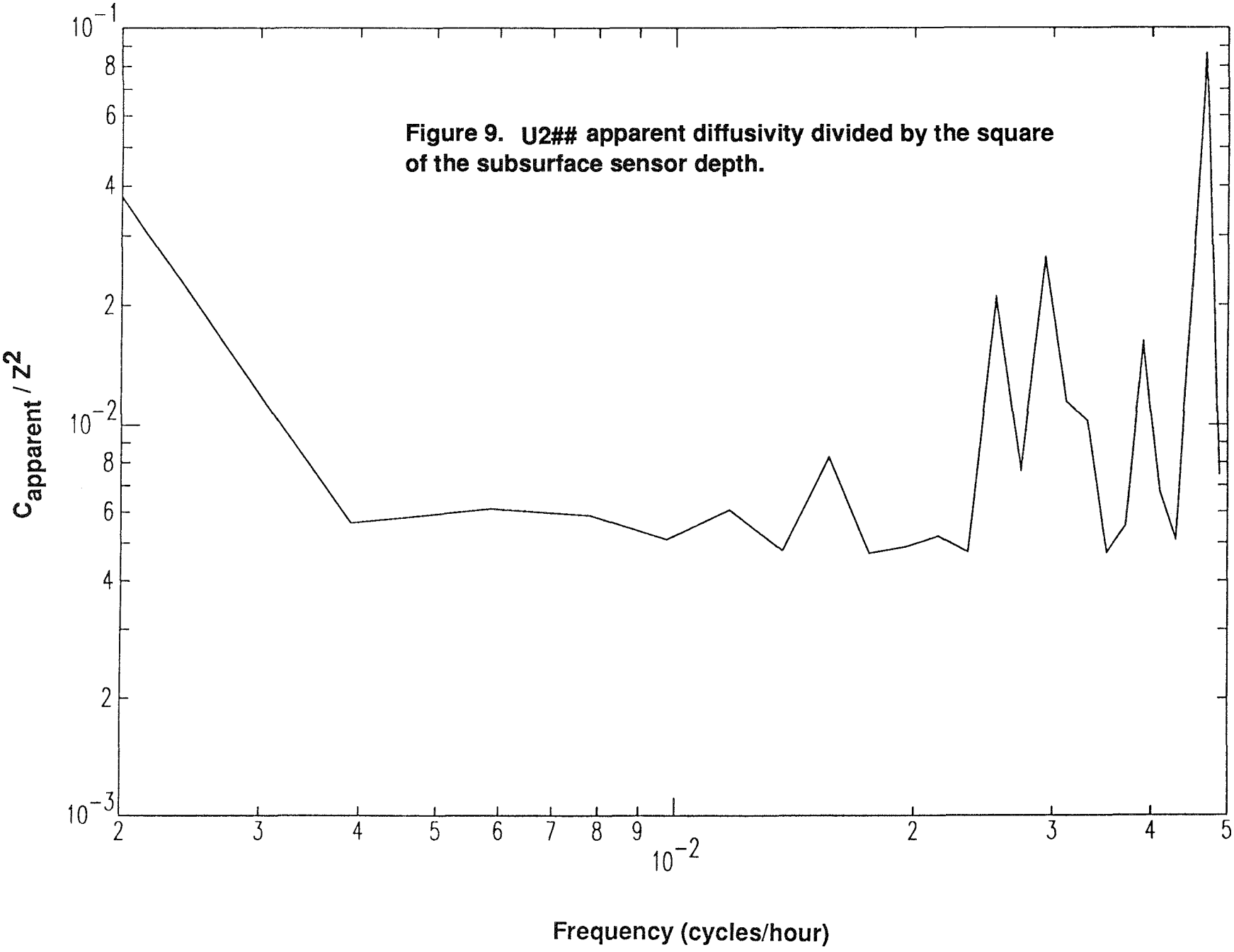

Figure 9. U2## apparent diffusivity divided by the square of the subsurface sensor depth.

Figure 10. U2## phase differences between the surface and subsurface sensor.

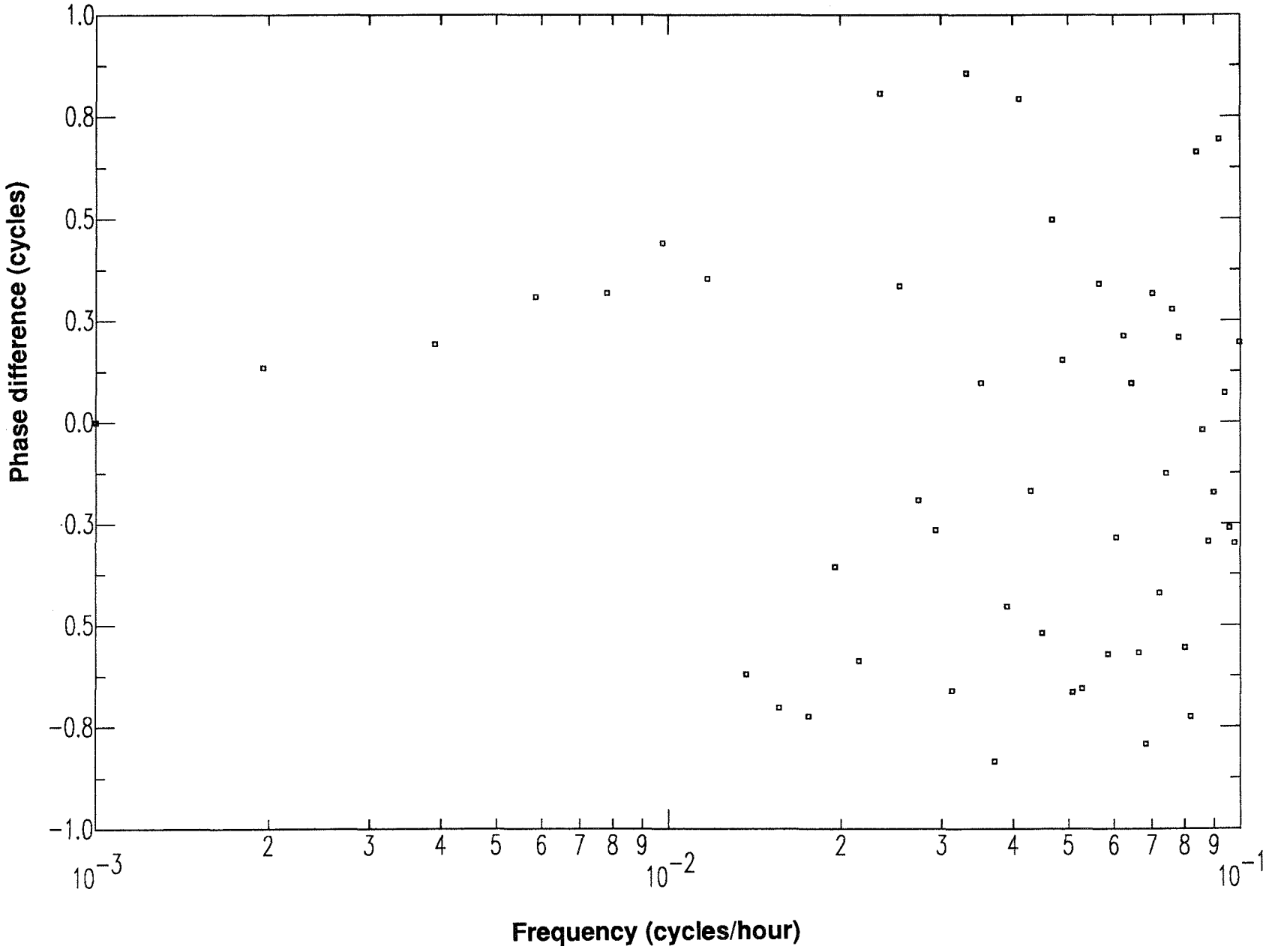

enough (most data sets are between 350-500 hours long). The driving factor in determining the length of data to record is the natural weather cycle at the NTS which produces the atmospheric pressure changes that we are interested in exploiting. Typically, an atmospheric pressure front (storm) typically occurs every 2-5 days at the NTS. This corresponds to pressure data in the frequency range of 0.008-0.02 cycles/hour. The data length that we can continuously record is limited by the size of the floppy disc to a maximum of about 40 days and by our "boredom factor" in wanting to acquire data in a finite time period. Fortunately, the natural weather cycle falls in between the time periods that we would get "bored" in gathering the data and the ones where the signal is contaminated.

These limits on frequency put real constraints upon our ability to resolve the diffusivity for a model and in our ability to distinguish between the simple models that we have proposed as interpretation aids. The plots of the theoretical Green's functions enable us to examine the uniqueness and resolution capabilities of the method. The conclusions that can be drawn from these plots would apply to the time domain results as well as any frequency domain results.

The frequency limitations mean that we can only put a lower bound on the depth of the water table and that we cannot use the data to determine the absolute depth of the water table. The locations of the bends in the curves in Figure 5 are the diagnostic tool for determining the depth of the water. For the U2## case, the data fell on the flat portion of the curves in Figure 5 (the ratio, $C_{apparent}/C = 1.0$). The smallest value of $\omega Z^2/C$ (for f = 0.004 cycles/hr) is about 4.5; thus the water table depth, L, must be greater than about 1.5 Z (or 400 m).

Two Layer Models

In the U2## example, we interpreted the data assuming a homogeneous half space. One can also ask: Do the data support a two-layer model interpretation? The interpretation process is somewhat more complex for the two layer model. First, master curves are constructed for the model under consideration. The parameters of the model are the diffusivities of the two layers, the permeabilities of the two layers, the thickness of the top layer, the depth to the water table, and the depth of the subsurface pressure sensor. One could construct master curves for apparent diffusivity as a function of these parameters; however, this would be a large number of plots. One possible way to proceed is to restrict the parameter space by using geologic knowledge of the problem under consideration. For example, the depth to the water table, the depth of the subsurface pressure sensor, and the thickness of the first layer could be constrained or even determined from geologic investigations. To illustrate the methodology, we have constructed a set of master curves for apparent diffusivity (Figure 11) and phase response (Figure 12) for the example in Table 2. We have constrained the ratio of permeabilities to be the same as the ratio of diffusivities (the connected porosity of both layers is the same). After calculating the apparent diffusivity from the measured pressure data, one does curve matching as was described in the previous section.

Examination of Figure 11 reveals some interesting features. Suppose that the apparent diffusivity data is basically constant (like the U2## example apparent diffusivity). Then the only diffusivity that we can really resolve is the diffusivity of the second layer, C_2. For example, suppose the apparent diffusivity is constant at 300 m^2/hr over the frequency band 0.004-0.02 cycles/hour. Then Figure 11 indicates the possibilities listed in Table 2.

Therefore, with apparent diffusivity data in the frequency band 0.004-0.02 cycles/hour, we would be unable to distinguish among any of the two layer cases listed in Table 2

Figure 11. Theoretical master curve for the apparent diffusivity, C, for a two layer model with a water table. The model used to construct these curves is listed in Table 2.

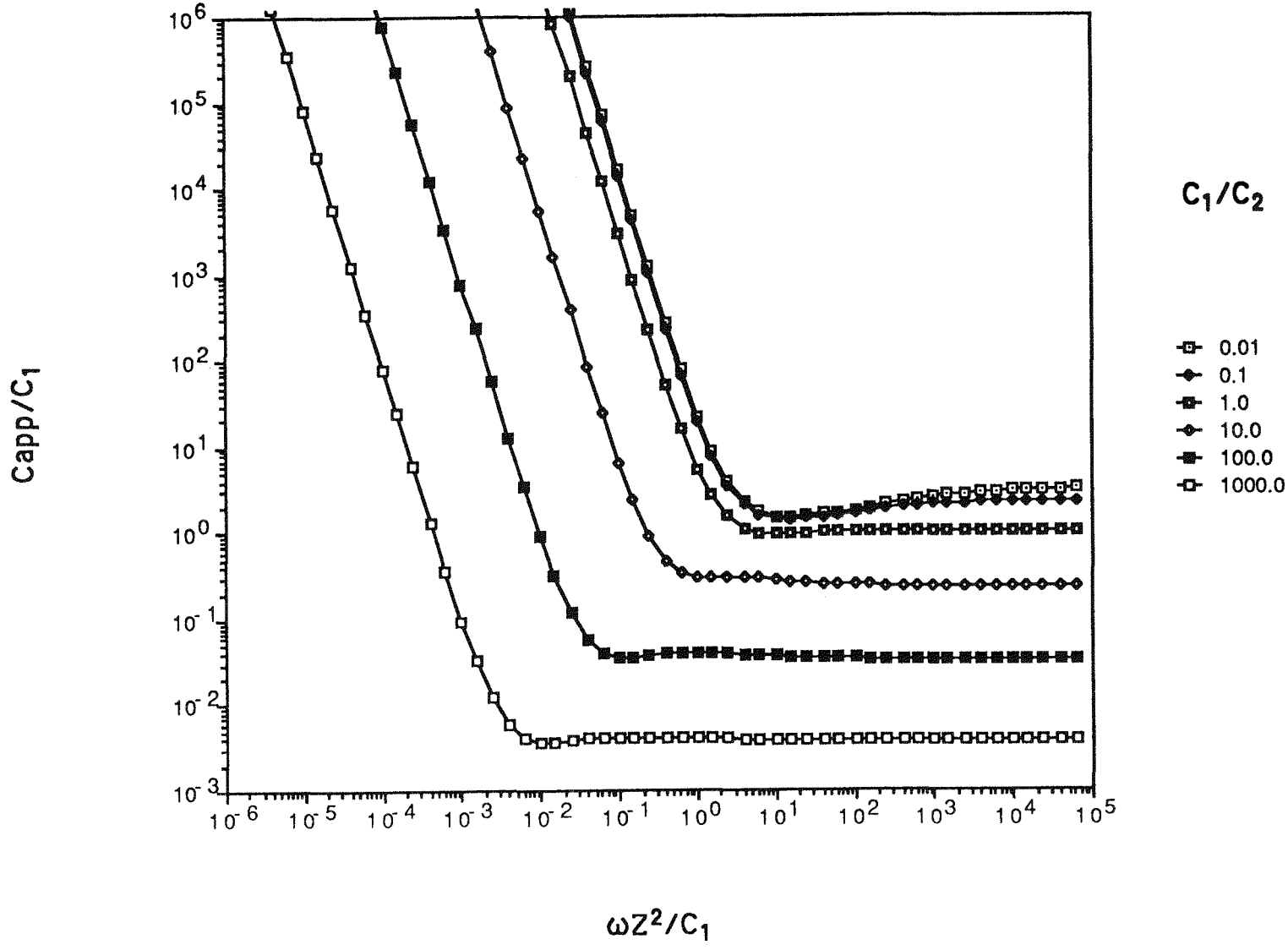

Figure 12. Theoretical master curve for the phase response for a two layer model with a water table. The model used to construct these curves is listed in Table 2.

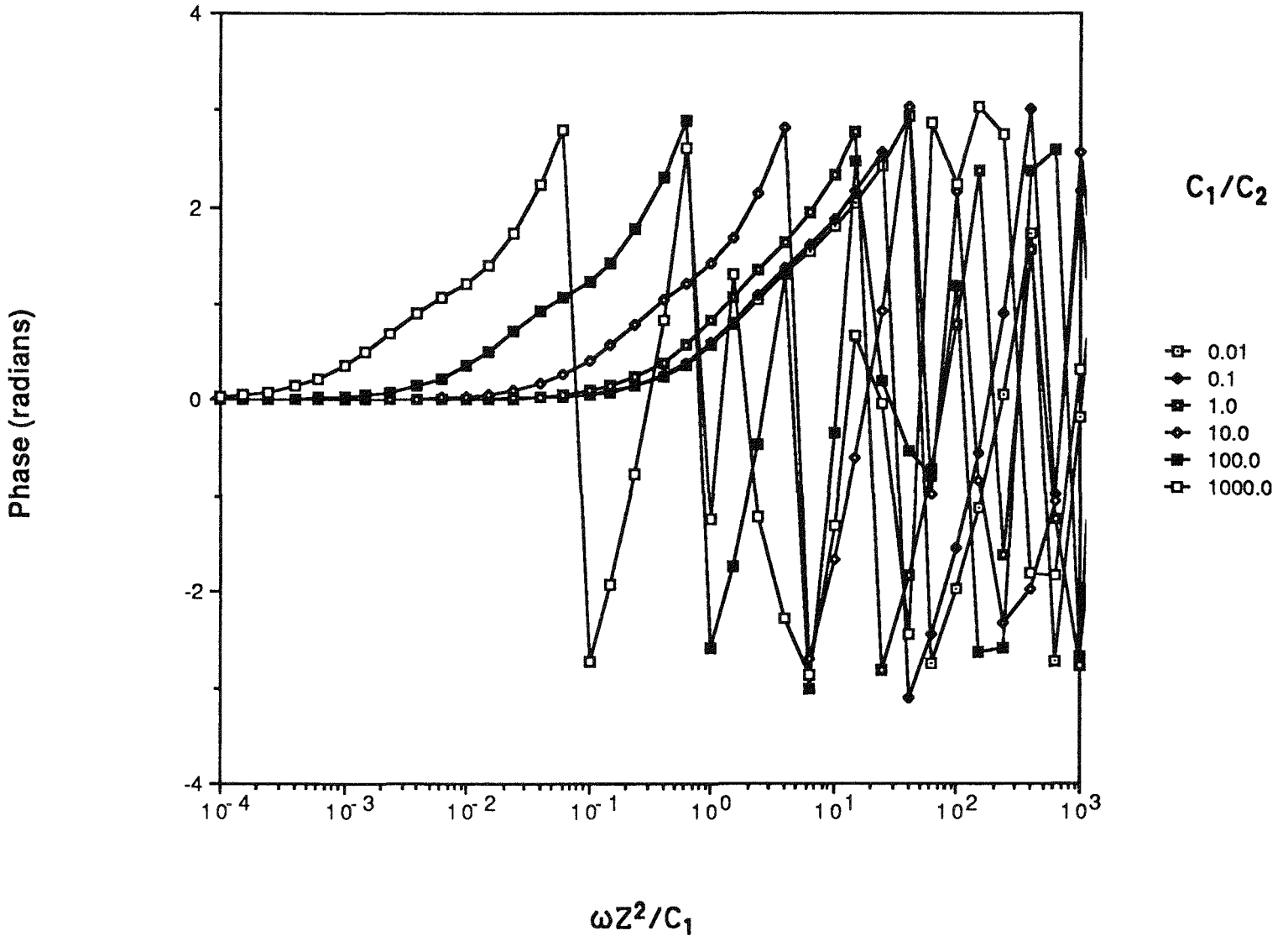

that have a C_1/C_2 ratio greater than or equal to 1.0. The small ratios are excluded because their corner frequencies fall outside the frequency range from 0.004-0.02 cycles/hour. Even with this restriction, we cannot really resolve the top layer's diffusivity. The top layer's diffusivity ranges from 300-78947 m^2/hour while the bottom layer varies over a range from 300-79 m^2/hour. It should be noted that we used the "eyeball" technique to determine where the curves in Figure 11 become "flat". Closer inspection might change the corner frequencies some; however, the effect is still the same. The ability to resolve the diffusivity of the top layer of a two-layer system with the pressure sensor in the second layer is severely limited (when the top layer is more diffusive and the apparent diffusivity data is band limited to a frequency range that corrsponds roughly to the atmospheric weather patterns). We are only really able to determine the smaller of the two layers' diffusivities.

Table 2

C_1/C_2	$C_{apparent}/C_1$	C_1	C_2	Corner Frequency (cycles/hour)
1000.0	0.0038	78947	79	0.003
100.0	0.033	9091	91	0.003
10.0	0.23	1304	130	0.003
1.0	1.0	300	300	0.003
0.1	2.2	136	1360	0.13
0.01	3.1	96	9677	1.9

$C_{apparent}$ = 300 m^2/hr

All diffusivities in m^2/hr

Depth of sensor = 400 m

Thickness of first layer = 200 m

Depth of water table = 600 m

Ratio of layer permeabilities is equal to the ratio of layer diffusivities.

Corner frequency is the frequency above which the apparent diffusivity data are flat for that particular C_1/C_2 ratio.

Figure 13 is an expanded version of Figure 11 for low ratios of C_1/C_2. Here the curves are not quite flat. However, the ability to distinguish between the master curves beyond a ratio of 0.01 is almost impossible. This means that when the top layer is more than 100 times less diffusive than the second layer for the parameters of the two layer model of Table 2, it would also be impossible to resolve the diffusivity of the bottom layer.

Effect of the Water Table

The water table takes up volume that would otherwise be a sink or source of air. The

Figure 13. Theoretical master curve for the apparent diffusivity, C, expanded for small ratios of C_1/C_2 for a two layer model with a water table. The model used to construct these curves is listed in Table 2.

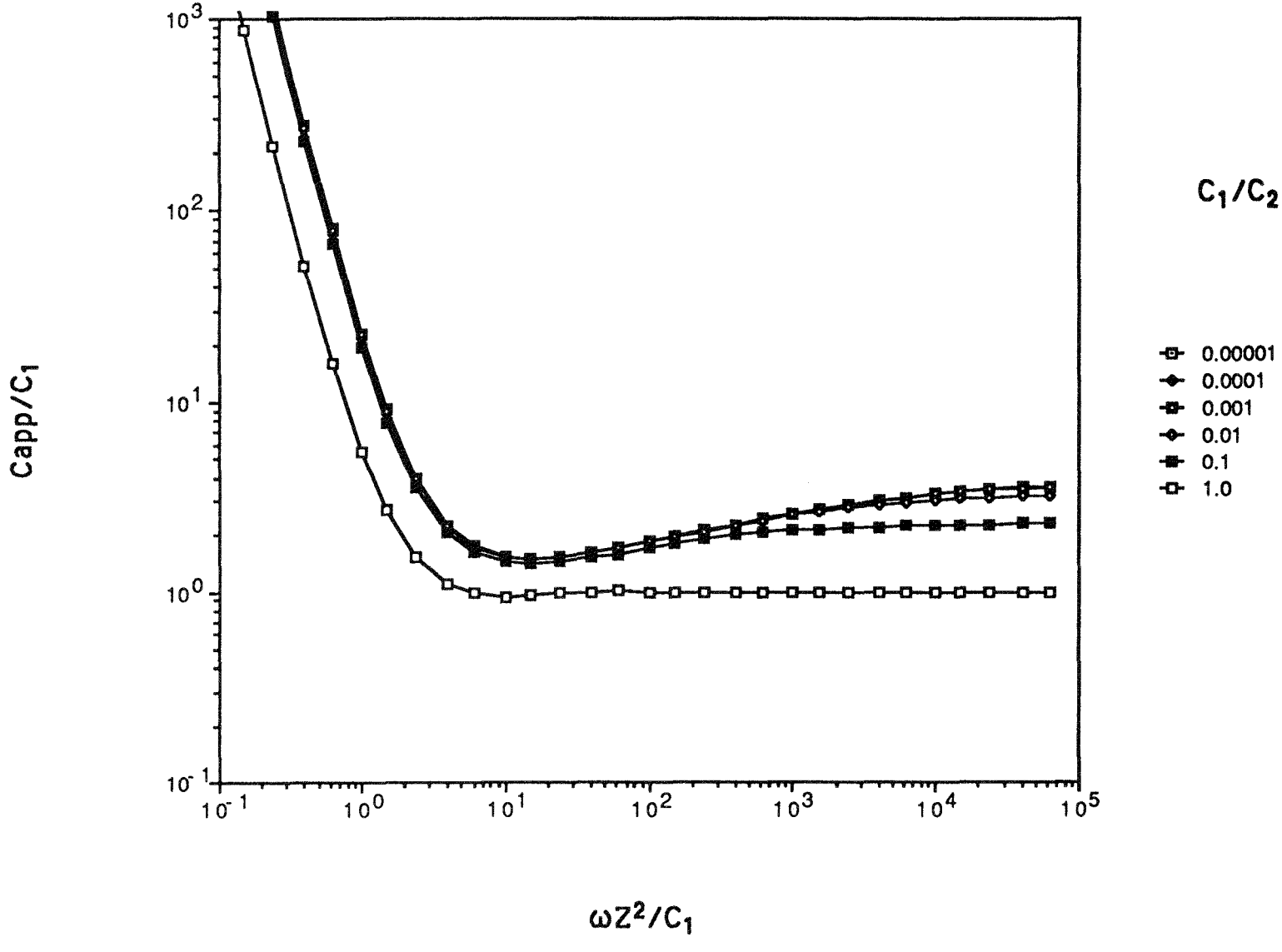

effect of the water table is readily seen in Figures 14, 15, 16, and 17. At high and very low values of $\omega Z^2/C$, the ratio of the Green's functions with and without a water table is unity as would be expected. At high frequencies, the pressure pulse never "sees" the water table as the water table is many diffusive "skin depths" deep. At very low frequencies, the pressure in the medium has time to equilibrate throughout the medium. In the intermediate frequency range, there is some enhancement of the amplitude of the pressure response at depth at most frequencies and very surprisingly also some frequencies at which the response is less. This part of the result is not well understood; however, we speculate that there is some type of resonant condition (like standing waves) that reduces the response at these particular frequencies. The enhancement was expected as the pressure waves "see" the water table and cannot propagate beyond it. For an impulse at the surface, the pressure response at depth would tend to build up more rapidly than if the volume below the water table had been available for storage of air.

Summary

Analytical expressions for the Green's functions of several simple models were calculated to aid in the interpretation of atmospheric pressure data for diffusivity structure.

The length of the impulse response for a typical NTS geologic setting can be quite long (>300 hr). The surface pressure history for time spans greater than 300 hr or the entire initial pressure distribution in the medium must be known before gas transport predictions can be reliably made from transport models, as the driving pressures for transport depend upon these initial conditions.

The range of diffusivities of chimneys measured to date is 132-31000 m^2/hr. These were calculated using a time domain finite difference technique. The bulk diffusivities calculated with the atmospheric pressure technique are a measurement on a large volume of material. The measurement includes the effect of the matrix and any fractures that might be present. The range of values for and the ability to resolve bulk diffusivity are important because bulk diffusivity is a key parameter in gas transport prediction models.

A frequency domain technique for estimating diffusivity has been developed. Examination of the master curves from this technique enable bounds to be established for our ability to estimate diffusivity. In two layer models, we can only resolve the smaller of the two layers' diffusivities.

The effect of the water table upon our data has been studied. In the intermediate frequency range, the presense of a water table near the downhole sensor enhances the pressure response.

Acknowledgements

This work was supported by the Nuclear Test Containment Program at Lawrence Livermore National Laboratory. It was performed under the auspices of the U. S. Department of Energy under Contract Number W-7405-ENG-48. Norman Burhard would like to acknowledge the very useful discussions with and stimulation provided by Paul Kasameyer on the interpretation methodology presented.

Figure 14. Amplitude ratio of Green's functions for homogeneous half space models with and without a water table.

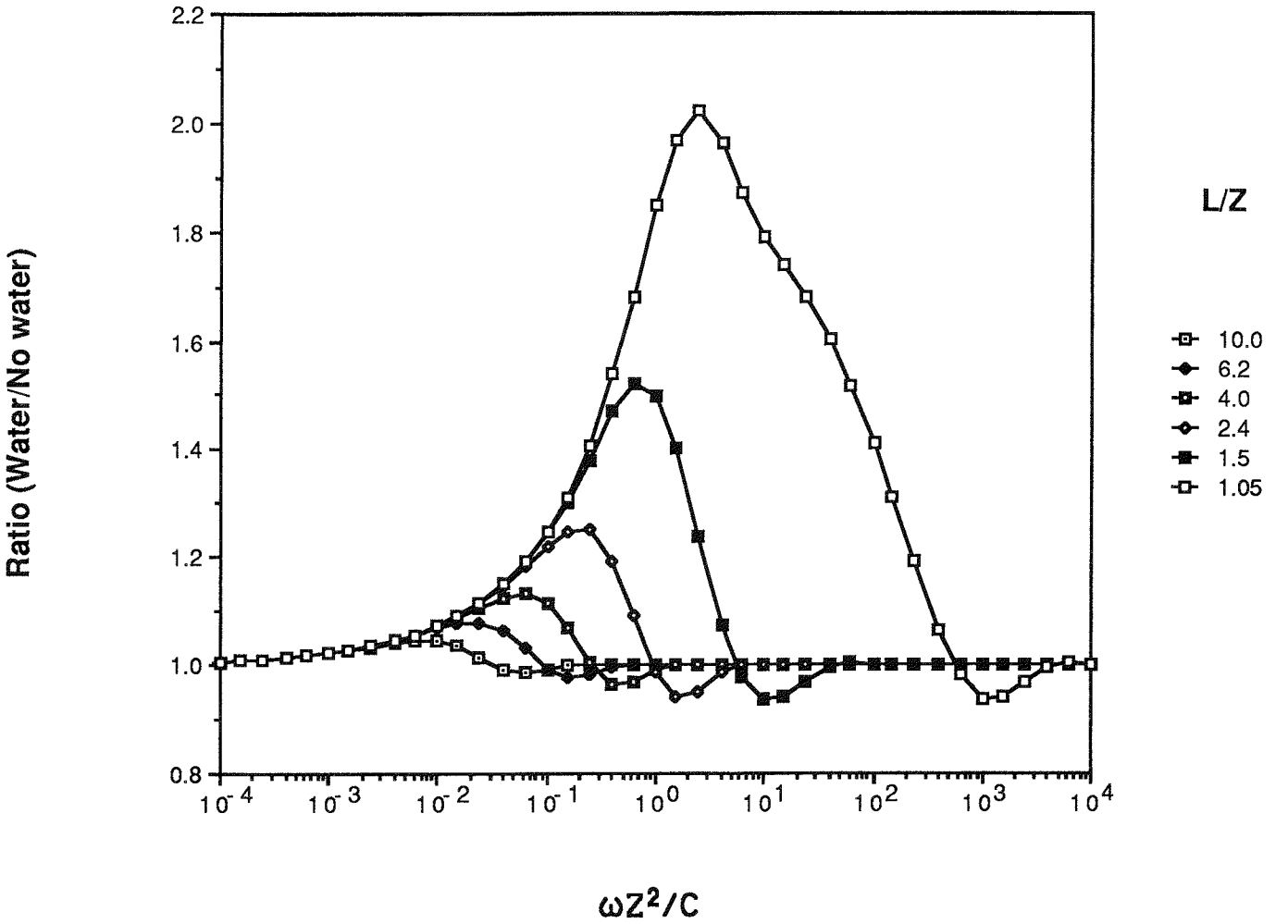

Figure 15. Phase difference of Green's functions for homogeneous half space models with and without a water table

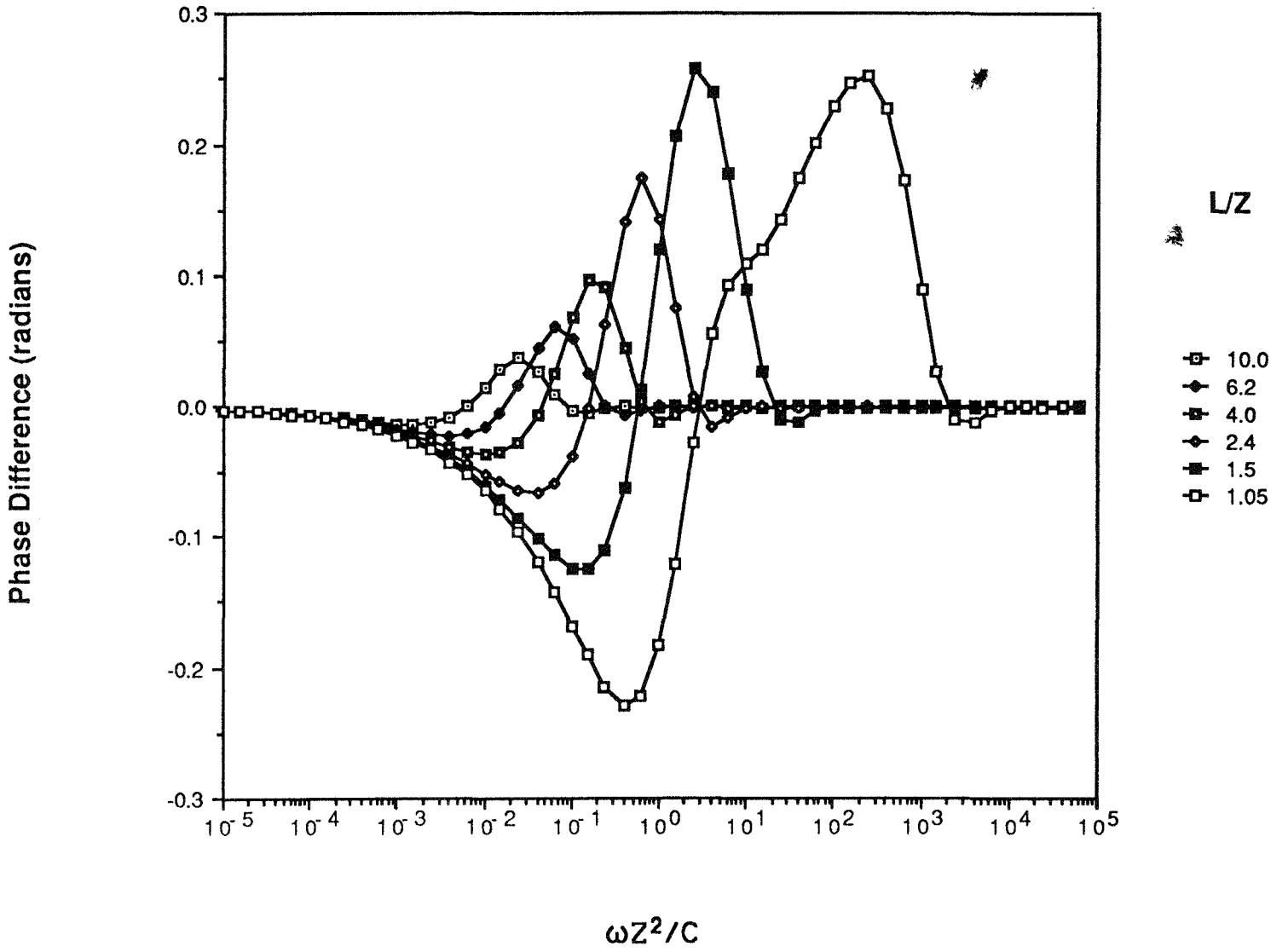

Figure 16. Amplitude ratio of Green's functions for two layer models with and without a water table. The model parameters are listed in Table 2.

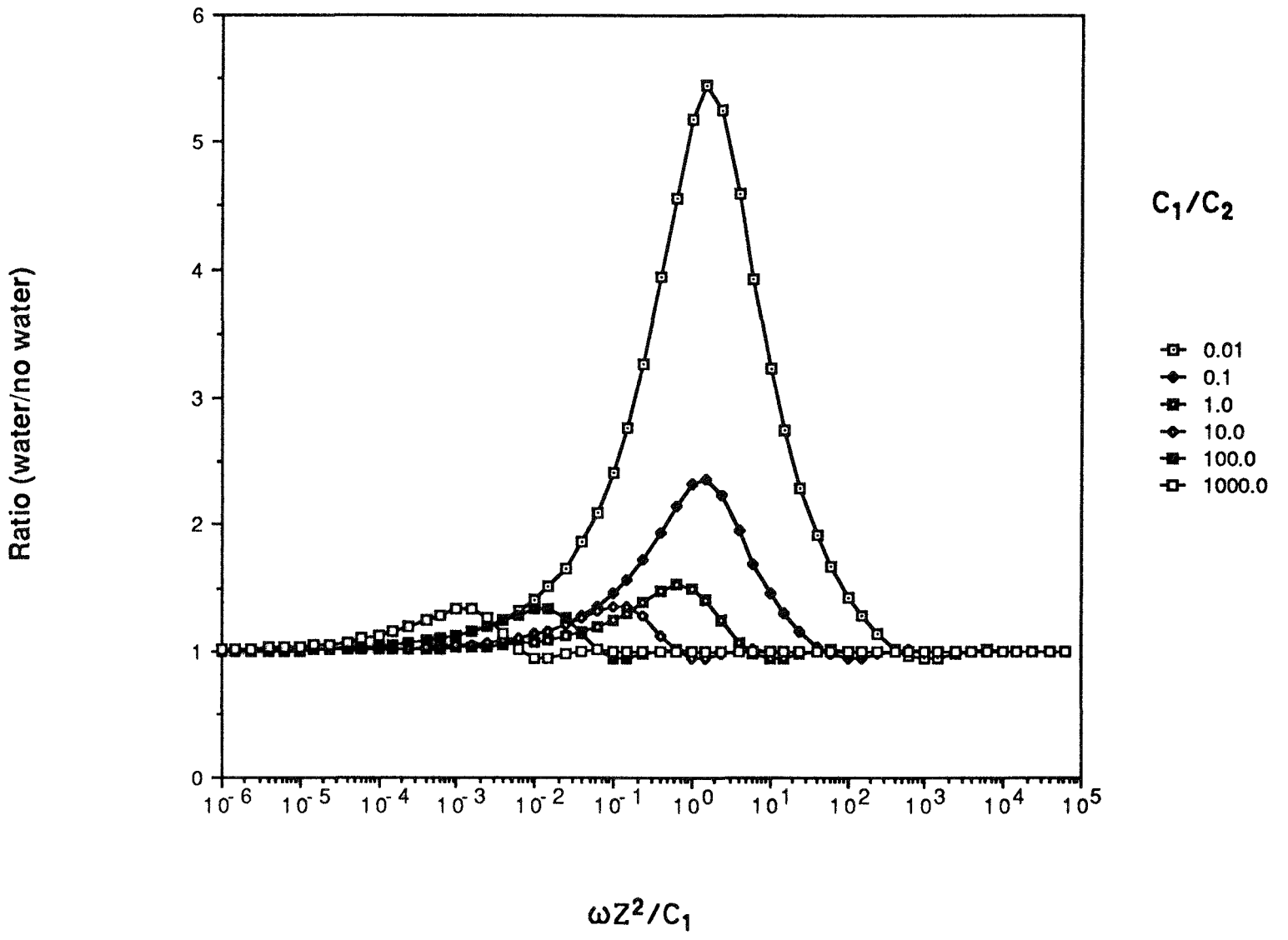

Figure 17. Phase difference of Green's functions for two layer models with and without a water table. The model parameters are listed in Table 2.

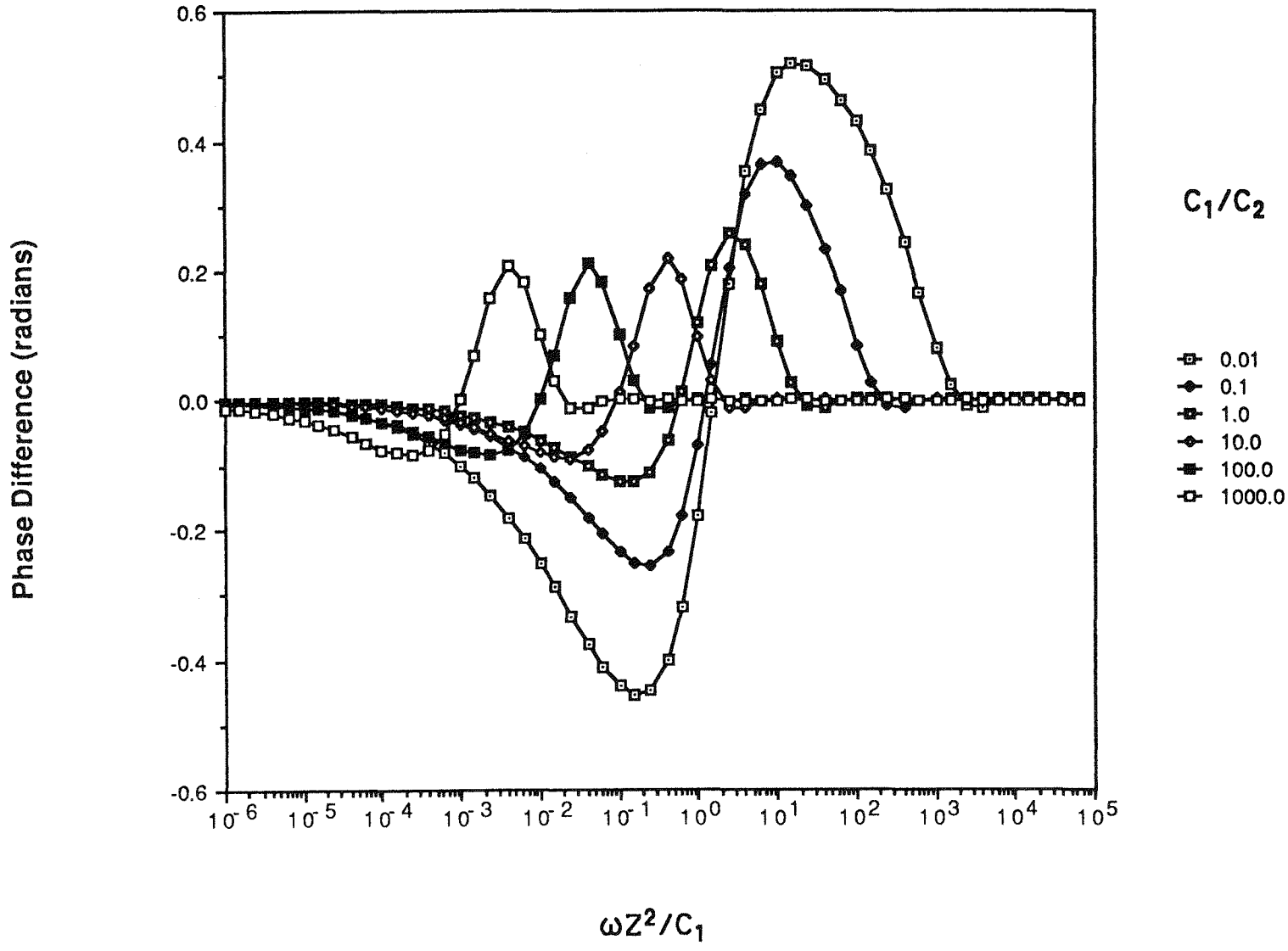

References

1. Nilson, R. H. and Lie, K. H., Numerical analysis of oscillatory gas motion and contaminant transport in a fractured porous medium, presented at the 4th Containment Symposium, this volume, 1987.
2. Nilson, R. H., Lie, K. H., and Peterson, E. W., Fickian filtering of cavity gases rising through a fractured permeable overburden, presented at the 4th Containment Symposium, this volume, 1987.
3. Hanson, J. M. and Hearst, J. R, Evaluation of permeability in the unsaturated zone at the Nevada Test Site using barometric pressure modeling, Proceeding of the Third Symposium on Containment of Underground Nuclear Explosions, Volume 1, LLNL CONF-850953, p. 392.
4. Rozsa, R. B., Snoeberger, D. F., and Baker, J., Chimney permeability data analysis, LLNL Report UCID-16440, January 30, 1974.
5. Snoeberger, D. F., Baker, J., Morris, C. J., and Rozsa, R. B., Permeability of a nuclear chimney and surface alluvium at the AEC Nevada Test Site, LLNL Report UCID-16479, April 17, 1974.
6. Snoeberger, D. F., Baker, J., Morris, C. J., Measurements and correlation analysis for nuclear chimney permeability, LLNL Report UCID-16302, July 10, 1973.
7. Hanson, J. M., Barometric pressure transient testing applications at the Nevada Test Site: Formation permeability analysis, TerraTek Report to LLNL, December, 1984, UCRL-15699.

SSS-R-88-8687

FICKIAN FILTERING OF CAVITY GASES RISING THROUGH A FRACTURED PERMEABLE OVERBURDEN

R. H. Nilson
K. H. Lie
E. W. Peterson
S-CUBED
A Division of Maxwell Laboratories, Inc.
P. O. Box 1620
La Jolla, CA 92038

ABSTRACT

In naturally or explosively fractured geologic media most of the permeability is associated with the fracture network, whereas most of the porosity resides within the matrix blocks. Thus, both levels of porosity, fracture and matrix, are important in controlling the transient migration of radioactive gases from an underground nuclear cavity to the earth's surface.

A numerical model of a double-porosity medium is used to investigate the upward transport of contaminant resulting from a moderate post-collapse overpressure in the chimney and/or cyclical pumping due to atmospheric pressure variations. It is found that the threat of rapid arrival through fractures is greatly mitigated by the process of Fickian diffusion which "filters" the contaminated gases as they rise through the fractures. Because of differences in concentration, contaminant species are drawn out of the rising gases into the surrounding porous matrix which contains relatively fresh air. The effectiveness of this Fickian filtering process depends on the aperture and spacings of fractures. Thus, consideration is given to the question of estimating these parameters of a double-porosity medium using field measurements such as the barometric pressure data reported by Hanson and Hearst at the previous containment symposium.

Although the fracture/matrix interaction can be beneficial in buffering a strong first arrival of radiation, it can also give rise to a ratchet-like dispersion mechanism during successive cycles of oscillatory motion, as described by Peterson, Lie and Nilson in this symposium.

* This work sponsored by the Nuclear Test Containment Program at Lawrence Livermore National Laboratory.

INTRODUCTION

It is generally accepted by the containment community that nearly all underground nuclear tests will eventually leak some radioactive gas to the atmosphere. Conservative burial practices and well-engineered stemming designs have successfully eliminated the early-time threat of gas transport driven by high-pressure steam in the cavity. But it is not unusual to observe the gradual arrival of a small amount of radioactive gas on the extended time scales of days, weeks, months, and even years after a test.

Although the associated levels of radioactivity have never posed a health hazard, the Containment Program at Lawrence Livermore National Laboratory has, over a number of years, made an effort to better understand these late-time seepage mechanisms. The goals of this work include: better prediction of the late-time seepage based on physical models, field measurements, and historical data; improved site selection practices; and the identification of practical preventive measures.

Fickian diffusion driven by concentration gradients cannot explain the observed radiation arrivals. Since gaseous diffusion coefficients are smaller than 10^{-5} m^2/s, significant arrivals from depths in excess of 200 meters should only occur on time scales of $L^2/D \sim 4 \times 10^9$ s $\sim$ 100 years. At the Second Containment Symposium R. G. Geil reported an experimental study of radiation levels in the soil gases of Yucca Flats. He found radiation levels two or three orders of magnitude greater than expected from Fickian diffusion, particularly along preexisting faults and the fissures produced by crater collapse, suggesting the likelihood of pressure-driven transport along preferential paths. But this was a relatively subtle form of pressure-driven transport, occurring months to years after quenching of the pressure in the cavity.

Weather patterns cause cylindrical variations in the barometric pressure having differential amplitudes on the order of 1/30 atm over periods of roughly 200 hours. As the barometer falls gases are drawn upward out of the permeable earth into the atmosphere. Conversely, as the barometric pressure increases, fresh air is pushed downward into the soil. At the Third Containment Symposium Hanson and Hearst[1] reported experimental measurements of the downhole pressure response occurring in capped emplacement holes as a result of this "atmospheric pumping" process. By observing the time lag and attenuation of the downhole response, compared to the surface forcing function, they were able to deduce the pore-fluid diffusivity which controls the speed of Darcian pressure disturbances moving through the permeable emplacement medium. In one particular hole on Pahute mesa they detected unusually large pore-fluid diffusivities which strongly suggested the presence of fractures, as

confirmed by the logging records. Post-shot monitoring of this hole indicated a connection between falling barometric pressure and surface detection of trace-level radiation, strengthening the association between atmospheric pumping, fractured media, and radioactive gas transport.

The present paper reports analytical and numerical studies of contaminant transport induced by atmospheric pumping. The mathematical model is based on a double-porosity [2,3] formulation which describes the interaction between fracture-porosity and matrix-porosity. Special emphasis is given to processes occurring in highly fractured media where one might expect to see cavity gases arriving at the surface during the first period of falling barometer. It is shown that the threat of rapid arrival through fractures is greatly mitigated by the process of Fickian diffusion which "filters" the contaminated gases as they rise through the fractures. Because of differences in concentration, contaminant species are drawn out of the rising gases into the surrounding porous matrix which contains relatively fresh air. This filtering mechanism has been previously studied by hydrologists[4] because it is thought to be beneficial in retarding the migration of contaminants carried by ground water.

A companion paper presented by Peterson, Lie and Nilson[5] at this symposium addresses the closely-related topic of dispersive mechanisms occurring during atmospheric pumping. The focus of that work is the ratcheting or boot-strap mechanisms which can bring contaminants to the surface after repeated cycles of oscillatory motion, even though the upward displacements associated with any single barometric cycle are small compared to the burial depth. In this class of medium Fickian diffusion is detrimental because it causes contaminants to be temporarily stored in the walls of a fracture in the interim between episodes of upward motion.

Overall, the upward transport in highly-fractured media is more benign than expected, whereas the opposite is true of the more homogeneous media. So there should be less of a disparity in behaviors than one would anticipate on the basis of simpler models which ignore the complex interactions between advective transport along fractures and the Fickian and Darcian diffusion into the surrounding permeable matrix.

PISTON-LIKE DISPLACEMENTS IN A SINGLE-POROSITY MEDIUM

First consider one-dimensional vertical transport in a homogeneous single-porosity medium. Let us begin by examining the case of quasi-static gas motions in which the pore-fluid diffusivity of the medium is so large that the air pressure throughout the medium adjusts itself instantaneously to variations in the surface

pressure. This provides a simple upper-bound estimate for the displacement of a contaminant during a cycle of atmospheric pumping.

The quasi-static displacement model is illustrated schematically in Figure 1 where a permeable layer of overall depth L is subjected to a surface pressure variation with a peak-to-peak amplitude of ΔP. The differential displacement ΔL of a gas particle or an interface (e.g., between contaminated versus fresh gas) can be estimated from the formula

$$\frac{\Delta L}{L_o} = \frac{\Delta P}{P_o} \sim \frac{2}{30} \tag{1}$$

in which P_o is the ambient pressure level and L_o is the depth of gas beneath the interface. This formula is based on the observation that the volume of gas below the interface ($V_o = A_{cc}\,\phi L_o$) expands into an incremental volume of $\Delta V = A_{cc}\phi\Delta L$ during an isothermal pressure change in which $\Delta V/V_o = \Delta P/P_o$. Note that the porosity, ϕ, of the medium must be uniform in order that $\Delta L/L_o$ be identical to $\Delta V/V_o$. Also, there must be a lower boundary to the gas-filled porous layer imposed by either a water table or a low permeability bed rock, as is generally true at NTS.

For the typical example of Figure 1, a pressure variation of $\Delta P/P_o = 2/30$ produces a differential displacement of only $\Delta L = 20$ meters for an interface located 300 meters above the water table. Such a small amount of upward displacement is probably of no concern, particularly since the contaminated gas would be pushed back down again during the next period of increasing barometric pressure.

This quasi-static model clearly illustrates the importance of overburden porosity in reducing the threat of radioactive gas migration. In essence, the overburden porosity provides a buffer volume between the cavity gas and the surface. During atmospheric lows, the cavity gas expands upward into this buffer volume. During atmospheric highs, the process is reversed. Stated most simplistically, if the volume of contaminated gas is V_o, and the fractional pressure change is 1/30, then a buffer volume of $V_o/30$ is marginally sufficient to prevent surface venting. It is emphasized that the capacitance effect of the buffer volume is achieved by displacement, not by pressurization: the contaminated gas flows upward into the bottom of the buffer as the fresh gas flows out the top.

The same basic argument is applicable either to a homogeneous porous medium, like sand, or to a uniform network of fractures which are separated by impermeable material. In either case, the buffer volume of the overburden seems more than sufficient to accommodate the differential expansion of the contaminated gas which lies beneath.

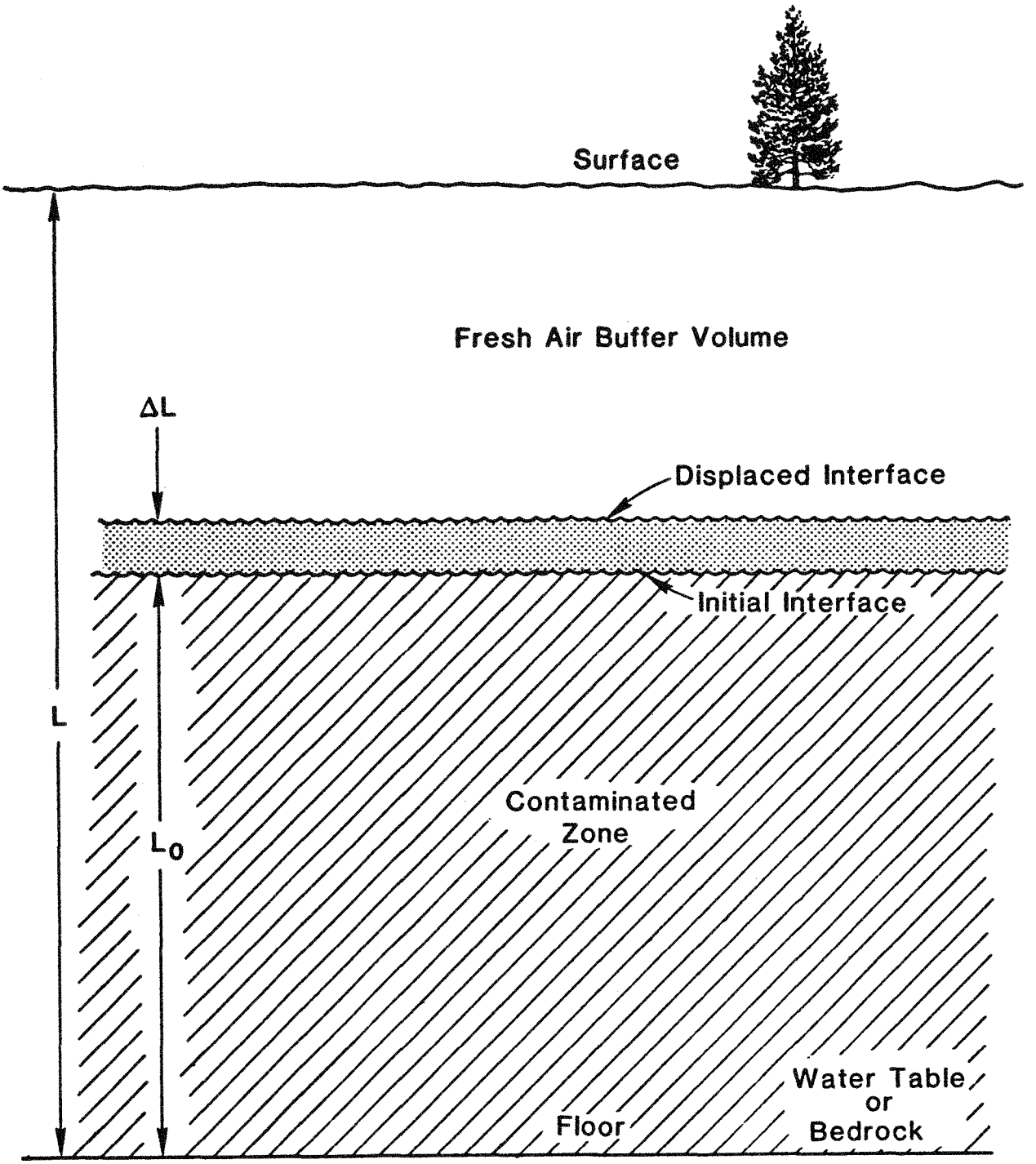

Figure 1. Schematic of a piston-like displacement caused by a pressure decrease at the surface of a homogeneous porous medium. Contaminated gas below the interface expands uniformly upward into the buffer volume of the overlying pore space.

Thus, it might appear that the upward displacement of contaminated gas should always be small, even if the diffusivity of the medium is extremely large, as we've assumed in this quasi-static model. A smaller diffusivity would reduce the amplitude of the pressure variations occurring at depth. Thus, there would be less volumetric expansion and contraction below the fresh/contaminated interface. So the upward displacements could only be smaller and even less threatening.

In reality, however, nonhomogeneities of the emplacement medium and, in particular, the presence of fractures, can cause significant departures from this very benign piston-like displacement model.

QUASISTATIC DISPLACEMENTS IN A DOUBLE POROSITY MEDIUM

The double-porosity model illustrated schematically in Figure 2 is a somewhat more realistic caricature of a nonhomogeneous geologic medium. The schematic illustrates the simplest possible situation in which fractures of width δ_f are separated by slab-like matrix blocks having a width δ_m, a permeability k_m, and an internal porosity, ϕ_m. The basic idea is that fluid moves one dimensionally along the fracture and one-dimensionally in and out of the porous matrix material. Thus, it is possible to accommodate matrix blocks which are slab-like (see Figure 2), match-like or cube-like by treating the one-dimensional flow within the blocks as either planar, cylindrical, or spherical in character, but here we restrict to slabs.

The two different levels of "porosity", fracture porosity and matrix porosity, are both important in controlling the transient flow response of the medium because most of the permeability generally resides within fractures, whereas most of the porosity resides within the matrix blocks. For example, consider a case with 1-millimeter fractures separated by 1-meter slabs having a porosity of 10% and a permeability of 1 millidarcy (i.e., 10^{-15} m^2). The ratio of capacitance volumes is then

$$\frac{V_{matrix}}{V_{fracs}} = \frac{\phi_m \delta_m}{\delta_f} \sim 100 \tag{2}$$

whereas the ratio of mass flows through fractures vs. blocks is

$$\frac{\dot{m}_{fracs}}{\dot{m}_{matrix}} = \frac{A_f}{A_m}\frac{u_f}{u_m} \sim \frac{\delta_f}{\delta_m}\frac{(\delta_f^2/12)}{k_m} \sim \frac{1}{12}\frac{\delta_f^3}{\delta_m k_m} \sim 10^5 \tag{3}$$

This ratio of flow rates implies that in a steady flow situation the cracks would carry 99.999% of the total mass flow through the composite medium. Even if the matrix permeability were as large as 1 Darcy or, alternatively, the fracture aperture as small as 10^{-4} m, the cracks would still carry 99% of the flow. Moreover, the cracks will

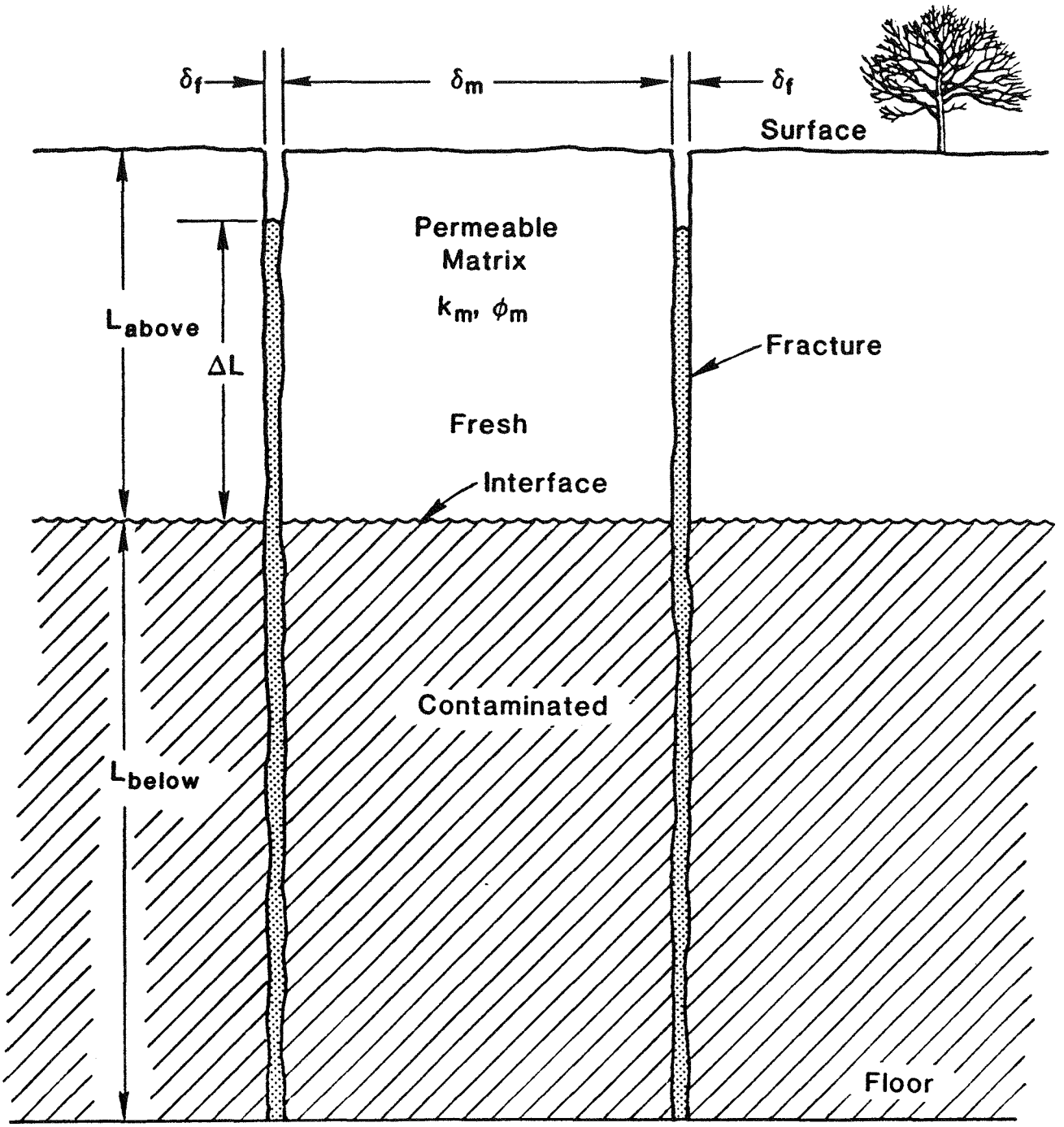

Figure 2. Schematic of a nonuniform displacement in a double-porosity medium. Contaminated gas from fractures and matrix blocks below the interface expands upward through the fractures. Only the relatively small fracture volume above the interface serves as a buffer.

carry an even greater share of the total flow in a transient situation because the contrast in the speed of pressure waves is even greater than the contrast in steady-flow permeabilities. Thus, we should be well justified in assuming that essentially all of the vertical flow travels through the cracks.

The first-order implications of the double-porosity model can be appreciated by again considering the "quasi-static" case in which the pore-fluid diffusivity of the medium is sufficiently large that the pressure everywhere within the medium closely follows the sinusoidal pressure variations which occur at the surface. The volumetric expansion of the gas is then the same as before, $\Delta V = V_o \Delta P/P_o$, where V_o includes the pore volume in the matrix as well as the cracks. But all of this expansion is now channeled upward through the cracks. So there is now a much smaller buffer volume to contain the differential expansion. Thus, the upward displacement of the fresh/contaminated interface is amplified by the volume ratio between matrix and fractures

$$\frac{\Delta L}{L_o} \sim \frac{\Delta P}{P_o}\left(\frac{V_m + V_f}{V_f}\right) \sim 100\,\frac{\Delta P}{P_o} \qquad (4)$$

such that even a modest decrease in barometric pressure (say 1 part in 100) could bring gases from a depth of 200 meters to the surface. The matrix blocks above the fresh/contaminated interface do not provide a temporary storage location for contaminated gas; they too are exhaling gas into the fractures during a period of falling barometer. So it would appear that contaminated gas should escape from our hypothetical fractured medium during any cycle of atmospheric pressure variation.

NUMERICAL SIMULATION OF A DOUBLE-POROSITY MEDIUM

There are, however, two physical mechanism which tend to mitigate the upward flow of radioactive gases through fractures. First, the flow resistance of the medium limits the penetration depth of pressure disturbances, so the vertical displacement of the gas tends to be smaller. Secondly, Fickian diffusion tends to filter the contaminated gases as they rise through fractures. Because of differences in concentration, contaminant species are drawn out of the rising gases into the surrounding porous medium which contains relatively fresh air. So the gas reaching the surface contains less contaminant. Both of these mechanisms have been incorporated in a mathematical model of the atmospheric pumping process.

A computational model of gas flow and contaminant transport in a double-porosity medium has been formulated and tested over the past year[3]. Flow along the fractures and within the permeable matrix blocks is locally one-dimensional. The interaction between fractures and blocks includes the Darcian seepage of fluid as well

as the Fickian diffusion of contaminant. To guard against artificial numerical diffusion, the FRAM filtering remedy and methodology of Chapman[6] is used in calculating the advective fluxes along fractures and within blocks. The entire system of equations including the interaction terms, is solved by a non-iterative algorithm which remains stable and conservative even when the computational time step is large compared to the cross-block transit time of Darcian pressure waves. The numerical accuracy has been tested by comparison with exact solutions for oscillatory and unidirectional flows, some of which include Darcian seepage or Fickian diffusion interaction between the fracture and the matrix.

In the example calculations presented here, the barometric pressure variation is assumed to be sinusoidal with a period of 200 hours and a peak-to-peak amplitude of 2/30 atmosphere. The medium has an impermeable floor at 500 meters and the contaminated gas initially occupies the region from a depth of 200 meters down to the floor. The matrix material has a porosity of $\phi_m = 0.1$ and a permeability of $k_m = 10^{-15}$ m^2 (1 millidarcy). As a prototypic case we suppose that fractures with an aperture of 1 millimeter are spaced 2 meters apart, but the aperture and spacing are both varied in the calculations to illustrate the role of each.

To show what might happen in the absence of Fickian filtering, we set the Fickian diffusion coefficient to zero in the first example. The most important result of the calculation is a history of the cumulative amount of contaminated gas which has escaped to the atmosphere, as indicated by the upper line on Figure 3. This cumulative outflow is expressed as a fraction of the contaminated gas initially present. Thus, it is seen that during the first barometric cycle, the fraction of contaminant which escapes is about 6% of the amount initially present, which is almost equal to the quasi-static estimate of $\Delta V/V_o = \Delta P/P_o = 2/30 = 0.067$. This outcome is not surprising since the pore-fluid diffusivity of the fractured medium is large, the buffer volume in fractures is small, and there is no Fickian filtering.

The instantaneous rate of flow of contaminant into the atmosphere is shown by the series of spikes on the lower part of Figure 3. Each spike corresponds to a positive phase of the motion when gas is being drawn out of the ground. During the intervening negative phases fresh air is pushed back down. The flow rate is expressed as a fraction of the initial amount which escapes per hour. Thus, if a flow rate of order 10^{-5} is maintained for a half-cycle of 100 hours the amount ofcontaminant which escapes is 0.1% of the amount initially present. After the first cycle, the rate of contaminant outflow decreases sharply because most of the gas being extracted from the lower region is then the fresh air which was pushed down on the previous cycles.

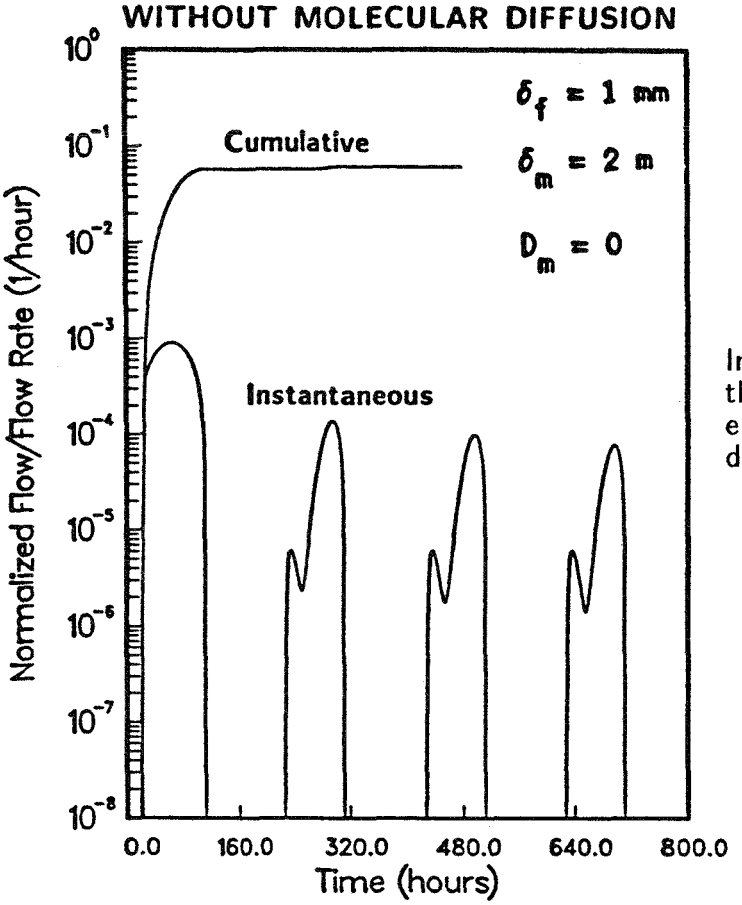

Figure 3.
In the absence of Fickian filtering more than 6% of the contaminated gas could escape during the first period of decreasing barometric pressure.

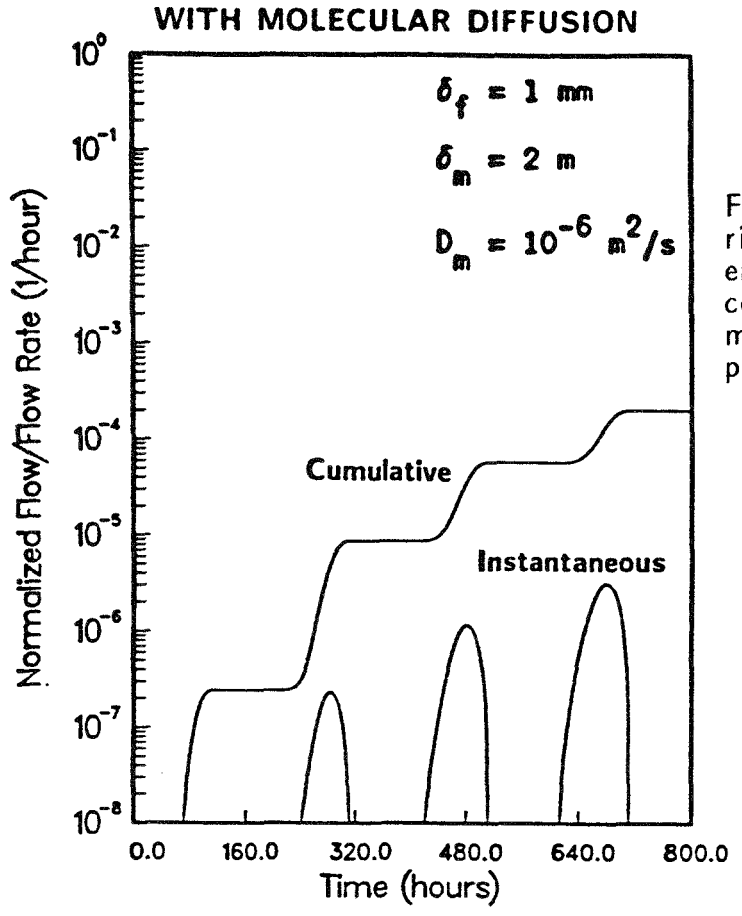

Figure 4.
Fickian filtering of contaminated gas rising through fractures causes an enormous reduction in the amount of contaminant which escapes from the medium during the first few cycles of pumping.

The dramatic effect of Fickian filtering is illustrated in Figure 4 which presents results for a case which is identical to the first, except that Fickian diffusion is now permitted to act with a relatively conservative coefficient of $D = 3 \times 10^{-6}$ m^2/s. The fraction of contaminant vented on the first cycle is now 2×10^{-7}, compared with 6×10^{-2} without Fickian diffusion. The reduction in contaminant venting is so great that five cycles of atmospheric pumping are now required to draw even 0.1% (10^{-3} on the plot) of the contaminated gas out of the ground. By that time, most of the radioactive species will have decayed somewhat. We did not, however, include any radioactive decay in this calculation in order to illustrate how effective the medium is in containing the gases.

A limited parameter study is now presented to provide some insight into the nature of the filtering process and to illustrate its sensitivity to the properties of the medium. The previous base-line calculation, which included Fickian diffusion, is therefore repeated with the fracture aperture increased to 3 millimeter and all other parameters held fixed at their previous values. As seen in Figure 5, the increase in aperture does slightly degrade the effectiveness of the filtering process, but this is only a factor-of-two degradation of a process which provides a four-order-of-magnitude attenuation in the early outflow. Thus, to the first approximation, these results are relatively insensitive to aperture.

Dispersive mechanisms discussed in [7] can increase the rate of contaminant transport both along the fracture and within the permeable matrix blocks. Since the primary origin of dispersive processes is the nonhomogeneity of a medium, the present double-porosity model directly accounts for the most severe first order effects. However, it must be recognized that fractures encountered in the field do not have a uniform aperture and that the matrix blocks themselves are certain to contain small-scale fractures and other nonhomogeneities. These second-order nonhomogeneities can be accounted for by including in the molecular diffusion coefficient a dispersive contribution which is calculated as a product of the local velocity and a length scale, d, called the dispersivity. A review of the groundwater literature suggests that the dispersivity along the fractures is probably on the order of $d \sim 1$ m, which results in an apparent diffusivity of roughly 10^{-2} m^2/s for the expected longitudinal velocity of 10^{-2} m/s. Even though this magnitude of apparent diffusivity is many orders of magnitude stronger than the Fickian diffusion along the fracture, it is still small compared to the advective transport along the fracture which was previously suppressed by the Fickian diffusion from the fracture into the matrix. Thus, it is seen in the calculation of Figure 6 that the dispersion process increases the contaminant outflow by only a factor of two or so, indicating that even much larger values of the dispersivity would be of little consequence. Dispersive processes occurring within the matrix blocks should be even less significant than this, because the lateral velocity is so small ($v \sim 0.1$ m/200 hr $\sim 10^{-7}$ m/s) that dispersive affects are certain to be orders of magnitude smaller than the Fickian diffusion which is already taken into account.

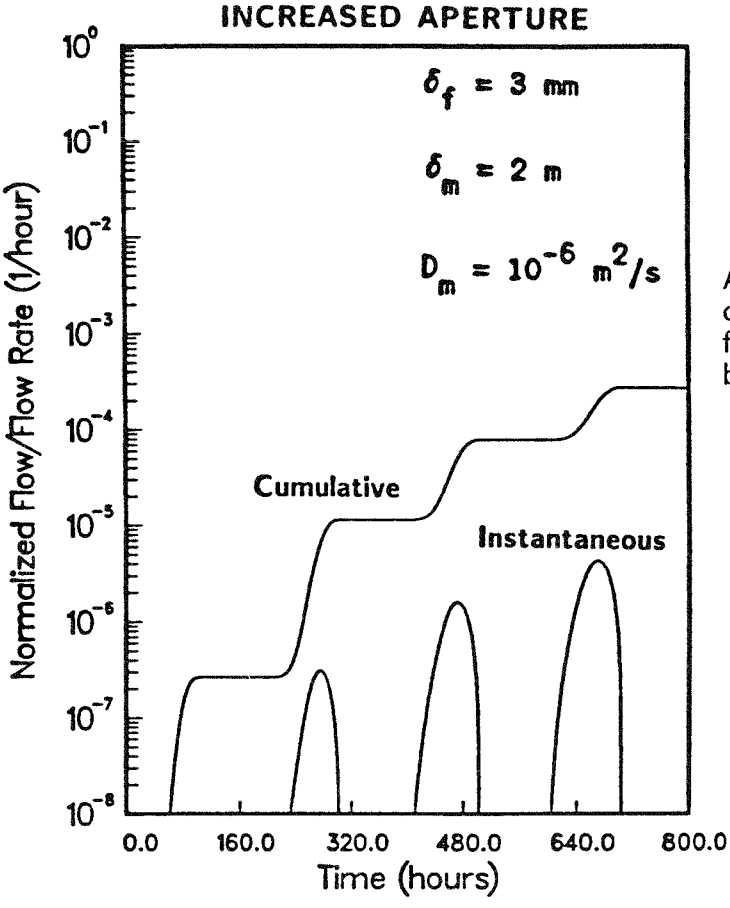

Figure 5.
An increase in the fracture aperture causes only a slight degradation of the filtering efficiency, as compared with the base case in Figure 4.

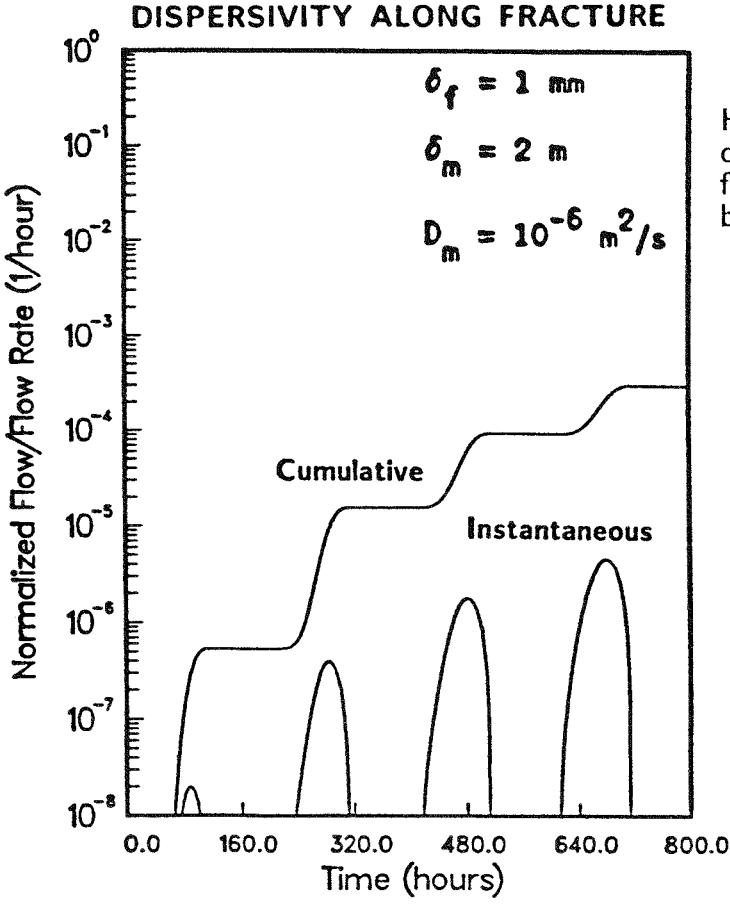

Figure 6.
Hydrodynamic dispersion processes should cause only a moderate reduction in the filtering efficiency, as compared with the base case in Figure 4.

The fracture spacing is very influential in controlling the Fickian filtering efficiency, as illustrated by the results in Figure 7 for an aperture of 1 millimeter and a spacing of 6 meters. Here, the early arrival of contaminant is about three orders of magnitude stronger than in the baseline case of 2-meter spacing (Figure 4) with the same aperture. The wider spacing permits a release of about 0.04% on the first cycle, as compared with the extremes of 6% unfiltered and 0.00004% well-filtered. Figure 8 for 3-millimeter fractures and 6-meter spacing reaffirms the importance of fracture spacing since, again, the early arrival is about three orders stronger than in the previous case (Figure 5) with a 3 millimeter aperture.

The effectiveness of Fickian filtering must eventually diminish when the filter becomes saturated with contaminant. Beyond that time, the behavior should follow a nearly cyclical pattern in which there is a close balance between the amount of contaminant which enters and leaves the filter during any cycle, such that the filter no longer provides any net benefit. Of course, there will still be a gradual decay of the outflow rate due to the overall depletion of the contaminant in the medium.

Although the calculations have not yet been extended to very late times, it would appear that something on the order of twenty cycles, or equivalently one year, would be required to pump most of the contaminated gas out of the ground. The amount of contaminant which escapes might be reduced somewhat by surface adsorption processes which are not presently included in the model. Also, it should be emphasized that no account has been taken of the radioactive decay process which will also reduce the magnitude of the radioactive release.

ANALYTICAL MODELING OF FICKIAN FILTERING

A simple analytical model can be used to describe the essence of the Fickian filtering process which extracts contaminants from gas streams rising through fractures. To this end, let us focus our attention on the "filtering" region which lies above the contaminated/fresh interface and suppose for the moment that there is no Darcian fluid motion occurring within the matrix material which lies above the interface, as through the permeability of the filter matrix were identically zero. The porosity of the filter matrix must, however, remain nonzero to permit Fickian diffusion from the fracture into the porespace. Under these conditions the equations which govern advective contaminant transport along the fracture coupled with Fickian diffusion into the matrix are analogous to those which govern advective heat transfer along a channel coupled with Fourier conduction into the channel walls.

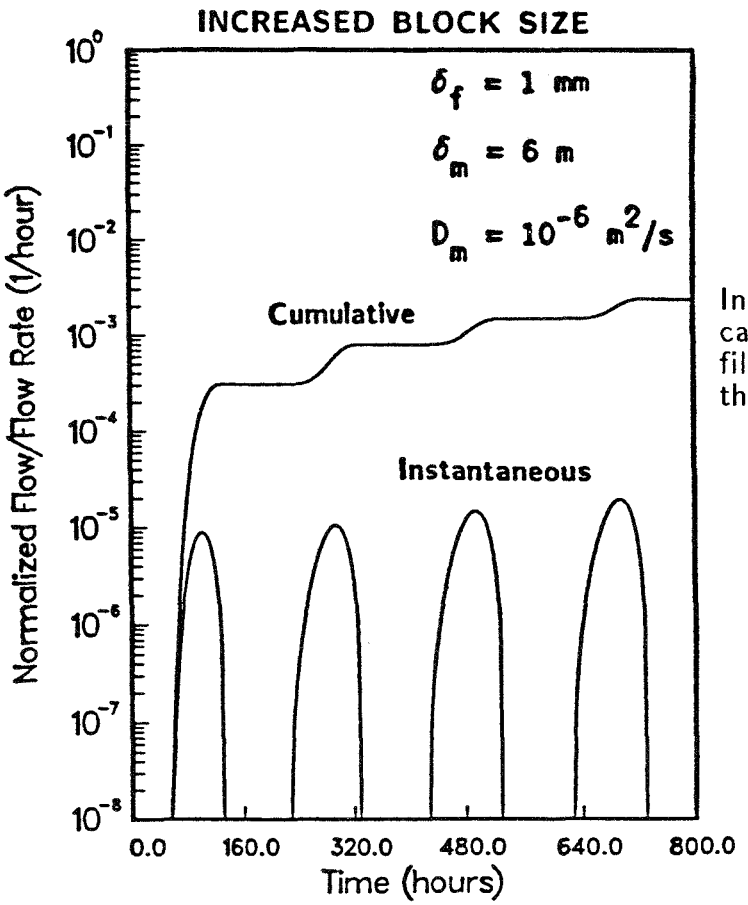

Figure 7.
Increased spacing between fractures causes a significant reduction in the filtering efficiency, as compared with the base case in Figure 4.

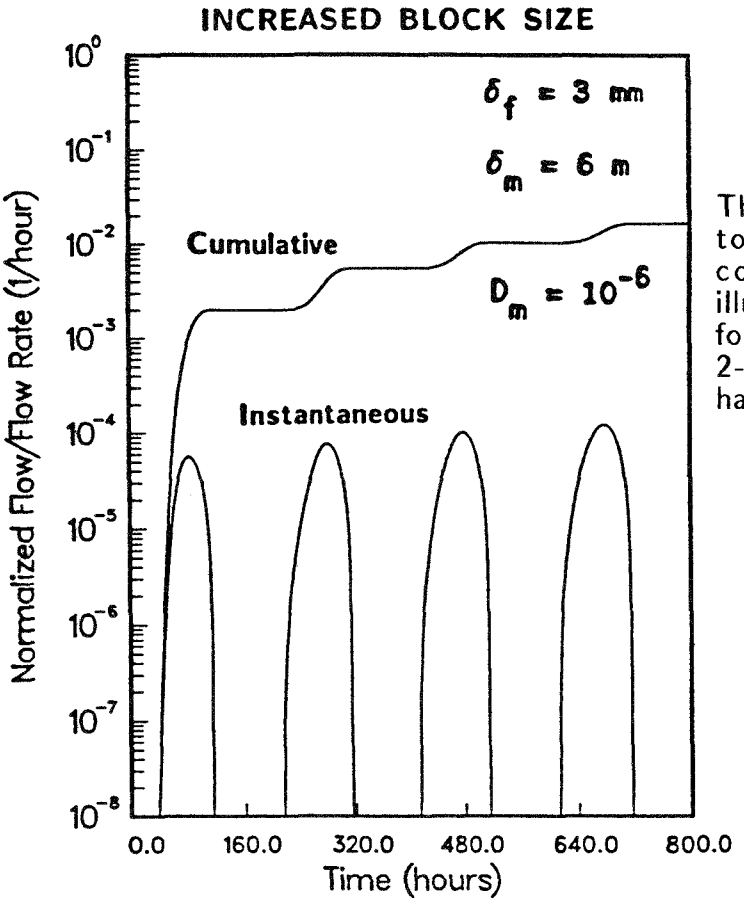

Figure 8.
The spacing between fractures appears to be the critical consideration in controlling the early arrival, as illustrated by comparing these results for 6-meter spacing with the previous 2-meter spacing in Figure 5, both having an aperture of 3 mm.

Carslaw and Jaeger[8] report the following analytical solution which applies to cases where the fluid velocity u is constant, the axial diffusion along the fracture is negligible, and the walls are infinitely thick.

$$\frac{C}{C_o} = \text{erfc}\left[\frac{x\ D\ \phi_m}{u\delta_f\left[D(t-x/u)\right]^{1/2}}\right] \tag{5}$$

Here, C_o is the prescribed concentration at the inlet to the channel and C(x,t) is the concentration in the channel as a function of position x, measured upward from the fresh/contaminated interface, and time, t. The upward velocity, u, can be estimated by channeling through the fracture the volumetric expansion of contaminated gas, $\Delta V/V_o = \Delta P/P_o$, which comes from the lower region, $V_o \sim L_b\delta_m\phi_m$, during a half-period of duration T/2.

$$u \sim \frac{\Delta V}{(T/2)}\frac{1}{\delta_f} \sim \frac{2L_b\ \phi_m\ \delta_m}{T\ \delta_f}\ \frac{\Delta P}{P_o} \sim 1\ \text{cm/s} \tag{6}$$

The numerical value of u ~ 1 cm/s corresponds to our prototypic case with L_b = 300 m, ϕ_m = 0.1, δ_m = 2 m, δ_f = 1 mm, T = 200 hr, and $\Delta P/P_o$ = 2/30.

The penetration of contaminant along the fracture is shown in Figure 9 for an overburden of L_a = 200 meters and the prototypic parameters of the previous paragraph. It is seen that the contaminant penetrates less than half way to the surface during a time of 200 hours. This amount of retardation is very significant since the contaminated gas would reach the surface in a time of t ~ L/u ~ 5 hours were it not for the Fickian filtering.

A simple rule-of-thumb containment criterion can be extracted from the analytical solution. If we require that the gases reaching the surface during the first falling barometer have a contaminant concentration no greater than 1 part in 10^5, then the argument of the error-function in equation (5) must be greater than 3. Since we can generally neglect x/u compared to t, this limitation can be stated as

$$\frac{x\ D\ \phi_m}{u\ \delta_f (Dt)^{1/2}} > 3 \tag{7}$$

in which x will be replaced by L_a for an observer stationed on the surface a distance L_a from the entrance of the filter channel. Then, by substituting our previous estimate of the velocity from equation (6), the criterion becomes simply

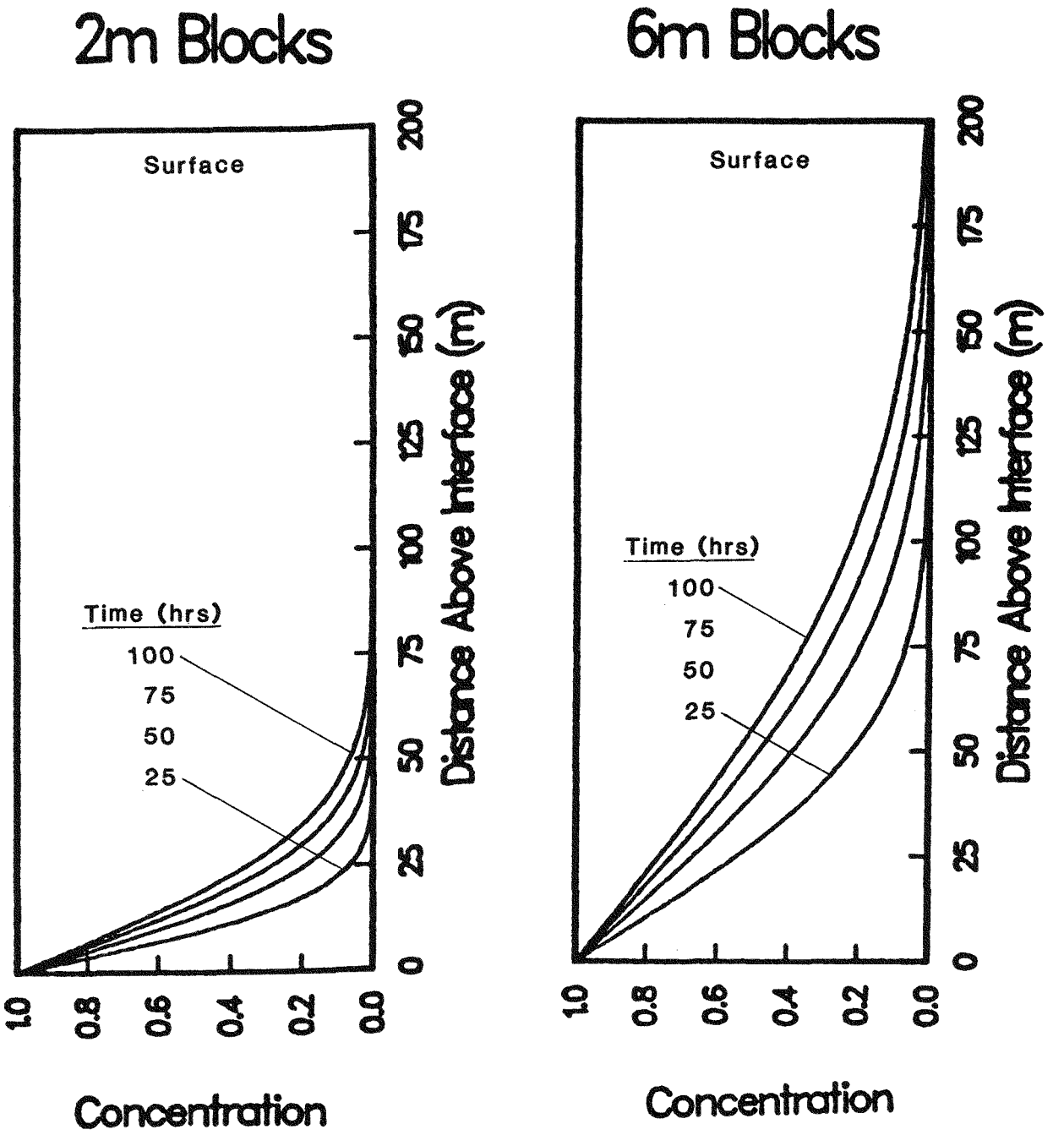

Figure 9. Concentration profiles along a vertical crack at various times for two different block sizes. Wider spacing of cracks increases the filtering load on each crack and, hence, permits greater penetration of contaminant along the cracks.

$$\delta_m < \frac{1}{3}\frac{L_a}{L_b}\frac{P_o}{\Delta P}(DT)^{1/2} \sim 4 \text{ meters} \qquad (8)$$

where the numerical value of 4 meters corresponds to the prototypic situation. This result is not very sensitive to the arbitrary choice of 1 part in 10^5 as an acceptance criterion; 1 part in 10 corresponds to an erfc argument of 1, and 1 part in 100 corresponds to an argument of 2, as compared with an argument of 3 for 1 part in 10^5.

It is somewhat surprising to find that the arrival criterion does not depend on the fracture aperture δ_f. However, it can be seen in Equation (5) that it is only the through-put $u\delta_f$ which matters, and this product is controlled by the volumetric expansion, since $u\delta_f = \Delta V/(T/2)$. Thus, the aperture is of secondary importance compared to the fracture spacing, in agreement with the numerical calculations of the preceding section.

The fracture spacing is of critical importance because it determines the "loading" on the filter. The amount of fluid passing upward along the fracture is proportional to the underlying volume which it services. This is true not only in the simple situation depicted in Figure 2, but also in the case of a partial collapse, since the total volume in the collapsed chimney region is then connected to the surface by a number of fractures which is inversely proportional to the fracture spacing. In this context it should be noted that the porosity "cancelled out" of the spacing criterion because it was assumed to be the same, ϕ_m, in both the "donor" region and the "filter" region, but this can be readily modified to accommodate an alternative chimney porosity.

One might argue that the size of the filter increases in proportion with fracture spacing and that this should exactly offset the increased throughput from below. This would be true if the Fickian diffusion process were always able to access all of the filter space in the time of interest. However, within a hundred-hour half-period the penetration depth of diffusion is limited to roughly

$$\delta_{Fickian} \sim 2\sqrt{DT} \sim 2 \text{ meter} \qquad (9)$$

which places a natural restriction on the fracture spacing which can be effectively filtered. This interpretation is consistent with the erfc-based criterion, as can be seen by collecting "donor" and "filter" variables on opposite sides of that equation to get

$$\delta_m L_b \frac{\Delta P}{P_o} < \frac{1}{3} L_a \sqrt{DT} \qquad (10)$$

which suggests that the accessible filter volume on the right must be about an order of magnitude greater than the through-put volume coming from the underlying donor region. It should be mentioned in this context that Darcian pressure waves travel through matrix blocks much faster than Fickian diffusion, so the permeability should not generally affect the spacing criterion, as further explained in the next section.

Having explored the implications of a very simplified analytical model, it is incumbent upon us to now review the validity of some underlying assumptions. In calculating the rate of Fickian diffusion from the channel into the porous matrix, we neglected the opposing seepage velocity which blows out of the blocks into the channel during a falling barometer. This simplification should be permissible provided that the outward displacement of the fluid in the blocks ($\sim\delta_m \Delta P/P_o$) is small compared to the Fickian penetration depth ($\sim\sqrt{DT}$), which poses an inequality almost equivalent to the previous containment criterion in equation (10). Thus, although the seepage motion in and out of blocks is critical in driving the much larger vertical displacement along the channel, it should not greatly alter the Fickian diffusion within the blocks.

Another simplification of the analytical solution is that the walls of the channel (i.e., matrix blocks) are assumed infinitely thick in calculating the Fickian diffusion losses from the channel. Although this supposition could certainly alter the behavior within the interesting parameter range, it probably would not affect the final containment criterion, since the accessible penetration depth of Fickian diffusion would then be the lesser of δ_m and $\sqrt{DT}$ which does not change the "cut-off" of the containment criterion. It is certainly possible to extend the analytical solution to accommodate a finite block-size, but the result would not be so simple and our primary purpose in this is only to gain a better understanding of the fully general numerical results which suffer no such restrictions.

ESTIMATING FRACTURE APERTURE AND SPACING FROM ATMOSPHERIC PUMPING DATA

To apply the double-porosity model to any particular emplacement region it is necessary to estimate the properties of the medium. The porosity and permeability of the matrix material can be adequately estimated from core-sample data, but the aperture and spacing of fractures are more difficult to estimate. Fortunately, it is mainly the upper filtering region which must be characterized in such detail, since the process should only be sensitive to the total well-connected pore-volume contained in the lower contaminated region.

Over the past few years LLNL has undertaken a field measurement program which provides useful information concerning the large-scale transport characteristics of the NTS geology.[1,9] After drilling, partially casing, and capping an emplacement hole, pressure transducers are used to measure the time variation of the barometric pressure at the earth's surface and within the hole. By observing the time lag and attenuation

of the down-hole signal, it is possible to infer the apparent bulk diffusivity of the formation. Even though it may not be the diffusivity which directly controls the post-shot transport of contaminated gas, this information can be used to estimate other parameters of interest, such as fracture aperture and fracture spacing. These parameters are important not only in the present context of atmospheric pumping processes but also in connection with hydrofracture propagation and early-time seepage driven by cavity pressure.

It should be strongly emphasized that the bulk "diffusivity" associated with pressure measurements is a pore-fluid diffusivity which describes the flow of a fluid through a permeable medium in response to a pressure gradient. This is entirely distinct from the Fickian diffusivity which describes the diffusion of one chemical component through another in response to a concentration gradient.

The bulk diffusivity which is measured in the field can be related to the more fundamental material properties by examining the pressure response of a double-porosity medium to a sinusoidal variation in surface pressure, as explained in [3]. The bulk diffusivity α_{fm} of the fractured matrix is related to the separate diffusivities α_f and α_m of the fractures and matrix, respectively, by the following formula

$$\alpha_{fm} = \left(\frac{\alpha_f}{1 + \frac{\delta_m \phi_m}{\delta_f} \frac{\tanh \lambda_m \sqrt{i}}{\lambda_m \sqrt{i}}} \right) \tag{11}$$

in which

$$\lambda_m = \frac{\delta_m}{\sqrt{\alpha_m T}} \tag{12}$$

and

$$\alpha_m = \frac{k_m p_o}{\mu \phi_m} \quad , \quad \alpha_f = \frac{\delta_f^2}{12} \frac{p_o}{\mu} \tag{13}$$

μ is viscosity, p_o is the ambient pressure level, and λ_m is analogous to a Fourier modulus in heat transfer problems.

Figure 10 illustrates the dependence of bulk diffusivity on the permeability of matrix blocks for three choices of fracture aperture and three choices of fracture spacing. The bulk diffusivity is highest when the matrix permeability is smallest, because pressure waves can then move rapidly along the fractures, unimpeded by seepage into the surrounding matrix blocks. As the permeability of the blocks increases, the seepage into the fracture walls reaches greater and greater penetration depths ($\sim\sqrt{\alpha_m T}$) on the time scale of interest. This slows the progress of pressure

waves because the fracture must supply more and more fluid to the wall in order to raise the local pressure. Once the penetration depth becomes comparable to the fracture spacing ($\lambda_m \geq 1$), the blocks are able to maintain pressure equilibrium with the fracture and the bulk diffusivity is reduced by the ratio of matrix volume to fracture volume ($\alpha_{fm} \rightarrow \alpha_f V_f / V_m$). The bulk diffusivity is then a hybrid quantity which reflects the permeability or "conductance" of the fractures together with the combined porosity or "capacitance" of the fractures plus the matrix.

Matrix permeabilities derived from core samples are typically on the order of millidarcies, which is sufficiently large to equilibrate even ten-meter blocks on the 100-hour time scale of interest. An immediate implication is that all of the connected pore space in fractures plus matrix should be used in data reduction and interpretation of atmospheric pumping data. Even a microdarcy permeability would be sufficient to equilibrate one meter blocks or, equivalently, a one-meter skin adjacent to widely spaced fractures.

Wider fracture spacing results in smaller diffusity because there is more "capacitance" associated with any one fracture. Thus, in view of the preceding contaminant transport analyses, one might argue that small diffusivities would be associated with threatful situations in which only a few fractures were serving as "breathing straws" for a huge underground air volume.

The diagonal line in the lower right corner of Figure 10 indicates the pore-fluid diffusivity of the matrix material itself as a function of the matrix permeability, assuming a matrix porosity of 10%. Thus, for a core-sample permeability of 1 millidarcy we might expect a pore fluid diffusivity of 10^{-4} m^2/s. Large-scale field measurements, such as the atmospheric pumping data from emplacement holes, generally indicate much higher diffusivities, which strongly suggests the presence of fractures.

The TIERRA emplacement hole, U19ac in Pahute mesa, exhibited a bulk diffusivity on the order of 10 m^2/s which corresponds to a permeability of hundreds of Darcies. As pointed out by Hanson and Hearst[1], this can only be interpreted as a fractured medium. Our prototypic example of 1 millimeter fractures spaced 2 meters apart was specifically chosen to be consistent with the TIERRA data. Other choices are, of course, possible since there is only one piece of data (bulk diffusivity) to constrain two unknowns (aperture and spacing), even if the porosity and permeability of the matrix are conceded as known.

Alluvium might also be interpreted as a double-porosity medium based on the atmospheric pumping data from emplacement hole U2fe in Area 2. The measured bulk diffusivity of around 1 m^2/s suggests a permeability of 30 Darcies and this is

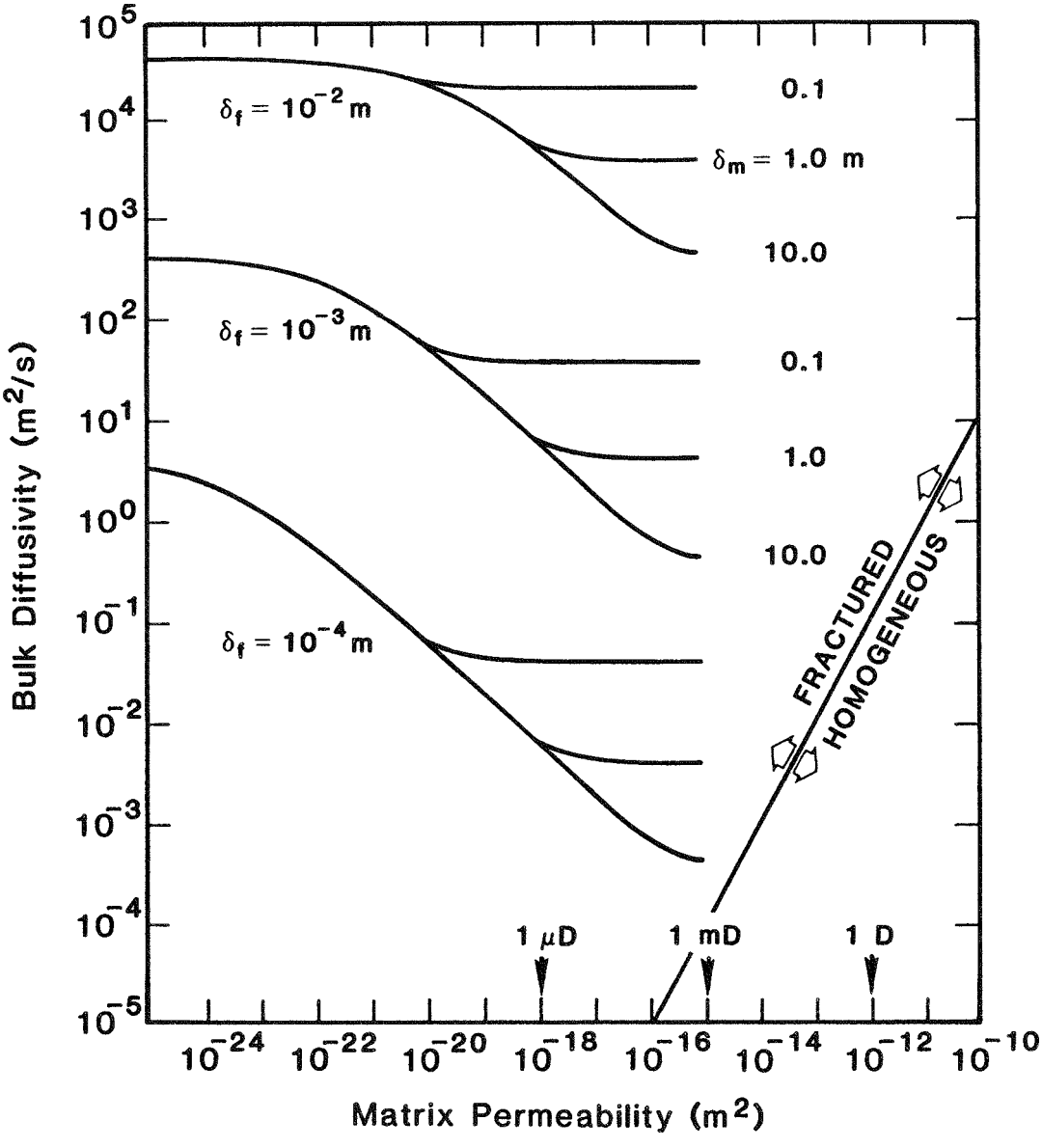

Figure 10. Bulk pore-fluid diffusivity of a fractured porous medium as a function of matrix permeability for three different choices of the fracture aperture and three different choices of the block size. Diagonal line indicates diffusivity of the matrix material. The apparent bulk diffusivity depends on the period of the sinusoidal pressure variation, here taken as 200 hours.

consistent with many previous borehole-scale injection tests in comparable media. One might attach the interpretation of a homogeneous medium which is undistinguishable from sand on the beach. An alternative double-porosity interpretation might be closely spaced fractures, say 1 centimeter apart, with aperture on the order of the grain size of 10^{-4} meter. The matrix permeability would not matter much so long as it was in the range from microdarcy to subdarcy. Undoubtedly there are more realistic choices than these, and, in alluvium, there would be some hope of using measurements at different scales to appropriately constrain the selection. The important point is that a double-porosity interpretation recognizes the existence of nonhomogeneities and, once recognized, it is possible to explore their consequences. The paper by Peterson, Lie, and Nilson[5] in this symposium addresses atmospheric pumping process in a nonhomogeneous double-porosity alluvium-like medium.

More information could perhaps be extracted from the atmospheric pumping experiments if the higher frequencies were not contaminated by diurnal heating of the transducers. The apparent bulk diffusivity of a double-porosity medium should be larger at higher frequencies because there is less opportunity for seepage interaction between fractures and matrix blocks. However, as noted previously, even 10 meter blocks are equilibrated by a 1 millidarcy matrix permeability within the 100-hour half-period used in constructing Figure 10. So the period would have to be at least 10 times shorter, and hence shorter than a day, to prevent equilibration. Even so, such frequency-response testing might be useful as a laboratory or borehole experiment aimed at characterizing the nonhomogeneity of a geologic medium.

SUMMARY

The atmospheric pumping experiments performed by LLNL[1,9] suggest that oscillatory gas motions penetrate all the way down to emplacement depths in fractured volcanic rocks as well as alluvium. Thus, atmospheric pumping seems a probable explanation for gradual seepage of radioactive gas on a time scale which is longer than the first hour or so of high cavity pressure but short compared to the years required for Fickian diffusion to reach the surface.

Piston-like vertical displacements of the gas in a uniform homogeneous medium should not draw contaminants out of the ground, regardless of how large the pore fluid diffusivity might be, because the buffer volume above the contaminated region is more than sufficient to accommodate the episodic expansions of the contaminated gas. This model is, however, overly optimistic, because it ignores the nonhomogeneities of the geologic emplacement media.

In a fractured porous medium nearly all of the vertical flow is carried by the fractures. So all of the volumetric expansion occurring within the contaminated chimney region is channeled upward through a relatively small fracture volume. Since the fracture volume would often be too small to accommodate the expansion, a few percent of the noncondensible radioactive gases produced by the explosion could be vented to the atmosphere during the first period of falling barometric pressure. This model is, however, overly pessimistic.

Fickian filtering of the contaminated gases rising through fractures tends to draw the contaminants out of the rising streams into the relatively fresh matrix blocks. This mechanism may often afford containment of essentially all of the radioactive gas during the first two or three barometric cycles, even in cases where substantial amounts of filtered cavity gas are exiting on each cycle.

The buffering effectiveness of Fickian filtering depends mainly on the spacing between fractures. Wider spacing increases the amount of expanding cavity gas which must be filtered by each fracture. Conversely, with denser fractures there is better access to the filtering matrix; greater contact area improves the filtering efficiency.

A double-porosity fracture/matrix model has been used to analyze the atmospheric pumping process and associated contaminant transport. This might be viewed as a zeroth-order treatment of a nonhomogeneous geologic medium, since fractures and pore space actually exist on a multitude of length scales in a fractal-like fashion. The two level double-porosity model, however, seems a well-balanced companion to the available experimental data, since it affords the opportunity to rationalize the enormous disparity between core-sample data and large-scale field measurement of transport properties. This recognition of nonhomogeneity has proved useful in understanding the atmospheric pumping process and it promises to add a new dimension to the analysis of hydrofracture containment, since that process is also moderated by the large-scale buffering ability of a prefractured permeable medium.

REFERENCES

1. J. M. Hanson and J. R. Hearst, "Evaluating Permeability in the Unsaturated Zone at the Nevada Test Site Using Barometric Pressure Modeling", Proc. Third Symp. on Containment of Underground Nuclear Tests, LLNL-CONF-850953, Vol. 1, p. 392-413, 1985.

2. T. D. Van Golf-Racht, Fundamentals of Fractured Reservoir Engineering, Elsevier Scientific Publishing, Amsterdam, 1982.

3. R. H. Nilson and K. H. Lie, "Numerical Analysis of Oscillatory Gas Motion and Contaminant Transport in a Fractured Porous Medium", SSS-R-87-8621, drafted April 1987.

4. G. E. Grisak and J. F. Pickens, "Solute Transport Through Fractured Media: The Effect of Matrix Diffusion," Water Resources Research, 16 (4), 719-730, 1980.

5. E. W. Peterson, K. H. Lie and R. H. Nilson, "Dispersion of Contaminant During Oscillatory Gas Motions Driven by Atmospheric Pressure Variations," this proceedings.

6. M. Chapman, "FRAM - A Nonlinear Damping Algorithm for the Continuity Equation," J. Comp. Phys. 44, 84-103, 1981.

7. J. J. Fried and M. A. Combarnous, "Dispersion in Porous Media," Advances in Hydroscience, Vol. 7, 169-282, 1971.

8. H. S. Carslaw and J. C. Jaeger, Conduction of Heat in Solids, Oxford: Clarendon Press, 1959.

9. N. R. Burkhard, J. R. Hearst, and W. Gersch, "Diffusivity Determinations at NTS," this proceedings.

DISPERSION OF CONTAMINANT DURING OSCILLATORY GAS-MOTIONS DRIVEN BY ATMOSPHERIC PRESSURE VARIATIONS

by
E. W. Peterson
K. Lie
R. H. Nilson

S-CUBED
A Division of Maxwell Laboratories, Inc.
P. O. Box 1620
San Diego, CA 92038

ABSTRACT

Cyclical variations in atmospheric pressure cause vertical oscillatory motions of gases within the permeable earth. In an idealized homogeneous porous medium having uniform velocity at every elevation the induced motions would be piston-like and reversible, and they would contribute nothing to the net vertical transport of radioactive gases. However, in any real geologic medium there are nonhomogeneities occurring on many different length scales (from the spacing of major fractures to the grain-size of the rock) which cause the oscillatory motions to be shaggy and irreversible and ratchet-like. The macroscale expression of these nonuniformities is diffusion-like in nature and it is generally referred to as dispersion.

A series of laboratory experiments were performed to better understand the dispersive mechanisms induced by oscillatory flow in a nonhomogeneous porous medium and to provide a quantitative check on analytical and numerical modeling. The apparatus consisted of a 2 meter Plexiglas column with plenums located at each end. After introducing a tracer gas into one plenum, its concentration was monitored at both ends. In some tests, oscillatory pumping motion was induced by operating a piston-device in one plenum.

Three different sequences of experiments were performed with the following results. (1) In a homogeneous sand column oscillatory motions cause no appreciable increase in the transport of tracer, as compared to a motionless experiment, in keeping with theoretical expectation. (2) Non-homogeneous media were first modeled using a central column of high permeability sand surrounded by an annulus of lower permeability sand. Dispersive transport along the column was substantially increased by the interaction between the two media, as verified by comparing results obtained for pumped columns with and without a partition tube between the central column and the annulus. (3) Another dispersive medium was constructed by emplacing a sequence of annular discs in a column of uniform sand. Results obtained with and without pumping were very different, in contrast with the homogeneous experiments in (1). Physical arguments, order of magnitude analyses, and numerical calculations are used to explain the outcome and to extrapolate to the field scale of interest.

* This work sponsored by the Nuclear Test Containment Program at Lawrence Livermore National Laboratory.

1. INTRODUCTION

Cyclical variations in barometric pressure cause an oscillatory up-and-down motion of gases within the chimney produced by an underground nuclear test. If the bulk permeability of the emplacement media were sufficiently small, the surface variations in pressure would be felt only at relatively shallow depths, and the contaminated gas within the chimney might remain almost stationary. However, large scale measurements of the pore-fluid diffusivity at NTS[1,2] indicate that the surface pressure variations are felt very strongly all the way down to burial depths on Pahute Mesa tuffs as well as in the alluvium on the flats. Thus, it is important to understand the fluid motion and the associated transport of radioactive gases which are caused by this atmospheric pumping process.

The laboratory experiments described here are being conducted to demonstrate some fundamental concepts, to verify analytical and numerical models, and, most importantly, to learn whether or not the oscillatory character of the atmospheric pumping process might significantly enhance the contaminant transport. The study is focused upon two specific issues.

- The distinction between homogeneous porous media and highly fractured media.

- The dispersive or ratchet-like transport mechanisms which occur in oscillatory flows.

One can easily imagine that a "ratchet mechanism" could carry contaminants to successively higher and higher elevations on the repeated upward phases of the motion. This sort of mechanism is known to be operative in homogeneous porous media at high enough frequencies (about ~1 cps or greater)[3]. Such enhancement can probably occur in fractured permeable media at much lower frequencies, because the porous walls of the fracture provide a temporary storage location in which the contaminant might reside between upward cycles.

The nonhomogeneity of a permeable medium is a critical consideration in controlling the radionuclide migration induced by atmospheric pumping. If the medium were entirely homogeneous at every horizon, gas particles at any given elevation would have identically the same vertical velocity. Thus, any interface between contaminated versus non-contaminated gas would necessarily move upward and downward in a piston-like fashion, without any dispersion of a sharp front. In reality, however, the gas will move faster and farther along preferential paths, such as fractures, than it does in the surrounding permeable matrix. Thus, nonhomogeneities can cause significant dispersion of the contaminant interface and greatly hasten the surface arrival of radioactive gases.

The primary physical mechanism of dispersion in unidirectional (i.e., non-oscillatory) flow is illustrated in Figure 1 for three different flow configurations.[4] In a channel or a capillary tube, the centerline velocity is greater than the fluid velocity near the wall, so the contaminant travels fastest up the center. The advance of the salient is, however, constrained by the fact that molecular diffusion in the lateral direction depletes the concentration in the central finger of contaminant.[5] An analogous effect occurs in a homogeneous porous medium due to the varying length (i.e., tortuosity) of adjacent stream tubes as well as varying velocity from one stream tube to the next.[6] An extreme case occurs in fractured porous media where both of the proceeding mechanisms are operative in a simultaneous fashion, and it is obvious that the fluid travels much faster along the fractures than through the blocks and the speed is different along fractures having different aperture.[7]

The oscillatory flows of interest in atmospheric pumping are subject to all of the dispersion mechanisms noted previously for unidirectional flow. In addition, there are a number of "ratchet mechanisms" which should also enhance the vertical dispersion, as noted in Figure 2. In an oscillating channel flow, some of the contaminant which travels rapidly up the center (during an upstroke) diffuses into the slow-speed boundary layers along the wall, where it will not be swept all the way down again (during the next downstroke).[8] If the wall of the channel is porous, as in a fractured permeable medium, this same sort of ratchet mechanism is further enhanced by two additional processes, since the contaminant can be carried into the porous walls of a fracture both by molecular diffusion[9] and by Darcian seepage. Thus, the walls provide a temporary residence where the contaminant can "hide" between successive upward cycles of motion.

In the geologic media of interest, all of the mechanisms noted above will be further modified by the nonhomogeneous arrangement of fractures, their degree of connectivity, and their inclinations to the predominant pressure gradient, as illustrated schematically in Figure 3. Also, one might expect that the vertically layered structure of a geologic medium might be another important consideration in the dispersion process. Considering the overall complexity of this transport problem, there is a need for laboratory experiments which clarify the issues as well as field experiments which characterize the media of interest.

The mathematical models describing the diffusion/dispersion phenomena responsible for movement of gas from a chimney to the surface will be described in Section 2. Results of laboratory experiments performed to demonstrate these concepts will be presented in Section 3. Conclusions are provided in Section 4.

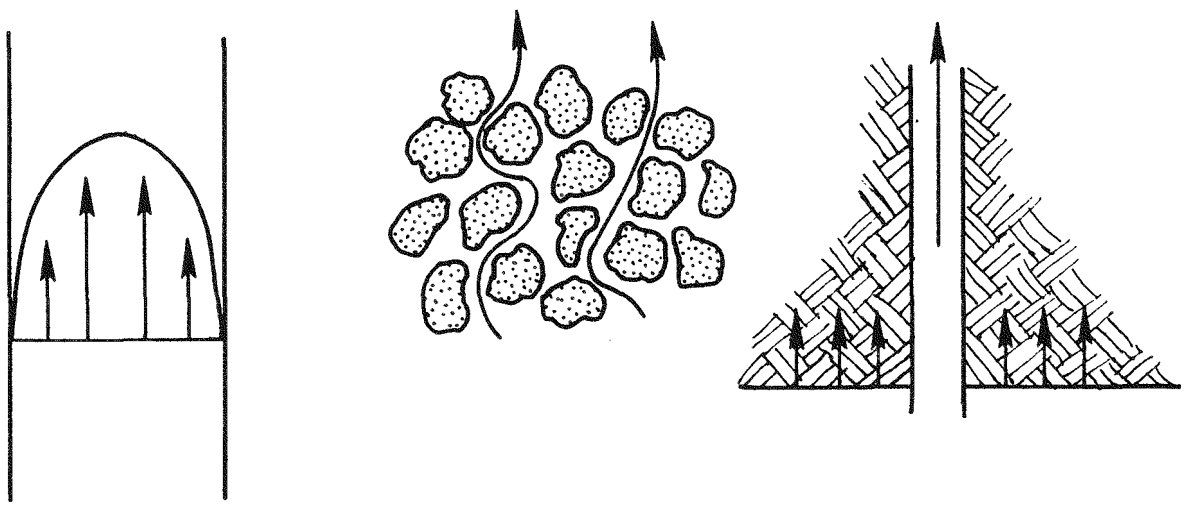

Figure 1. Nonuniformity of the fluid velocity causes dispersion of contaminants in channel flows, porous media and in fractured porous media, even in the absence of oscillatory motions.

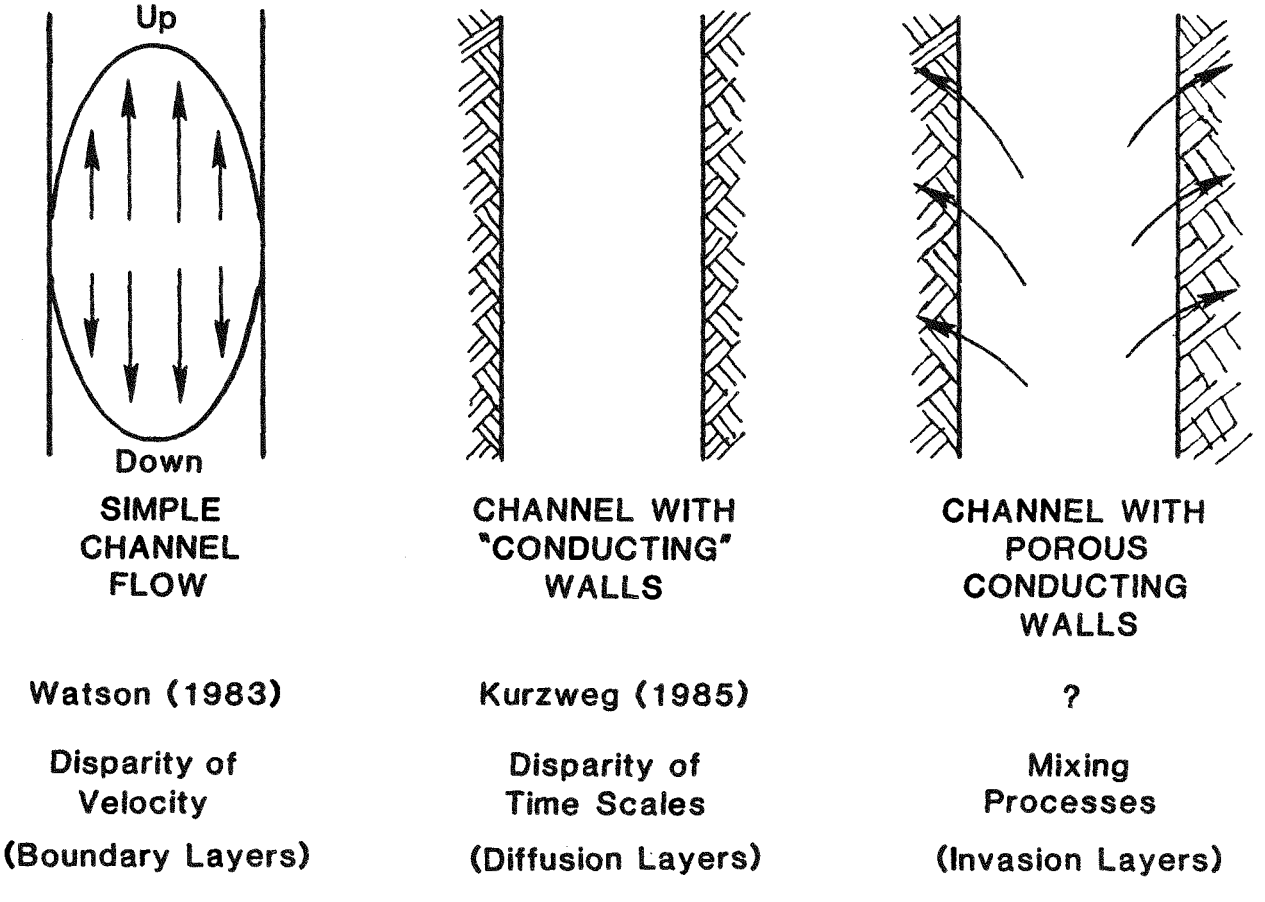

Figure 2. Oscillatory motions can enhance dispersion because of "ratchet" mechanisms which carry contaminant to higher and higher elevations at each successive upstroke of motion.

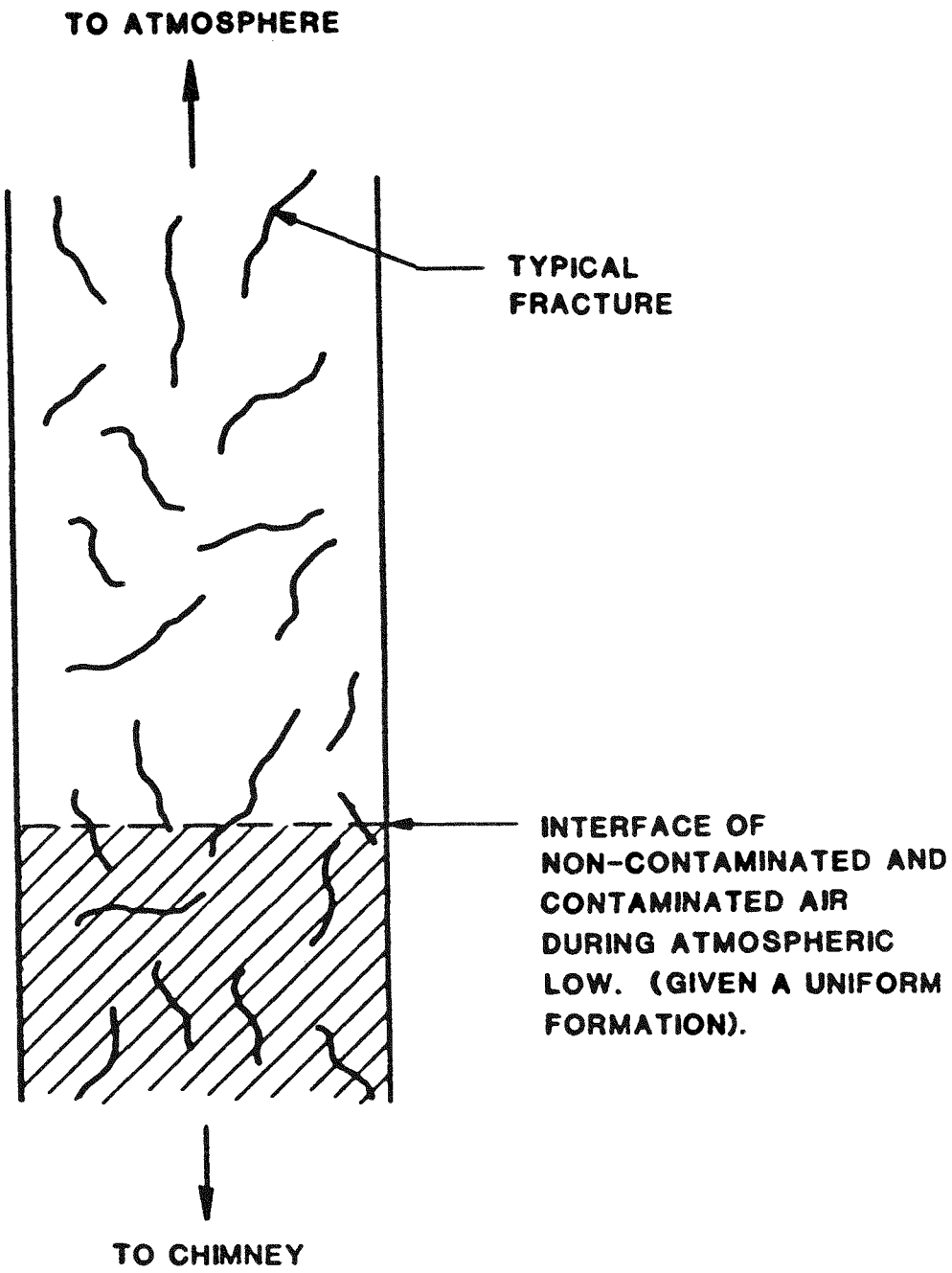

Figure 3. Nonuniformity of fracture orientation, relative to pressure gradient, causes irreversibilities during upward and downward phases of flow.

2. MATHEMATICAL MODELS

Even though dispersive effects are generally multidimensional in origin, they are often modeled in a one-dimensional fashion by analogy with molecular diffusion. The one-dimensional equation for conservation of an inert chemical component travelling through a porous medium is

$$\frac{\partial C}{\partial t} + \frac{\partial}{\partial x}\left(\frac{u}{\phi} C\right) = \frac{\partial}{\partial x}\left(D \frac{\partial C}{\partial x}\right) \tag{1}$$

in which C is the concentration, u is the superficial velocity of the gas, ϕ is the porosity, and D is the dispersion coefficient which includes the effects of molecular diffusion as well as the mechanical dispersion caused by the multidimensionality of the flow

$$D = D_{molecular} + D_{mechanical} \tag{2}$$

Typically, the molecular diffusion coefficient for gases moving through air is of the order 10^{-1} m^2/hr, but in a porous medium this value is reduced in accordance with the following relationship in which τ is the tortuosity[10]

$$D_{molecular} \sim \frac{D_o \phi}{\tau} \sim 10^{-2}\ m^2/hr \tag{3}$$

where the numerical value of 10^{-2} m^2/hr also reflects the fact that the tracer gases used in the experiments have a relatively large molecular weight, M, and D is inversely proportional to the square root of M.

The mechanical dispersion coefficient is usually assumed to depend linearly on the interstitial velocity, u/ϕ, such that (for the high Peclet numbers of interest here)[4]

$$D_{mechanical} \sim \frac{u}{\phi} \delta \tag{4}$$

which serves as a defining equation for the so-called dispersivity coefficient

$$\delta = \text{dispersivity} \tag{5}$$

Previous laboratory investigations indicate that the mechanical dispersivity of granular media (such as the sand used in the present experiments) is on the order of 1 to 10 times the grain size, for a nonoscillatory flow in a uniform bed.[11]

The flow along a single fracture experiences a moderate amount of dispersion because of the non-uniform velocity across the fracture. However, the effective diffusion coefficient derived by Taylor[5] for a parabolic velocity profile is on the order of

$$D_{Taylor} \sim \frac{a^2 u^2}{192 D_{molecular}} \qquad (6)$$

which is usually very small for the fracture apertures, a, and fluid speeds, u, encountered in geologic media.

The ratchet-like dispersion mechanisms pictured in Figure 2 depend upon the interaction between a primary flow channel and the bounding walls which provides a storage location where contaminants can reside between successive upward motions. Following Kurzweg's[9] analysis of an analogous heat transfer problem, a relatively simple exact solution can be derived[12] for the peak value of the effective diffusivity (D_{eff}) induced by an oscillating flow with $u = u_o \sin(2\pi t/T)$. It can be shown that for the experimental conditions described in Section 3 that

$$D_{eff} \sim \frac{1}{10} \frac{(\Delta L)^2}{T} \qquad (7)$$

where T is the period of oscillation and $\Delta L \sim u_o T$ is the longitudinal displacement or "stroke" of the oscillatory motion.

A number of dispersive effects have just been described. The associated diffusion or dispersion coefficients will be used in the following section to provide rough but comparative estimates of certain phenomena which can in turn be used as an aid to understanding the experimental results.

3. LABORATORY EXPERIMENTS

A series of laboratory experiments were undertaken to better understand the physical mechanisms which are important in the vertical transport of contaminated gases during atmospheric pumping. The experiments described here provide some qualitative and quantitative information concerning the roles of molecular diffusion and mechanical dispersion. In particular, it was found that atmospheric pumping does not enhance contaminant flow through a uniform porous medium. In contrast, the interaction between a simulated fracture and its permeable surroundings (i.e., the ratcheting mechanism illustrated on the right side of Figure 2) can significantly hasten the surface arrival of radioactive gases.

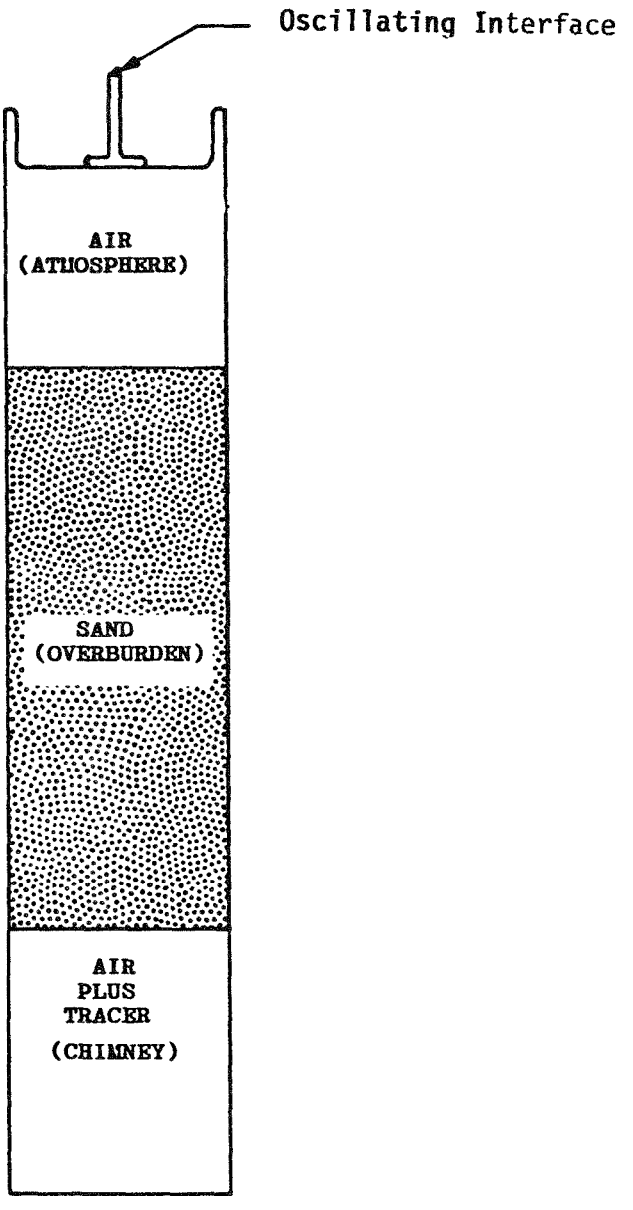

Figure 4. Experimental apparatus induces an oscillatory motion by reciprocating motion of a piston.

The experimental apparatus is illustrated schematically in Figure 4. The sample holder is a lucite tube 10 cm in diameter by 2 m long. The sample is constrained between perforated plates leaving plenum chambers at both ends. An oscillatory pressure variation is be produced within the upper plenum by a piston-like reciprocating motion. At the onset of an experiment, a tracer gas is injected into the lower plenum to simulate the radioactive gas at the bottom of a nuclear chimney. During an experiment, gas samples are periodically extracted from the upper and lower plenums by insertion of a hypodermic needle through a septum seal. After each extraction of a sample, a compensating amount of clean air is reinjected to offset the slight pressure reduction caused by the extraction. A gas chromatograph is used to determine the concentration of tracer gas within each sample, providing a time history of the concentration in each plenum.

Typical pressure histories at the top and bottom of the column are shown in Figure 5. The peak to peak pressure variation is on the order of 0.4 psi, comparable to the atmospheric pumping process of interest. The period of the pressure oscillation is, however, much shorter in the laboratory (~1 min) than in the field (~100 hr), to provide many cycles of oscillation in a short time and, also, to compensate for the shorter length scale used in the laboratory. The experiment was designed such that the pressure at the bottom would have a moderate degree of time lag and attenuation to approximate the behavior which has been observed during atmospheric pumping experiments in emplacement holes on Pahute Mesa. The differential displacement, ΔL, of the contaminant interface was on the order of 4 cm, corresponding to roughly 2% of the overall sample length.

To characterize the sands used in the pumping simulations, a number of preliminary experiments were performed. Porosity was determined by comparing bulk sample density with the density of SiO_2. Porosity was on the order of 35% for all of the samples. Permeability was determined from measurements of pressure drop during steady flow of nitrogen, with the flow rate deduced from the long-term pressure drop in the nitrogen bottle. Permeability was around 30 Darcies versus 200 Darcies, for samples having mesh sizes of 60-100 versus 20.

Results of the preliminary, proof of concept tests, are reported in Figure 6. These data were obtained using two identical experimental systems. In one system,, atmospheric pumping was simulated while in the other there was no pumping. The test results therefore provide a comparison between molecular diffusion and mechanical dispersion. As shown on Figure 6, the two results are essentially equivalent, given the overall data scatter.

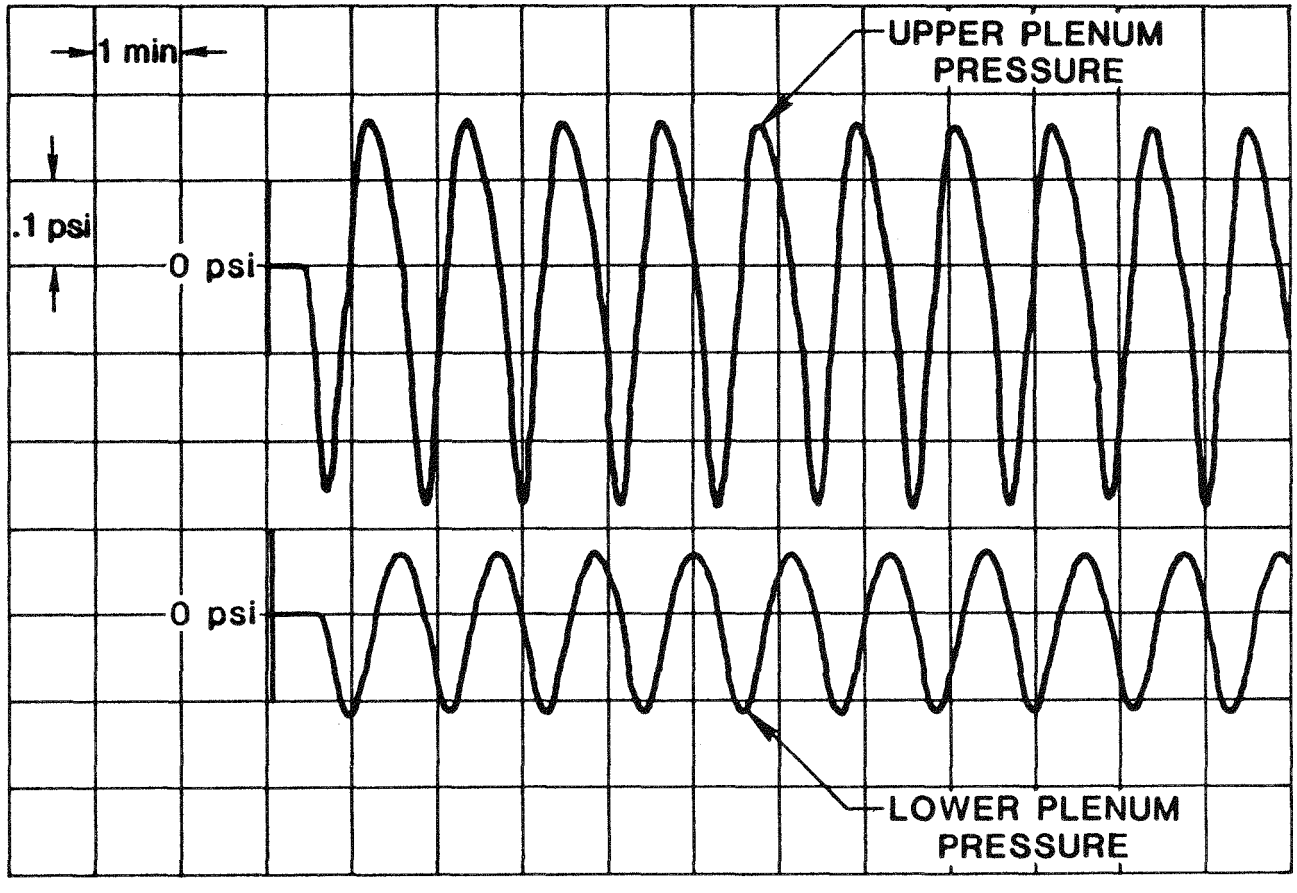

Figure 5. Typical pressure history at the top and bottom of the sand column during the laboratory experiments.

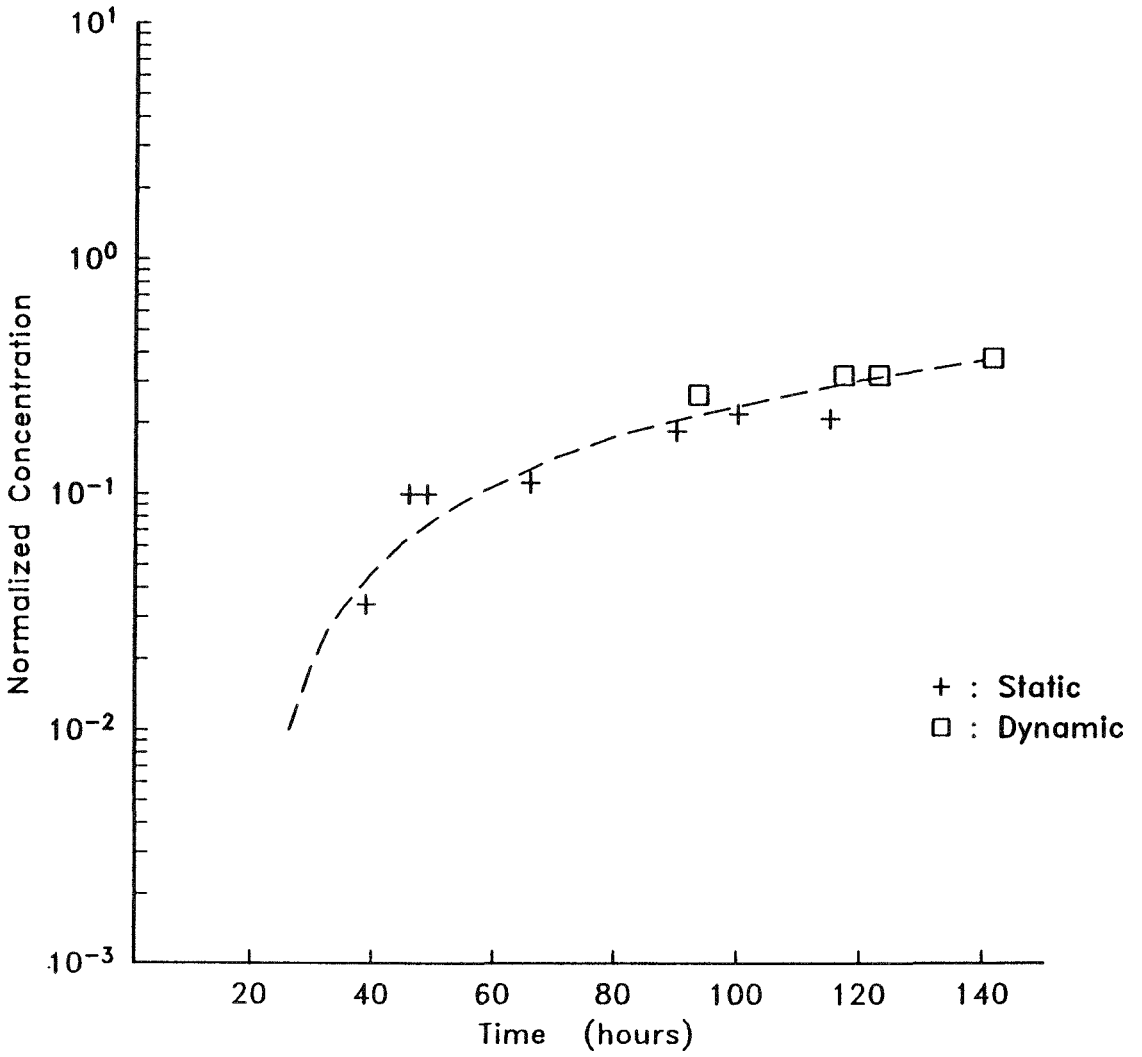

Figure 6. Comparison of atmospheric pumping and diffusion test results obtained during the short duration proof of concept test conducted using a uniform column filled with 60-100 mesh glass spheres.

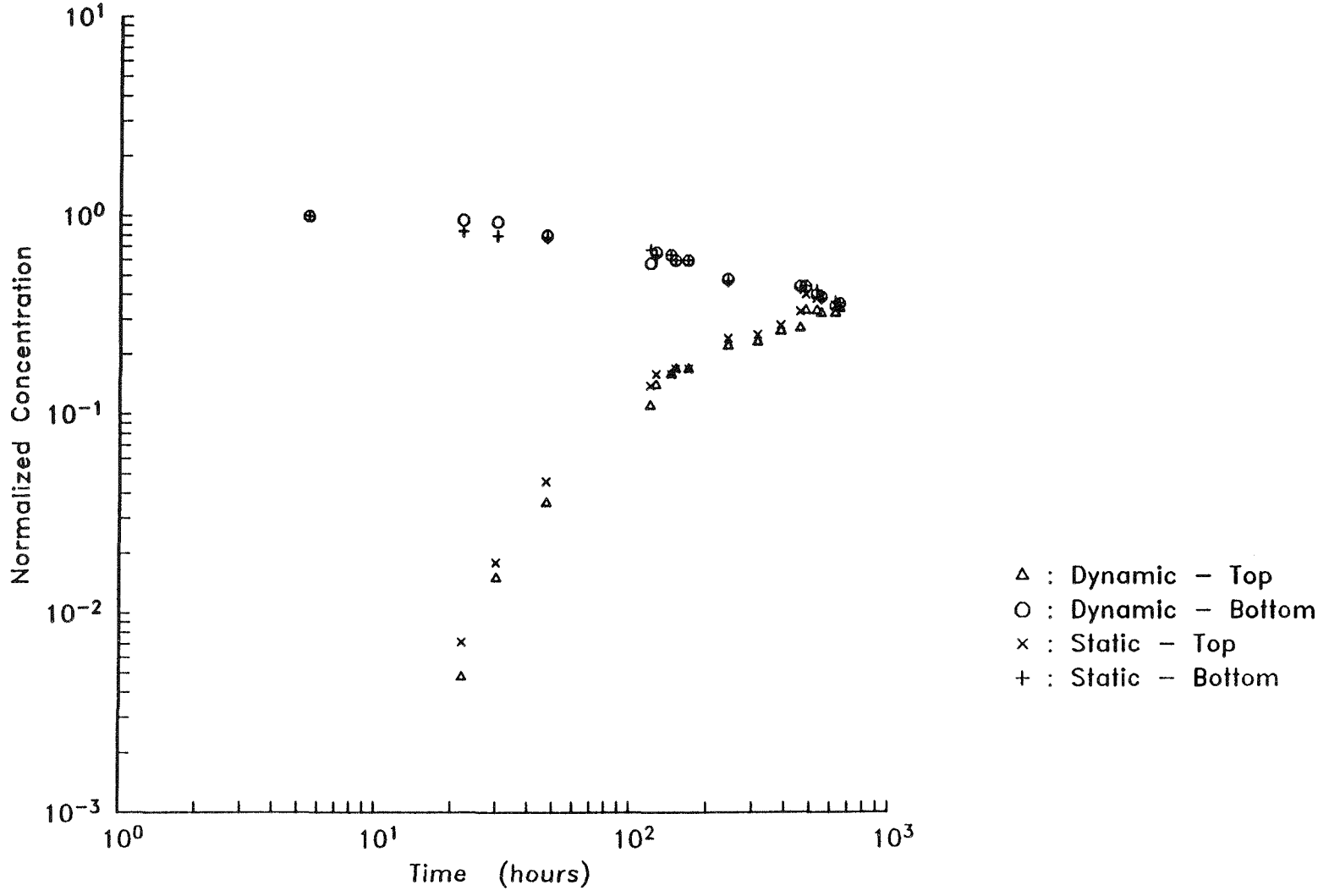

Figure 7. Comparison of atmospheric pumping and diffusion test results obtained using a uniform column filled with 60-100 mesh glass spheres.

Two additional tests, whose results are shown on Figure 7, were conducted to confirm the preliminary results. Again, it can be seen that cyclical pumping did not enhance dispersion and hasten the tracer arrival.

In these tests, the normalized tracer concentration in the upper plenum approached the .10 level within 50 to 90 hours. This compares fairly well with the following rough estimate of the time required to achieve a concentration of this level at the top (L ~ 2m) of the sand column by a process of molecular diffusion.

$$t \sim \frac{0.1 \times L^2}{D_{molecular}} \sim 40 \text{ hrs} \qquad (8)$$

Also, the rate of decrease in concentration in the lower plenum is in agreement with the analytical solution for molecular diffusion out of a reservoir into a semi-infinite porous column. So both of these order-of-magnitude checks confirm that the outcome of the homogeneous sand-column experiments, unpumped and pumped, is controlled primarily by molecular diffusion.

The close correspondence between pumped and unpumped results shown on Figures 6 and 7 may, at first, seem surprising. However, in homogeneous granular materials like sand, the dispersivity is generally on the order of 10^{-3} m or less.[13] So with a pore velocity of about $u \sim \Delta L/T \sim 4$ cm/1 min. ~ 2 m/hr, the mechanical dispersion coefficient should be around

$$D_{mechanical} \sim 10^{-3} \text{ m}^2/\text{hr} < D_{molecular} \sim 10^{-2} \text{ m}^2/\text{hr} \qquad (9)$$

suggesting that mechanical dispersion should not be noticeable in a unidirectional flow with this velocity, in keeping with the experimental outcome.

Conceptually, the ratchet or boot-strapping processes shown on the left hand sketch given on Figure 2, could be active in these oscillatory experiments. Within the initial 30 hours of pumping, there were about 2000 cycles of motion, each with a 4 cm upstroke. This adds up to a total cumulative upward displacement of about 100 meters for a demonic gas particle who always rides with the updraft and then holds his position during the downdraft. The ratchet or boot-strap mechanism, however, is not operative in a capillary tube or a homogeneous granular medium when the diffusion time across the micro-pore flow channels, $t = d^2/D$ is considerably less than the period of oscillation, because transverse molecular diffusion will then dissipate the horizontal concentration gradients which are essential to the mechanism. In our experiment with a grain size $d < 10^{-3}$ m, a molecular diffusion coefficient of $D \sim 10^{-2}$ m^2/hr, and a period of T ~ .02 hr,

$$\frac{t}{T} \sim 10^{-2} < < 1 \qquad (10)$$

Thus, the theory predicts that in a homogeneous sand column there should be no enhanced tracer motion associated with ratcheting, and none was observed in the experiments.

Additional tests were performed, using the experiment designs shown schematically in Figure 8 to illustrate the ratchet mechanism which we do expect to occur in fractured geologic media. Results of these experiments will be described in the following paragraphs.

To simulate the presence of a fracture or a high permeability path, we emplaced a 1 inch tube of coarse 200 Darcy sand along the centerline of the larger lucite tube, surrounding it with the finer 30 Darcy glass beads used in the previous experiments. In one case, the emplacement tube was left in position throughout the experiment, thus maintaining an impermeable barrier between the fracture and its permeable surroundings. In the other case, the tube was carefully removed during pouring and compaction of the annular sandpack, to allow free communication between the "fracture" and its surroundings.

The results of these two fracture-simulation experiments are shown in Figure 9. The arrival is clearly much earlier when the guard tube is removed, and the slope of the data is much steeper, suggesting a greater vertical flux. We believe that this enhancement is caused by the ratchet mechanisms pictured on the right side of Figure 2. Contaminated gas moves up the central column, and some of it travels outward into the surrounding annular sand pack, both by Darcian seepage and by molecular diffusion. Since the horizontal path length is now d ~ 3 cm, the transverse diffusion time of $t \sim d^2/D \sim 10^{-1}$ hr is now somewhat longer than the period of oscillation.

$$\frac{t}{T} \sim \frac{10^{-1}\text{hr}}{2 \times 10^{-2}\text{hr}} > 1 \qquad (11)$$

suggesting that there should be horizontal gradients within the column and that ratcheting should occur from diffusion effects alone. This ratcheting would be expected to be further enhanced by the effects of Darcian seepage. These ratcheting effects therefore provide a likely explanation for the early arrival and enhanced contaminant flux observed in the simulated fracture experiment in which the guard tube was removed.

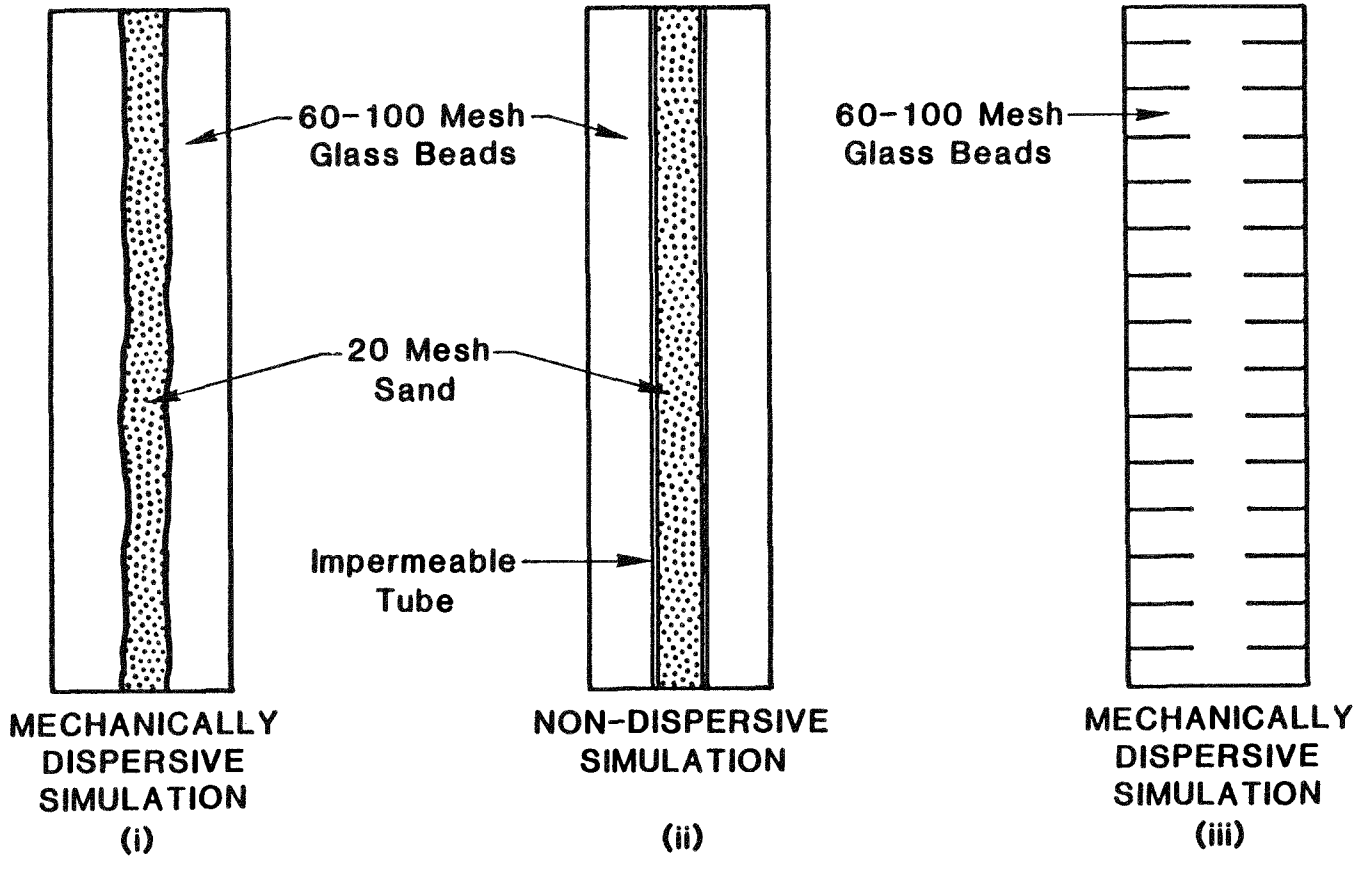

Figure 8. Interaction between a fracture and the surrounding porous medium as simulated by a high-permeability central column surrounded by an annulus of lower-permeability material and by a column whose vertical flow is limited by emplaced discs. Note that in some experiments, an impermeable guard-tube was used to prevent crossflow between the "fracture" and its "porous" surrounding.

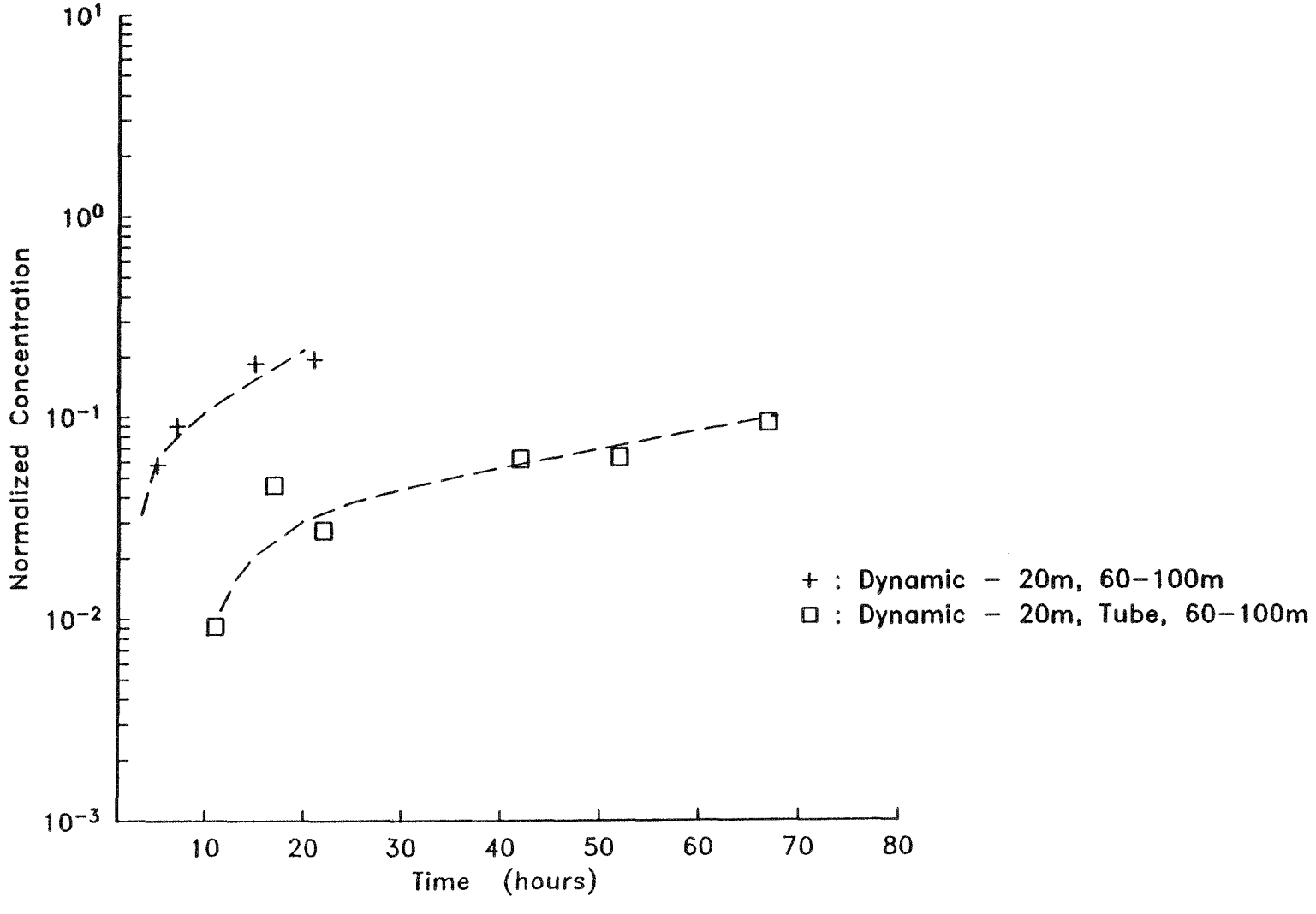

Figure 9. Comparison of results obtained with and without the guard-tube suggests that sideward communication between the "fracture" and its surroundings cause significant enhancement of the upward transport of the contaminant.

Comparison of the simulated fracture experiments with and without the guard tube helps to confirm the origin of the enhanced transport. The presence of the guard tube clearly delays the arrival and reduces the contaminant flux, even though the presence of the tube should tend to increase the upward displacement, ΔL, which occurs in the central column during each successive cycle. (The guard tube prevents lateral seepage from the central column into the surrounding annulus, which should increase the stroke of the motion ΔL.) Indeed, with the guard tube in place the contaminant has the opportunity to reach further toward the top on any given upstroke, but it cannot "hold" its position during a downstroke unless it is allowed access to a hiding place in the surrounding sand pack. The ratchet mechanism can only be effective if there is a transverse storage mechanism which has a relatively slow response time.

The tracer transport time shown on Figure 9 for the fracture experiment with the tube absent is clearly faster than obtained for the tests whose results are shown on Figures 6 and 7. The fracture experiment with the tube in place has a fairly quick arrival at the surface, but the late time flux (slope) is comparable to those shown previously. These two observations (arrival and slope) together seem to suggest the following explanation: the arrival and the late time flux are both controlled by molecular diffusion; It's just that the larger differential displacement, $\Delta L \sim 1$ m, of the experiment with a central tube should reduce the path length, and associated arrival time, for diffusion to the surface.

A second series of experiments were performed to demonstrate the ratchet mechanism using the disc design shown on Figure 2. This design was selected as the geometry is well suited for analysis using a recently developed numerical code specifically designed to simulate these cyclical motions without introducing prohibitive quantities of numerical diffusion.

Results of the series of experiments with the disc configuration are shown on Figure 10. The latest slowest transport of tracer is seen to occur with the static column. The dynamic test, having a 4 cm upward displacement of gas at the bottom of the sand column and .02 hr period had the intermediate transport characteristics. Finally, the dynamic test having a 12 cm upward displacement but .07 hr period showed the fastest transport. These series of tests demonstrate the importance of the ratcheting mechanism and how this mechanism is enhanced if the upward gas displacement is increased.

The order of magnitude of the observed ratcheting enhancements can be checked against the analytical estimate given previously

$$D_{eff} \sim \frac{1}{10} \frac{(\Delta L)^2}{T} \sim 10^{-2} \frac{m^2}{hr} \leftrightarrow 1 \frac{m^2}{hr} \qquad (12)$$

where the low end of the range corresponds to a displacement of $\Delta L = 4$ cm and the upper end to a displacement of $\Delta L = 1$ m, both with a period 0.02 hr. Upon comparing this range with the magnitude of molecular diffusion ($D_{molecular} \sim 10^{-2}$ m^2/hr) one would expect to see a moderate, but noticeable, enhancement in the intermediate data set of Figure 10 (for $\Delta L \sim 4$ cm) and a very substantial enhancement for the unguarded high-permeability central column in Figure 9 ($\Delta L \sim 1$ m), in keeping with the experimental observations.

4. CONCLUSIONS

The described experiments, whose results are consistent with estimates based on simple diffusion and dispersion arguments, strongly suggest that;

- Contaminant transport in the vertical direction through a homogeneous porous medium is not enhanced by atmospheric pumping.

- Contaminant transport in the vertical direction through a non-homogeneous porous medium is enhanced by atmospheric pumping.

The rate of transport through a homogeneous porous medium was found to result from molecular diffusion. In a non-uniform medium, typical of most real geologic medium, the transport rate could be greatly increased as a result of atmospheric pumping. Key parameters determining the transport rate include the magnitudes and periods of the pressure variations, the degree of non-uniformity (i.e., possible fracture extent), the bulk medium permeability and porosity, and the system geometry (i.e., cavity or chimney size, depth of burial, layering, etc.).

Future work involves the continued development of the numerical model used to describe contaminant transport through real geologic media resulting from cyclical atmospheric pressure variations. Work is also continuing to apply these results to field applications.

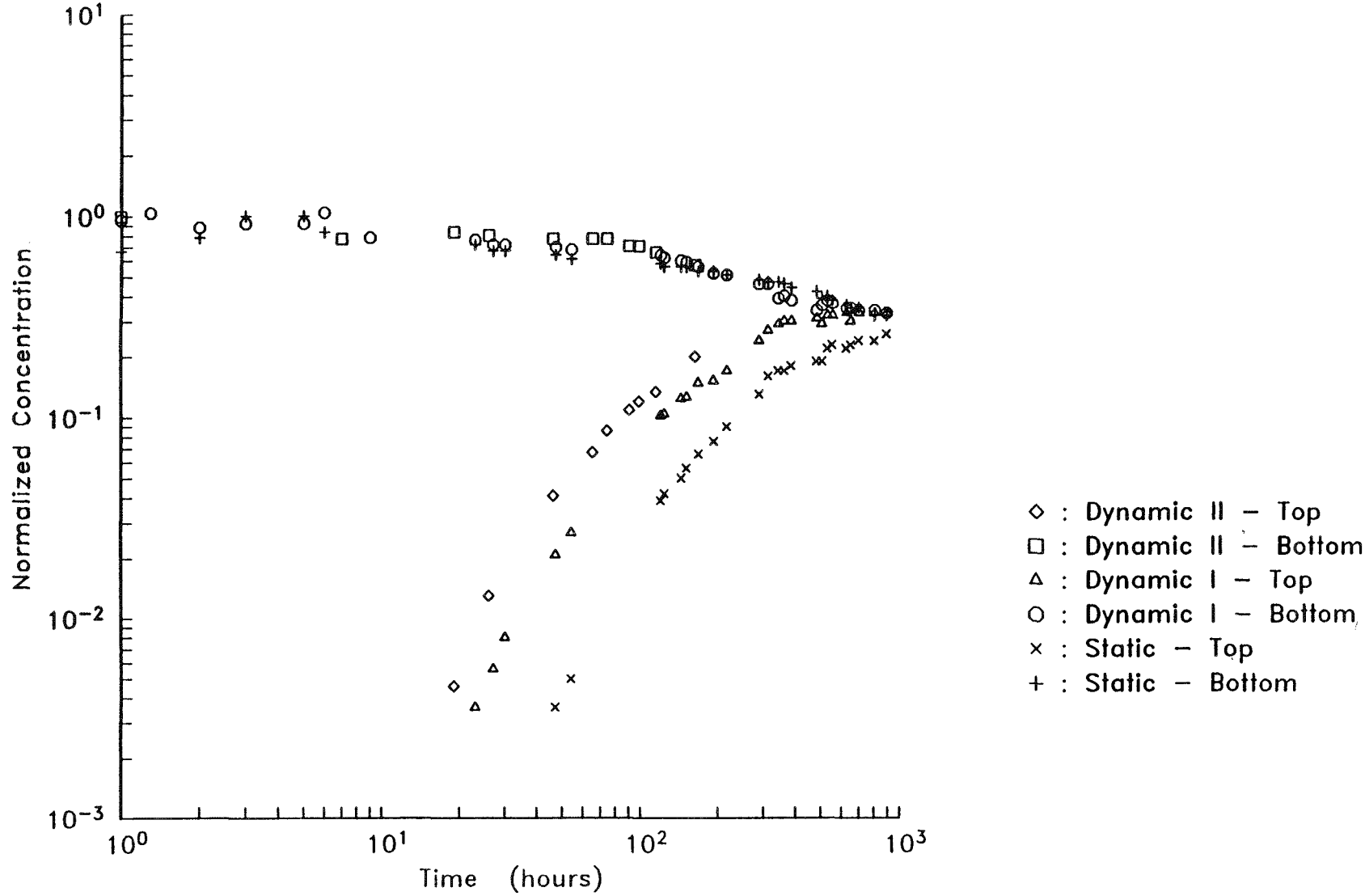

Figure 10. Comparison of the static and dynamic transport characteristics obtained using a column whose vertical flow in an annular region is limited by emplacement of impermeable discs.

REFERENCES

1. J. M. Hanson and J. R. Hearst, "Evaluation of Permeability in the Unsaturated Zone at NTS Using Barometric Pressure Modeling," Proc. Third Symp. Containment UGT, Vol. 1, p. 392-414, 1985.

2. N. R. Burkhard, J. R. Hearst, and W. Gersch, "Diffusivity Determination at NTS," this proceedings.

3. U. H. Kurzweg and L. Zhao, "Heat Transfer by High-Frequency Oscillation: A New Hydrodynamic Technique for Achieving Large Effective Thermal Conductivity," Physics of Fluids 27 (11), 2624-2627, 1984.

4. A. E. Scheidegger, The Physics of Flow through Porous Media, Univ. of Toronto Press, Toronto, Canada, 1963.

5. G. I. Taylor, "Dispersion of Soluable Matter in Solvent Flowing Slowly Through a Tube," Proc. Royal Soc. London, A, 219, 186-203, 1953.

6. P. G. Saffman, "A Theory of Dispersion in a Porous Medium," J. Fluid Mech., 6, 321-349, 1959.

7. H. K. Endo, J.C.S. Long, C.R.Wilson, P.A.Witherspoon, "A Model for Investigating Mechanical Transport in Fracture Networks," Water Res. Research, 20, (10), 1390-1400, 1984.

8. E. Watson, "Diffusion in Oscillatory Pipe Flow," J. Fluid Mech. 133, 233-244, 1983.

9. U. H. Kurzweg, "Enhanced Heat Conduction in Oscillating Viscous Flows Within Parallel-Plate Channels," J.Fluid Mech.,156, 291-300, 1985.

10. D. M. Smith, "Restricted Diffusion through Pores Within Periodic Constrictions," AIChE Journal 32 (6), 1039-1042, 1986.

11. D. L. Koch and J. F. Brady, "Dispersion in Fixed Beds," J. Fluid Mech. 154, 399-427, 1985.

12. R. H. Nilson and K. Lie, "Numerical Analysis of Oscillatory Gas Motion and Contaminant Transport in a Fractured Porous Medium, SSS-R-87-8621, S-CUBED, 1987.

13. R. A. Freeze and J. A. Cherry, Groundwater, Prentice-Hall, Englewood Cliffs, NJ, 1979.

Hydrology and Radionuclide Migration

DO NOT MICROFILM
THIS PAGE

HIGH FLUID LEVELS IN DRILL HOLES, YUCCA FLAT, NEVADA TEST SITE

Hoover, D.L., U.S. Geological Survey,
Box 25046, MS 913,
Denver, Colorado, 80225
and
Trudeau, Douglas A., U.S. Geological Survey,
1500 E. Tropicana, Suite 201,
Las Vegas, Nevada, 89132

ABSTRACT

Between 1962 and 1986, the sustained effects of underground nuclear tests on water levels were investigated in six drill holes in Yucca Flat. This report identifies 33 drill holes that have high fluid levels (levels of any drilling fluid that are above the water table of Doty and Thordarson, 1983) or high water levels (formation water levels that are above previously measured static water levels). We conclude that (1) high fluid levels are more abundant where 20 or more nuclear tests within a 2,440-m radius were detonated near or below the water table, (2) high fluid levels are probably cumulative, and (3) the top of complete zeolitization of volcanic rocks has no apparent relation to drill holes that have high fluid or water levels.

MEASURED EFFECTS OF UNDERGROUND NUCLEAR TESTS ON WATER LEVELS

On June 21, 1962, the water level in well 7 in east-central Yucca Flat (fig. 1, 2) was found to be 17.1 m above measurements that were made two months previously. The cause of the high water level was tentatively related to the nuclear test in U3amS which took place 40 days before the measurement (M.S. Garber, U.S. Geological Survey, written commun., 1963). The U3amS nuclear device was detonated 307 m from well 7 and 71.3 m above the water table. Later measurements indicated an exponentially decreasing rate of decline of the water level in well 7. Fourteen months after the rise of the water level was first noted, the water level was still 8.5 m above water levels measured prior to the U3amS nuclear test.

During and after the nuclear test in U3cn on September 13, 1963, water levels were monitored in three wells in Yucca Flat. The nuclear test in U3cn was detonated approximately 213 m below the static water level. At U3cn#4, 610 m from U3cn, instrumentation to measure water levels was disabled by the nuclear test, but a manual measurement 16 hours later showed the water level to have risen 148 m above the pretest level. The maximum water level rise was estimated at 244 m (W.E. Hale, I.J. Winograd, and M.S. Garber, U.S. Geological Survey, written commun., 1963). At well 7, 1173 m from U3cn, the water level rose 13.8 m in 4 hours after the nuclear test fell 3.7 m after 18 1/2 hours, and finally, rose to 21.3 m above the pretest level 17 days after the nuclear test. After 446 days, the water level was still 2.2 m above the pretest level (G.E. Brethauer and William Thordarson, U.S. Geological Survey, written commun., 1973). At well E, 2423 m from U3cn, the water level rose about 3.4 m 18 seconds after the nuclear test. Later water tests indicated that flow was plugged off between the well and the rocks.

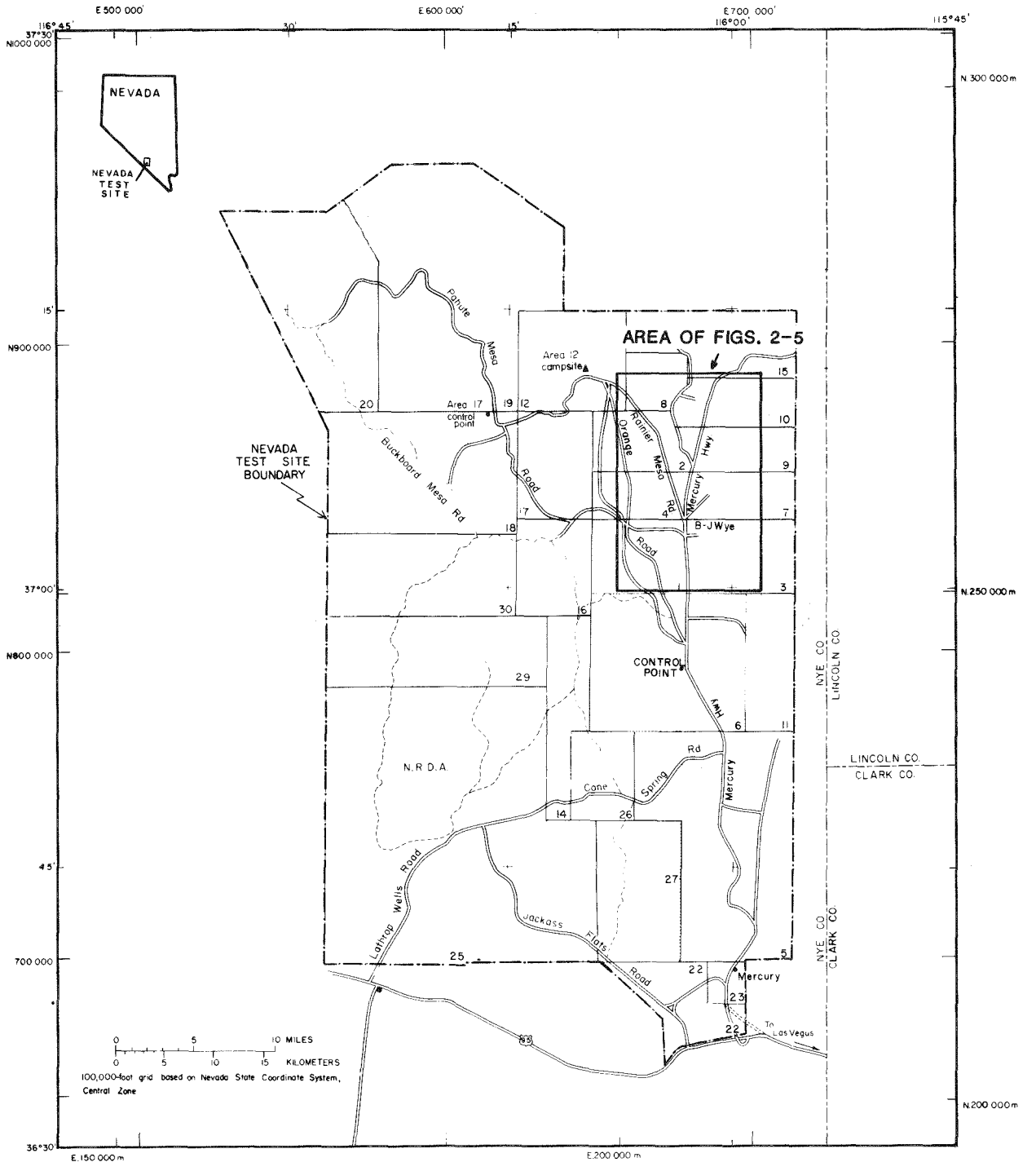

Figure 1.--Location of Nevada Test Site and numbered testing areas.

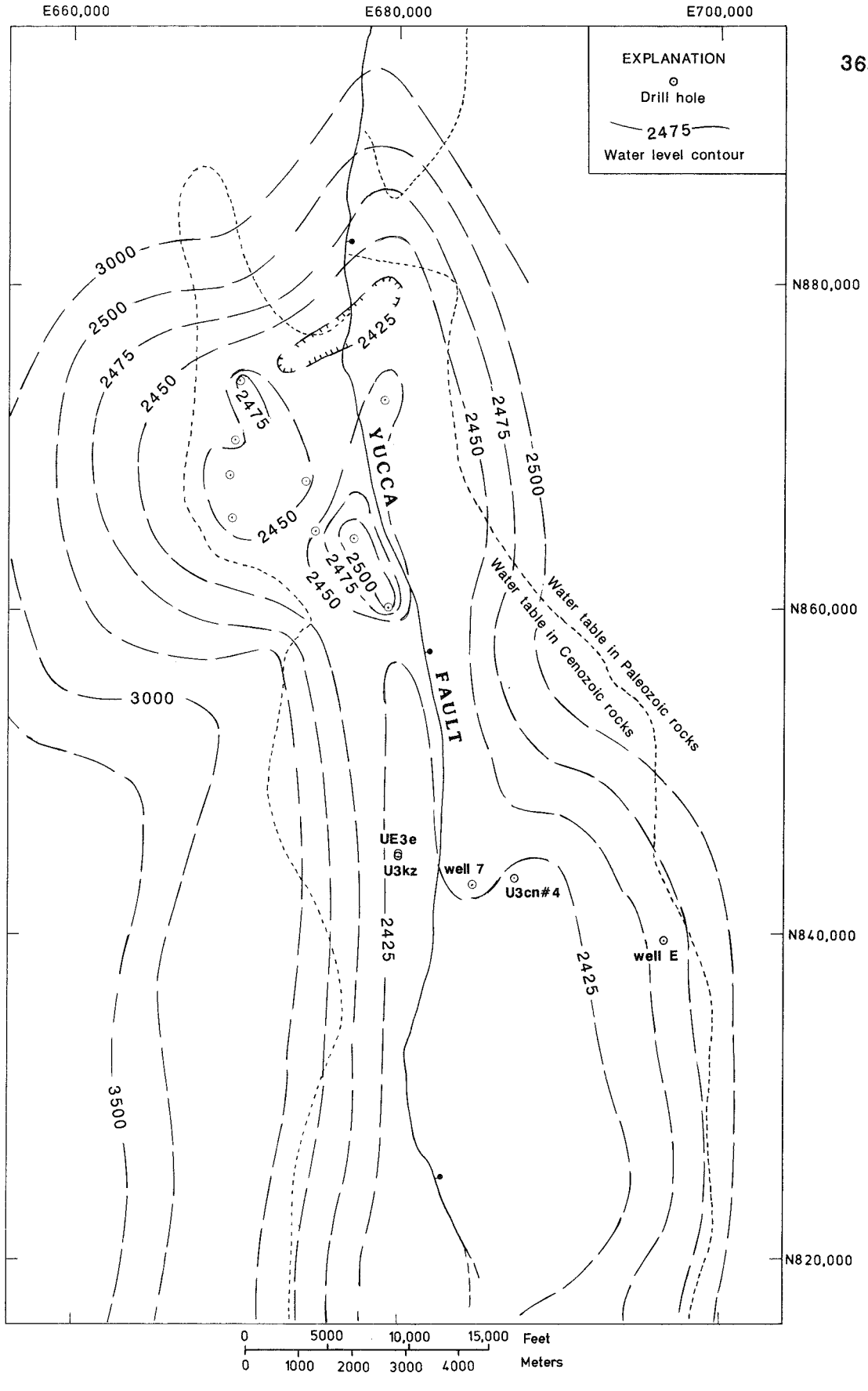

Figure 2.--Water table in rocks of Cenozoic and Paleozoic age, Yucca Flat, Nevada Test Site (modified from Doty and Thordarson, 1983).

Measurements of water levels continued for 18 days in U3cn#4 after the nuclear test in U3cn and for 446 days in well 7. Mathematical analysis of these measurements (G.E. Brethauer and William Thordarson, U.S. Geological Survey, written commun., 1973) indicated that:

1. Only data from well 7 were usable for mathematical analysis.
2. Measurements in other drill holes were needed to express a mathematical model that could be applied to other nuclear tests.
3. The rise and decline of water levels in response to an underground nuclear test was complex, and could involve more than one mechanism.

Water level measurements made in 1980 were used to compile a water table map of Yucca Flat (Doty and Thordarson, 1983). Figure 2 shows two ground-water mounds that have a relief of 15 to 23 m above the surrounding water levels in northern Yucca Flat. The ground-water mounds are not related to lithologic characteristics. Although the water table elsewhere in Yucca Flat follows the configuration of the alluvial basin and is not affected by faults, the two ground-water mounds are bounded on the east and west by faults. At well 7, the water table contours form a nose that has a relief of about 10 m above the water table of the surrounding area. Again, lithologic characteristics provide no reason for the high water level at well 7, but a fault is present. Other drill holes that have high fluid levels are also close to faults, but data are insufficient to determine a relationship between high fluid levels and faults.

After completion of the U3kz drill hole and cementing of a liner from 449 to 670 m in 1985, the liner leaked at the bottom and allowed entry of water that contained detectable radioactivity. The water level rose and stabilized 13.7 m above the top of the liner or 71.6 m above the water table of Doty and Thordarson (1983). UE3e, 60.7 m north of U3kz, was drilled to a depth of 765 m to investigate the source of radionuclides found in U3kz. In an open hole, the water level in UE3e apparently stabilized 45.1 m above the water table. Geophysical logs indicated that the probable source of the water and of radionuclides in UE3e was from fractures at a depth of 658 m. When the drill hole was shut in below 646 m by packers, the water level rose 253 m above the water table of Doty and Thordarson (1983) and was still rising after 11 days. It was concluded from radionuclide analyses and data from the two drill holes that the nuclear test in U7aq, 355 m north of U3kz, was the probable cause of the high fluid levels and the source of radionuclides in U3kz and UE3e (D.C. Sewell, U.S. Department of Energy consultant, written commun., 1987).

HIGH FLUID LEVELS

The radionuclides and high water levels in U3kz and UE3e were believed to be confined to the fault block that contains the two drill holes (D.C. Sewell, U.S. Department of Energy consultant, written commun., 1987). Geologic investigation of the fault block led to the discovery that some drill holes outside of the fault block also had apparent high fluid levels. Fluid level and pertinent drilling operation data were summarized from drill-hole histories for all drill holes in Yucca Flat that penetrated below the water table (Doty and Thordarson, 1983) or to less than 100 m above the water table. Winograd (1970) recognized that anomalous, high fluid levels could

occur in drill holes because of drilling methods, density contrasts between drilling fluids and formation water, and anomalous formation-water temperatures. To eliminate these factors, the following criteria were used to screen these summaries of fluid level history:

1. At least two fluid level measurements after cessation of drilling operations other than logging or sidewall coring;
2. All measurements in an open hole or in open drill pipe or casing;
3. Last measurement at least 2 weeks after cessation of drilling operations;
4. Bottom of hole below the water table of Doty and Thordarson (1983);
5. Cave or fill substantially less than fluid level rise;
6. Purge of drilling fluid before measurements;
7. Drilling fluid other than mud.

These criteria were met by six drill holes (fig. 3) that have definite high fluid levels. Eighteen drill holes that do not meet one or more of the last four criteria are termed possible high fluid levels (fig. 3). In addition to the 6 definite and 18 possible high fluid levels, the 8 wells that define the 2 ground-water mounds (fig. 2) and well 7 are included on figure 3.

For most of the drill holes examined, fluid level measurements, after drilling operations ceased, were made for operational reasons and did not meet the criteria. Thus, drill holes with high fluid levels may be more abundant than indicated on figure 3. Except for the eight drill holes with high water levels that are included from figure 2 and high water levels in U3kz and UE3e, the high fluid levels cannot be used in hydrologic investigations except to indicate where the problem of high fluid levels is present.

DENSITY OF NUCLEAR TESTS

All announced nuclear tests in Yucca Flat that were detonated below the water table or less than 100 m above the water table were used to compile the map of nuclear test densities (fig. 3). The nuclear tests took place from 1962 through 1986. The density of nuclear tests was obtained by contouring density values on equally-spaced grid points. The density values were obtained by counting all nuclear tests within a 2440-m radius of each grid point. This radius is the approximate distance between U3cn and well E (HTH "E"), the longest distance for which the effects of a nuclear test on water levels have been noted in Yucca Flat. All of the high fluid levels are within areas that have a density of five or more nuclear tests within a 2440-m radius. Twenty-five of the 33 drill holes that have high fluid or water levels are within areas that have a density of 20 or more nuclear tests.

The map of nuclear test densities is an empirical device that does not take into account distance from nuclear tests, time since nuclear tests and hydrologic factors, such as rock compressibility and hydraulic diffusivity. The major deficiency of the map is that time since the nuclear tests used to compile the map is not incorporated in the map. Thus, areas that contain nuclear tests that occurred early in the period of compiled nuclear tests (1962-1986) and areas that have high hydraulic diffusivity are probably overemphasized. A map that incorporates density as a direct function of yield and inverse functions of distance from nuclear tests and time since nuclear tests might provide a better empirical relationship to high water levels.

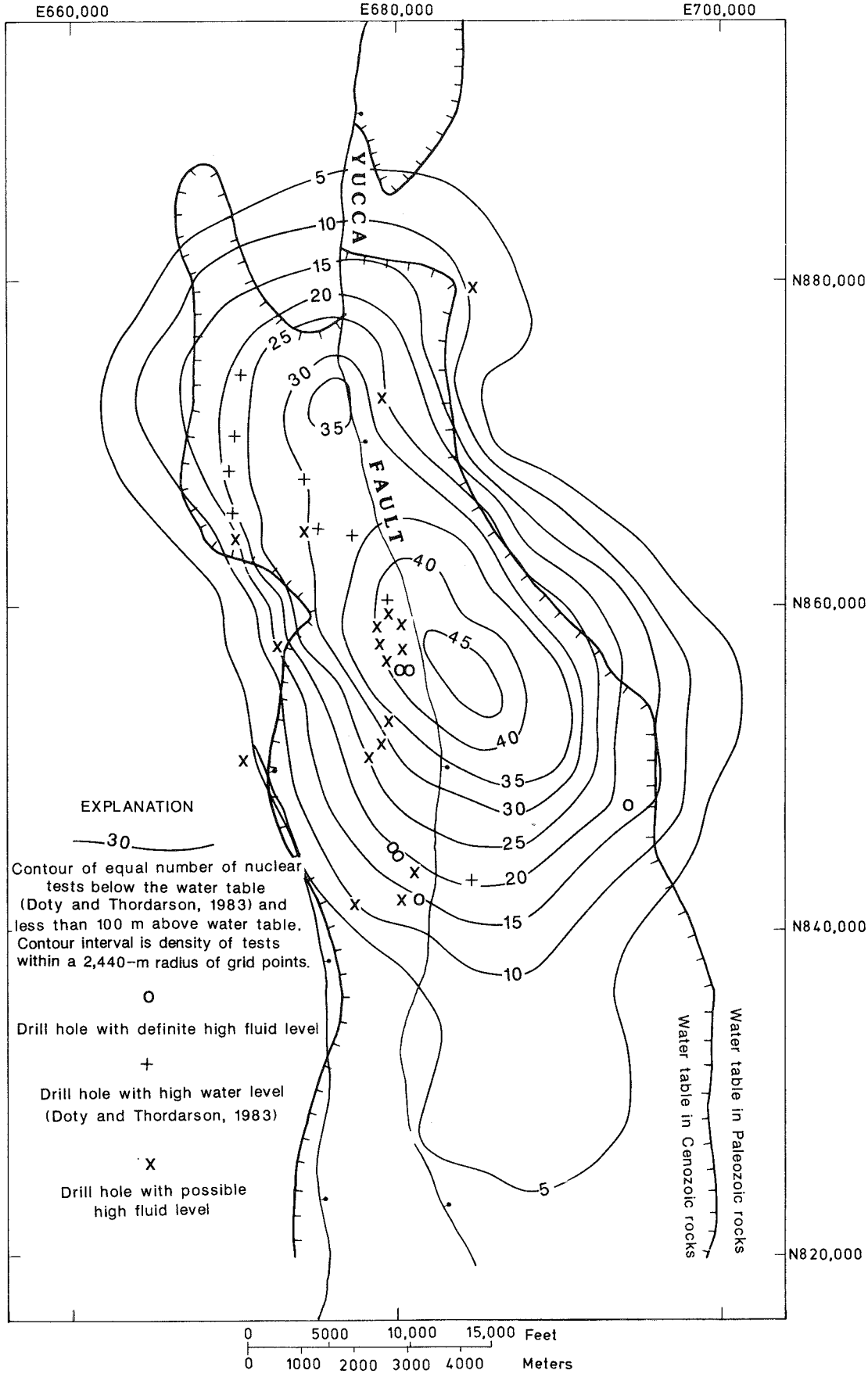

Figure 3.--Drill holes with high fluid levels and density of nuclear tests.

ZEOLITIZATION

Zeolitization of vitric volcanic rocks greatly reduces permeability. To determine whether a relationship between high fluid or water levels and zeolitization existed, a structure contour map on top of completely zeolitized rocks was compiled from lithologic logs of more than 200 drill holes (fig. 4). The structure contour and water table maps were used to compile an isopach map of the interval between the top of completely zeolitized rocks and the water table (fig. 5). Drill holes that have high fluid or water levels are almost equally divided between areas where completely zeolitized rocks are above the water table and areas where they are below the water table.

SUMMARY

The effects of underground nuclear tests in Yucca Flat on water levels have been measured at distances of at least 2400 m from a nuclear test. Post-test measurements of high water levels caused by nuclear tests indicate that water levels require months or years to return to pretest levels. The location of the 33 drill holes that have high fluid or water levels indicates that a density of 20 or more nuclear tests near or below the water table and within a 2440-m radius may cause significant effects on water levels. This density and the long period of time for water levels to return to pretest levels indicates that the effects of nuclear tests on water levels are probably cumulative. Drill holes with high fluid or water levels are about equally divided between areas where the top of zeolitized rocks are above and where they are below the water table.

Fluid level measurements in most drill holes are made for purposes of drilling operations and their suitability for defining areas of high water levels in this report was fortuitous. Hydrologic data holes are needed to define the hydrologic factors of rocks that affect high water levels and the rate at which the high water levels will decline. Fluid level measurements made for hydrologic purposes in instrument or emplacement holes, where drilling and completion programs permit, would better define the area of high water levels.

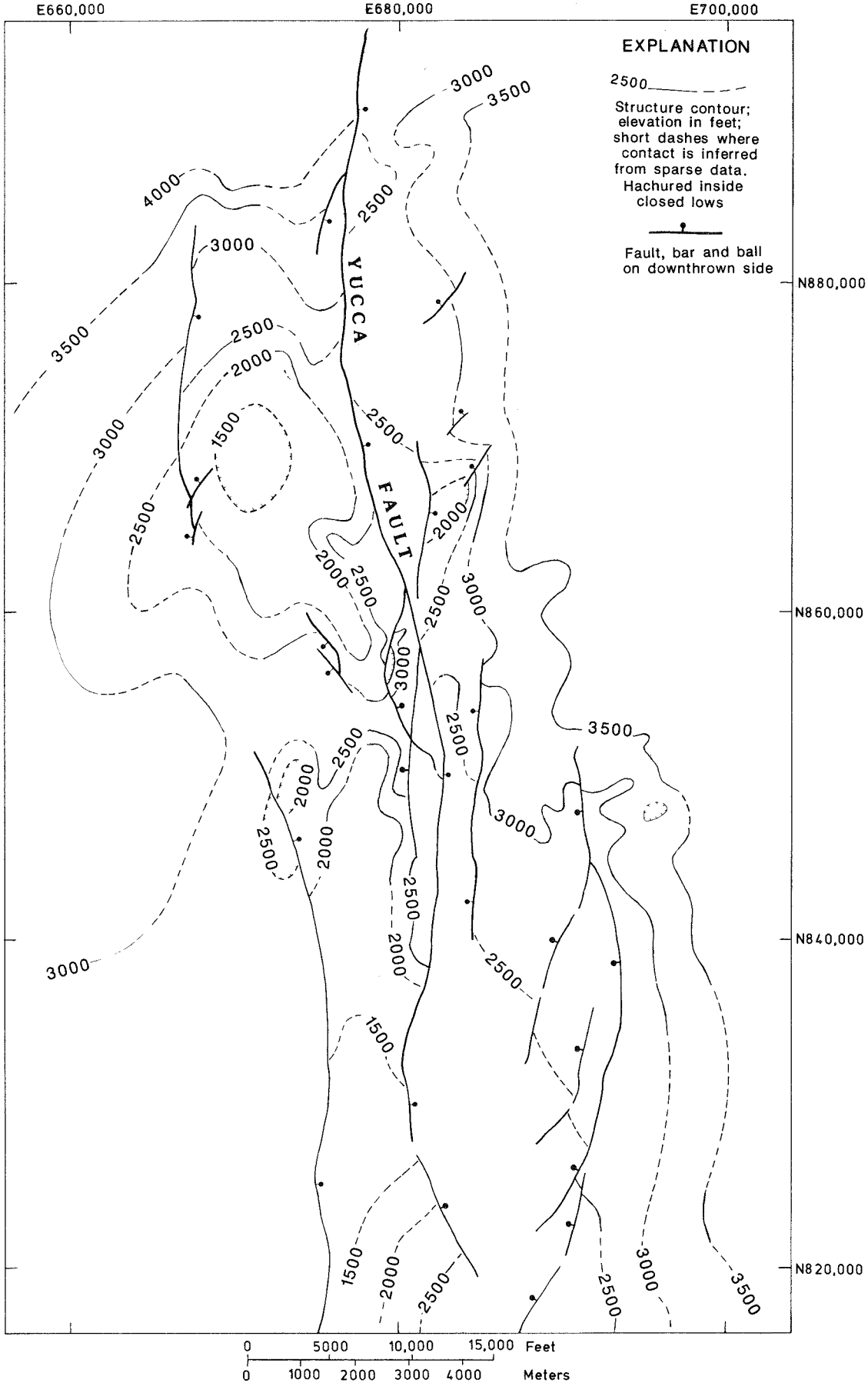

Figure 4.--Elevation of top of zeolitized rocks. Contour interval: 500 feet.

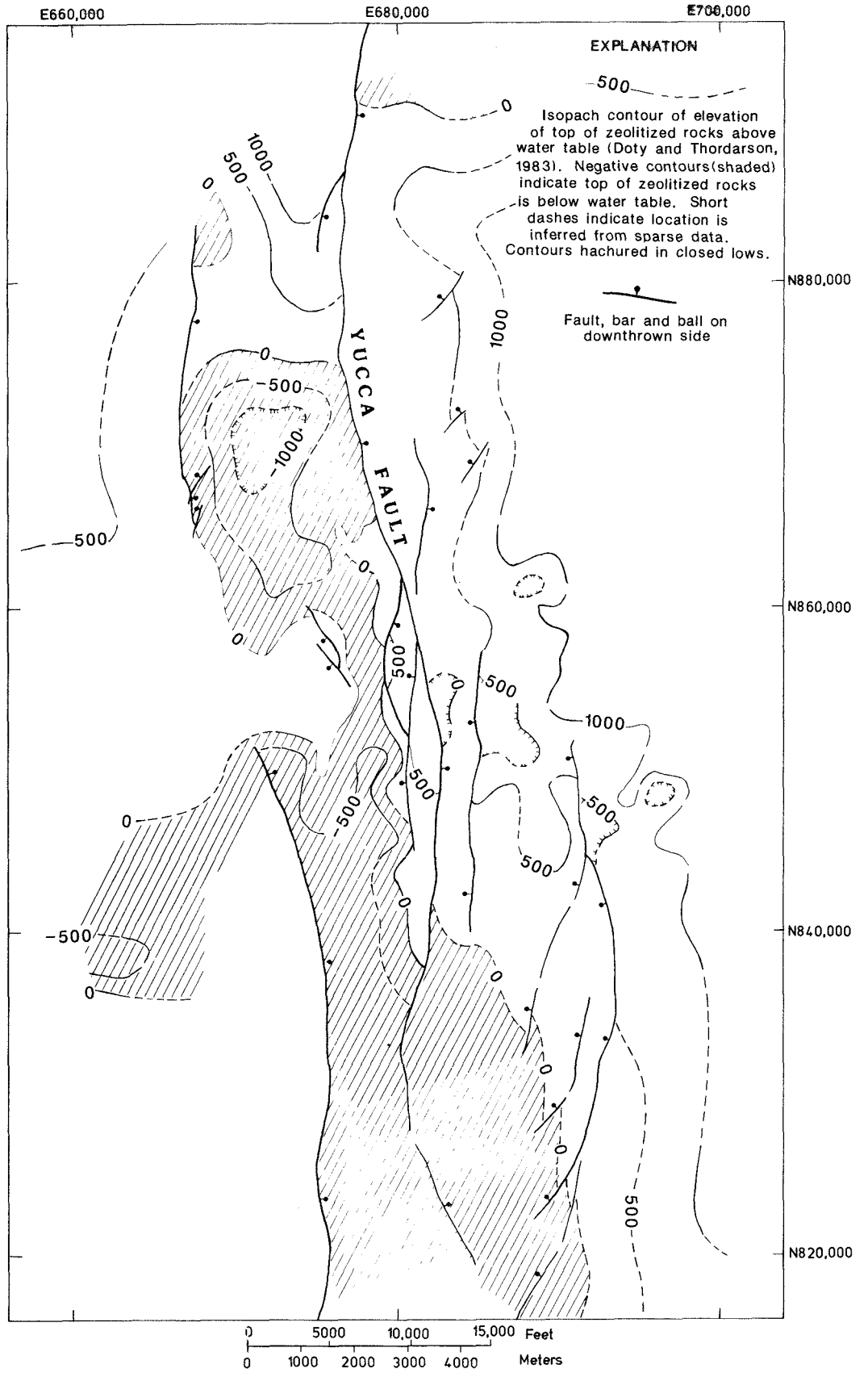

Figure 5.--Isopach map between top of zeolitized rocks and water table (Doty and Thordarson, 1983). Contour interval: 500 feet.

REFERENCES CITED

Doty, G.C., and Thordarson, William, 1983, Water table in rocks of Cenozoic and Paleozoic age, 1980, Yucca Flat, Nevada Test Site, Nevada: U.S. Geological Survey Water-Resources Investigation Report 83-4067. Map scale 1:48,000.

Winograd, I.J., 1970, Noninstrumental factors affecting measurement of static water levels in deeply buried aquifers and aquitards, Nevada Test Site: Ground water, v. 8, p. 19-28.

Winograd, I.J., and Thordarson, William, 1975, Hydrogeologic and hydrochemical framework, south-central Great Basin, Nevada-California, with special reference to the Nevada Test Site: U.S. Geological Survey Professional Paper 712-C, p. C1-C126.

TEMPERATURE LOGGING AS AN AID TO UNDERSTANDING GROUNDWATER FLOW IN NTS BOREHOLES

John Conaway
Los Alamos National Laboratory

ABSTRACT

A temperature log in a thermally stable borehole through a uniform geologic formation would normally show essentially a straight line, with the temperature increasing slowly with depth at a rate corresponding to the local geothermal gradient. Changes in the slope of this line can result from many factors. In the case where groundwater is entering the borehole at one depth and exiting at another depth (or at the surface) the temperature disturbance resulting from this flow is likely to be a prominent feature of the temperature profile of the borehole.

Temperature logs have been run using special procedures in exploration and satellite holes, where unusual groundwater behavior has been noted, at the NTS. These logs are useful in understanding the groundwater flow in those boreholes.

I. INTRODUCTION

A temperature log in a thermally stable borehole through a uniform geologic formation would normally show essentially a straight line, with the temperature increasing slowly with depth at a rate corresponding to the local geothermal gradient. Changes in the slope of this line can result from many different factors, including the following:

(1) Variations in thermal resistivity of the rock with depth along the borehole (Roy, 1963; Beck, 1976; Conaway and Beck, 1977).

(2) Surface climatic changes (Beck, 1977).

(3) Thermal effects of drilling and engineering procedures in the borehole (Lachenbruch and Brewer, 1959; Smith and Steffensen, 1970 and 1975; Keys and Brown, 1978; Fagley et al, 1982; Murphy, 1982)

(4) Local heat sources, such as radionuclides in the rock or cement setting outside casing, or heat sinks, such as groundwater movement outside the borehole (Bredehoeft and Papadopulos, 1965; Sorey, 1971; Cook, 1979).

(5) Thermal disturbances of the borehole fluid, such as free convection or fluid flow in the borehole (Diment, 1967; Gretener, 1967; Sammel, 1968; Sass et al, 1974; Gupta, 1981; Grant et al, 1983; Beck and Shen, 1985).

(6) Distortion of heat flow by complicated geologic structure (Lee and Henyey, 1974).

At one time or another, temperature logs have been used to study all of the above factors, many of which are also reviewed by Kappelmeyer and Haenel (1974). Clearly, a given factor could be considered to be either signal or noise depending on the goal of the temperature survey, and on any given log several of these effects may be evident. For this reason, temperature logs are not as reliable as many of the geophysical logging techniques. Still, temperature logs can be very useful under favorable conditions, and in some cases can provide unique and valuable information.

In the case where groundwater is entering the borehole at one depth and exiting at another depth (or at the surface) the temperature disturbance resulting from this flow is likely to be a prominent feature of the temperature profile of the borehole. Temperature logs acquired in small diameter NTS boreholes are useful in understanding the groundwater flow observed in those holes.

II. SOME IDEALIZED THERMAL SIGNATURES

Some simplified examples of what an ideal temperature log might look like under various circumstances will help illustrate how the factors listed above can affect the log. In the illustrations presented in this section, the borehole environment is considered ideal and thermally stable in every respect except for the one factor being illustrated in each case. In practice, several of these factors are likely to be present on the same log, and interpretation may be difficult or impossible. The illustrations given here are intended as a starting point in visualizing these effects rather than as a definitive catalog. Since some thermal disturbances, such as those caused by groundwater flow in the borehole, are time-dependent, a given illustration may or may not be representative in a particular case.

In Figure 1, Curve a shows an ideal temperature survey through a uniform formation. There are no disturbances of any kind. The slope of the line depends on the thermal resistivity of the rock, and Curve b shows a log through three different formations having three different thermal resistivities. Curve c shows what the effect of a warming trend on the surface of the ground might be. Curve d shows the effect of the exothermic reaction involved in fresh cement setting behind the casing.

In Figure 2, Curve a shows how a permeable zone can appear on a temperature log in a borehole after a period of circulation of liquid colder than the rock in that region. Curve b shows the effect of liquid entering the borehole in the middle region of the log and flowing downward. Curve c shows the effect of liquid entering the borehole in the middle of the log and flowing upward. Curve d shows the same condition as Curve c, but with the liquid flowing much faster. An actively producing gas zone can also cause similar results.

In Figure 3, Curve a is ambiguous, showing either warmer liquid entering the borehole at the bottom and flowing slowly upward, exiting near the middle of the borehole, or cooler liquid entering the borehole at the top and exiting near the middle. Curve b shows liquid entering the borehole in the upper part of the hole and flowing downward to exit in the bottom part of the hole. Curve c shows what might happen if the tool hangs up on the way down the hole, and then drops free after a short period of time.

III. INSTRUMENTAL CONSIDERATIONS

Accuracy is generally not a prime consideration when it comes to many applications of temperature logs. One notable exception to this is the study of heat flow from the earth. For most purposes an accuracy of a few tenths of a degree is adequate. The accuracy specification for the work at the NTS is +/- 1 C. The calibration is currently performed before each log, using a bucket of water and a mercury thermometer as the standard of comparison. Although accurate enough for engineering purposes, this crude calibration has caused some problems in comparing the detailed character of logs run in the same hole on different dates.

The more important specifications of a temperature logging system for the purposes described in this paper are useful precision and the thermal time constant of the sensor. The useful precision of

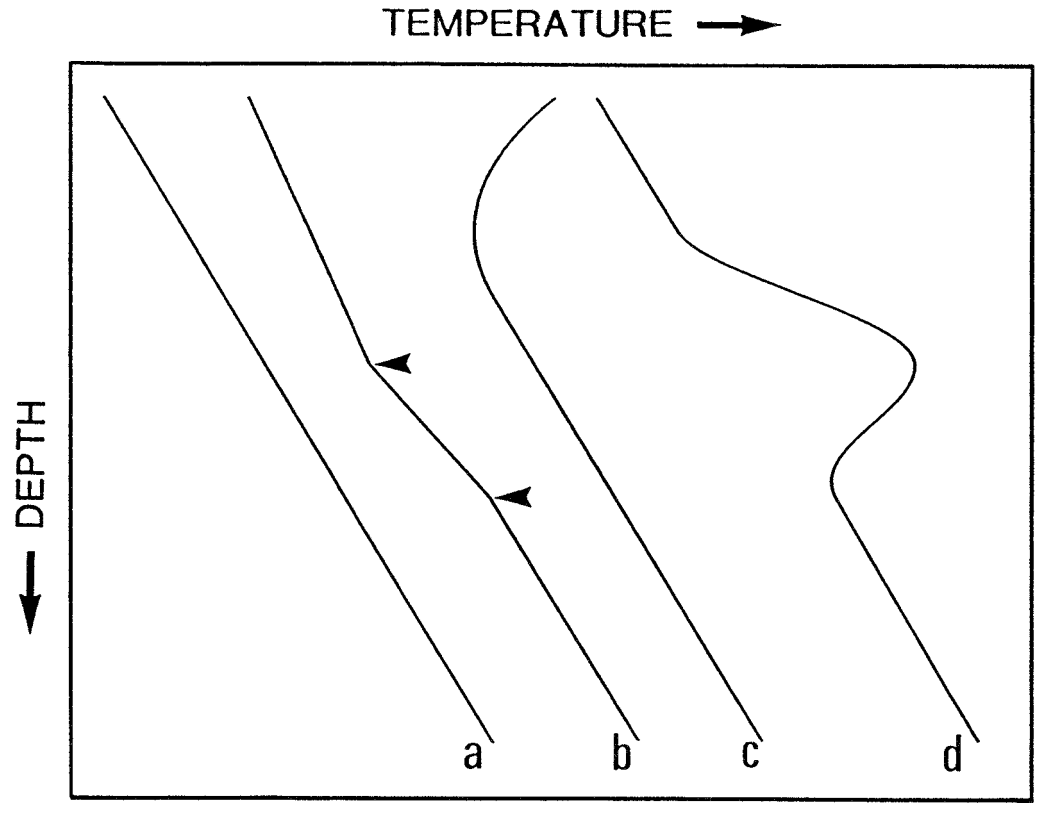

Figure 1 - *Curve a* shows a temperature survey in a thermally stable borehole through a uniform, homogeneous formation. There are no disturbances of any kind. For the ideal, steady-state situation, the slope of the line (thermal gradient) is proportional both to thermal resistivity and to the heat flow parallel to the borehole. *Curve b* shows a log through three different parallel, homogeneous formations having three different thermal resistivities. The bed boundaries are indicated by the two arrows. In the ideal case of constant, uniform heat flow parallel to the borehole and negligible influence of the borehole, the measured temperature gradient is proportional to the thermal conductivity of the rock. *Curve c* shows what the effect of a warming trend on the surface of the ground might be. Depending on the depth and temperature scale this could be seasonal (penetrating a few meters) or a long-term climatic variation (penetrating hundreds or thousands of meters into the ground). *Curve d* shows the effect of the exothermic reaction involved in fresh cement setting behind the casing. Locating the top of the cement has been a routine application of temperature logs in the petroleum industry for decades.

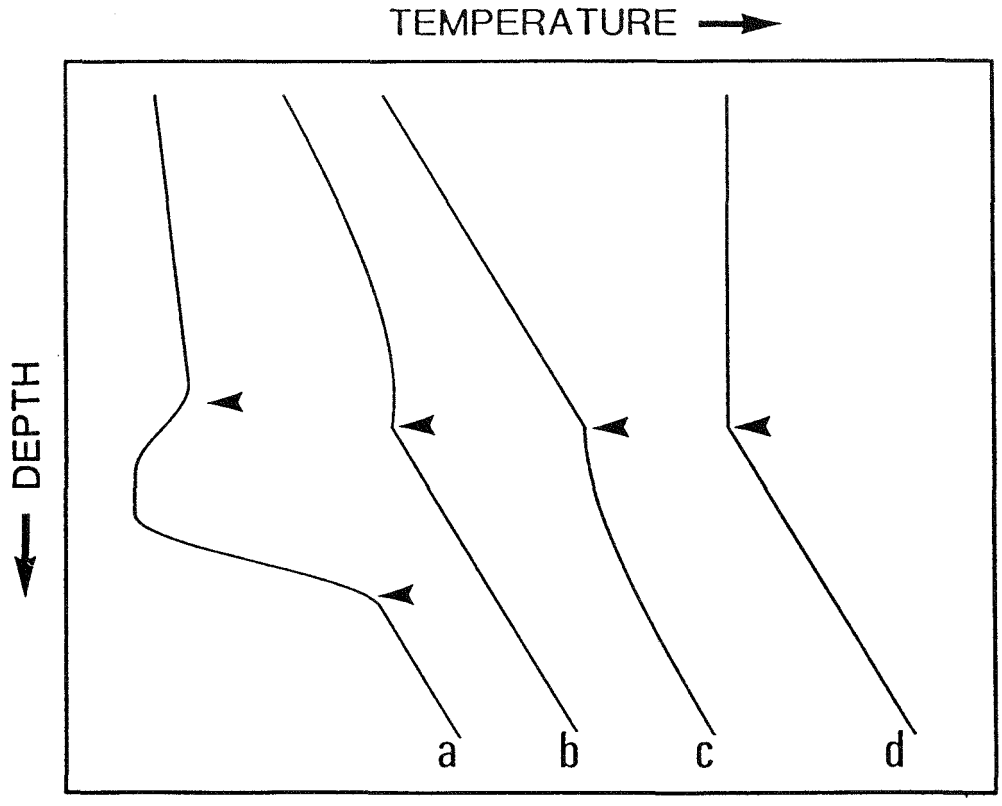

Figure 2 - *Curve a* shows how a permeable zone can appear on a temperature log in a borehole after a period of circulation of liquid colder than the rock in that region. The permeable zone is bracketed by the two arrows. The thermal gradient in the upper portion of the borehole has be changed a great deal by the circulating liquid, and the permeable zone where circulation was lost stands out as an anomalous low-temperature region. If the circulating liquid had been warmer than the rock, the temperature anomaly in the permeable zone would have been positive. *Curve b* shows the effect of liquid entering the borehole at the arrow and flowing downward. The effect of liquid flowing in the borehole can be manifested in the temperature log in many ways depending on flow rate, flow direction, properties of the rock, and number and nature of the zones of entry and exit of the liquid. Several other simple situations are illustrated in Figure 2 c and d and Figure 3 a and b. *Curve c* shows the effect of liquid entering the borehole at the arrow and flowing upward. *Curve d* shows the same condition as Curve b, but with the liquid flowing much faster. An actively producing gas zone can also cause similar results, and also may cause localized cooling.

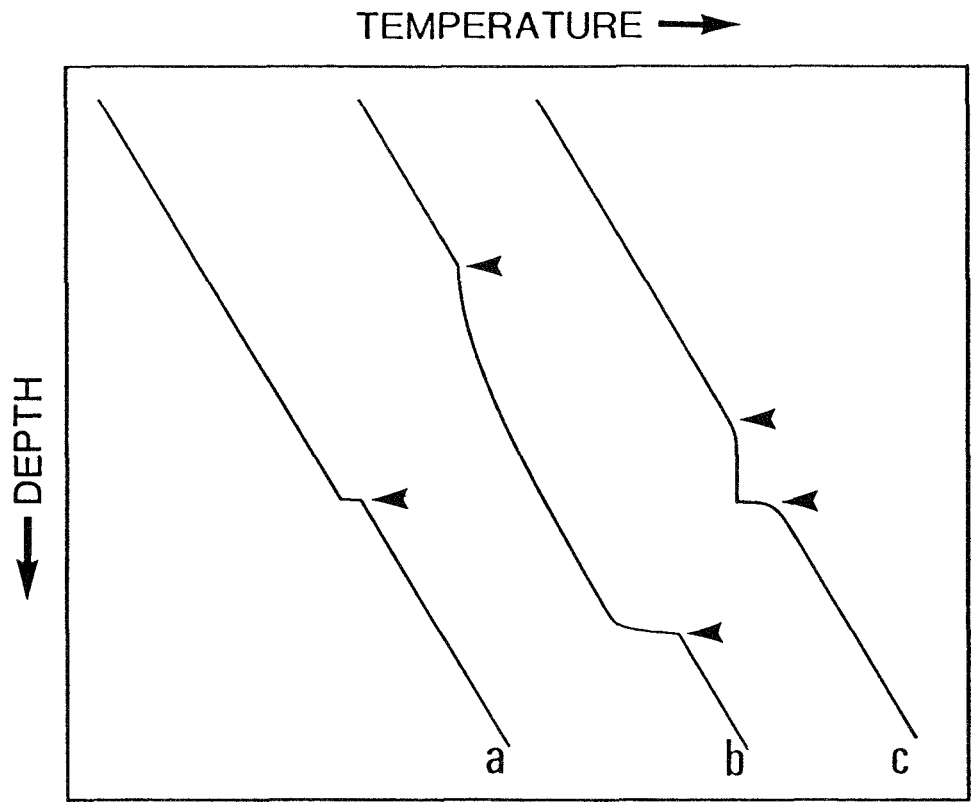

Figure 3 - *Curve a* shows either liquid entering the borehole at the bottom and flowing slowly upward, exiting at the arrow, *or* liquid entering at the top and flowing slowly downward, exiting at the arrow. *Curve b* shows liquid entering the borehole at the upper arrow and flowing downward to exit at the lower arrow. *Curve c* shows what might happen if the tool hangs up on the way down the hole, and then drops free after a short period of time. The tool hangs up at the upper arrow, but the shaft encoder continues to indicate increasing depth for some time as cable is fed into the hole, even though the tool has stopped. Of course, if the tool does not drop free the situation will soon become obvious on the surface. In this example, the tool drops free at the moment (*apparent* depth) indicated by the lower arrow. Convection cells in the borehole fluid also appear as an isothermal region in the borehole, but these are generally only a few borehole diameters in depth extent.

a given system is determined by the actual output precision (the number of decimal degrees available in the recorded temperature reading) and by the thermal-equivalent electrical noise level of the logging system in decimal degrees. A useful precision of 0.001 C is a good target for precise work, and an even higher precision may be useful in some cases. This figure sometimes generates controversy in the logging community, but the only real criterion for what is useful precision should be the magnitude of the thermal signal compared with the thermal noise level in the borehole. Assuming that the sample interval in the borehole is 0.1 m, and the geothermal gradient through a given formation is 10 C/Km, the average temperature increment between readings is 0.001 C. Since thermal noise levels at least as low as 0.0001 C have been documented in a borehole under good conditions (Bristow and Conaway, 1984), it is clear that a precision of 0.001 C or better may indeed be useful in some cases. For an example, see Conaway and Beck (1977).

The time constant of the thermal sensor is important because it degrades (smooths) the signal *before* electrical noise is added. Thus, the signal strength is reduced by the sensor time constant while the noise is not affected (except for thermal noise in the borehole). From this it is apparent that sensor having a short time constant will give the best log, all else being equal. Time constants on the order of 1 s are achievable and this is a good target. Occasionally, the thermal sensor will pick up a glob of grease or mud on the way down the borehole and its thermal response time will be greatly increased; this can sometimes be recognized by the unusually sluggish behavior of the resulting log.

Under some conditions, accurate "stabilized" temperature data can also be extracted from the *continuous* or *dynamic* temperature log (that is, a log made with the tool constantly moving) at any desired depth by application of a simple inverse filter to remove the effect of the sensor time constant. A suitable filter for an exponential response has been given by Conaway (1980). Given proper survey techniques (Appendix A), temperature readings obtained from the moving tool are less susceptible to errors resulting from the thermal mass of the tool than are stationary readings. In dynamic logging the tool is constantly entering undisturbed fluid, whereas in static logging the fluid temperature in the vicinity of the stationary sensor can be significantly altered by the thermal mass of the tool. Once again, a high precision tool system with a short thermal time constant will give the best results.

IV. QUANTITATIVE INTERPRETATION

Historically, as new logging techniques are developed they tend to be qualitative in nature. Only after a great deal of effort has been expended on development of interpretation theory do reliable quantitative results begin to emerge. In the case of temperature logs, the process of making them quantitatively useful has met with mixed success depending on the application, and in general a qualitative interpretation is the most that can be expected.

In the case of fluid flows in the borehole, attempts to derive flow rates from the temperature log tend to be based on assumptions the validity of which is unknown in most cases. For this reason, no effort is being expended at present to derive flow rates from the temperature logs recorded at the NTS. Some discussion of the problem of extracting quantitative information regarding flow rates and similar phenomena from temperature logs may be found in Boldizsar (1958), Ramey (1962), Murphy (1982), and Beck and Shen (1985), among others.

V. A CASE STUDY: U4t Sat. #1 and Ue4t

U4t Satellite Hole #1 is located about 10 m from U4t emplacement hole in southeastern Area 4. TD was reached at 639.5 m on May 1, 1986. On June 4, TD was tagged at 619 m and the water level in the hole was tagged at 321.3 m, well above the supposed water table in that region. The hole was blown dry and the water level was tagged on a number of occasions, documenting a steady rise in the water in the borehole over a period of weeks.

The presence of unusual amounts of water in the borehole was a source of some concern, and consequently part of the logging effort in this hole was directed toward understanding where the

water was entering the hole and where it was leaving the hole. As part of this effort, temperature logs were run by Dresser Atlas using the old Birdwell temperature tool on June 6, June 18, and July 2. These are shown in Figure 4, Curves a, b, and c, respectively; Curves d and e are from borehole Ue4t and will be discussed later. The drop in temperature seen on all three runs at about 320 m indicates the water level in the borehole. An additional temperature log was run on July 9, but the noise level of that tool is too large to permit detailed analysis of the log.

The temperature logs in U4t Sat #1 were run while lowering the tool into the borehole to minimize the extent to which the borehole thermal environment was disturbed by the tool. Logging speed was a slow 3 m/min. The logs were intended to be run without stopping, but run 1 was erroneously interrupted for stationary temperature measurements and some 35 m of data are missing, and run 2 was interrupted due to technical difficulties. As an additional problem, the temperature calibrations for the three runs, performed on-site with a mercury thermometer as described earlier, are different and not precisely known.

The drilling operation at U4t Sat #1 ended on May 1. Drilling disturbs the temperature regime of the borehole, and that disturbance takes some time to die away. Consequently, the longer one waits to log the hole after drilling, the better the log is likely to be. On June 6, bottom was tagged to determine TD, and the Dresser induction log was run; both of these procedures took place *before* the temperature log was run. Thus, run 1 is quite noisy due to disturbance of the water in the borehole.

Runs 2 and 3 are better logs than run 1, and some conclusions can be drawn based on those runs. The interpretation presented here is somewhat speculative, however, and other interpretations are no doubt possible. Looking at run 2 first (Figure 4b), groundwater seems to be entering the borehole at or near the bottom. The lower 50 m of the borehole is roughly isothermal, with irregular temperature changes with depth due perhaps to mixing of inflowing water with water already in the borehole. The water appears to be flowing up the borehole and leaving the borehole at a number of levels, indicated by offsets in the temperature profile. These are presumably relatively permeable zones, including but not restricted to faults and fractures.

Run 3 shows many of the same temperature offsets as run 2 at the same depths, tending to confirm that these features are related to fixed depths in the borehole (i.e. probably geological features) rather than noise features such as equipment problems or convection cells. Some of these offsets have been marked by arrows in this figure.

Some of the offsets seen in runs 2 and 3 have less obvious counterparts in run 1, once again indicating that these are not noise or transient disturbances. The bottom 50 m of run 1 is partially obscured due to missing data, but some sign of the possible water inflow with mixing can be seen in the bottom 20 m.

Exploration borehole Ue4t was drilled after U4t Sat #1 to help understand the groundwater behavior in the area. Ue4t is located roughly 200 m south of U4t Sat #1. Two temperature logs were run in the hole by Dresser Atlas, on February 19 and March 13, 1987. Both logs appear to be good logs (Figure 4 Curves d and e). Similar offsets to those seen in the logs from U4t Sat #1 are seen in those from Ue4t, and the explanation for these is undoubtedly the same in both cases.

Figure 5 shows the portion of runs 2 and 3 in U4t Sat #1 between 400 and 550 m (Curves a and b, respectively), and the same portion of runs 1 and 2 in Ue4t (Curves 3 and 4). This expanded view helps pick out the details, but can still be improved upon for spotting the offsets resulting from waterflows. Figure 6, Curves a and b, show the thermal gradient profiles from U4t Sat #1 and Ue4t corresponding to the temperature logs shown in Figure 5. These gradient profiles have been generated by numerical differentiation of the corresponding temperature logs, and have been smoothed with a cosine bell filter extending over about 1 m of depth. Peaks on the temperature gradient profile indicate zones where the temperature increases rapidly with depth over a short depth interval. Many of the prominent peaks seem to indicate exit zones for the groundwater flowing up the hole.

Figure 6 also shows a decrease with time in the water-flow temperature signatures. In other words, the large peaks seen in curves a and c are much reduced in curves b and d. The volumetric flow rate may be dwindling with time, perhaps due to plugging of the permeable exit zones by silt.

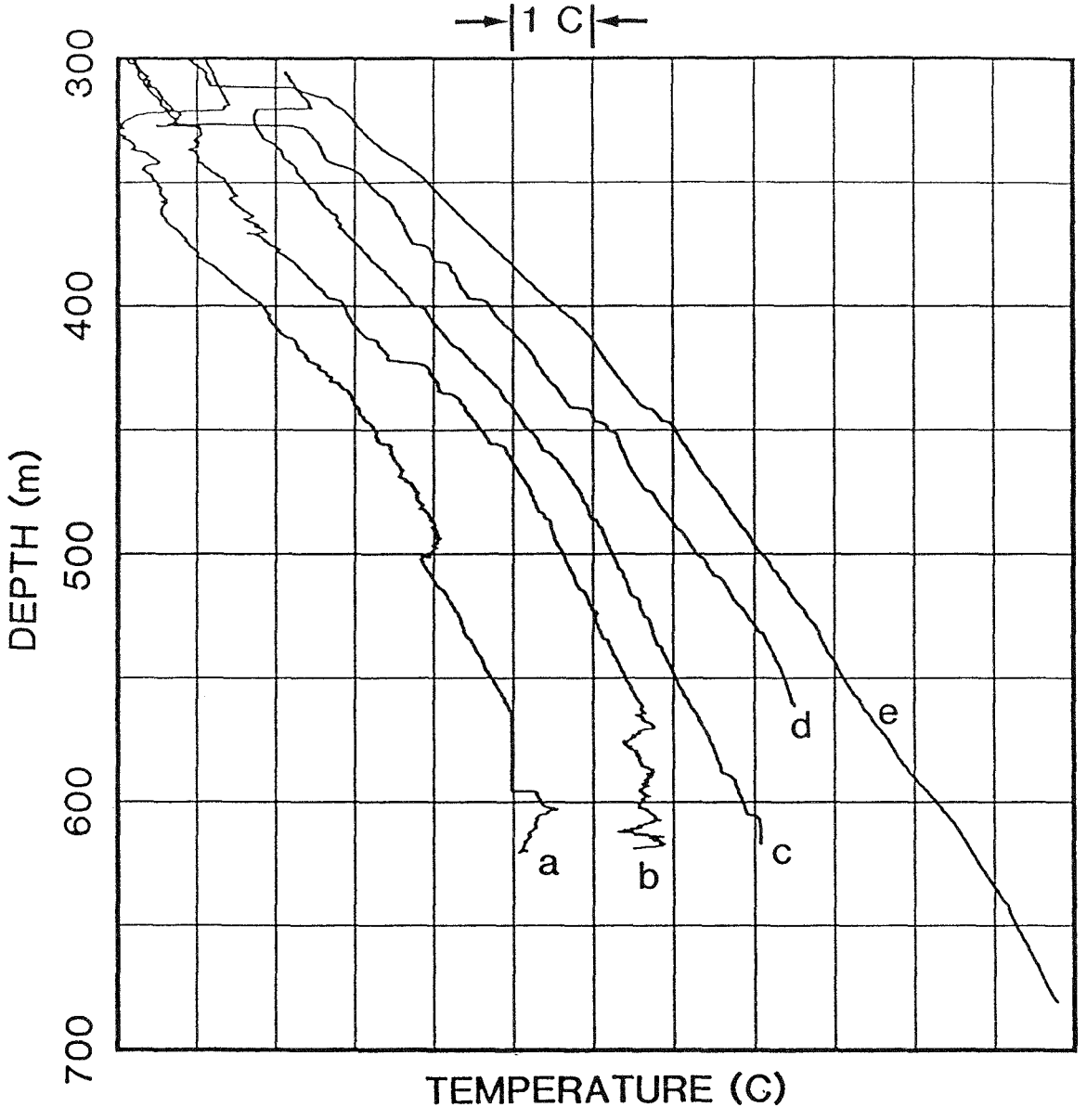

Figure 4 - Temperature logs from U4t Sat #1 and Ue4t. *Curves a, b, and c*, show runs 1, 2, 3, respectively, in borehole U4t Sat #1. *Curves d and e* show runs 1 and 2, respectively, in borehole Ue4t. The curves have been temperature shifted by an arbitrary amount for clarity; 1 division equals 1 C. The portion of run 1 (Curve a) between 565 and 595 m is missing due to an error in the logging procedure.

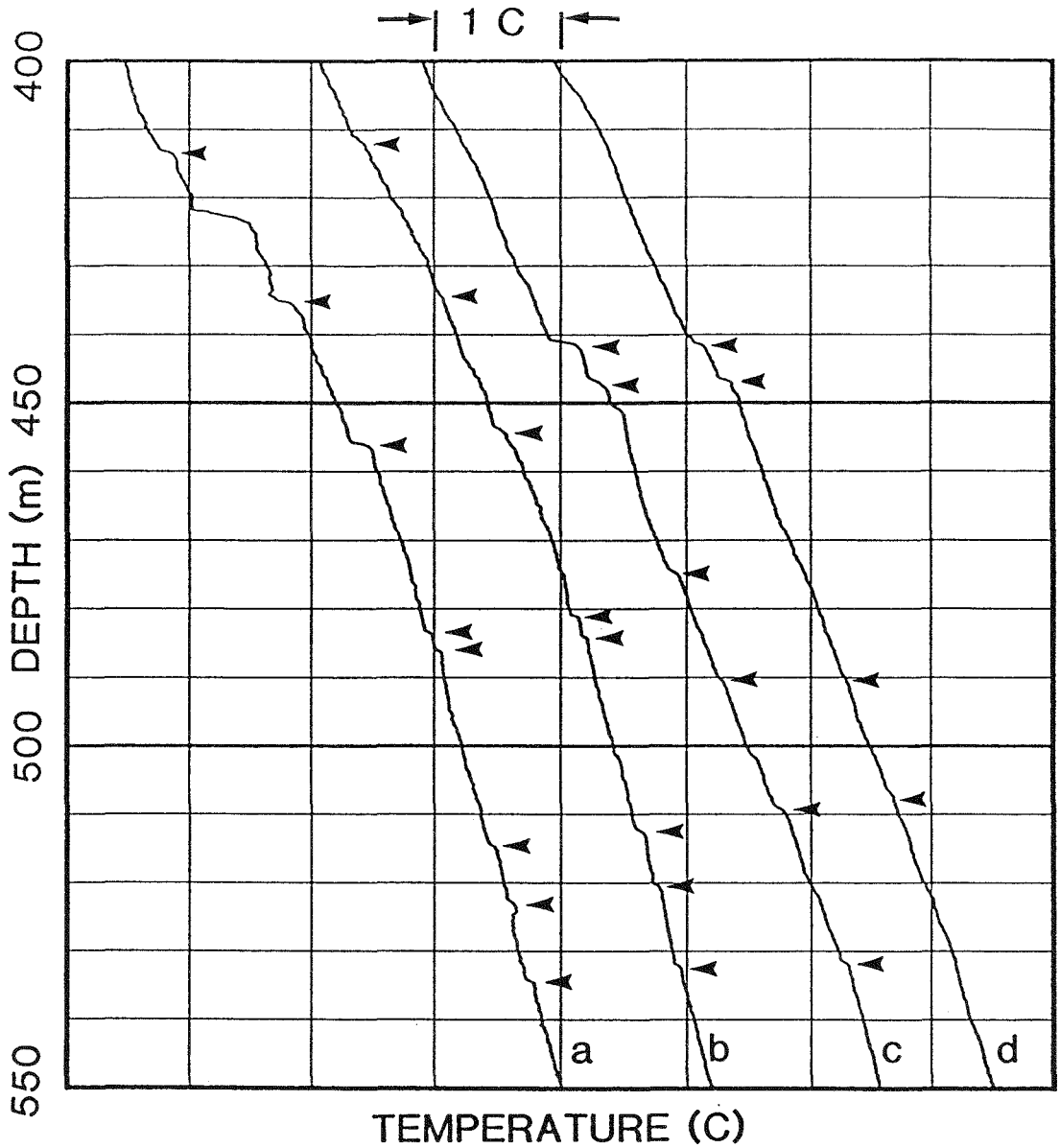

Figure 5 - Temperature logs from U4t Sat #1 and Ue4t on an expanded depth scale. *Curves a and b* show runs 2 and 3, respectively, from U4t Sat #1. *Curves c and d* show runs 1 and 2, respectively, from Ue4t. The curves have been temperature shifted by an arbitrary amount for clarity. On the abscissa, 1 division equals 1 C.

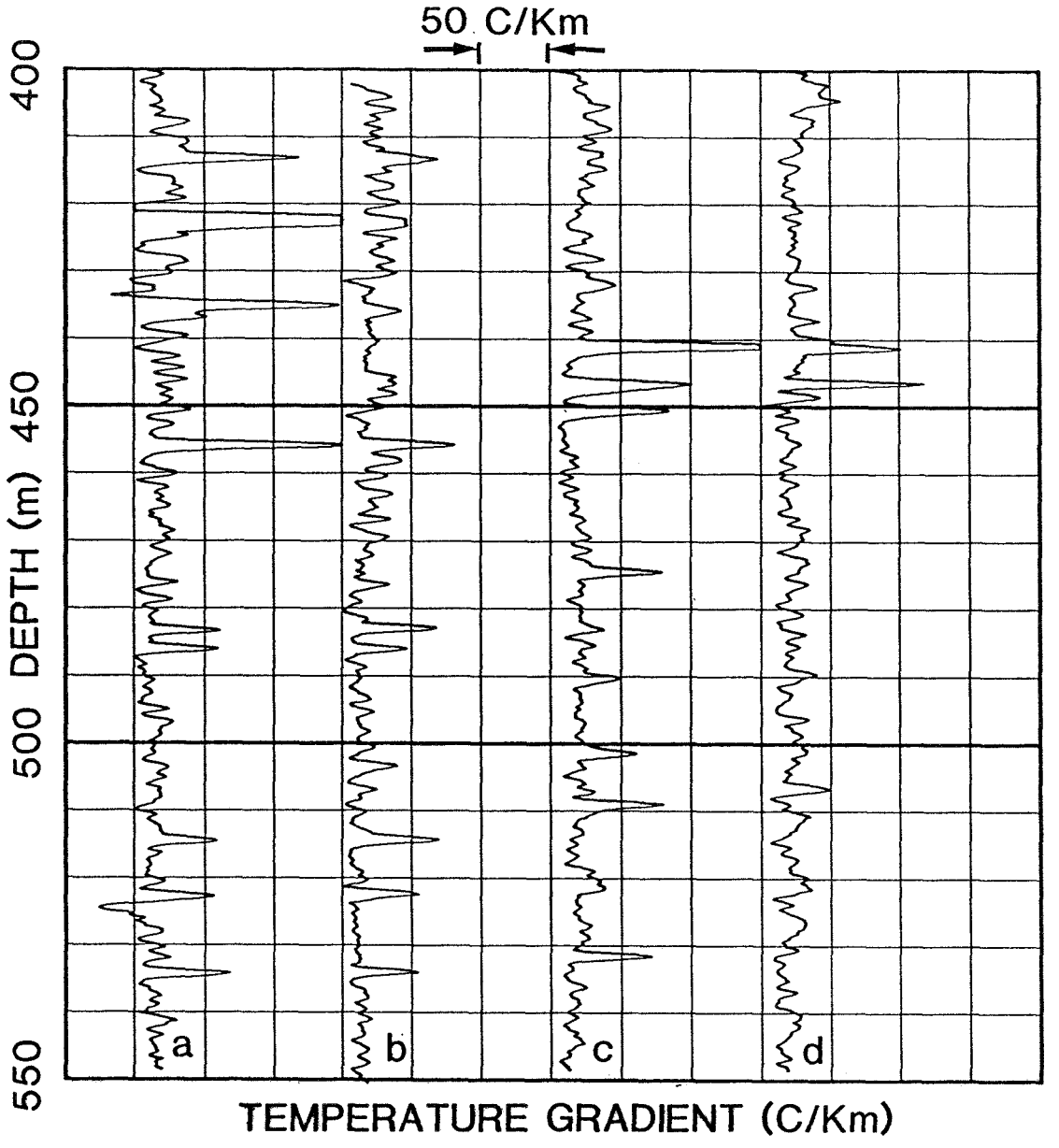

Figure 6 - Temperature gradient profiles from U4t Sat #1 and Ue4t, obtained by numerical differentiation and smoothing of the temperature logs. *Curves a and b* show runs 2 and 3, respectively, from U4t Sat #1. *Curves c and d* show runs 1 and 2, respectively, from Ue4t. For clarity, Curves a, b, c and d have been shifted by 50, 200 and 350 and 500 C/Km, respectively, along the temperature gradient axis; 1 division equals 50 C/Km. The higher peaks have been truncated at 150 C/Km on all four curves to avoid interference on this plot.

The suspected zones of exit of water from the borehole seen on the temperature logs and temperature gradient profiles generally correspond with electrical resistivity lows. This seems reasonable. Penetration of liquid into a dry or partially saturated formation would be expected to lower the electrical resistivity of the medium. Furthermore, the exit zones often correlate with hole enlargements as indicated by the caliper log. This also is expected, since zones of enhanced permeability often are associated with faults, fractures, friable zones and poorly consolidated materials, all of which are less competent than normal undisturbed rock and are therefore susceptible to hole enlargement.

VI. DISCUSSION AND CONCLUSIONS

Temperature logs are influenced by many factors, including thermal resistivity of the rock, geologic structure, free convection of the borehole fluid, groundwater flows, and heat sources and sinks. Because of their sensitivity to many factors, temperature logs are not always useful in a given application. In studying groundwater flows in boreholes at the NTS, however, temperature logs can indicate zones of entrance and exit of the water.

The temperature logs run in Ue4t and U4t Sat #1 were run to test whether the logs would be useful in studying groundwater flow. From the results presented in this paper that is clearly the case. Optimum procedure was not followed in running these logs, and the interpretations given here are necessarily limited in scope. For more definitive results in studying a given hole, a program should be set up before the hole is completed. The program would include temperature logs run using proper procedure (Appendix A) at regular intervals after the hole is completed. Frequent water level tags after the hole is completed can also be useful. For more intensive study, the temperature logs can be used to help plan packer and tracer surveys.

VII. ACKNOWLEDGEMENTS

This work is supported by the United States Department of Energy.

VIII. REFERENCES

Beck, A. E., "The use of thermal resistivity logs in stratigraphic correlation," *Geophysics,* 41, 300 - 309 (1976).

Beck, A. E., "Climatically perturbed temperature gradients and their effect on regional and continental heat-flow means," *Tectonophysics,* 41, 17 - 39 (1977).

Beck, A. E., and Shen, P. Y., "Temperature distribution in flowing liquid wells," *Geophysics,* 50, 1113-1118 (1985).

Boldizsar, T., "The distribution of temperature in flowing wells," *Am. J. Sci.,* 256, 294-298 (1958).

Bredehoeft, J. D., and Papadopulos, I. S., "Rates of vertical groundwater movement estimated from the Earth's thermal profile," *Water Resources Res.,* 1, 325-328 (1965).

Bristow, Q., and Conaway, J. G., "Temperature gradient measurements in boreholes using low noise high resolution digital techniques," in *Current Research*, Part B, Geological Survey of Canada Paper 84-1b, 101 - 108 (1984).

Conaway, J. G., "Exact inverse filters for the deconvolution of gamma-ray logs," *Geoexploration,* 18, 1 - 14 (1980).

Conaway, J. G., and Beck, A. E., "Fine-scale correlation between temperature gradient logs and lithology," *Geophysics,* 42, 1401 - 1410 (1977).

Cook, C. E., "Radial differential temperature (RDT) logging - a new tool for detecting and treating flow behind casing," *J. Pet. Tech.*, 31, 676-682 (1979).

Costain, J. K., "Probe response and continuous temperature measurements," *J. Geophys. Res.*, 75, 3969 - 3975 (1970).

Diment, W. H., "Thermal regime of a large diameter borehole: Instability of the water column and comparison of air- and water-filled conditions," *Geophysics,* 32, 720 - 726 (1967).

Fagley, J., Fogler, H. S., Davenport, C. B., and Millhone, R. S., "An improved simulation for interpreting temperature logs in water injection wells," *Soc. Pet. Eng. J.*, , 709-718 (1982).

Grant, M. A., Bixley, P. F., and Donaldson, I. G., "Internal flows in geothermal wells: their identification and effect on the wellbore temperature and pressure profiles," *Soc. Pet. Eng. J.*, , 168-176 (1983).

Gretener, P. E., "On the thermal instability of large diameter wells - An observational report," *Geophysics,* 32, 727 - 738 (1967).

Gupta, B. S., "Case Histories of temperature surveys in Kuwait," *J. Pet. Tech*, 33, 2505-2514 (1981).

Ibrahim, M. W., "Discussion of 'Case histories of temperature surveys in Kuwait' by B. S. Gupta, with a reply by the author," *J. Pet. Tech*, 34, 2403-2405 (1982).

Kappelmeyer, O., and Haenel, R., "Geothermics, with Special Reference to Application," Geopublication Associates, Gebruder Borntraeger, Stuttgart (1974).

Keys, W. S., and Brown, R. F., "The use of temperature logs to trace the movement of injected water," *Ground Water,* 16, 32-48 (1978).

Lachenbruch, A. H., and Brewer, M. C., "Dissipation of temperature effect in drilling a well in Arctic Alaska," U. S. G. S. Bull. 1083-C, 73 - 109 (1959).

Lee, Tien-Chang, and Henyey, T. L., "Heat-flow refraction across dissimilar media," *Geophys. J. R. Astr. Soc.,* 39, 319-333 (1974).

Murphy, H. D., "Enhanced interpretation of temperature surveys taken during injection or production," *J. Pet. Tech.,* 34, 1313-1326 (1982).

Ramey, H. J., "Wellbore heat transmissions," *J. Pet. Tech.*, 14, 427-435, 1962.

Roy, F. R., "Heat flow measurements in the United States," Ph.D. Thesis, Harvard University (1963).

Sammel, E. A., "Convective flow and its effect on temperature logging in small-diameter wells," *Geophysics,* 33, 1004 - 1012 (1968).

Sass, J. H., Munroe, R. J., and Moses, T. H., "Heat flow from eastern Panama and northwester Colombia," *Earth and Planet. Sci. Let.,* 21, 134-142 (1974).

Smith, R. C., and Steffensen, R. J., "Computer study of factors affecting temperature profiles in water injection wells," *J. Pet. Tech.*, 22, 1447-1458, 1970.

Smith, R. C., and Steffensen, R. J., "Interpretation of temperature profiles in water-injection wells," *J. Pet. Tech.*, 27, 777-784, 1975.

Sorey, M. L., "Measurement of vertical groundwater velocity from temperature profiles in wells," *Water Resources Res.*, 7, 963-970 (1971).

APPENDIX A

OPTIMUM LOGGING TECHNIQUES FOR HIGH-RESOLUTION TEMPERATURE LOGS

The equilibrium thermal regime in a borehole is delicate and easily disrupted. Temperature logs must be run properly to minimize the effect of the logging process on the in situ temperatures. A few observations about temperature logs and some guidelines to follow in running the logs are given in this appendix.

1. In general, smaller diameter boreholes will give better temperature logs than larger diameter boreholes. Smaller boreholes are less prone to free convection, and the disturbing effects of the drilling process on the borehole temperature regime do not last as long. Also, for a given temperature regime, the more viscous the fluid, the larger the borehole must be before free convection sets in.

2. If true formation temperatures are desired, the temperature log should generally be run as late as possible after drilling to minimize errors due to the circulation of drilling fluid. Obviously, if the fluid is pumped out and replaced or circulated after the drilling is finished the hole will require some time to reach equilibrium temperature.

3. The temperature log should be the first log run on a given day.

4. The log should be run down the hole rather than up so that the thermal sensor is entering undisturbed fluid.

5. The log should be run in a single continuous pass. The tool should not be stopped in the borehole until the entire downward run is completed.

6. Running the log slowly helps improve precision, especially if the sensor time constant is relatively long.

7. Accurate "equilibrium" temperature data can be extracted from the dynamic temperature log in some cases by application of a simple inverse filter to remove the effect of the sensor time constant. Temperature readings obtained in this manner are less susceptible to errors resulting from the thermal mass of the tool than are stationary readings.

8. For best results, more than one log should be run, especially if the logs are run shortly after drilling is completed (within a few days, weeks, or months depending on the drilling method). This allows the analyst to discriminate more effectively between noise and desired information. The hole should be allowed to stabilize at least overnight after a log before running additional temperature logs.

9. If high-resolution temperature gradients are to be computed from a temperature log, the thermal sensor must have very high precision and low noise. A precision of .001 C with a noise level at or below that figure makes a good target when specifying temperature logging equipment.

GEOLOGIC AND HYDROLOGIC INVESTIGATIONS AT THE ALEMAN (U3KZ) SITE, AND OTHER SITES IN YUCCA FLAT, THE NEVADA TEST SITE

Ward L. Hawkins
Los Alamos National Laboratory

Anne P. Cavazos
Peter H. Thompson
Fenix and Scisson, Inc.

ABSTRACT

Over the years many interesting geohydrologic observations have been made in Yucca Flat. Anomalously high water levels have been measured in some drill holes and radioactivity was discovered associated with fractures in a few of these holes. Water removed from U3kz, an emplacement hole (ALEMAN) which had developed a leak in the liner, was found to contain large amounts of tritium and some fission products. The source, at least for the fission products, is believed to be an event 337 m to the north of U3kz conducted nine years earlier. Ue3e, a nearby exploratory hole (65 m north of U3kz) drilled to investigate these findings, made similar discoveries. A packer test in Ue3e revealed unexpectedly high hydraulic pressures at depth. Hole U3cn #5 was drilled a little more than two years after the detonation of BILBY (U3cn) in September, 1963, approximately 122 m southwest of the event. Fractures in core from this hole were found to contain radionuclides (Garber and Johnston, 1967). Similarly a cored exploratory hole (Ue4g #2) drilled in late 1977 for the ICEBERG event, encountered radionuclides in fractures. These fission products are believed to have traveled some 320 m from the source event (LATIR) executed in February 1974.

Three sites (including ALEMAN) near the center of the valley, just west of the Yucca Fault, have revealed unanticipated hydrologic conditions. All are in a similar geologic setting. These sites were drilled with large diameter (> 1.5 m) emplacement holes and have smaller diameter nearby exploratory or satellite holes. The emplacement holes were lined from below the working point to above the predicted top of the static water level (SWL). Two of the three emplacement holes developed leaks in their liner. Five other sites in the same general area had water flowing into the hole over the top of the liner and another site had a liner which leaked. These conditions may have been the result of hydraulic pressures greater than anticipated. Hydrologic data from three of these recent sites is reviewed.

I. BACKGROUND

Forty days after the AARDVARK (U3ams) event in May, 1962, the SWL in test well 7, located 305 m to the west, was found to be about 17 m higher than the previous measurement made in the summer of 1961 (Garber, 1963). The previous level had not fluctuated more than 0.6 m in over three years. From the rate of decline records, a projection of two years was made for the fluid level to drop to the pre-test level. After the BILBY event (1963) in hole U3cn, measurements of fluid level changes were made in four nearby holes (Hale, et al, 1963). This data also indicated immediate increase of water table altitude and subsequent slow decline in the tuff aquifer. There was a suggestion that the response differed for the Paleozoic carbonate rocks. It is yet to be determined if the elevated fluid levels found are the result of actual elevation increases of the water table or slowly dissipating pore pressure increases.

In the last ten years there have been nine emplacement sites within or near the geologically well known Tuff Pile 1 near the center of Yucca Flat which have required remedial actions to make them acceptable for event execution (Fig. 1). At five of the sites (U7au, U7av, U7ba, U4j and U4l) the

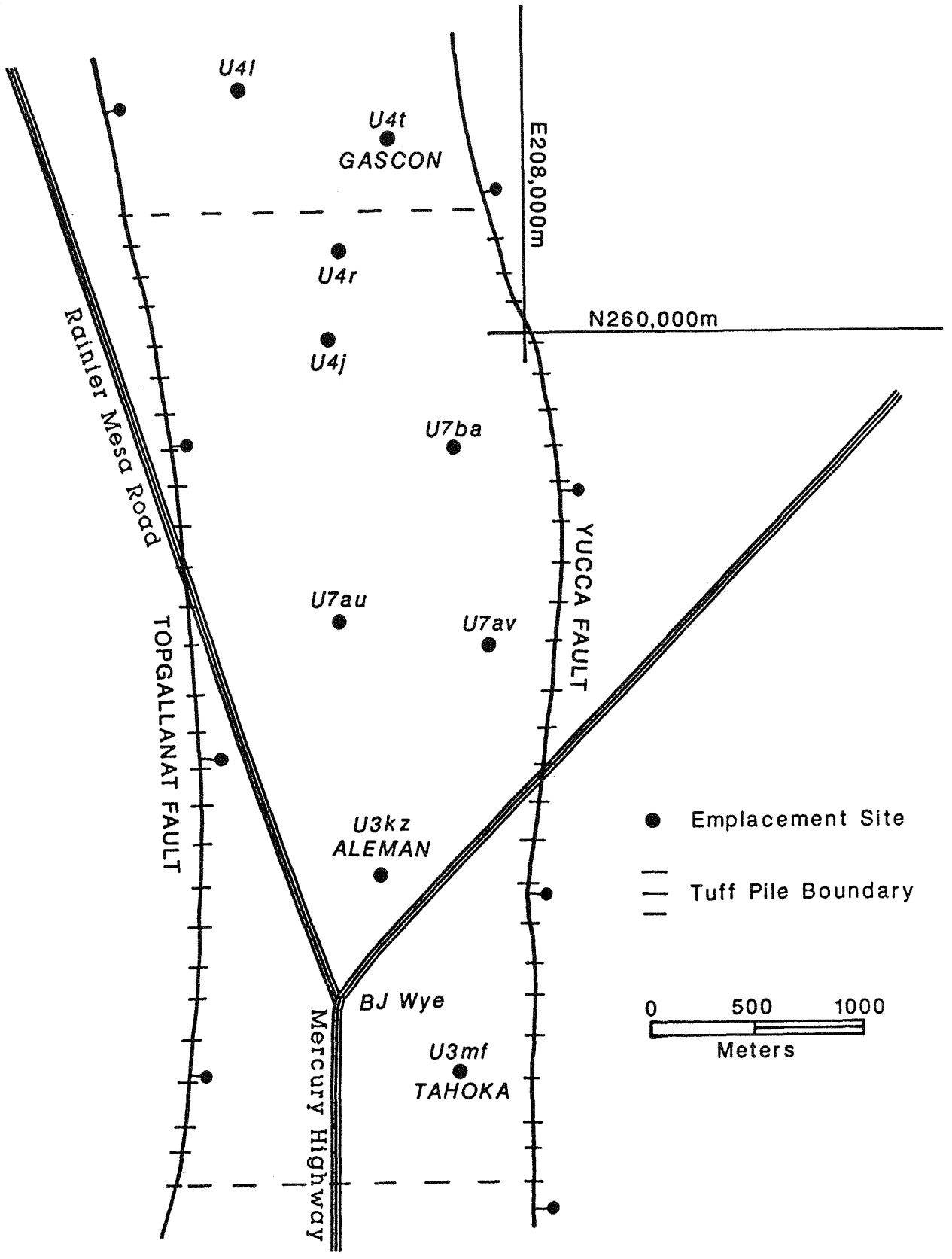

Fig. 1. Emplacement sites included in study.

large diameter (>1.5 m) emplacement holes had water entering the hole over the top of the liner. (Liners are installed in emplacement holes above what is believed to be the top of the SWL to below the working point to provide a dry environment for the experiment.) The only remedial action necessary on four of the five holes was a fines layer as a moisture barrier at the top of the liner. However, the first of these holes (U7au) had 27 m of liner added to the top of the existing liner and subsequent designs have included additional liner. Three sites (U4r, U3kz and U4t) had liners in the emplacement hole which leaked. All the leaks were within 20 m of the bottom of the liner. After failed repair attempts at U3kz and U4r, the holes were used at much less than their intended depth. At U4t the hole was successfully repaired. A packer test in exploratory hole Ue3e, 60 m north of U3kz, indicated much higher hydraulic pressures than the liner was designed to accommodate. A satellite hole (U4t sat #1) and a exploratory hole (Ue4t; drilled to study radionuclide migration) near U4t (GASCON) also indicated hydraulic pressures in excess of the design limits of the liner. The liner design for the TAHOKA (U3mf) emplacement hole was based on hydraulic measurements made in a nearby exploratory hole (Ue3mf). This report reviews the hydrologic data collected at the ALEMAN, TAHOKA and GASCON sites.

II. ALEMAN SITE

At the ALEMAN site (Fig. 2a; Fig. 2b), the 2.44 m diameter emplacement hole, U3kz, was lined with a 1.88 m inner diameter liner from a depth of 449 m to 670 m. Forty seven days after the lined hole was dewatered, the fluid level was found to have risen 50 m. The hole was dewatered again. Video inspection of the hole revealed a leak in a weld less than a meter from the bottom of the liner. Further examination of the hole revealed no water entering the hole from above the liner implying that the sole source of the fluid was the leak in the liner. The fluid level was monitored for the next thirteen months (Fig. 3). After about 6 months the water had risen at a fairly consistent 1.5 m per day to a depth of approximately 435 m or 14 m above the top of the liner and 64 m higher than the predicted water table (Doty and Thordardson, 1983). An attempt was made to seal the liner by cementing a large mandrel into the lower portion. This mandrel was primarily a 15 m length of 1.71 m outer diameter prefilled casing. The attempted repair had no apparent effect on the inflow of fluid.

The fluid level was again allowed to rise. Within four months the fluid level stabilized at a depth of 436 m, 13 m above the top of the liner and approximately 64 m higher than the predicted SWL (Fig. 3). During dewatering and remedial activities at U3kz, water samples were taken from the sump and the borehole. It was in these samples that high levels of tritium (5×10^4 pCi/ml) and, upon further investigations in the spring of 1986, the fission products were discovered. The source for the fission products is believed to be the SANDREEF event in U7aq, 337 m to the north of U3kz (Fig. 1). The ALEMAN RNM panel was formed by DOE Nevada Operations Office to consider these discoveries.

An exploratory hole (Ue3e) located approximately 65 m to the north of U3kz and on a line with U7aq, was drilled to determine if the zone of contamination could be effectively investigated following the execution of the ALEMAN event in U3kz. In an attempt to learn something about the hydrologic conditions, Ue3e was drilled in three phases with a waiting period between each phase to monitor the fluid level. The 0.25 m diameter hole was drilled to a depth of 520 m for phase one; 642 m for phase two, and 735 m for phase three. The ALEMAN RNM panel (referring to the ICEBERG/LATIR experience) recommended obtaining data through the depth interval where the Grouse Canyon stratigraphic unit might be found. (Later information indicates there is an insignificant thickness of Tbg at this site.) Although the hole was drilled through this depth (~700 m) during Phase 3, loss of hole depth due to sloughing excluded some of the geophysical logging in this interval. To ensure adequate data acquisition, the hole was cleaned out and deepened to 765.0 m. After the drilling of phases one and three, and the final deepening, the depth-to-fluid in the open hole stabilized within a few meters of 470 m (Fig. 4). The shallower, apparently stabilized depth-to-fluid following phase two is unexplained, however, a corresponding loss of total depth also occurred.

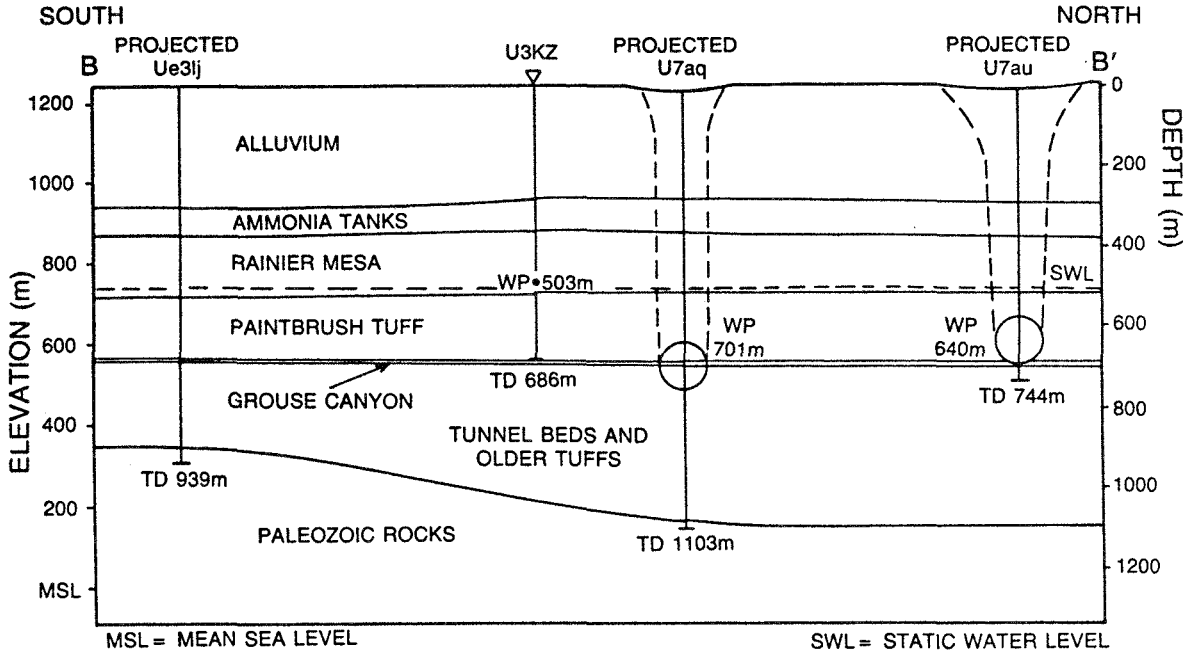

Fig. 2a. ALEMAN south to north cross section.

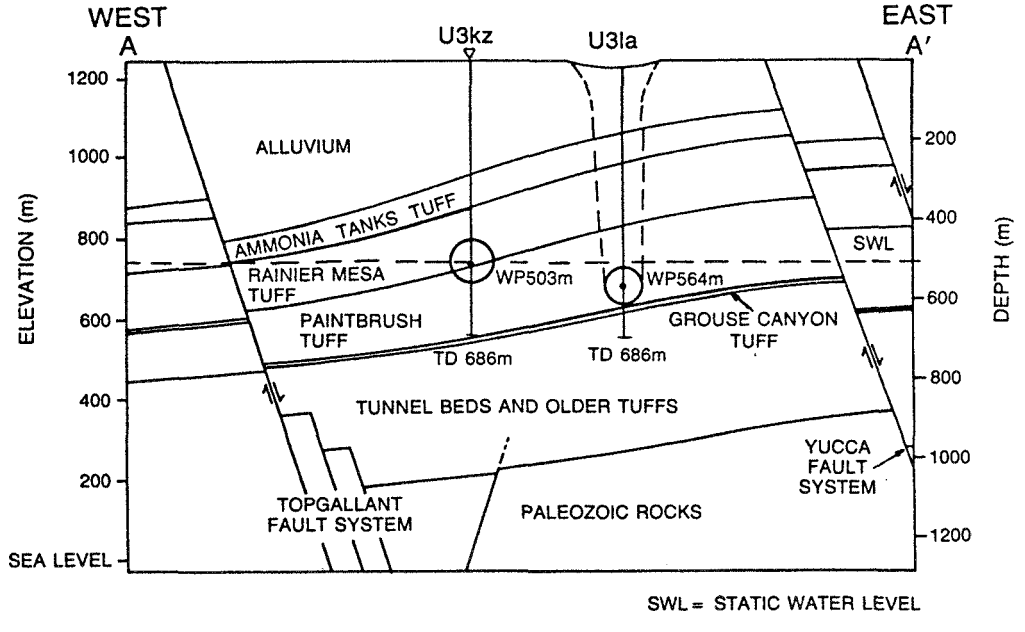

Fig. 2b. ALEMAN west to east cross section.

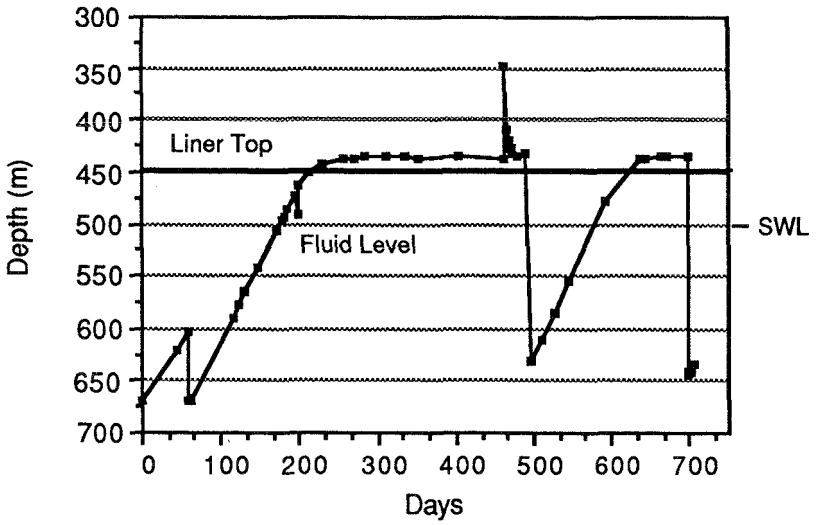

Fig. 3. U3kz liner fluid levels

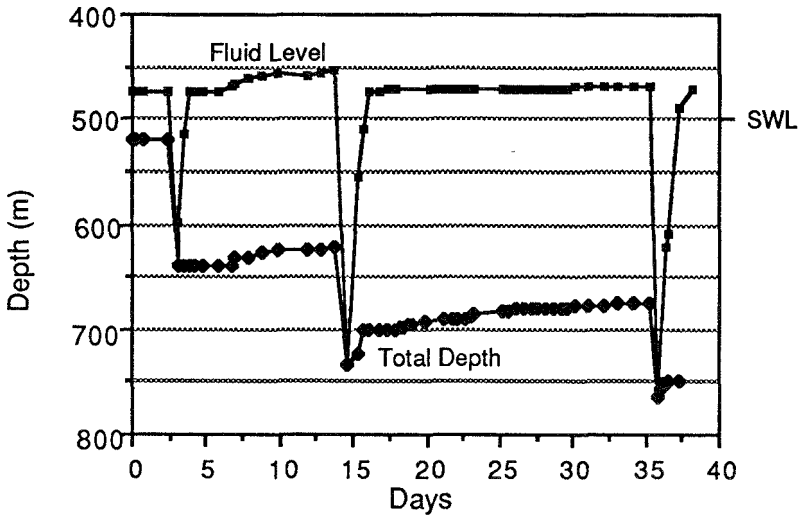

Fig. 4. Fluid levels during drilling of Ue3e

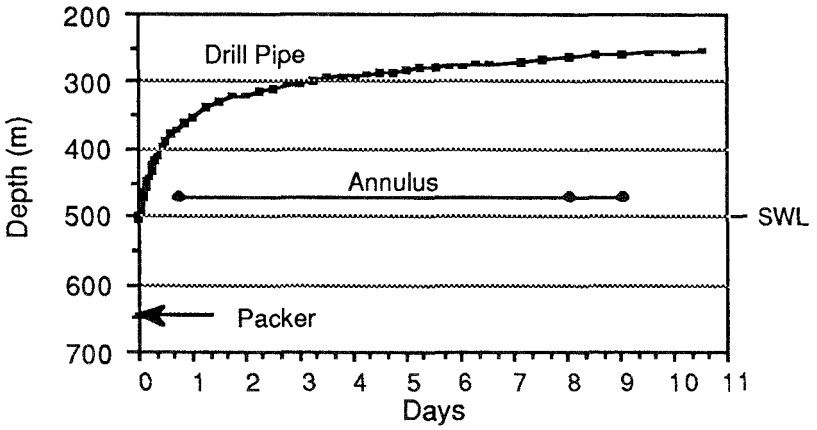

Fig. 5. Ue3e packer test

Fluid samples monitored during the drilling indicated elevated levels of tritium beginning at a depth of 661 m. A natural gamma log showed a spike of activity at 659 m depth and a sidewall sample taken in that interval contained a trace of cesium (Cs 137). Based on this information it was decided that the ALEMAN test could proceed in U3kz without jeopardizing future studies.

In an attempt to determine hydraulic pressures at depth, a flow-through packer was set in the Ue3e open hole at a depth of 646 m. Fluid rose in the pipe running through the packer to a measured depth of 255 m, more than 250 m higher than the predicted SWL (Fig. 5). The fluid level had not stabilized after ten and a half days. Projected depths of stabilization are approximately 30 m shallower. The fluid in the annulus stabilized within 24 hours at a depth of 470 m.

Six months after the execution of the ALEMAN event, Ue3e#2, an exploratory hole was drilled 12 m to the north of Ue3e. The primary objective of this hole was to obtain continuous core through the zone where the Cs 137 was found in Ue3e. A hole 0.20 m diameter was drilled to 594 m and 0.11 m diameter casing was set but not cemented in the hole. Continuous core was recovered (~100% recovery) from 594 m to 723 m. However, the zone of interest found in Ue3e was not penetrated. This implies that the Cs 137 contamination is not evenly distributed along a bedding plane but may be only in a small channel, perhaps associated with a high angle fracture or fault.

Fluid level tags are being made in Ue3e#2. A month after fluid sampling and logging, the fluid level in Ue3e#2 was discovered at a depth of 205 m both in the casing and in the annulus. The level at the time of this writing (8/7/87) is at a depth of 177 m, and is still gradually rising. Because there is communication between the fluid in the casing and the fluid in the annulus, Ue3e #2 is considered, for hydrologic purposes, as uncased. However, the hole was rotary drilled from the surface to 594 m with air foam and the core drilling below 594 m used a gel and polymer mud. These drilling fluids, especially the latter, probably reduce the ability of the formation to take fluid. The height of the fluid in Ue3e#2 is surprising, especially with the data from the packer test in Ue3e, 12 m to the south.

III. GASCON SITE

The GASCON test was conducted in emplacement hole U4t, just north of the Tuff Pile 1 boundary (Fig. 1; Fig. 6a and Fig. 6b). U4t was lined from 441 m to 601 m with a 1.9 m diameter liner for an estimated depth to the SWL of 506 m. During the month following insertion of the liner, slowly rising fluid levels were detected. After dewatering, video inspection revealed a collapsed section of liner with a leak about 5.5 m above the liner bottom. Fluid was not seen entering the over the liner from the top. The fluid level in U4t had not stabilized before the liner was repaired by cementing a smaller diameter liner inside it.

Twelve meters to the west of U4t, satellite hole U4t sat #1 was drilled. Two months after the completion of this 0.31 m diameter, 640 m deep, uncased instrument hole, the depth-to-fluid was 323 m. The fluid level stabilized after another two months at a depth of 315 m, or 191 m above the predicted static water level of 506 m and over 100 m above the U4t liner top. During the borehole video run just prior to the emplacement of the device, fluid was seen seeping into U4t, probably from the satellite hole.

Ue4t was drilled for RNM and hydrologic investigations and is located 168 m south, and 15 m west of U4t. This 0.25 m diameter hole was rotary drilled in three phases using air-foam to a total depth (TD) of 736 m. Fluid levels were monitored after each phase of drilling. Data gathered during this process seems to indicate the presence of pressurized zones, as the depth-to-fluid decreased with drilled depth (Fig. 7). Tags following phase one drilling were insufficient for projection of a stabilized fluid level. The stabilized phase two fluid level was at a depth of approximately 320 m. As of 8/7/87, the phase three fluid level seems to be stabilizing at a depth of about 265 m. No elevated levels of tritium or fission products have been detected in any of the holes at the GASCON site.

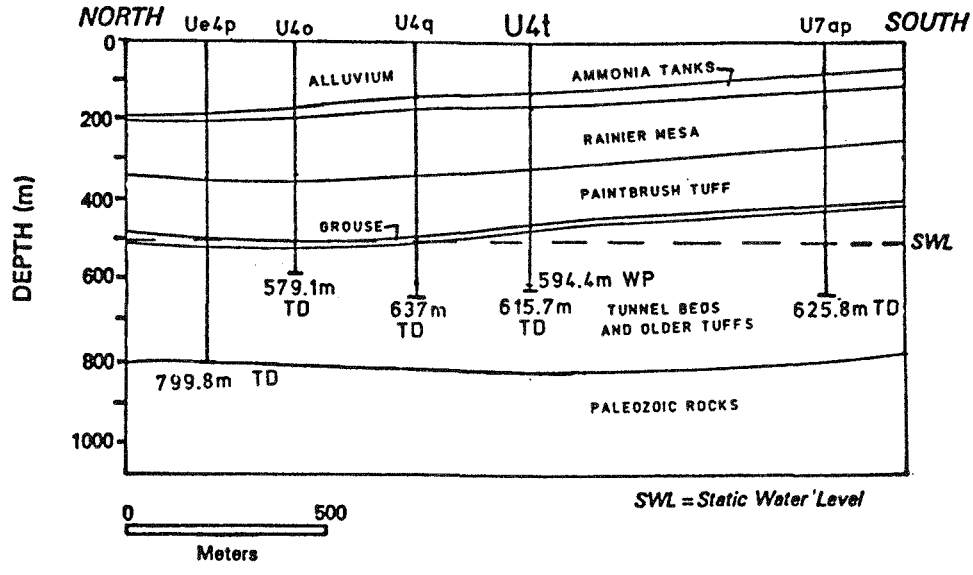

Fig. 6a. GASCON north to south cross section.

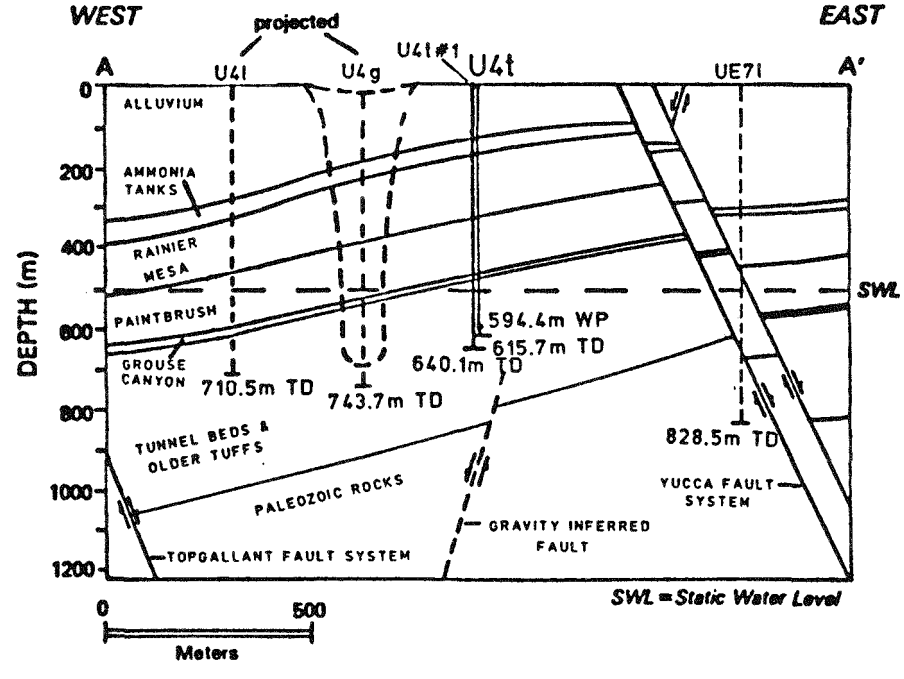

Fig. 6b. GASCON west to east cross section.

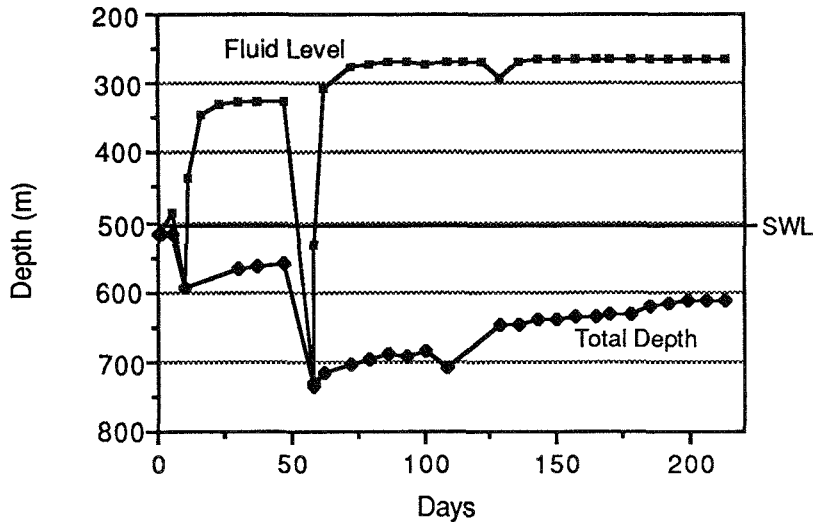

Fig. 7. Fluid levels following drilling at Ue4t

IV. TAHOKA SITE

The TAHOKA event was executed in hole U3mf which is in Tuff Pile 1 in a very similar geologic setting to ALEMAN and GASCON (Fig. 8a; Fig. 8b). To avoid problems with the liner at this site an exploratory hole (Ue3mf) to determine hydraulic pressures was drilled 13 m to the southeast of the planned emplacement site. Ue3mf was drilled in three phases with air-foam. Fluid levels were monitored after each of the first two phases (Fig. 9). The 0.31 m diameter hole was initially drilled to a depth of 518 m or 25 m below the predicted depth of the water table. Fluid level tags indicated the depth-to-fluid would stabilize above a depth of 488 m. At a drilled depth of 640 m, the fluid level appeared to be stabilizing at a depth slightly above 439 m. In phase three the hole was drilled to a final TD of 732 m. The fluid level had not stabilized prior to the first packer test.

Three single packer tests were run in Ue3mf. The packer was first set on the 0.11 m diameter drill pipe at a depth of 577 m. Figure 10 indicates the fluid levels in both the annulus and the drill pipe were nearing stabilization when drilling of emplacement hole U3mf disrupted the packer test. After about fifteen days, the fluid level in the drill pipe and the annulus were at depths of 415 m and 435 m respectively, when both levels began dropping. Apparently, there was communication from the exploratory hole to the emplacement hole.

Based on the fluid level information obtained in the first packer test, the liner for emplacement hole U3mf was set from a depth of 655 m to 411 m (82 m above the predicted water table). The liner was also reinforced with stabilizer rings.

Two additional packer tests were performed in Ue3mf. The main objective of these packer tests was to define the water table. Packer test depths were determined using information from the staged drilling. After the first stage of drilling (TD of 518 m) the depth-to-fluid of less than 488 m was higher than the predicted water table of 493 m. Therefore, the actual water table was believed to be somewhere between 518 m and 493 m depth. The packer was emplaced at a depth of 516 m for the second test. Fluid level in the drill pipe stabilized at approximately 431 m below the surface and the fluid level in the annulus stabilized at approximately 452 m (Fig. 13). The annulus fluid level was 36 m higher, than the fluid level in the open hole during the first phase of drilling, indicating that the fluid level had not stabilized.

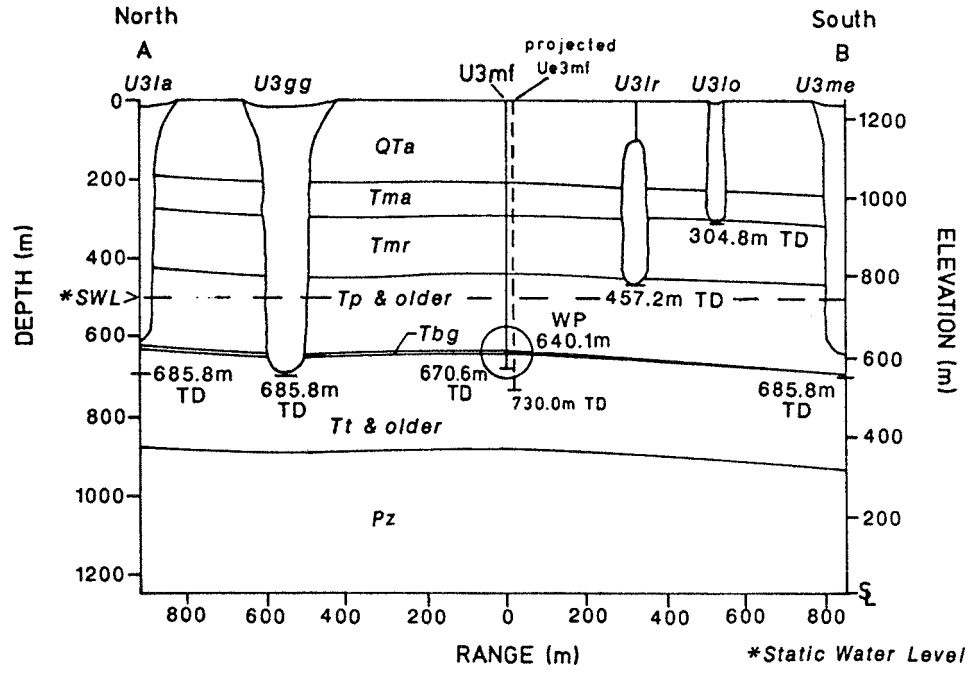

Fig. 8a. TAHOKA north to south cross section.

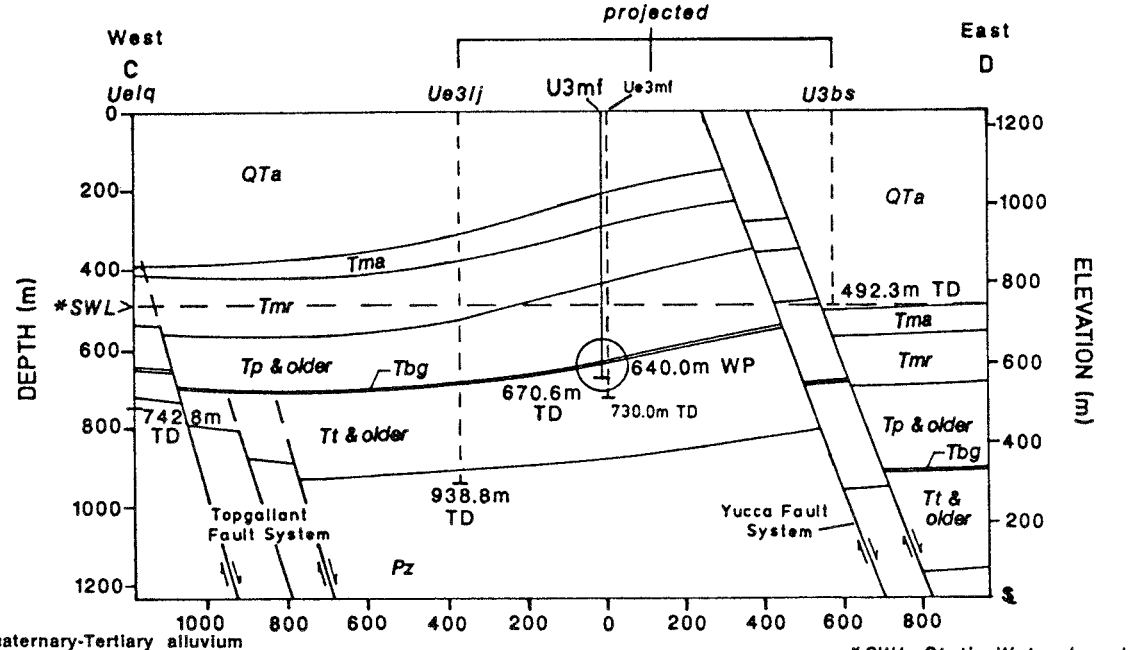

QTa--Quaternary-Tertiary alluvium
Tma--Ammonia Tanks Member, Timber Mountain Tuff
Tmr--Rainier Mesa Member, Timber Mountain Tuff
Tp & older--Paintbrush Tuff and older tuffs
Tbg--Grouse Canyon Member, Belted Range Tuff
Tt & older--Tunnel Beds tuff and older
Pz--Paleozoic rocks, undifferentiated

Fig. 8b. TAHOKA west to east cross section.

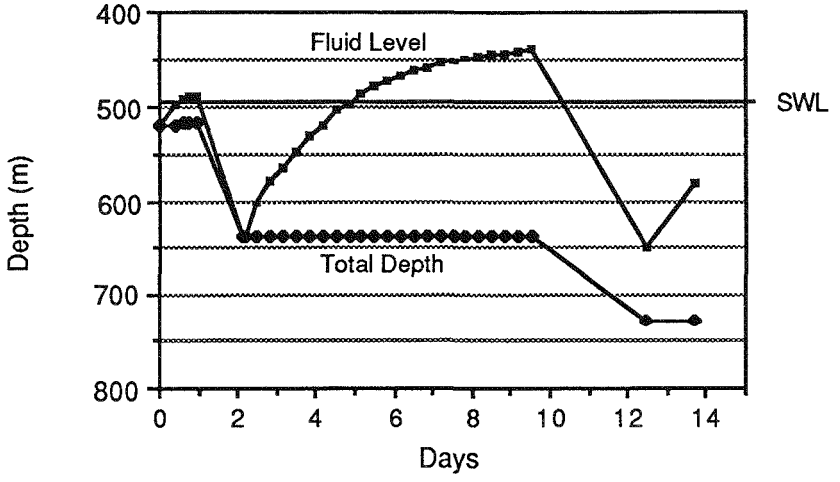

Fig. 9. Fluid levels during drilling of Ue3mf

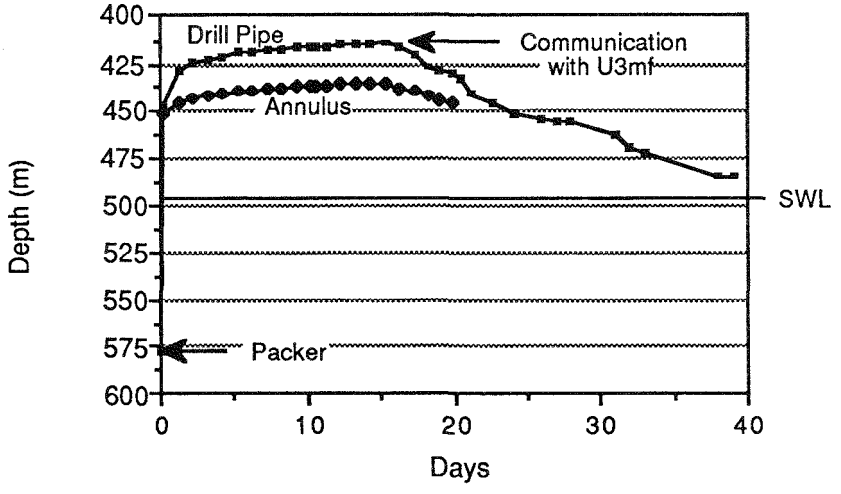

Fig. 10. First packer test in Ue3mf

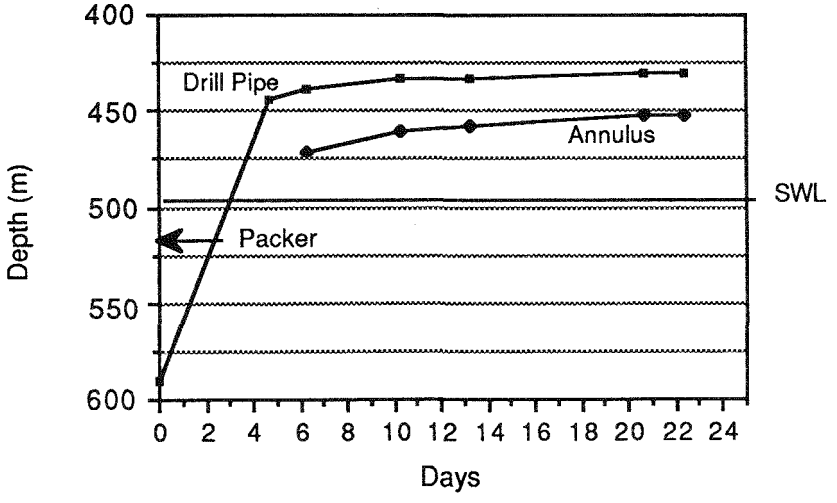

Fig. 11. Second packer test in Ue3mf

The packer was set at 480 m for the third test. When the packer was inflated, the fluid level in both the annulus and the drill pipe was at a depth of 472 m. Four days later, fluid levels were again measured. The fluid in the drill pipe was found to have risen to 436 m below the surface and no fluid was observed in the annulus. After another three days, the fluid in the drill pipe was measured at 434 m and again, no fluid was found in the annulus.

A test was performed to determine if the PAIL (photon annulus investigation log) tool was working properly. Fluid level changes were monitored after 1590 liters of water were poured into the annulus. This volume of water translates into a fluid rise in the annulus of approximately 23 m above the 3 m long packer. The fluid level in the annulus was immediately found to have risen to 455 m, exactly the 23 m expected. Two hours after addition of the water, the fluid in the annulus dropped 2 m. The fluid level remained at approximately 457 m for the next seven days. The test was then abandoned in order to continue operations necessary to the TAHOKA event. Results from the third packer test thus proved to be inconclusive in determining the water table. No elevated levels of tritium or fission products were detected in either the emplacement hole or the exploratory hole at the TAHOKA site.

V. SUMMARY

Data from the three sites discussed above although not conclusive does indicate anomalous hydrologic conditions. At the ALEMAN site high levels of tritium and some radionuclides were discovered in drill holes. Depths-to-fluid in open holes and during a packer test were much higher than predicted. Fluid in the Ue3e#2 open hole is now more than 320 m higher than the predicted elevation of the water table. Higher than expected fluid levels were also found at the GASCON site but no elevated levels of tritium or radionuclides were discovered. The staged drilling of Ue4t suggests increasing hydraulic pressure with depth. Ue3mf at the TAHOKA site revealed the complexity of the hydrologic conditions through three packer tests. A concerted effort to determine the water table was inconclusive.

The effects of these zones of relatively high pressure are obvious for hole construction and related containment concerns such as saturated stemming materials but other effects may not be as obvious. Certainly the hydrogeologic system in central Yucca Flat should be perceived as one of complex hydraulics.

VI. ACKNOWLEDGEMENTS

The authors wish to express their appreciation to the USGS, especially the Water Resources Division in Las Vegas, Nevada, the Desert Research Institute in Reno, Nevada, and the Field Test Division at Los Alamos National Laboratory for their support of these hydrologic studies.

This work supported by the United States Department of Energy.

VII. REFERENCES

Doty, G. C., and Thordardson, W., 1983, Water table in rocks of Cenozoic and Paleozoic age, 1980, Yucca Flat, Nevada Test Site, Nevada, U.S. Geol. Survey, Water Resources Investigations Report 83-4067, map.

Garber, M. S., 1963, Large rise and following decline of water level in Well 7, Area 3, Nevada Test Site--An effect from the Aardvark underground nuclear explosion: U.S. Geol. Survey Tech. Letter Yucca-48, 9 p.

Garber, M. S., and Johnston, R. H., 1967, A summary of lithologic data, aquifer tests, and construction of hydraulic test well U3cn-5, Nevada Test Site: U.S. Geol. Survey Tech. Letter NTS-200, 34 p.

Hale, W. E., Winograd, I. J., and Garber, M. S., 1963, Preliminary appraisal of close-in aquifer response to the Bilby event, Yucca Flat, Nevada: U.S. Geol. Survey Tech. Letter NTS-63, 32 p.

Collapse Phenomena

DO NOT MICROFILM
THIS PAGE

DEVELOPMENT FOR CENTRIFUGE MODELING OF BURIED EXPLOSIONS

Joseph. A. Brown
Jack W. House
Kenneth H. Wohletz
Los Alamos National Laboratory

Edward S. Gaffney
Ktech Corp.

ABSTRACT

We are developing test bed construction and instrumentation techniques for monitoring ground shock of contained subscale HE bursts (~45 gm C-4) that will be conducted on a large centrifuge. Reproducibility of the test medium has been a problem, but construction in a series of lifts of known volume and mass appears to produce good results. Instrumentation has included several types of stress transducers (piezoresistive: manganin and carbon; and piezoelectric polyinylidene fluoride), a mutual inductance particle velocity gauge, and accelerometers. Good ground shock records have been obtained. We have assembled a multichannel digital data acquisition system which can be transported to other sites such as a centrifuge facility. We have also obtained measurements of cavity and collapse crater sizes. Initial centrifuge tests will begin in the fall of 1987.

I. INTRODUCTION

The underground nuclear test community has long been interested in the formation and collapse of explosion cavities and other post-event phenomena. These are directly applicable to designs for the containment of radioactivity for future nuclear tests as well as problems related to the location of new test holes in proximity to previous events.

At the Second Containment Symposium, we discussed several potential applications of geotechnical centrifuge testing technology to the containment of nuclear tests (Gaffney and Cheney, 1983). Since that time we have undertaken a program to develop methods for conducting such experiments on a large centrifuge such as the National Geotechnical Centrifuge Facility at University of California at Davis. This facility was recently commissioned and is currently operating with the capability of taking a 4 ton payload to 16 g's in a swing bucket. We have scheduled our first experiments on this machine for the Fall of 1987. Our program has concentrated on developing test bed preparation techniques and instrumentation for monitoring the ground shock produced by small HE charges, both by methods applicable to centrifuge implementation.

II. TEST DESCRIPTION

A test bed consisting of washed sand provides a simple setup for testing stress gauges and accelerometers in a spherical geometry. With this material simple placement of an explosive charge and a gauge array in a specified horizon facilitates measurement of a spherically diverging stress wave in a soil-like medium as well as post-shot inspection of the shot horizon and gauge condition. This experimental setup was chosen especially for its ease in construction.

The spherical explosive charges of C-4 are 38 mm in diameter (approximately 46 g) and initiated by Reynolds RP-87 detonators; the stress wave reaches the sand at about 5.4 microseconds after detonation. Detonator leads are run out of the test bed on a radial well removed from gauges and signal leads.

Gauge arrays are set up to measure stress and accelerations at two radial distances, typically from 50 to 200 mm on a horizontal plane. A photograph of one array at shot level is shown in Figure 1. Although much care is taken to achieve specific gauge location and orientation, minor gauge movement may occur during backfill of the test bed.

In early experiments the test bed consisted of two levels separated by a shot-level template with a 1.5 m diameter test horizon. The upper level was emplaced after charge and gauge layout, and the template provided a means for locating the post shot excavation. Burial depths range from 600 to 700 mm. A photograph of the test bed is shown in Figure 2. The washed sand used ranged in approximate grain diameters (one standard deviation) from about one-half millimeter to several millimeters with infrequent large grains up to several centimeters. Sand, sieved through 2 mm screens, was carefully placed around gauges and the charge to insure as much homogeneity as possible. Wet sand density was typically 1.6 to 1.7 Mg/m^3 at 5 weight percent saturation. However, heterogeneity was difficult to overcome in construction of the test bed. In more recent shots the test bed within about 0.3 m of shot depth is placed in lifts of known mass within a 1 m^2 frame of 2 x 4 lumber. This permits more precise control of test bed density and water content.

III. MEASUREMENTS

The measurement of ground shock from small explosions has been accomplished numerous times. SRI International has reported an extensive program of measurements in grout (intended to simulate volcanic tuff) and reconstituted alluvium (Florence et al., 1984). Most of their measurements were of the lagrangian radial velocity, although they did make some measurements of the radial stress. The velocity measurements were made by monitoring the current induced in a circular coil concentric about the charge as it moved outward while cutting lines of flux in a uniform

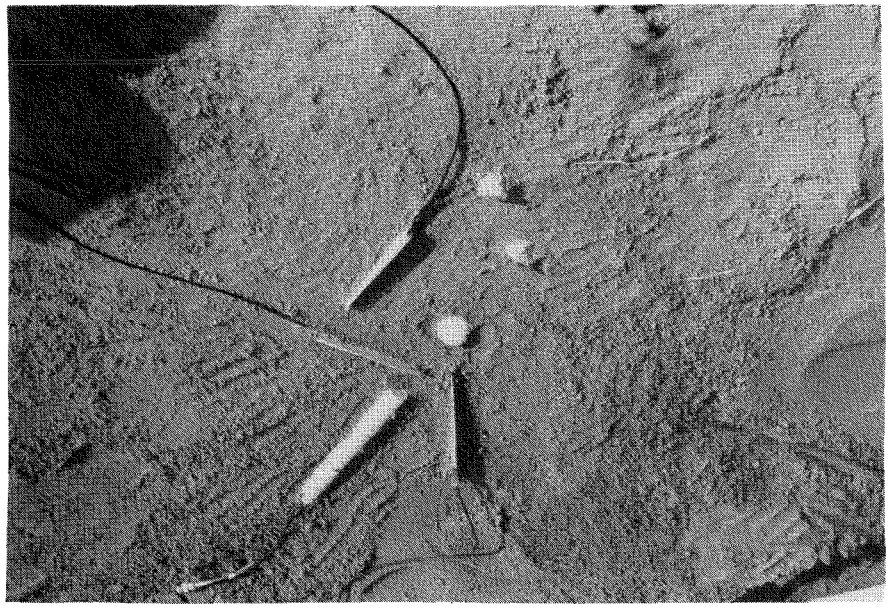

Figure 1 Photograph of the gauge array used in shot 86-2. The test bed is shown at shot level with spherical C-4 charge in center, carbon gauges (wedge shaped), manganin gauge (cylindrical), and accelerometers (small blocks), oriented around the charge. The total diameter of controlled space in the test bed is about 1.5 meters.

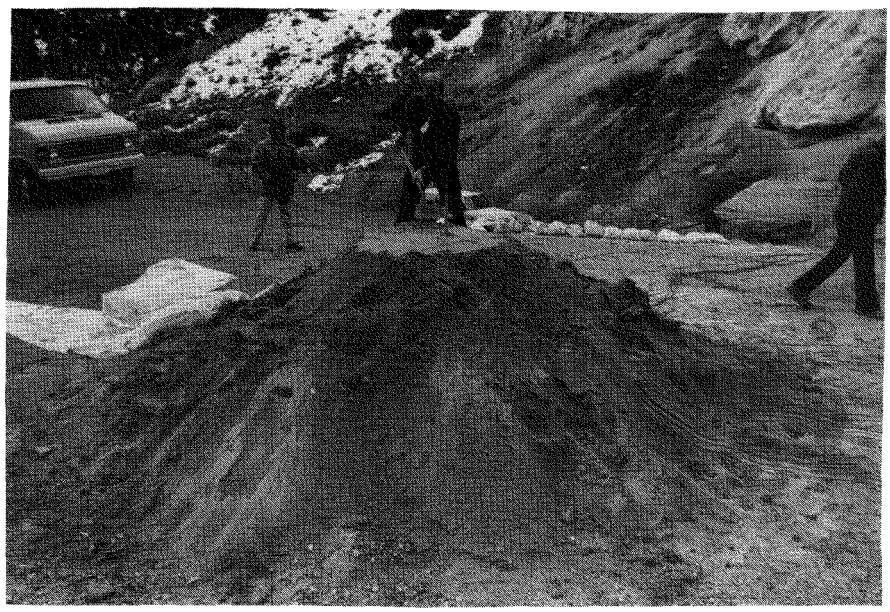

Figure 2 Photograph of the test bed after it has been back-filled over shot layer. The back-filled over shot layer. The back fill is such that its depth above the charge is sufficient to allow formation of a collapse crater, and its surface diameter is several times larger than that of the expected collapse crater.

magnetic field. This has proven to be a very reliable technique; unfortunately, it would be impossible to implement on a centrifuge test because the uniform field is produced by a pair of large Helmholtz coils. The mass of these coils is too great for incorporation in a centrifuge test. In addition, the power required would be beyond the limits which could be delivered to the centrifuge arm.

Manganin Stress Gauges

Our manganin gauge design was previously described (Gaffney et al., 1985); it is a probe-like package in which the gauge element is mounted on a polycarbonate support such that the gauge leads are at right angles to the sensitive element. This arrangement, along with a coaxial shorting pin (for triggering recording devices), is potted in epoxy to insure mechanical stability. The epoxy may be treated to obtain reasonable impedance matching with the test bed. However, the radial probe nature of this gauge package does not promote lagrangian measurements, especially in semi-compressible media such as our sand test beds. Results obtained include dynamic and reflected stress components that must be unfolded in order to obtain free-field stress. Still, the package appears to be rugged and capable of surviving stress waves of several tens of MPa in the sand test beds. The coaxial trigger pin is not required with the digital recording system but is ultimately necessary for adequate oscilloscope records.

Carbon Piezoresistive Stress Gauges

Carbon piezoresistive film stress gauges have been used in a flat-pack configuration to measure radial stress-time histories at medium ranges, corresponding to pressure of tens to hundreds of MPa. As commercially supplied[1], the 50Ω piezoresistive film and foil leads are encapsulated between thin (.025 mm) layers of kapton. For greater survivability, we have added a layer of .25 mm thick mica to each side of the gauge, and gradually increased the flat-pack thickness from 0.55 mm at the gauge sensing element (7.6 mm x 12.7 mm), to 6.5 mm at the end of the gauge where the coaxial cable lead (RG-174) exits, by filling between the mica strips with fast-setting epoxy. The final gauge package is thus a wedge shape of 115 mm x 25 mm cross section. This arrangement maximizes the chances of gauge survival while preserving the lagrangian response of the gauge and mimimizing the inclusion effect at the sensing element.

Carbon gauges of this type are valuable for their high sensitivity in the low stress (<1 GPa) regime, and because their sensing elements form a single wide strip rather than a conducting grid, they are less susceptible to destruction through puncture by individual material grains. The response of these gauge packages in the current test configuration will be described below.

[1]Dynasen, Inc., Goleta, CA

Polyvinylidene Fluoride Stress Gauges

We have had good success with stress gauges using a polyvinylidene fluoride (PVDF) transducer for measuring both ground shock amplitude and stresses associated with ground flow. The PVDF stress transducer has been described by Reed (1987). We have used these in a probe configuration[2] similar to that described above for manganin gauges. The PVDF gauge is particularly suited for applications where the arrival time of the shock wave is not well predicted because it requires no pulsed power for operation. We have used gauges of this type both with and without charge amplifiers, but even with the charge amplifiers only a steady low voltage current of a few milliamps is required. Several of these gauges were included on two centrifuge cratering events conducted at Cambridge University in August 1987, with good data return. Peak stresses in the range from less than one to tens of MPa were recorded on eight of the twelve gauges fielded.

Other Active Measurements

Preliminary measurements of acceleration are made using a micro-miniature shock accelerometer. Endevco model 2291[3] is a piezoelectric transducer capable of withstanding 100,000 g in any direction. Its small mass (1.3 grams) and high resonance frequency (250 kHz) make it adequate for acceleration measurements at ranges of greater than 100 to 200 mm where stresses have decayed to under 100 MPa and stress rise times are nearly 100 microseconds long. Still, higher frequency records are desired, and since particle velocity records are the required data, we do not anticipate further development of acceleration measurements, since data integration is required to get velocities. Accelerometers have been mounted on squares of various plastics in order to facilitate orientation of the gauge and to improve coupling to the test medium. Our best results with this type of gauge has been for measuring acceleration near surface ground zero (SGZ).

Because of the difficulty of implementing other particle velocity measurement techniques on a centrifuge, we have attempted to adapt a technique from field methods. The mutual inductance particle velocity (MIPV) gauge (Florence, et al., 1983) consists of two nearly coincident coils in the shape of a long, thin rectangle whose long axis lies on a radius from the charge. A constant current of several tens of amperes flowing through one coil links flux through the other. As the coils are deformed the mutual inductance is changed producing a current in the other coil, which is proportional to the velocity for the end of the coils nearest the charge. At the time of this writing we have constructed such a gauge with the necessary power supply in a package that can be mounted an operated on a centrifuge.

---

[2]Ktech Corporation, Albuquerque, NM

[3]Endevco, San Juan Capistrano, CA

Data Acquisition

For this study, we have constructed a multi-channel digital data acquisition system which was designed to be reasonably portable for transport to and use at remote facilities. The system is computer controlled, utilizing the CAMAC (IEEE-583) interface standard.

Signals from the carbon and manganin piezoresistive stress gauges are obtained from pulsed-d.c. Wheatstone bridge power supplies[4], which are typically triggered for a duration of 500 microseconds, resulting in less than 5 percent decay of the voltage applied to the gauges. We use excitation voltages of 70v and 200v for the carbon and manganin gauges, respectively, representing an optimum balance between gauge sensitivity and joule heating effects in the gauge packages. The dual-channel power supplies can be triggered independently, resulting in flexibility in timing the gauge activation with respect to arrival of the stress wave at the various gauge positions. Voltage records from the accelerometers are obtained from charge amplifers, and other types of gauges that supply voltage or current signals can be accommodated.

The data recording system resides in two CAMAC crates and consists of multi-channel, timing delay units, trigger generators, amplifier/alternators, and transient waveform digitizers with associated memory modules. The nine waveform digitizers are of two types (LeCroy 2264/8800 and 8818/8105)[5], which together allow recording of signals at rates from 1 MHz to 100 MHz for up to 14 channels of data and durations of several milliseconds per channel. A mini computer(DEC LSI 11/23)[6] controls the recorders and acquires the data through two crate controllers (Kinetic Systems 3912-ZIG)[7] The timing delay system with the detonator trigger as a source supplies appropriately timed trigger signals for the bridge power supplies and the waveform recorders. This system allows positioning of the stress wave within the bridge excitation time with the latter being within the duration of the recording "windows."

Following data collection, the computer reads the contents of memory for each data channel sequentially, storing the information in files of binary format on flexible disk and/or magnetic tape cartridge. These media can then be transported to a large computer for later display and analysis.

---

[4]Dynasen, Inc., Goleta, CA

[5]LeCroy Research Systems Corp., Spring Valley, NY

[6]Digital Equipment Corp., Maynard, MA

[7]Kinetic Systems Corp., Lockport, IL

Post-Test Measurements

Post shot measurements consist of two data sets. The first is accurate measurement of the test bed deformation such as collapse pit dimensions, fracture geometry, and compaction. The second requires excavation back to the shot level without disturbing gauges and detonation products. After excavation a reasonable measure for transient cavity dimensions is made by noting location of detonation products. The final location and integrity of gauge packages is important for interpreting gauge records and also as a valuable aid in guage development, so the type of gauge destruction and movement are noted.

IV. RESULTS

An important goal of this study is to investigate the suitability of various techniques for measuring free-field stresses during small-scale explosive tests carried out on a centrifuge. The gauges should be sensitive enough to measure stresses at ranges of several cavity radii in highly attenuating media such as dry desert alluvium, but rugged enough to survive the strong spherical flow environment at close ranges. Also, aspects of gauge response in spherical flow, such as strain sensitivity and transverse stress response, must be understood and characterized. In this section we show some early records obtained from stress gauges, and give a preliminary qualitative discussion of some of their features.

Another important aspect of this work is the analysis of the post-shot condition of the test bed. Below we describe this post-test inspection process for a typical experiment in unsaturated wet sand.

Gauge Records

Figure 3, shows a record obtained from a manganin gauge. The gauge package was oriented to measure radial stress at a range of 200 mm. The horizontal scale in the figures refers to elapsed time since charge initiation. Because of the higher-than-anticipated stress, the signal's peak exceeds the preset range of the recording system. However, several features remain to be interpreted.

One can see the induced noise shortly following detonation. The large transient signal at approximately 100 microseconds is the beginning of the power supply current pulse, followed by some "settling" behavior that seems to result from significant deviations from the 50Ω nominal initial gauge resistance, which in this case was about 45Ω. The signal then follows a slow decrease in baseline, showing a decrease in gauge resistance as it heats up. This record is not corrected for joule heating effect. In practice, we obtain a baseline gauge record of joule heating for each gauge after building the test bed but before firing, so that the effect can later be subtracted from the recorded data.

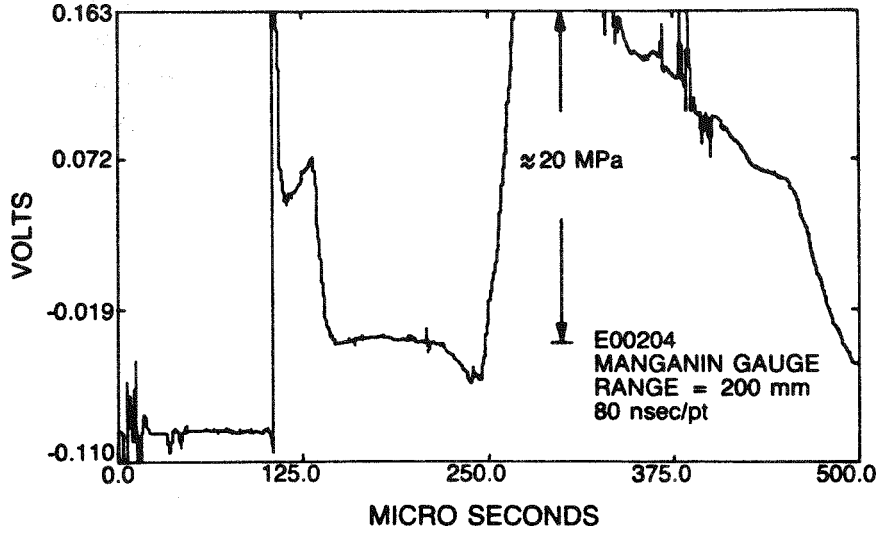

Figure 3 Plot of manganin gauge response versus time. Note that the stress wave produces a positive response that exceeded the recording limit, and that the power supply turn-on characteristic at 100 microseconds lasts for over 20 microseconds.

The design of the manganin gauge package precludes a lagrangian response to the flow, and the impedance mismatch to the surrounding medium is such that one expects the recorded stress to be approximately twice that of the free field. The positive-going signal reflects the increase of manganin's piezoresistivity with increasing compressive stress. The risetime of the stress signal is longer than but consistent with that measured with carbon gauges, at smaller ranges. The extended duration is presumably an effect of the massive gauge package and its radial orientation. This gauge did not fail during the test and survived intact.

Figure 4 shows stress histories recorded on a 2 gram cratering experiment using the PVDF stress gauge. These records were recorded with a 20 KHz FM recording system and hence do not show the true peak initial shock stress. The sharp spikes at zero time are electromagnetic pickup of the detonation pulse. However, they show the dynamic stress of the saturated sand medium flowing past the nearly Eulerian gauge, which begins at about 0.5 ms and lasts about 15 ms. The negative portion of the record beginning about 7 ms may represent reduction of pore pressures to zero during dilation of the flowing sand, a phenomenon which would not be seen in the partially saturated media that is of most interest to containment. Each of these gauges had been used on a previous test, indicating the survivable return.

Post-shot Test Bed Analysis

Post-shot examination of the test bed shows formation of a collapse crater, radial and concentric fractures extending away from and around the crater, and inward dipping slump faults on the crater's inside slopes. Figure 5 is a photograph of post-shot, test-bed deforation. A typical collapse crater may range from 30 to 50 cm in diameter and 10 to 15 cm deep. Major concentric fractures are spaced from 5 to 15 cm apart, while radial fractures are oriented at 20 to 40 degree intervals. The whole test-bed surface shows several centimeters of subsidence. SGZ accelerometer records indicate that the test bed deformation and crater collapse occur within one second after detonation.

Excavation of the test bed reveals that gauges have been displaced and damaged, especially those located within 100 mm of the charge. This observation is not surprising because existence of detonation products up to 200 mm from ground zero suggests considerable growth of a transient explosion cavity. As shown in Figure 6, detonation products are typically found within a radius 150 mm. We believe that this value is a characteristic measure of the transient cavity radius, because the relatively massive gauge packages placed within this region have been displaced outward to the observed limit of detonation products, and the cavity volume corresponding to this radius is approximately that of the collapse crater (i.e. the cavity has been filled in primarily by collapse of roof materials).

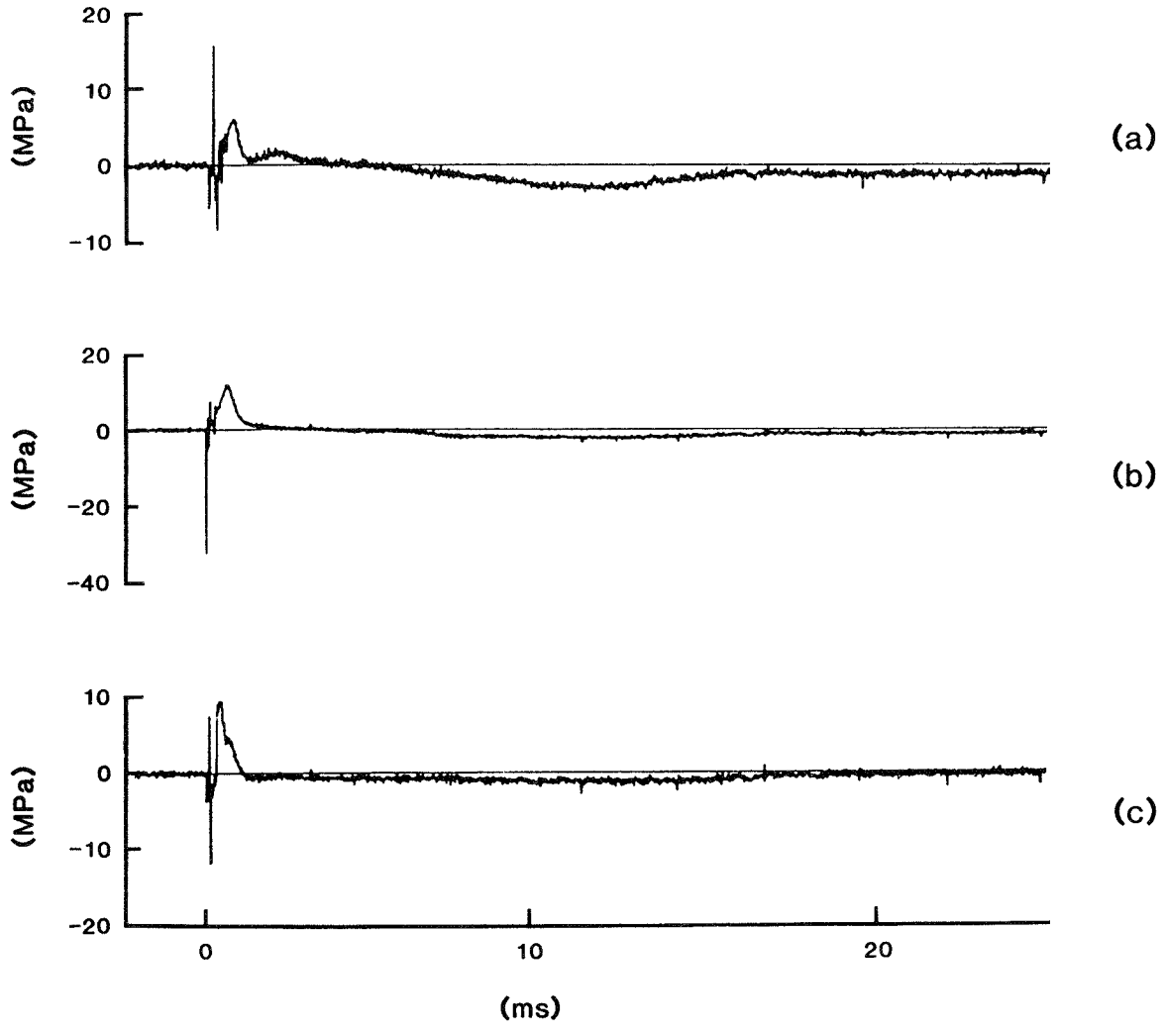

Figure 4 Plots of PVDF gauge response versus time for a cratering experiment conducted on a centrifuge. Sharp spikes at zero time are detonator noise. These are followed by positive peaks produced by the propagating stress wave.

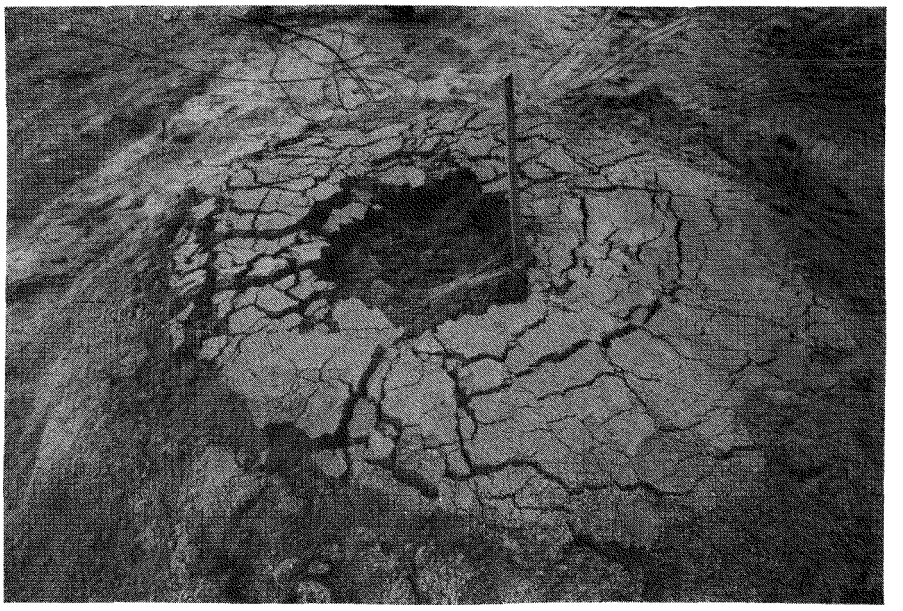

Figure 5 Photograph showing test-bed deformation: a collapse crater nearly 50 cm in diameter and 15 cm in depth and uniformly spaced concentric and radial fractures surrounding the collapse crater.

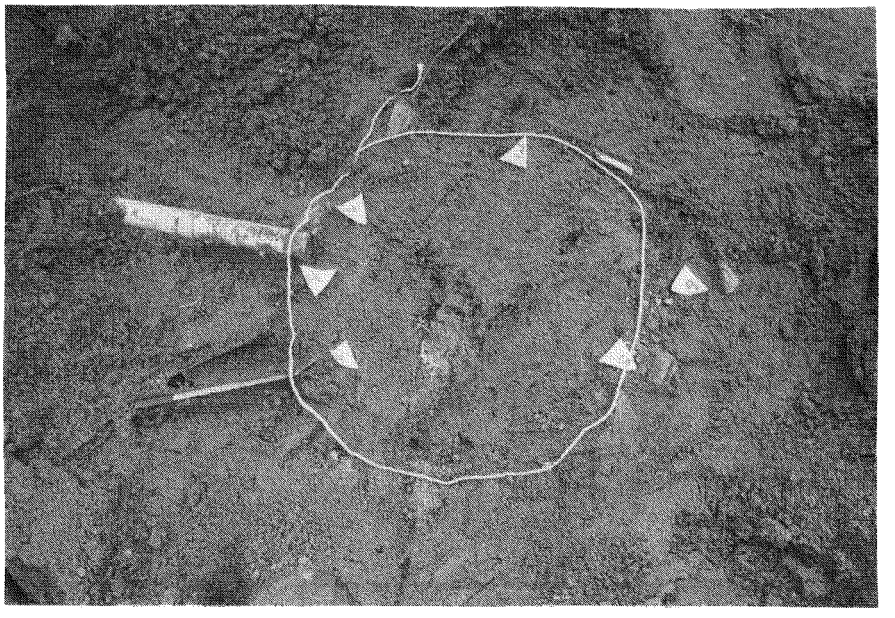

Figure 6 Photograph of the post-shot excavation (86-2). Numbers refer to: (1) carbon gauge package with an initial tangential orientation at 70 mm, (2) carbon gauge package with an initial radial orientation at 70 mm, (3) carbon gauge package initially at 120 mm, (4) manganin gauge initially at 120 mm, (5) accelerometer initially at 120 mm, and (6) accelerometer initially at 200 mm. Gauge displacements and damage are readily apparent in this picture as is an approximate radius of the transient cavity.

As noted above, all the gauges are displaced during propagation of the strain wave produced by the detonation. Least affected are the probe-like manganin and PVDF packages and greatest displacement is noted for the carbon flat packs. Accelerometers show up to several cm of radial displacement as well as rotation. Typically, the carbon flat packs show damage dependent upon their initial position. Gauges placed normal to radial stresses show one or several breaks transverse to the long axis, while gauges placed to measure hoop stress split along the long axis where the gauge is bonded to the mica backing. When damaged, manganin gauges are broken transverse to their long axes and along interfaces between the gauge support and surrounding epoxy. However, we note that both carbon and manganin gauge packages are reuseable when they have been placed at ranges near 200 mm. In fact one manganin gauge has survived two shots while providing good stress records on both. PVDF probes at 120 mm have also been reused. Finally, no damage has been noted on accelerometers.

IV. CONCLUSIONS AND SUMMARY

An interest in the processes of cavity formation and collapse resulting from contained nuclear explosions, as well as modeling of crater formation from buried conventional munitions, has led us to initiate a program at Los Alamos National Laboratory to model these effects using small-scale high-explosive tests. We are concentrating thus far on gauge construction and performance, and on techniques for test-bed construction and post-test evaluation.

The very difficult problem of construction of test beds in media such as unsaturated wet alluvium, is also being investigated. Uniform and well characterized density, accurate gauge emplacement, and test bed characteristics required to produce burst containment, cavity collapse, and crater formation are being studied. Also, techniques for accurate post-test analysis of these effects are of concern, as well as examination of final gauge condition as an aid in design of survivable gauge packages.

Gauges under study include: carbon and manganin piezoresistive stress gauges; polyvinylidene fluoride piezoelectric gauges; small, high-frequency accelerometers; and a new type of mutual inductance particle velocity gauge. The response of these gauges in spherically diverging flow is of primary interest.

From our initial results we can reach some conclusions regarding gauge packaging for these small HE tests. First, although a flat-pack gauge provides the best assurance of measuring the stress desired, these gauges are very fragile in the strongly divergent flow field produced by small HE events. The Eulerian probes, which we have used with both manganin and PVDF transducers, provide a package which is rugged enough to survive the environment and to produce good records. However, the interpretation of these records is less straightforward than for Lagrangian gauges.

REFERENCES

Gaffney, E. S., and Cheney, J. A., 1983, Containment science on a centrifuge. 2nd Symposium Containment of Underground Nuclear Explosions Vol. 2, 365-378.

Gaffney, E. S., Wohletz, K. H., and McQueen R. G., The Measurement of Shock in Explosive Centrifuge Model Tests. Proceedings of the 2nd Symposium on the Interaction of Non-nuclear Munitions with Structures, 15-19 April 1985, Panama City Beach, FL., p. 413-417.

Florence, A. L., Cizek, J. C., and Keller, C. E., Laboratory Experiments on Explosions in Geologic Materials. Shock Waves in Condensed Matter - 1983, 521-4, Elsevier, New York (1984).

Florence, A. L., Keough, D. D., and Mak, R., Calculational Evaluation of the Inclusion Effect on Stress Gauge Measurements in Rock and Soil. Symposium Proceedings, Part 2, Interaction of Non-nuclear Munitions with Structures, US Air Force Academy, CO, 10-13 May 1983, pp. 7-11 (1983).

Reed, R. P., 1987, Recent developments in piezoelectric polymer stress gauges, Range Commanders Council, 14th Transducer Workshop.

DEVELOPMENT OF CENTRIFUGE MODELING FOR EVALUATING THE MECHANISMS OF COLLAPSE OF UNDERGROUND OPENINGS

DAVIS, B. C., Nuclear Test Engineering Division,
Lawrence Livermore National Laboratory, Livermore, CA 94550
KUTTER, B. L. and CHANG, J. D. L., Department of Civil Engineering,
University of California, Davis, CA 95616

ABSTRACT

Improved prediction of surface collapse above an underground cavity is important in many LLNL programs, including nuclear testing. To improve our predictive capability it is necessary to achieve a better understanding of the mechanisms involved in the process of collapse. Our research aims to develop the centrifuge technique for modeling mechanisms of underground collapse in soil. We will also evaluate the adequacy of existing constitutive or flow models of soils in relation to the problem of underground collapse.

Scale model tests, if carefully conducted, can provide useful data when full-scale results are difficult or impossible to obtain. One advantage of centrifuge scale modeling is the easy observation of deformation mechanisms. In scale model tests involving problems such as underground collapse where gravity is a major driving force, the forces of gravity must be scaled to make the model simulate the actual event or prototype. Gravity can be scaled by placing the models in a centrifuge, where they are subjected to a steady centripetal acceleration many times greater than the earth's gravity. We also consider other factors in our effort to maintain similarity between model and prototype. Mechanical properties such as permeability, shear strength, density, and moduli must be the same in the model as in the prototype. The stress fields in the model and prototype must also be the same, since the mechanical properties of the model are highly dependent on the confining pressures. Accurate modeling requires that the mechanical properties of the model maintain an appropriate stress dependence to the prototype.

The modeling tests were performed in Monterey 0/30 sand, Fountainbleau sand or Nevada Test Site (NTS) Area 2 alluvium. Development of the method consisted of testing several different scale models (at varying gravity levels). This is called "modeling of models." If the various models predict the same prototype behavior, then the scaling laws and test procedure are verified over the range of scale factors spanned by the models. The test results validated the modeling laws as applied in the experiments reported here.

INTRODUCTION

The objective of this research is to develop the centrifuge technique for modeling mechanisms of collapse in underground openings in soil, and also to evaluate the adequacy of existing constitutive models of soil or granular flow theory for use in modeling this type of collapse.

When an opening is excavated in a geologic medium, the load formerly carried by the excavated material will be shared by media surrounding the opening and support forces within the opening. If strains within the elastic limit are generated, this redistribution of stress can be readily approximated with elastic theory, physical models or numerical techniques. However, the geometry of stress redistribution and the resulting deformations are difficult to calculate when large, nonlinear strains are involved because of the complex interaction of the various mechanisms that come into play. As a consequence, we cannot now adequately predict what happens when collapse occurs.

In connection with a quasi-static formulation of the underground collapse problem, we investigated various model parameters, including the strength parameters of the surrounding geologic media, the distance of the opening below ground surface, and the effect of gravity on these parameters, as well as the boundary effect of the scale modeling. The initial results left us with some questions about the validity of the model we were using and/or the validity of the Ten Diameter Rule. We continued testing to further explore the above parameters and to determine of we did have a valid modeling method.

We initiated the centrifuge scale-modeling research using the Schaevitz Centrifuge (see Table 1) at the University of California, Davis, with joint funding by the Engineering Research Program and the Nuclear Test Program. Part of the funding we received was used to ready the National Geotechnical Centrifuge for testing. Currently, we are continuing to use the Schaevitz Centrifuge, but will be moving to the National Geotechnical Centrifuge, the largest machine of its kind in the world, which will allow evaluation of larger models.

CENTRIFUGE MODELING

Scale model tests, if carefully conducted, can provide useful data when full-scale results are difficult or impossible to obtain. In scale model tests involving problems such as underground collapse where gravity is a major driving force, the forces of gravity must be scaled to make the model simulate the actual event or prototype. Gravity can be scaled by placing the models in a centrifuge, where they are subjected to a steady centripetal acceleration many times greater than the earth's gravity.

Table 1. Specifications of U.C. Davis Centrifuges.

N.G.C.--Swing bucket centrifuge	
Radius to surface of platform	30 ft
Max Area of Model	6 x 7 ft
Max Height of Sample	5 ft
Max Payload Mass	4 tons
Max Acceleration (estimated)	
1987	25 g
1988	100 g
1990	300 g
Schaevitz --Swing bucket centrifuge	
Radius to surface of platform	43 in
Max Area of Model	18 in x 18 in
Max Height of Sample (approx)	16 in
Max Capacity (Sample weight x acceleration)	10,000 g-lb (e.g., 100 lb x 100 g)
Max Acceleration	175 g
Drum Centrifuge*	
Radius to Surface of Drum	2 ft
Circumference of model	12.6 ft
Width of Model	10 in
Max Height of Model	6 in
Max Payload Mass	600 lb
Max. acceleration	300 g

* Model is continuous around circumference of centrifuge.

We also consider other factors in our effort to maintain similarity between model and prototype. Mechanical properties such as permeability, shear strength, density, and moduli must be the same in the model as in the prototype. The stress fields in the model and prototype must also be the same, since the mechanical properties of the model are highly dependent on the confining pressures. For example, using the traditional Mohr-Coulomb equation:

$$\tau_f = c + \sigma_n \tan \phi \ , \qquad (1)$$

the shear stress on a failure plane τ is defined as a function of two soil parameters, namely the cohesion (c) and the friction angle (ϕ), where the frictional contribution to the strength is proportional to σ_n, the normal stress on the failure plane.

Accurate modeling also requires that the mechanical properties of the model maintain an appropriate stress dependence to the prototype. As an example of stress dependence, particulate geologic media such as sand and soil tend to change volume (dilate or contract) during shear in a nonlinear and stress-dependent fashion. Thus the condition of identical stress is imposed:

$$\sigma_{model}/\sigma_{prototype} = \sigma^* = 1 \ . \tag{2}$$

This condition of identical stress leads to a set of scaling ratios (see Table 2), which must be maintained.

Limitations of Centrifuge Modeling

When applying the scaling laws to a particular problem, the researcher must keep in mind certain important limitations of centrifugal modeling. For example, the largest soil particle size must be much smaller that the critical, i.e., smallest model dimensions. The Ten Diameter Rule for particle size which is followed in gravity scale modeling maintains that the largest soil particle size must be less than or equal to one-tenth the critical model dimension. If this condition is not met, then the particle size must be scaled as all other dimensions are scaled, with special effort taken to maintain a similarity of the mechanical properties of the model soil (with adjusted grain size) to those of the prototype soil.

In addition, the centrifuge produces a non-uniform radial acceleration field proportional to the radius of rotation. This means that the bottom of the model will be subjected to greater acceleration than the top. To minimize errors due to this non-uniform acceleration field, we keep the model dimensions much smaller than the centrifuge radius.

Relative motion within a model in a rotating reference frame can cause Coriolis accelerations. These accelerations are equal to

$$a_{cor} = 2\omega \, v_{rel} \ , \tag{3}$$

where ω is the angular velocity of the centrifuge. These forces are generally insignificant for quasi-static problems when v_{rel} is very small and also for most dynamic problems when the model accelerations or the model gravity factor is much greater than the Coriolis accelerations.

Table 2. Summary of gravity-scaling ratios

For all events		For Dynamic events	
Quantity	Model dimension / Prototype dimension	Quantity	Model dimenson / Prototype dimension
Stress	1	Time	1/N
Strain	1	Frequency	N
Length	1/N	Velocity	1
Area	$1/N^2$	Acceleration	N
Volume	$1/N^3$	Strain Rate	N
Mass	$1/N^3$		
Density	1		
Force	$1/N^2$		
For Self Weight		**For diffusion events**	
Time	Not Applicable	Time	$1/N^2$
Acceleration	N	Velocity	N^2
		Acceleration	N^3
		Strain Rate	N^2

Note: This table assumes that the model and prototype are constructed of material with identical mechanical properties; that the rate of strain does not affect the mechanical properties; and that no two important scaling ratios are conflicting.

These limitations, and other possible scaling or boundary effects, indicate that centrifugal modeling should be verified by a model study that validates the modeling laws for the particular problem being studied. The best check on scaling laws would be a comparison to full-scale test data, but this is usually not possible. An alternative method evaluates the scaling laws by performing the same test at different scale factors. The testing of two different scale models is called "modeling of models." If both models predict the same prototype behavior, then the scaling laws and test procedure are verified over the range of scale factors spanned by the models. This method was used to test model cavities of 2-in. diameter and 6-in. depth at 38 g (N = 38), and cavities of 1-in. diameter and 3-in. depth at 76 g (N = 76). The 1-in. cavity was used as a model of the 2-in. cavity, and both represent a prototype cavity of 76-in. diameter and 228-in. depth. The test results only marginally validated the modeling laws as applied in the experiments. Further testing has concentrated on verifying whether the marginal results were due mainly to density effects or grain size effects (scale effect).

EXPERIMENTAL PROGRAM

Our tests begin with a container (the so-called model bucket or sample bucket) holding sand or alluvium soil, whose relevant properties, such as particle size, are carefully controlled. A schematic view of the test arrangement is shown on Fig. 1. The underground opening is simulated by a model cavity (MC), which is a molded rubber (latex) bag filled with water and buried in the sand or soil at the appropriate depth. To balance the soil overburden pressure on the MC and prevent its premature collapse, an appropriate water level is set in the supply reservoir with valve SV1 open and valve SV2 closed. During tests the water level in the supply reservoir and the pressure in the MC are monitored by pressure transducers. With this arrangement the increase in overburden pressure as the centrifuge comes up to speed is exactly balanced by the accompanying increase in hydrostatic pressure inside the MC. After the centrifuge reaches the desired acceleration, SV1 is closed. To initiate the collapse of the MC, SV2 is opened, letting water drain from the MC into the collection reservoir, whose volume is monitored by another pressure transducer. The flow restriction shown at A prevents oscillations in the system due to the operation of SV2. Figure 2 shows the test setup in place on the Schaevitz Centrifuge at U.C. Davis, and Table 3 summarizes conditions and crater data for the 27 tests performed thus far.

TEST PROCEDURE

The tests initially were performed in Monterey 0/30 sand or Nevada Test Site (NTS) Area 2 alluvium. The NTS alluvium provided to us contained a significant amount of gravel and small boulders. We removed all particles larger than 0.2 in. by sieving to produce the grain size distribution labeled "coarse alluvium" in Fig. 3. This soil was used for most of the tests requiring a cavity of 2-in. diameter. For tests with a cavity of 1-in. diameter the alluvium was further sieved, removing all particles larger than 0.11 in., to produce the grain size distribution labeled "fine alluvium" in Fig. 3, which also includes the grain size distribution for the Monterey sand and the Fountainbleau sand.

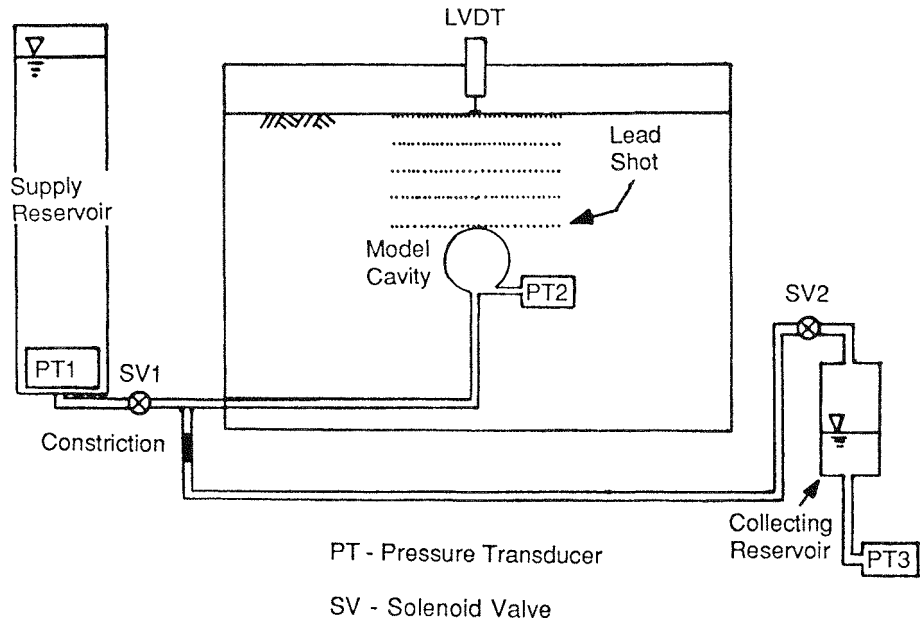

Figure 1. Schematic view of the test setup.

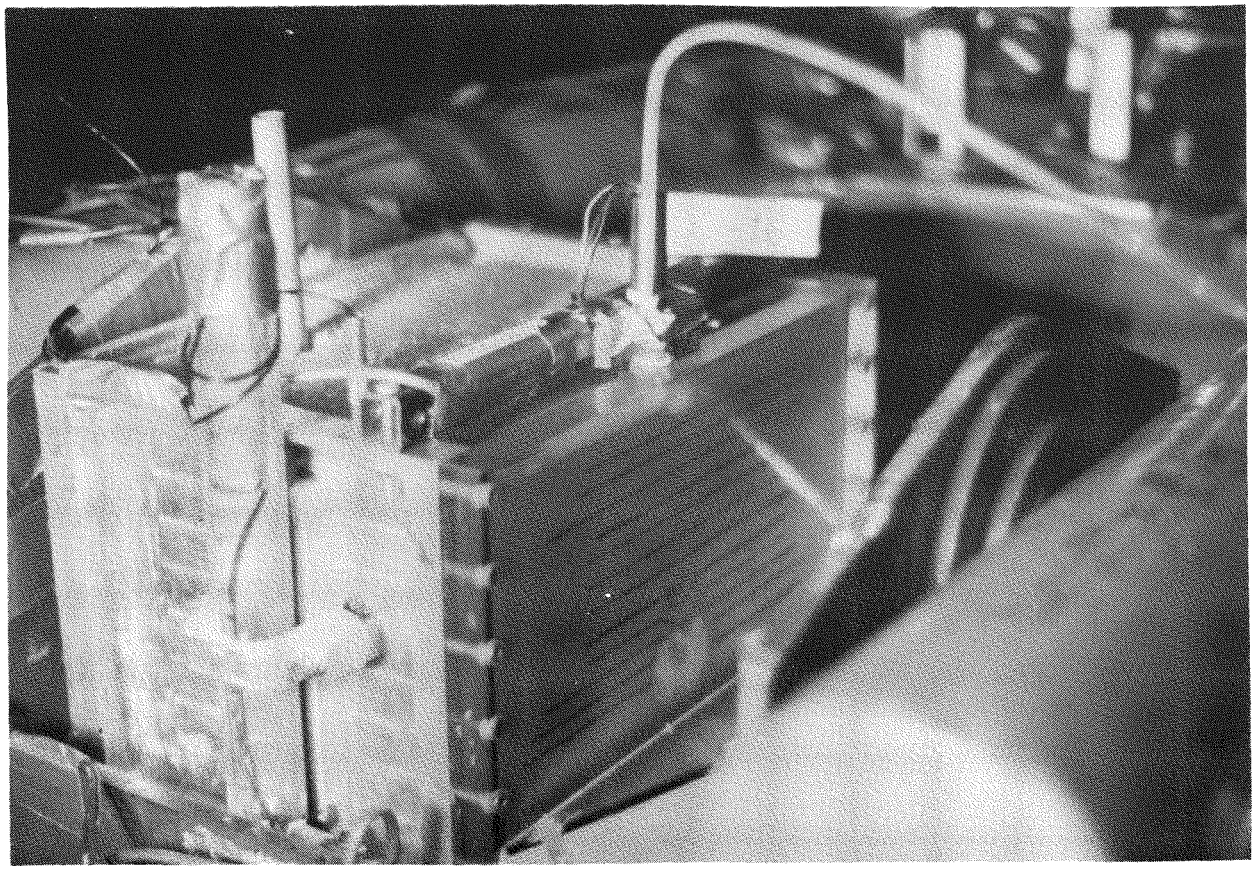

Figure 2. Test setup installed in the Schaevitz Centrifuge.

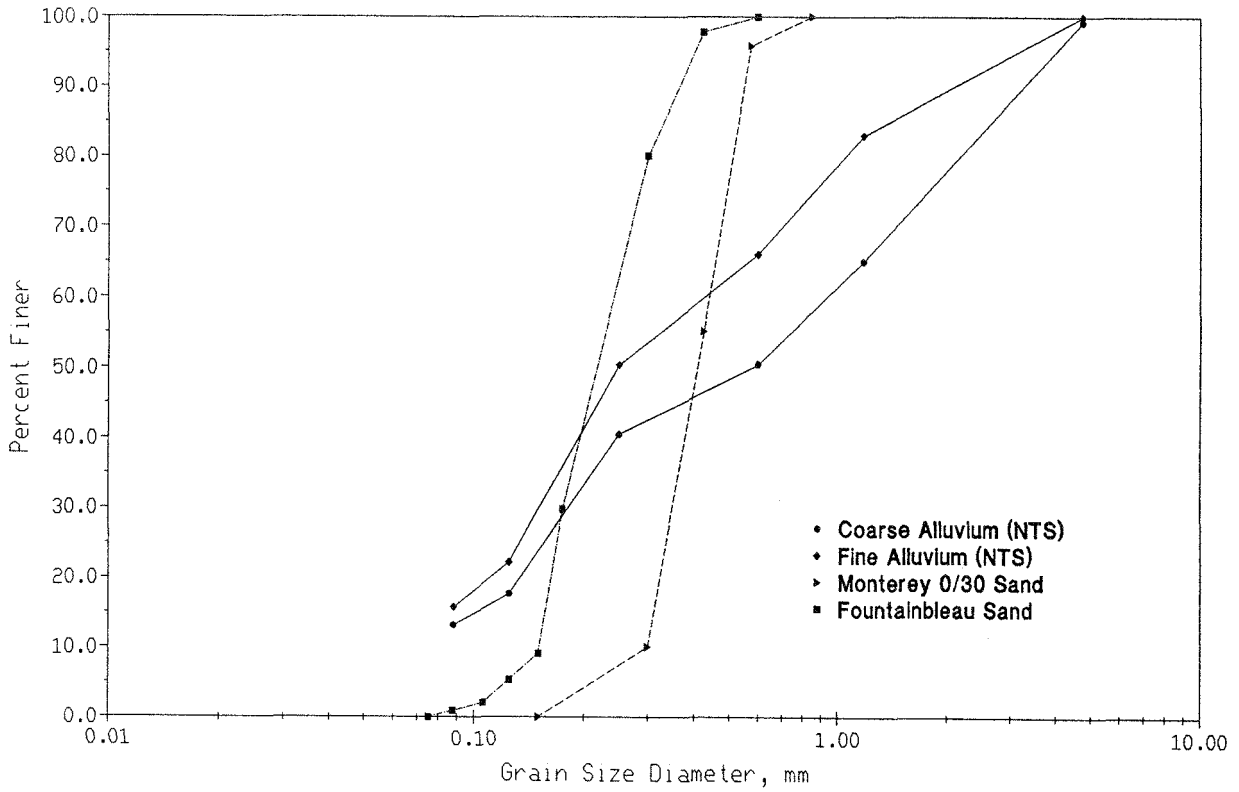

Figure 3. Grain size distribution of experimental soils.

Before the soil was placed in the model bucket, the model cavity (rubber bag) was installed either next to the Plexiglas window or centrally in the model bucket. A pluviator was then used to place the sand at a uniform density. Due to the gravel content of the NTS alluvium, a hand-pouring method was used for this material to avoid possible damage to the pluviator. The alluvium was poured from a height of about 10 in. from the top of the model bucket. When the model bucket was half full, it was vibrated at 65-68 Hz for 15 min and then the bucket was completely fill and vibrated again. In some tests (CC86-1 thru CC86-13 and also CC86-16 and -17 of Table 3) thin layers of an oil-based clay were used to indicate the deformation pattern. Colored alluvium was used for this purpose in tests CC86-14 and -15. While a line of lead shot was placed at 1 in. lift intervals in tests CC87-1 thru CC87-10. The lead shot allowed us to take radiograph pictures of the test prior to testing and after testing, and thus document the deformation.

During the spin of the centrifuge, for tests with hemispherical cavities (see Table 3) located against the Plexiglas window, the propagation of the chimney was monitored by a TV camera spinning with the sample bucket and aiming at the reflecting mirror placed in front of the Plexiglas window. In addition to the TV camera, pictures were taken by a 35-mm camera

Table 3. Summary of test conditions and crater data.

Test*	Test Descrip. Code**	Soil Density (pcf)	Centrifuge Acceleration (g)	Degree of Saturation (%)	Crater Vol. / Initial Cav. Vol.	Cavity Vol. Change / Initial Cav. Vol.
CC86-2	M3H2	107.4	76.5	0	.50	
CC86-3	M3H2	111.9	76.5	0	0.45	0.78
CC86-4	M6H2	111.7	82.8	0	0.24	0.58
CC86-5	M6H2	110.6	82.8	0	0.44	0.80
CC86-6	C6H2	96.7	82.8	0	0.35	0.72
CC86-7	C6H2	101.0	82.8	0	0.52	0.67
CC86-8	A6H1	99.0	82.8	0	0	0.97
CC86-9	A3H1	100.0	76.5	0	0	0.93
CC86-10	A6H2	100.3	38.2	0	0.26	0.93
CC86-11	C6H2	100.0	38.2	0	0.12	0.87
CC86-12	A3H1	102.4	76.5	0	0.24	0.71
CC86-13	A3H1	102.4	76.5	0	0.38	0.67
CC86-14	C6H2	96.8	38.3	0	0	0.44
CC86-15	C6H2	98.9	38.3	0	0.19	0.58
CC86-16	C6H2	109.9	38.3	48+	0	0.81
CC86-17	C6H2	124.1	38.3	100	0	0.87
CC87-3	M6H2	105.8	72	0	0	0.86
CC87-4	M6S2	105.6	36	0	0.36	0.95
CC87-5	M6H2	106.3	36	0	0.19	0.97
CC87-6	F6S2	102.3	36	0	0.50	0.98
CC87-8	F3S1	103.9	72	0	0.33	0.89
CC87-9	M3S1	109.2	72	0	0.13	0.92
CC87-10	M6S2	96.6	36	0	0.34	0.96

* Data lost on tests not listed

** Test description code: e.g.,

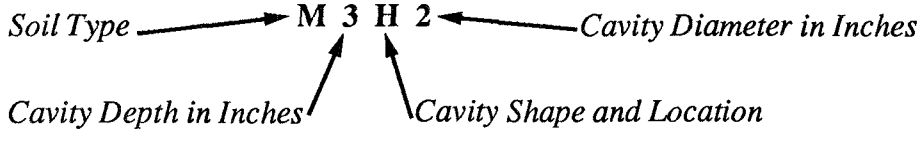

M = Monterey 0/30 sand
F = Fountainbleau sand
C = Coarse Alluvium
A = Fine Alluvium
H = Hemisperically placed against window
S = Spherical in middle of sample bucket

\+ This is an average degree of saturation. The water content actually increases with depth from about 8% to 14%.

mounted on top of the centrifuge. A synchronized strobe light provided the necessary light. In both the hemispherical and spherical cavity tests, the final configuration of the chimney was revealed by the x-ray radiograph pictures taken after each test. Comparison of the final radiograph to the initial radiograph allowed us to calculate the relative movement or flow of each one inch layer. The radiographs also indicated the shape of the collapsed model cavity.

MECHANISMS OF COLLAPSE

One advantage of centrifuge testing is the easy observation of deformation mechanisms. Figure 4 shows the gradual development of the collapse of a cavity as we have observed it in our testing. The collapse begins just above the cavity and the chimney gradually progresses upward as the cavity fluid is allowed to drain out of the model cavity. When the zone of collapsing soil reaches the surface, a crater begins to form. As the crater slopes approach the angle of repose, surrounding material begins to slide into the crater. Figure 5 shows the final shapes of chimneys determined from the x-ray radiography results for four different tests.

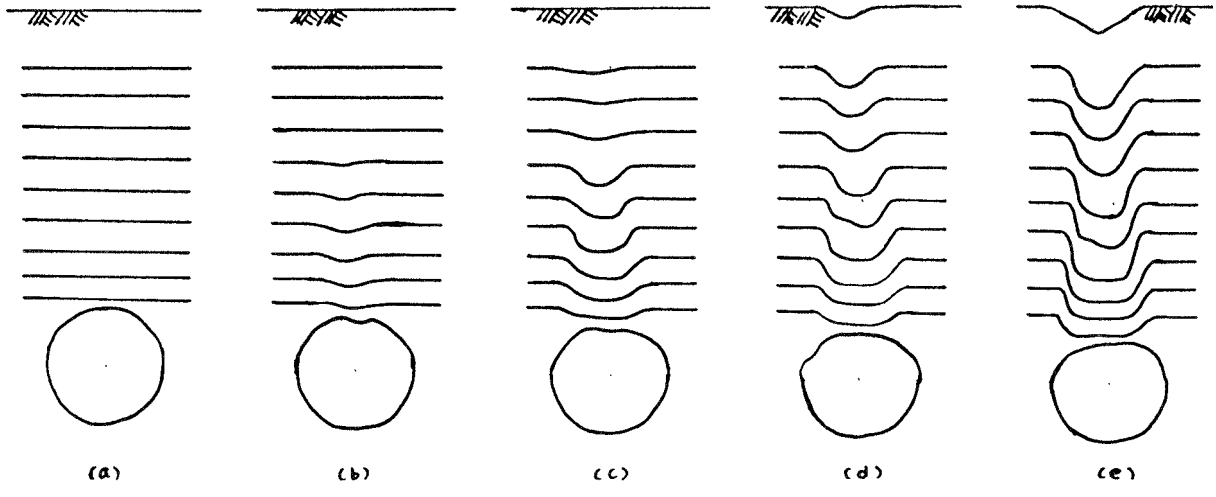

Figure 4. Propagation of a collapse chimney.

The four tests shown in Fig. 5 also demonstrate modeling of models. While the draw patterns for all the tests are similar, the crater volumes are smaller for the small diameter cavities. Further, the crater dimensions for the Fountainbleau sand are more accurately reproduced. It is these results coupled with the results from the previous year which suggest that there may be a grain size effect that increases as the particle size increases. The results of this years this years testing also confirmed the significance of the edge effects. The testing of hemispherical cavities against the observational window results in a restricted collapse process. The friction on the window produces incomplete collapse of the model cavity and reduced crater dimensions.

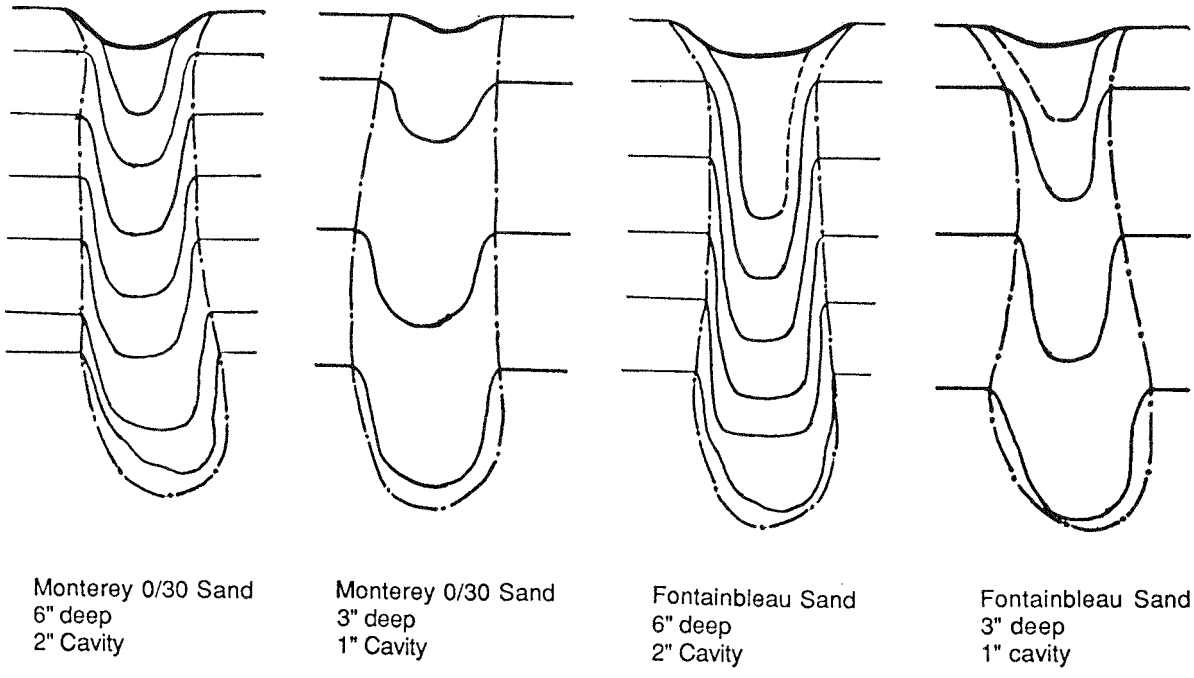

Figure 5. Chimney shapes, for four different tests, determined from x-ray radiography.

Figure 6 illustrates the relation between observed crater volume and the cavity volume change. Scale effects and experimental errors are magnified in this figure since crater volume is roughly proportional to the cube of the crater dimensions. We observed the following trends:

1) The collapse of larger model cavities (and hence lower scale factors) resulted in larger craters.
2) The collapse of hemispherical cavities at the Plexiglas window produced smaller craters due to edge effects.
3) The agreement in modeling of models tests was better for the finer sand (Fountainbleau) than for the coarser sand (Monterey 0/30).

Our results also show that the crater volume is less than the cavity volume change. This difference is explained by the dilation of the dense sand as it flows in to the collapsing cavity. This assumption of dilation is supported by Fig. 7.

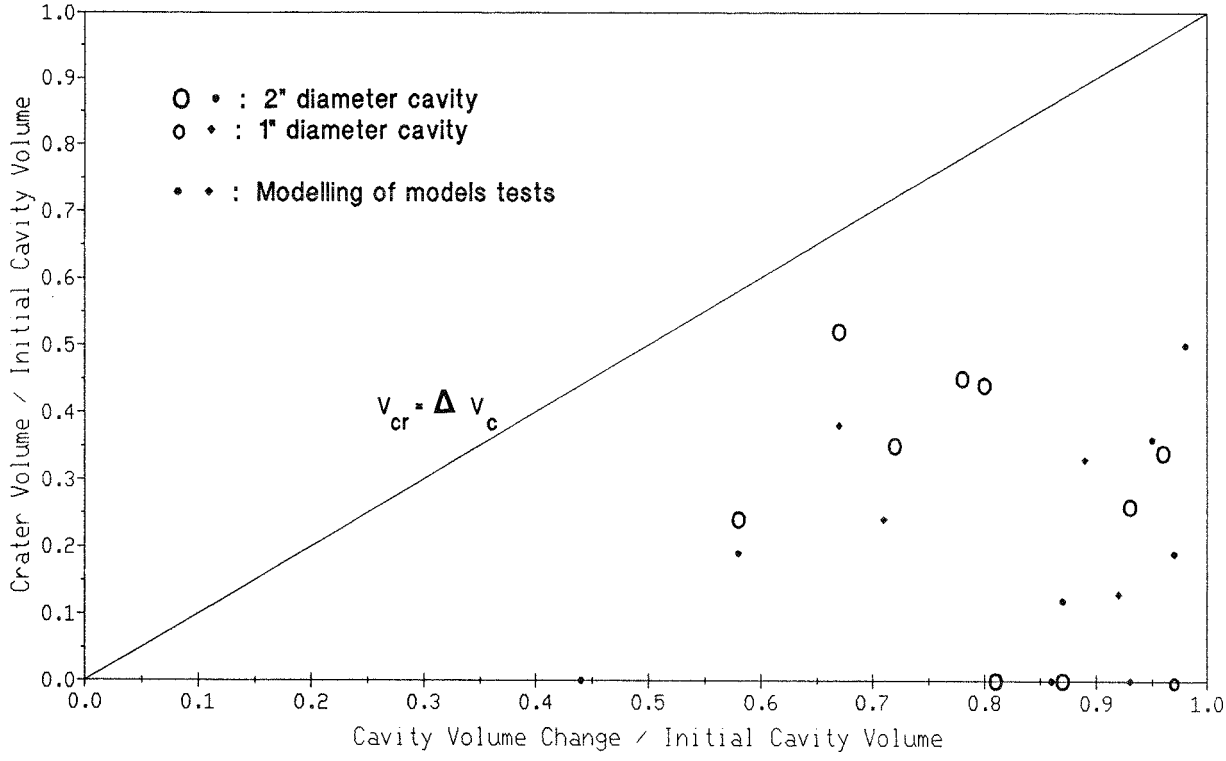

Figure 6. Crater volume vs change in cavity volume (normalized values).

Figure 6. Crater volume vs change in cavity volume (normalized values).

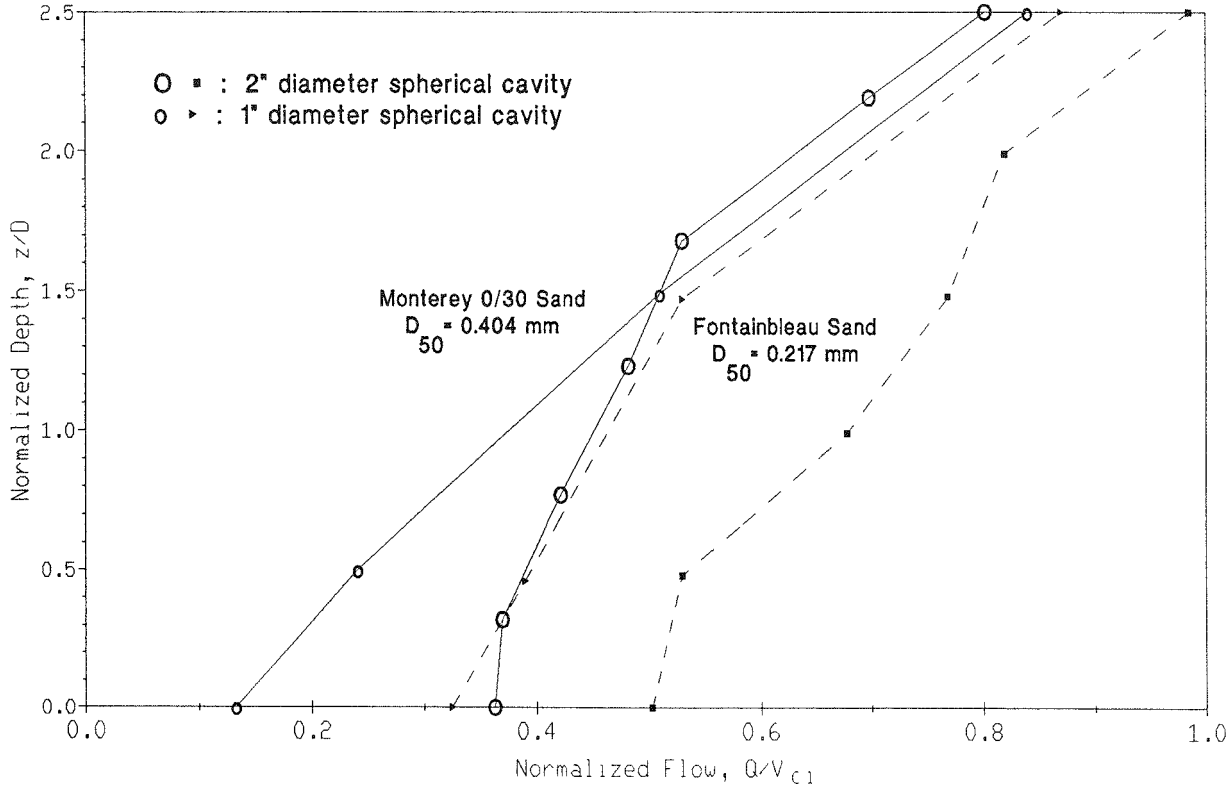

Figure 7. Sand flow vs depth (normalized values).

The four radiographs taken at the end of the spherical cavity tests were analyzed by calculating the volume of soil, Q, that flowed past the horizontal planes corresponding to the initial levels of lead shot. This was accomplished by assuming that the chimney was axisymmetric. The flow, Q, was then normalized by the initial cavity volume. The normalized flow is plotted as a function of depth (normalized). For incompressible soil, the relationship should be a vertical line. The reduction in volumetric flow of soil as elevation above the cavity increases is indicative of the dilation of the soil during the collapse process. We quantified the amount of dilation by assuming that the difference between the cavity volume change and the crater volume is caused by a uniform dilation of the soil in the collapse chimney. The collapse chimney was assumed to by cylindrical with an average diameter (measured from the radiographs) of 1.45 cavity diameters. The resulting average final relative density of the soil in the chimney after collapse is given in Table 4. The tests with spherical cavities in Monterey sand (tests CC87-4 and -9) produced chimneys with average relative densities of about 50% and the Fontainbleau chimney (tests CC87-6 and -8) had final relative densities of about 60% after the collapse. The tests with hemispherical cavities produced estimated relative densities significantly less that that for spherical cavities, but this may be an artifact due to the asymmetrical shape of the chimney due to edge effects.

Table 4. Summary of density changes due to soil dilation.

Test	Test Descrip. Code	Initial Density (pcf)	Vol. of Influenced Zone Before Test (in^3)	Vol. of Influenced Zone After Test (in^3)	Final Gross Density (pcf)	Density Decrease (%)
CC87-4	M6S2	105.6	13.93	16.40	89.7	15.1
CC87-6	F6S2	102.3	13.78	15.79	89.3	12.7
CC87-8	F3S1	103.9	1.48	1.78	86.8	16.5
CC87-9	M3S1	109.2	1.95	2.37	90.1	17.5
CC87-10	M6S2	96.6	20.50	23.16	85.6	11.4

The low relative densities reached during collapse of the chimney are probably a result of the soil approaching its critical density for the low confining pressures that are occurring in the chimney during collapse.

Relationship of Cavity Pressure to Volume Change

We have compared normalized pressure in the model cavity to normalized change in cavity volume (Figs. 8 and 9). The normalized cavity volume is simply the change in cavity volume (ΔV) divided by the initial cavity volume (V). The normalized pressure, which we interpret as a measure of the driving force causing collapse, was obtained by dividing the cavity pressure recorded by the overburden pressure at the midpoint of the cavity, using the equation

$$P^* = [P_{PT2} - N\gamma_w h] / N\gamma z \ , \qquad (4)$$

where P_{PT2} is the cavity pressure recorded by transducer PT2 (see Fig. 1), N is the centrifuge acceleration, γ_w is the unit weight of water at 1 g, h is the difference in radius between PT2 and the center of the cavity, γ is the unit weight of the soil, and z is the depth from the surface to the center of the cavity.

The five tests shown on Figs. 8 and 9 represented cavities with the same prototype diameter and depth. The results all follow a similar pattern, the tests all began with P* of approximately 1. When the cavity begins to drain, the cavity pressure rapidly drops to between 0 and 5% of the overburden pressure. Next the cavity pressure begins to rise to about 10 to 15% of the initial overburden pressure, and the cavity pressure eventually drops below zero. The negative pressure is an artifact of the subtraction. When the cavity is nearly collapsed there may in fact be no fluid in the center of the cavity, while the pressure at the bottom of the cavity is positive. If the positive pressure at the bottom of the cavity is less than the value of w, a negative cavity pressure is calculated. The hemispherical cavity had a distinctly lower cavity pressure than the spherical cavities, presumably due to edge effect. The results for 2-in. diameter cavities are expected to be more accurate since the volume change was 8 times larger than for the 1-in. diameter cavity.

The cavity pressure can be predicted by adapting the arching equations developed by Terzaghi (1943) [for a plane strain cavity] to axisymmetric conditions. This yields the following expression

$$P_c = \frac{D_p \gamma \left(1 - e^{-4 \tan \phi \, z_p / D_p}\right)}{4 \tan \phi} \qquad (5)$$

where P_c is the predicted cavity pressure, D_p is the cavity diameter corresponding to the prototype, z_p is the cavity burial depth corresponding to the prototype, ϕ is the friction angle, and γ is the soil density. The minimum cavity pressure is estimated by using the peak friction angle corresponding to the initial dense state. For he dense Monterey sand, the friction angle assumed for calculations is 38^0 (γ = 110 pcf). This results in a predicted normalized cavity pressure P* of 0.155 which compares to a measured normalized cavity pressure of 0.133 and 0.158 for tests on the 1-in. and 2-in. cavities respectively (see Fig. 8).

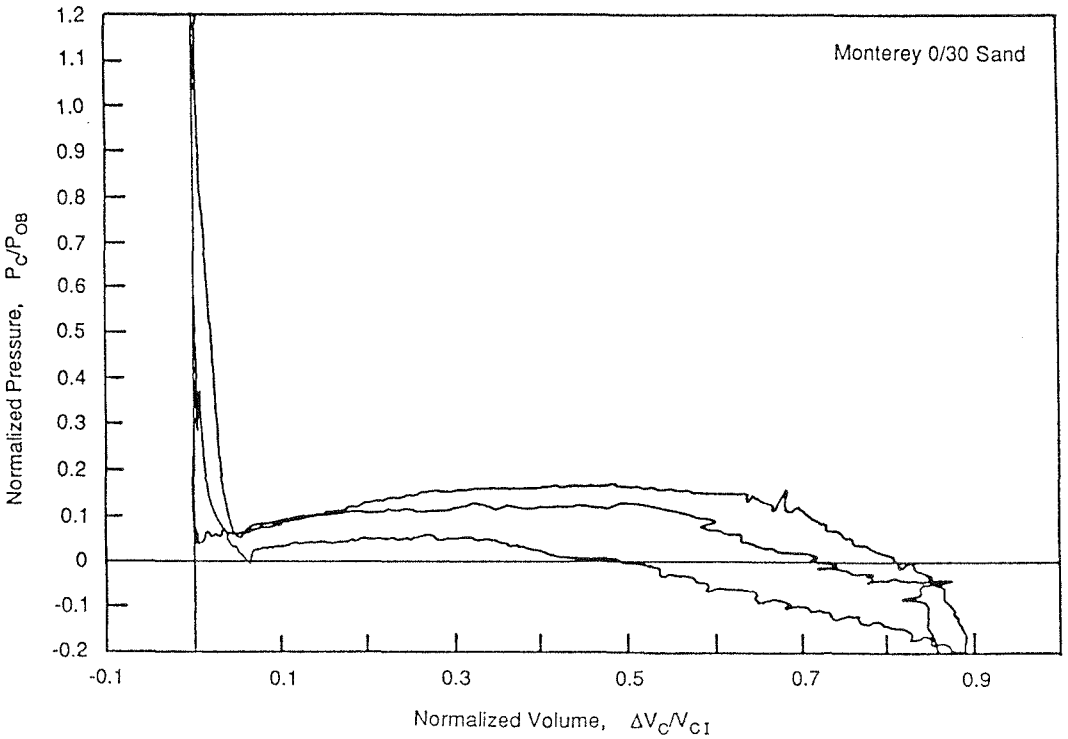

Figure 8. Cavity pressure vs change in cavity volume (normalized) for Monterey 0/30 Sand.

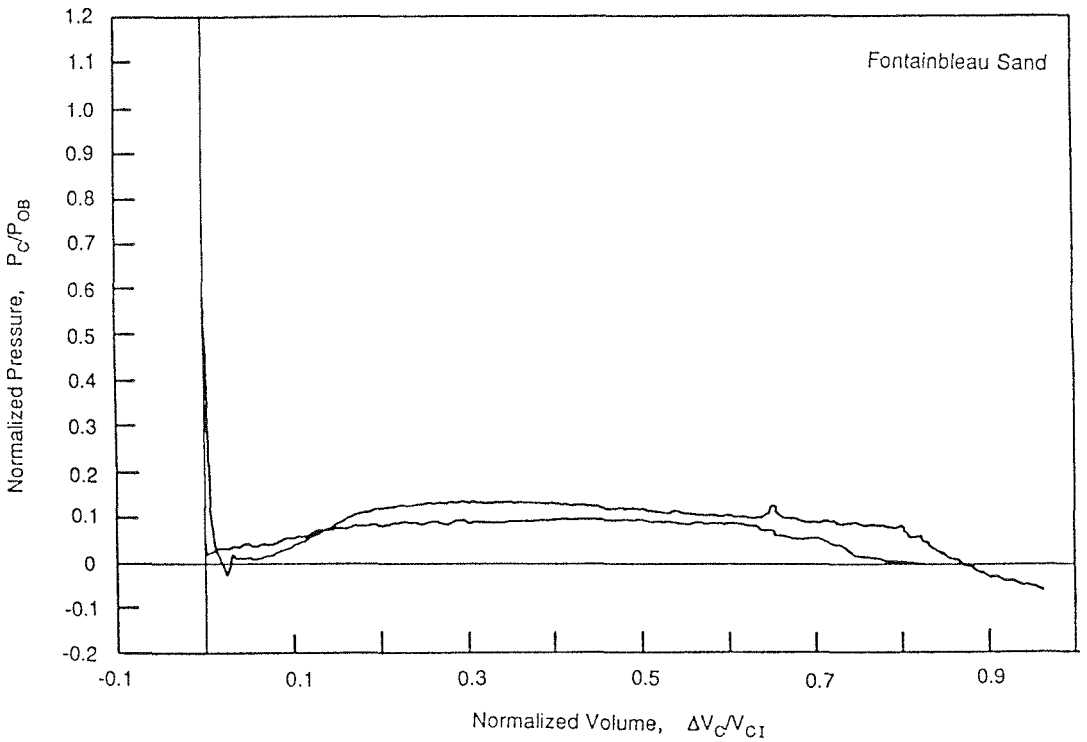

Figure 9. Cavity pressure vs change in cavity volume (normalized) for Fontainbleau Sand.

Since the soil dilates during collapse the friction angle of the soil reduces. Using a friction angle of 33^0 (γ = 90.5 pcf) for loose Monterey sand provides an estimated cavity pressure of P* of 0.153 which compares to the measured values of 0.133 and 0.158 for the 1-in. and 2-in. diameter cavities respectively.

CONCLUSIONS

Cavity collapse is related to studies of flow in bunkers or silos and sublevel caving except that the amount of flow is limited (ie, in the above examples material is removed at a draw point). In the cavity collapse problem volume of flow is limited to about D3 where D is the diameter of the chimney. We have devised a method for centrifugal gravity-scale modeling of the collapse of an underground opening. Our experiments have indicated that in flow problems, the critical dimensions are not necessarily the model dimensions but the dimensions of the chimney developed. Testing will continue so that we can quantify the grain size effect. Our objective is to continue to quantitative define the contribution of density and grain size to the dynamics of underground collapse. This will be done is conjuction with continued numerical modeling.

BIBLIOGRAPHY

Butkovich, T.R. (1976), "Cavities Produced by Underground Nuclear Explosions," Lawrence Livermore National Laboratory, Livermore, CA, UCRL-52097.

Hakala, W.W. (1970), "Subsidence Caused by an Underground Nuclear Nuclear Explosion," Proc. Sym. Eng. Nuclear Explo., Vol 2, 1428-1455, National Bureau of Standards, Springfield, Ill.

Janelid, I. and R. Krapil (1966), "Sublevel Caving," Int. J. Rock Mech. Min. Sci., 3:129-153.

Krapil, R.(1982), "The Mechanics and Design of Sublevel Caving Systems," W.A. Hustralid (ed.), *Underground Mining Methods Handbook*, 880-897, Society of Mining Engineers-AIME, New York.

Peter, D.C. (1984), "Physical Modeling of the Draw Behavior of Broken Rock in Caving," Colo. Sch. Min. Quart., 79(1).

Siskind, D.E., H.R. Hardy, Jr., and S.S. Alexander (1973), "A Study of Pressurized Underground Storage Cavities: Theoretical and Laboratory Investigations," Int. J. Rock Mech. Min. Sci. and Geomech. Abstr., 10:133-150.

Terzaghi, K. (1943), "Theoretical Soil Mechanics," 66-76, John Wiley and Sons, N.Y.

Thigpen, L. (1984), "On the Mechanics of Strata Collapse Above Underground Openings," Lawrence Livermore National Laboratory, Livermore, CA, UCID-20152.

Yenge, L.I. (1980), "Analysis of Bulk Flow of Materials Under Gravity Caving Process. Part 2: Theoretical and Physical Modeling of Gravity Flow of Broken Rock," Colo. Sch. Min. Quart., 76(3).

TRENDS IN CAVITY COLLAPSE DATA

Robert G. Deupree
Susan D. Noel
Clayton A. Watson

Los Alamos National Laboratory

ABSTRACT

Los Alamos National Laboratory has now measured the dynamics of cavity collapse using time domain reflectometry on over thirty Los Alamos nuclear weapons tests. A new system which greatly facilitates the collection and storage of this data is described. We have studied this collection of data and have been able to form a few conclusions: 1) the average rate of fall varies from 5 to 95 m/s, but most events fell into a group with average fall rates between 20 and 50 m/s, 2) the rate of fall generally increases toward the surface, and 3) the final (i.e., post-surface collapse) crush of the cable is generally located 25 – 100 m to the surface, suggesting that the material located above this depth tends to fall as a block. This depth may be location dependent. While these general trends are present, it should be noted that at least one counter example can be found for nearly every conclusion.

I. INTRODUCTION

The cliper concept was developed by Clyde Sisemore at Lawrence Livermore National Laboratory in the mid 1960's (Sisemore and Stefani 1971). The concept uses time domain reflectometry, which sends a pulse down a coaxial cable and waits for a reflected pulse to return. By knowing the time required for a pulse to travel down the cable and return and the velocity of an electrical pulse in the cable, one can determine the physical length of the cable and thus the location of its end. During cavity collapse it is presumed that the cable is continually broken as the collapse occurs, so that the physical length of the cable is continually shortened.

The actual picture appears to be not quite so simple, as the cable appears to break discreetly rather than continually. An example is shown in Figure 1, a plot of the depth below the surface of the end of the cable versus time. The solid line provides the point to point connection, while the dashed line gives our picture of how the collapse may actually be taking place. It should be remembered that such interpretation is involved in our future discussion of the collapse process.

Over the past year we have made the collection, retrieval, and analysis of data considerably less personnel intensive. A few years ago raw data was printed exclusively on paper. Recently,

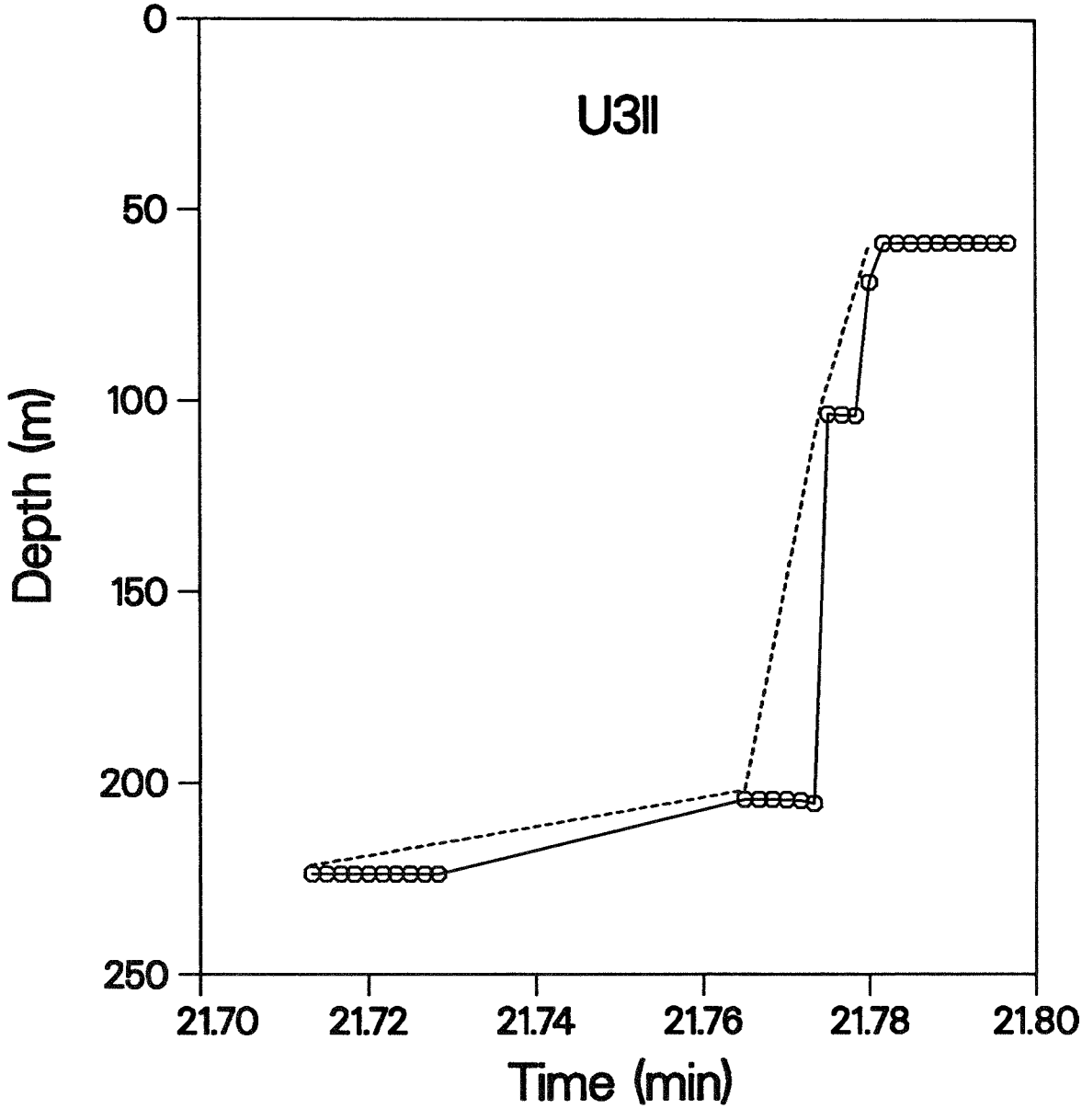

Fig. 1 - Plot of depth beneath SGZ versus time from detonation. The circles represent EXCOR data, which are connected by the solid lines. The dashed line gives our picture of how the cavity collapse might actually occur (Section II).

EG&G Los Alamos Operations developed for both Los Alamos and Livermore National Laboratories the EXCOR box which is a microprocessor controlled time domain reflectometer. We have developed menu driven software on a MicroVax which allows us to interact with the EXCOR microprocessor from a terminal in the Los Alamos Monitor Room in CP-1. From this location we can arm the EXCOR box, perform calibration sequences, retrieve, reduce, and plot data, write data files, and terminate data acquisition. Complete details of this system, which has been successfully employed on all Los Alamos FY87 tests, are given by Watson (1987). With this software all data retrieval and analysis can be completed within roughly ten minutes of collapse. This new real time capability is important as it provides more complete information to the Test Controller and Test Director for scheduling their post-shot activities. Transmission of the data to the GEODES database (Winterkamp, et. al. 1985) is currently performed by tape, but in the future will be done by a link between Los Alamos and the Monitor Room. Both current and proposed configurations are shown in Figure 2. The future configuration would allow all operations except supplying power and cable to the MicroVax and EXCOR to be performed from Los Alamos. Both raw and reduced data are stored in GEODES, where they are accessed through software using the FORTRAN interface and data reduction parameters for analysis.

At the time of writing this paper, we currently have cavity collapse data for 34 Los Alamos nuclear weapons test. The hole designations are listed in Table I, for which we have: 28 collapses to the surface, five (U4i, U4o, U19ae, U19ak, U19ar) subsurface collapses, and one (U19ad) for which no collapse occurred.

Table I: Holes in the Database

U19ad	U19ae	U19ak	U19ar	U3kk	U3la	U3lc
U3ld	U3lh	U3lj	U3ll	U3lm	U3lo	U3ls
U3lt	U3lv	U3lw	U3lz	U3me	U3mg	U4i
U4j	U4o	U4p	U4t	U6d	U7ao	U7bd
U7bh	U7bl	U7bo	U7bp	U7bu	U7bv	

We now turn to a discussion of the properties of cavity collapse. We shall first discuss the average rate of fall and then examine the variation in fall rates within a given hole. Another property we will explore is the final depth that EXCOR records. This can be well under the surface, even for surface collapses because the last section of collapse does not break the cable, but rather pulls the cable with the material as it falls. We conclude with some comments on the generality of our results.

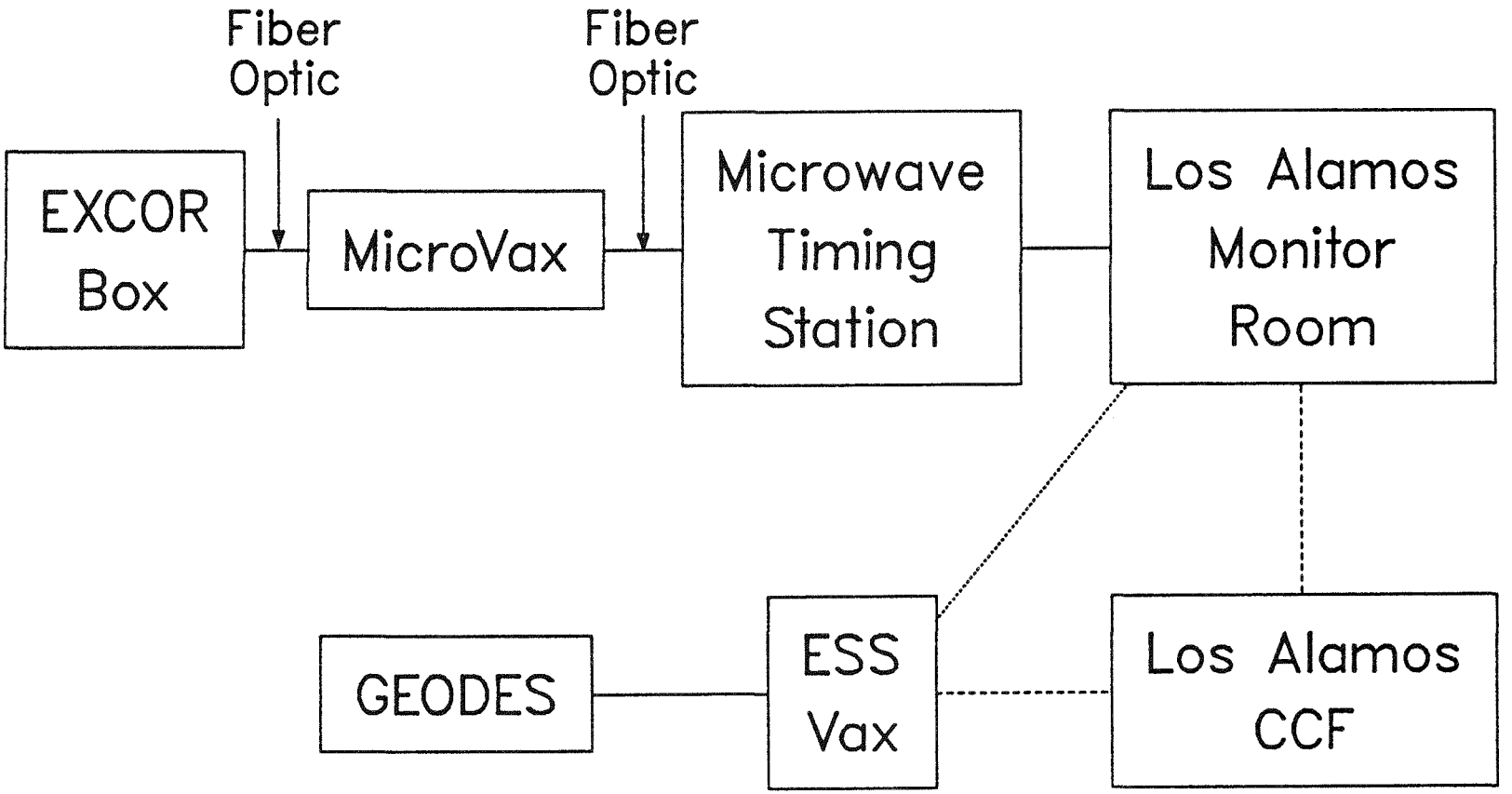

Fig. 2 - Block diagram represents the components of the current data acquisition system. The dashed lines donate the links that are not complete, and the dotted line a "foot link" that is currently employed.

II. COLLAPSE VELOCITIES

We have computed collapse velocities for 33 of the 34 events in the database. The omission is U19ad, for which no post-shot cable shortening occurred during the roughly four days of monitoring. The monitoring was terminated when it was time to remove the trailer to another event.

The method of calculation of the velocities is outlined with respect to Figure 1. The velocities are the slopes of the dashed lines, with the average taken as the slope of a line which begins at the point where the first dashed line begins and ends as the final point of the last dashed line. One should note that the initial cavity collapse information comes neither from the working point nor the cavity radius, but where the ground shock ceased to crush the cable.

We present a histogram of these average velocities in Figure 3. While there is clearly a wide range of average velocities, there is a clear concentration (half the sample) at velocities in the range 20-50 m/s. There are also some interesting associations for those events outside this central clump. Two of the three Area 19 events (U19ar and U19ak) are among the five with average velocities less than 20 m/s. A third member of this group, U6d, is our sole representative of a staged collapse, to which we shall return in Section IV. Of the eight events with average velocities greater than 60 m/s, six of them (U7bl, U3me, U3la, U7bp, U7bo, and U4j) have depths of burial greater than 500 m. However, there are many neighboring deeply buried events whose average velocities are not extraordinary. The only plausible explanation we have for the preponderance of deeply buried events with higher average velocities is the fact that the velocity appears to increase with time during the collapse, to which we now turn.

The method by which we have chosen to examine velocity variations within an event may be explained again with reference to Figure 1. We consider each dashed line as a time interval over which a velocity can be measured. We then compute the ratio of the velocity in each time interval to the velocity of the first time interval. We have subdivided the holes by NTS area and present these ratios in Figures 4-8. The impression these figures provide is one of chaos, but it is clear that there are many more points whose value exceeds one (indicating an accelerating rate of collapse) than not. While it may be possible to assign a physical meaning to this, we do not care, with this data, to go beyond noting the general trend.

III. THE FINAL RECORDED DEPTH

We have been able to understand how the collapse near the surface occurs from a feature built into data acquisition software. As the geophone activity picked up on the TORNERO event, Deupree sent the command asking how many data points had been collected. The answer was 40 data points.

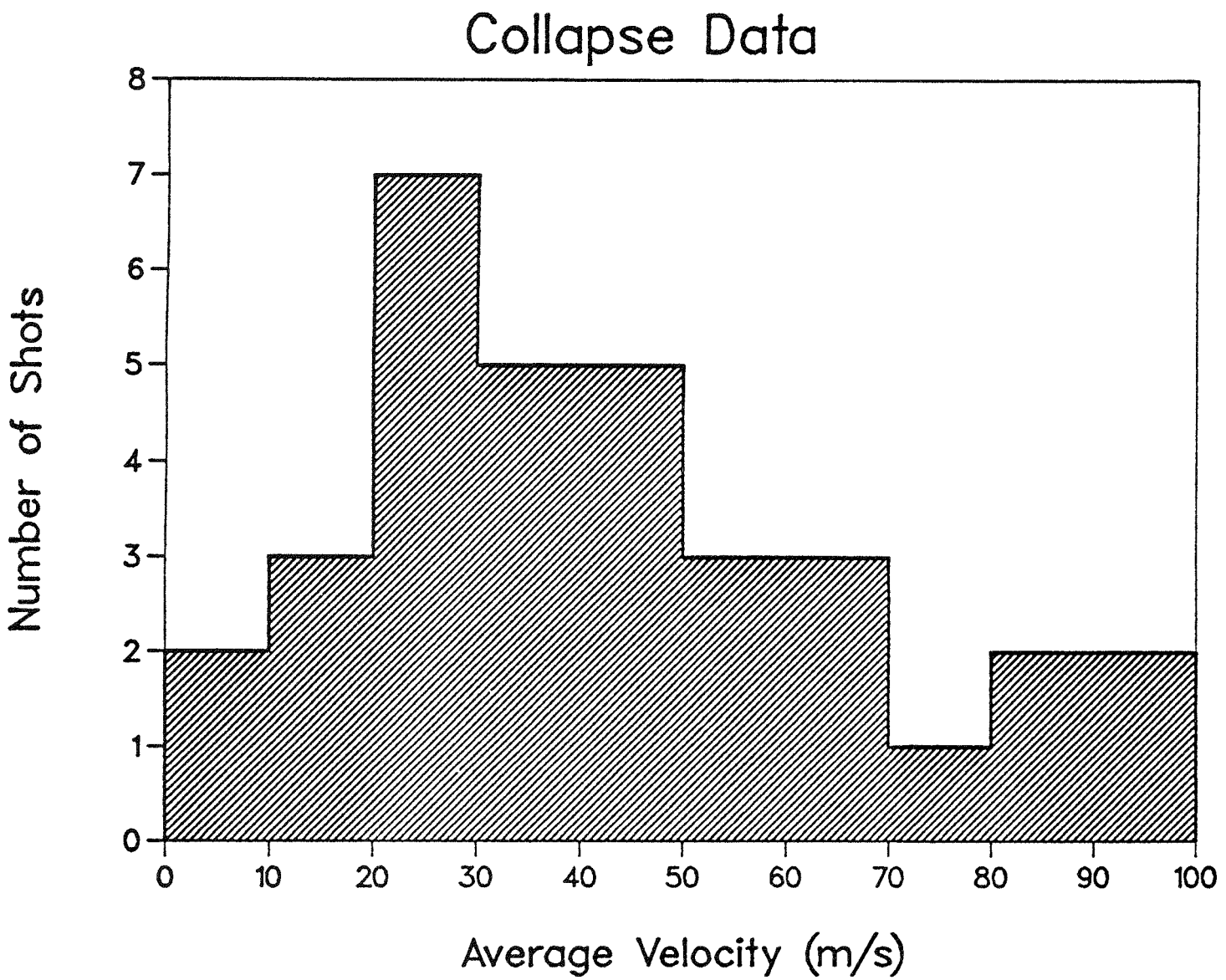

Fig. 3 - Distribution of the average collapse velocity.

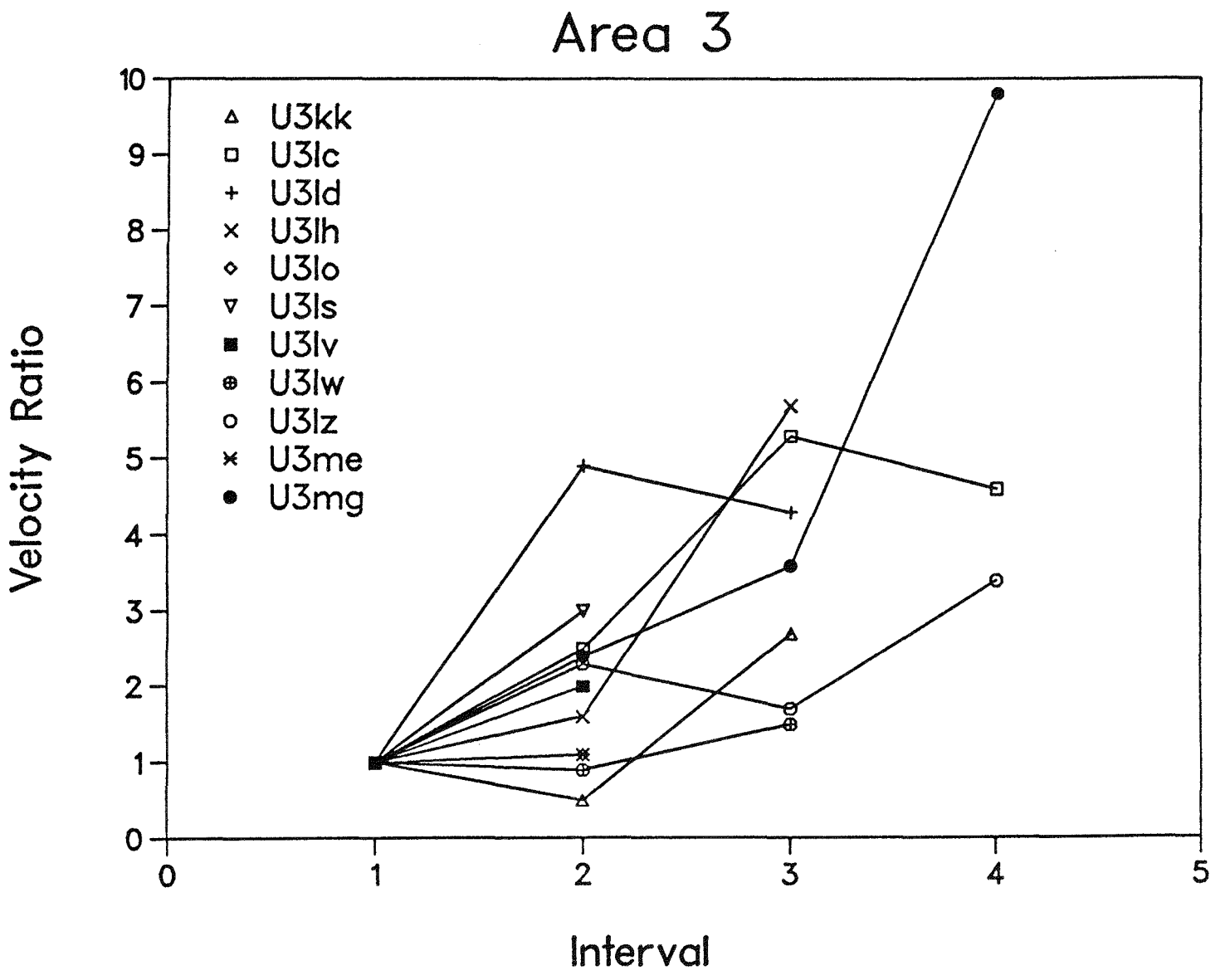

Fig. 4 - Ratio of the velocity in each interval during the collapse to that of the first interval for events in Area 3.

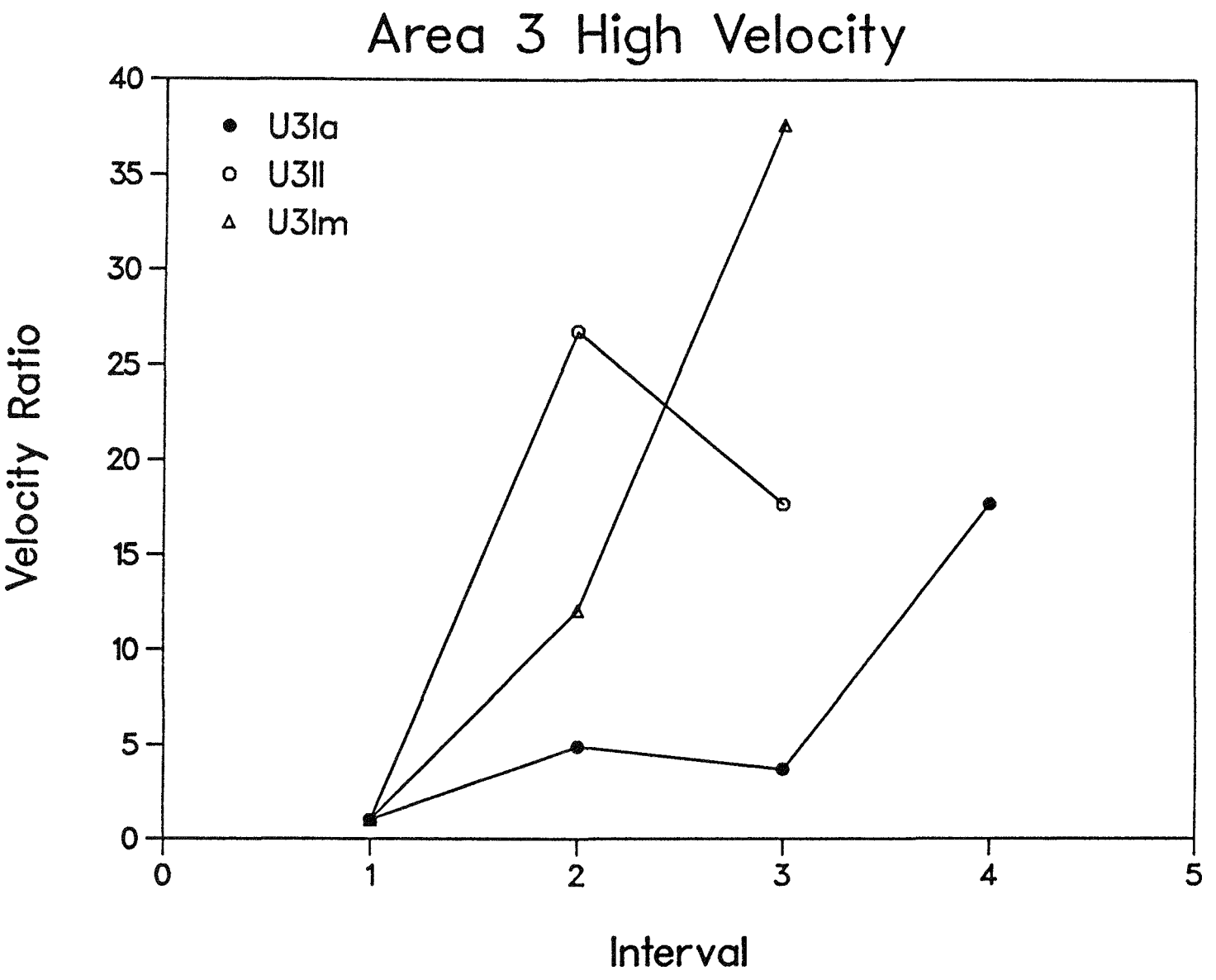

Fig. 5 - Same as in Fig. 4 for other events in Area 3.

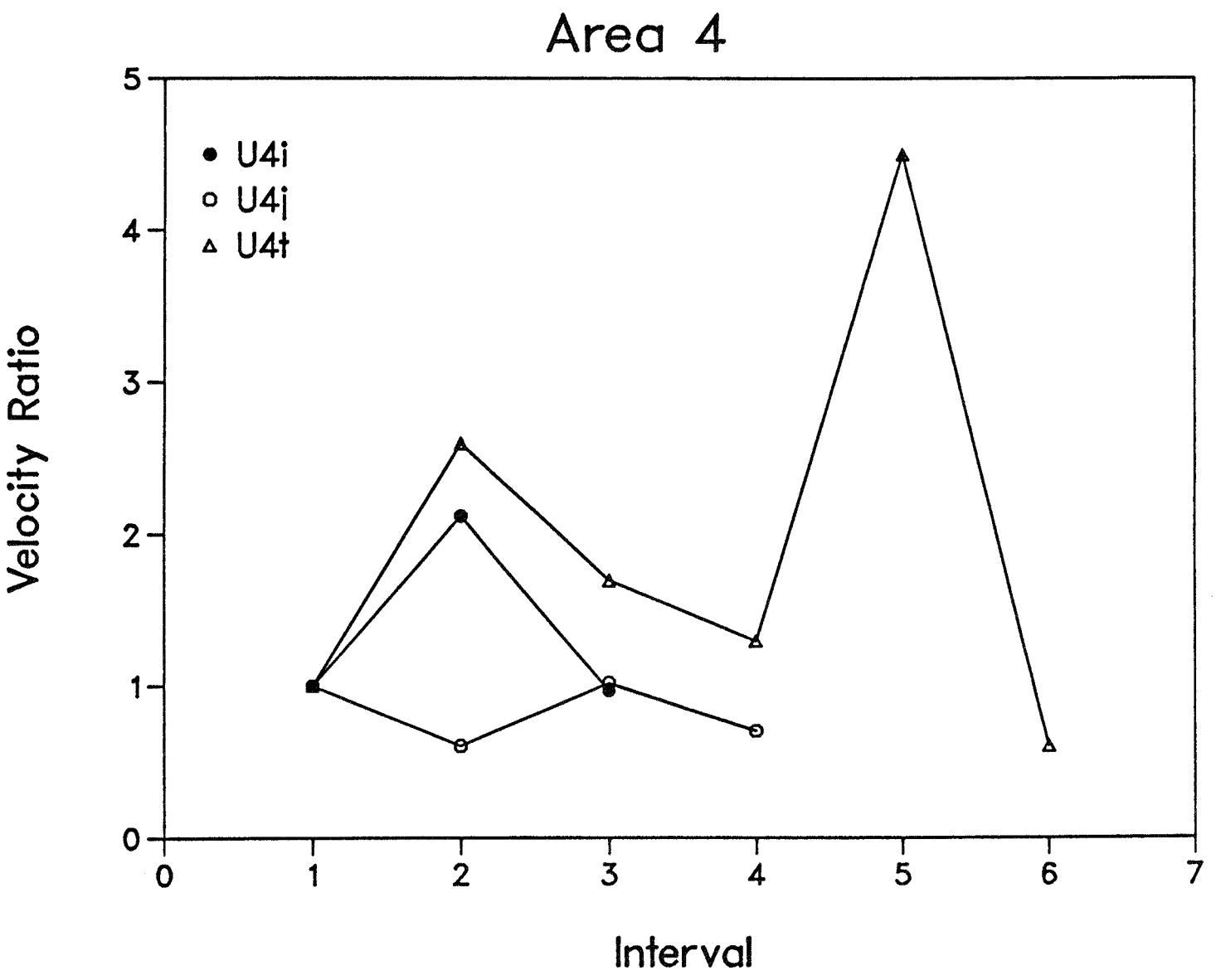

Fig. 6 - Same as in Fig. 4 for events in Area 4.

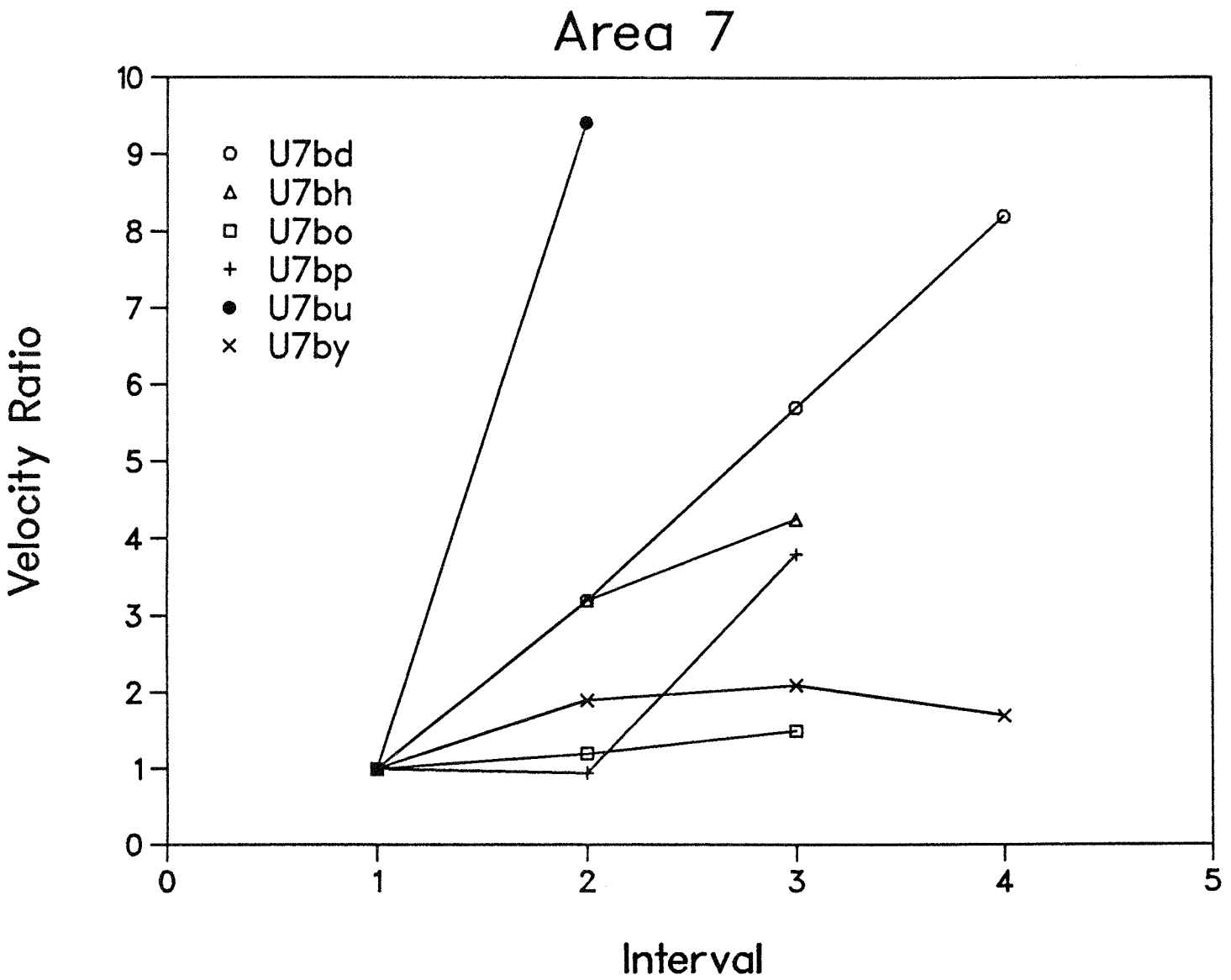

Fig. 7 - Same as in Fig. 4 for events in Area 7.

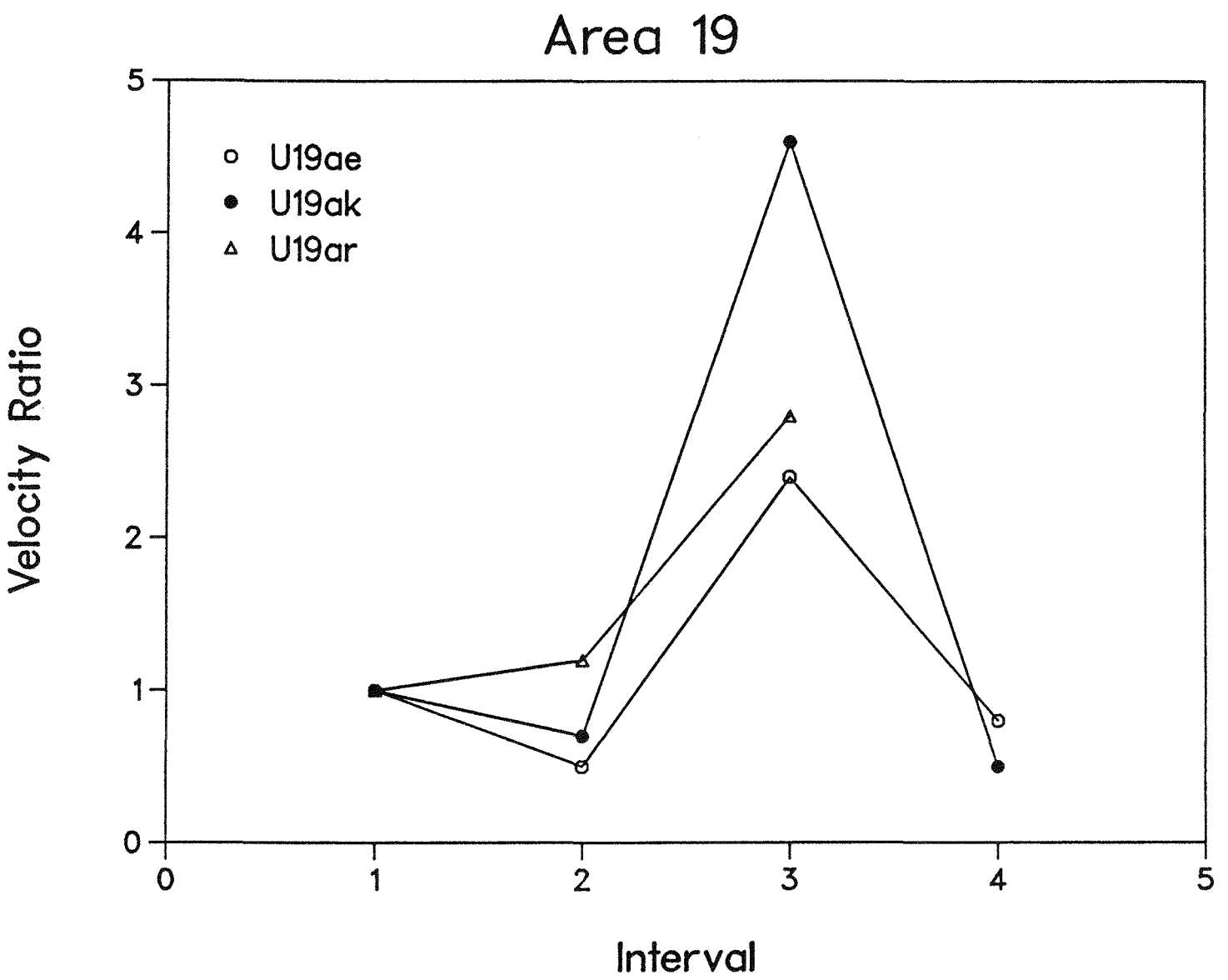

Fig. 8 - Same as in Fig. 4 for events in Area 19.

After the answer was received, he looked at the television monitor just in time to see the surface start to fall. A second query after this revealed that still 40 datapoints had been recorded. This lends support to our contention that this last fall to the surface occurs as a block (otherwise it would break the cable) and that it is in some sense distinct from the previous collapse.

A histogram of the final depth measurement recorded is presented in Figure 9. The five events that did not collapse to the surface (three in Area 19) are clearly discernable. The other two events were overburied. The event with a final depth at 145 m, U7by, had a surface casing to that depth, which indicates that a surface casing may help isolate at least that material inside the original hole from the collapse. In none of the other holes with values of the ending depth greater than 75m is this the cause. However, it may explain why the majority of holes fall in the 25-50 m interval, since many of Los Alamos surface casings are 37 m deep. It is interesting to note that, with the exception of U7by, whose value originates from a different cause, all the events with ending depths greater than 75 m fall in a line along the Area 4 - Area 7 and Area 1 - Area 3 boundary. This is shown in Figure 10. Other events with shallower ending depths also fall along this line, so that it is not clear what can be deduced from this. More events may confirm or deny this trend.

IV. DISCUSSION

We have tried to identify general trends in the data for the 34 events that we have. This is complicated by the fact that nearly every trend also has at least one counter example. Some of these, such as U7by in the previous section, can be explained, but others remain mysterious.

One of the most interesting anomalies is U6d, the only event in our sample to show a staged collapse. The data is shown in Figure 11. It is in this case that the correlation between cable crush and actual fall of material is most uncertain. An example is that the last recorded crush of the cable was not accompanied by any geophone activity, and that some recording cables survived even longer. If we suspect a staged collapse in the future, we may have to pay more attention to how these particular cables fit in the cable bundle.

We have found some trends in the limited amount of data we have so far obtained. We hope that, in addition to being able to supply our containment scientists with real time information about the collapse, we will be able to explore these trends more fully as we collect more data.

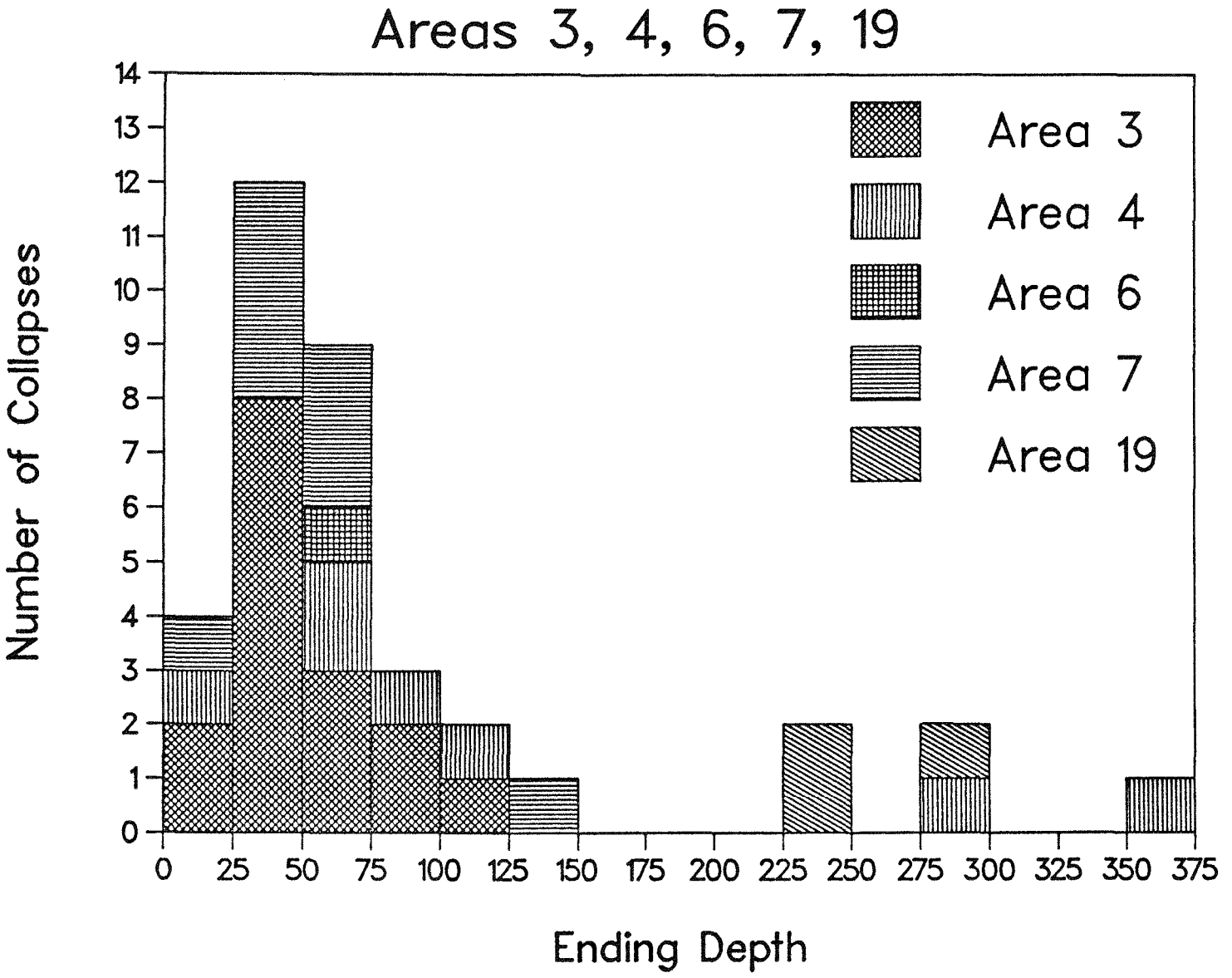

Fig. 9 - Distribution of the final EXCOR depth.

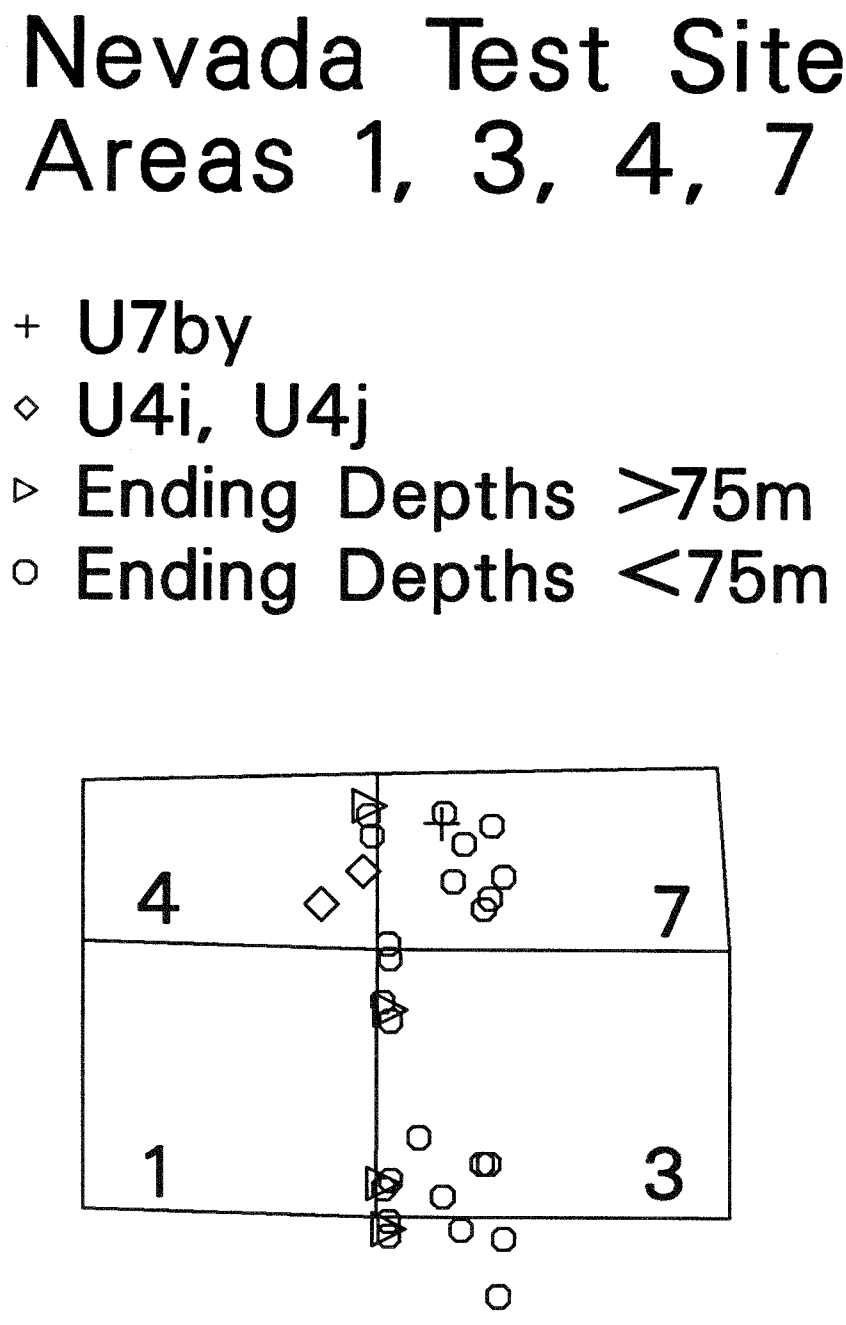

Fig. 10 - Locations of events with various ending EXCOR depths. See text for explanation.

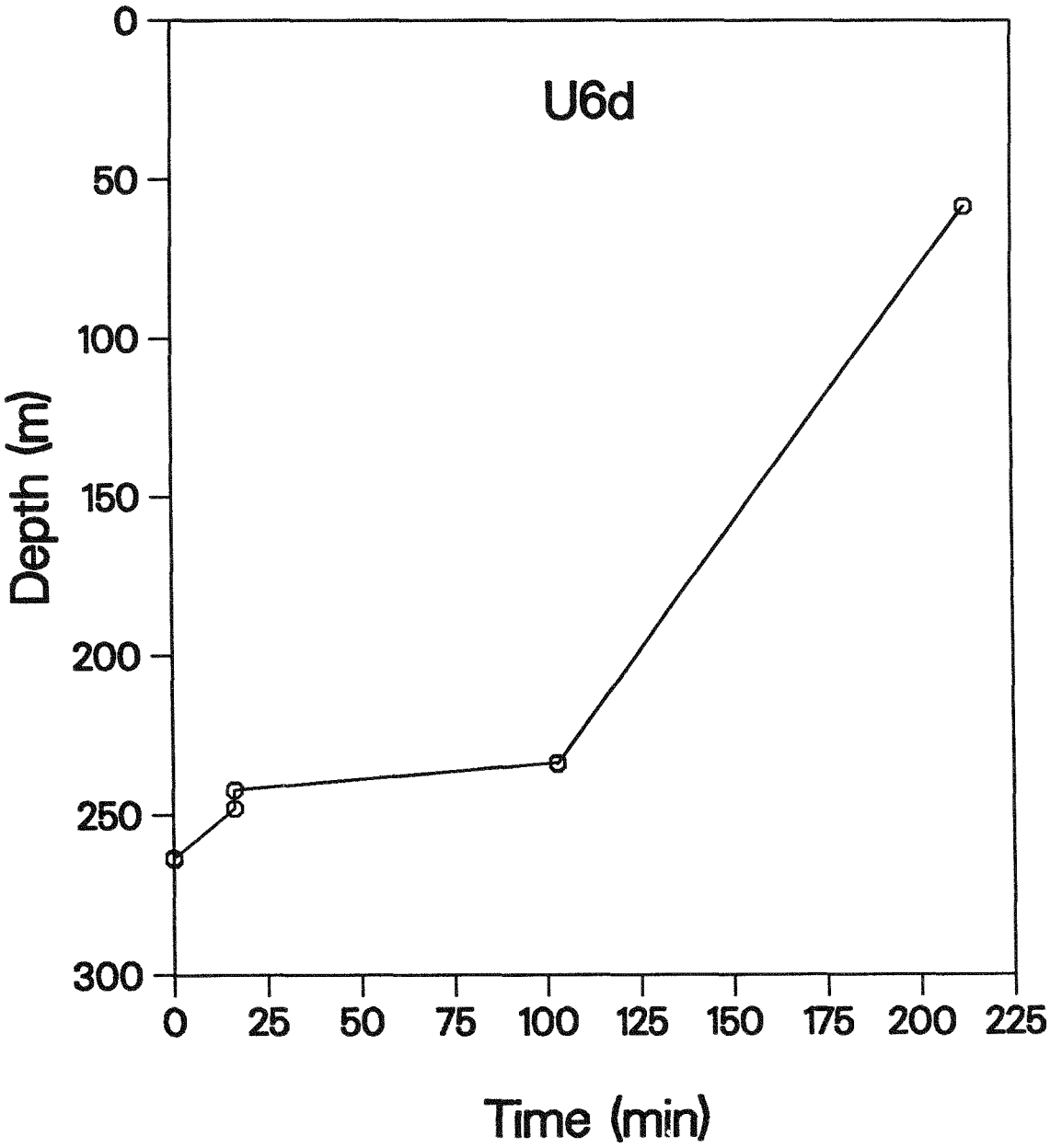

Fig. 11 - Collapse data for U6d.

V. ACKNOWLEDGEMENTS

It is a pleasure to thank Don Eilers, Stuart Flicker, Jack House, Michael O'Conner, Connon Odom, Jake Perea, Denis Whann, and the Los Alamos J-Division Office, especially Tom Scolman and Walt Wolff, for their assistance and cooperation. This work has been supported by the United States Department of Energy.

REFERENCES

Sisemore, C. J. and Stefani, R. E. 1971, "Rock Fracture Measurements". A New Use for Time Domain Reflectometry," Journal of Applied Physics, 42, 2701.

Winterkamp, J. L., Neergaard, J. R., Mills, C. F., and Watson, C. A. 1985, "GEoscience Data Evaluation System", Proceedings of the Third Symposium on Containment of Underground Explosions, 2, 141.

Watson, C. A. 1987, "The Cliper Data Acquisition System, "Los Alamos Report, LA-11059-MS.

PHOTOGRAMMETRIC METHOD FOR DETERMINING SINK VOLUMES AT THE NEVADA TEST SITE

GARCIA, M.N., U.S. Geological Survey, Box 25046, MS 913, Federal Center, Denver, CO 80225

ABSTRACT

A procedure has been developed that utilizes a computer-assisted PG-2 photogrammetric plotter to measure the volumes of sinks formed following detonation of underground nuclear devices. Volumes determined by this procedure are more precise than those measured in the field. A detailed field measurement of the sink cannot be made because of possible hazards, thus, the few measurements commonly simplify the sink dimensions and ignore the sag zone, the area of minor subsidence just beyond the sink's perimeter. This sag zone commonly accounts for 5-20 percent of the sink's total volume and must be included in the final volume measurement. Field measurements are also time consuming and may not be recorded until days or weeks after surface collapse. As the photogrammetric procedure relies on photographs taken as soon as possible after collapse, and because the dimensions of the sink, including the sag zone, can be measured more precisely, a better interpretation of the effects of the explosion can be made.

INTRODUCTION

Since 1962 approximately 550 announced nuclear tests have been conducted below the surface of the Nevada Test Site (NTS) (fig. 1). Approximately 80 percent of these tests have a related ground surface collapse commonly called a sink (Houser and Eckel, 1962). The formation of a sink helps contain the radioactive gases generated after a subsurface nuclear explosion. Few of these sinks have the appearance of a perfect circle centered on surface ground zero. The sinks formed on the NTS range from deep, steep-sided, "cookie-cutters" to shallow, broadsided, inverse cones. The dimensions of the sinks in Yucca Flat range from 3 to 345 meters in radius and 0.6 to 60 meters in depth. The larger sinks have volumes approaching 21 million cubic meters.

Houser recognized five distinct morphological zones observed in most of the sinks (fig. 2). Zone 1, the central part of the sink where the greatest amount of subsidence occurs, to Zone 5, where no obvious deformation occurs (Houser, 1970). The sinks can be further systematically classified based on similarities between depth of emplacement and yield of the explosion, and characteristics of the testing medium (T.D. Kunkle, Los Alamos National Laboratory, written commun., 1984). Recognizing the characteristics of each sink and accurately measuring the dimensions, particularly volumes, are important, because phenomenological information associated with the nuclear explosion can be derived from these observations and measurements.

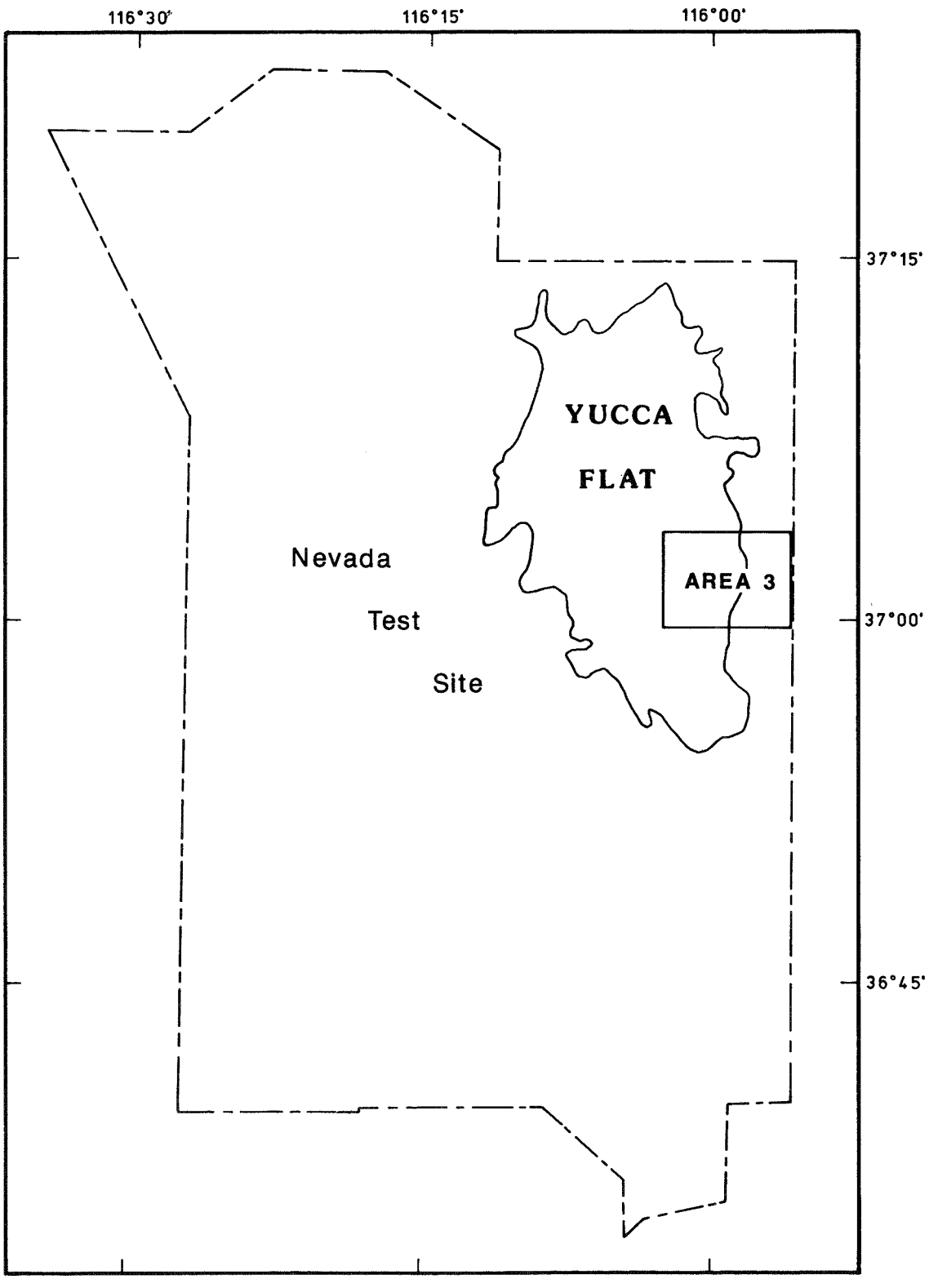

Figure 1.--Index map of the Nevada Test Site, showing Yucca Flat and the boundaries of Area 3.

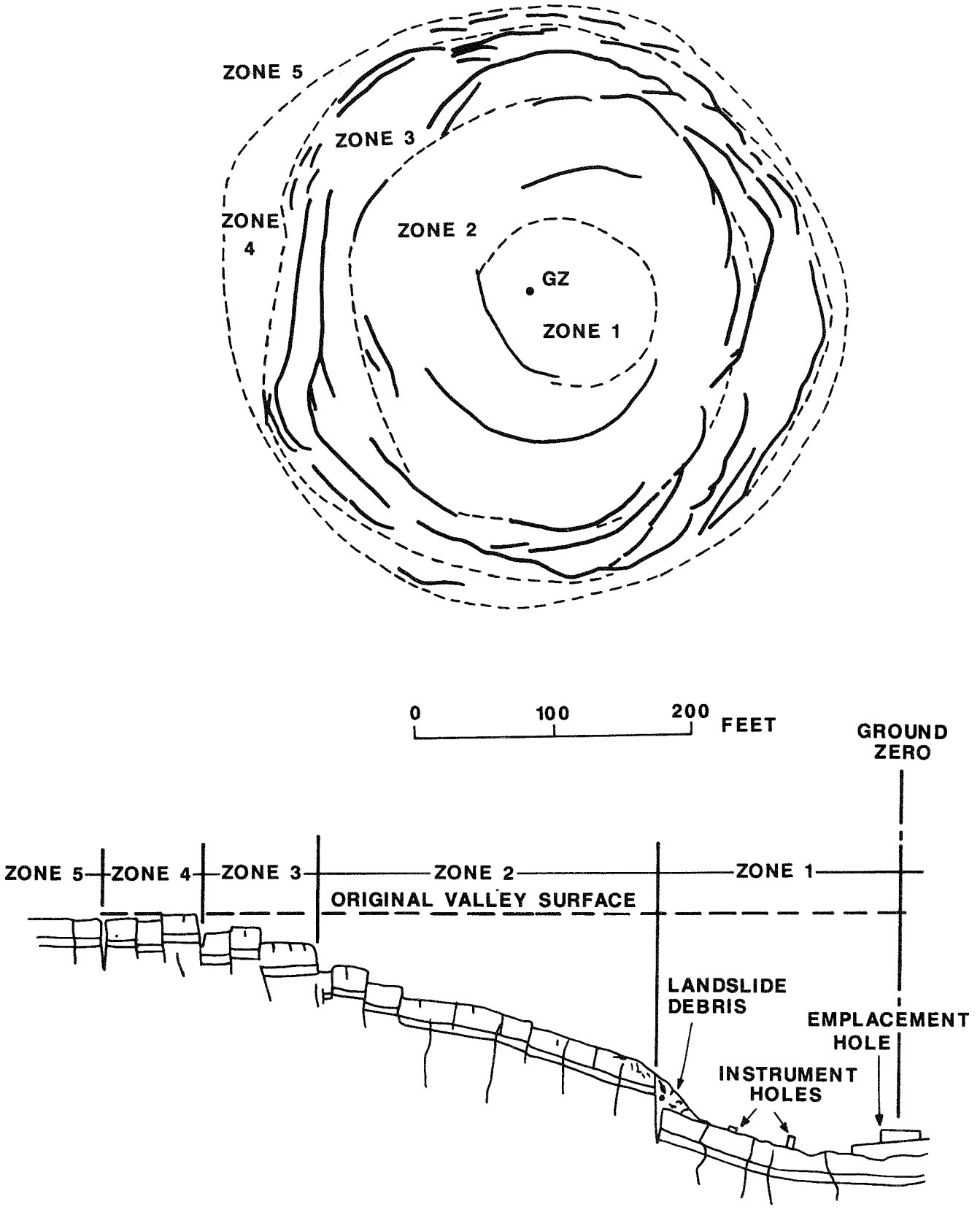

Figure 2.--Generalized view and section of morphologic zones of a typical sink in Area 3, Yucca Flat, NTS (modified from Houser, 1970).

MEASUREMENT OF SINK VOLUMES

However field measurements of the sinks are made, safety restrictions at the NTS restrict field mappers from entering the sinks. Thus, precise ground surface measurement cannot be made, and the sink dimensions are often oversimplified (fig. 3). Additionally, the peripheral sag zone associated with subsidence, or Houser's Zone 4 (fig. 2), is commonly left unmeasured. Houser (1970) indicates that Zone 4 is not only an integral part of the subsidence process, but may be a truer reflection of the degree of subsidence than the topographic sink edge. The calculated volume from this sag zone accounts for 5-20 percent of the total volume of the sink.

Before 1970, sink volumes were determined photogrammetrically, but volume measurements were in error because they assumed a conical sink (Jones, 1979). With the advances in photogrammetric technology, a procedure has been developed to precisely map sink dimensions. The procedure utilizes the Computer-assisted Photogrammetric Mapping System (CPMS). The CPMS allows the operator to map contours of the sink. The contours represent the trace of the intersection of horizontal planes with the walls of the sink. The computer then calculates the volume of the irregularly shaped space between two contours. The collapse volume of the sink is calculated by tracing sufficient contours in the sink to adequately represent the configuration of the walls of the sink. A total volume measurement for each sink is made from the combined volume measurements of material between each contour. A complete discussion of the CPMS and its application for geologic studies can be found in Pillmore and others (1981).

The procedure relies on large-scale aerial photographs taken of the site of the test following collapse of the surface. The large-scale (1:4,800) photographs make it possible to map all topographic features of the sink, including the sag zone.

COMPARISON OF RESULTS

CPMS volume measurements were made of six sinks (U3ks, U3lh, U3li, U3ls, U3lt, and U3lw) in Area 3 (fig. 4). To check the reliability of the CPMS-measured volumes, profiles (fig. 5) were plotted on the CPMS from post-test photographs. From these profiles, volumes could be geometrically calculated (as a frustum of a cone) and compared with the CPMS values. Because the sides of the sinks in profile are not straight, the calculated profile volumes were slightly larger than the CPMS-generated volumes. The difference ranged from 4-16 percent; the more irregular sinks produced the greater difference.

A comparison of the CPMS volume measurements was made with volume measurements from four of the field-surveyed sinks (fig. 6). (Surveys for U3li and U3lw were unavailable.) The comparisons, shown in table 1, indicate a difference from 10-15 percent between volumes calculated using the two different approaches. The field-measured sink volumes of U3ks and U3lh were less than those measured on the CPMS, while field-measured volumes of U3ls and U3lt were greater than the CPMS values. Field measurements were then compared with the CPMS-generated profiles (fig. 6). This comparison showed that field measurements of U3ks and U3lh failed to take into account large portions of the sink, thus, the conical field measurements of U3ks and U3lh underestimated the volume. Comparisons of U3ls and U3lt showed larger field-measured volumes

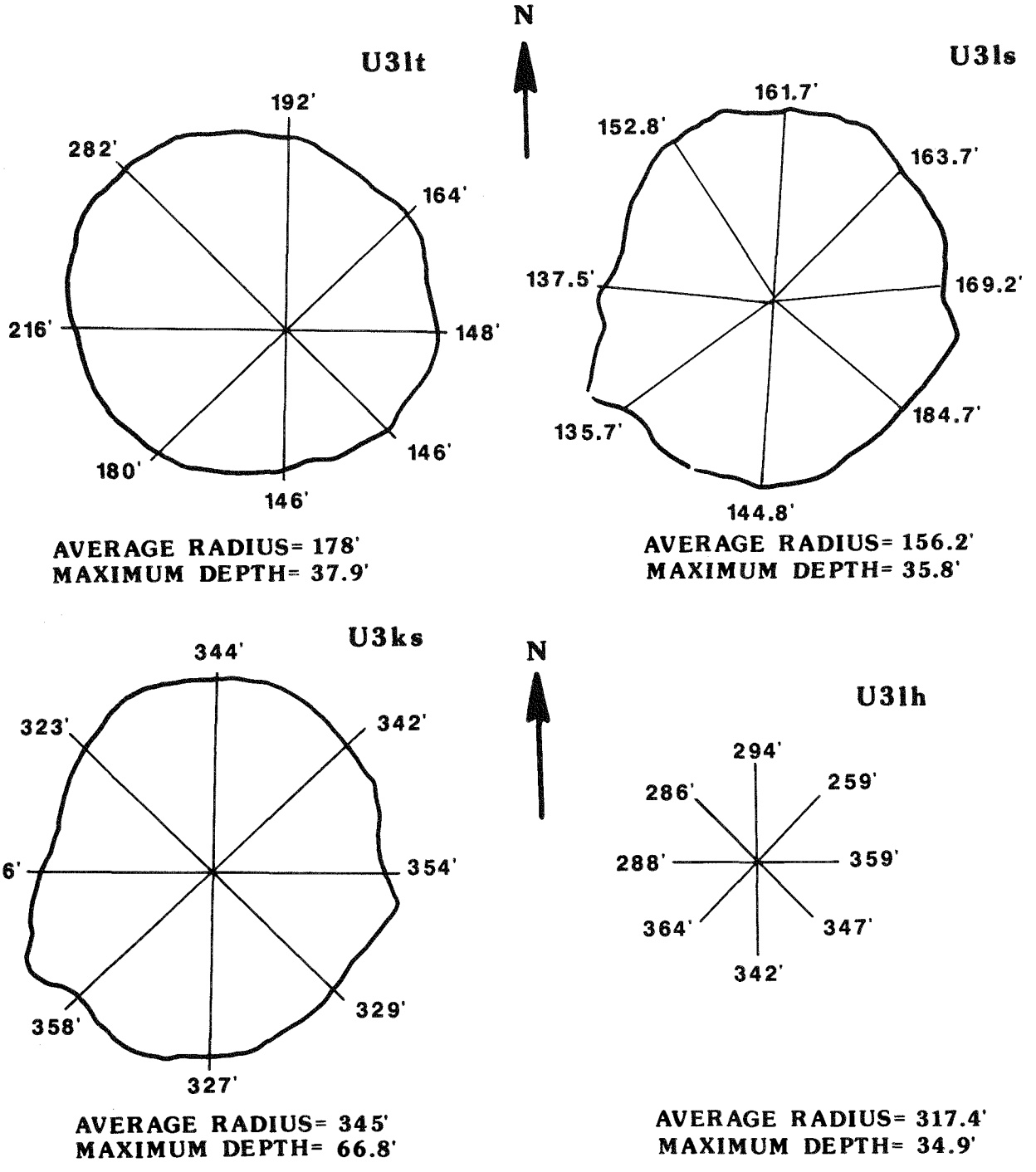

Figure 3.--Field measurements (not to scale) of sinks U31t, U31s, U31h, and U3ks (from Holmes and Narver, Inc., 1987).

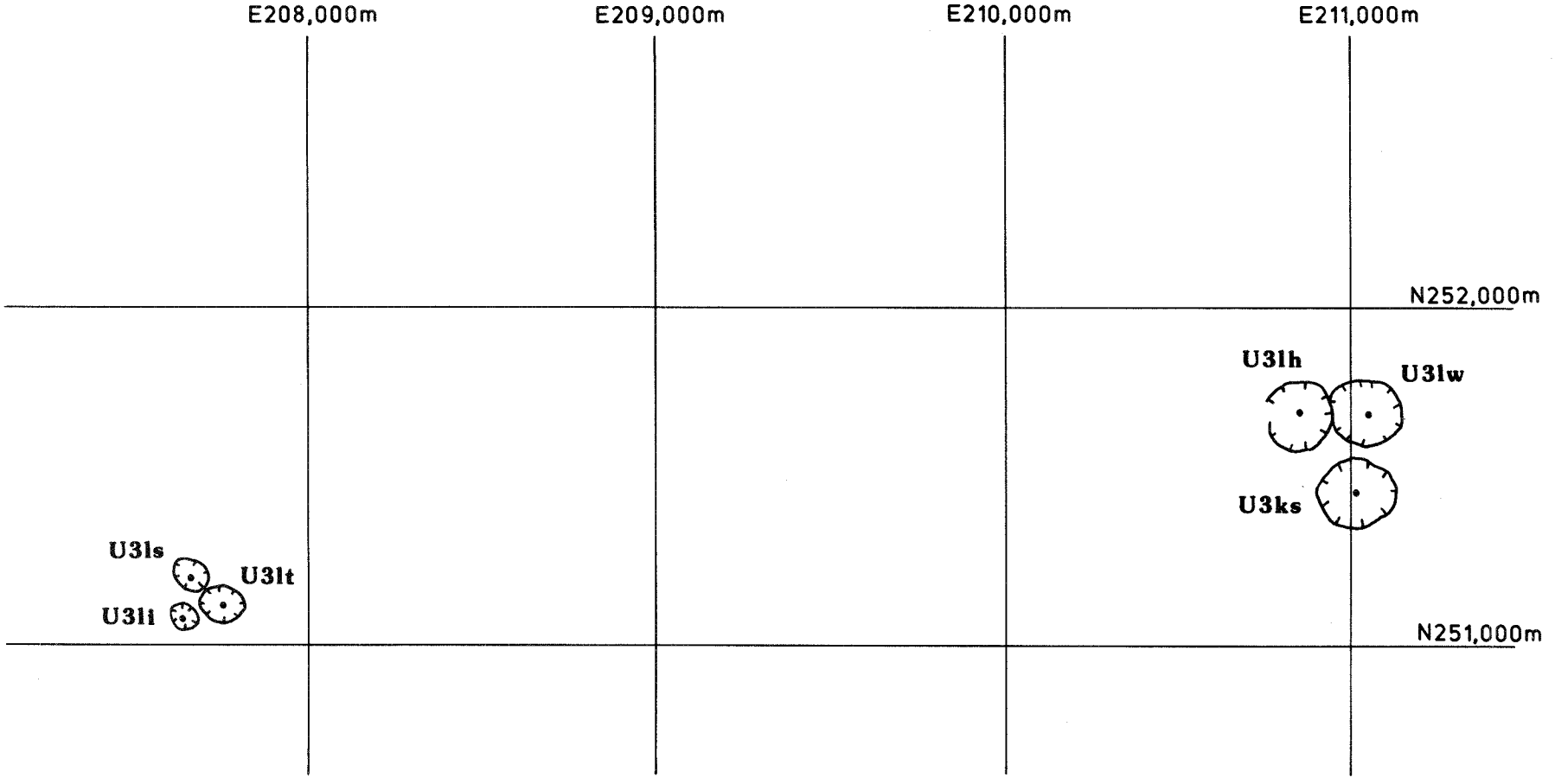

Figure 4.--Location of sinks measured using CPMS.

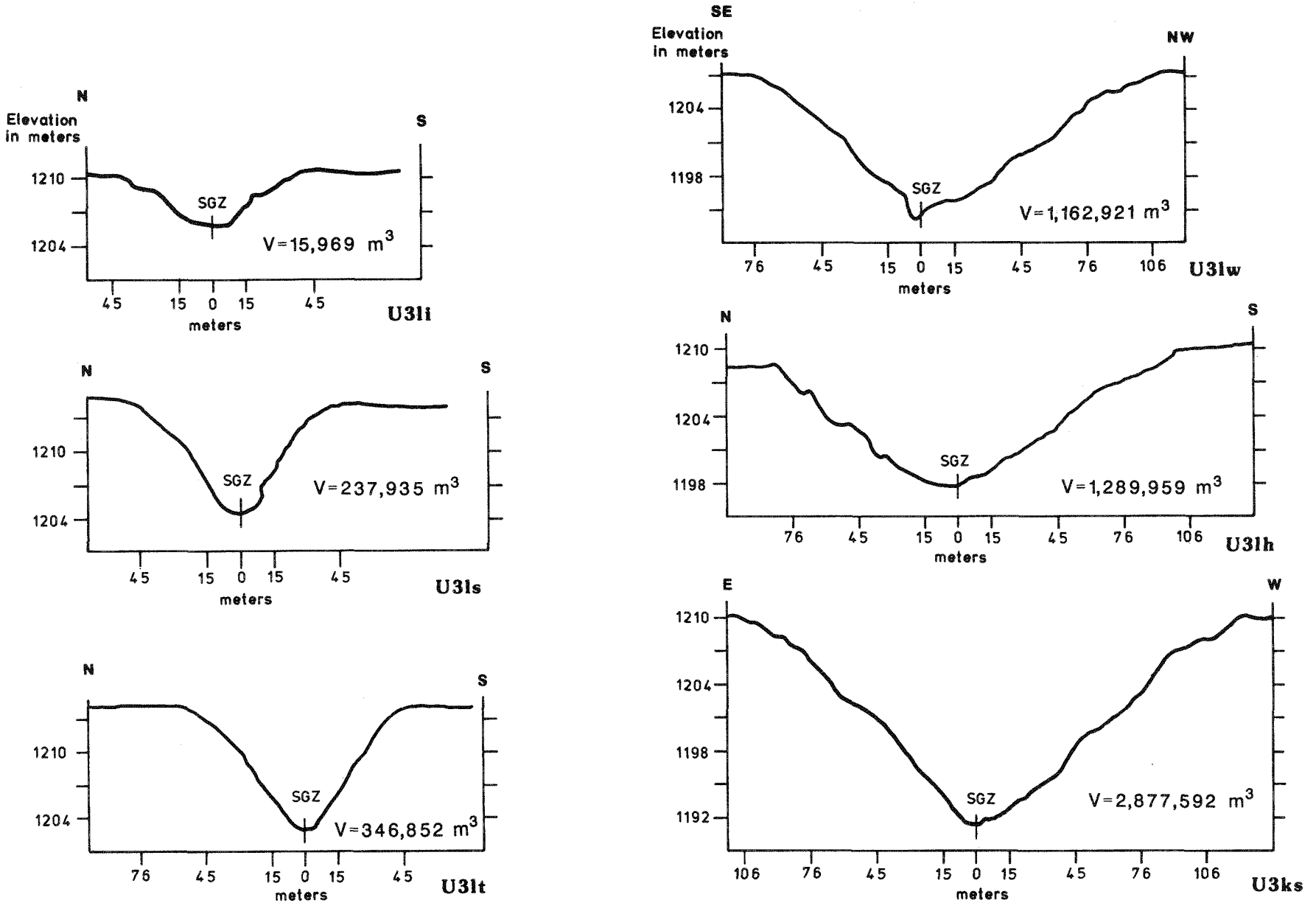

Figure 5.--CPMS-generated profiles of U3ks, U3li, U3lh, U3ls, U3lt, and U3lw (V = volume).

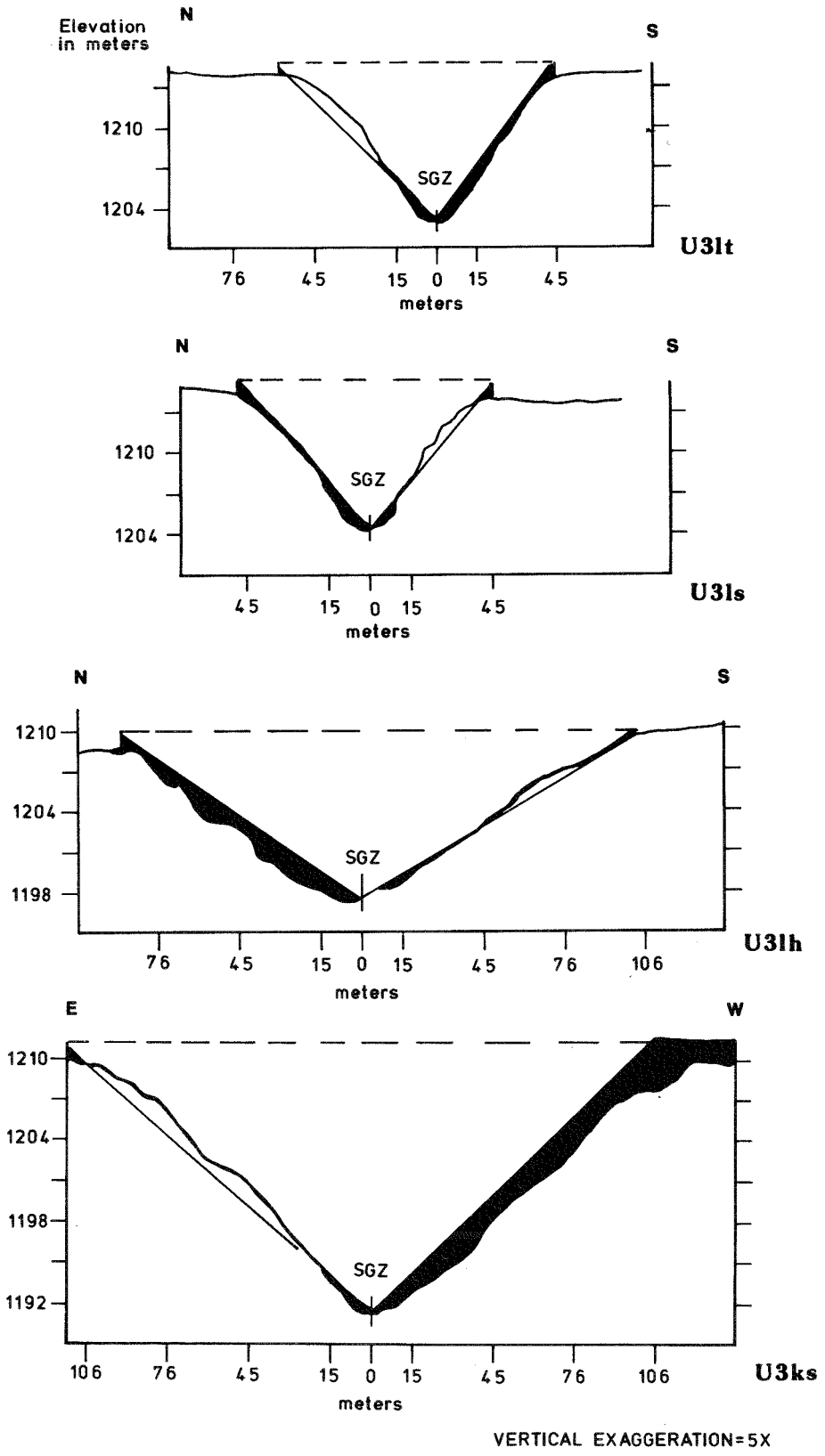

Figure 6.--Comparison of CPMS-generated profiles and field measurements. Shaded areas indicate areas not included in the field-measured volumes.

Table 1. Comparison of CPMS and field-measured volumes for selected sites in Area 3, NTS.

Site	CPMS-generated volume (in cubic meters)	Field-measured volume (in cubic meters)	Percent Difference
U3ks	2,877,592	2,536,518	12
U31i	85,969	Unavailable	--
U31h	1,289,956	1,121,663	13
U31s	237,935	278,655	15
U31t	346,852	383,091	10
U31w	1,162,921	Unavailable	--

that are related to the irregular sides of the sinks. Because field mappers cannot enter the sink to measure these irregularities, their measurements are commonly imprecise. Because the CPMS divides the sink into a finite number of horizontal planes, it is able to map irregularities that field mapping cannot determine.

CONCLUSIONS

The CPMS method for determining volumes is more accurate than previous methods. However, the method has only been applied in Area 3. Studies should be continued in other areas on the NTS. Advantages of using the CPMS method include: little or no time required in the field; easily obtainable and correctable results; a three-dimensional view of sink for volume determinations; recognizable irregularities and profiles that check the reliability of CPMS-generated volumes. The photogrammetric procedure is not foolproof. Problems encountered with poor quality photographs have to be corrected, but the advantages of the photogrammetric procedure far outweigh this disadvantage.

REFERENCES

Houser, F.N., 1970, A summary of information and ideas regarding sinks and collapse, NTS: U.S. Geological Survey report USGS-474-41, 129 p.; available only from U.S. Department of Commerce National Technical Information Service, Springfield, Va. 22161.

Houser, F.N., and Eckel, E.B., 1962, Possible engineering uses of subsidence induced by contained underground nuclear explosions: U.S. Geological Survey Professional Paper 450-C, p. C17-C18.

Jones, E.M., 1979, Nuclear Cavities and Craters in NTS/Area 3 Alluvium (U): Los Alamos National Laboratory Report, LA-7834-MS, 33 p.

Pillmore, C.L., Dueholm, K.S., Jepsen, H.S., and Schuck, C.H., 1981, Computer-assisted photogrammetric mapping system for geologic studies--A progress report, in Proceedings 14th Congress of the International Society of Photogrammetry, Hamburg, West Germany, 1980, v. 36, p. 159-171.

External Distribution:

AFWL/ NTCO
Kirtland AFB, NM 87115-5000
Attn: Albert Alexander

Field Command/DNA
Test Directorate
P.O. Box 98539
Las Vegas, NV 89193
Attn: Joseph W. LaComb

Field Command/DNA
P.O. Box 98518
Las Vegas, NV 89193
Attn: Roger Thompson

Field Command/DNA
Kirtland AFB, NM 87115-5000
Attn: Dale Glover

U.S. Department of Energy
M/A MA 232.21
Attn: Energy Library, T-A
P.O. Box A
Germantown, MD 20874
For: Ray Ferry, HQ
Irv Williams, HQ

U.S. Department of Energy
Nevada Operations Office
P.O. Box 98518
Las Vegas, NV 89193-8518
Attn: Richard Hague
Richard Navarro
Grace Plummer
Nick Aquilina

U.S. Department of Energy
Oak Ridge Operations Office
P.O. Box E
Oak Ridge, TN 37831
Attn: Lawrence Whitehead
NTIC

Los Alamos National Laboratory
Mail Station 5000
P.O. Box 1663
Los Alamos, NM 87545
For: Fred App
Joseph Brown
Robert Brownlee
Wendee Brunish
John Conaway
Ruth Demuth
Robert Deupree (5 copies)
Thomas Dey
Richard Fenster
Ward Hawkins
Jack House (6 copies)
Robert Kirby
Don Krier
Tom Kunkle
Carol La Delfe
Mark Matthews
James Neergard
Sue Noel
Jay Norman
A. Ogard
B. Roy Saunders
Tom Scolman
Joe Thompson
Bryan Travis
Bruce Trent
R. G. Warren
Clay Watson
Judy Winterkamp
Ken Wohletz
Report Library

Lawrence Livermore National Laboratory
P.O. Box 808
Livermore, CA 94550
For: Bob Addis, L-113
Gordon Anderson, L-203
Joe Behne, L-49
Norm Burkhard, L-203
Dick Carlson, L-203
R. Corallo (LLNL-N), L-777
James Carothers, L-1
Chris Cordill, L-113
H. A. Dockery
James D. Donithan (LLNL-N) L-777
Al Duba, L-203
Don Felske, L-777
Larry Ferderber, L-49
Lew Glenn, L-203
Hal Goldwire, L-203
Joe Hearst, L-203
Francois Heuze, L-203
Billy Hudson, L-203
Bob Kuckuck, L-49
A. S. Kusubov, L-201
Don Larson, L-203
Andy Lundberg, L-113
John Mercier, L-113
Mel Millet, L-777
Bill Moran, L-203
Robin Newmark, L-203
Cliff Olsen, L-203 (10 copies)
Gayle Pawloski, L-203
Steve Pratuch, L-113
John T. Rambo, L-203
Larry Schwartz, L-203
Clyde Sisemore, L-203
Ray Stout, L-203
Robert Swift, L-203
John Toman, L-389
Jeff Wagoner, L-203
Vern Wheeler, L-203
Erv Woodward, L-203
Library

EG&G
Amador Valley Operations
Attn: Classified Material Control
P.O. Box 9051
Pleasanton, CA 94566
For: Tom Edwards, AVO
Melton Hatch, AVO
John Kalinowski, AVO
T. Stubbs

EG&G
Attn: Document Control
P.O. Box 1912
Las Vegas, NV 89101
Attn: Del Wallace, NLVF
Bill Webb, NLVF

Fenix & Scisson, Inc.
P.O. Box 93265
Las Vegas, NV 89193-3265
Attn: Grant Bruesch
A. P. Cavazos
S. L. Drellack, Jr.
W. T. Hughes
P. H. Thompson

Ernest Fickas
Geo-Centers, Inc.
2350 Alamo Ave., SE, Suite 302
Albuquerque, NM 87106

Holmes & Narver, Inc.
Las Vegas Division
Attn: Facility Control Station
P.O. Box 14340
Las Vegas, NV 89114-4340
For: Dave Bedsun
Ralph Haak
Joe LaComb, Jr.
Leroy Ryan
Richard Ivy

Pacifica Technology
P.O. Box 148
Del Mar, CA 92014
Attn: Robert Allen
Martin Fogel
Dan Patch
D. Ranta
Colby Swan

S-Cubed
P.O. Box 1620
La Jolla, CA 92038
Attn: Charles Dismukes
Russell Duff
E. Halda
Michael Higginbotham
Diana Hollis
Kay Lie
Bob Nilson
Dan Peterka
Edward Peterson
Len Reed
Norton Rimer
Rachel Sandmann
John Wiehe
David Yates

SRI International
P.O. Box 725
Menlo Park, CA 94026-0725
Attn: A. L. Florence
Geza Nagy

Science & Engineering Associates
612 Old Santa Fe Trail
Santa Fe, NM 87501
Attn: C. Keller

Ktech
901 Pennsylvania, NE
Albuquerque, NM 87110
Attn: E. S. Gaffney

Planetary Geosciences Division
University of Hawaii
2525 Correa Road
Honolulu, HI 96822
Attn: J. C. Gradie

U.S. Geological Survey
Central Regional Geology Branch
Box 25046, MS 913
Denver, CO 80225
Attn: M. N. Garcia
D. L. Hoover
Evan Jenkins
Paul Orkild
Security Officer

U.S. Department of Energy
Attn: Richard Navarro
P.O. Box 98518
Las Vegas, NV 89193-8518
(Hold for Harry Covington,
U.S. Geological Survey)

Terra Tek
University Research Park
420 Wakara Way
Salt Lake City, UT 84108
Attn: Sidney Green
W. Klauber
John Lupo

Desert Research Institute
Water Resources Center
P.O. Box 8086, University Station
Reno, NV 89507
Attn: Paul Fenske

G. H. Higgins
P.O. Box 1991
Woodland, CA 95695

University of California, Davis
Department of Civil Engineering
Davis, CA 95616
Attn: B. L. Kutter
L. Chang

Sandia Internal Distribution:

1513 R. C. Dyknuizen
1513 A. J. Ratzel
1523 L. M. Taylor
1531 S. L. Thompson
Attn: T. K. Bergstresser
J. S. Rottler
3312 J. H. Metcalf
7100 C. D. Broyles
7110 J. D. Plimpton
7111 J. R. Banister
7111 R. C. Bass
7111 L. R. Hill (5 copies)
7112 C. R. Mehl
7112 A. J. Chabai
7112 C. W. Smith
7116 S. R. Dolce
7116 C. W. Cook
7116 R. P. Reed
7116 R. C. Shear
8244 S. K. Griffiths
3151 W. I. Klein
For DOE/OSTI (NWD Index) (2 copies)

*U.S. GOVERNMENT PRINTING OFFICE: 1988-0-573-036/80019

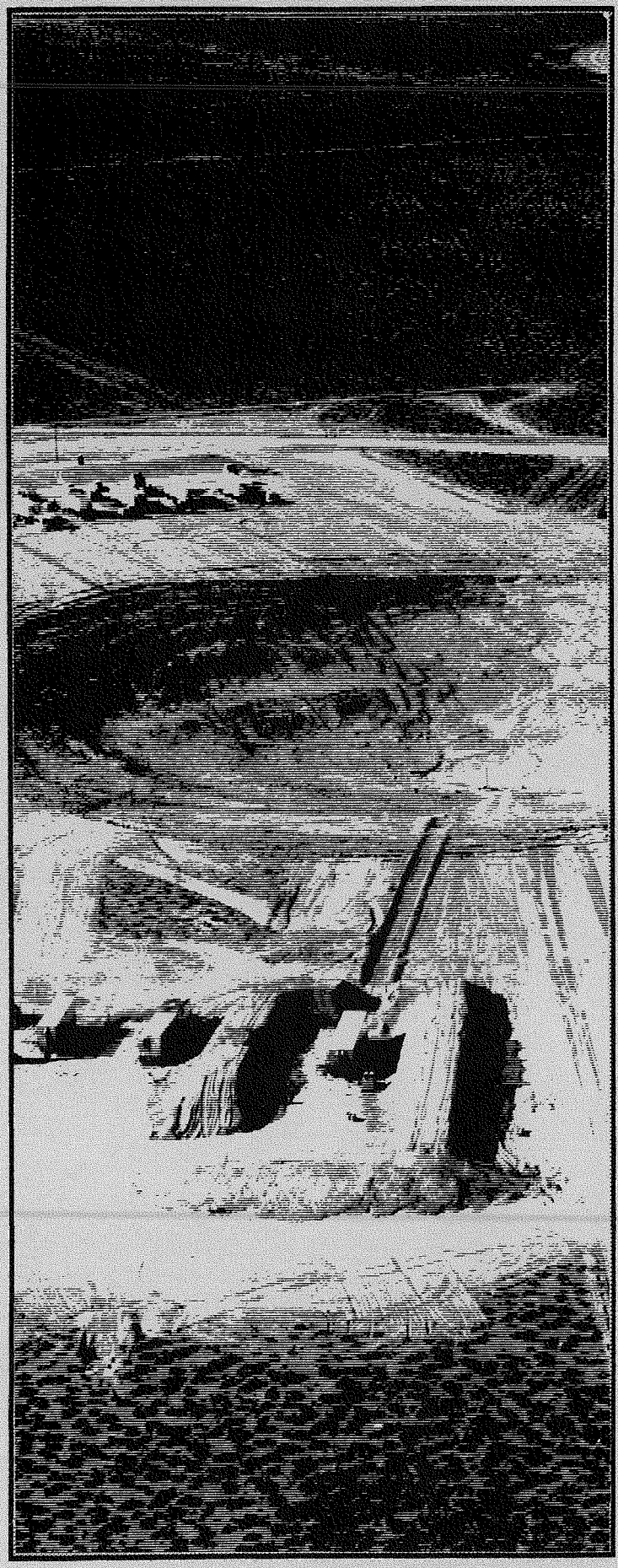

Fourth Symposium on Containment of Underground Nuclear Explosions

United States Air Force Academy, Colorado Springs, Colorado Sept. 21-24, 1987

Volume 2 PROCEEDINGS

CONF-870961

Erratum

G-4
"Making Sense of the Mixed Alluvium in the Yucca Flat Basin"

J. L. Wagoner
Lawrence Livermore National Laboratory
Livermore, CA

DISCLAIMER

This document was prepared as an account of work sponsored by an agency of the United States Government. Neither the United States Government nor the University of California nor any of their employees, makes any warranty, express or implied, or assumes any legal liability or responsibility for the accuracy, completeness, or usefulness of any information, apparatus, product, or process disclosed, or represents that its use would not infringe privately owned rights. Reference herein to any specific commercial products, process, or service by trade name, trademark, manufacturer, or otherwise, does not necessarily constitute or imply its endorsement, recommendation, or favoring by the United States Government or the University of California. The views and opinions of authors expressed herein do not necessarily state or reflect those of the United States Government or the University of California, and shall not be used for advertising or product endorsement purposes.

Proceedings of the Fourth Symposium on Containment of Underground Nuclear Explosions— **Volume 2**

Erratum
Conference paper G-4

United States Air Force Academy,
Colorado Spring, Colorado

Sept. 21–24, 1987

Clifford W. Olsen, Scientific Editor
Maureen L. Donohue, Publication Editor
Sandra Wander, Editor

MAKING SENSE OF THE MIXED ALLUVIUM IN THE YUCCA FLAT BASIN*

J. L. Wagoner
Lawrence Livermore National Laboratory
Livermore, CA 94550

Introduction

The purpose of this study is to define stratigraphic units in the mixed alluvium that can be correlated between drill holes in the Yucca Flat basin. This will provide a better understanding of the three-dimensional stratigraphic framework of the alluvial pile, help us to understand the geologic history and development of the basin, and aid in the prediction of working point lithology and physical properties.

The mixed alluvium consists of coarse-grained fluvial sediments that are transported very short distances from the source areas. Lateral facies changes are abrupt because of the localized nature of the sedimentation, and because the source areas change rapidly through geologic time and laterally within the basin.

Individual alluvial fans generally drain a single canyon along the basin margin. The source rocks in the drainage area provide a specific suite of detritus to the alluvial fan. As new formations are exposed by erosion, new rock types become available to the sediments.

I have reviewed most of the lithologic logs constructed for holes in the northern part of the basin. Some holes were not adequately described, but the majority of the logs contained useful descriptions of the character of the alluvial sediments. Seven stratigraphic units were defined based on the lithology of the dominant source rock described in the log. These units are not time-stratigraphic, but rather are controlled by the locations of the available source rocks.

I have also investigated the average CO_2 content of the individual units in the basin. The CO_2 content of the working point medium is a major concern, since even moderate amounts of CO_2 may lead to late-time seeps from underground nuclear events.

General Geologic Setting of Yucca Flat

Yucca Flat is a fault-bounded arid basin that trends north-south and encompasses an area of 525 km^2. The basement beneath Yucca Flat and the adjacent ranges consists of late Precambrian and Paleozoic carbonate and clastic sedimentary rocks. Deposited on top of the basement are Tertiary volcanic rocks. These sedimentary and volcanic rocks represent the major sources of detritus for the basin-filling alluvium.

*This work was performed under the auspices of the U.S. Department of Energy by Lawrence Livermore National Laboratory under contract No. W-7405-Eng-48.

Structurally, the basin is characterized by gently step-faulted margins that lead to deep grabens near the center. The deep basin structure is controlled by the Carpetbag and Yucca Faults. The initial alluvial deposits were derived from a terrane blanketed almost totally by middle to late Tertiary pyroclastic volcanic deposits. These alluvial deposits contained predominantly volcanic detritus. With continued basin subsidence and uplift of the surrounding ranges, erosion eventually unroofed the Paleozoic sedimentary rocks, providing a new source of detritus. The character of the deposits thus changed from a basal volcanic-rich alluvium to a mixed alluvium containing variable percentages of both volcanic and basement sedimentary clasts.

The two types of alluvium routinely identified in northern Yucca Flat are termed mixed alluvium and basal tuffaceous alluvium. These are defined on the basis of the clast composition and stratigraphic position.

The basal tuffaceous alluvium by definition contains <5% Paleozoic sedimentary rock fragments and >95% Tertiary volcanic fragments. The deposit is the oldest alluvium in the basin and always occurs stratigraphically between the overlying mixed alluvium and underlying volcanics. The sediments are typically coarse-grained gravelly sands, with local coarse gravels.

The mixed alluvium contains >5% Paleozoic sedimentary fragments and <95% Tertiary volcanic fragments. These deposits are mainly gravelly sediments, with subordinate sand and finer grained deposits. The mixed alluvium is typically coarser grained than the basal tuffaceous alluvium.

Methods Employed in the Study

In this study, I have reviewed all of the available lithologic logs for the LLNL field test area located north of Nevada coordinate N 262000 in Yucca Flat (Figure 1). These holes are located in Areas 2, 8, 9, and 10. Some of the older lithologic descriptions were too vague to offer the information necessary to define the contacts of the stratigraphic units. In these cases, I did not use the data.

Seven stratigraphic units were defined on the basis of the character of the dominant detrital clast lithology (Figure 2). No holes contained all of the units. A database was constructed of all of the holes having reliable stratigraphic data. These data were then used as input into the ISM code, an interactive surface mapping program on the Containment VAX computer. ISM was written by Dynamic Graphics, Inc., in Berkeley, California. The scattered data were gridded and then contoured. I also calculated the average CO_2 content for each unit in each hole, and these data were then added to the database and contoured.

Isopach and structural contour maps were constructed for each unit to show the distribution of the units in relation to the major faults and the basin margin. Cross sections were also constructed to show the facies relationships and thickness of the units. I also constructed maps showing the variation of the CO_2 content in each stratigraphic unit. Because of the large number of maps, the structural contour maps are not included in this document. These maps will appear in a future publication.

Definition of the Stratigraphic Units

This study defines seven stratigraphic units, based on the character of the dominant source rock in the sediment. The following is a brief definition of the units:

Unit 1 -- Paleozoic noncarbonate clasts are dominant, generally >50% of the clast population. The top of the unit is always at the surface.

Unit 1a-- Paleozoic noncarbonate clasts are dominant. This unit differs from Unit 1 in that the top of the unit is never at the surface.

Unit 2 -- Paleozoic carbonate clasts are dominant, generally >50% of the clast population.

Unit 3 -- Tertiary volcanic tuff clasts are greater than or equal to Paleozoic clasts. The top of this unit is always at the surface.

Unit 3a-- This unit is the same as Unit 3 except that the top of the unit is never at the surface.

Unit 4 -- Paleozoic carbonate clasts are dominant. This unit is restricted to the east side of Area 9.

Unit 5 -- Basal tuffaceous alluvium. Tertiary volcanic tuff comprises >95% of the sediment.

These working units are defined only by the criteria stated and there is no inference of sediment textural classification or general grain size. It is assumed that the depositional setting was probably much the same for most of the units. The deposits were mostly laid down under semi-arid, nonmarine fluvial/alluvial conditions. The units as defined are useful for a first cut at correlating and constructing the three-dimensional stratigraphic model.

Discussion of the Maps

I have constructed several maps showing both the lateral and vertical distribution of the lithostratigraphic units in the alluvium in the Yucca Flat basin. In general, the lateral distribution of the units reflects the areal extent of the datapoints. For example, Unit 1 (Figure 3) probably extends to the western basin margin, since Paleozoic clastic rocks are exposed in the Eleana Range. I have chosen to extend the zero isopach line only as far as is reasonable for the available stratigraphic data.

Two types of maps are available in this paper. The isopach map shows the thickness and lateral distribution of the individual units across the basin. The second map shows the variation of the CO_2 content for each unit in the basin.

Unit 1 contains dominantly clasts of Paleozoic clastic sedimentary rocks, and by definition, the top of this unit is always at the surface of the valley. Figure 3 is an isopach map of Unit 1. This is the most widespread unit, mainly receiving detritus from the Paleozoic Eleana Formation exposed along the western and northwestern margins of the basin. The unit thins over the Carpetbag Ridge and is thickest between the Carpetbag and Yucca Faults. Unit 1 is rare east of the Yucca Fault.

Figure 4 shows the variation of the CO_2 content in Unit 1. Thirty-three holes had CO_2 data for Unit 1. The values ranged from 0.1-4.83%, with an average of 2.27% for the basin. West of the Carpetbag Ridge there is an increase in CO_2 toward the south. Between the Carpetbag and Yucca Faults, the highest values seem to be concentrated toward the center of the basin.

Unit 1A consists of the same material as Unit 1 except that by definition, the top of Unit 1A never occurs at the valley surface. This unit is older than most of Unit 1 and is much less common (Figure 5), indicating that most of the Paleozoic clastic formations were buried during this time and unroofed later in the development of the basin. Unit 1A is most common in the south-central portion of the study area. This sedimentary section decreases in thickness away from the Carpetbag Ridge and probably represents a buried alluvial fan.

Figure 6 shows the variation of the CO_2 content in Unit 1A. Only seven holes in Unit 1A had CO_2 measurements. The data ranged from 1.65-4.45%, and averaged 2.82%. The highest measured CO_2 values were on the west side of the Carpetbag Ridge.

Unit 2 is composed dominantly of Paleozoic carbonate detritus. Most of Unit 2 is located between the Carpetbag and Yucca Faults (Figure 7). The source of this deposit was the buried Carpetbag Ridge and sediments generally became thin away from the ridge. Three holes drilled into the ridge encountered Paleozoic carbonate rocks in contact with the mixed alluvium, indicating that the carbonate was locally exposed to erosion and provided detritus to the basin.

Unit 2 is also found in the northeastern corner of the basin and locally west of the Carpetbag Ridge. The deposits in the northeastern area probably were derived form the Paleozoic carbonate rocks exposed at the Smoky Hills.

Figure 8 shows the variation of the CO_2 content for Unit 2. Twenty-five holes had measured data, which ranged from 1.58-8.69%, with an average of 4.82%. In general, the CO_2 values increase toward the probable source areas for the deposits. Note especially the section between the two major faults, where the values tend to increase toward the Carpetbag Ridge. This suggests an increase in the percentage of carbonate clasts toward the source area.

Unit 3 consists mainly of Tertiary volcanic detritus and subordinate clasts of Paleozoic rocks. This unit is mainly restricted to the southeastern portion of the study area (Figure 9). The northernmost deposits derived material from Tertiary volcanic rocks exposed northeast of the map border. The deposits in the southeast corner derived material from the rocks exposed at Balloon Hill. The thick section of Unit 3 between the Carpetbag and Yucca Faults may be partly fault-controlled.

Figure 10 shows the variation of the CO_2 content in Unit 3. Twelve holes had data, which ranged from 1.20-6.70% and averaged 2.67%. There is considerable variation of the CO_2 within the basin.

Unit 3A is basically the same as Unit 3 except that the top of the unit is never at the valley surface. This unit has much the same distribution as Unit 3 (Figure 11), and is thickest between the two major faults. These sediments

probably derived detritus from the uplifted blocks along the two major faults as the Tertiary volcanic rocks were being partially stripped away.

Figure 12 shows the variation of the CO_2 content in Unit 3A. Twenty holes had data, ranging from 0.21-5.05% and averaging 2.13%. As in Unit 3, there is no systematic variation in the CO_2 content.

Unit 4 consists dominantly of Paleozoic carbonate clasts. This unit is restricted to the east side of the basin, and represents a series of alluvial fans at the base of Banded Mountain (Figure 13).

Figure 14 shows the variation of the CO_2 content in Unit 4. Only two holes had measured CO_2 data, ranging from 26.20-27.52% and averaging 26.86%. These sediments are extremely carbonate-rich, and this is reflected in the high CO_2 contents.

Unit 5 is the basal tuffaceous alluvium. This is the oldest alluvial deposit in the basin and always occurs stratigraphically between the mixed alluvium and the Tertiary volcanic rocks. Unit 5 is concentrated mainly in the central portion of the basin between the two major faults (Figure 15). When the basin development started, most of the surrounding terrane was blanketed by thick deposits of Tertiary volcanics. Unit 5 was the product of erosion of these faulted and uplifted volcanic deposits. The initial mixed alluvium sediments were formed when the Paleozoic bedrock was unroofed by erosion.

Figure 16 shows the variation of the CO_2 content in Unit 5. Measured data were provided for 34 holes ranging from 0.40-6.56% and averaging 2.65%. Because Paleozoic clasts comprise <5% of the sediment, the majority of the CO_2 found in Unit 5 is derived from secondary calcite cement. As with Units 3 and 3A, there is a large variation in the CO_2 content.

Figures 16 and 17 are schematic cross sections across the basin. These sections show the lateral and vertical facies relationships of the units in the alluvium, and were constructed using structural contour maps of the top and base of each unit.

Conclusions

In an attempt to unravel the stratigraphy of the mixed alluvium in the Yucca Flat basin, I have reviewed lithologic descriptions for most of the exploratory and emplacement holes in northern Yucca Flat and have identified seven types of alluvial deposits. These lithostratigraphic units are defined by the percentage of detritus derived from the three main source terranes: Paleozoic clastic and carbonate rocks and Tertiary volcanic rocks; they are independent of the clast size of the sediment. Isopach and structural contour maps have been constructed for each unit. Distribution of the deposits is a function of the source areas exposed during deposition of the sediments. The sources change with time as the rocks are uplifted along faults, denuded by erosion, and/or buried by subsequent younger deposits. I have also calculated the average CO_2 content for each unit and constructed maps showing the spatial variation of the CO_2 content. These data not only help us understand the geologic evolution of the basin, but also aid in the planning for future emplacement sites in the Yucca Flat basin.

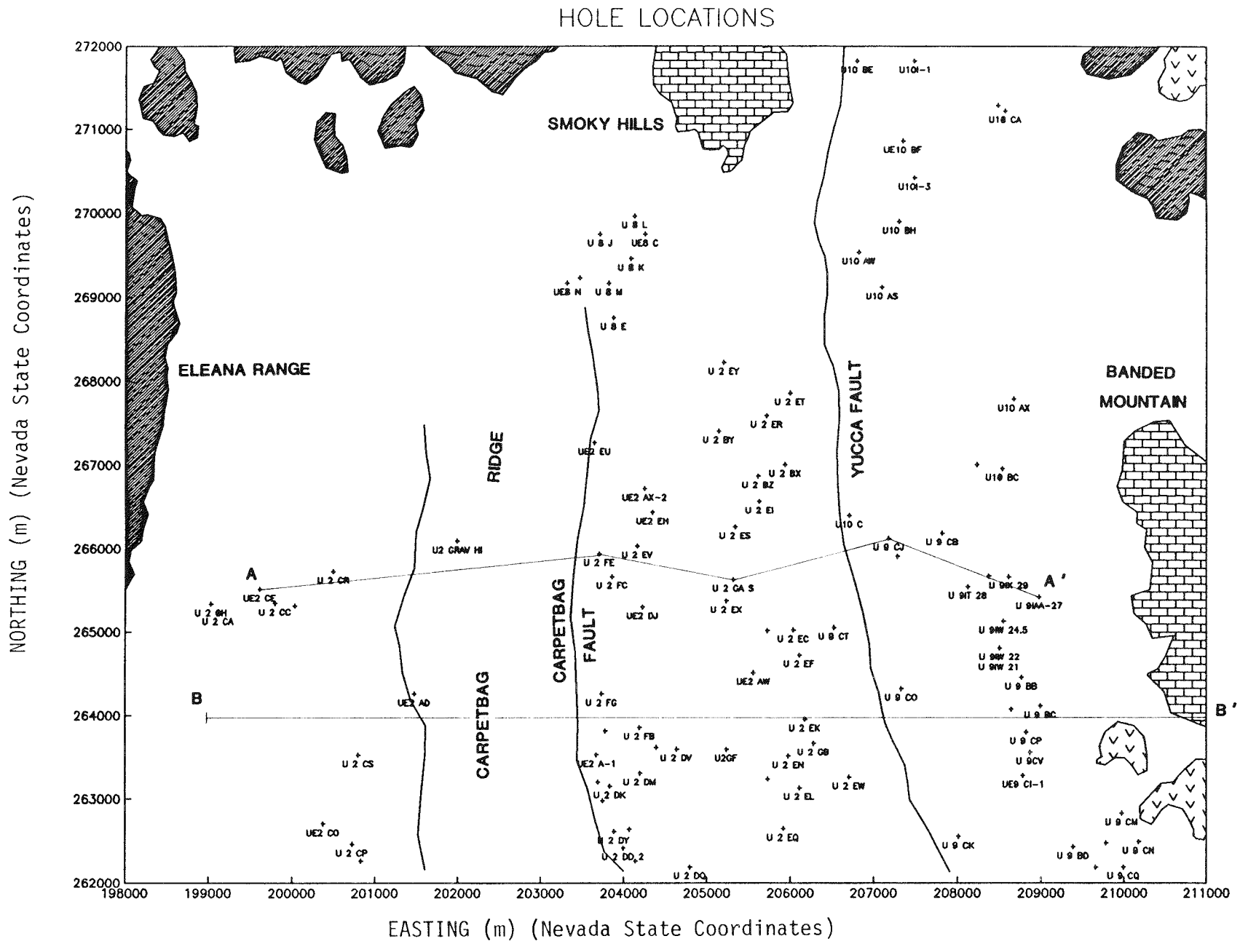

Figure 1. Locations of holes used in the study. The basin margin rocks are defined as Paleozoic clastic (angled lines), Paleozoic carbonate (brick pattern), and Tertrary volcanic ('v' shapes). The lines of section A-A^{1} and B-B^{1} refer to the cross sections in figures 17 and 18.

Stratigraphic Column

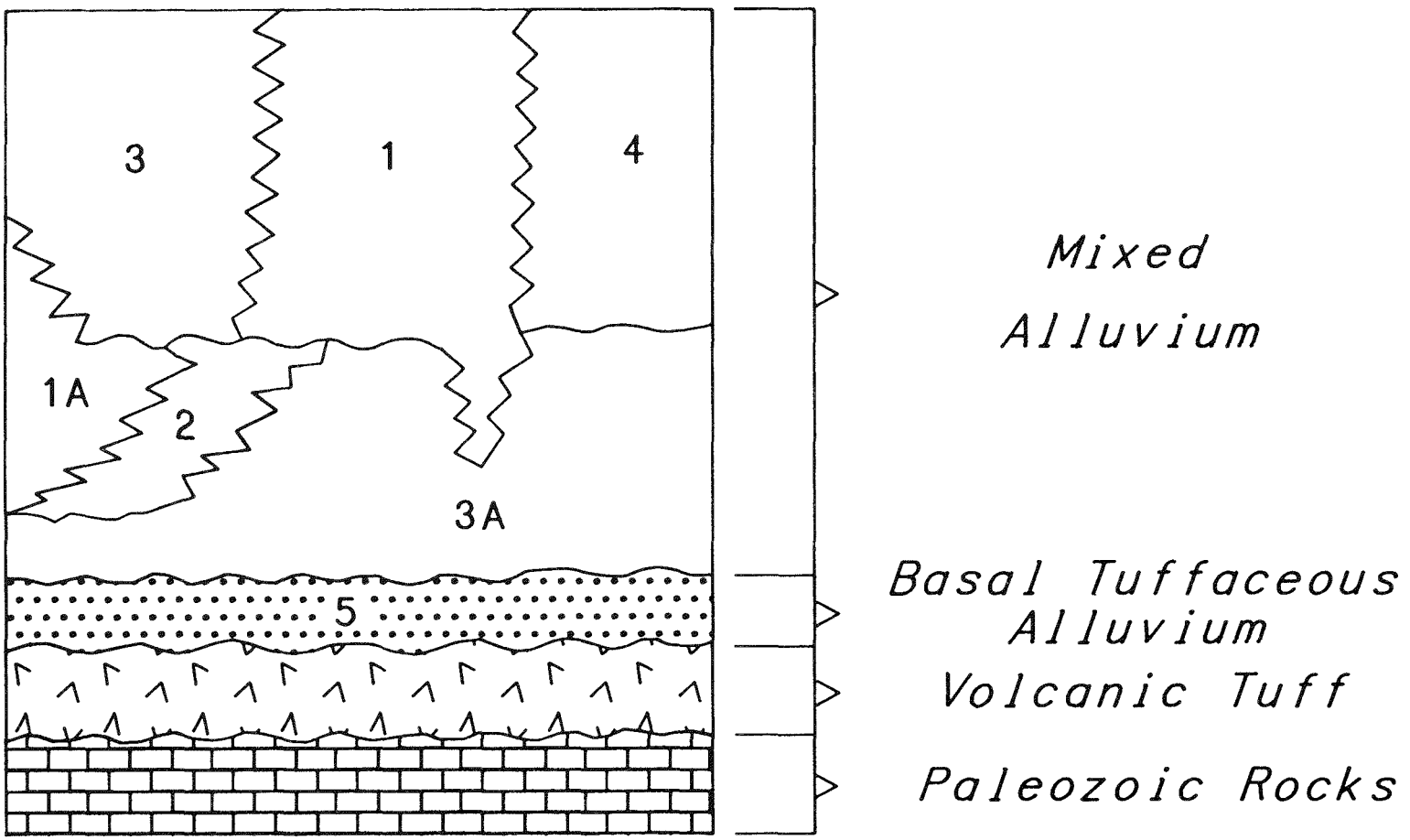

Figure 2. Schematic stratigraphic column.

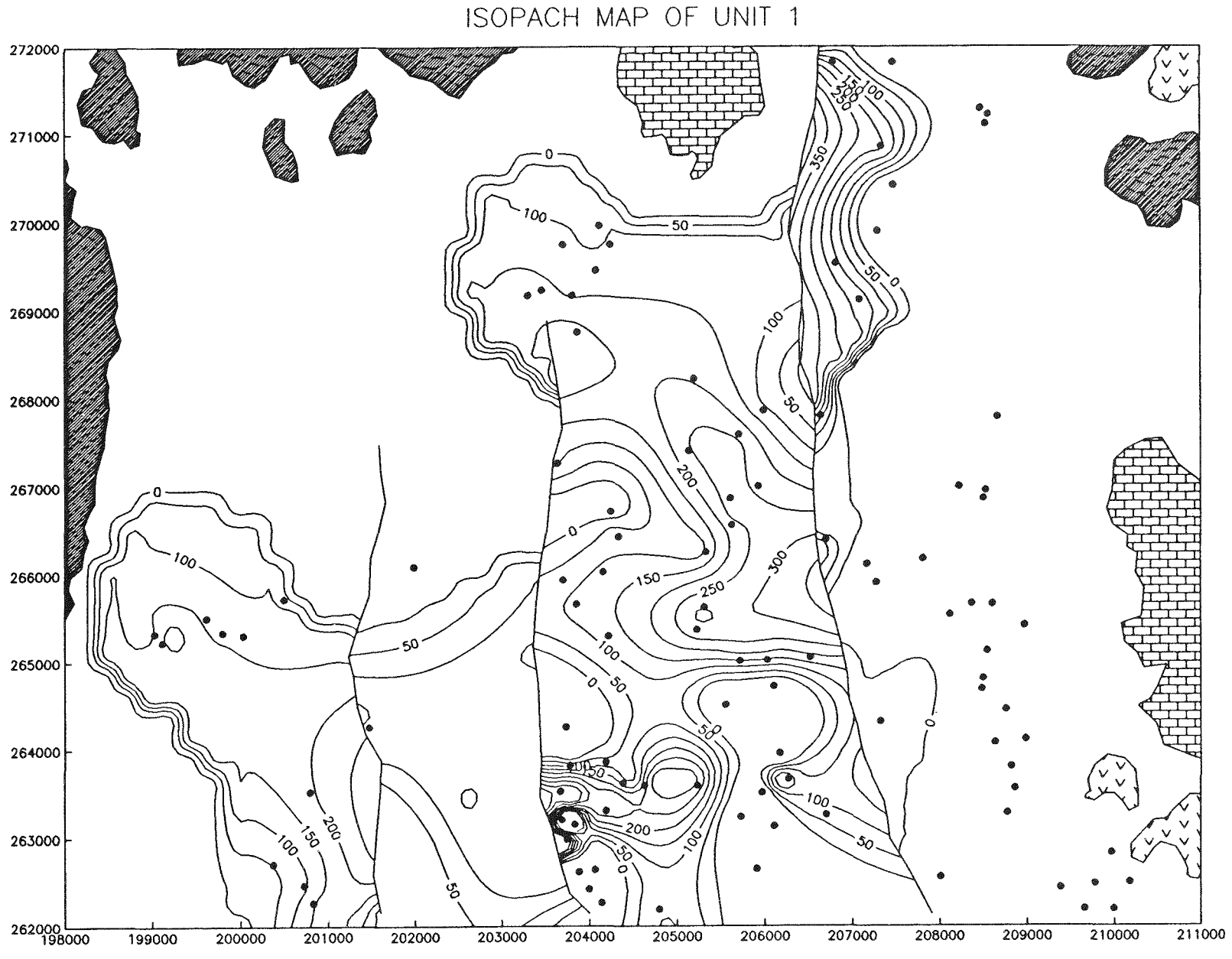

Figure 3. Isopach map of unit 1. Contour interval is 50 m.

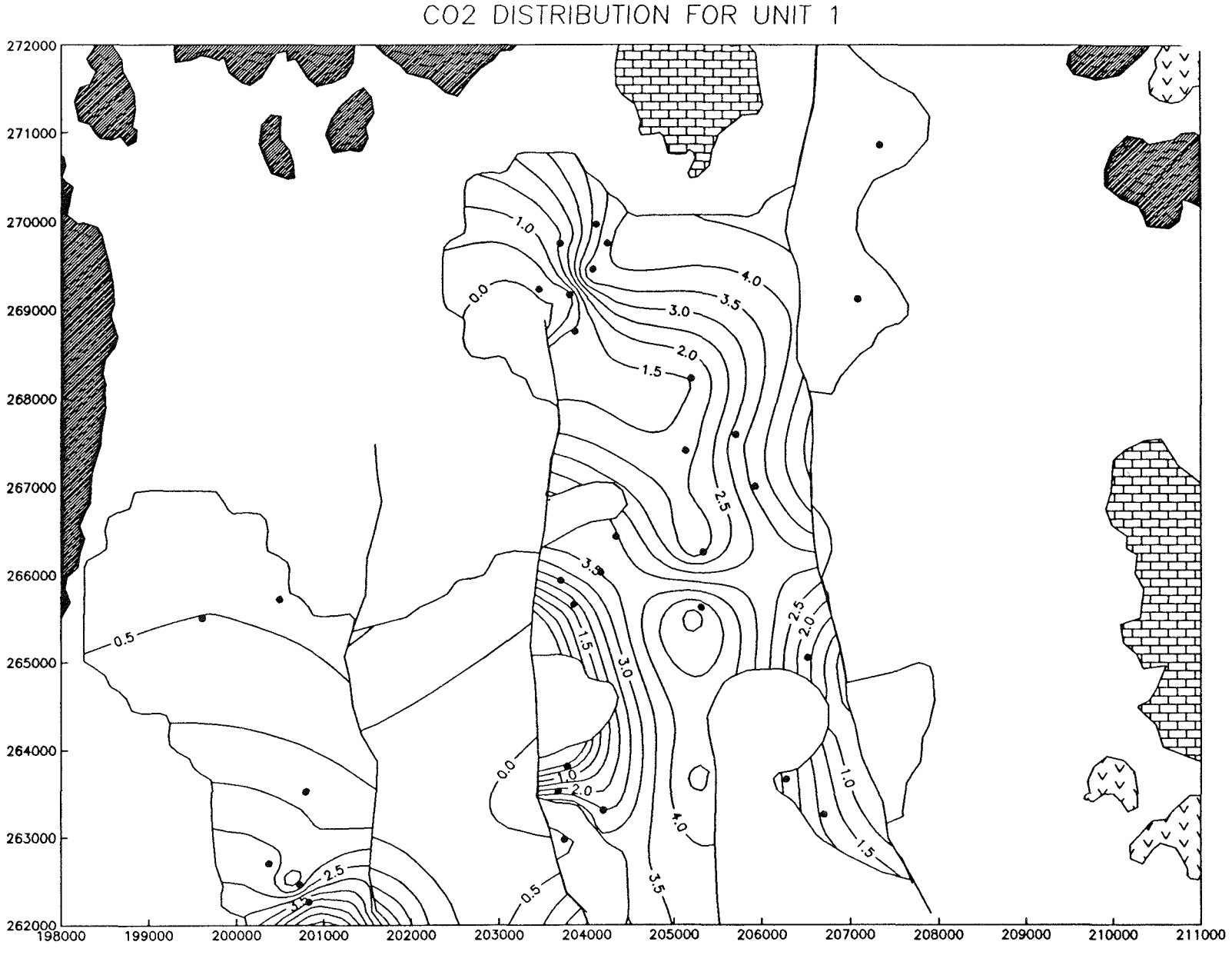

Figure 4. Variation of CO_2 content for unit 1. Contour interval is 0.5%.

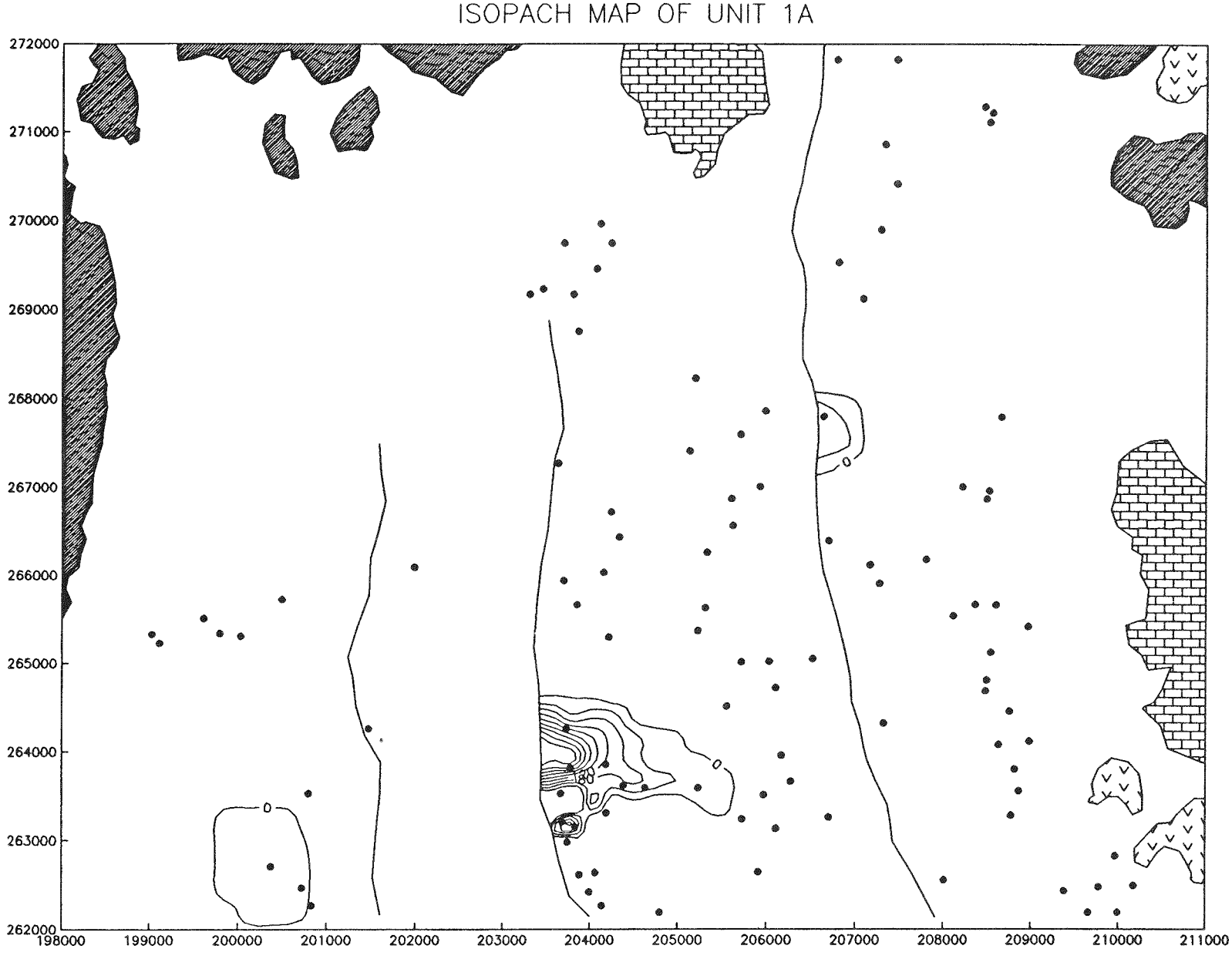

Figure 5. Isopach map of unit 1A. Contour interval is 40 m.

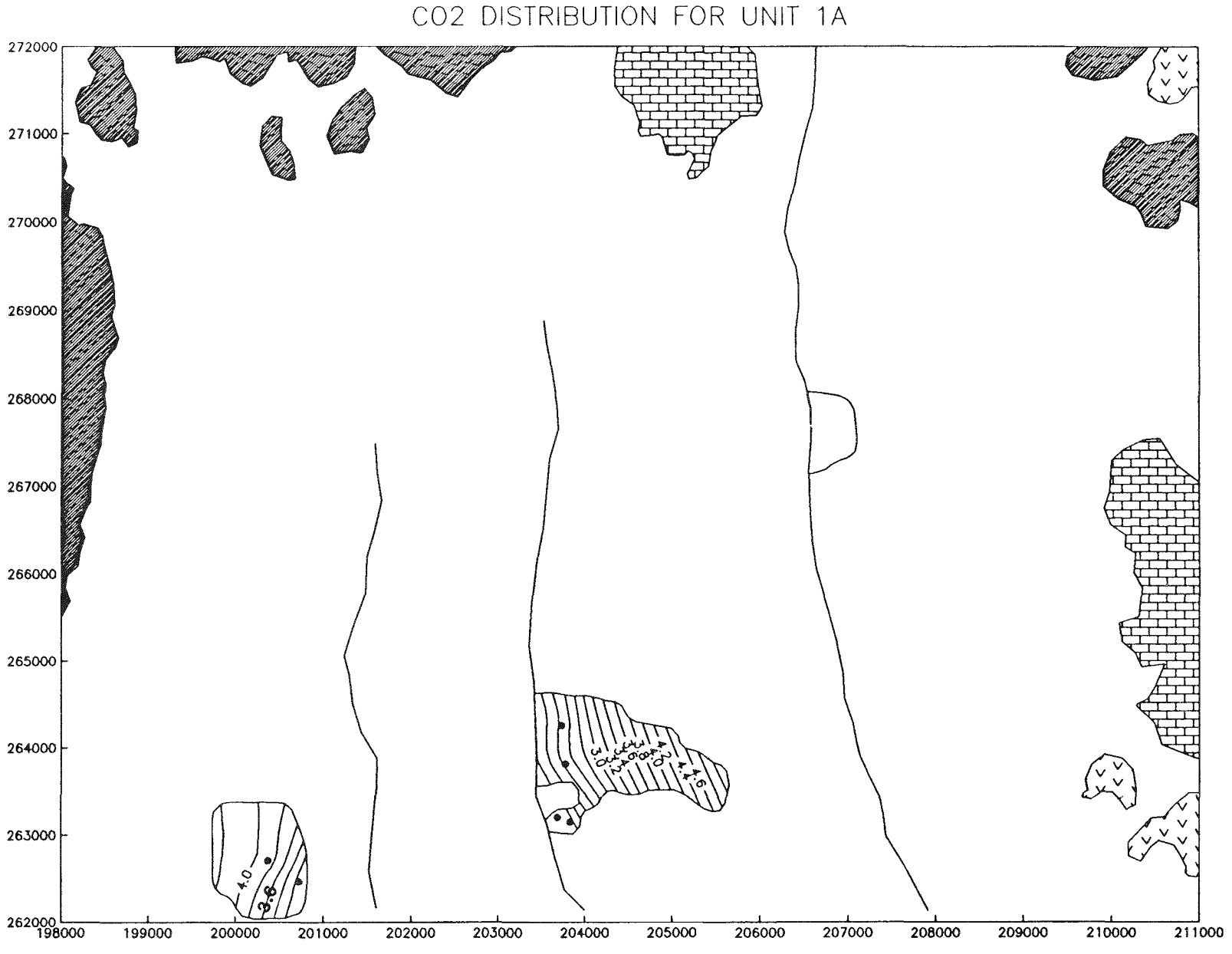

Figure 6. Variation of CO_2 content for unit 1A. Contour interval is 0.2%.

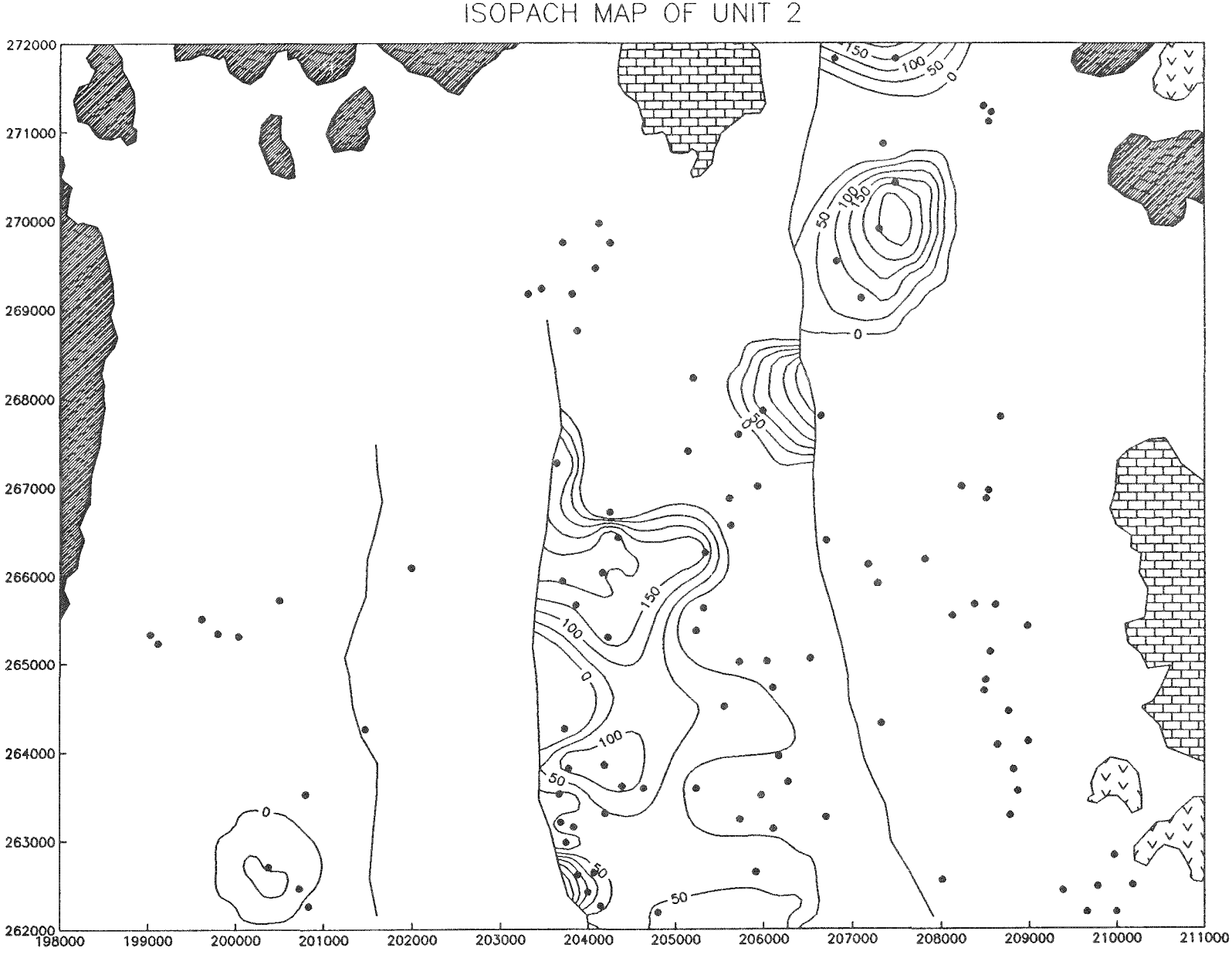

Figure 7. Isopach map of unit 2. Contour interval is 50 m.

Figure 8. Variation of CO_2 content for unit 2. Contour interval is 0.5%.

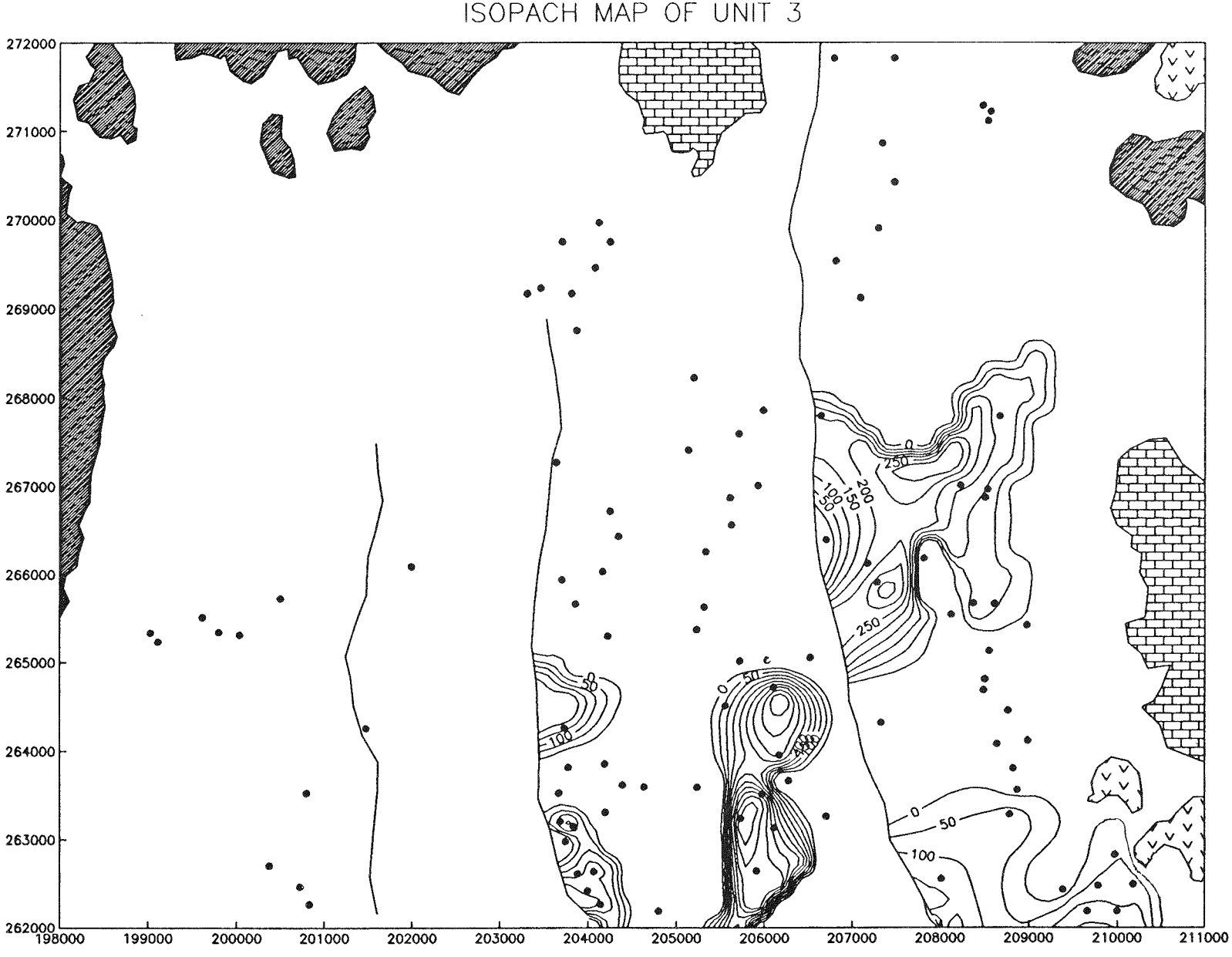

Figure 9. Isopach map of unit 3. Contour interval is 50 m.

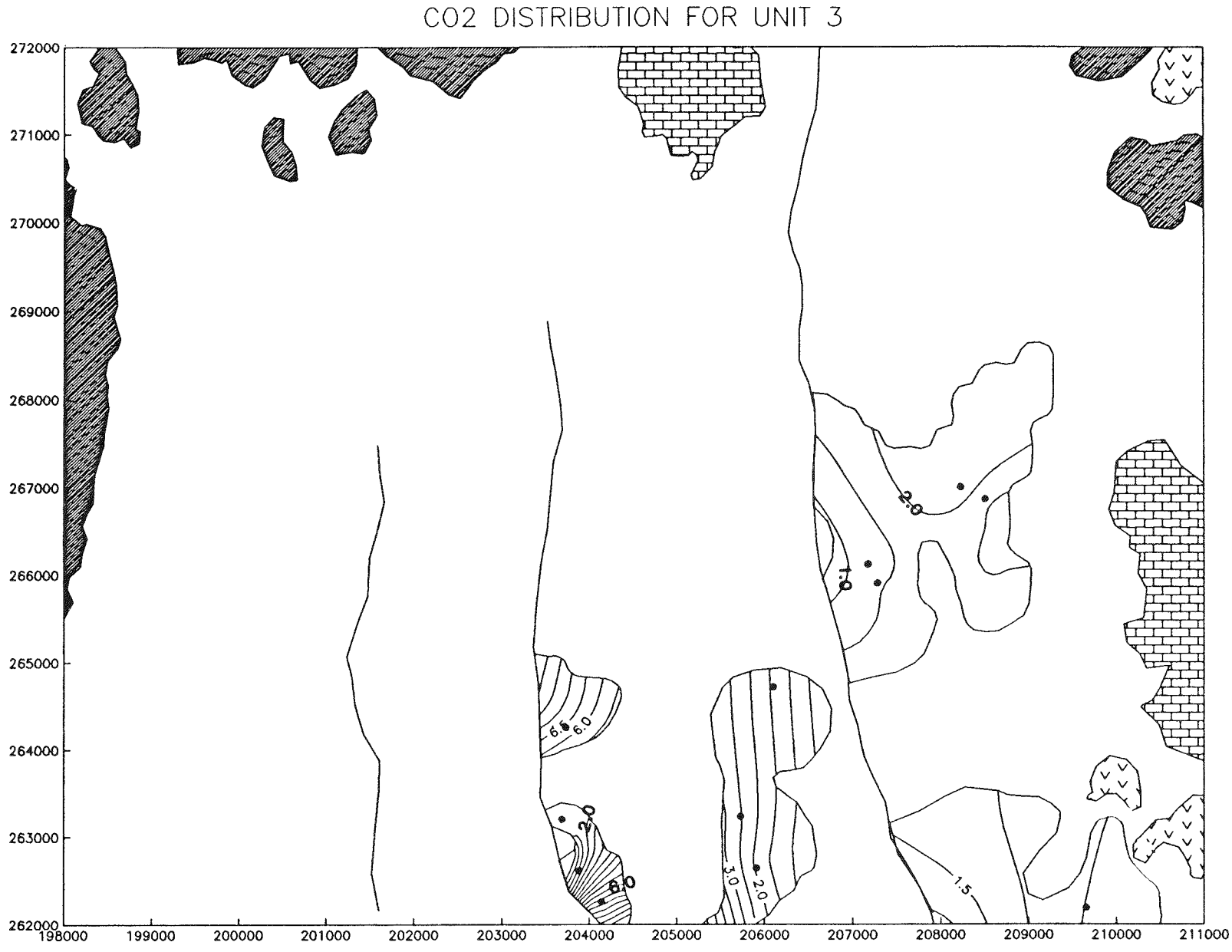

Figure 10. This map shows the variation of the CO_2 content for unit 3. Contour interval is 0.5%.

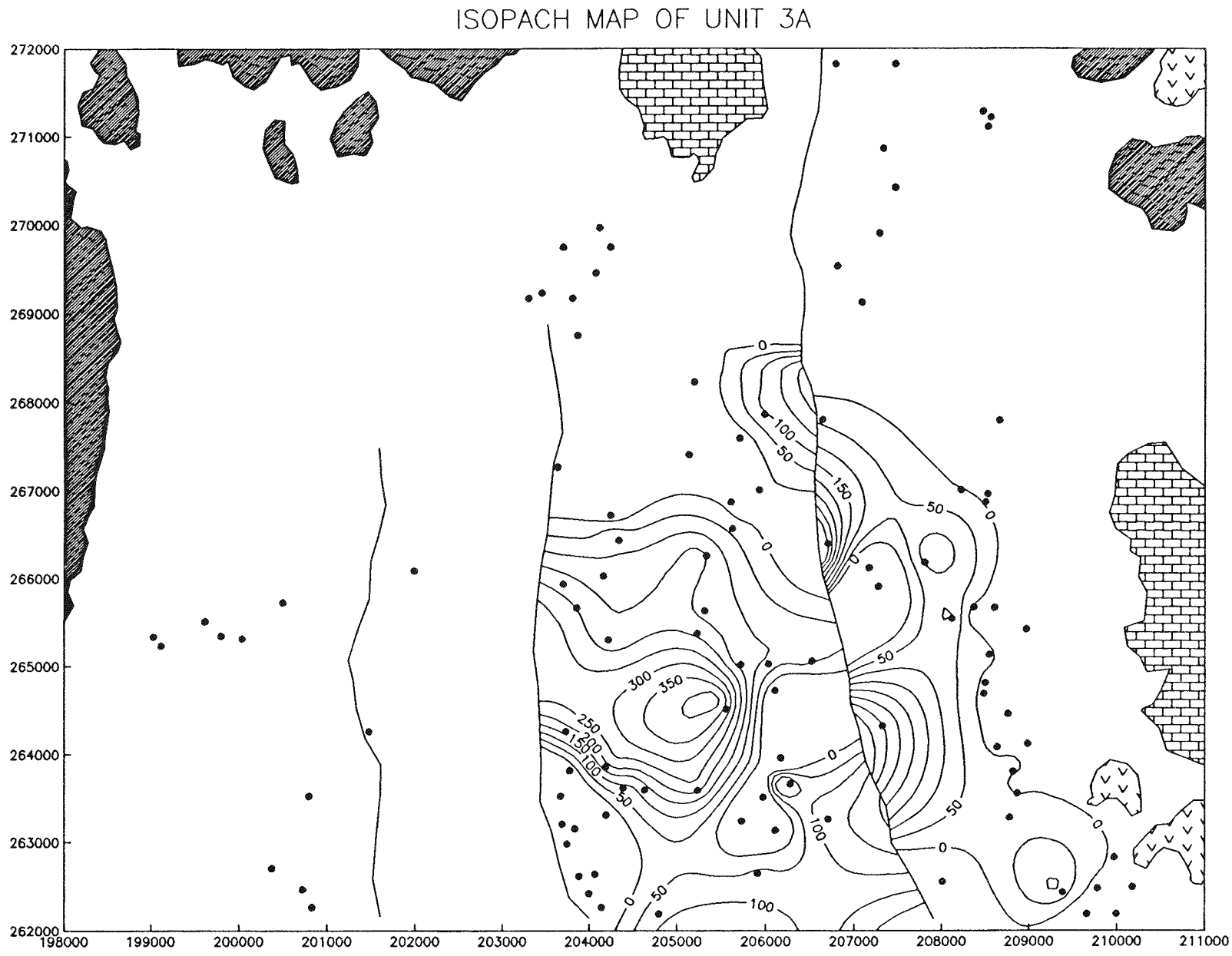

Figure 11. Isopach map of unit 3A. Contour interval is 50 m.

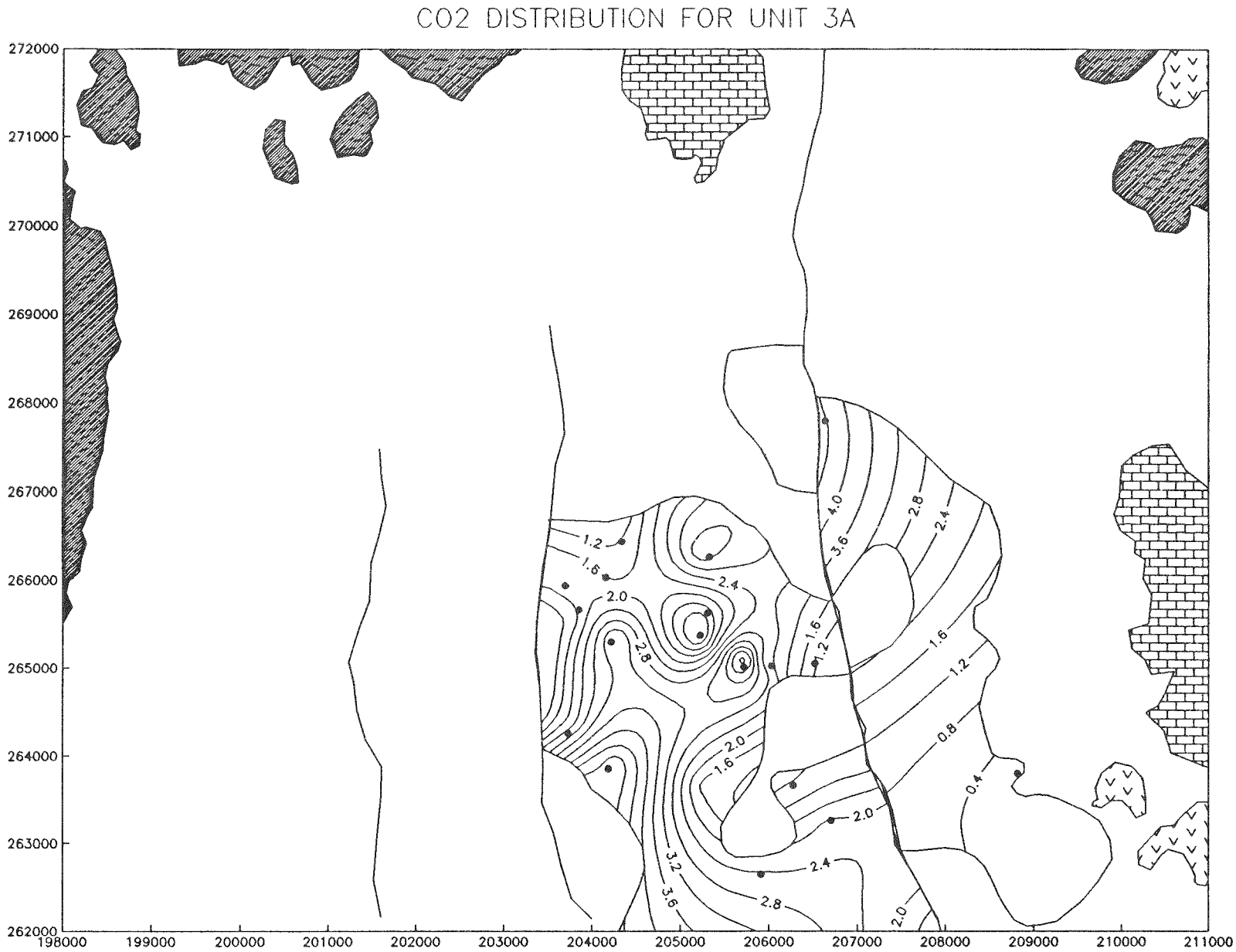

Figure 12. This map shows the variation of the CO_2 content for unit 3A. Contour interval is 0.4%.

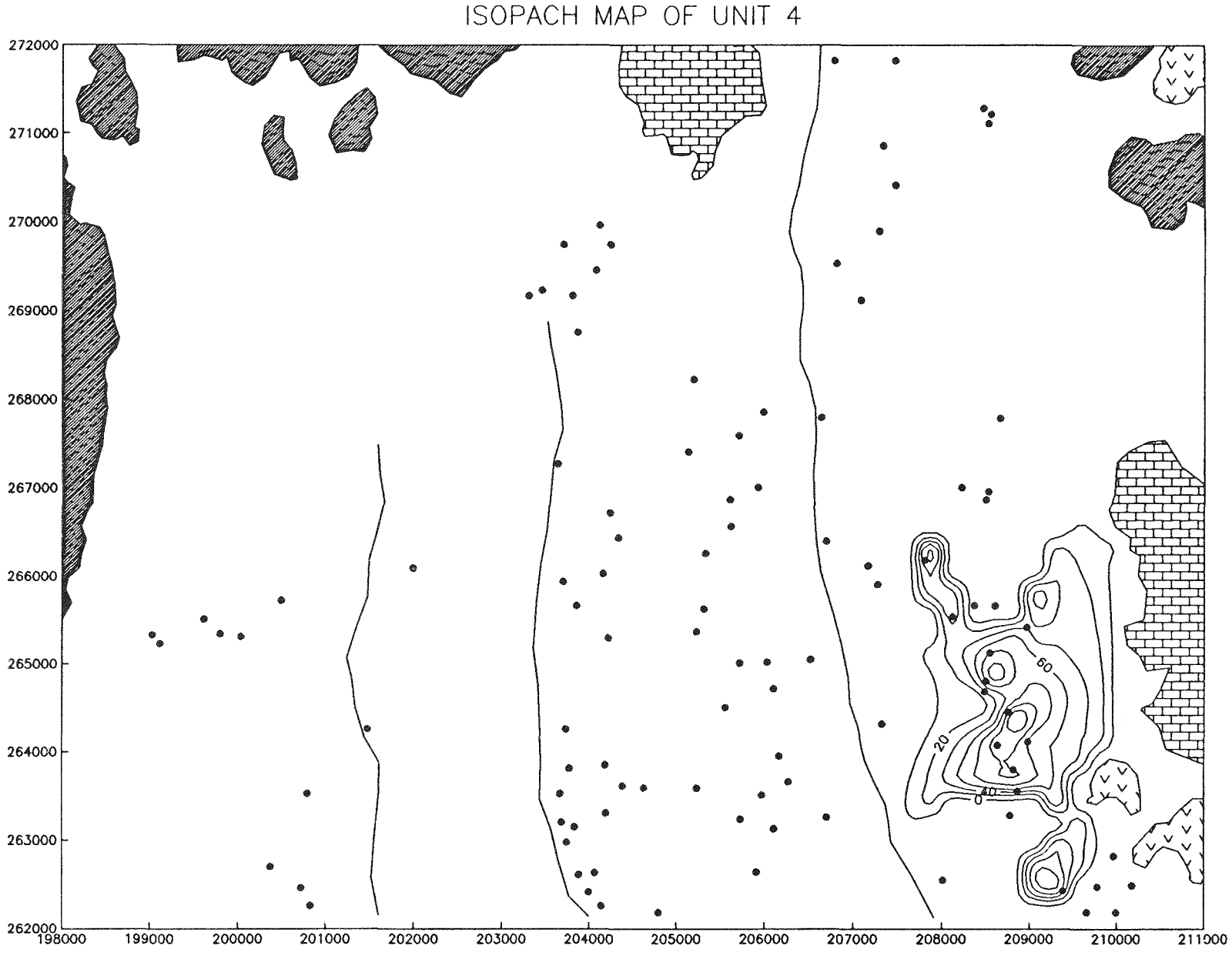

Figure 13. Isopach map of unit 4. Contour interval is 20 m.

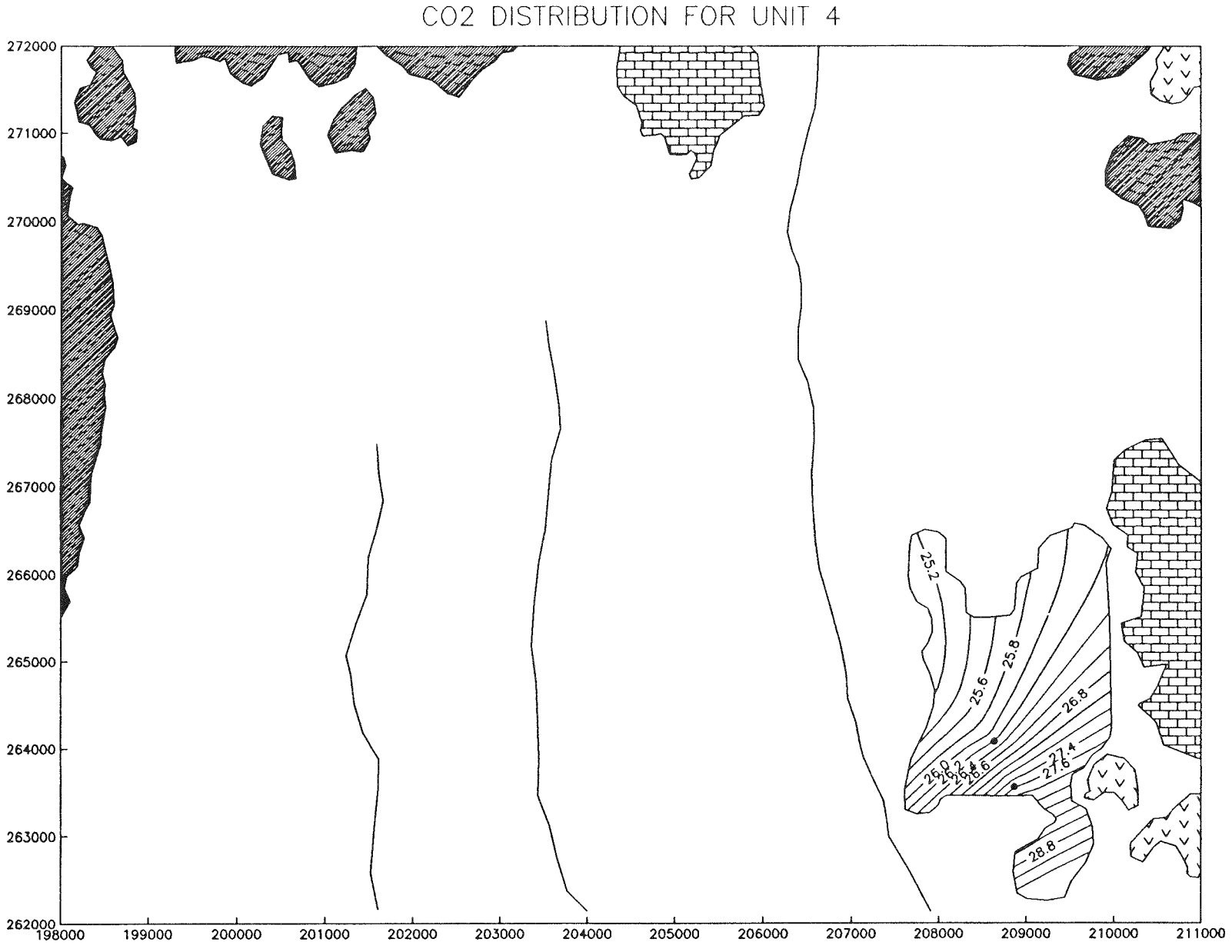

Figure 14. This map shows the variation of the CO_2 content for unit 4. Contour interval is 0.2%.

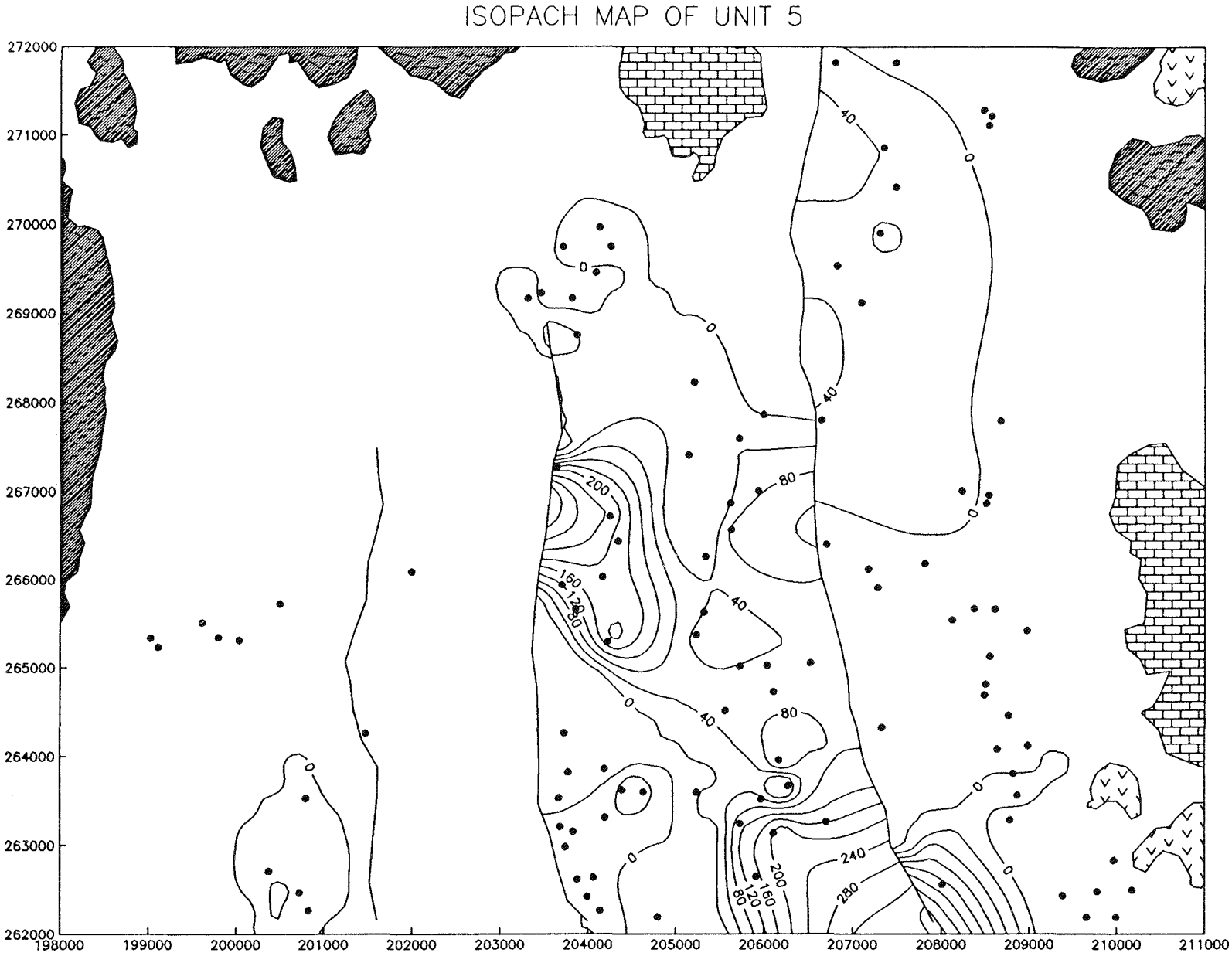

Figure 15. Isopach map of unit 5. Contour interval is 40 m.

Figure 16. This map shows the variation of the CO_2 content for unit 5. Contour interval is 0.5%.

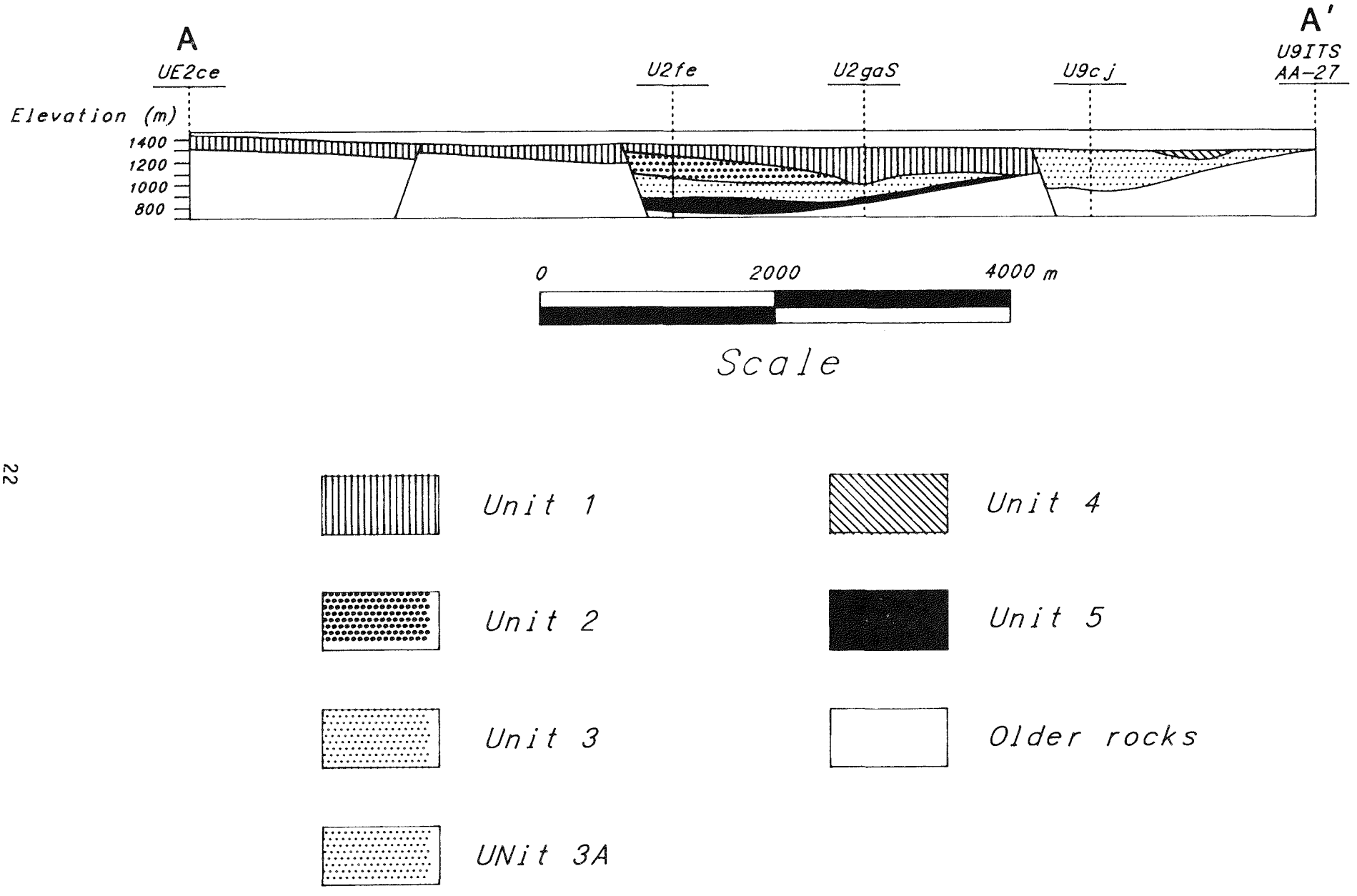

Figure 17. Schematic cross section through 5 holes across the Yucca Flat basin.

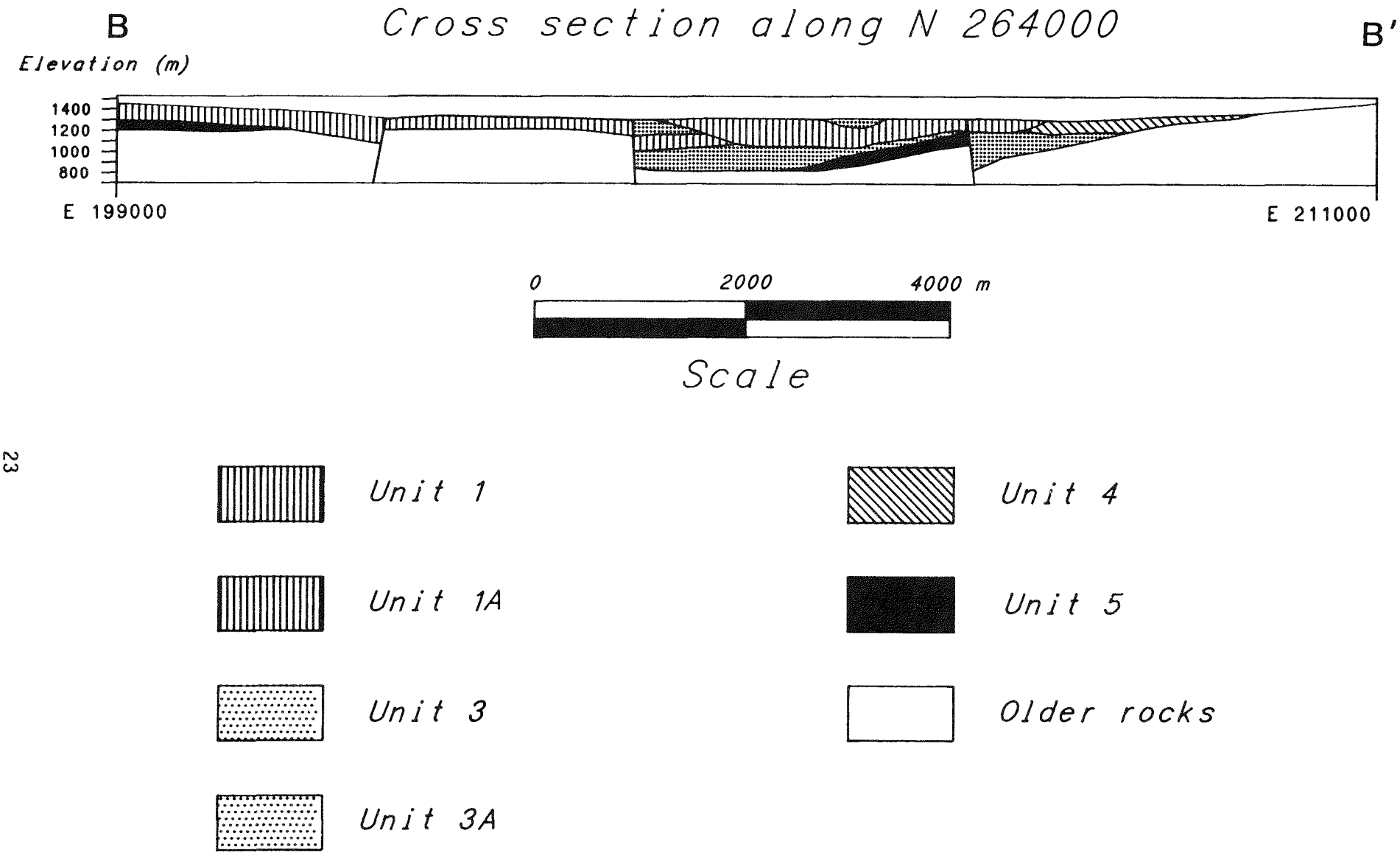

Figure 18. Schematic cross section along Nevada coordinate N 264000.

External Distribution:

AFWL/ NTCO
Kirtland AFB, NM 87115-5000
Attn: Albert Alexander

Field Command/DNA
Test Directorate
P.O. Box 98539
Las Vegas, NV 89193
Attn: Joseph W. LaComb

Field Command/DNA
P.O. Box 98518
Las Vegas, NV 89193
Attn: Roger Thompson

Field Command/DNA
Kirtland AFB, NM 87115-5000
Attn: Dale Glover

U.S. Department of Energy
M/A MA 232.21
Attn: Energy Library, T-A
P.O. Box A
Germantown, MD 20874
For: Ray Ferry, HQ
Irv Williams, HQ

U.S. Department of Energy
Nevada Operations Office
P.O. Box 98518
Las Vegas, NV 89193-8518
Attn: Richard Hague
Richard Navarro
Grace Plummer
Nick Aquilina

U.S. Department of Energy
Oak Ridge Operations Office
P.O. Box E
Oak Ridge, TN 37831
Attn: Lawrence Whitehead
NTIC

Los Alamos National Laboratory
Mail Station 5000
P.O. Box 1663
Los Alamos, NM 87545
For: Fred App
Joseph Brown
Robert Brownlee
Wendee Brunish
John Conaway
Ruth Demuth
Robert Deupree (5 copies)
Thomas Dey
Richard Fenster
Ward Hawkins
Jack House (6 copies)
Robert Kirby
Don Krier
Tom Kunkle
Carol La Delfe
Mark Matthews
James Neergard
Sue Noel
Jay Norman
A. Ogard
B. Roy Saunders
Tom Scolman
Joe Thompson
Bryan Travis
Bruce Trent
R. G. Warren
Clay Watson
Judy Winterkamp
Ken Wohletz
Report Library

Lawrence Livermore National Laboratory
P.O. Box 808
Livermore, CA 94550
For: Bob Addis, L-113
Gordon Anderson, L-203
Joe Behne, L-49
Norm Burkhard, L-203
Dick Carlson, L-203
R. Corallo (LLNL-N), L-777
James Carothers, L-1
Chris Cordill, L-113
H. A. Dockery
James D. Donithan (LLNL-N) L-777
Al Duba, L-203
Don Felske, L-777
Larry Ferderber, L-49
Lew Glenn, L-203
Hal Goldwire, L-203
Joe Hearst, L-203
Francois Heuze, L-203
Billy Hudson, L-203
Bob Kuckuck, L-49
A. S. Kusubov, L-201
Don Larson, L-203
Andy Lundberg, L-113
John Mercier, L-113
Mel Millet, L-777
Bill Moran, L-203
Robin Newmark, L-203
Cliff Olsen, L-203 (10 copies)
Gayle Pawloski, L-203
Steve Pratuch, L-113
John T. Rambo, L-203
Larry Schwartz, L-203
Clyde Sisemore, L-203
Ray Stout, L-203
Robert Swift, L-203
John Toman, L-389
Jeff Wagoner, L-203
Vern Wheeler, L-203
Erv Woodward, L-203
Library

EG&G
Amador Valley Operations
Attn: Classified Material Control
P.O. Box 9051
Pleasanton, CA 94566
For: Tom Edwards, AVO
Melton Hatch, AVO
John Kalinowski, AVO
T. Stubbs

EG&G
Attn: Document Control
P.O. Box 1912
Las Vegas, NV 89101
Attn: Del Wallace, NLVF
Bill Webb, NLVF

Fenix & Scisson, Inc.
P.O. Box 93265
Las Vegas, NV 89193-3265
Attn: Grant Bruesch
A. P. Cavazos
S. L. Drellack, Jr.
W. T. Hughes
P. H. Thompson

Ernest Fickas
Geo-Centers, Inc.
2350 Alamo Ave., SE, Suite 302
Albuquerque, NM 87106

Holmes & Narver, Inc.
Las Vegas Division
Attn: Facility Control Station
P.O. Box 14340
Las Vegas, NV 89114-4340
For: Dave Bedsun
Ralph Haak
Joe LaComb, Jr.
Leroy Ryan
Richard Ivy

Pacifica Technology
P.O. Box 148
Del Mar, CA 92014
Attn: Robert Allen
Martin Fogel
Dan Patch
D. Ranta
Colby Swan

S-Cubed
P.O. Box 1620
La Jolla, CA 92038
Attn: Charles Dismukes
Russell Duff
E. Halda
Michael Higginbotham
Diana Hollis
Kay Lie
Bob Nilson
Dan Peterka
Edward Peterson
Len Reed
Norton Rimer
Rachel Sandmann
John Wiehe
David Yates

SRI International
P.O. Box 725
Menlo Park, CA 94026-0725
Attn: A. L. Florence
Geza Nagy

Science & Engineering Associates
612 Old Santa Fe Trail
Santa Fe, NM 87501
Attn: C. Keller

Ktech
901 Pennsylvania, NE
Albuquerque, NM 87110
Attn: E. S. Gaffney

Planetary Geosciences Division
University of Hawaii
2525 Correa Road
Honolulu, HI 96822
Attn: J. C. Gradie

U.S. Geological Survey
Central Regional Geology Branch
Box 25046, MS 913
Denver, CO 80225
Attn: M. N. Garcia
D. L. Hoover
Evan Jenkins
Paul Orkild
Security Officer

U.S. Department of Energy
Attn: Richard Navarro
P.O. Box 98518
Las Vegas, NV 89193-8518
(Hold for Harry Covington,
U.S. Geological Survey)

Terra Tek
University Research Park
420 Wakara Way
Salt Lake City, UT 84108
Attn: Sidney Green
W. Klauber
John Lupo

Desert Research Institute
Water Resources Center
P.O. Box 8086, University Station
Reno, NV 89507
Attn: Paul Fenske

G. H. Higgins
P.O. Box 1991
Woodland, CA 95695

University of California, Davis
Department of Civil Engineering
Davis, CA 95616
Attn: B. L. Kutter
L. Chang

Sandia Internal Distribution:

1513 R. C. Dyknuizen
1513 A. J. Ratzel
1523 L. M. Taylor
1531 S. L. Thompson
Attn: T. K. Bergstresser
J. S. Rottler
3312 J. H. Metcalf
7100 C. D. Broyles
7110 J. D. Plimpton
7111 J. R. Banister
7111 R. C. Bass
7111 L. R. Hill (5 copies)
7112 C. R. Mehl
7112 A. J. Chabai
7112 C. W. Smith
7116 S. R. Dolce
7116 C. W. Cook
7116 R. P. Reed
7116 R. C. Shear
8244 S. K. Griffiths
3151 W. I. Klein
For DOE/OSTI (NWD Index) (2 copies)